UNIVERSITY OF SOUTHAMPTON

FACULTY OF ENGINEERING AND THE ENVIROMENT

Engineering Materials

Microstructural Evolution and Mechanical Properties of Oxygen-free Copper Processed by Severe Plastic Deformation

by

Meshal Y. Alawadhi

September 2017

UNIVERSITY OF SOUTHAMPTON

ABSTRACT

FACULTY OF ENGINEERING AND THE ENVIROMENT

Doctor of Philosophy

MICROSTRUCTURAL EVOLUTION AND MECHANICAL PROPERTIES OF OXYGEN-FREE COPPER PROCESSED BY SEVERE PLASTIC DEFORMATION

Meshal Y. Alawadhi

This thesis presents a study on the microstructural evolution and mechanical properties of oxygen-free copper processed by equal-channel angular pressing (ECAP) and high-pressure torsion (HPT) at room temperature. Experiments were systematically conducted to examine microstructural stability and deformation mechanisms, and their influence on the mechanical properties.

A significant grain refinement was attained after deforming the material by 24 passes of ECAP and 10 turns of HPT. The microstructure in the steady-state condition consisted of equiaxed ultrafine grains (UFGs) with high-angles of misorientation. Hardness values increase with increasing number of ECAP passes and HPT turns, and the microhardness distribution was relatively homogenous.

ECAP and HPT samples were pulled to failure at room temperature using strain rates of 1.0×10^{-4} s^{-1}, 1.0×10^{-3} s^{-1} and 1.0×10^{-2} s^{-1}. The direct influence of recovery behaviour on the tensile properties was investigated. A simultaneous increase in strength and ductility were observed with increasing number of ECAP passes as well as HPT turns. This is due to occurrence of dynamic recovery at an equivalent strain of ~12 that decreases

the total dislocation density and restores the work hardening ability of oxygen-free copper. Both grain boundary and dislocation strengthening mechanisms contribute to the strength of oxygen-free copper. Higher ductility but lower strength was observed when using lower strain rates.

UFG copper samples produced by HPT were stored at room temperature for 12 months to investigate microstructural stability and self-annealing phenomena. The results show that the samples processed by a low number of turns exhibit lower thermal stability after storage of 12 months in comparison to the samples processed by a high number of turns. A significant decrease in the hardness was recorded near the edges of the discs processed by 1/4, 1/2 and 1 turn due to recrystallization and grain growth whereas a minor drop in hardness values were observed in the samples processed by 3, 5 and 10 turns, and this drop was related to the recovery mechanism. Tensile tests were repeated after 12 months and the results showed that the ductility was enhanced in compensation for strength.

To investigate the deformation mechanism and thermal stability under high strain rates, copper samples were subjected to 1, 4 and 8 passes of ECAP and further deformed by dynamic testing. A significant grain refinement was produced in the ECAP specimens after dynamic testing which is comparable to the grain refinement produced by severe plastic deformation (SPD) techniques such as ECAP and HPT. The grain refinement mechanism was mainly by dislocation slip in the specimen processed by 1 pass whereas it was through dynamic recrystallization for the specimen processed by 8 passes. This is due to the difference in the dislocation densities and stored energy between the ECAP specimens. A 1 pass specimen has better stability than 4 and 8-pass specimens during dynamic testing. It was also shown that increasing the testing temperature and/or the strain rate can highly influence the deformation mechanism.

Contents

List of Tables

List of Figures

Declaration of Authorship

I, Meshal Alawadhi, declare that this thesis and the work presented in it are my own and has been generated by me as the result of my own original research.

Microstructural evolution and mechanical properties of oxygen-free copper processed by severe plastic deformation

I confirm that:

1. This work was done wholly or mainly whilst in candidature for a research degree at the University of Southampton;
2. Where any part of this thesis has previously been submitted for a degree or any other qualification at this University or any other institution, this has been clearly stated;
3. Where I have consulted the published work of others, this is always clearly attributed;
4. Where I have quoted from the work of others, the source is always given. With the exception of such quotations, this thesis is entirely my own work;
5. I have acknowledged all main sources of help;
6. Where the thesis is based on work done by myself jointly with others, I have made clear exactly what was done by other and what I have contributed myself.

Parts of this work have been published or to be published as:

- M.Y. Alawadhi, Y. Huang, T.G. Langdon, Evolution of homogeneity in oxygen-free copper processed by either ECAP or HPT, Review on advanced Materials Science, Vol. 50, pp. 47-54, 2017.

- M.Y. Alawadhi, S. Sabbaghianrad, Y. Huang, T.G. Langdon, Direct influence of recovery behaviour on mechanical properties in oxygen-free copper processed using different SPD techniques: HPT and ECAP, Journal of Materials Research and Technology (in press), doi:10.1016/j.jmrt.2017.05.005

- M.Y. Alawadhi, S. Sabbaghianrad, Y. Huang, T.G. Langdon, A critical investigation of the paradox of strength and ductility in oxygen-free copper processed by equal-channel angular pressing (Submitted to supervisor for review).

- M.Y. Alawadhi, S. Sabbaghianrad, Y. C. Wang, Y. Huang, T.G. Langdon, The Influence of the initial microstructural condition on grain refinement and mechanical properties in oxygen-free copper under high strain rate deformation (Submitted to supervisor for review).

- M.Y. Alawadhi, S. Sabbaghianrad, Y. Huang, T.G. Langdon, The Effect of Self-annealing Behaviour at Room Temperature on the Microstructure and Mechanical Properties of Oxygen-free Cu Processed by HPT (In preparation).

- M.Y. Alawadhi, Y. Huang, T.G. Langdon, Microstructural evolution and mechanical properties of oxygen-free copper processed by severe plastic deformation, PGR conference, Southampton, UK, 22 October 2014.

- M.Y. Alawadhi, Y. Huang, T.G. Langdon, The Paradox of strength and ductility in oxygen-free copper processed by high-pressure torsion, PGR conference, Southampton, UK, October 2015.

Signed:_____

Date:_____

Acknowledgements

Undertaking this PhD has been a truly life-changing experience for me and it would not have been possible without the support and guidance that I received from many people.

I would like to express my sincere debt of gratitude to my supervisors, Professor Terence G. Langdon and Dr. Yi Huang for their vision, guidance and encouragement throughout my PhD journey at the University of Southampton.

I am indebted to the Public Authority for Applied Education and Training (PAAET) in Kuwait for financial support for my PhD studies. I also would like to thank the Kuwait Foundation for the Advancement of Science (KFAS) for their financial support which enabled me to attend conferences.

I would like to acknowledge and thank Dr. Shima Sabbaghianrad of the University of Southern California, USA, for her assistance with EBSD testing. My appreciation also extends to Professor Yingchun Wang and her research group in Beijing Institute of Technology, China, for their help with the dynamic tests.

Special thanks to my mother on her patience and sacrifice during my 12 years of studying abroad. I know that allowing me to enroll on a PhD was the hardest decision she made, especially after my father passed away in 2010 and her poor health forced her to be in hospital most of her time. Although she needed me during that time, she did not stop me from achieving my dream. Thank you mother, I owe you everything and I love you the most.

I wish to thank my father who passed away in 2010 during my studying of Master's degree. He was my driving force and inspiration. I wish if I could have the chance to show him the moment he was waiting for.

Finally, I would like to thank my loving wife and state publicity how much I appreciate her sacrifices for me. She provided me with the strength through this journey and this PhD study would not have been possible without her support.

I dedicate this thesis to

my great mother, my lovely wife, and my beloved children

for their constant support and unconditional love.

Also, to the soul of my father

I love you all dearly.

Abbreviations

ARB	-	Accumulative roll-bonding
BCC	-	Body centred cubic
CEC	-	Cyclic extrusion and compression
CW	-	Cold work
DPD	-	Dynamic plastic deformation
DRX	-	Dynamic recrystallization
EBSD	-	Electron backscatter diffraction
ECAP	-	Equal-Channel Angular Pressing
El.	-	Elongation to failure
FCC	-	Face centred cubic
GBS	-	Grain boundary sliding
GND	-	Geometrically necessary dislocations
HAGBs	-	High-angle grain boundaries
HESP	-	High energy shot peening
HPT	-	High-Pressure Torsion
Hv	-	Vickers microhardness
LAGBs	-	Low-angle grain boundaries
LNT	-	Liquid nitrogen temperature
LSP	-	Laser shock processing

MD	-	Molecular dynamic
MDF	-	Multi-directional forging
MEMS	-	Microelectromechanical systems
MST	-	Micro systems technology
OFHC	-	Oxygen-free high conductivity
OIM	-	Orientation-imaging microscopy
OM	-	Optical microscopy
RT	-	Room temperature
RUE	-	Repetitive upsetting-extrusion
SEM	-	Scanning electron microscopy
SFE	-	Stacking-fault energy
SHPB	-	Split Hopkinson pressure bar
SIBM	-	Strain induced boundary migration
SMAT	-	Surface mechanical attrition treatment
SPD	-	Severe plastic deformation
TE	-	Twist extrusion
TEM	-	Transmission electron microscopy
UEL	-	Uniform elongation
UFG	-	Ultrafine-grained
UTS	-	Ultimate tensile strength

XRD	-	X-ray diffraction
YS	-	Yield stress

Nomenclature

A_b	-	The area of the cross-section of the Hopkinson pressure bar
A_s	-	The area of the cross-section of the compression specimen tested using split Hopkinson pressure bar system
b	-	Burgers vector
C_0	-	Speed of sound
C_V	-	Specific heat capacity
d	-	Grain size
D_c	-	The average crystallite size
$D\gamma$	-	The incremental shear strain
E	-	Young modulus
G	-	Shear Modulus
h	-	Initial thickness of HPT disc
H_0	-	Materials constant from Hall-Petch relationship
HV_C	-	The average hardness values in the central region of HPT disc
HV_R	-	The average hardness values in the peripheral region of HPT disc
k_y	-	Constant of yielding in the Hall-Petch relationship
L_s	-	The length of the compression specimen used in split Hopkinson pressure bar system
M	-	Taylor factor
m	-	Strain rate sensitivity

N	-	Number of revolutions in HPT
N_{ECAP}	-	Number of ECAP passes
Q	-	Activation energy
R	-	Universal gas constant
r	-	Radial distance from the centre of the HPT disc
t	-	Time
T_H	-	Homologous temperature
T_m	-	Melting temperature
Z	-	Zener-Hollomon parameter
α	-	A numerical factor depending on the arrangement of dislocations
α	-	The degree of homogeneity parameter
ε	-	True strain
$\langle \varepsilon^2 \rangle^{1/2}$	-	Lattice microstrain
ε_{eq}	-	Von Mises equivalent strain imposed during HPT
ε_I	-	Incident strain pulse acquired during split Hopkinson pressure bar test
ε_N	-	Equivalent strain imposed during ECAP
ε_R	-	Reflected strain pulse acquired during split Hopkinson pressure bar test
ε_T	-	Transmitted strain pulse acquired during split Hopkinson pressure bar test
$\dot{\varepsilon}$	-	Strain rate

ρ	-	Dislocation density
σ	-	True stress
σ_0	-	Friction stress (the starting stress for dislocation movement)
σ_{dis}	-	Stress from dislocation strengthening
σ_{GB}	-	Stress from grain boundary strengthening
σ_y	-	Yield stress
Φ	-	The channel angle of intersection of the two channels in ECAP die
Θ	-	Work-hardening rate
Ψ	-	The angle of the outer arc of curvature in the ECAP die
ω	-	The angular velocity of the rotating anvils during HPT

Chapter 1: Introduction

1.1 Background

Producing materials with superior mechanical and physical properties such as high strength and good ductility has become a goal in several industries. Grain size is an important factor in polycrystalline materials since, according to the Hall-Petch relationship, materials will exhibit greater strength as grain size is reduced [1,2]. Additionally, materials with a stable, small grain size tend to have exceptional superplastic properties at elevated temperatures that are much superior to those of their coarser counterparts [3,4].

Over the last two decades severe plastic deformation (SPD), obtained by applying very high strain to the bulk material, has been shown to produce ultrafine-grained (UFG) materials very effectively. Exceptional grain refinement is achieved through the use of very large hydrostatic pressure with special tool geometries to prevent the free flow of material to retain the sample's shape. Conventional thermomechanical processing reduces the grain size of the materials and enhances their properties, but the refinement is limited to a few micrometres while SPD is capable of producing an average grain size of less than 1 μm.

UFG materials are bulk materials that have a homogenous microstructure, with equiaxed grains having high-angle misorientation grain boundaries [5]. UFG materials are produced by imposing a very high strain on the coarse grains in order to introduce a high density of dislocations in the bulk solid, in which movement and rearrangement form an array of grain boundaries. As a result, bulk ultrafine-grained materials are produced without compromising the overall dimensions [3].

When UFG materials have a grain size below 100 nm they are termed nanocrystalline materials. Conventional procedures such as rolling, drawing and extrusion face limitations on the deformation process during the imposition of high strain in the deformation process, due to the reduction in cross-sectional dimensions and low workability at room temperature. Thus, various SPD techniques have been developed

recently that are capable of introducing intensive strain at low temperature, including high-pressure torsion (HPT), equal-channel angular pressing (ECAP), accumulative roll bonding (ARB), cyclic extrusion and compression (CEC), twist extrusion (TE) and multi-directional forging (MDF). HPT and ECAP are the leading methods in producing UFG materials; experiments have demonstrated that HPT is the most effective at producing very small grains, due to strain accumulated during the process [6,7], while ECAP can produce larger samples, making it the most favoured method for industrial applications [8–10].

Copper has attracted many researchers in various fields because it is considered one of the most important commercial metals in building construction, electrical and electronic products, industrial machinery and equipment, transportation equipment and architectural and biological applications. It is suitable for many applications due to its high electrical and thermal conductivity, corrosion resistance, colour, malleability and ease of fabrication [11].

The demand for copper in the electronics industry has been increased in the past two decades due to its relatively high strength and high electrical conductivity. More than 50% of all copper is consumed by electrical and electronic applications. Copper is used in chemical plants due to its high thermal conductivity, malleability and corrosion resistance. The ease of fabrication makes it easy to form into complex shapes as well as into wires, strips and sheets. Copper is also used in sanitary systems, waste, water and gas pipes due to its resistance to corrosion by chemicals and soil.

1.2 Motivation

This thesis has been motivated by the importance of enhancing the mechanical properties of copper to provide a better potential candidate in materials selection for many applications. Several methods have been proposed to enhance the mechanical properties of copper and copper alloys including cold working, solid solution and precipitation hardening; however, grain refinement using SPD methods improves the mechanical properties without changing the chemical composition and the shape of the sample. On the other hand, the size of the sample is a major limitation.

Initial investigations of the mechanical properties of UFG copper were driven by industry's worries concerning the micro-miniaturisation of mechanical parts to be used in the field of microelectronics materials including microelectromechanical system applications, electro-technical systems and connections and high standard microelectronics devices. The concerns originated in the knowledge that when the dimensions of an object are less than a few tens of micrometers its mechanical properties are size dependant. Two reasons have been given to explain this phenomenon: (i) the grain size (microstructural scale) depends on the size of the object and, (ii) observations where plastic deformation was confined to samples of dimensions of only a few nanometres have shown a new phenomenon where the measured mechanical properties depend on the sample size [12]. It follows that grain size will be an important factor in determining the minimum size of geometrical features produced by micro-forming.

Another motivation was the great potential for UFG copper in micro-forming, the production of parts with at least two dimensions in the submillimeter range (see Section 2.9). Reducing dimensions of parts to less than a few microns is difficult because the ratio of microstructural parameters and part dimensions changes with miniaturization [13]. As a result, parts produced by conventional forming processes are hardly ever used in micro-forming. Rather, SPD produced UFG materials with high strength and good ductility are more suitable for micro-forming applications.

1.3 Aims and Objectives

The aim of the present research is to acquire knowledge about the microstructural evolution of oxygen-free copper processed by two SPD techniques, ECAP and HPT, and to study strength and ductility after deformation at room temperature. The present work also aims to carry out the first systematic study of the relation between ECAP and HPT processing, the resulting structure and its properties. Such an investigation will assist the transfer of knowledge from basic research to the industrial development of oxygen-free copper for better use of its superior properties.

The main objectives of this research are to investigate:

- The microstructural evolution of oxygen-free copper processed by ECAP and HPT at room temperature.
- The microhardness homogeneity in oxygen-free copper processed by ECAP and HPT at room temperature.
- The microstructural stability of UFG oxygen-free copper during the processes of HPT and ECAP at room temperature and its direct influence on the mechanical properties.
- The microstructural stability of UFG oxygen-free copper after a long period stored at room temperature and its influence on microstructural evolution and mechanical properties.
- The microstructural stability and deformation mechanism in UFG oxygen-free copper under high strain rate deformation.

1.4 Contribution to knowledge

Although there is a wealth of studies in pure copper, the overwhelming majority of published papers have concentrated on particular areas such as individual mechanical properties, microstructural evolution or processing, therefore, it is a challenge to obtain an overview of the inter-relations between the different areas. This research will make a contribution to the study of the strengthening and softening mechanisms of oxygen-free copper when extensively deformed by different imposed strain using various SPD techniques at room temperature and enriches the knowledge available.

Contradictions in published results obtained to date, have been observed. The majority of studies have suggested that pure copper shows hardening behaviour without softening during both HPT and ECAP at room temperature. Nevertheless, very limited studies have reported a softening behaviour of pure copper during HPT and ECAP processing at room temperature. This research has aims to reinvestigate the softening behaviour of oxygen-free copper at room temperature and its direct influence on the mechanical properties.

Most of the experiments performed on pure copper have reported high strength but low ductility at room temperature due to the decrease in the work hardening ability after SPD. Although the increase in ductility was associated with increasing the processing temperature, very few studies have reported an increase in strength and ductility in pure copper processed by ECAP at room temperature. To date, there is no study concerning the simultaneous enhancement of strength and ductility of pure copper after HPT, especially at room temperature. Thus, the current research aims to examine the possibility of improving the strength and ductility of oxygen-free copper by ECAP and HPT at room temperature as well as providing a systematic investigation regarding the mechanism of this improvement.

Although a great deal is now known about the thermal stability of pure copper processed by different SPD methods, there is still little evidence of strain softening after long term storage at room temperature. Limited experiments have been conducted into the application of HPT in pure copper to investigate microstructural stability at room temperature after the deformation process. These were isolated studies each of which conducted the experiment using different storage period (hours, months, years) and one selected processing condition, thus it was hard to draw a general conclusion. Therefore, this research aims to provide a systematic and a comprehensive study of the microstructural stability and mechanical properties of oxygen-free copper processed by HPT then stored at room temperature for 12 months using several different processing conditions from low to high strained samples.

Recent studies have been testing copper using high strain rate dynamic tests in which the material is impacted by high speed projectiles. These studies have focused on the influence of temperature, strain rate and their coupling effect on the deformation mechanisms and mechanical properties of pure copper during dynamic testing. However, there are no reports discussing the influence of the initial microstructural condition on the mechanical properties, nor on grain refinement mechanisms after dynamic testing. Uniquely, this research aims to investigate the influence of initial microstructure developed by ECAP prior to dynamic testing on the microstructural stability of oxygen-free copper deformed at high strain rate. Also, to examine the influence of strain rate and temperature on the microstructure and mechanical properties of oxygen-free copper deformed by ECAP and subject to further dynamic testing

1.5 Thesis Structure

The thesis is comprised of 10 chapters. Chapter 2 presents a thorough literature review that covers the definitions, objectives, procedures, methods and applications of SPD. Also, it provides a description of the principles of high-pressure torsion (HPT), equal-channel angular pressing (ECAP) and dynamic testing. Chapter 3 presents the material and experimental procedures used in this study. The microstructural and microhardness evolutions of oxygen-free copper processed by ECAP at room temperature. In Chapter 5, the microstructural and microhardness evolutions in oxygen-free copper processed by HPT at room temperature are presented and discussed. Chapter 6 presents the paradox of strength and ductility in UFG oxygen-free copper processed by HPT and ECAP at room temperature. The effect of self-annealing behaviour at room temperature on the microstructure and mechanical properties of oxygen-free copper processed by HPT is presented in Chapter 7. Chapter 8 presents the microstructural stability and deformation mechanism of oxygen-free copper deformed by a high strain rate dynamic test. Chapter 9 provides a general discussion on the different softening mechanisms produced by SPD at room temperature. Conclusions are presented in Chapter 10, where the outcomes and findings from experimental work are revealed and includes suggestions for future work.

Chapter 2: Literature Review

2.1 Severe Plastic Deformation

Researchers became interested in severe plastic deformation and the characteristics of small-grained materials after a report published in 1988 indicated the huge potential in changing a bulk solid from coarse- to fine-grained (in the submicrometer range) by this method [14].

SPD is defined as a metal-forming method where the bulk solid undergoes extensive hydrostatic pressure, involving very high strain, to produce an ultrafine-grained structure without permitting the free flow of the material to compromise the sample's overall dimensions [15]. SPD is capable of producing finer grains than the conventional thermomechanical process. Moreover, strength and ductility are both improved by SPD; although thermomechanical processing can improve strength, it decreases ductility [16].

2.1.1 Objective of SPD processing

Average grain size has been proved to have a significant impact on crystalline materials' mechanical and physical properties such as strength, ductility and resistance to plastic flow. In general, fine-grained materials tend to be superior to coarse-grained materials [15], thus the main objective of processing metals by SPD is to refine their grain size to enhance strength and ductility without changing the bulk dimensions, in other words, producing bulk UFG materials. These are defined as bulk materials having an homogenous microstructure with equiaxed grains (less than 1 μm) and high-angle misorientation grain boundaries [17]. When UFG materials have a grain size below 100 nm they are termed nanocrystalline materials, and when they have nanostructural elements such as grain boundary precipitates, nanotwins and dislocation substructures they are termed nanostructured materials [17]. The relationship between the strength of any polycrystalline material and its grain size is expressed by the Hall-Petch equation, as follows:

$$\sigma_y = \sigma_0 + k_y d^{-1/2} \tag{2.1}$$

where σ_y is the yield stress, σ_0 is the friction stress (the starting stress for dislocation movement), k_y is a yield constant often referred to as the Petch parameter and is material specific, and d is the grain size [1,2]. It is clear from Equation 2.1 that there is an inverse relationship between strength and grain size: the smaller the grain size, the higher the material's strength. During the SPD process, the free flow of the material is constrained by different tools, depending on the method used. These constraining tools create significant hydrostatic pressure on the material, leading to high strain that creates high densities of lattice defects in the material [17].

2.1.2 Procedures for UFG microstructures synthesis

Materials with UFG microstructures can be synthesized by two different procedures: bottom-up and top-down [18]. The bottom-up procedure is when individual atoms are consolidated to construct the bulk material. The main advantage of this procedure is to produce materials with very small grain size, below 10 nm. However, it has some limitations such as contamination of the material, porosity and the production of small and limited size samples.

The top-down procedure involves refining the grain size of bulk coarse-grained solid materials by imposing a very high strain and dislocation density, which leads to grain refinement to at least submicrometer level [15]. SPD as a synthesis method commonly uses this top-down approach.

Despite the slight change in its overall dimensions during SPD, the shape of the sample is preserved by using tools with special geometries to prevent the free flow of material. This generates a very high hydrostatic pressure on the sample [17] that imposes a very high strain and introduces high dislocation densities within the grains. The rearrangement of the dislocation densities within the grains creates new grain boundaries and, as a result, UFG materials are produced [19].

2.1.3 SPD methods

Bulk metals with a small grain size in the order of few micrometres may be produced by a conventional procedure known as thermomechanical processing, but it is limited to the production of micrometre-size grains, while SPD has been proven to achieve a grain size at submicrometer or even nanometre levels [3]. The two most common SPD methods are Equal-Channel Angular Pressing (ECAP) and High-Pressure Torsion (HPT). ECAP is sometimes favoured because it allows the use of larger samples than HPT, yet smaller grain sizes – at nanometre level – are achieved by the latter [20].

2.1.4 Applications of SPD-processed materials

The techniques of SPD processing have recently improved and the resulting materials possess outstanding properties such as high strength, ductility, machinability, forgeability, formability and low processing cost [18]. They have microstructures with a smaller grain size that is different from their course-grained counterparts, providing unique mechanical and physical properties. Due to these unique properties, SPD-processed materials are used in numerous applications in fields such as medical, electrical, electromechanical, structural and many others.

Pure titanium processed by SPD is used in biomedical applications for medical implants. It is the material with the greatest biocompatibility with living organisms, but unprocessed titanium is not used in the medical field because it has only low strength. Processing pure titanium by SPD increases its strength and fatigue properties, creating a nanostructured material that overcomes the strength limitation to render it suitable for medical implants. Figure 2.1 shows different types of nanostructured titanium screws used as implants in biomedical applications [21]. Another nanostructured material used in medical application is Ni–Ti alloy. This is used as bone replacement material because of its low elastic modulus, considered to be the closest to that of human bone.

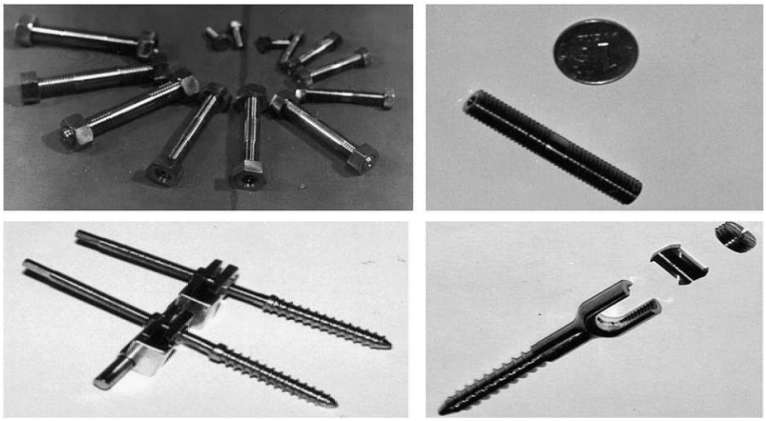

Figure 2.1 Nanostructured titanium screws used as biomedical implants [21].

Several properties make magnesium and its alloys ideal material for hydrogen storage, were it not for their poor hydrogen absorption-desorption kinetics below 350ºC. SPD processing of magnesium alloy produces a nanostructured material that shows a reduction in grain size and, in addition, an increase in hydrogen absorption-desorption kinetics [22,23].

Metallic materials proceed by SPD are also used in micro-devices such as components for microelectromechanical systems (MEMS). Nanostructured materials can be fabricated into micro-parts with complex shapes such as MEMS gears [24] and high-strength aluminium wires [25].

Further, nanostructured aluminium alloys produced by SPD are used for the fabrication of high-strength aluminium alloy sheets and rods. These are used in structural applications in sectors such as civil and defence. Also, SPD enhances the strength and conductivity of aluminium to produce unconventional electric conductors [26]. Nanostructured steels demonstrate high strength, and good formability and machinability. They are used in the production of small screws, shafts, rods, strips, sheets and wires.

2.2 High-Pressure Torsion

The fundamental concept of HPT originated when Professor Bridgman, the Hollis Professor of Mathematics and Natural Philosophy at Harvard University, conducted series of experiments in 1943 that tried to combine torsional straining with very high

pressure on solids [15]. His methodology was to apply longitudinal compression and simultaneously to twist the sample.

The specimen was in shape of a bar with two reduced-radii sections, as shown in Figure 2.2. The bar had two fixed ends where longitudinal compression was applied. The two reduced sections were rotated by the central piece of the specimen, which induced torsional straining in the two reduced sections. This procedure produces an increase in torsional strength [27]. Later, in the 1980s, a research group from Russia used the principles of HPT to process many metallic alloys [28]. Today, HPT is one of the most common SPD methods used to process nanostructured materials.

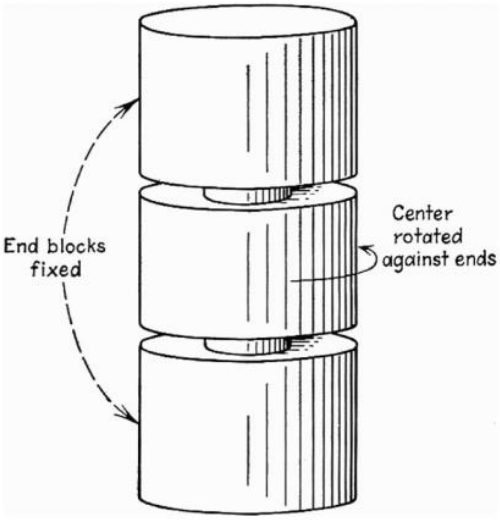

Figure 2.2 Schematic illustration showing the combination of torsional straining and longitudinal compression on a solid sample [27].

2.2.1 Principle of high-pressure torsion

HPT is commonly performed at room or higher temperatures by placing the sample between two anvils. The upper anvil remains stationary while the lower rotates, and both feature circular cavities of the same dimensions as the sample, which is in the form of a disc. The sample is subjected simultaneously to a high compressive pressure, P, and torsional straining, as shown in Figure 2.3. The applied compressive pressure is several GPa, while the torsional straining is enforced by the rotation of the lower anvil. The disc is deformed by shearing due to the surface frictional forces created by the applied pressure and torsion. Thus, deformation of the disc continues under quasi-hydrostatic pressure.

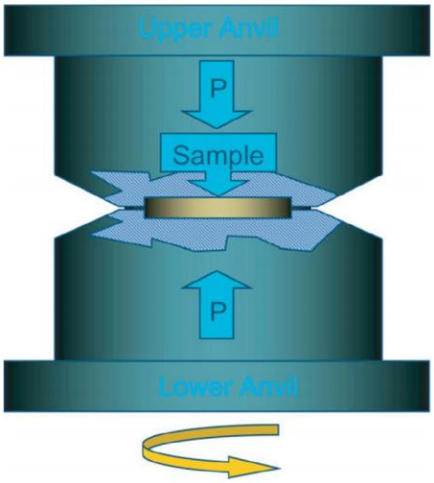

Figure 2.3 Schematic illustration of HPT processing illustrating the pressure applied on the sample (disc) and the torsional straining induced by the rotation of the lower anvil [29].

2.2.2 Imposed strain in HPT

The strain imposed on the disc during the HPT process is calculated by using the variables illustrated in Figure 2.4. The incremental shear strain, dγ, is estimated by the displacement, dl, and the disc thickness, h.

$$d\gamma = \frac{dl}{h} \tag{2.2}$$

For an infinitely small rotation, dθ is accounted and dl is equal to rdθ, where r represents the radius of the disc sample. Thus, the incremental shear strain dγ is written as [6]:

$$d\gamma = \frac{rd\theta}{h} \tag{2.3}$$

Since the thickness of the disc is assumed to be independent of the rotation angle, where θ = 2πN and N is the number of revolutions, the shear strain is given by:

$$\gamma = \frac{2\pi N.r}{h} \tag{2.4}$$

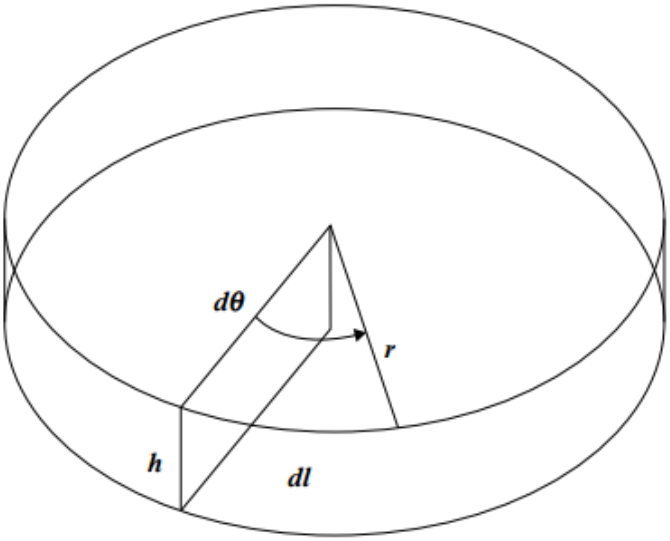

Figure 2.4 Variables used in calculating the total imposed strain during HPT [6].

According to von Mises, the equivalent strain is given by [30]:

$$\varepsilon = \frac{\gamma}{\sqrt{3}} \tag{2.5}$$

Substituting Equation 2.4 into Equation 2.5, the von Mises equivalent strain is:

$$\varepsilon_{eq} = \frac{2\pi N.r}{h\sqrt{3}} \tag{2.6}$$

It has been demonstrated that taking the number of revolutions imposed on the disc to represent the HPT strain, instead of the calculated strain values, is more practical for analysis of the microstructure evolution of an HPT sample. This is due to the difficulty in precisely detecting the centre of the disc, which leads to miscalculation of the HPT true strain values [30].

2.2.3 Types of HPT processing

Based on how the sample is placed between the upper and lower anvils in the HPT facility, there are two different processing types: unconstrained and constrained, as illustrated in Figure 2.5 [31]. Figure 2.5(a) shows unconstrained HPT, where the disc is placed on the lower anvil then pressure and torsional straining applied. The material flows freely outwards under the pressure, while there is limited back-pressure as a result of the frictional forces between the surface of disc and the anvils [6]. This set-up is not favoured due to the continual decrease in the thickness of the sample that might cause the anvils to come into contact and destroy the machine [32]. Constrained HPT, as shown in Figure 2.5(b), is where the disc is placed on the lower anvil within a cavity of the same shape and size of the disc, then load and torsional strain is applied. This method prevents the material flowing outward during the process, and the disc is strained by full back-pressure. Yet, this is not the ideal constrained condition for practical HPT processing as, in fact, it is very difficult to achieve.

The most common constrained method used for HPT processing is quasi-constrained, as depicted in Figure 2.5(c). In this approach, the disc is fitted between cavities machined in each anvil. A small gap between the two anvils during the process allows a limited outward flow of material [33].

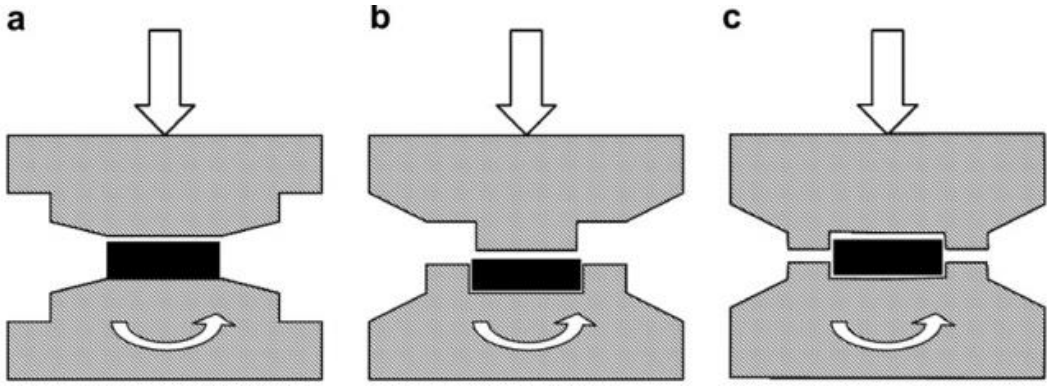

Figure 2.5 Schematic illustration of HPT facility: (a) unconstrained, (b) constrained and (c) quasi-constrained conditions [31].

2.2.4 Variation in homogeneity across an HPT disc

A crucial limitation to HPT processing is the disparity in homogeneity across the processed disc, a consequence of variation in the strain imposed. Theoretically, the strain value is zero at the centre of the disc, increasing linearly to a maximum strain value near the periphery. Equation 2.6 represents this relationship and shows that strain rises with increasing distance from the disc centre. It clearly shows that a disc processed by HPT will exhibit an inhomogeneous microstructure in the early stages of processing. The variation in the imposed strain across the disc for different values of r, is illustrated in Figure 2.6 as a function of the number of revolutions.

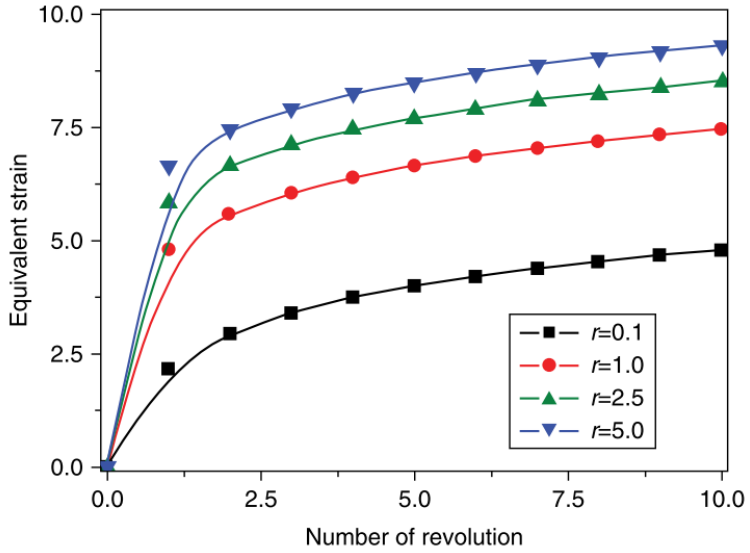

Figure 2.6 Equivalent strain as a function of the number of revolutions shows the variation of the imposed strain across the disc, r in mm [31].

Microstructural homogeneity is studied by measuring microhardness values and analysing its evolution on the disc, capturing microstructural images using transmission electron microscopy (TEM) for comparison. Results support the finding of variation in homogeneity across the diameter of the disc, with lowest and highest microhardness values at the centre and edges respectively [33–35]. A study of the microstructural homogeneity of austenitic steel was performed after processing the samples by HPT by up to 16 turns at a nominal hydrostatic pressure of 5.3 GPa [33]. This study found that the centre of the disc remained undeformed even after 16 turns of HPT, as shown in Figure 2.7. Thus, formation of a completely homogeneous microstructure is unattainable.

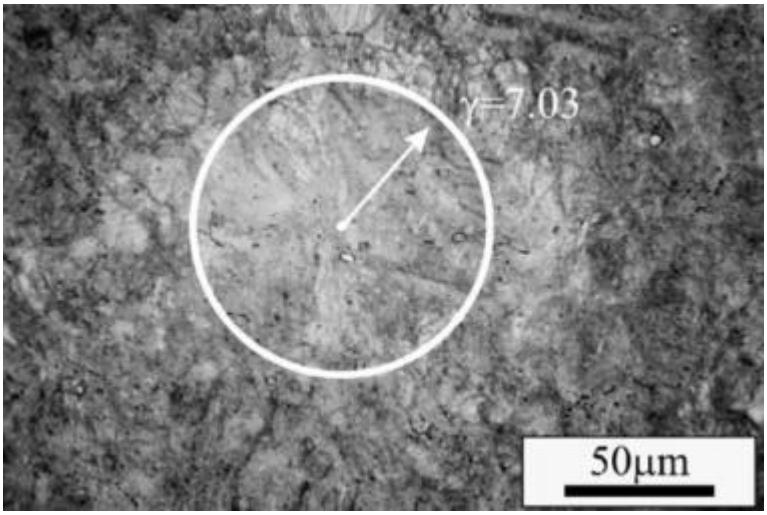

Figure 2.7 Optical micrograph of centre of austenitic steel disc after deformation by HPT to 16 turns [33].

Many experimental reports have revealed the potential to achieve reasonable homogenous microstructure after reaching sufficient strain and sufficiently high imposed pressure, despite the fact that in the early stages of HPT processing the disc centre has only low hardness values [7,29,31,36–40]. Three-dimensional representations of hardness distribution over the surface of Al-606 discs show a gradual evolution towards a homogeneous microstructure, as in Figure 2.8 [40]. Another approach to representing hardness variation on the disc surface is to produce colour-coded hardness contour maps, as in Figure 2.9 [40].

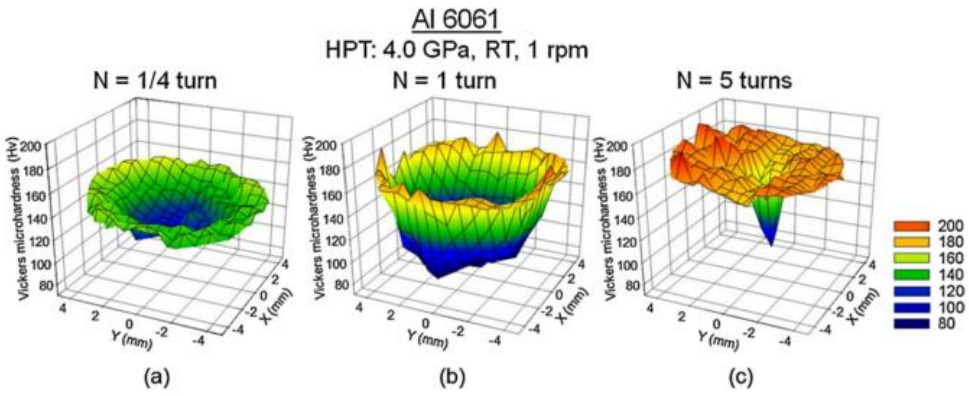

Figure 2.8 Three-dimensional representations of hardness distribution for Al-6061 alloy: (a) after 1/4 turn, (b) after 1 turn and (c) after 5 turns [40].

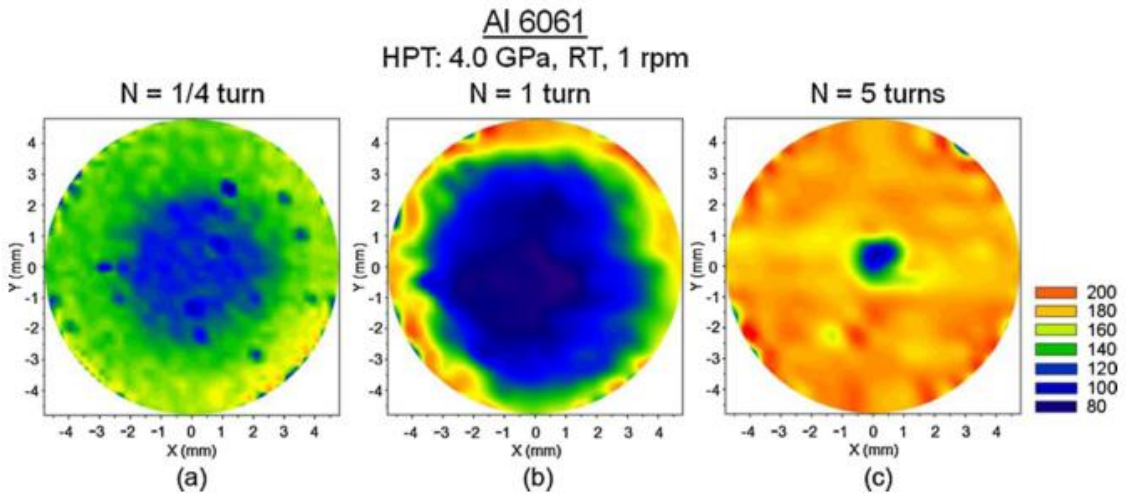

Figure 2.9 Colour-coded hardness contour maps for Al-6061 alloy: (a) after 1/4 turn, (b) after 1 turn and (c) after 5 turns [40].

Some studies on high-purity aluminium of (99.99%) have reported results deviating from the theoretical strain relationship. They show that hardness at the centre of the disc is higher than at the periphery in the initial stages of HPT processing. Upon increasing torsional strain, the hardness values at the centre of the disc decrease until the total surface of the disc attains a balanced level of hardness distribution and reasonable homogeneity [40–42]. This behaviour has been recorded in hardness measurements made by three different methods. The first takes the hardness measurements across the diameter of the disc, as shown in Figure 2.10 [41]. The second takes the hardness measurements across the total surface area of the disc and presents the results as colour-coded contour maps, as shown in Figure 2.11 [40]. The third method takes the hardness measurements over the total area of the disc and represents them three-dimensionally, as in Figure 2.12 [40].

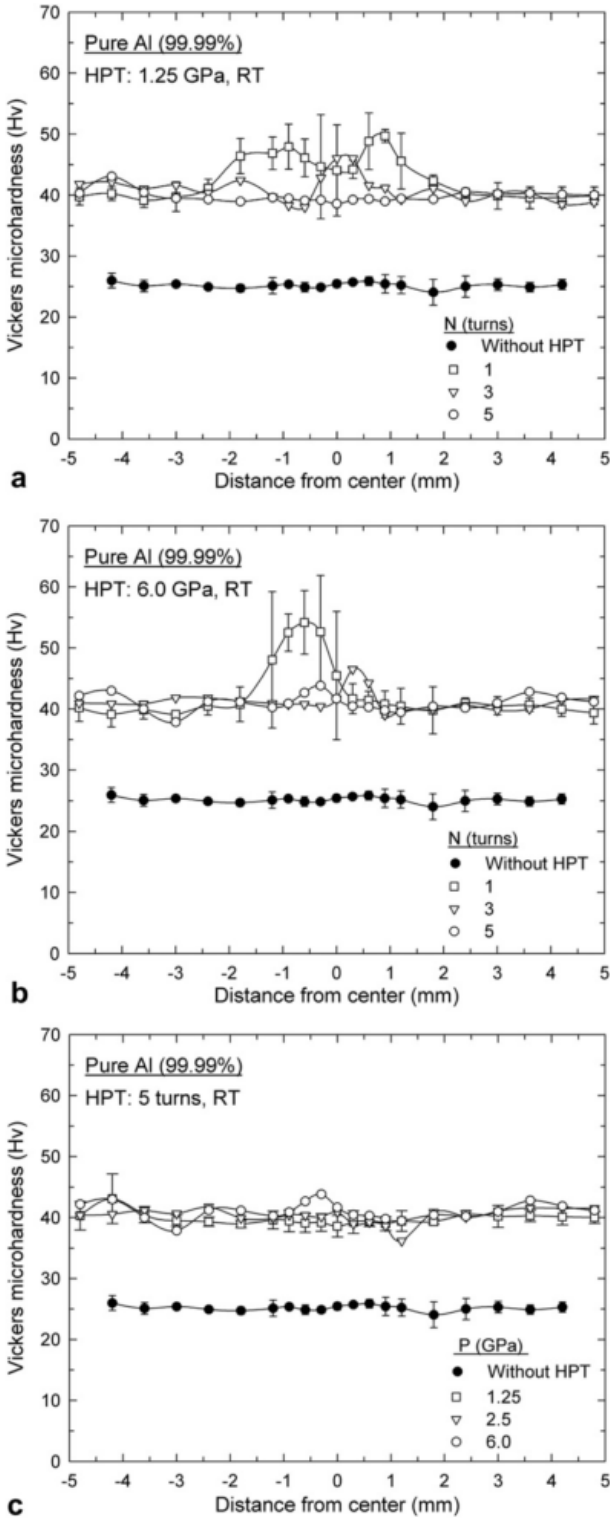

Figure 2.10 Microhardness values across the diameter of a disc: (a) under applied pressure of 1.25 GPa, (b) under applied pressure of 6.0 GPa and (c) under different pressures after 5 turns [41].

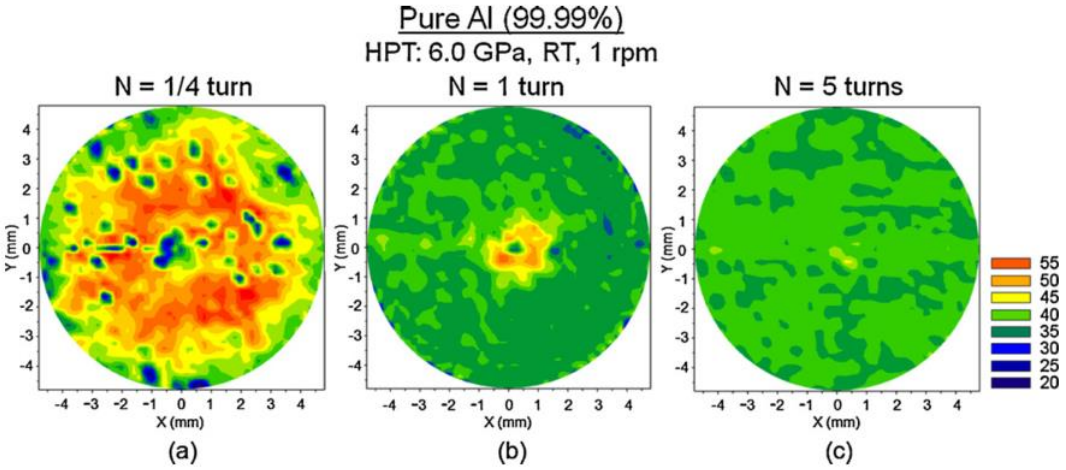

Figure 2.11 Colour-coded maps showing the evolution of hardness homogeneity for pure Al discs processed by HPT for: (a) 1/4 turn, (b) 1 turn and (c) 5 turns [40].

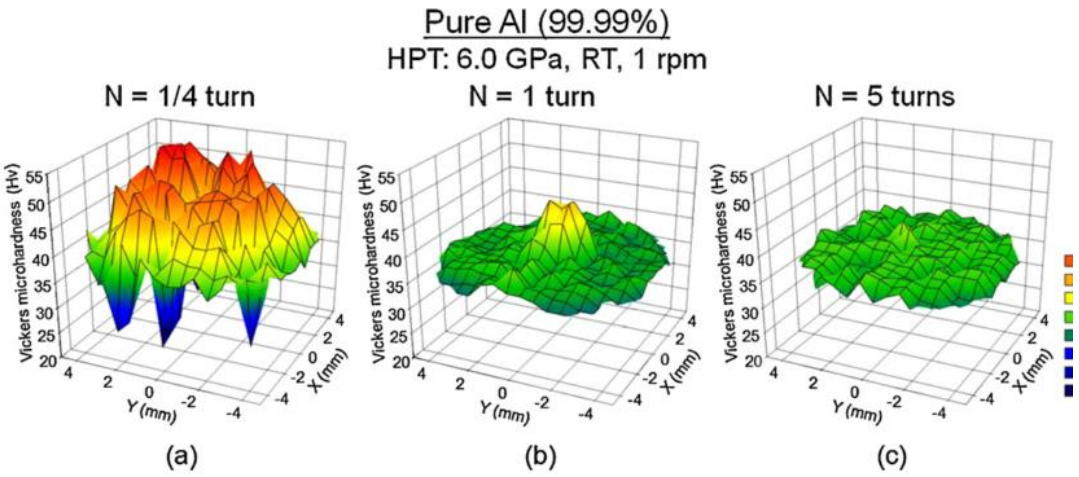

Figure 2.12 3D representations showing the development of hardness homogeneity for pure Al discs processed by HPT for: (a) 1/4 turn, (b) 1 turn and (c) 5 turns [40].

2.2.5 Influence of applied pressure on evolution of microstructure

The applied pressure, hydrostatic pressure, is a major parameter impacting on grain refinement during HPT. By increasing the applied pressure on the disc, the imposed strain increases and introduces a high density of lattice defects, achieving a significant increase in hardness and an excellent grain refinement [6,7,17,36]. High-purity nickel (99.99%) discs processed by HPT were investigated after five turns using pressures of 1, 3, 6 and 9 GPa [6]. Figure 2.13 shows three-dimensional meshes for all microhardness

data acquired during HPT. Initially, the nickel discs had an inhomogeneous microstructure and non-uniform hardness distribution across their diameter. The hardness values were lower at the centre than the edge, and the initial hardness value and grain size were ~1.4 GPa and ~100 nm, respectively. As depicted in Figure 2.13 and Figure 2.14, the increase in the applied pressure from 1 to 9 GPa led to a rise in hardness values all over the discs' surface, especially at the centre, with recorded hardness values of greater than 3 GPa. Homogeneity is enhanced by increasing the applied pressure [6,7].

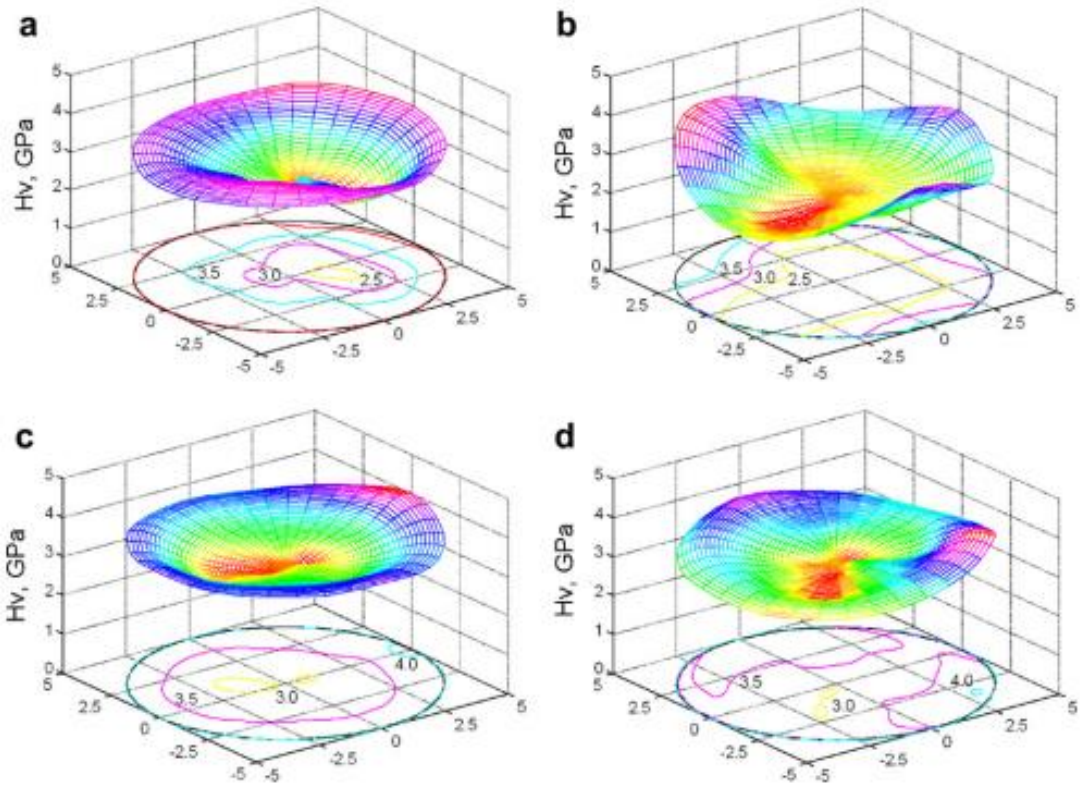

Figure 2.13 3D representation of microhardness distribution as a function of applied pressure for Ni processed by HPT: (a) 1 GPa, (b) 3 GPa, (c) 6 GPa and (d) 9 GPa [6].

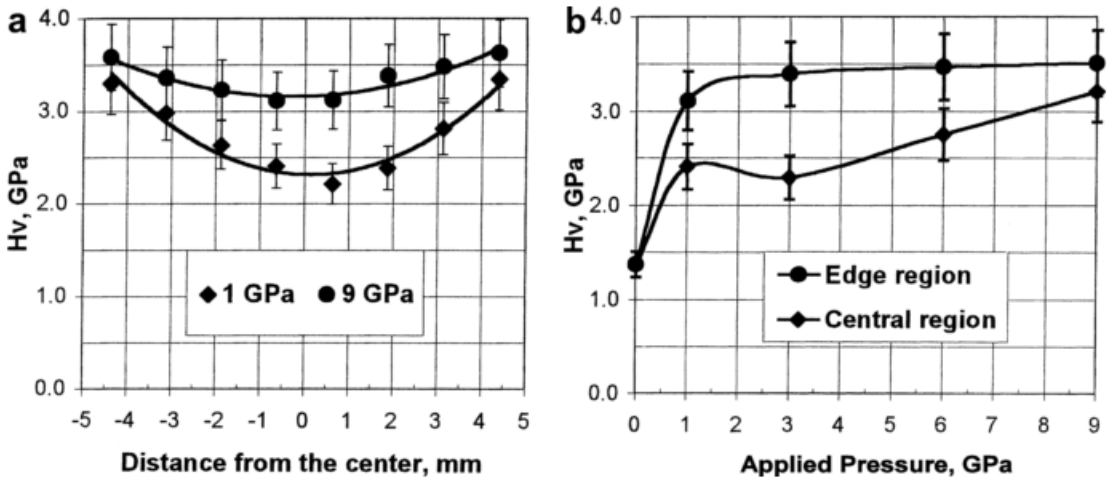

Figure 2.14 (a) Average microhardness across the diameter of Ni discs at pressures of 1 and 9 GPa; and (b) Average microhardness versus the applied pressure for both centre and edge of Ni discs [7].

In addition, TEM was conducted on nickel discs processed by HPT for five turns under three different applied pressures of 1, 3 and 9 GPa, as shown in Figure 2.15 [6]. The upper row represents the centres of the discs and the lower row represents the edges. TEM images for the samples processed by 1 GPa show a large difference in mean grain size between the centre and edge of the disc with the mean grain size at the centre greater than at the edge. At an applied pressure of 3 GPa, the difference in mean grain size between the centre and edge of the disc becomes less. The grains at the edges become more equiaxed, while at the centre they are elongated. At a pressure of 9 GPa the mean grain size is similar at the centre and the edges, and the grains become equiaxed in both regions.

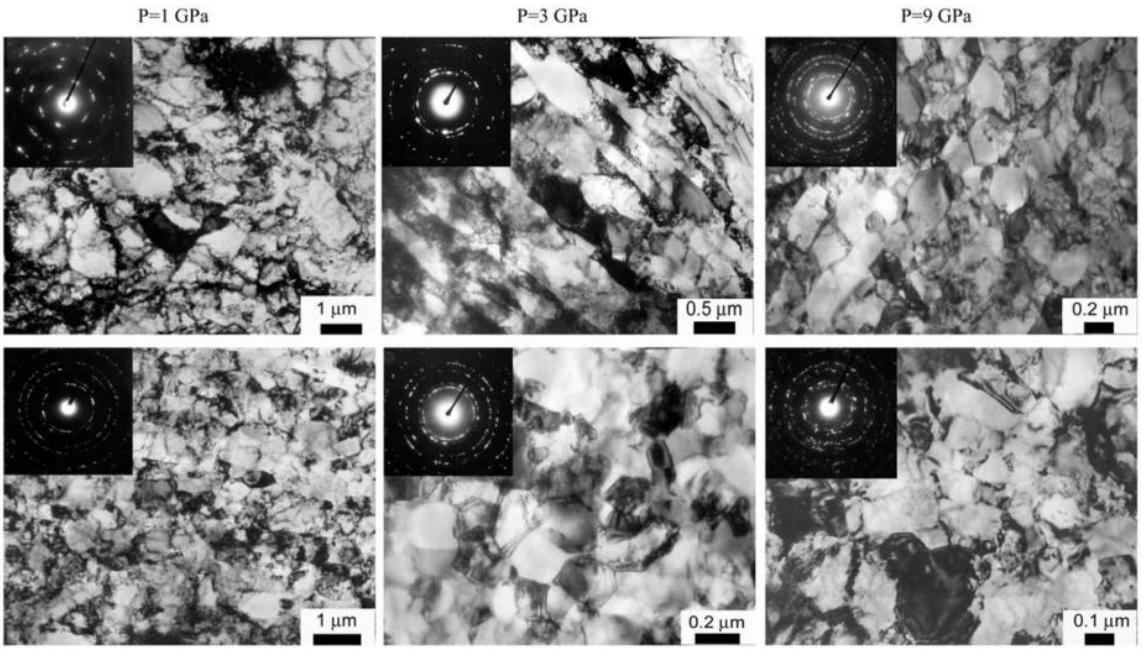

Figure 2.15 TEM images for Ni discs processed by HPT for five turns under three different applied pressures of 1, 3 and 9 GPa [6].

2.2.6 Influence of number of revolutions

The total imposed strain plays a crucial role in grain refinement during HPT processing and, as mentioned above, is measured by the number of revolutions. Several studies have shown that by increasing the number of revolutions, overall hardness values rise and a reasonable homogeneity is attained [6,7,36]. This relationship is illustrated in Figure 2.16 and Figure 2.17, showing the influence of the total number of revolutions on microhardness in high-purity nickel discs.

The discs were processed by HPT for 1/2, 1, 3 and 7 turns under an applied pressure of 6.0 GPa [6,7]. In the early stages, the hardness values at the centre of the discs were lower than at the edges, and the initial value of microhardness was 1.4 GPa. After 7 revolutions, the overall hardness values increased to more than 3 GPa and became uniform across the disc surface. That is, a certain homogeneity was achieved.

Figure 2.18 illustrates the evolution of hardness homogeneity across the diameter of discs of Al-3% Mg-0.2% Sc alloys as a function of number of turns. It is clear that

increasing the number of turns boosts the hardness significantly in the central region of the disc and reaches saturation at the edges. Consequently, increasing the number of turns from 1 to 7 increases hardness across the disc and achieves a reasonably homogenous distribution [36].

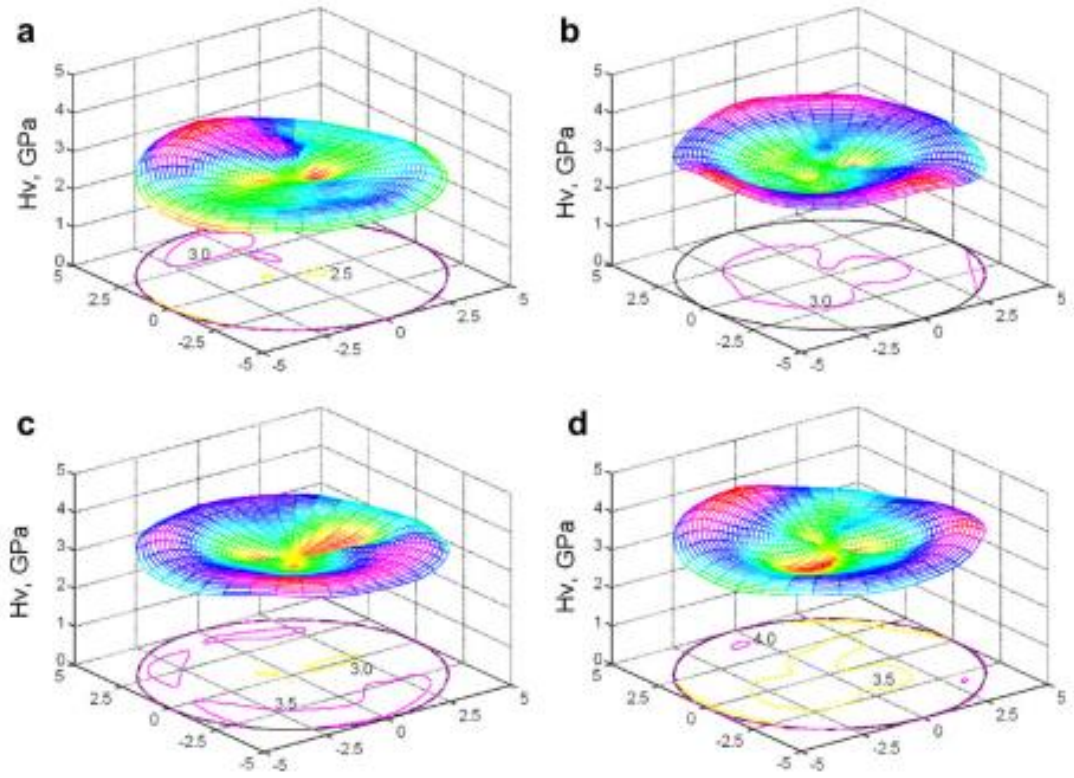

Figure 2.16 3D representation of microhardness distribution as a function of the number of turns for Ni processed by HPT under a pressure of 6.0 GPa: (a) 1/2 turn, (b) 1 turn, (c) 3 turns and (d) 7 turns [6]. (X and Y axis are in mm)

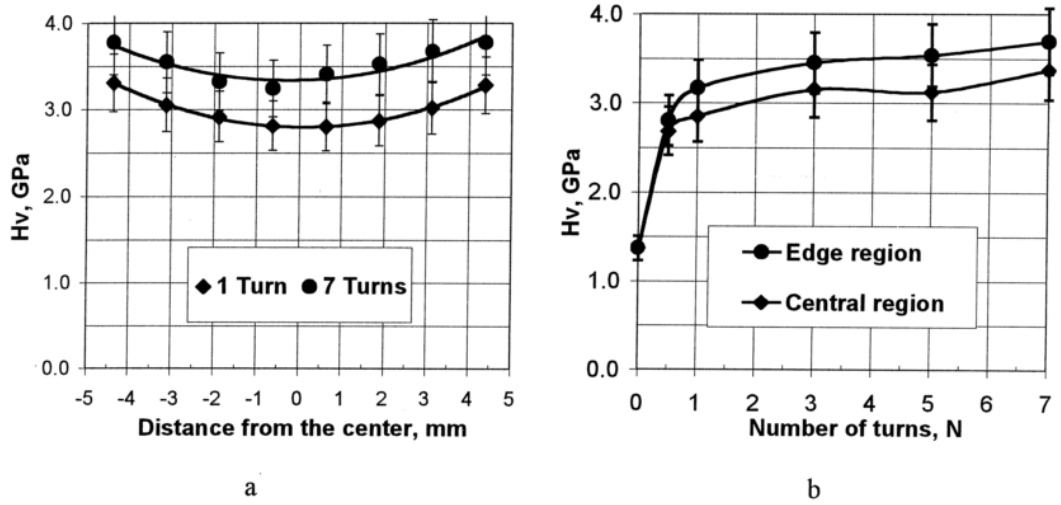

Figure 2.17 (a) Average microhardness across the diameter of Ni discs at 1 and 7 turns; (b) average microhardness against number of turns for both centre and edges of the Ni discs [7].

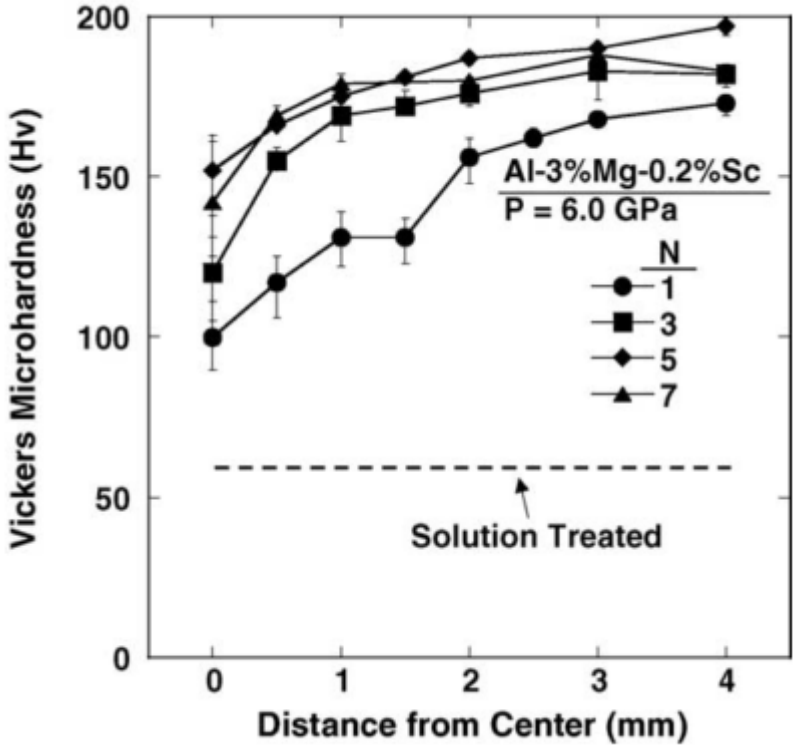

Figure 2.18 Vickers microhardness measurements radially across the discs of Al-3% Mg-0.2% Sc alloy processed by HPT under a pressure of 6.0 GPa with increasing number of turns [36].

2.2.7 Influence of stacking-fault energy

Stacking-fault energy (SFE) is considered one of the most important factors in determining the deformation behaviour of cubic structured materials. It controls the extent of the separation between the partial dislocations. Materials with high SFE tend to have only a small separation between the partial dislocations and a thin stacking fault, while materials with low SFE have a large separation between the partial dislocations and a wide stacking fault [43]. Table 2.1 illustrates SFE values for different metals and alloys.

Table 2.1 SFE values for various metals and alloys [43].

Metal	**Stacking-fault energy ($mJ\ m^{-2}$)**
Brass	< 10
303 Stainless steel	8
304 Stainless steel	20
310 stainless steel	45
Silver	~ 25
Gold	~ 50
Copper	~ 80
Nickel	~ 150
Aluminum	~ 200

Plastic deformation in metals is significantly affected by their SFE. Metals with low SFE have a fast strain hardening rate and tend to twin easily during annealing [43].

Moreover, SFE influences the development of microstructural homogeneity after processing by HPT. Two behaviours in the variation of hardness across the diameter of the disc in the early stages of HPT processing have been reported [41]. The variation is directly related to the rate of recovery in materials; materials with high SFE have a high recovery rate and easy cross-slip, and vice versa.

Earlier studies on high-purity aluminium with high SFE found higher hardness values in the central region than at the periphery in the early stages of processing, due to the dynamic recovery at the edge of the disc. Also, there was a gradual evolution towards hardness homogeneity with increasing numbers of turns [38,41,44].

Studies on low SFE materials such as commercial-purity aluminium and aluminium alloys [29,31,39,45], and copper and copper alloys [37,46–52] have reported lower hardness values in the central region than at the periphery in the early stages of deformation. These studies show a gradual evolution towards hardness homogeneity when increasing torsional strain in the absence of recovery. The variation in Vickers microhardness across the diameter of the disc in the early stages of deformation of materials with fast and slow recovery rates is depicted schematically in Figure 2.19.

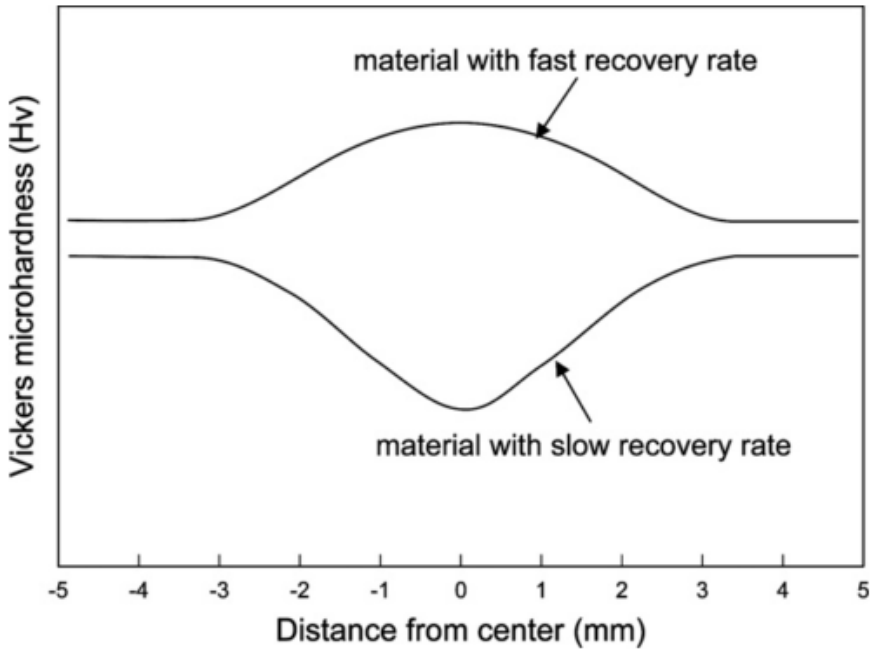

Figure 2.19 Schematic illustration of variation in Vickers microhardness across the diameter of the disc in the early stages of deformation for materials with fast and slow recovery rates [41].

The variation in hardness with equivalent strain is affected by the rate of recovery. During HPT, the microstructure tends to saturate at high strain rates with increasing numbers of turns. Figure 2.20 illustrates three distinct ways to achieve saturation of hardness with equivalent strain. The annealed (unprocessed) condition is denoted by a small bar on the hardness axis. Figure 2.20(a) shows an increase in hardness in the early stages of straining until the sample becomes saturated at a certain value without recovery. Most metals exhibit this type of behaviour. In Figure 2.20(b), an initial increase in hardness value is followed by a subsequent decrease, then saturation. This type of behaviour occurs in materials with a high SFE due to their easy cross-slip and their fast rate of recovery. The third behaviour is depicted in Figure 2.20(c), clearly showing hardness values below the values of the annealed condition in the early stages of processing. Further weakening is due to the high pressure imposed during HPT [53].

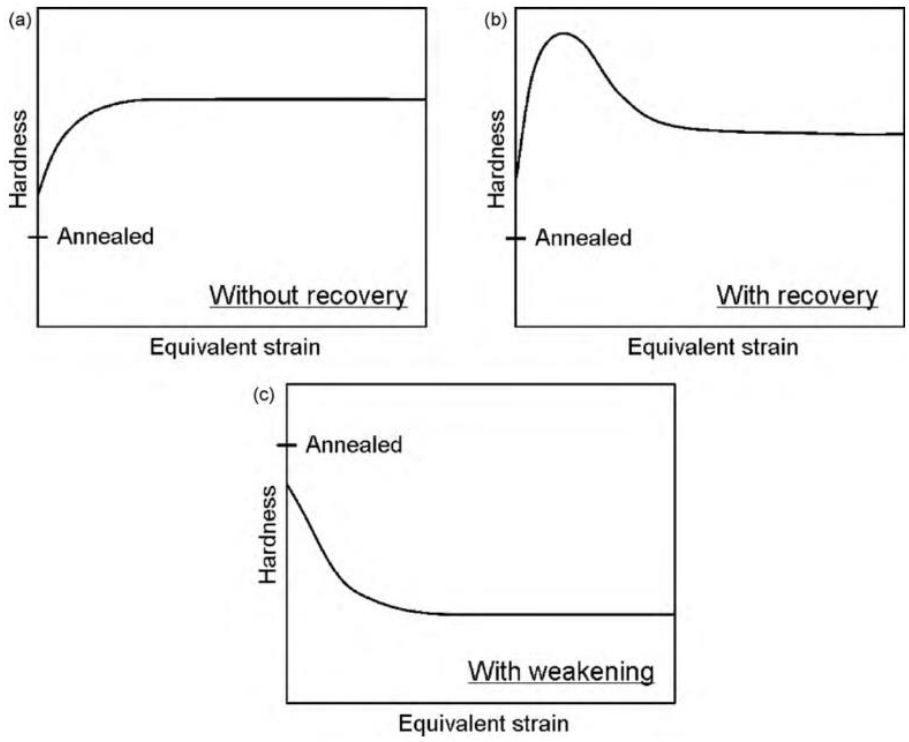

Figure 2.20 Three distinct behaviours for the saturation of hardness with equivalent strain during HPT processing: (a) without recovery, (b) with recovery, and (c) with weakening [53].

2.2.8 Advantages and disadvantages of HPT

A primary advantage of HPT is the production of materials with ultrafine grain while retaining the initial shape and dimensions [15]. HPT produces finer microstructures than other SPD methods due to the hydrostatic pressure imposed during the deformation [54], with the additional benefit of an ability to process metals that are difficult (brittle/hard) to process by other SPD methods [55]. Another advantage is producing grains with higher-angle boundaries than achieved under ECAP [6,54,56]. On the other hand, major limitations of the HPT process include the shape and size of the HPT sample. The shape has to be that of a disc, which is a problem for the many applications that require complex shapes. Also, the disc size is limited to ~10–20 mm diameter and ~1 mm in thickness. This is very small for industrial applications [57]. Likewise, after HPT processing the variation in the microstructure across the disc is considered a limitation. As mentioned earlier, this is due to a difference in imposed strain across the disc with distance from the centre [58]. As a result, as reported in some studies, a completely homogeneous microstructure is not always achievable [33].

2.3 Equal-Channel Angular Pressing (ECAP)

In the 1970s and 1980s, ECAP was introduced by Segal and his associates at the Physical-Technical Institute of Minsk in the former Soviet Union [59]. They succeeded in using simple shear to impose high strains on metal billets without changing the cross-sectional dimensions. ECAP attracted scientific interest in the 1990s because the processed metals had an UFG at submicrometer level, thus exceptional properties were achieved [8,60]. ECAP has received yet more attention recently beacuse:

- it is quite a relatively simple procedure
- it can be applied to large billets, with potential for structural applications
- it can be applied to materials with different crystal structures
- it can achieve reasonable homogeneity by increasing the number of passes, and
- it has the potential to be modified to handle larger billets [61].

2.3.1 Principle of Equal-Channel Angular Pressing (ECAP)

A schematic illustration of the general principles of ECAP is given in Figure 2.21 [62]. The ECAP tool uses a special die that contains a channel of uniform cross-section. The channel of the die is bent through the internal channel angle ϕ and the curvature angle Ψ. This internal channel angle ϕ is that between the two sections of the bent channel, while the curvature angle Ψ is the angle at the outer arc of curvature, where the two parts of the channel intersect, as illustrated in Figure 2.22 [63]. Depending on the shape of the die channel, the ECAP sample takes the form of a bar with square cross-section, as in Figure 2.21, or a rod with a circular cross-section, as in Figure 2.22. The sample is pressed through the die channel by applying pressure with a plunger, then deformed by simple shear as it passes through the die channel angle. Very high strain is achieved by pressing the sample repeatedly, using several passes. The pressed sample has three orthogonal planes: the transverse plane (X) is the plane perpendicular to the flow direction; the flow plane (Y) is the parallel plane to the side face of the sample at the exit point; and the longitudinal plane (Z) is the plane parallel to the top surface of the sample at the point of exit from the die [61]. The sample exits the die with the same initial cross-sectional dimensions, despite the very high strain during the process. There are several fundamental parameters that characterize the process, such as the imposed strain in each separate pass, the processing route, and the slip systems operating during the process.

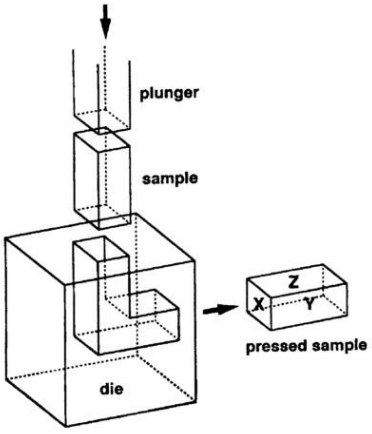

Figure 2.21 Schematic illustration of a typical ECAP facility [62].

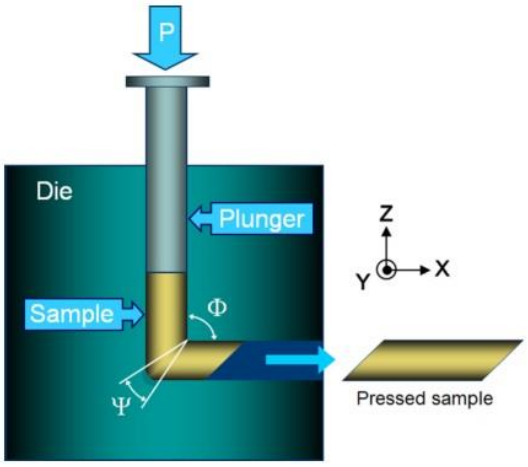

Figure 2.22 Schematic illustration of the channel angle ϕ and the curvature angle Ψ used in ECAP [63].

2.3.2 Imposed strain in ECAP

The imposed strain is one of the fundamental parameters of the ECAP process, and it influences the UFG structure of materials processed by ECAP. The amount of strain induced in the sample during each pass depends on the number of passes, the channel angles (ϕ) and the angle of curvature (Ψ) as shown in Figure 2.22 [63]. The equivalent strain imposed during ECAP processing after N_{ECAP} passes, ε_N, is given by [64]:

$$\varepsilon_N = \frac{N_{ECAP}}{\sqrt{3}}\left[2\cot\left(\frac{\Phi}{2}+\frac{\Psi}{2}\right)+\Psi\,\mathrm{cosec}\left(\frac{\Phi}{2}+\frac{\Psi}{2}\right)\right] \tag{2.7}$$

It is assumed that the billets are well lubricated before entering the ECAP channel, to minimize frictional forces. It is readily apparent from Equation 2.7 that equivalent strain increases with increasing numbers of ECAP passes as well as decreasing the channel angles.

2.3.3 Processing routes in ECAP

During ECAP, the samples are pressed by one of four different processing routes. The mechanism of these routes is described by the rotation of a sample around its longitudinal axis during adjacent passes. These routes are shown in Figure 2.23 [65] and are termed: Route A when these is no rotation to the sample between each separate pass; Route B_A when the sample is rotated by 90º in alternate directions between each separate pass; Route B_C when the sample is rotated by 90º in the same direction between each separate pass; and lastly Route C when the sample is rotated by 180º between passes. It has been demonstrated that rotating the sample between each pass initiates different slip systems, which result in different microstructures [66–68].

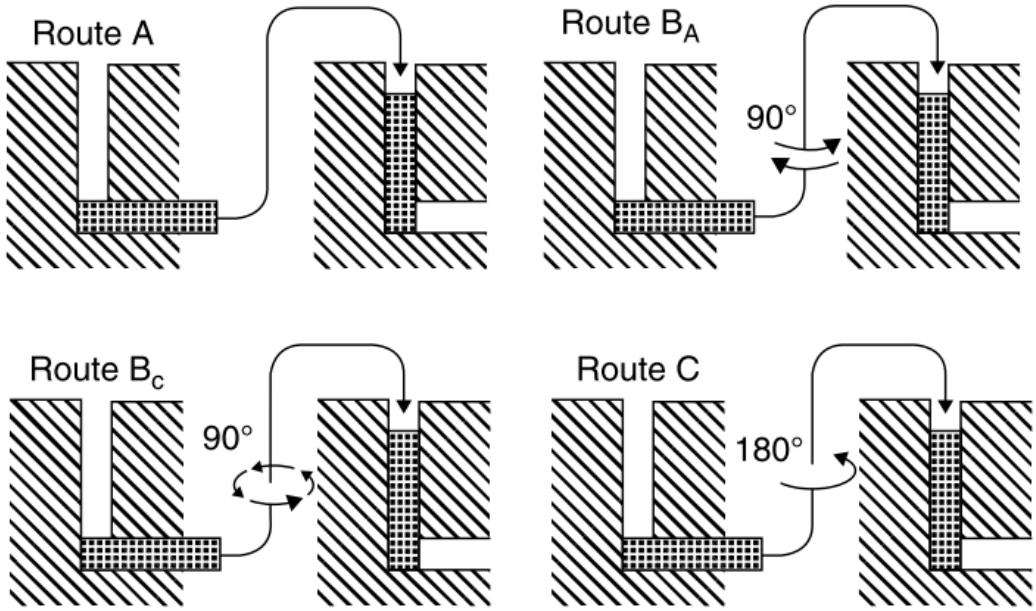

Figure 2.23 Four processing routes used in ECAP: Route A; Route B_A; Route B_C; and Route C [65].

Several studies on high-purity aluminium have shown that Route B_C is the best at rapidly achieving equiaxed ultrafine grains [69–71]. Other studies on aluminium alloys have reported that Route A is more efficient than Route B_C in ECAP processing [72]. Later studies have shown that processing using Route A produces a higher fraction of high-angle boundaries, however; elongated grains are formed instead of equiaxed [73]. More recently, an experiment was conducted on oxygen-free copper processed by ECAP by up to 25 passes [74]. The results revealed that Route B_C produced more equiaxed and smaller grains after 25 passes; Route A produced a higher fraction of high-angle boundaries. Route B_C provided the highest of yield stress, ultimate tensile stress and ductility after 10 passes.

Figure 2.24 shows the microstructures in the X-plane for pure aluminium processed by ECAP through 4 passes using different processing routes. They are Route A [71], Route B_A [69], Route B_C [71] and Route C [71]. These micrographs display elongated grains after 4 passes in each of the Routes A, B_A and C, but an array of equiaxed ultrafine grains is achieved after processing using Route B_C.

Route B_C is also the most efficient processing route to enhance the superplastic formability of materials, since it leads to an equiaxed grain structure, which is an important factor in superplasticity at high temperatures. A supporting study conducted on Al–Mg–Sc alloy to investigate superplastic ductility after processing by ECAP through different processing routes [75] concluded that Route B_C leads to maximum elongation.

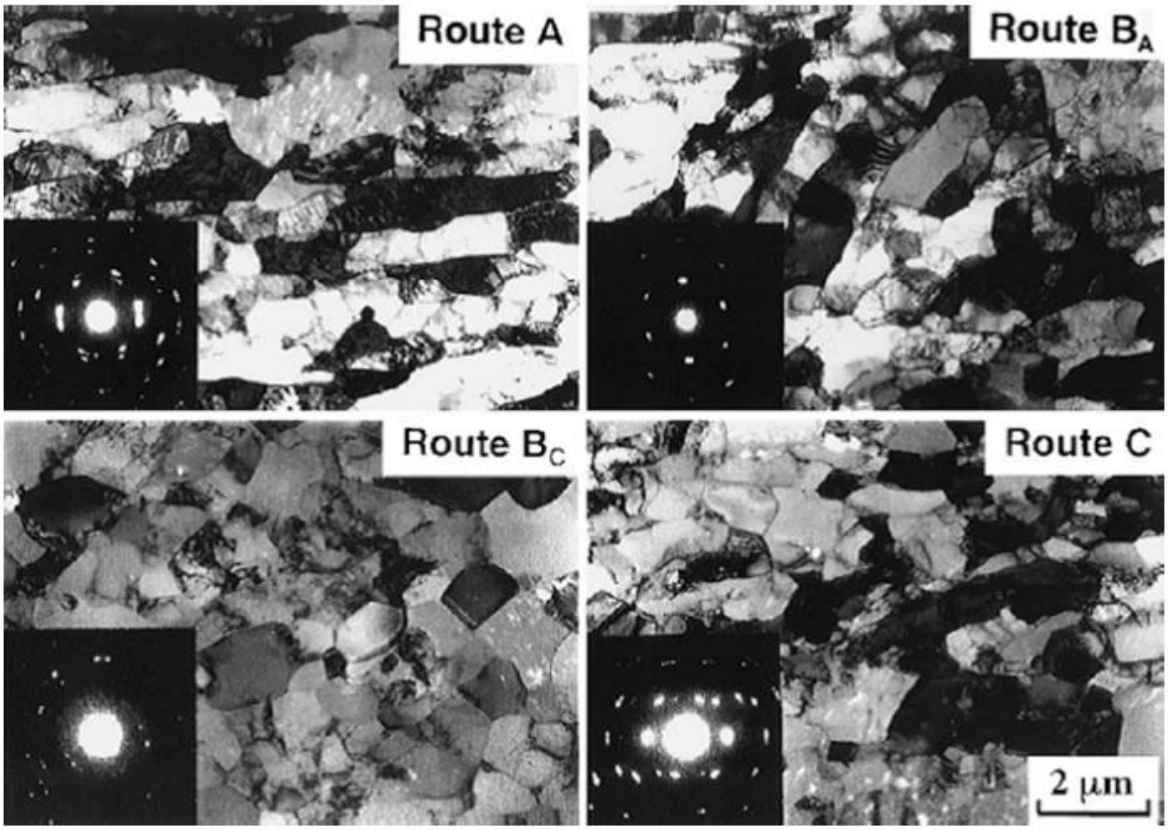

Figure 2.24 Photomicrographs showing X-plane microstructures for aluminium processed by ECAP through 4 passes using different processing routes: Route A [71], Route B_A [69], Route B_C [71] and Route C [71].

2.3.4 Slip planes introduced during ECAP

During the ECAP process, each route introduces different slip planes on the sample. These are shown in Figure 2.25 [66]. Each plane is labelled by a number corresponding to the number of passes for each processing route. As seen, the slip planes are numbered 1, 2, 3 and 4 for the first four ECAP passes, the X, Y and Z planes are orthogonal planes, as described above.

Route A has two distinct shearing planes that intersect at an angle of 90º, while Route B_A has four distinct shearing planes that intersect at an angle of 120º. Both Routes B_C and C are considered redundant strain processes because in Route B_C, the slip plane in the third pass cancels the slip plane in the first pass, and the slip plane in the fourth pass cancels that in the second. In Route C, shear occurs on the same plan and the direction of the shear is reversed in each sequential pass. Routes A and B_A are not considered redundant strain processes, because the strain accumulates with increasing numbers of ECAP passes.

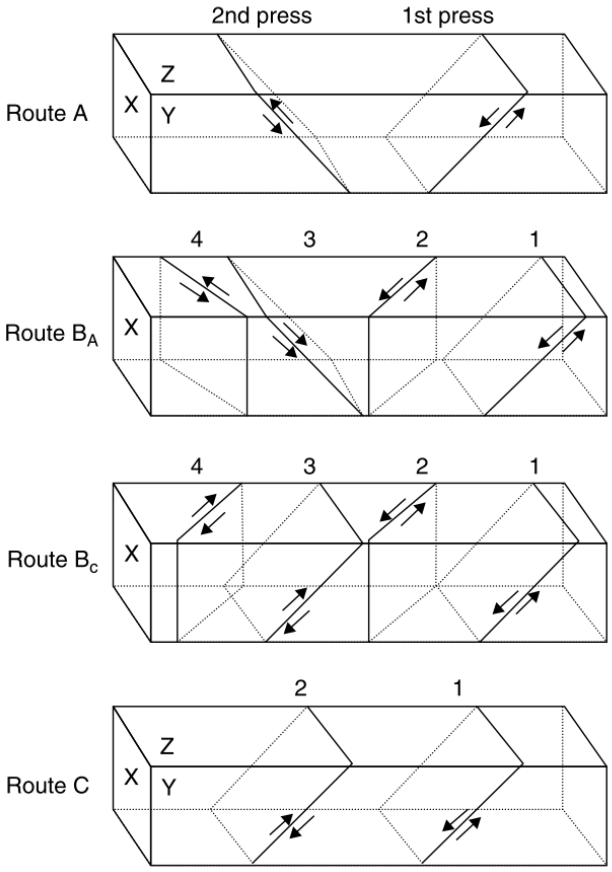

Figure 2.25 Slip planes for Route A, Route B_A, Route B_C and Route C [66].

When processing the samples by ECAP using the different processing routes (A, B_A, B_C and C) for different numbers of passes, distortions are introduced into the cubic elements. Figure 2.26 demonstrates these distortions for each processing route on the three orthogonal planes by up to 8 passes [76]. Route A shows no distortion on the Z plane: the distortions occur on the X and Y-planes. The degree of distortion is heightened

with increasing numbers of passes. The distortions in Route B_A occur on all planes and increase with the number of passes. In Route B_C, the cubic element is distorted on all orthogonal planes, but the cubic element is restored every 4 passes. In Route C, the cubic element is distorted on the X and Y-planes only, and there is no distortion on the Z plane. The cubic element is restored every 2 passes.

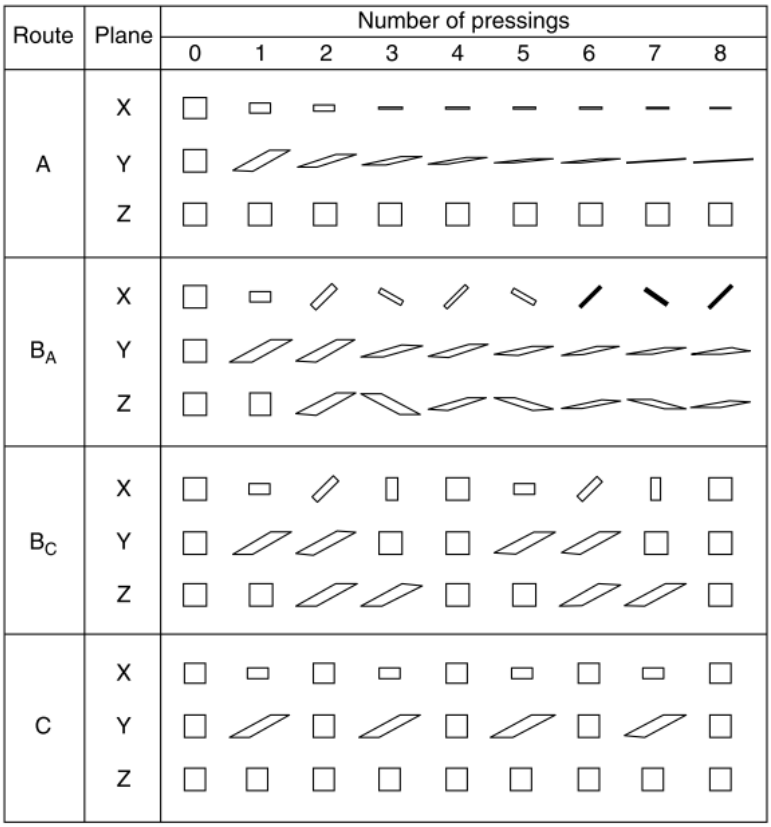

Figure 2.26 Distortions visible on the faces of the cubic element in ECAP processing with up to 8 passes using different processing routes (A, B_A, B_C and C) and shown on the three orthogonal planes [76].

2.3.5 Factors affecting ECAP

The microstructural characteristics of the sample are affected by numerous factors during the ECAP process such as the channel angle Φ, the angle of curvature Ψ, pressing speed, pressing temperature, back-pressure and internal heating.

2.3.5.1 Channel angle Φ

The channel angle, Φ, has a major influence on the microstructure of the sample. Studies have shown that a channel angle of 90º provides the best results in terms of

microstructure and imposed strain. It has been shown that using a die with a channel angle of 90º imposes very significant plastic strain on the sample, thus attaining ultrafine equiaxed grains with boundaries having high angles of misorientation [77]. A deviation from the ideal channel angle ($\Phi \approx 90º$) is sometimes necessary, using larger or smaller channel angles. For example, low ductility materials such as tungsten will crack during ECAP using the 90º channel angle, so a wider channel angle is more favourable. Figure 2.27 shows billets of pure tungsten processed using Route B_C and a channel angle Φ of 110º for 8 passes [78].

Figure 2.27 Tungsten billet processed by ECAP using Route B_C and ϕ = 110º for 8 passes [78].

Increasing the channel angle leads to a decrease in the processing temperature [79], thus smaller grains are achieved. Nevertheless, in order to attain a high value of total imposed strain with larger channel angles, high numbers of ECAP passes are required. The larger the channel angle, the higher the number of passes needed [77]. On the other hand, channel angles that are less than 90º tend to increase the total imposed strain during ECAP process and therefore provide smaller grains than those produced by a 90º channel angle [80]. However, for the samples to be extruded by ECAP without cracking requires high pressure.

TEM was used to analyse the microstructure of pure aluminium (99.99%) after processing by ECAP using Route B_C through four different internal angles Φ = 90º, 112.5º, 135º and 157.5º [77]. Figure 2.28 illustrates the microstructures produced after

processing using each internal angle. It is concluded that an internal channel angle of 90º is the most efficient at producing fine-grained structures and, by increasing the channel angle, subgrains with low-angle grain boundaries increase in the microstructure.

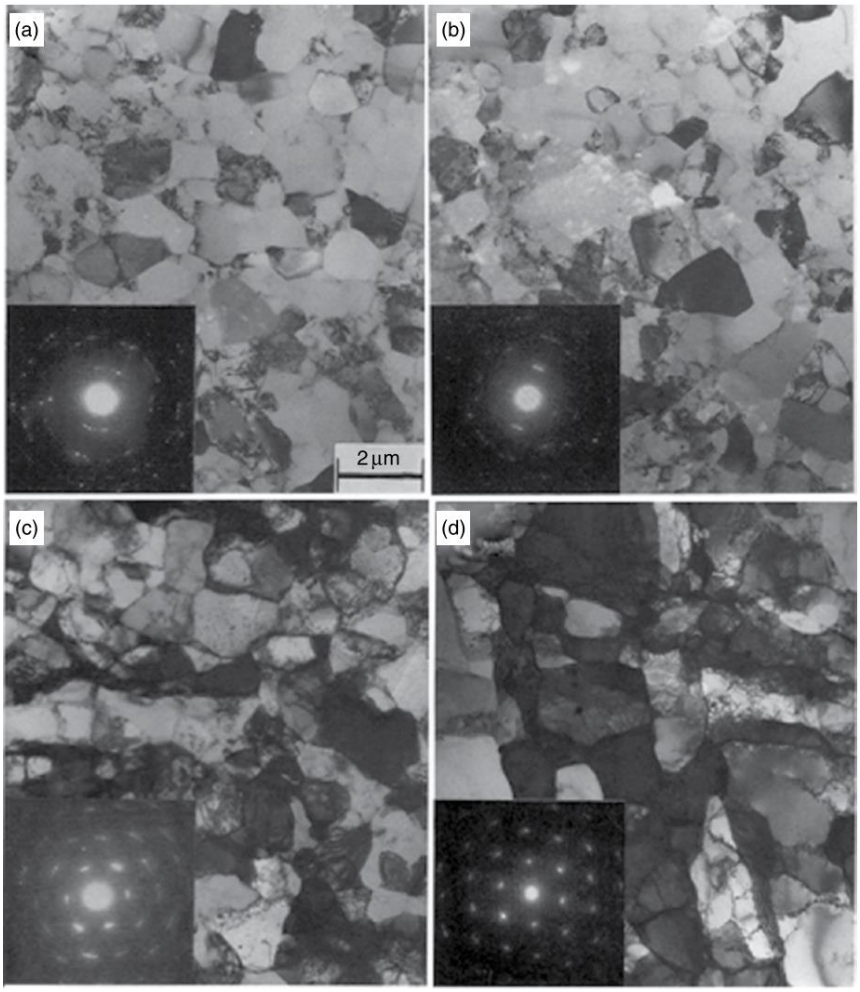

Figure 2.28 TEM micrographs showing microstructures of pure Al after processing by ECAP using Route B_C through multiple internal channel angles Φ: (a) 90°; (b) 112.5°; (c) 135°; and (d) 157.5° [77].

2.3.5.2 Angle of curvature, Ψ

The angle of curvature Ψ has only a minor influence on the strain, yet it influences the production of ultrafine grains. Studies have ascertained that using an outer angle of curvature of Ψ = 20º and a channel angle of Φ = 90º with no arc of curvature at the inner point, where the two parts of the channel intersect, is the best way to increase microstructure homogeneity and minimize the effect of the 'dead zone'. This is the area

at the outer corner of the die channel where the billet has no contact with the die walls during pressing, thus reducing the microstructural homogeneity [61].

2.3.5.3 Pressing speed

The pressing speed has a very minor influence on the equilibrium size of the ultrafine grains produced by ECAP [62,81]. It is limited to the production of more equally sized ultrafine grains, due to the associated recovery. Yield stress against pressing speed for Al- 1%Mg alloy processed by ECAP through 1 to 4 passes using Route B_C is depicted in Figure 2.29 [62], showing that the pressing speed has a very minor effect on the yield stress.

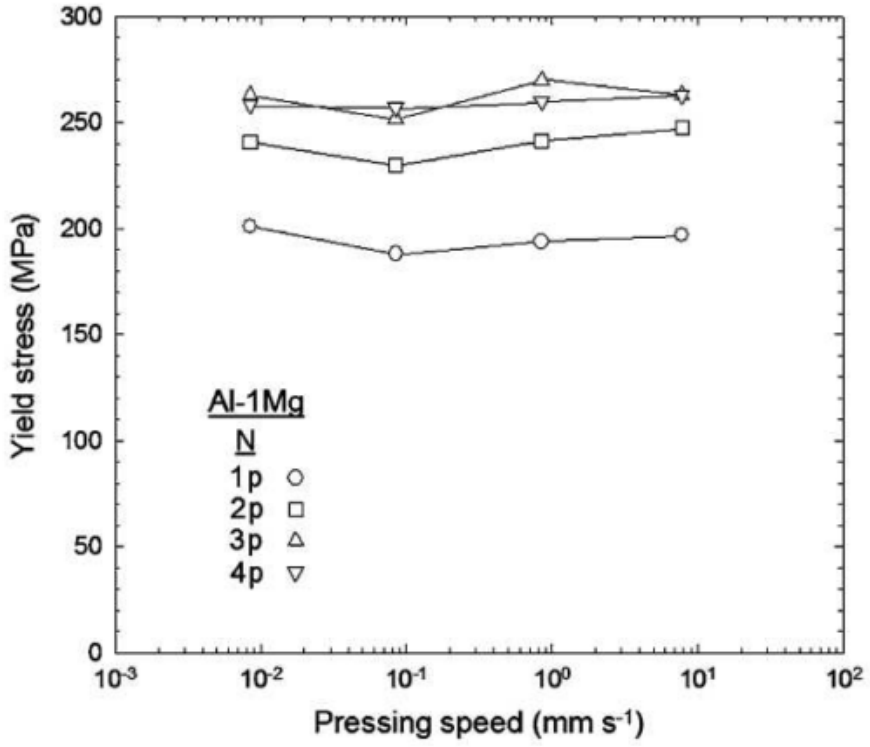

Figure 2.29 Yield stress against pressing speed for Al- 1% Mg alloy processed by ECAP through 1 to 4 passes using Route B_C [62].

Figure 2.30 shows microstructures of high-purity aluminium (99.99%) processed by ECAP for 4 passes using Route B_C through a channel angle of $\Phi = 90°$ with two speeds of ~8.5×10^{-3} mm/s and ~7.6 mm/s [62]. Both speeds produced similar fine-grained microstructures with the same average grain size of ~1.3 μm.

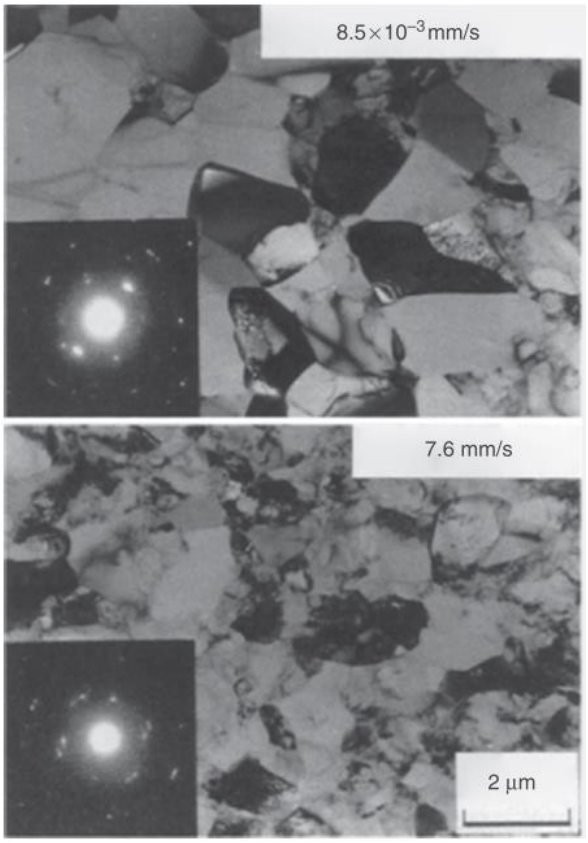

Figure 2.30 Microstructure of high-purity aluminium (99.99%) processed by ECAP for 4 passes using Route B_C through a channel angle of $\Phi = 90°$ with two speeds of ~8.5×10^{-3} mm/s and ~7.6 mm/s [62].

2.3.5.4 Pressing temperature

A major factor in ECAP processing is the pressing temperature. Experiments have shown that raising the pressing temperature increases the equilibrium grain size and, in addition, the fraction of low-angle grain boundaries (LABs <5º). Thus, using the lowest possible temperature achieves the smallest grain size and the highest fraction of high-angle boundaries (HABs >15º). Since the pressing temperature can be controlled, the best pressing temperature is the lowest at which ECAP processing may be executed without introducing defects into the billet [82–86]. Figure 2.31 shows the microstructure of pure aluminium processed by ECAP at different temperatures: room temperature; 373 K, 473 K and 573 K [82]. It is clear that the largest grain size is formed at the highest temperature of 573 K. Another study was undertaken on 5052 aluminium alloy billets processed by ECAP at six different temperatures: 50 ºC; 100 ºC; 150 ºC; 200 ºC; 250 ºC; and 300 ºC

[83]. It is obvious from Figure 2.32 and Figure 2.33 that the higher the pressing temperature, the greater the fraction of low-angle boundaries.

In addition, an internal rise of temperature is noticed during the ECAP process. After investigation, it was concluded that the factors affecting internal heating in ECAP are the strength of the material and the ram speed. Increasing the strength of the material and the ram speed during pressing, increases internal heating [81,87].

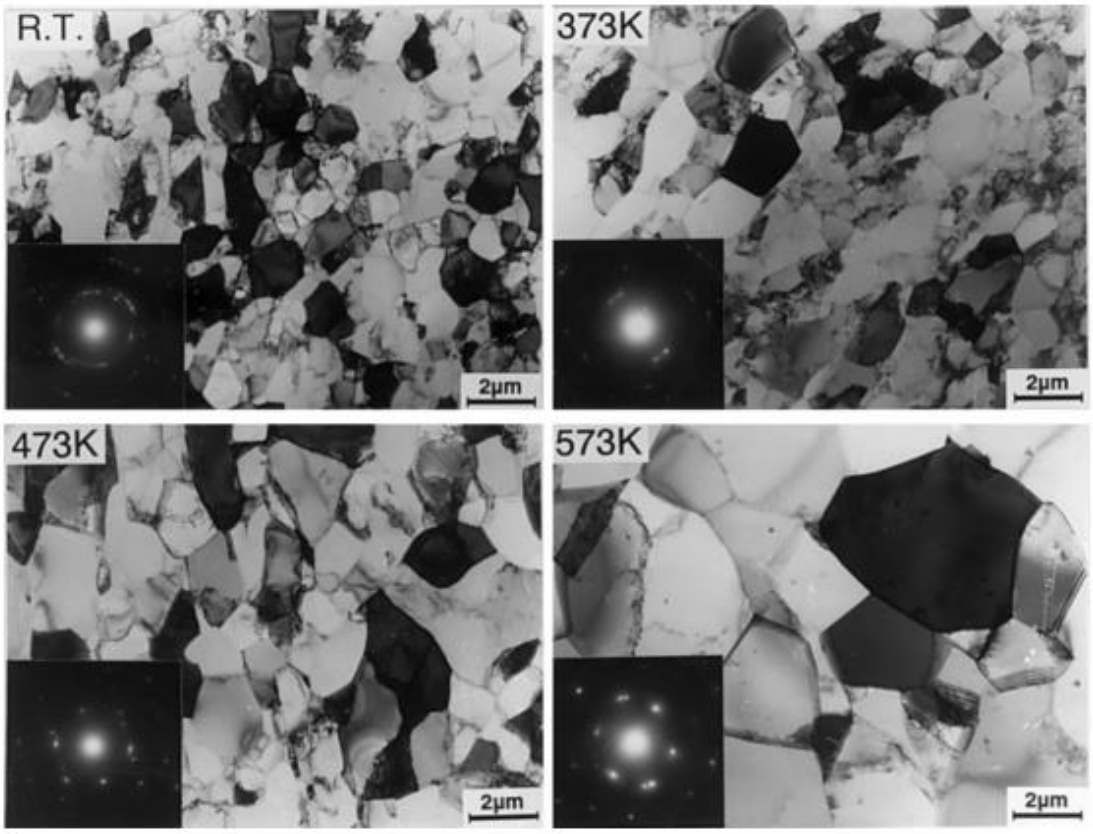

Figure 2.31 Microstructures of pure aluminium processed at different temperatures: RT; 373 K; 473 K; and 573 K [82].

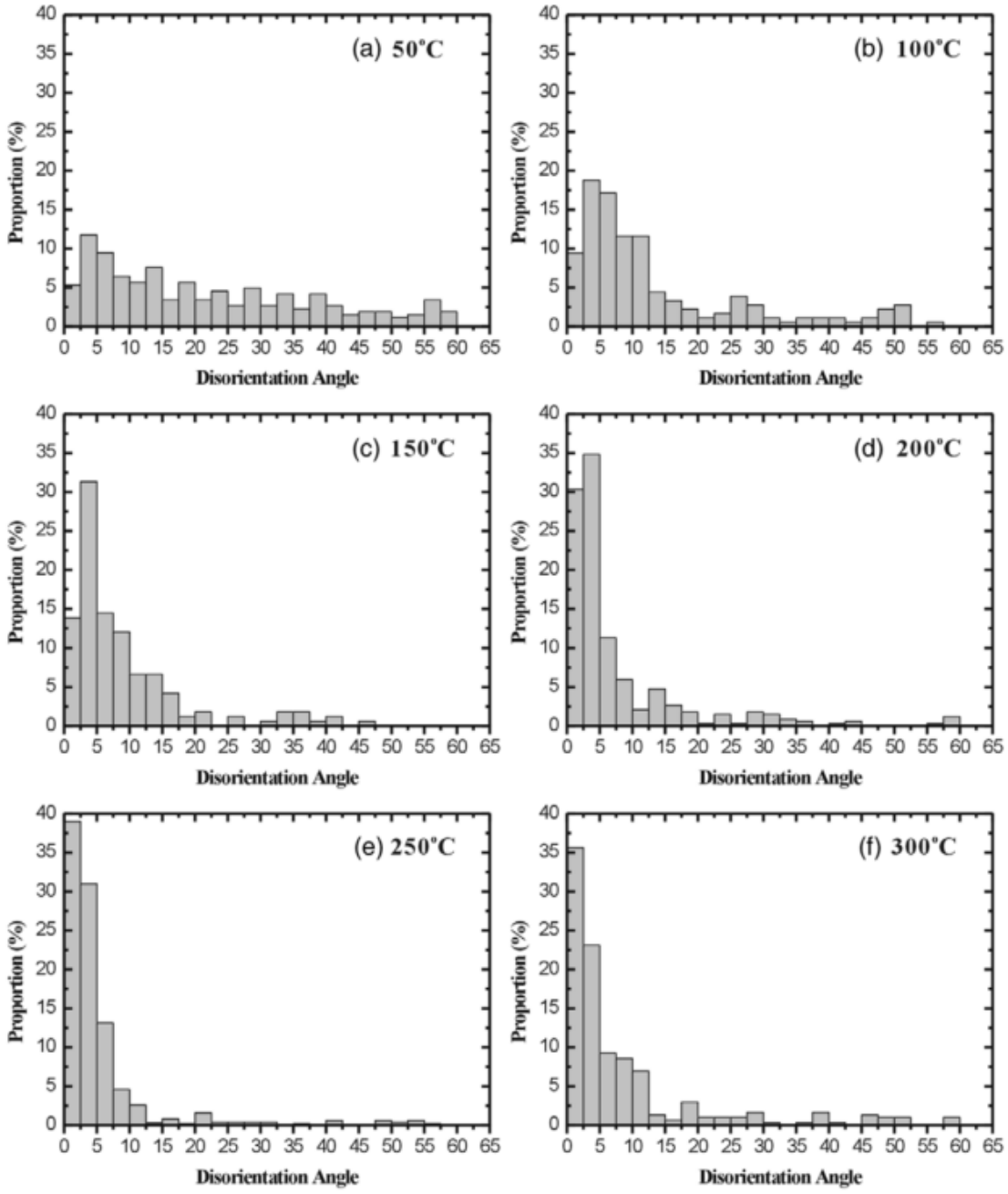

Figure 2.32 Histograms illustrating the proportion of high and low-angle boundaries produced in 5052 aluminium alloy at: (a) 50 °C; (b) 100 °C; (c) 150 °C; (d) 200 °C; (e) 250 °C; and (f) 300 °C [83].

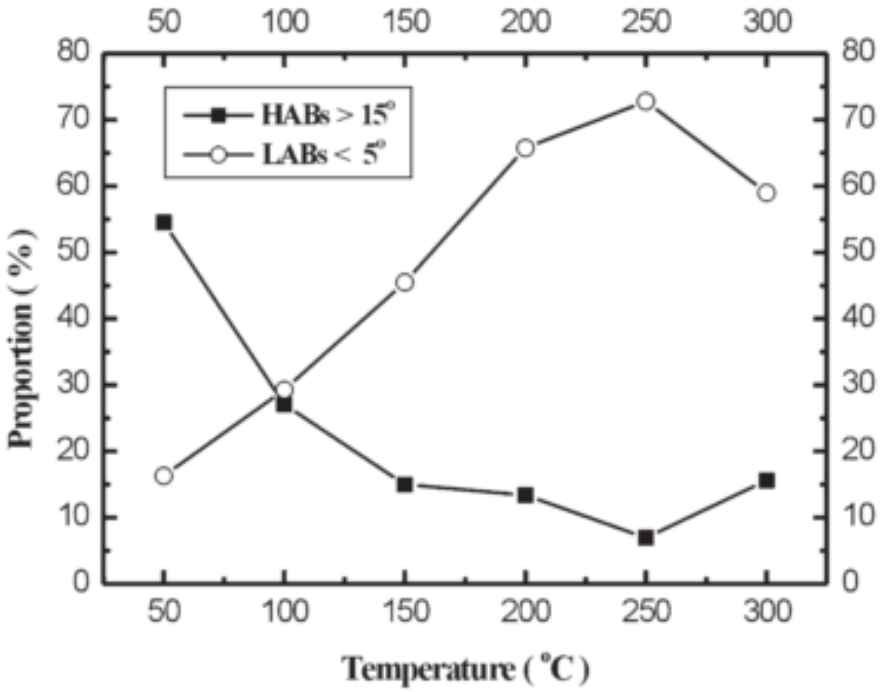

Figure 2.33 Influence of pressing temperature on the proportion of low and high angle boundaries [83].

2.3.5.5 Back-pressure

Back-pressure improves the workability of the sample during the ECAP process, as well as assisting in reaching a higher number of ECAP passes without introducing cracking of the sample [88–90]. Back-pressure increases the homogeneity of the microstructure of the sample by reducing the effect of the dead zone on the sample during ECAP [91]. Additionally, the presence of back-pressure during processing has an impact on the refinement of the grain. Samples processed by ECAP with back-pressure have a smaller grain size than those without, improving mechanical properties such as strength and ductility [90].

2.3.6 Evolution of homogeneity during ECAP processing

As mentioned earlier, during ECAP the billet is pressed through a bent channel within a die and deformed by simple shear. Theoretically, the strain distribution is homogenous across the billet [92,93]. Likewise, the microstructure is homogenous. However, there are some influences on the imposed strain that affect the homogeneity of the microstructure of the pressed billet: first, the lack of contact between the billet surface and the die wall at the outer arc of curvature in the so-called dead zone [94–97] and; secondly, the friction between the surface of the pressed billet and the channel walls of the die while pressing [94,95]. This disturbs the distribution of the imposed strain during ECAP and leads to microstructural inhomogeneity.

Several experiments investigated the evolution of microstructure homogeneity for samples processed by ECAP [98–100]. A study was conducted on billets of commercial-purity aluminium Al-1050 alloy processed by ECAP at room temperature through 1, 2, 4 and 6 passes using Route B_C [98]. The billets were cut on the cross-sectional (X) and longitudinal (Y) planes and the results of the microhardness measurements were presented as colour-coded contour maps, shown in Figure 2.34 and Figure 2.35, respectively. The results indicated microstructure inhomogeneity, where the top and bottom regions had lower hardness values than the centre of the billet after the first pass. This inhomogeneity decreased with increasing number of passes as the lower values of microhardness in the top and bottom regions increased, and both planes reached reasonable homogeneity.

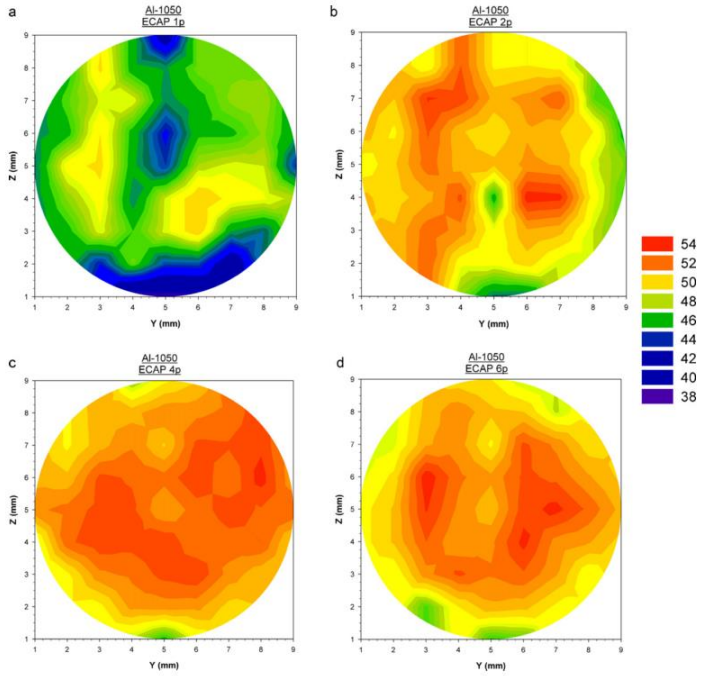

Figure 2.34 Colour-coded contour maps showing microhardness distribution on the cross-sectional planes of Al-1050 alloy after: (a) 1 pass, (b) 2 passes, (c) 4 passes and (d) 6 passes [98].

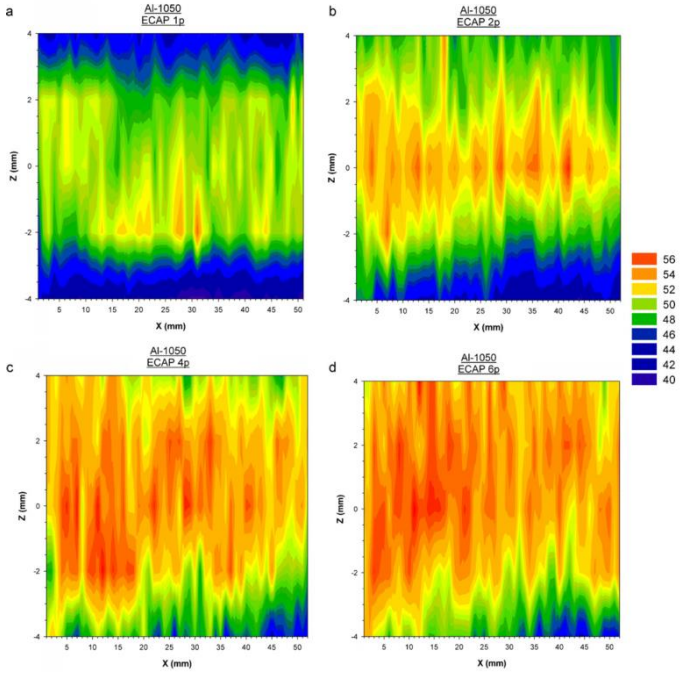

Figure 2.35 Colour-coded contour maps showing microhardness distribution on the longitudinal planes of Al-1050 alloy after: (a) 1 pass, (b) 2 passes, (c) 4 passes and (d) 6 passes [98].

2.4 Dynamic Testing

Tensile and compression are the most common conventional mechanical tests used to investigate the deformation mechanisms and mechanical properties of UFG materials under low strain rate, in the range up to ~10^1 s^{-1}. Today, methods used to test the mechanical properties of UFG materials at high strain rates include split Hopkinson pressure bars (SHBP) [101,102], the Taylor impact test [102,103] and shock loading by plate impact [102]. These different dynamic test techniques have been enhanced to provide similar conditions to ballistic impact [102]. Figure 2.36 is a schematic diagram showing the strain rate range for different mechanical testing methods [102]. It is readily apparent that the strain rate regime for SHBP dynamic test is between 10^1 s^{-1} to 10^4 s^{-1}.

Figure 2.37 is a schematic diagram of split Hopkinson pressure bar system. It can be seen that the specimen is contained between the incident and transmitted bars. A pressurized gas is used to push the striker bar towards the incident bar. When the striker bar hits the incident bar, it creates an elastic compression wave transmitted towards the specimen. At each interface a fraction of the wave will be transmitted and the remainder reflected, so that some wave energy will pass through the transmitted bar and some will be reflected back towards the incident bar. Thus, the specimen is strained and deformed plastically.

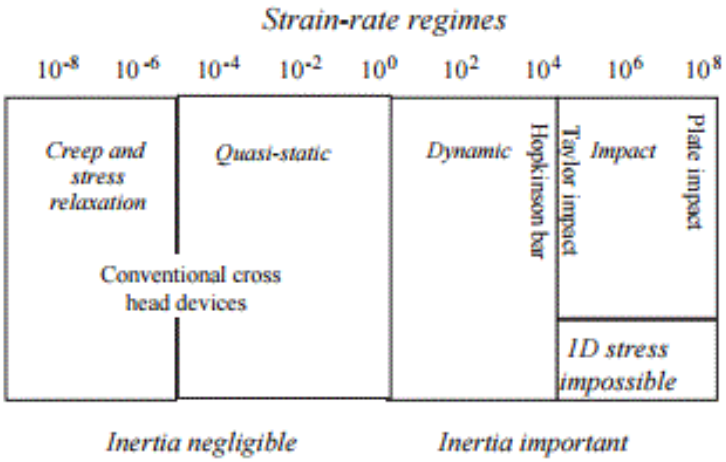

Figure 2.36 Schematic diagram showing the strain rate range (s^{-1}) for different mechanical testing methods [102].

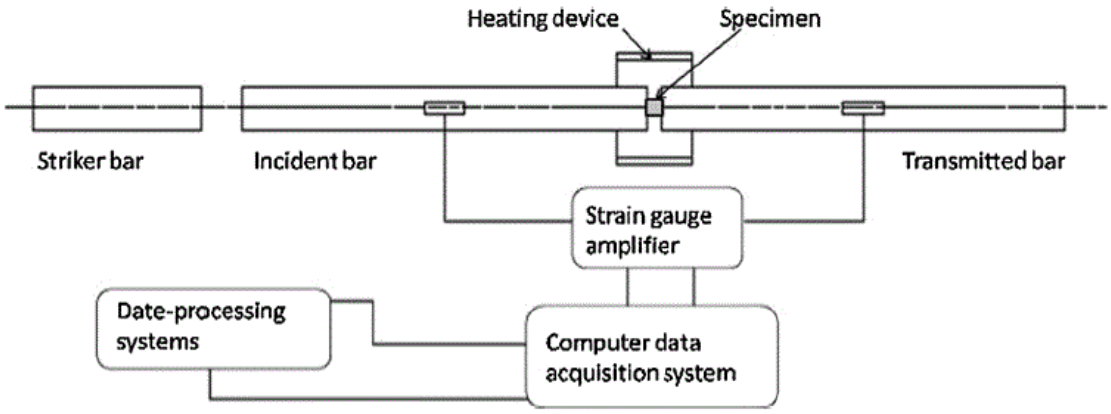

Figure 2.37 Schematic diagram of split Hopkinson pressure bar system [101].

The true stress (σ), true strain (ε) and strain rate $\dot{\varepsilon}$ are calculated using the following equations [104]:

$$\sigma(t) = \frac{E\,A_b}{A_s}\,[\varepsilon_I(t) - \varepsilon_R(t) - \varepsilon_T(t)] \tag{2.8}$$

$$\varepsilon(t) = \frac{C_0}{L_s}\int_0^t [\varepsilon_I(t) - \varepsilon_R(t) - \varepsilon_T(t)]\,dt \tag{2.9}$$

$$\dot{\varepsilon}(t) = \frac{C_0}{L_s}\,[\varepsilon_I(t) - \varepsilon_R(t) - \varepsilon_T(t)] \tag{2.10}$$

where E is the Young modulus, A_b is the area of the cross-section of the bar, A_s is the area of the cross-section of the compression specimen, C_0 is the speed of the sound in the bar, l_s is the length of the compression specimen and t is time, ε_I, ε_R and ε_T are strain pulses obtained during the SHPB test defined as the incident, reflected and transmitted strain pulses, respectively.

The deformation of UFG materials at high strain rates has attracted attention because materials with very small grain sizes produced by dynamic testing have great potential for use in aeronautic and aerospace applications [105]. Several studies have investigated the mechanical properties and deformation mechanisms of dynamically deformed materials. Adiabatic shear bands are produced within very short time during dynamic testing, as a result of high speed impact within very short time [106,107]. New recrystallized grains with high-angle grain boundaries are produced by dynamic

recrystallization in the interior of the shear bands due to the temperature rise during the deformation [106,108,109]. In other cases, the temperature rise during the dynamic testing is not sufficient to act as a driving force for dynamic recrystallization and therefore it is a mechanically driven process controlled by the increase of misorientation between the neighbouring subgrains [107,110,111].

The mechanical properties of materials deformed by dynamic testing are highly influenced by the grain size, strain rate and testing temperature. A study on Oxygen-free high thermal conductivity copper (OFHC Cu) tested at a high strain rate of 3.0×10^3 s^{-1} showed that the strength increases as the grain size decreases as shown in Figure 2.38 [108]. It is also well established that the higher the strain rate used during dynamic testing, the higher is the strength of the material [106,108,112,113]. Figure 2.39 [113] presents the influence of the strain rate on the flow stress of 7075 aluminium alloy. It is readily apparent that flow stress increases with increase of strain rate, regardless of the testing temperature. Studies have also shown that the testing temperature can highly alter the strength of the material deformed by dynamic testing. Inspection of Figure 2.40 [113] shows that the flow stress decreases as the temperature increases at a constant strain rate.

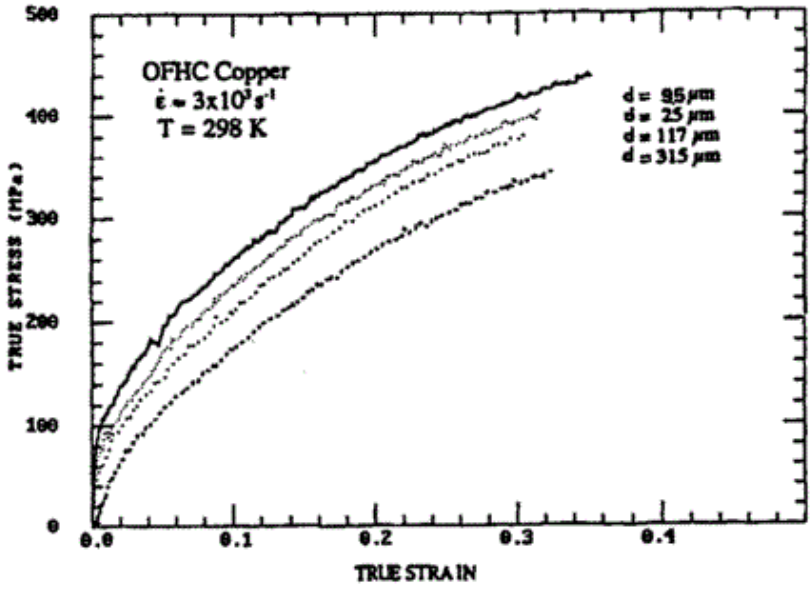

Figure 2.38 True stress-true strain curves for OFHC Cu specimens with various grain sizes deformed by dynamic test at 298 K using high strain rate of 3.0×10^3 s^{-1}.

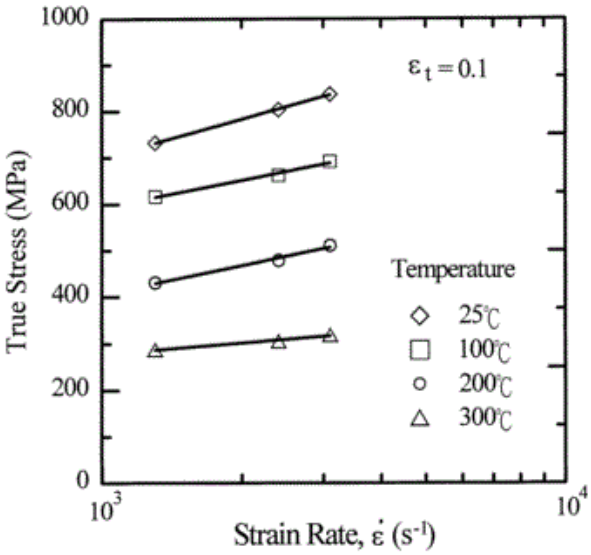

Figure 2.39 The flow stress with respect to the strain rate for 7075 aluminium alloy as a function of temperature [113].

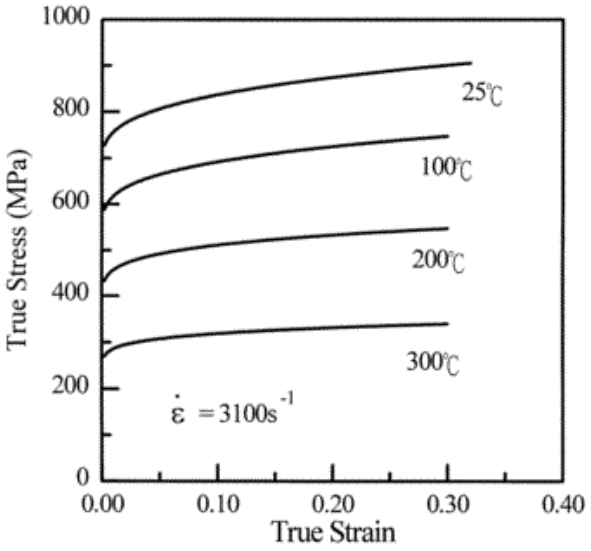

Figure 2.40 True stress-true strain curves for different testing temperatures used during the deformation of 7075 aluminium alloy at strain rate of $3.1\times10^3\ s^{-1}$ [113].

2.5 Copper and Copper Alloys

Pure copper is a relatively soft, ductile, malleable metal with a reddish-orange colour. Copper and copper alloys are one of the largest groups of commercial metals and

their consumption of copper is in third place after iron/steel and aluminium [114]. Copper and copper alloys are widely used in sectors such as building construction, electrical and electronic products, industrial machinery and equipment, transportation equipment and so on. They are popular because of their high electrical and thermal conductivities, corrosion resistance, strength and fatigue resistance, ductility and malleability, colour and ease of fabrication [11].

Copper and its alloys are shaped by such fabrication processes as rolling, extrusion, forging, drawing and stamping, not to mention forming at elevated temperatures. Copper is an ideal metal for decorative purposes as it can be polished, textured, plated or coated. Pieces are joined by processes such as welding, soldering, brazing, crimping, staking, riveting and bolting [114].

Pure copper is considered a soft, ductile, malleable metal with a reddish-orange colour. The atomic number and atomic weight of copper are 29 and 63.546 respectively. Some of the physical, electrical, thermal and mechanical properties of copper are listed in Table 2.2.

Table 2.2 Physical, electrical, thermal and mechanical properties of copper.

Property	**Value**
Density	8.94 g/cm³
Melting point	1084.62 ºC (1357.8 K)
Boiling point	2562ºC
Electrical resistivity	16.78 nΩ·m
Thermal conductivity	401 $W \cdot m^{-1} \cdot K^{-1}$
Thermal expansion	(25°C) 16.5 $\mu m \cdot m^{-1} \cdot K^{-1}$
Young's modulus	110–128 GPa
Shear modulus	48 GPa
Vickers hardness	369 MPa
Atomic number	29
Atomic weight	63.546

2.5.1 Applications of copper and copper alloys

Due to its high electrical conductivity, pure copper is used for cables, including telecommunications, electronic, power cables and automotive components. The increase in the use of electronic components in cars has raised the amount of copper used in automotive industry. For example, copper and its alloys are used for LED brake lights, keyless entry, airbag control, cruise control, ABS, suspension control and so on. Moreover, they are used in solar panels, heating systems, heat exchangers, car radiators due to their excellent heat conductivity. Since they have high corrosion resistance, they can be used for pipes, valves and fittings in systems using fluids [114]. Table 2.3 [114] lists the major end-use applications for copper and copper alloys, with the reason(s) for choosing copper for each particular application.

However, despite the fact that copper is a noble metal, it is susceptible to hydrogen embrittlement and stress-corrosion cracking by certain reagents and environments [114].

2.5.2 Classification of copper and copper alloys

Copper and copper alloys may be classified into nine major groups, based on the alloying element and quantity. Each is identified by a Unified Numbering System (UNS) designation prefixed ‘C’, followed by five numbers. These differentiate between wrought and cast alloys. The UNS for wrought alloys is given by C1xxxx to C7xxxx, while the UNS for cast alloys is given by C8xxxx to C9xxxx. Table 2.4 shows the nine major groups along with their UNS designations [11].

Table 2.3 Major end-use applications of copper and copper alloys, with reason(s) for choosing copper [114].

Application	**Mill product**	**Principal reason(s) for using copper**
Telecommunications	Copper wire	Electrical properties
Automotive: automobiles, trucks and buses	Brass and copper strip, copper wire	Corrosion resistance, heat transfer and electrical properties
Plumbing and heating	Copper tube, brass rod, castings	Corrosion resistance, machinability
Building wiring	Copper wire	Electrical properties
Heavy industrial equipment	All	Corrosion resistance, wear resistance, electrical properties, heat transfer, machinability
Air conditioning and commercial refrigeration	Copper tube	Heat transfer, formability
Industrial valve and fittings	Brass rod, castings	Corrosion resistance, machinability
Power utilities	Copper wire and bar	Electrical properties
Appliances	Copper wire and tube	Electrical properties and heat transfer
Lighting and wiring devices	Alloy strip, copper wire	Electrical properties
Electronics	Alloy strip, copper wire	Electrical properties
Fasteners	Brass wire	Machinability, corrosion resistance
Military and commercial ordnance	Brass strip and tube	Ease of fabrication
Coinage	Alloy and copper strip	Ease of fabrication, corrosion resistance, electrical properties, aesthetics
Builders' hardware	Brass rod and strip	Corrosion resistance, formability, aesthetics
Heat exchangers	Alloy tube and plate	Heat transfer, corrosion resistance

Table 2.4 Nine major groups of copper and copper alloys, along with their UNS designations [11].

UNS	Group
Wrought Alloys	
C1xxxx	Coppers (contain a minimum of 99.3% Cu) and high-copper alloys (contain up to 5% of alloying elements)
C2xxxx	Copper–zinc alloys (brasses, contain up to 40% Zn)
C3xxxx	Copper–zinc–lead alloys (leaded brasses)
C4xxxx	Copper–zinc–tin alloys (tin brasses)
C5xxxx	Copper–tin alloys (phosphor bronzes, contain up to 10% Sn and 0.2% P)
C6xxxx	Copper–aluminium alloys (aluminium bronzes, contain up to 10% Al), copper–silicon alloys (silicon bronzes, contain up to 3% Si) and miscellaneous copper–zinc alloys
C7xxxx	Copper–nickel alloys, copper–zinc–nickel alloys
Cast Alloys	
C8xxxx	Cast coppers, cast high-copper alloys, the cast brasses of various types, cast manganese–bronze alloys and cast copper–zinc–silicon alloys
C9xxxx	Cast copper–tin alloys, copper-tin–lead alloys, copper–tin-nickel alloys, copper–aluminium–iron alloys, copper–nickel–iron and copper–nickel–zinc alloys (nickel silvers, contain up to 27% Zn and 18% Ni)

2.5.3 Oxygen-free coppers

Oxygen-free coppers are classified as a type of wrought copper. They are classified on the basis of their oxygen and impurity content. Oxygen-free coppers do not contain oxide or deoxidants, and are not affected by hydrogen embrittlement. Oxygen-free coppers are termed electrical coppers, due to their outstanding electrical conductivity [11]. They are used in applications that require high conductivity with high ductility, where hydrogen embrittlement is not permitted and in low gas permeability applications [114]. They are used in electronics as speaker wires, amplifier wires and audio/video connector cables. Similarly, they can be used in producing electromagnets, magnetometers and superconductors.

Oxygen-free copper is classified into five types based on nominal composition: 1) oxygen-free electronic copper (99.99 Cu); 2) oxygen-free copper (99.95 Cu); 3) oxygen-free extra-low-phosphorus copper (99.95 Cu, 0.003 P); 4) oxygen-free silver-bearing copper (99.95 Cu); and 5) oxygen-free low-phosphorus copper (99.95 Cu, 0.009 P) [114].

2.5.3.1 C10300 Oxygen-free, extra-low-phosphorus copper

The material used in this study is C10300 oxygen-free, extra-low-phosphorus copper. Its purity is 99.95%, and it contains a very small amount of phosphorus, about 0.003% P. Its tensile strength is between 221 to 379 MPa and its yield strength 69 to 345 MPa. It has high electrical conductivity, good forgeability and superb hot/cold workability. C10300 is used in applications that demand good conductivity and good welding or brazing properties, such as electrical conductors, busbars and tubular bus [114].

2.6 Severe Plastic Deformation of Copper and Copper Alloys

2.6.1 Influence of HPT on homogeneity in copper and copper alloys

Investigations of the influence of HPT on the homogeneity of copper and its alloys have used microhardness tests and microstructure characterization techniques such as optical microscopy, scanning electron microscopy (SEM), transmission electron

microscopy (TEM), electron back-scatter diffraction (EBSD) and X-rays [46,51,52]. These studies show inhomogeneous microstructures during the early stages of HPT processing, when the centre of the copper disc has coarser grains than the periphery. Grains at the centre of the disc are gradually refined with further rotation, so there is a gradual evolution towards microstructural homogeneity. This behaviour is shown in Figure 2.41 by optical microscopy images of the centre of oxygen-free copper (99.99+ wt% purity) discs processed by HPT at ambient temperature for 1/4, 1/2, 1 and 5 revolutions under a pressure of 6.0 GPa [52].

Another approach to evaluate the microstructural homogeneities is taking microhardness measurements across the diameter of HPT discs. The results for Cu-0.1 %Zr alloy processed by HPT at room temperature by up to 10 turns under an applied pressure of 6.0 GPa [51] are shown in Figure 2.42. It is clear that the hardness values at the centre are lower than at the edge, certainly for less than 5 turns. Initial hardness values for 1/4 turn are Hv ~110 and Hv ~160 at centre and edge, respectively. The hardness gradually increases in the centre with increasing numbers of turns and reaches Hv ~ 160 after 5 turns, while at the edge it remains at Hv ~160.

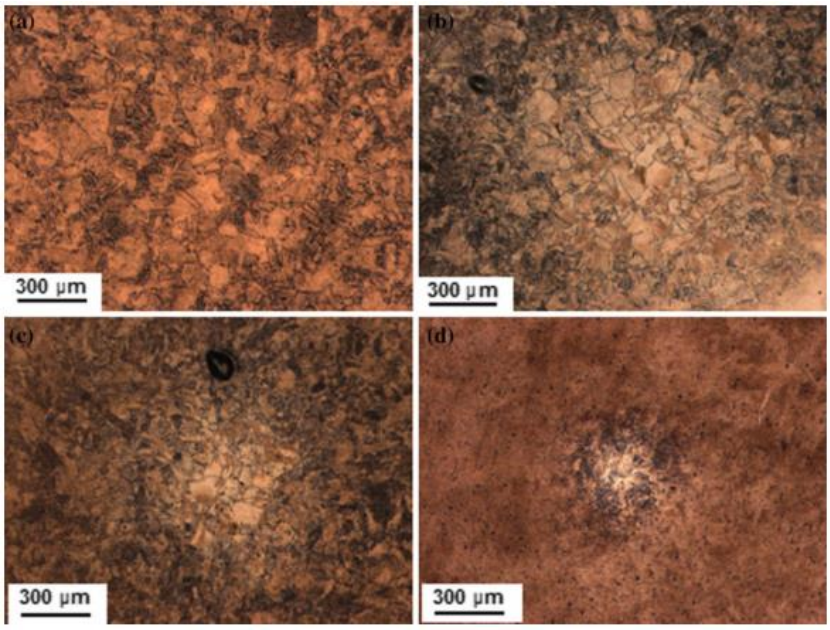

Figure 2.41 Optical microscopy images showing the evolution of homogeneity at the centre of copper discs processed at various number of turns: (a) N = 1/4 ; (b) N = 1/2; (c) N = 1, and; (d) N = 5 [52].

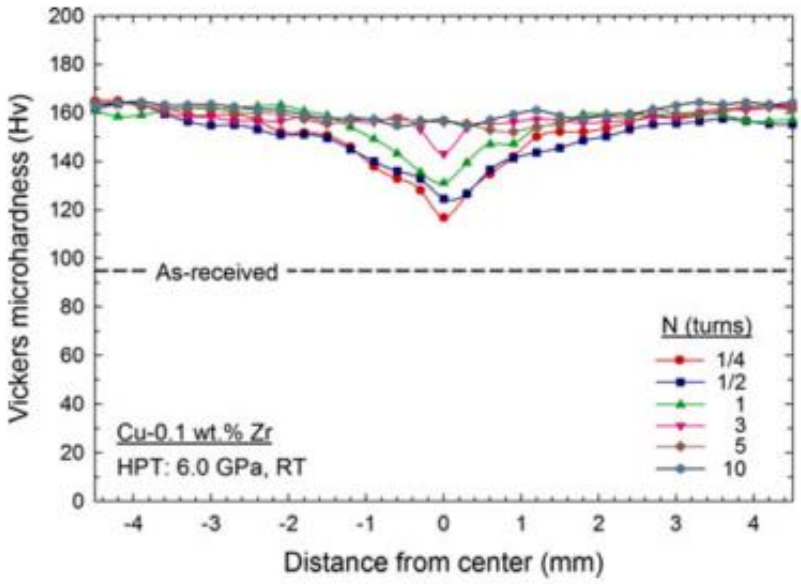

Figure 2.42 Microhardness values across diameter of Cu-0.1 %Zr alloy discs processed by HPT up to 10 turns [51].

A new method to evaluate the microstructural inhomogeneities for the same Cu-0.1 %Zr discs takes microhardness measurements in a rectilinear grid pattern and producing colour-coded contour maps [50]. These illustrate the variation in microhardness distribution over the surface of the disc, as in Figure 2.43. It is clear that the microhardness distribution over the cross-section of the disc is inhomogeneous during the early stages of the HPT process (N = 1/4). There are low hardness values in the central region of the disc, but this region decreases (hardness increases) with further turns. The whole surface of the disc becomes homogenous and reaches the same level of hardness distributions at higher strains (N = 5 turns).

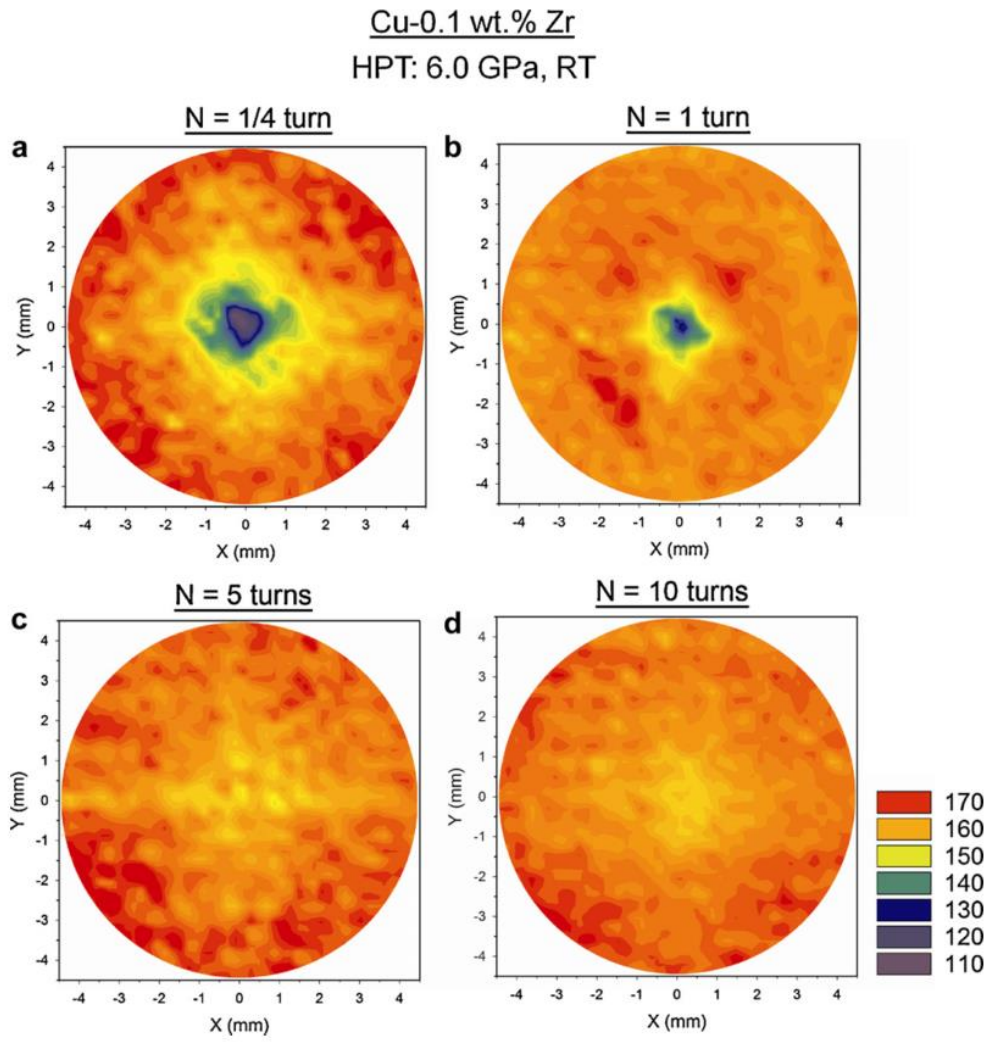

Figure 2.43 Colour-coded contour maps for microhardness distribution over the surface of Cu-0.1 %Zr discs processed by HPT for: (a) N = 1/4 turn; (b) N = 1 turn; (c) N = 5 turns, and; (d) N = 10 turns [50].

2.6.2 Microstructural evolution of copper and copper alloys processed by HPT

Two investigations of oxygen-free copper of 99.99+ wt% purity [52] and Cu-0.1 %Zr alloy [51] provide detailed analysis of microstructural evolution during HPT. The average grain size measurements for oxygen-free copper are shown in Table 2.5 when the discs are processed at ambient temperature through 1/4, 1/2, 1 and 5 revolutions under a pressure of 6.0 GPa [52]. It is clear that the average grain size at the centre, mid-radius and near-edge positions across the disc decrease with increase in the number of

revolutions. At N = 5 turns, the results show an average grain size of ~0.45 μm at mid-radius and near-edge positions, while the average grain size at the centre is ~1.8 μm. Accordingly, the microstructure becomes reasonably homogenous.

The development in the distribution of misorientation angles is presented in Figure 2.44. When N = 1/4, the majority of the misorientation angles at the centre of the disc are LABs with misorientation angles <5º, see Figure 2.44(a). The proportion of LABs in the mid-radius is less, with a slight increase in the HABs, misorientation angles >15º, as shown in Figure 2.45(b). At the near-edge (Figure 2.44(c)), the misorientation angles increase to 60º and HABs are formed. When N = 5, the centre of the disc shows a slight increase in relative frequency of misorientation angles >5º (Figure 2.44(d)). Conversely, there is a significant increase in HABs in the mid-radius and near-edge positions of the disc, as shown in Figure 2.44(e) and Figure 2.44(f), which show the evolution of homogeneous microstructures in highly strained regions.

Table 2.5 Average grain size of OFHP copper at three radial positions in disc plan: centre, mid-radius and near-edge [52].

Sample/position	Average grain size (μm)		
	Center	Mid-radius	Near-edge
$N = 1/4$	15.7	0.68	0.57
$N = 1/2$	8.7	0.63	0.48
$N = 1$	8.4	0.56	0.47
$N = 5$	1.8	0.47	0.45

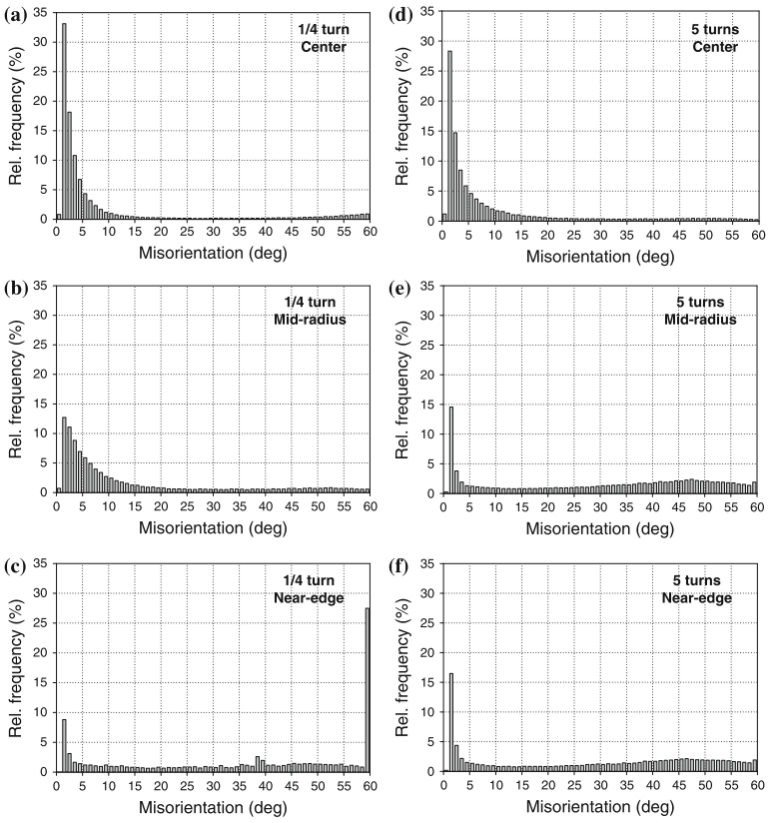

Figure 2.44 Distribution of misorientation angles for N = 1/4 (a–c) and 5 turns (d–f) [52].

Figure 2.45 provides an EBSD mapping of Cu-0.1%Zr discs processed by HPT for 1 and 5 turns under a pressure of 6.0 GPa [51]. These images show the orientation of each grain in different colours. At N = 1 turn, the average grain size at the centre and edge of the disc are ~580 nm and ~410 nm, respectively. With an increase to N = 5 turns, the average grain size in the central region decreases to ~500 nm while the grains at the edges show no change in size. It may be clearly seen in these EBSD maps that the grains are elongated and the microstructure inhomogeneous at N = 1, while at N = 5 the grains become smaller in size and more equiaxed.

The distribution of the misorientation angles of grain boundaries at the centres and edges of the disc are depicted in Figure 2.46. At N = 1, the centre of the disc shows 46% of HABs, that is, lower than at the edges, where the figure is 68%. However, after rotating the disc for 5 turns using HPT, the percentage of grain boundary misorientation becomes 70% at both the centre and edge of the disc.

Figure 2.47 [50] depicts TEM images showing the evolution of microstructures in the discs. After N = 1/4 turn, the central region shows many dislocations of cell structures with unclear (sub)grain boundaries. However; the grains at the edge of the disc are smaller and finer though many of the sub(grain) boundaries are still unclear. After N = 1 turn, there is no noticeable change in the central region of the disc. However, the grain boundaries become sharper and most of the grains more equiaxed. After N = 5 turns, the microstructure becomes uniform, having equiaxed grains with very sharp boundaries.

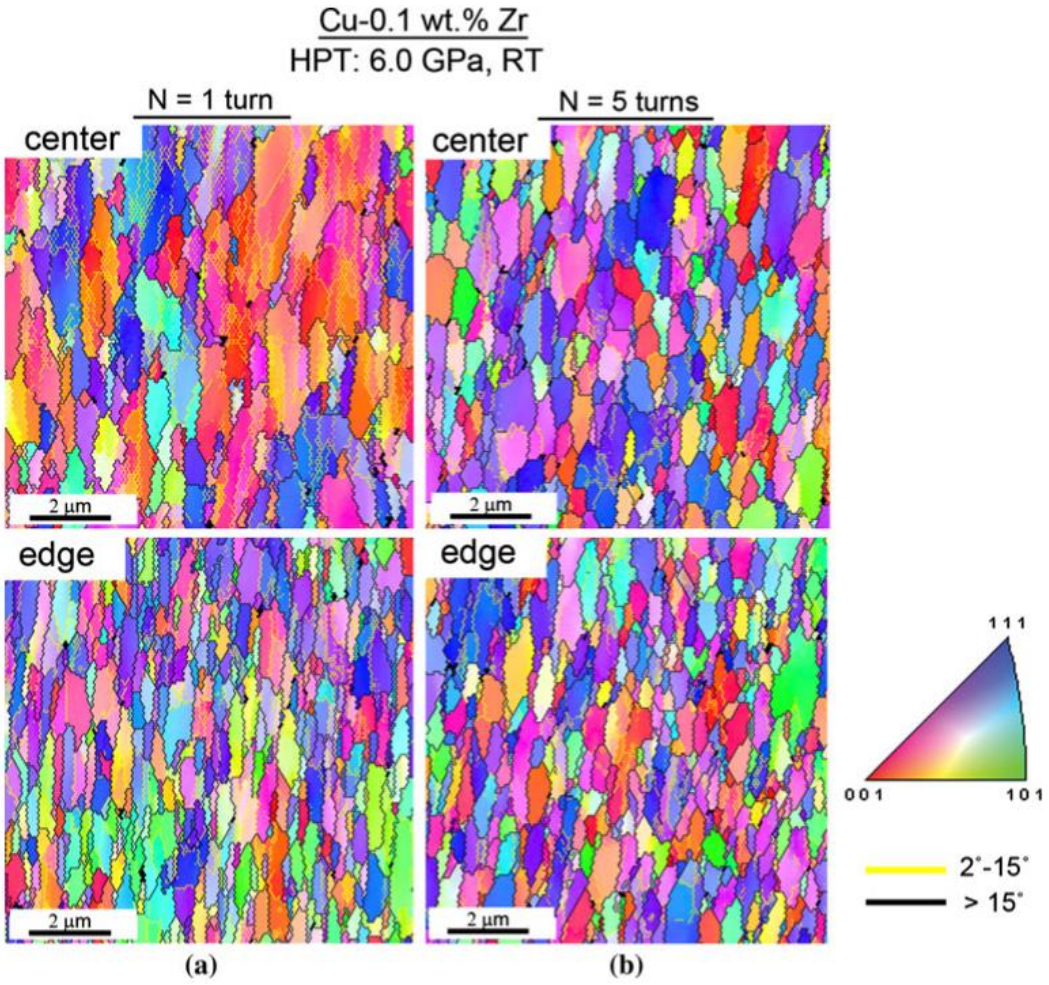

Figure 2.45 EBSD mappings of grain orientation of Cu-0.1 %Zr discs processed by HPT for 1 and 5 turns, for the centre and edge regions [51].

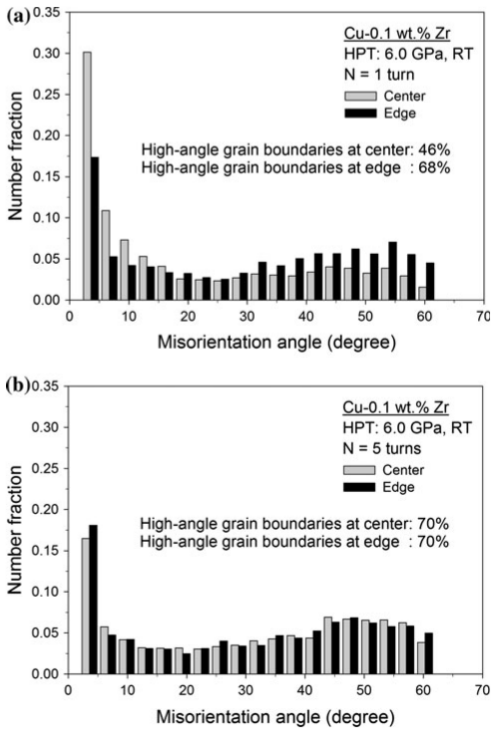

Figure 2.46 Distribution of misorientation angles of grain boundaries at centres and edges of disc [51].

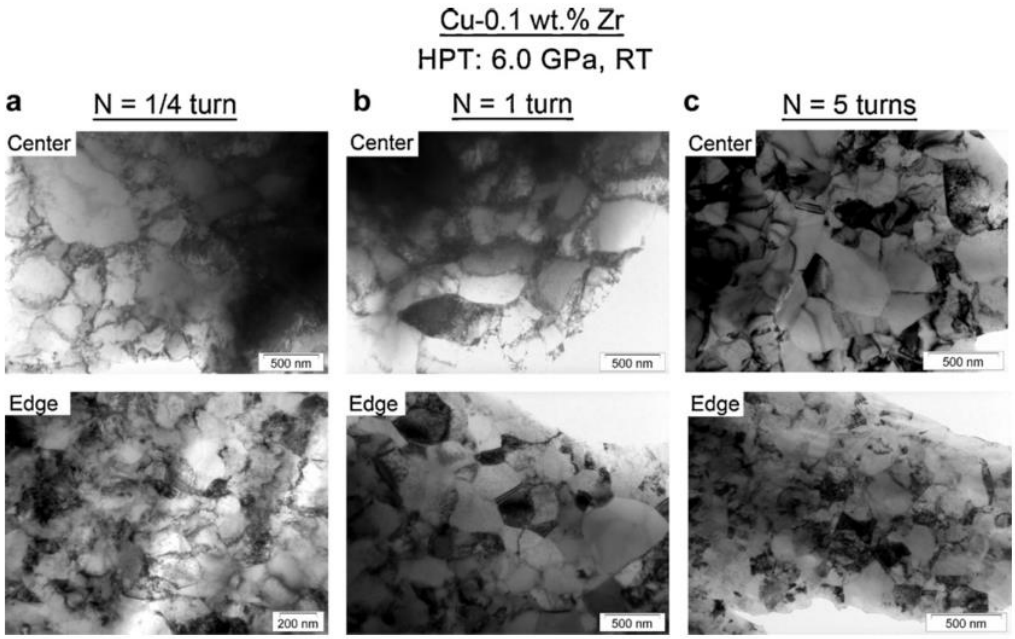

Figure 2.47 TEM images for centre and edge regions of Cu-0.1%Zr discs processed by HPT for: (a) N= 1/4, (b) N = 1 and (c) N = 5 [50].

2.6.3 Influence of ECAP processing on microstructural homogeneity of copper and its alloys

Various studies have been conducted to assess the potential for achieving microstructural homogeneity of copper and copper alloys after processing by ECAP [49,99,115]. A Cu–0.1% Zr alloy was processed by ECAP at room temperature using a channel angle of $\Phi = 110°$ and up to 8 passes [99]. Vickers microhardness measurements were taken on the cross-sectional X-plane, as shown in Figure 2.48, and longitudinal Y-planes of the billet, as shown in Figure 2.49. The results are presented as colour-coded contour maps. It is concluded that the lower region of the billet has lower hardness in the early stages of deformation on both X and Y-planes. Hardness increases with further numbers of passes. After 8 passes, both planes display complete homogeneity, reached at the same rate.

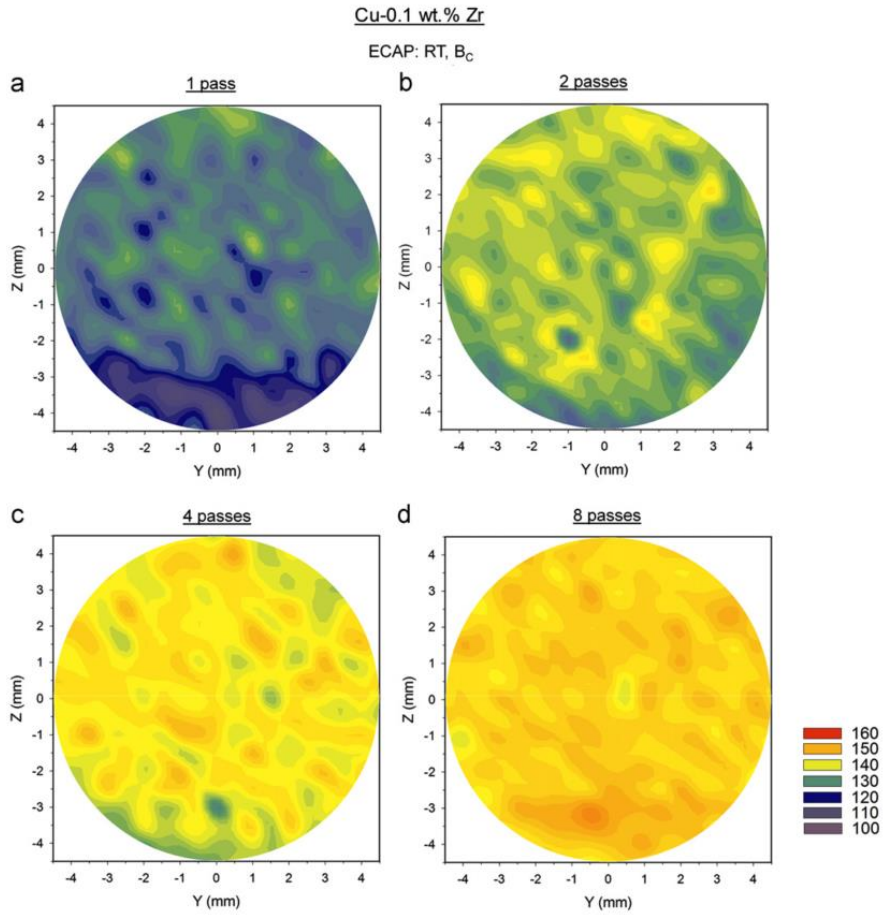

Figure 2.48 Colour-coded contour maps on cross-sectional X-planes for Cu-0.1 wt% Zr processed by ECAP at room temperature for: (a) 1, (b) 2, (c) 4 and (d) 8 passes [99].

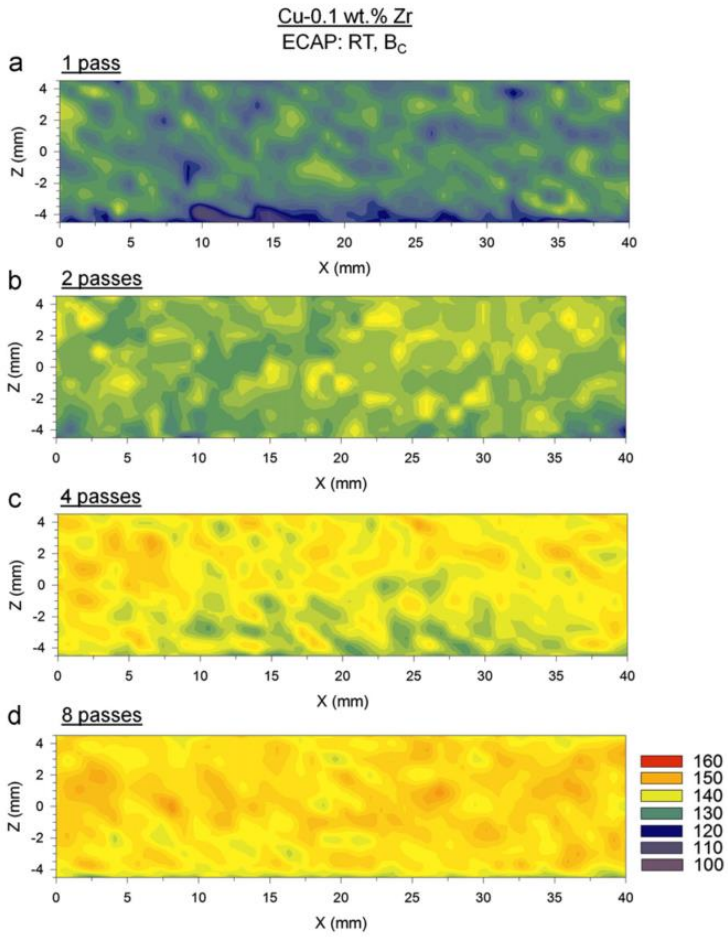

Figure 2.49 Colour-coded contour maps on the longitudinal Y-planes for Cu-0.1 wt% Zr processed by ECAP at room temperature for: (a) 1, (b) 2, (c) 4Pand (d) 8 passes [99].

2.7 Dislocation density and grain size

Dislocation density and grain size are essential microstructural parameters in SPD. Grain size decreases while the fraction of HABs and dislocation densities both increase during the process. The grain size and dislocation density reach saturation level at a certain imposed strain during the SPD process, dependent on technique and the type of material. For example, the saturation level of dislocation density in pure copper is 37×10^{14} m^{-2}, while it is 34×10^{14} m^{-2} for nickel after processing by HPT at room temperature [116]. The values obtained for these materials after processed by HPT are higher than those obtained when the same materials were processed by ECAP at the same temperature, due to the extensive hydrostatic pressure imposed during HPT. Grain size

and crystallite size are plotted as a function of dislocation density for different metals processed by various SPD techniques, as shown in Figure 2.50 [117]. It is clear that the crystallite size is less than the grain size. Also, the smaller the grain and/or crystallite size, the higher the dislocation density; this is associated with the arrangement of dislocations into grain/subgrain boundaries during processing. Saturation level is reached when there is a balance (equilibrium state) between the generation of dislocations and dynamic recovery, where dislocations are annihilated at grain boundaries (GBs).

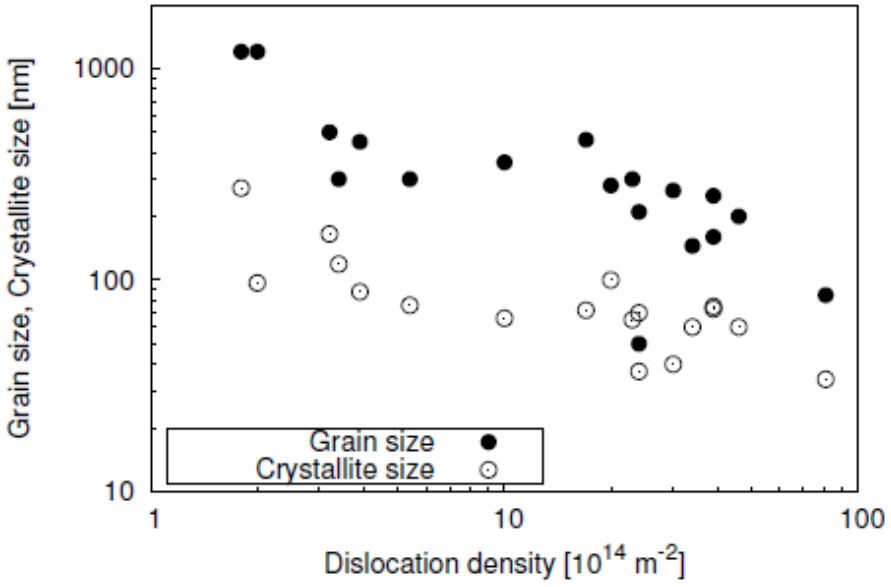

Figure 2.50 Grain size and crystallite size, plotted as a function of dislocation density for different metals processed by various SPD techniques [117].

2.8 Strength and Ductility of SPD-processed Materials

As mentioned earlier, SPD processes have been proven to reduce the grain size of materials to submicron or nanometre level. This grain refinement increases the mechanical strength of materials [118–120]. Also, SPD processing introduces a high density of dislocations, which leads to an increase in strength, while the ductility of the SPD-processed materials decreases [89,121]. Strength and ductility are important mechanical properties for every material, but difficult to achieve together; the strength of materials is enhanced at the expense of ductility and vice versa. Obtaining high strength and good ductility in the same material is the aim of many industries using advanced structural applications for aerospace and sporting goods.

A study of six different aluminium alloys processed by ECAP at room temperature [121] found that there is an abrupt increase in the strength of Al alloys at an equivalent strain of ~1 (see Figure 2.51(a)). Beyond this, increasing the imposed strain yields a gradual increase in strength. Meanwhile, ductility – represented by elongation to failure – after the first pass decreases in several aluminium alloys and remains almost the same under increased strain, as shown in Figure 2.51(b).

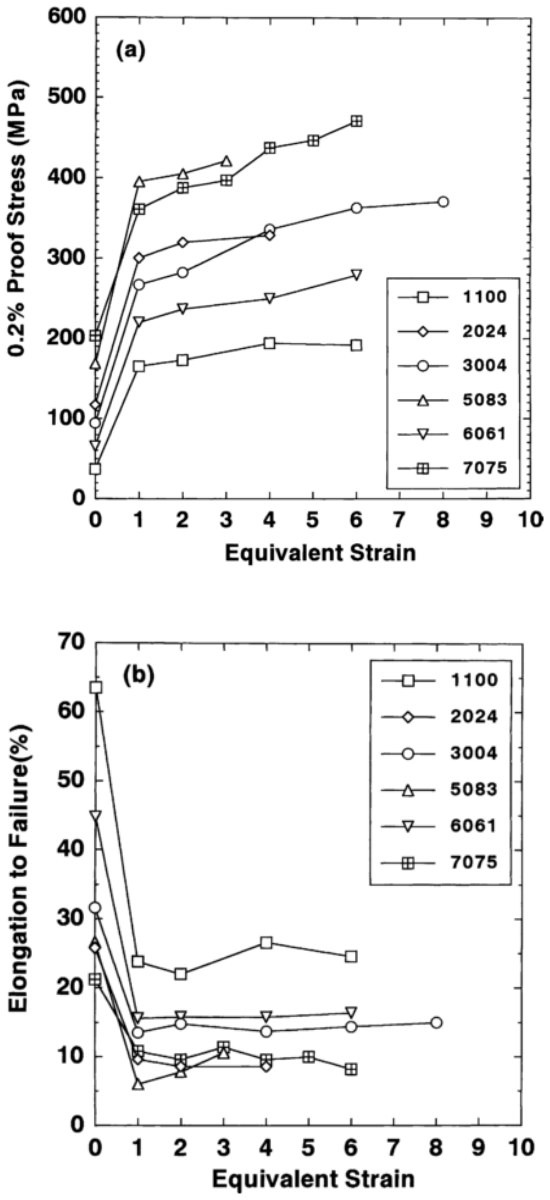

Figure 2.51 For several Al alloys processed by ECAP at room temperature: (a) 0.2 proof stress as a function of equivalent strain; and (b) elongation to failure as a function of equivalent strain [121].

Strength and ductility are strongly affected by the processing method. For example, producing nanostructured materials by consolidating nanopowders introduces defects such as oxidation and porosity that make the material highly brittle [122]. SPD-processed materials are free of porosity and contamination, and have better ductility than materials processed by conventional processes such as drawing, extrusion and rolling. An experiment was conducted on Al-3004 alloy processed by ECAP and cold rolling (CR) [121]. Both processes provided an increase in strength by increasing the equivalent strain, as shown in Figure 2.52(a), however ductility beyond an equivalent strain of ~1 was retained by ECAP processing yet decreased under cold rolling, as shown in Figure 2.52(b).

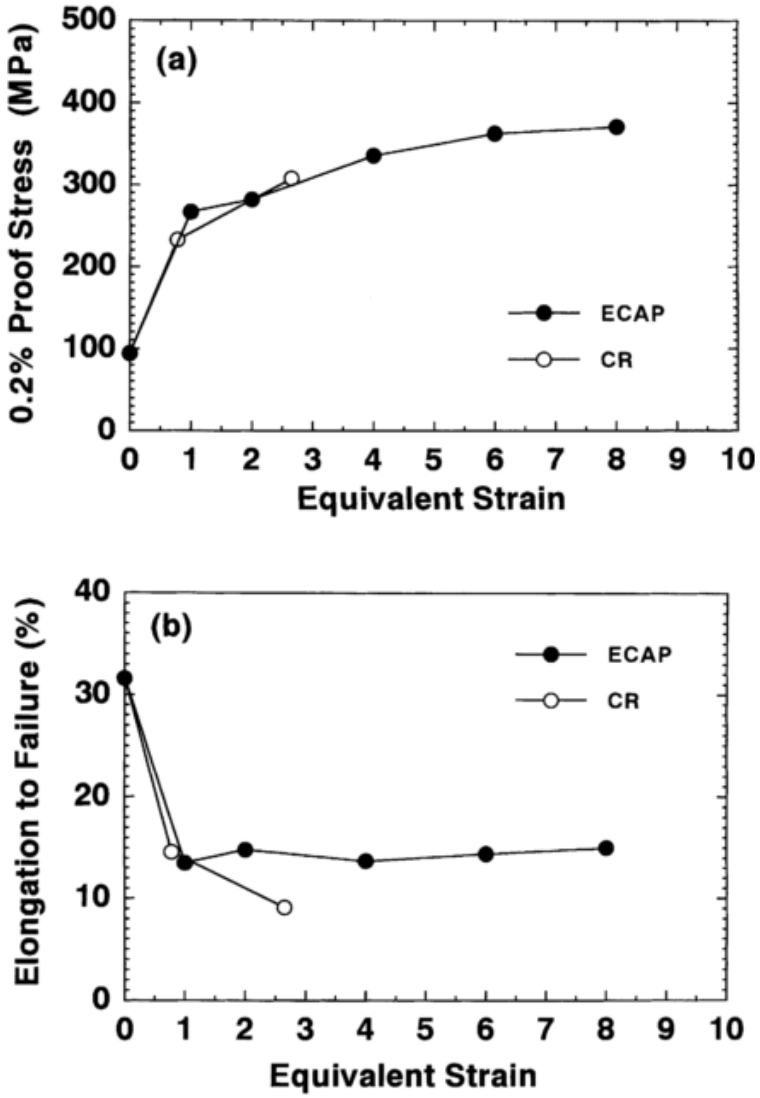

Figure 2.52 For Al-3004 processed by ECAP and cold rolling: (a) strength; and (b) ductility against equivalent strain [121].

Several studies have reported achieving high strength and good ductility in different UFG metals produced by SPD [89,123–128]. These studies suggest various possible mechanisms. The first is a change in the deformation mechanism, from dislocation or twinning to grain boundary sliding [89]. The study was conducted on pure copper (99.996%) and pure titanium (99.98%), processed by ECAP and HPT respectively. The grain boundaries generated by SPD were HABs in a non-equilibrium state. In addition, the strain rate sensitivity increased in both metals after SPD processes, which facilitated grain boundary sliding, thus ductility was improved.

Another possible mechanism is the formation of bimodal structures [123]. Pure copper with a commercial purity of (99.99%) was processed by ECAP at room temperature, then further processed by cold rolling at 93% cold work (CW). The workpiece was cooled at liquid nitrogen temperature (LNT) between consecutive rolling passes, then was annealed for 3 minutes at 200 °C. The result was a bimodal structure of large grain size, at micrometer level, embedded in a matrix of nanocrystalline grains. Thus, strength was increased by the nanocrystalline grains while ductility was enhanced by the larger grains, as shown in Figure 2.53. The same approach when conducted with nickel failed; despite the formation of a bimodal microstructure, strength and ductility were not enhanced simultaneously due to SFE in nickel being higher than in copper. This causes a higher recovery rate during annealing [129]. Another study on cryo-rolled UFG copper at LNT shows an increase in both strength and ductility due to the grain refinement and increase in the fraction of HAGBs. It also shows that the flow stress decreases with reduced thickness of the tensile specimen [126].

Pure copper (99.95%) was processed by ECAP with up to 16 passes, showed increased in strength and elongation with increasing number of passes. This behaviour is explained by the annihilation of dislocations by dynamic recovery, which leads to a decrease in total dislocation density. The work-hardening ability of copper was restored and ductility improved [124].

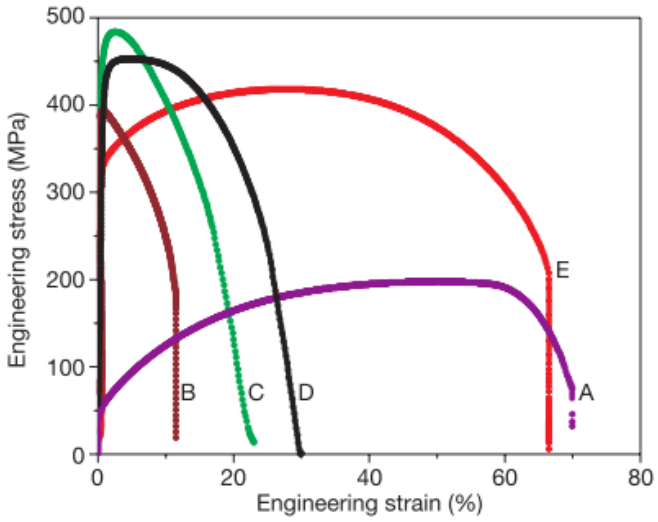

Figure 2.53 Engineering stress–strain curves for pure copper: (a) annealed; (b) rolled to 95% CW at room temperature; (c) rolled to 93% CW at LNT; (d) rolled to 93% CW + 180 °C for 3 mins and; (e) rolled to 93% CW + 200 °C for 3 mins [123].

Another approach to achieving high strength and ductility is to age the material after SPD processing. Nanostructured materials have very small grains, therefore the accumulation of dislocations is limited due to low work-hardening. As a result, nanostructured materials have low ductility. An experiment was conducted on Al-10.8 %Ag alloy processed by ECAP then treated by ageing for 100 hours at a temperature of 373 K to enhance its work-hardening capacity [125]. The results show that hardness values increase, as shown in Figure 2.54.

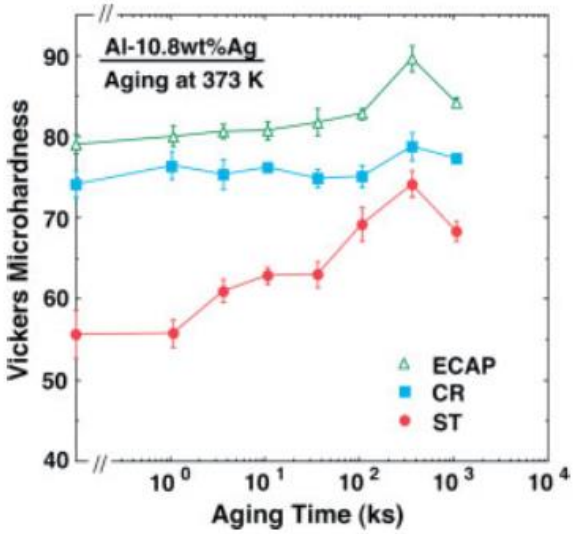

Figure 2.54 Vickers microhardness values against ageing time for Al-10.8 Wt%Ag at 373 K [125]. (CR is cold rolling and ST is solution treatment)

The stress–strain plot in Figure 2.55 again indicates that ductility is enhanced by processing the alloy by ECAP then ageing to increase the work-hardening capacity, which in turns increases the grains' ability to further accumulate dislocations.

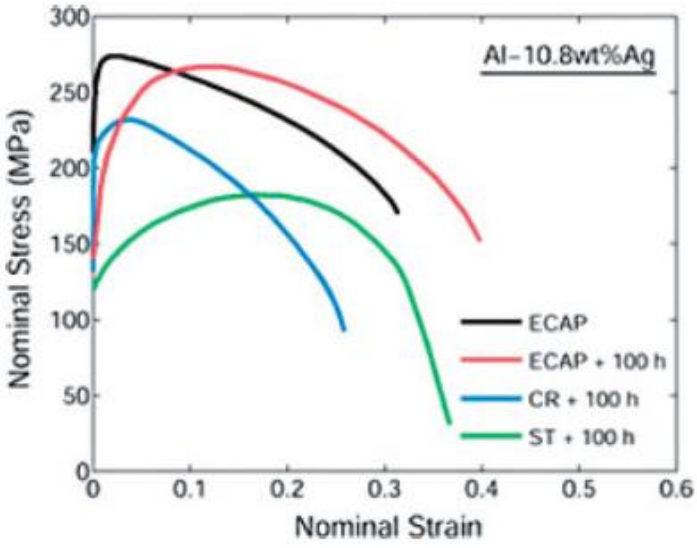

Figure 2.55 Stress–strain curves for Al-10.8 Wt%Ag after various treatments [125].

Introducing a controlled heat treatment to the material after SPD processing has been shown to enhance the strength and ductility of the material. Commercially pure titanium was processed at room temperature by HPT then annealed at temperatures up to 350 ºC for 10 minutes [127]. Analysis reveals that strength is enhanced after annealing the sample at 300 ºC and 350 ºC, as shown in Figure 2.56. The best result is observed by annealing the titanium sample at 300 ºC, when both high strength and good ductility are achieved, as seen in Figure 2.57.

The rearrangement of defects starts at an annealing temperature of 250 ºC without introducing grain growth. The defects in the grain interiors move to near grain boundaries and form two distinct regions of dislocation arrays. One is a highly disordered region that enhances the strength, and the other is a finely ordered structure that improves the ductility of the titanium, as seen in Figure 2.58.

Other studies have reported an enhancement in the ductility at the cost of strength, obtained by applying short-term annealing on metals having low and medium SFE [128]. A copper sample exhibits a yield stress of 600 MPa and low uniform elongation of 1%

after processing by dynamic plastic deformation. After annealing the sample at 120 °C for an hour, the uniform elongation increases to about 8%, but the yield strength decreases to about 300 MPa due to the significant decrease in defect (dislocation) density during the annealing process [128]. It can be seen from previous studies that short-term annealing is a successful method of recovering ductility after processing metals by SPD. However, retaining the strength of UFG metal is a challenging target, as recovery and grain growth are controlled during the heat treatment process.

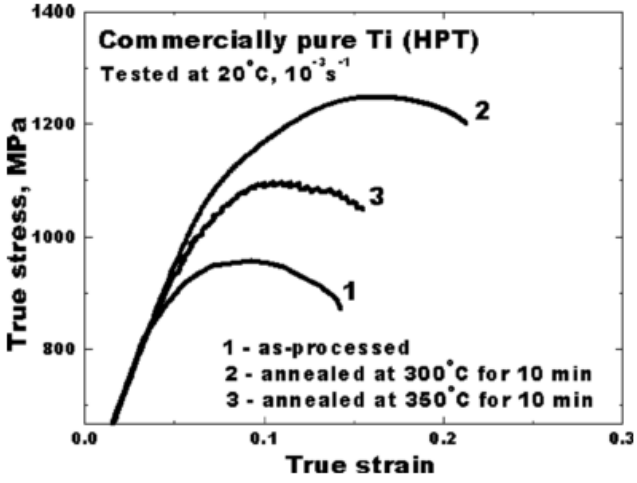

Figure 2.56 True stress–strain curves for Ti: (1) as-processed (HPT); (2) annealed at 300 °C; and (3) annealed at 350 °C [127].

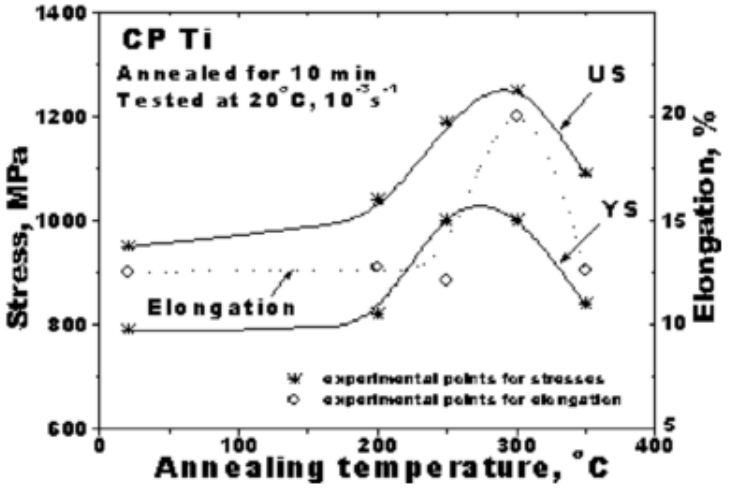

Figure 2.57 Effect of annealing temperature on ultimate strength (US), yield stress (YS) and elongation of Ti processed by HPT [127].

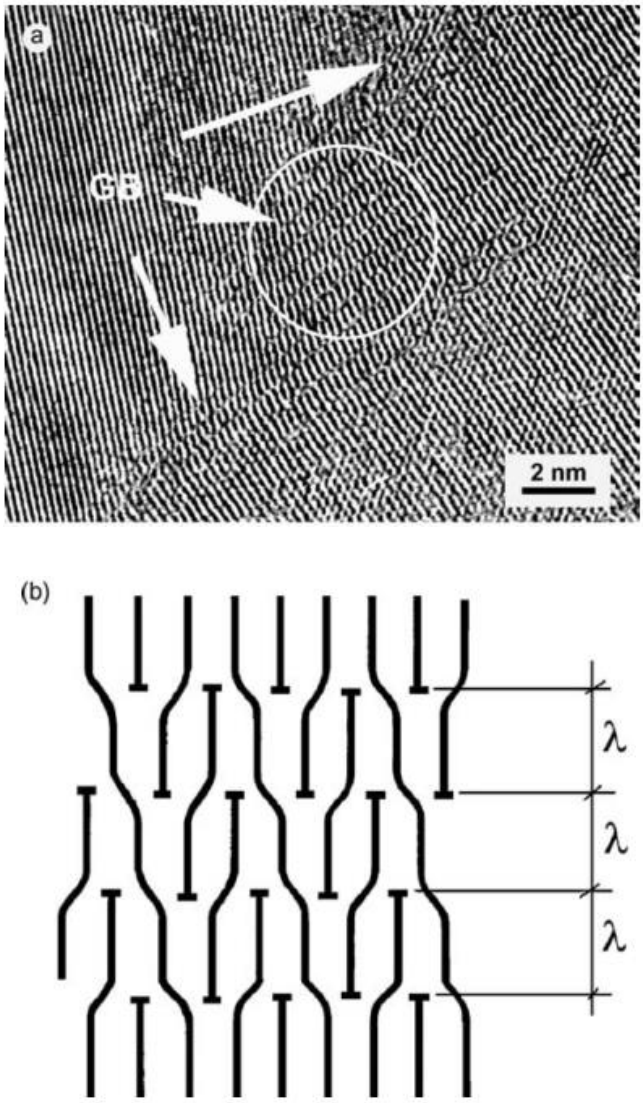

Figure 2.58 (a) HREM shows grain boundary region after annealing titanium at 250 °C for 10 minutes; and (b) ordered defect structure scheme for titanium [127].

2.9 The significant potential for using UFG materials in micro-forming operations

Micro-forming technology is a manufacturing process that produces very small parts with at least two dimensions in the submillimeter range and is essential for electronic components such as micro systems technology (MST), cellular phones and MP3 players in addition to mechanical parts such as connector pins, miniature screws and contact springs [130]. The demand for these products has increased recently which has made

micro-forming an attractive manufacturing method due to its capability for mass production with controlled quality and low cost [131].

The grain size is an important factor affecting the minimum size of geometrical features produced by micro-forming [132,133]. Reducing the dimensions of miniature parts to less than few microns is difficult because the ratio between the microstructural parameters and the part dimensions changes with miniaturization [13]. As a result, the parts produced by conventional forming processes are hardly used in the micro-forming process. Thus, UFG materials with high strength and good ductility produced by SPD show high suitability for micro-forming applications.

A recent study was conducted on high purity aluminium (99.999%) to investigate the effect of grain size and specimen dimensions on the micro-forming process [134]. The samples were initially processed by ECAP with 8 passes at room temperature using a die with an internal angle of 90°. After ECAP, the samples were tested for their suitability for micro-compressing. The results revealed: (i) that decreasing the grain size and increasing the dimensions of the sample increases the flow stress, (ii) flow stress curves show a transition from strain hardening to strain softening with smaller grain size during the process; and (iii) the surface roughness is enhanced after micro-compression when UFG Al is used. The study shows a significant potential for using UFG materials processed by SPD in micro-forming operations.

2.10 Summary

The definition, objectives, procedures, methods and applications of SPD were briefly explained. The fundamental concept and principles of HPT and ECAP were also explained, as were the experimental factors affecting the processes with their advantages and disadvantages. Furthermore, the basic characteristics of Copper and Copper alloys and their classification and applications have been presented. The effect of both processes on the evolution of microstructural homogeneity of Copper and Copper alloys has been explained. Due to the importance of grain size and dislocation density, the relationship between the two were reviewed.

Strength and ductility behavior for various metals processed by SPD and the method used to enhance both parameters were reviewed in Section 2.8. Since the grain size is a limiting factor in micro-forming operations, there is a significant potential for using UFG materials processed by SPD in micro-forming operations as discussed in Section 2.9.

It can be seen from the literature review that grain size and dislocation density are essential factors affecting the strength and ductility of metals. Several approaches were reported to simultaneously enhance the strength and ductility by grain boundary sliding, bimodal structure, aging, dynamic recovery mechanism and short-term annealing.

Chapter 3: Materials and Experimental Procedures

3.1 Materials

The experiment was conducted using a commercial C10300 oxygen-free copper of a nominal composition of 99.95 % Cu, 0.003 % P. The metal was supplied by Smith Metal Centre in UK in the form of a rod 4000 mm long and ~15.90 mm in diameter.

The diameter of the rod was reduced to 10 mm by machining. For HPT the rod was sliced into discs ~1.5 mm thick, and for ECAP the rod was cut into billets 65 mm long and 10 mm in diameter. The discs and billets were first annealed for an hour at a temperature of 600 °C using a vacuum tube furnace to prevent oxygen contamination during the heat treatment process. Before HPT processing, the thickness of each annealed disc was carefully reduced from ~1.5 mm to ~0.83 mm by mechanical polishing using abrasive SiC papers of 800 and 1200 grit. Optical microscopy and Vickers microhardness were conducted on the annealed disc to provide information regarding the initial condition before SPD processing.

3.2 SPD Techniques

3.2.1 HPT processing

The discs were processed by the HPT facility shown in Figure 3.1 at room temperature under quasi-constrained conditions [135] permitting a limited outflow of material between the anvils for various numbers of turns: N = 1/4, 1/2, 1, 3, 5 and 10. This facility consists of an upper and lower anvil, each of which has a circular depression of 10 mm diameter and 0.25 mm depth. Both were cleaned thoroughly with ethanol to assure a contamination-free process. The disc was placed in the depression on the lower anvil, then the lower anvil was moved upward until the disc was compressed by an applied compressive pressure of 6.0 GPa. Torsional strain was imposed on the disc by rotating the lower anvil at a speed of 1 rpm, and the applied pressure was maintained throughout.

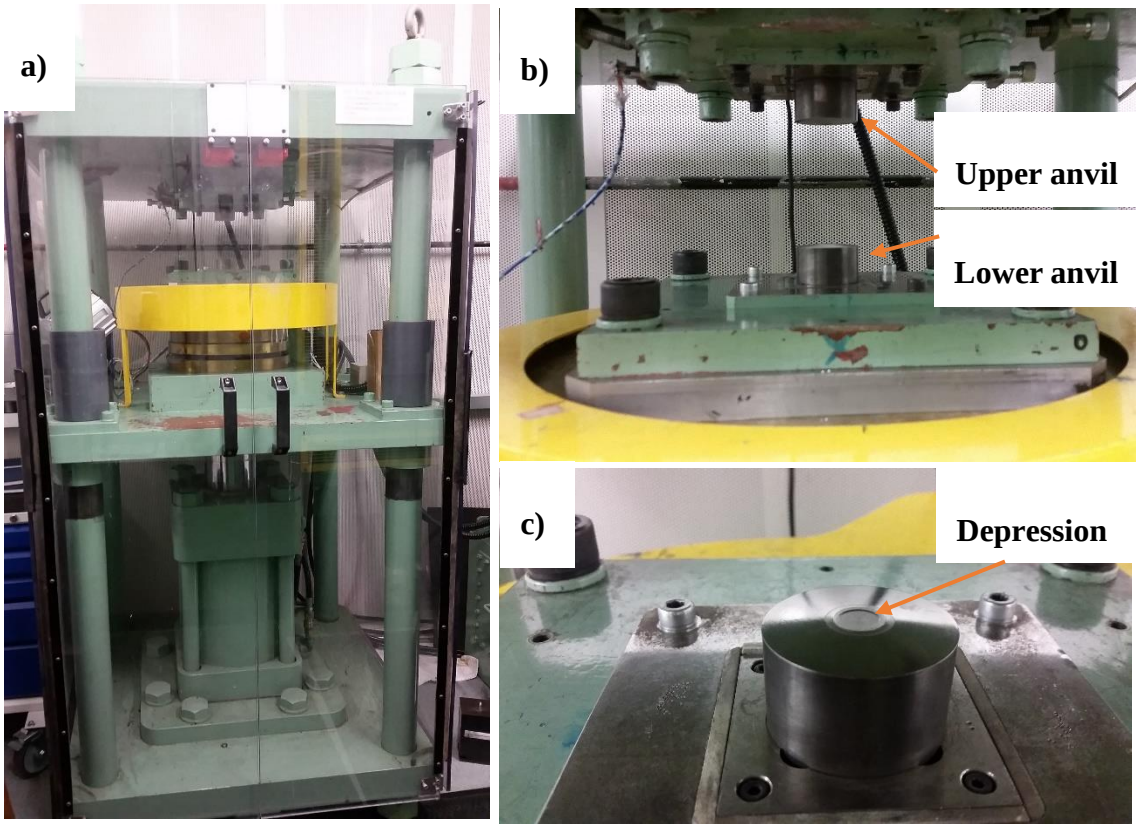

Figure 3.1 High-pressure torsion facility in SPD lab: (a) HPT machine; (b) upper and lower anvils; and (c) depression on the face of the anvil.

Since slippage is possible during the HPT process, it is necessary to ensure there is no slippage before conducting the HPT experiment. A straight line was drawn on one side of the disc from the centre to the perimeter. A second line was drawn on opposite face of the disc from the centre to end at the same point as the first line, so the lines were on top of each other. Then the HPT process was carried out at room temperature under an applied pressure of 6.0 GPa for a single turn. The two drawn lines were found to be in their initial positions, indicating that there had been no slippage during the process; if there had been a shift in the position of the lines, this would have indicated the presence of slippage.

The applied pressure of 6.0 GPa corresponds to an applied load of 48 tons. A simple conversion is illustrated below:

The applied load = 48 tons, which equals to 48000 kg

$$\frac{48000\ kg}{0.1019\ kg/N} = 471050\ N = Force$$

$$A = \pi r^2 = \pi(0.005\ m)^2 = 7.854x10^{-5}\ m^2$$

$$Pressure, P = \frac{Force, F}{Area, A}$$

Thus,

$$P = \frac{F}{A} = \frac{471050\ N}{7.854x10^{-5}\ m^2} = 5.99x10^9\ \frac{N}{m^2} = 6.0\ GPa$$

3.2.2 ECAP processing

The ECAP facility is shown in Figure 3.2. The billets were pressed through a solid die that had a channel bent through an internal angle of Φ = 110º and an outer arc of curvature of Ψ = 20º at a ram speed of 3 mm/s. The billets were pressed at room temperature and using a plunger made of H13 tool steel, through 1, 2, 4, 8, 16, 20 and 24 passes. A Molybdenum disulphide (MoS_2) lubricant was used on the billets, plunger and the walls of the die channel before each pass to minimize the friction forces acting on the billets during the pressing. The billets were processed using Route B_C in which the sample is rotated 90° in the same direction between each pass [76]. The heads and tails of the billets were clearly marked, as well as the tops and bottoms as shown in Figure 3.3. Equation 2.7 [64] was used to calculate the equivalent strain after each pass of ECAP. Accordingly, the imposed strain after each pass is ~0.76 and the maximum accumulated imposed strain was ~18.

$$\varepsilon_N = \frac{N_{ECAP}}{\sqrt{3}}\left[2\cot\left(\frac{\Phi}{2}+\frac{\Psi}{2}\right)+\Psi\mathrm{cosec}\left(\frac{\Phi}{2}+\frac{\Psi}{2}\right)\right]$$

For N_{ECAP} = 1; $\varepsilon_1 = 0.76 \times 1 = 0.76$

For N_{ECAP} = 8; $\varepsilon_8 = 0.76 \times 8 = 6.08$

For N_{ECAP} = 24; $\varepsilon_{24} = 0.76 \times 24 = 18.2$

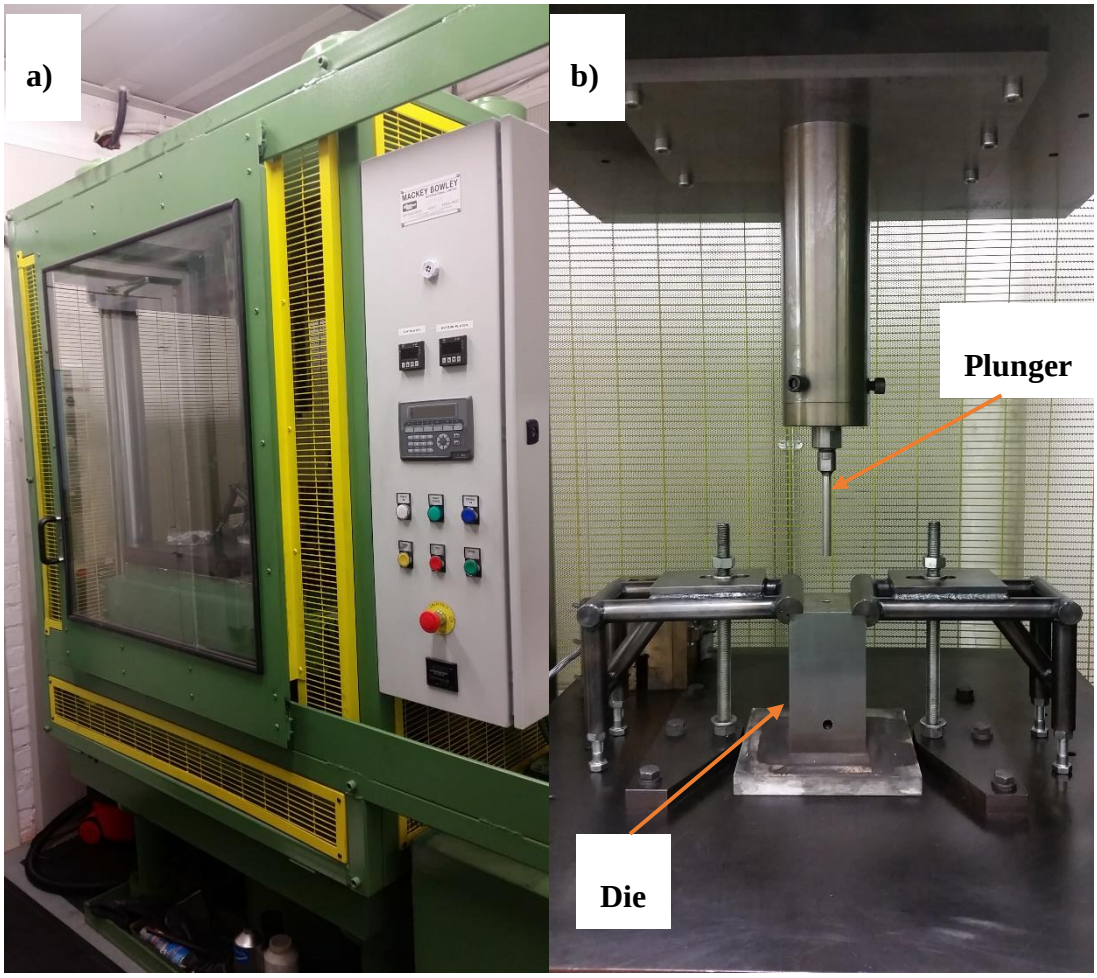

Figure 3.2 ECAP Facility in SPD lab: (a) ECAP machine; (b) Plunger and die used in the process.

3.2.3 ECAP followed by dynamic testing at high strain rate

After ECAP processing, a number of deformed billets were selected to be further deformed by high strain rate dynamic testing methods. The testing conditions are presented in Table 3.1. Billets deformed by 1, 4 and 8 passes were used for the subsequent dynamic testing. Tests were conducted on a Gleeble 3500 machine using a strain rate of 10 s^{-1} at 298 K and 473 K. Other tests were performed using a split Hopkinson pressure bar (SHPB) system with a higher strain rate of 5.5×10^{3} s^{-1}, again the tests were performed at the two temperatures, 298 K and 473 K. Figure 3.3 shows the schematic diagram of the ECAP billet after ECAP processing. Dynamic testing specimens were machined from the ECAP-deformed billets as shown in Figure 3.4. Each specimen was in the shape of cylinder 5 mm in length and 5 mm in diameter.

Table 3.1 Conditions used for dynamic testing.

ECAP conditions (Passes)	Strain rate (s^{-1})	Temperature (K)	Dynamic Testing Method
1, 4, 8	10	298	Gleeble 3500
1, 4, 8	10	473	Gleeble 3500
1, 4, 8	5500	298	SHPB
1, 4, 8	5500	473	SHPB

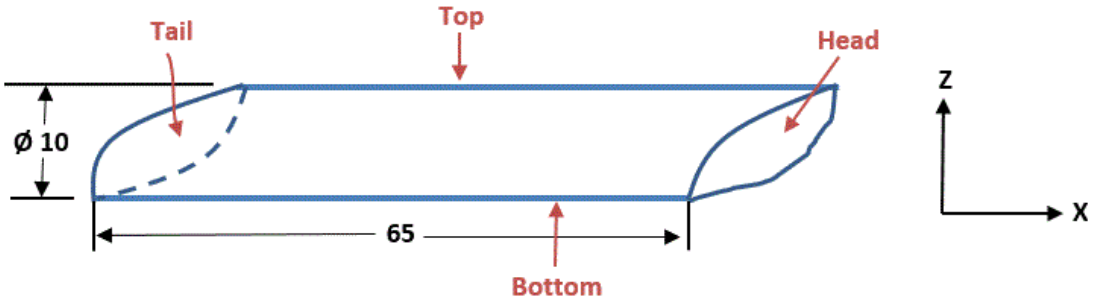

Figure 3.3 Schematic diagram of ECAP billet shape and dimensions after ECAP processing. (Units: mm)

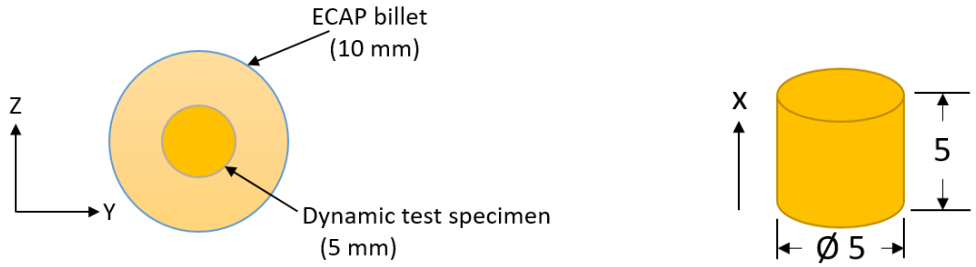

Figure 3.4 Schematic diagrams of wire cutting compressive sample for dynamic testing from the billet after ECAP at a) cross-sectional and b) longitudinal axes (Units: mm).

3.3 Microstructural Characterization

3.3.1 Optical Microscopy

Optical microscopy was carried out using an Olympus BX61 microscope. All HPT and ECAP samples (as-received, annealed and processed) were cold-mounted using Struers EpoFix Kit (resin + hardener). The epoxy cold-mounting was used instead of Bakelite because during Bakelite mounting the temperature reaches to ~175 °C and it may cause a change in microstructure. Samples were ground gradually using 800, 1200 and 4000 grit SiC paper. Afterwards, primary polishing was undertaken using a 1.0 µm diamond paste abrasive, and finally the samples were polished using 0.05 µm colloidal silica solution on a MetPrep cloth known as Chemicloth to attain a mirror-like finish. These surfaces were etched using aqua regia, a solution of nitrohydrochloric acid in a 3:1 mixture of hydrochloric acid and nitric acid.

3.3.2 Electron Backscatter Diffraction (EBSD)

The microstructural characteristics of the oxygen-free copper were investigated in the annealed condition and after processing by HPT and ECAP. All samples were ground with SiC paper of up to 4000 grit. They were then polished with 9, 6, 3 and 1 µm polishing suspensions and finally by a vibratory polishing machine using colloidal silica solution of 0.4 µm. The microstructural data were obtained using an analytical field emission scanning electron microscope, JEOL JSM-7001 F, at an operating voltage of 15 kV. The microstructural data were recorded using EBSD and orientation-imaging microscopy (OIM™). OIM software and a TSL orientation-imaging system were used to collect the data. The EBSD patterns were collected at a working distance of 15 mm with a sample tilt of 70°. The OIM images were plotted using a step size of 0.05 µm. Using the software, high-angle grain boundaries were classified as those with a misorientation between neighbouring measuring points of >15°, with a misorientation difference of 2° to 15° for low-angle grain boundaries (LAGBs).

3.3.3 X-ray Diffraction (XRD)

The X-ray samples were prepared by the same conventional metallographic grinding and polishing as for optical microscopy and then the samples were slightly etched by a mixture of 50 ml of distilled water and 50 ml of nitric acid to remove the thin, deformed, surface layer. A Bruker D2 Phaser X-ray diffractometer equipped with a copper target using Cu Kα (λ= 0.15406 nm) radiation was used to analyse the sample surfaces. XRD patterns were recorded by performing scans of θ–2θ, with 2θ from 30° to 100°. Materials analysis using diffraction (MAUD) software were used to measure the microstructural parameters such as crystallite size, microstrain and lattice parameter. MAUD analysis is based on Rietveld method [136–138], a full-pattern fitting procedure. The pseudo-Voigt functions were used to model the XRD pattern in which the intensities depend on the structure of the phases existing in the specimen [139]. Crystallite sizes and microstrains are determined from the angular dependence of the Cauchy and Gaussian components of the half-width at half-maxima (HWHM) of the diffraction peaks, respectively, according to the Delf model [137].

The dislocation density ρ was calculated by using the microstructural parameters data obtained by MAUD software using equation [140,141]:

$$\rho = \frac{2\sqrt{3}\langle \varepsilon^2 \rangle^{1/2}}{D_c b} \tag{3.1}$$

where $\langle \varepsilon^2 \rangle^{1/2}$ is the lattice microstrain, D_c is the average crystallite size and b is the Burgers vector. Copper is an FCC metal that normally slips on {111} planes in <110> directions and the Burgers vector is $\frac{a}{2}\langle 110 \rangle$, which means b can be written as $\frac{a}{\sqrt{2}}$, where *a* is the lattice parameter representing a close-packed direction, with the shortest repeated length in the crystal [142].

3.4 Mechanical Properties

3.4.1 Microhardness test

Each billet processed by ECAP was cut into two sections, cross-sectional (X-plane) and longitudinal (Y-plane), as depicted in Figure 3.5 and Figure 3.6, respectively. The X-plane is perpendicular to the pressing direction, and the Y-plane is parallel to the side of the billet at the die exit point, see Figure 2.21.

Discs were cut in the cross-sectional direction (X-plane) from the ECAP billets. All sections were gradually ground using 1200 and 4000 grit SiC papers. Afterwards, a final polishing using an abrasive of 1.0 µm diamond paste was used to attain a mirror-like surface finish. The microhardness test was conducted using a Vickers indenter. The microhardness measurements were taken using a Future-Tech Microhardness tester, FM-300, by applying an indentation load of 100 gf and a dwell time of 15 s. Two different procedures were used to measure the microhardness. First, the average values were recorded along the diameter of each disc of ECAP X-plane with 0.3 mm between each point. Four actual indentations were measured around each of these points, separated by a distance of 0.15 mm, then the average of these four points was calculated as depicted in Figure 3.7. In order to avoid any interaction with plastic deformation zones around each indentation, the distance between the indentations was three times the size of the indentation.

Second, Vickers microhardness measurements were recorded over the total surface of the planes of the ECAP billet, using a rectilinear grid pattern as depicted in Figure 3.8. The dots in Figure 3.8 represents the indentation positions over the X and Y planes. For the X-plane, the spacing between each separate indentation was 0.5 mm. These datum points were used to construct colour-coded contour maps that provide a visual display of the distribution of microhardness over the entire surface of each plane. The same procedure was conducted on the surfaces of the HPT discs. For the Y-plane, the spacing between each separate indentation was 1 mm in the pressing direction and 0.5, 1.0, 2.0, 3.0, 4.0, 5.0, 6.0, 7.0, 8.0, 9.0 and 9.5 mm in the vertical direction.

Hardness measurements on HPT samples has the same procedure as the X-plane of ECAP billet. The microhardness tests for HPT were conducted on the annealed and

processed discs at N = 1/4, 1/2, 1, 3, 5 and 10 turns, and for the ECAP billets the hardness measurements were recorded at 1, 2, 4, 6, 8, 16 and 24 passes.

Vickers microhardness measurements were recorded at random positions over the surfaces of the cylindrical specimens used during dynamic testing. The average microhardness value were calculated by recording 25 individual indentations on each specimen.

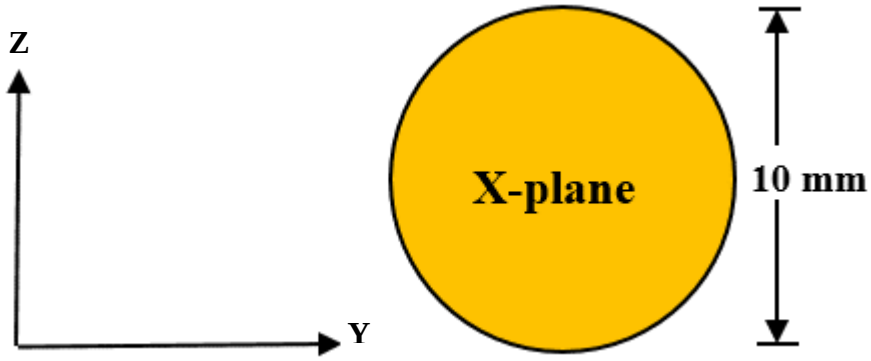

Figure 3.5 Schematic illustration showing the cross-sectional plane (X-plane) of ECAP billets.

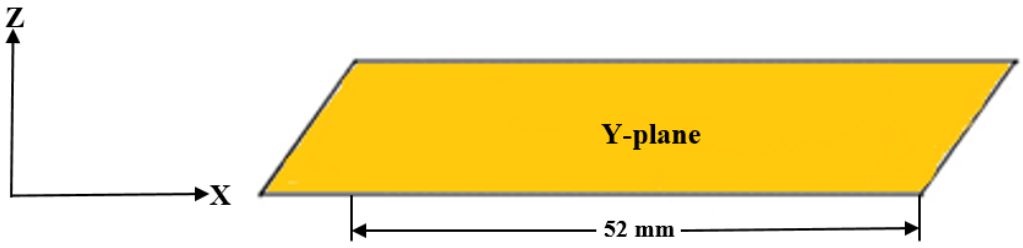

Figure 3.6 Schematic illustration showing the longitudinal plane (Y-plane) of ECAP billets.

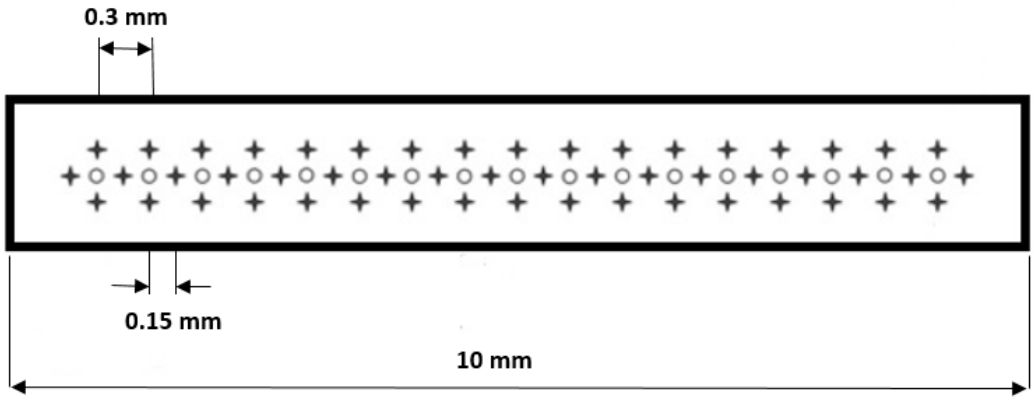

Figure 3.7 Schematic illustration showing the positions of hardness measurements across disc diameter.

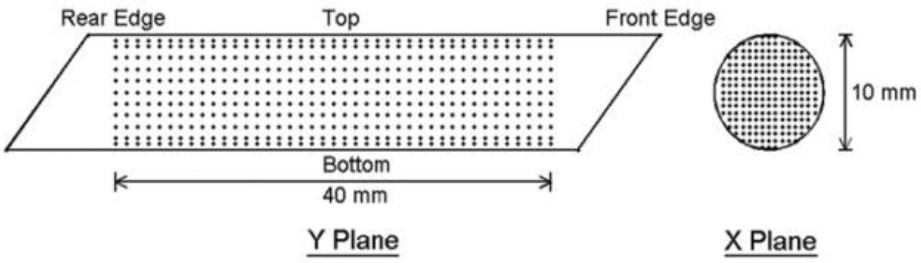

Figure 3.8 Locations of microhardness measurements on cross-sectional (X-plane) and longitudinal (Y-plane) sections of oxygen-free copper billet processed by ECAP [99].

3.4.2 Tensile test

Tensile tests were conducted at room temperature using a Zwick tensile testing machine, and the specimens were pulled to failure for initial strain rates of 1.0×10^{-2} s^{-1}, 1.0×10^{-3} s^{-1} and 1.0×10^{-4} s^{-1}. Two miniature tensile specimens, as shown in Figure 3.9, were cut from each HPT disc using a wire electrical discharge machine. The centre of each tensile specimen was 2 mm from the centre of the disc, to avoid the non-uniform microstructure in the central region. The gauge length was 1.0 mm with cross-sections of 1.0×0.7 mm^2. Four specimens were cut from each ECAP billet with gauge lengths of 4 mm and cross-sections of 3.0×2.0 mm^2, as shown in Figure 3.10. Uniaxial tensile tests are more appropriate than compression tests to assess the ductility of materials, due to the crack propagation and ductile failure instabilities associated with compression tests.

The load and displacement data were recorded using testIIXpert software. These data were used to plot the engineering stress-strain curves and true stress-strain curves. The elastic modulus of copper was used to correct the elastic shifting caused by the machine.

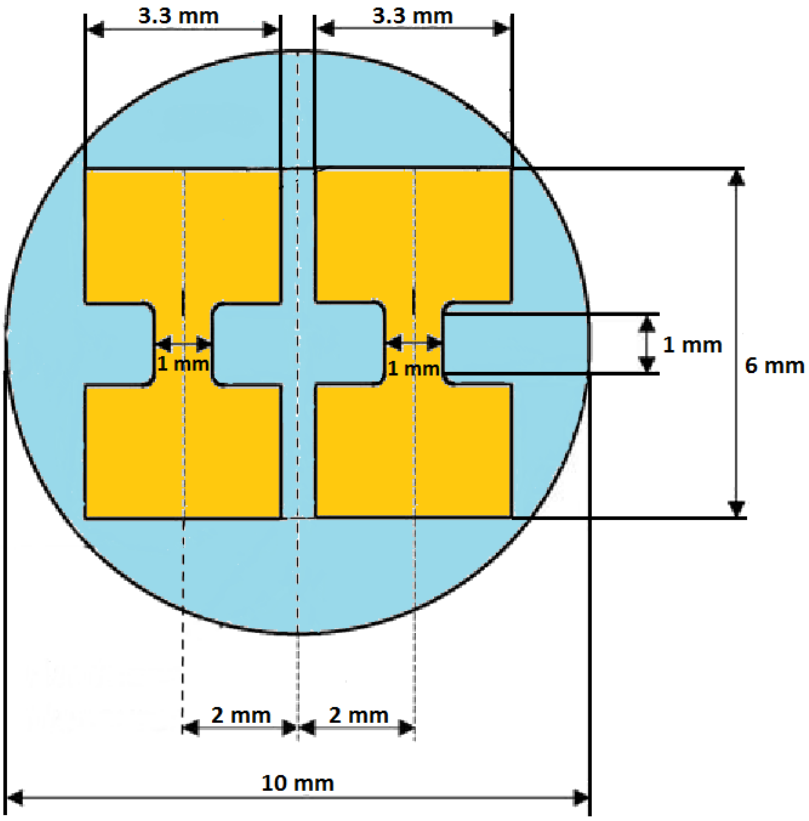

Figure 3.9 Dimensions of the miniature tensile specimens cut from the HPT disc.

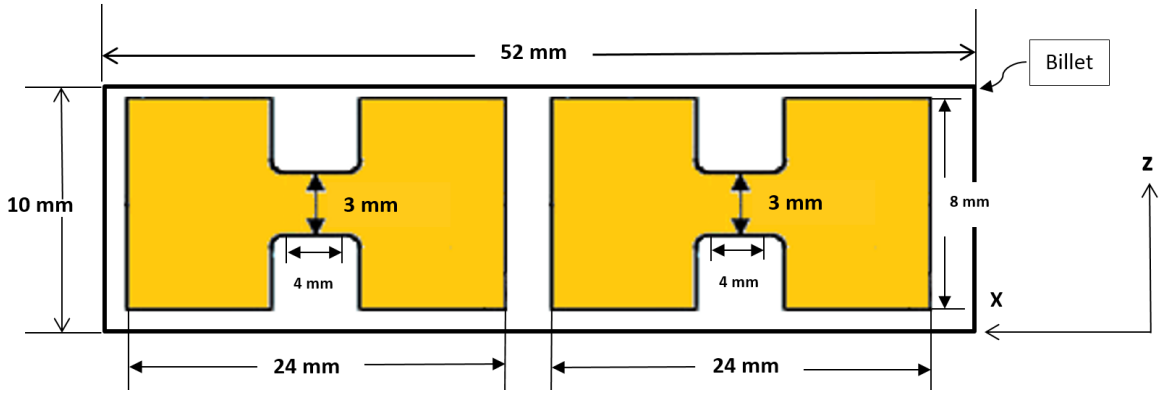

Figure 3.10 Dimensions of the miniature tensile specimens cut from the ECAP billet.

Chapter 4 Microstructural and Microhardness Evolutions of Oxygen-free Copper Processed by ECAP at Room Temperature

4.1 Introduction

The extent of the strengthening of metals by SPD is most effectively measured by recording the hardness values after processing. There are now many reports of hardness measurements after SPD with the values recorded on different sectional planes within the samples. In ECAP, the hardness values are generally measured on cross-sectional planes cut perpendicular to the pressing direction [143] but there are also reports of measurements on longitudinal planes along the lengths of the billets [144]. In HPT, hardness measurements are generally recorded on the upper surface after processing [29,41] but there are also reports of measurements on planes cut vertical to the disc upper surfaces [145] and on various planes cut parallel to the upper surface [38]. All of these results confirm that there is a reasonable level of hardness homogeneity in the billets processed by ECAP whereas in HPT the situation is more complex because the strain varies across the disc diameter and this leads initially to inhomogeneities in both the hardness and the microstructure. By processing HPT discs through fractional numbers of turns such as 1/8 and 1/4 turn, it was established that the hardness gradually evolves with increasing strain to produce a reasonable level of homogeneity [146]. This evolution has been explained theoretically using strain gradient plasticity [147] and the development of a hardness evolution has been examined and summarized for a large number of metallic systems [148].

Both of Chapter 4 and Chapter 5 were prompted by the recognition that most reports of hardness evolution in ECAP or HPT relate to the use of different materials, or possibly even to similar materials but obtained from different sources, in order to document the individual hardness values and the gradual evolution with straining. This use of different materials makes it difficult to obtain an accurate assessment of the true differences between the hardness evolution in ECAP and HPT. Accordingly, the present investigation was initiated specifically to make use of the same material, oxygen-free copper of commercial purity, for processing by either ECAP (Chapter 4) or HPT (Chapter

5) and by conducting all processing at room temperature to avoid any thermal effects. Oxygen-free copper was selected as the test material both because of the interests in using this material in industrial applications and because of very recent reports demonstrating the development of unusual effects in the hardness evolution in this material in the earliest stages of HPT processing [52,149,150].

4.2 Results

In this chapter, the microstructural evolution of oxygen-free copper processed by ECAP for 1, 2, 4, 6, 8, 16 and 24 passes at room temperature are investigated using optical microscopy, EBSD and X-ray diffraction while the hardness evolution is examined using Vickers microhardness test.

4.2.1 Optical microscopy observations

The microstructures of the as-received and annealed oxygen-free copper samples prior to processing, as revealed by optical microscopy, are presented in Figure 4.1. The average grain size of 9.1 μm was measured by the line intercept method. The annealed samples were created by applying a homogenization annealing heat treatment on the as-received sample at 600 °C for 1 hour.

Figure 4.2 shows the optical microstructures (OM) at the cross-sectional planes of oxygen-free copper samples processed by ECAP at room temperature through 1, 2, 4, 6 and 8 passes using a 110º die. Inspection shows that grains become elongated after a single pass. After two passes, the microstructure still consists of elongated grains, detectable by OM. After the fourth pass, the grains become finer and more equiaxed with a higher fraction of distorted grain boundaries, increasing the difficulty of detecting the grain by OM. After 6 and 8 passes, the microstructure is so highly refined that grains cannot be observed by OM. While the severe deformation introduced into the samples makes the microstructure hard to observe, OM images still clearly show that increasing the number of passes increases the grain refinement.

Transmission electron microscopy (TEM) or electron back-scatter diffraction (EBSD) is required for more detailed microstructural analysis.

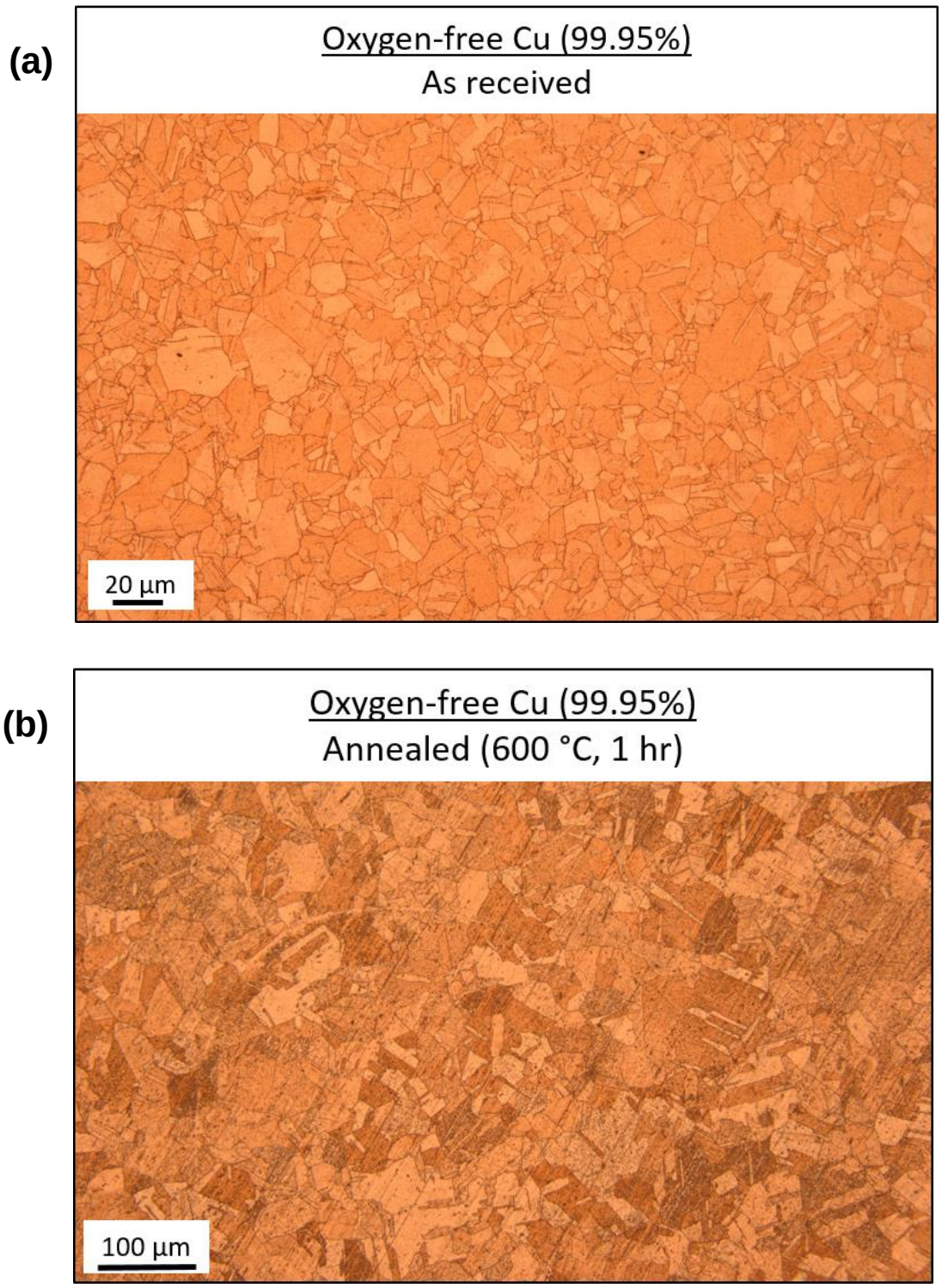

Figure 4.1 Optical micrograph of microstructures of a) as-received and b) annealed oxygen-free copper.

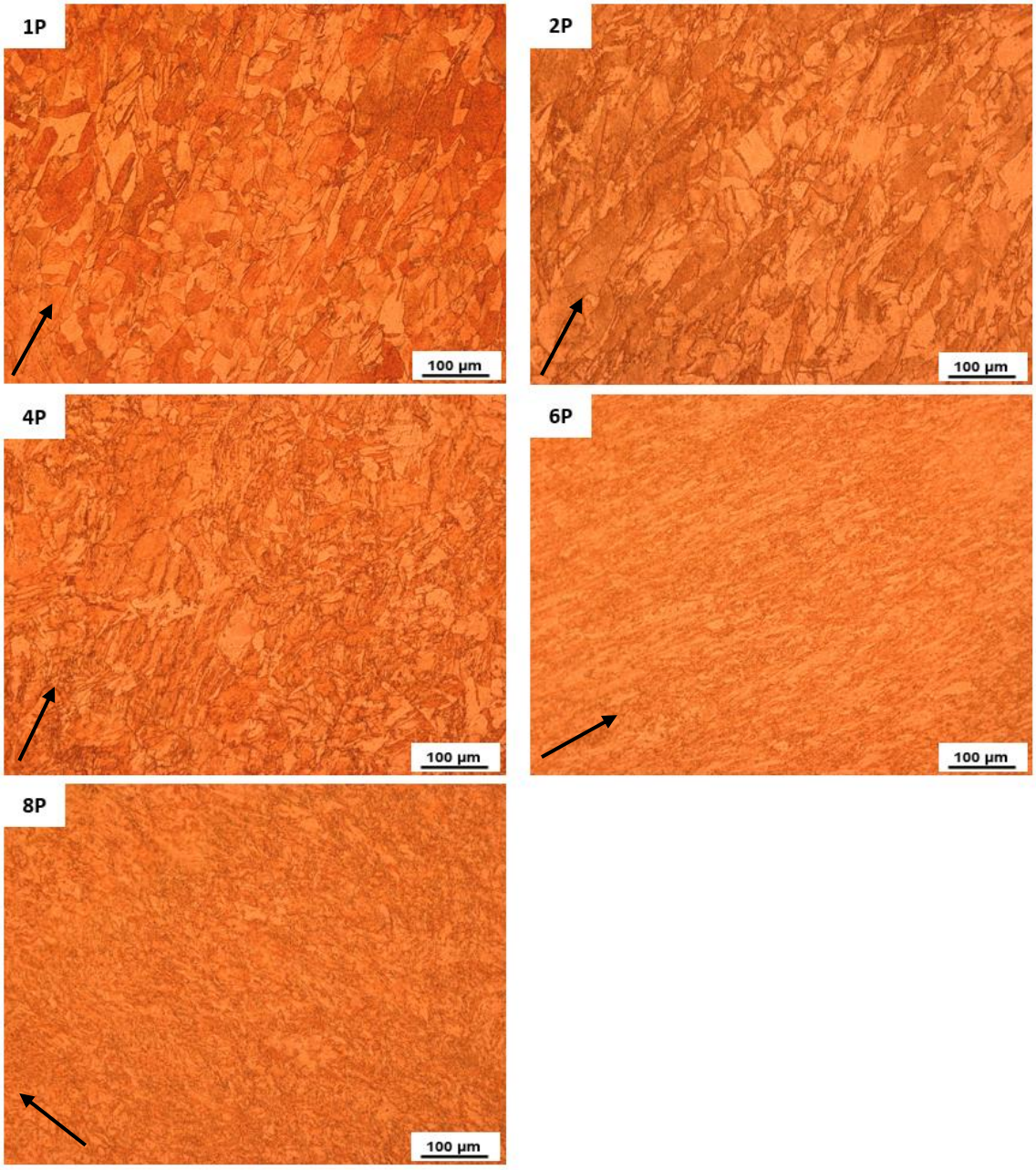

Figure 4.2 Optical microstructures for oxygen-free copper (99.95%) processed by ECAP at room temperature for 1, 2, 4, 6 and 8 passes using Route B_C. (The arrows indicate the pressing direction).

4.2.2 Electron-backscatter diffraction measurements

The microstructures of the annealed and processed copper samples were examined by EBSD. Figure 4.3 presents the initial microstructure of the annealed copper specimens prior to ECAP processing.

OIM was conducted on the longitudinal planes (Y-planes) of the processed billets, as in Figure 4.4 (2 passes), Figure 4.5 (4 passes), Figure 4.6 (8 passes), Figure 4.7 (16 passes) and Figure 4.8 (24 passes). Each colour represents a different grain orientation, as depicted by the triangular legend located alongside each OIM image, and shows the extrusion direction (ED). The grain size was determined by the average spacing between the HAGBs (excluding subgrains).

Inspection of the OIM in Figure 4.3(a) shows that the microstructure of the initial annealed sample was of relatively large grains of average size ~24 μm, as shown in the histogram in Figure 4.3(c). The distribution of misorientation angles for the annealed sample contains a high percentage (~18%) of twin boundaries (annealing twins), and ~70% of high-angle grain boundaries (HAGBs), as shown in Figure 4.3(b).

After 2 passes of ECAP, the microstructure shows large and elongated grains with an average grain size of ~14 μm and ~64% HAGBs, as shown in Figure 4.4. Increasing the number of passes to 4 reduced the average grain size significantly to ~4.4 μm, while the percentage of HAGBs increased slightly to ~66%, see Figure 4.5. A close inspection of the OIM image in Figure 4.5 shows a microstructure with some areas of small grains and some of large, elongated grains.

The microstructure after 8 passes of ECAP has a structure containing both equiaxed grains and elongated grains, see Figure 4.6. The average grain size dropped to ~2.9 μm and the proportion of HAGBs increased to ~71%. With increasing strain, 16 passes, as seen in Figure 4.7, the microstructure became more equiaxed and shows evidence of the presence of coarser grains. After 16 passes of ECAP, the average grain size decreased to ~1.3 μm and the proportion of HAGBs increased significantly to ~80%. Lastly, after 24 passes the microstructure became homogenous with well-defined equiaxed grains of average size ~0.6 μm and ~88% HAGBs, as shown in Figure 4.8.

From the results presented above, it is concluded that the formation of UFG microstructure for oxygen-free copper processed by ECAP is achieved by imposing high strain. The average grain size decreases while the proportion of HAGBs increases with increased number of ECAP passes.

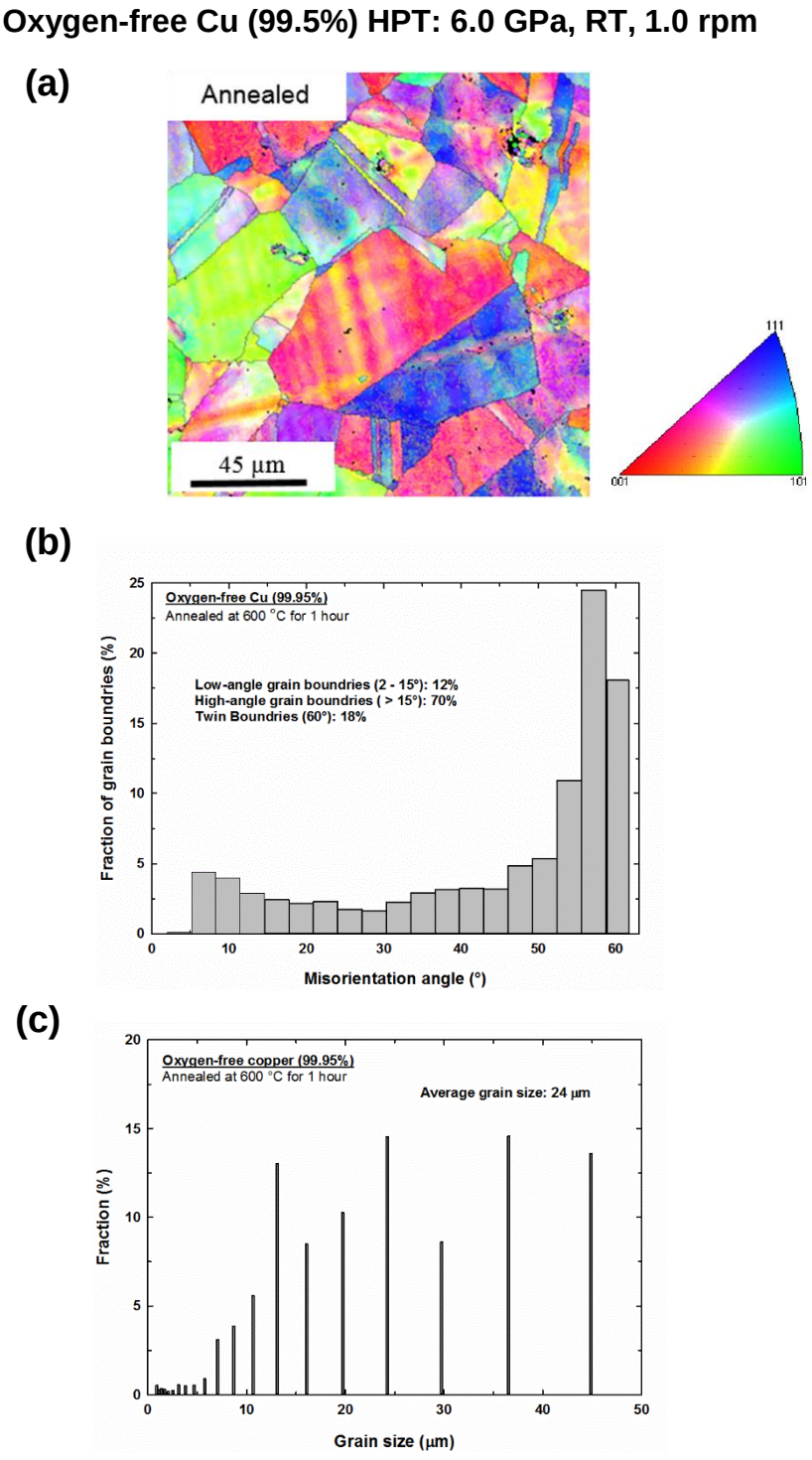

Figure 4.3 Images of annealed oxygen-free copper before processing: (a) EBSD orientation image; (b) distribution of proportion of misorientation angles of grain boundaries, and; (c) average grain size.

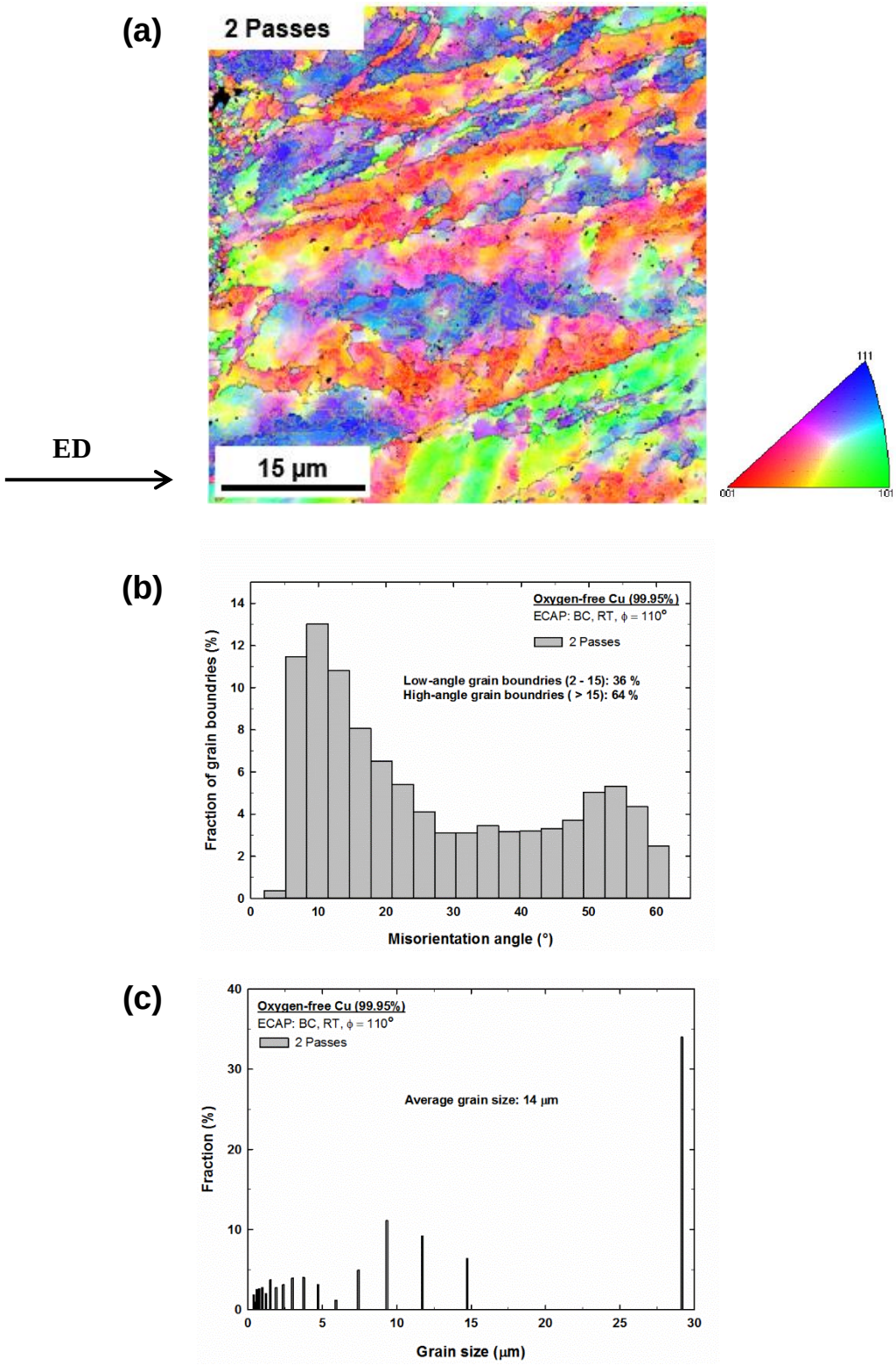

Figure 4.4 Images of oxygen-free copper processed by ECAP for 2 passes: (a) EBSD orientation image; (b) distribution of proportion of misorientation angles of the grain boundaries and; (c) average grain size.

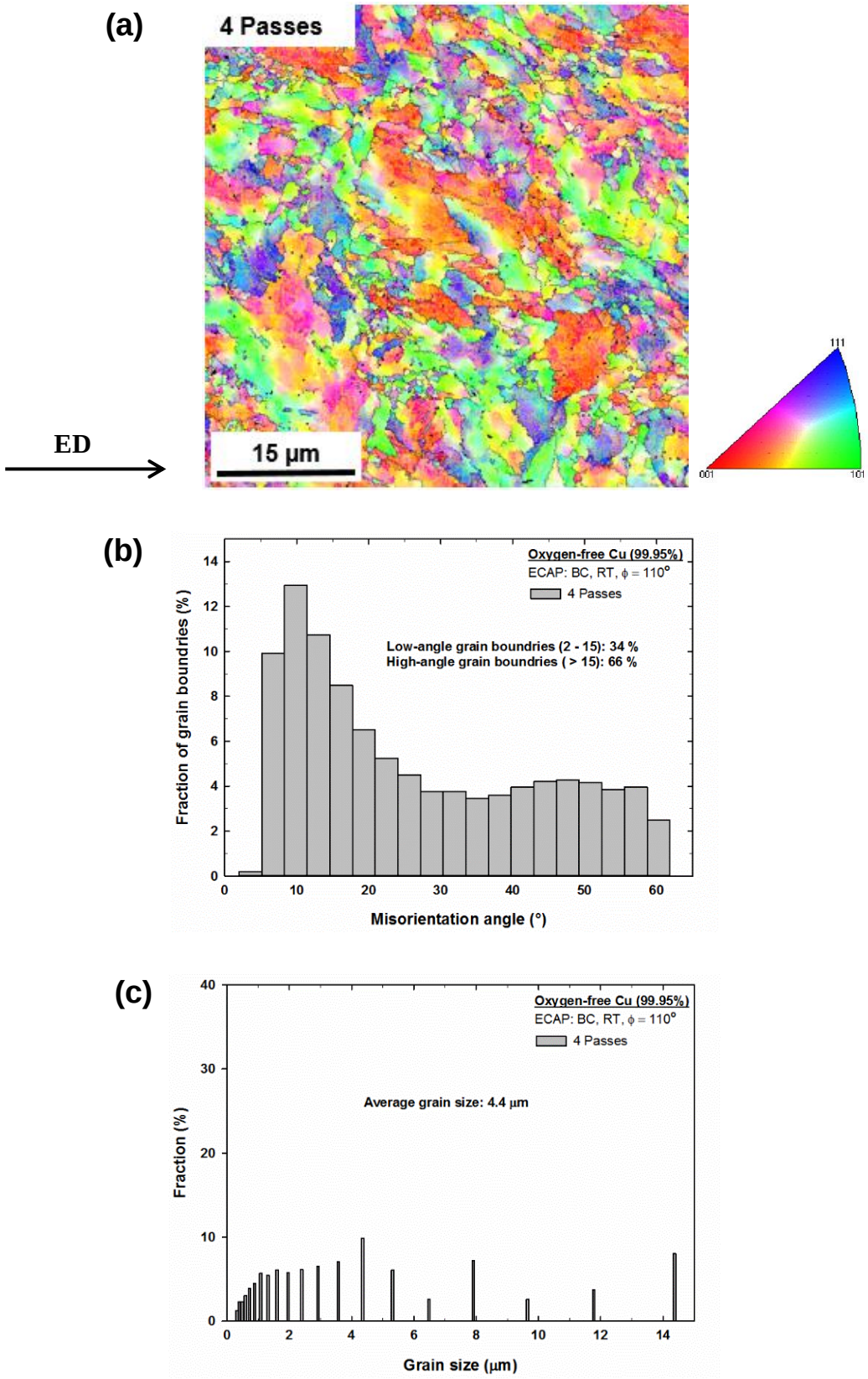

Figure 4.5 Images of oxygen-free copper processed by ECAP for 4 passes: (a) EBSD orientation image; (b) distribution of proportion of misorientation angles of the grain boundaries and; (c) average grain size.

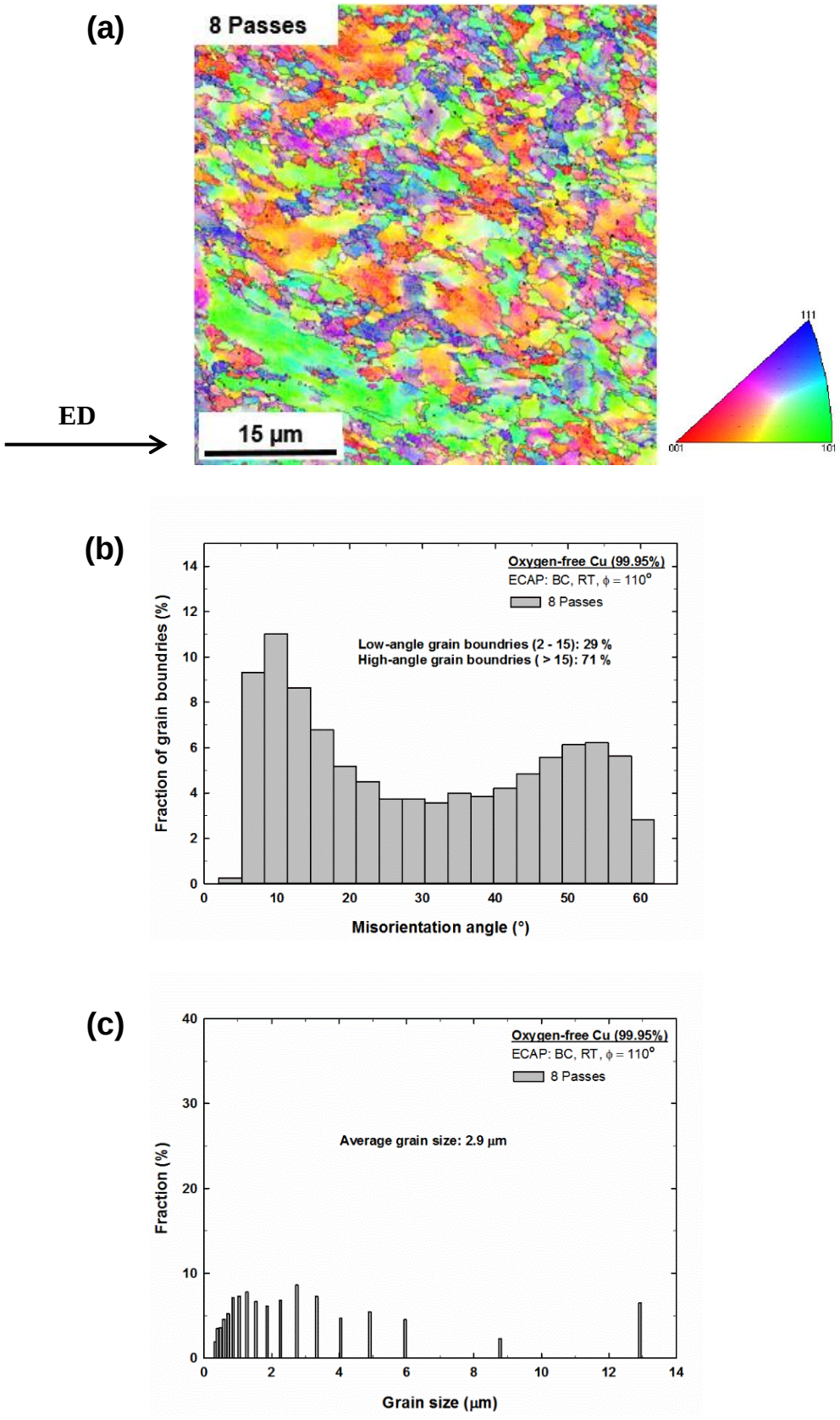

Figure 4.6 Images of oxygen-free copper processed by ECAP for 8 passes: (a) EBSD orientation image; (b) distribution of the proportion of misorientation angles of grain boundaries; and (c) average grain size.

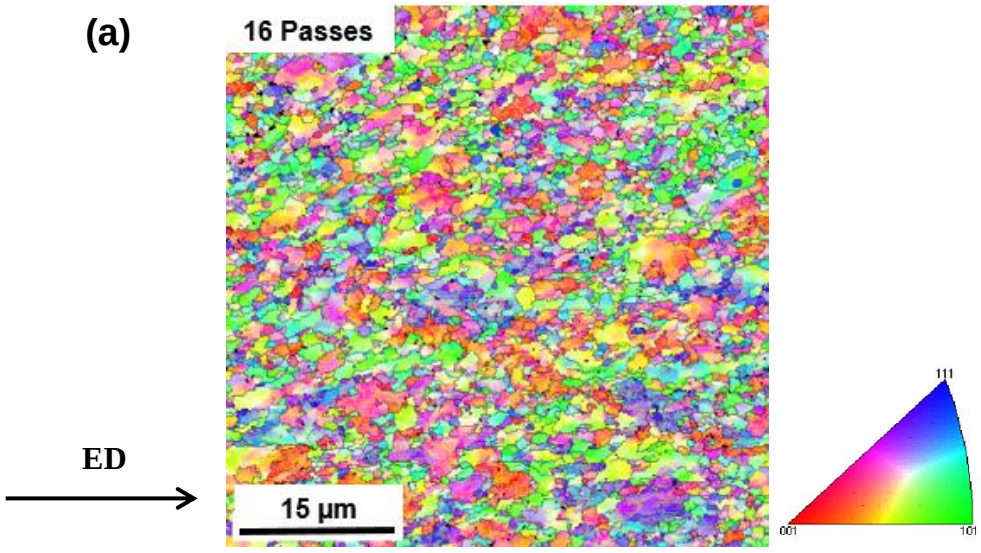

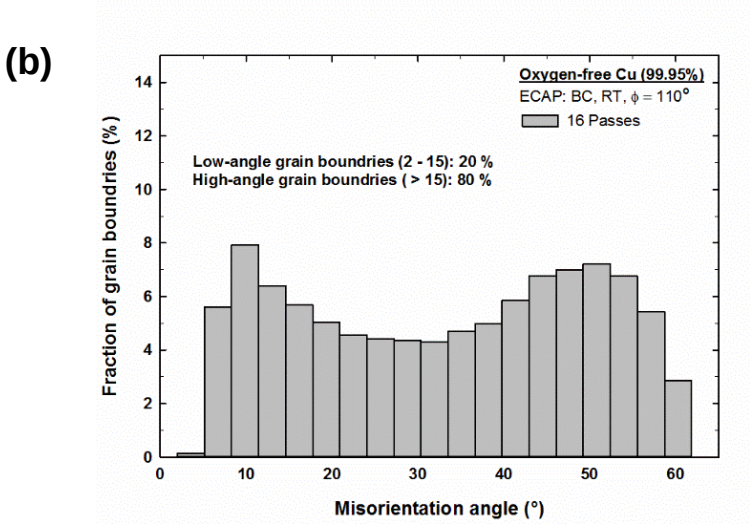

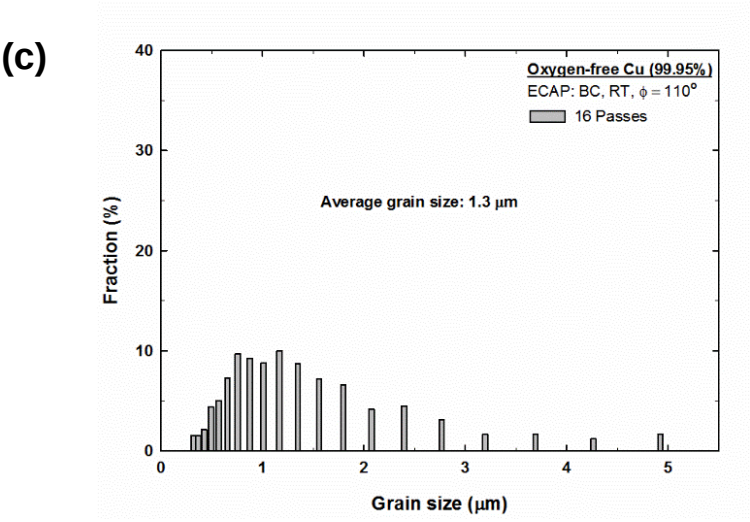

Figure 4.7 Images of oxygen-free copper processed by ECAP for 16 passes: (a) EBSD orientation image; (b) distribution of proportion of misorientation angles of grain boundaries; and (c) average grain size.

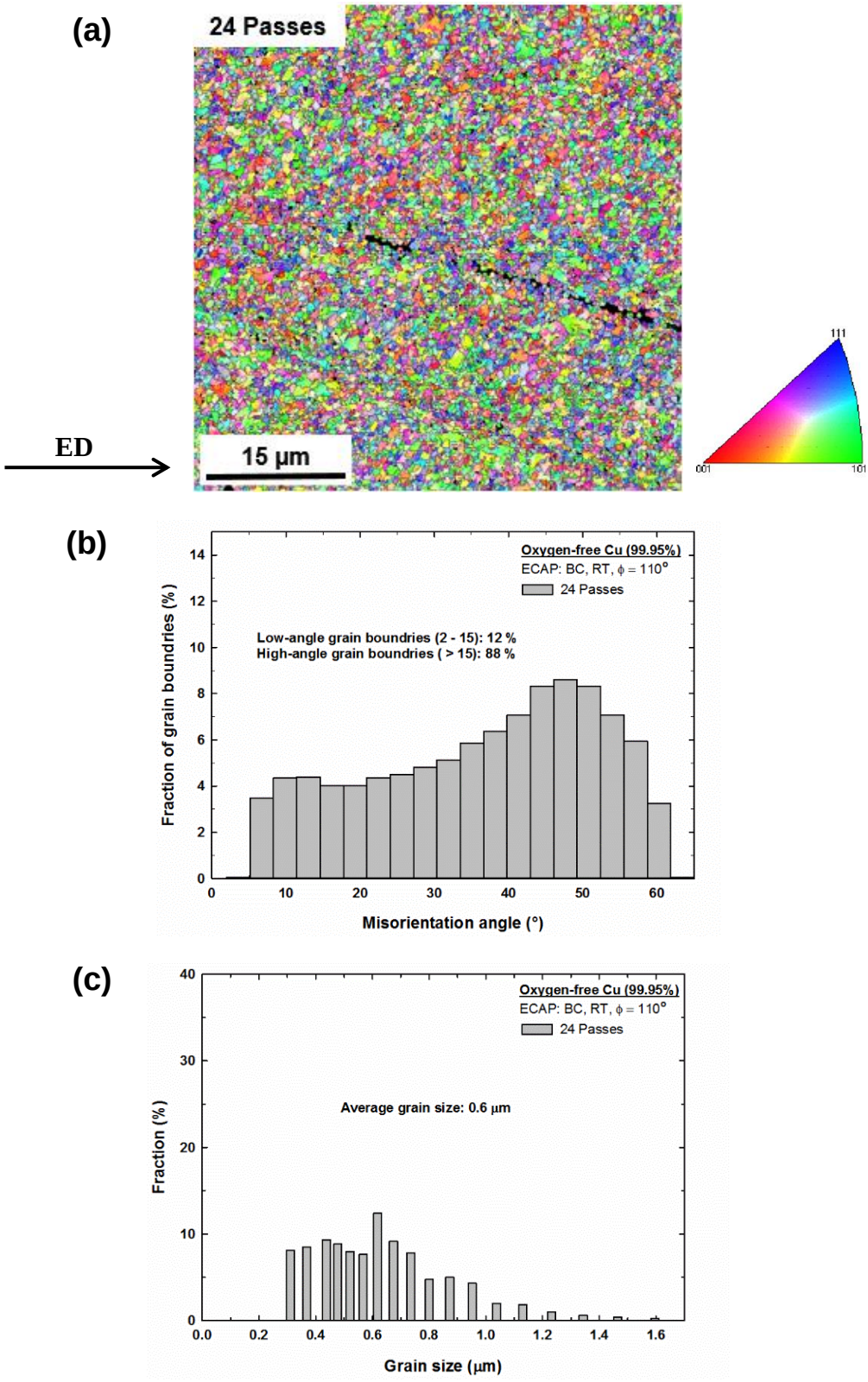

Figure 4.8 Images of oxygen-free copper processed by ECAP for 24 passes: (a) EBSD orientation image; (b) distribution of proportion of misorientation angles of the grain boundaries and; (c) average grain size.

4.2.3 X-ray diffraction analysis

Figure 4.9 shows the XRD patterns of annealed oxygen-free copper samples after processing by ECAP through 2, 4, 8, 16 and 24 passes. Each diffraction peak is marked with its related reflection plane, as follows: (111), (002), (022), (113) and (222). It can be seen from Figure 4.9 that the intensity of the (002), (022), (113) and (222) peaks decreased after 24 passes, whereas the intensity of the (111) peak increased. Moreover, the peaks of the ECAP samples processed through 24 passes show more line-broadening than the annealed sample. This line-broadening is used to calculate the crystallite size for each condition [151,152].

XRD profile broadening is affected mainly by two parameters: the internal microstrain and the small grain size. Figure 4.10 shows the crystallite sizes and microstrain values obtained from analysis of the X-ray diffraction line-broadening, with the error bars calculated using Maud software. A decrease in the crystallite size was observed with increasing number of passes up to 16 passes, followed by a minor recovery after 24 passes. The crystallite sizes after 2, 4, 8, 16 and 24 passes are ~194 nm, ~172 nm, ~126 nm, ~111 nm and ~134 nm, respectively, whereas the average grain size is ~14000 nm, ~4400 nm, ~2900 nm, 1300 nm and ~600 nm, respectively. It can be seen that the crystallite size value determined by XRD after each processing condition is smaller than the average grain size measured by EBSD. This may be due to the fact the EBSD measures the sizes of the grain with HAGBs while XRD measures the mean size of the domains [153,154].

The measured microstrain from the XRD peak-broadening is depicted in Figure 4.10. It characterizes the concentration of crystallite defects in the oxygen-free copper samples. It is apparent from the results that microstrain increases with increasing number of turns to 16 passes, then decreases after 24 passes.

The dislocation density, ρ, was calculated on the basis of the X-ray data using equation 3.1 [140,141]. Dislocation density is defined as 'the total dislocation length per unit volume or, equivalently, the number of dislocations that intersect a unit area of random section' [155]. Figure 4.11 displays the calculated values for the dislocation density and the crystallite size as a function of the number of passes. It is obvious from

Figure 4.10 and Figure 4.11 that the dislocation density and microstrain demonstrate the same tendency after deformation to different number of passes.

The dislocation density in the annealed sample was ~3.9×10^{12} m^{-2} and increased to ~6.8×10^{13} m^{-2} and ~8.2×10^{13} m^{-2} after 2 and 4 passes, respectively. The dislocation density increased significantly to a value of ~3.6×10^{14} m^{-2} after 8 passes, followed by a further increase to a value of ~4.0×10^{14} m^{-2} after 16 passes. Later, a decrease in the dislocation density to value of ~2.2×10^{14} m^{-2} was observed after 24 passes, which shows evidence of some dynamic recovery taking place after 16 passes of ECAP. These results are similar to those reported in pure Cu processed by simple shear extrusion (SSE) through 12 passes [156]. It was observed that dislocation density increased with increasing number of passes from 1 – 8 passes then it was decreased beyond 8 passes.

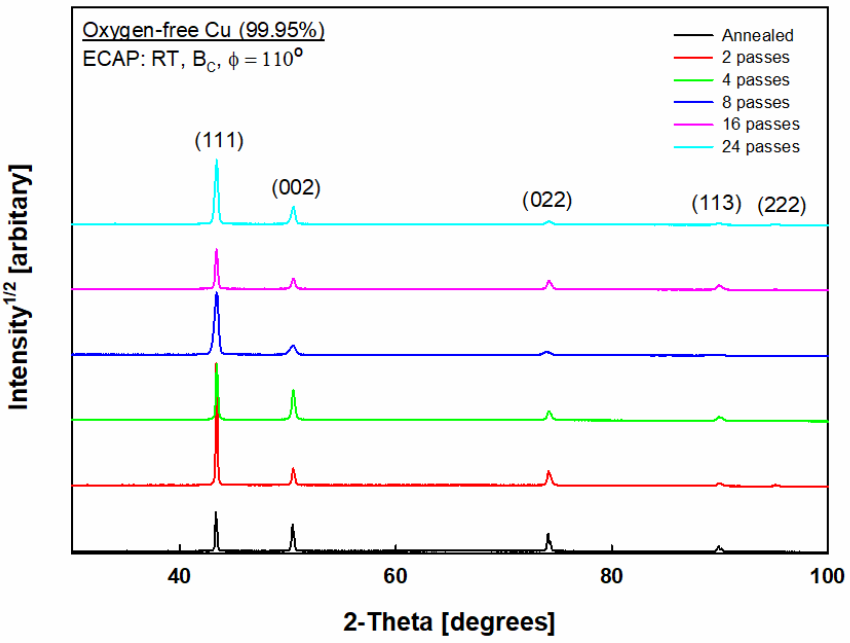

Figure 4.9 XRD patterns for oxygen-free Cu showing the annealed condition and after processing by ECAP through 2, 4, 8, 16 and 24 passes.

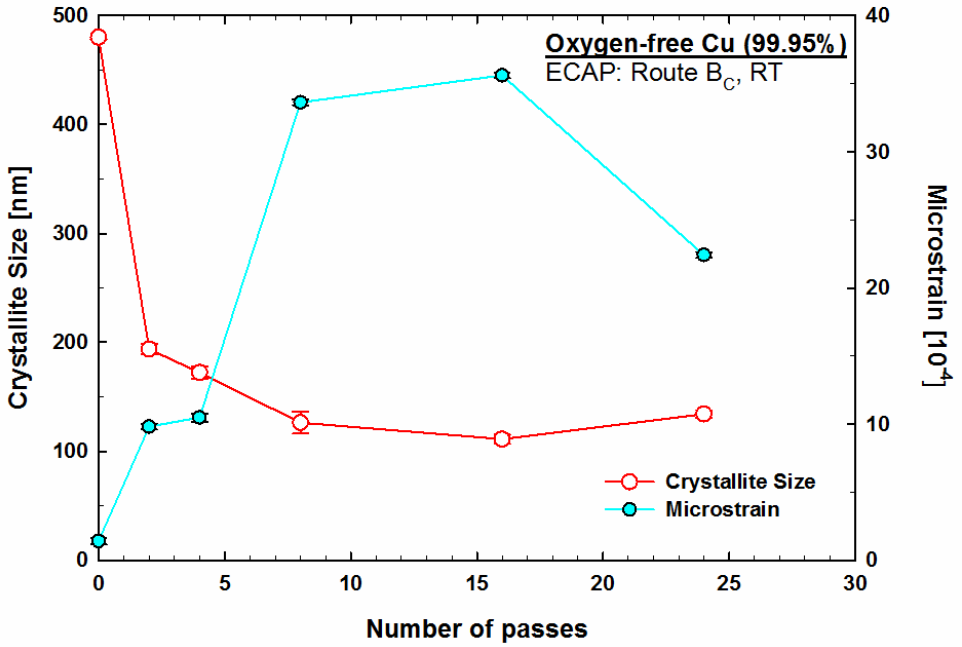

Figure 4.10 Crystallite size and microstrain plotted as a function of number of ECAP passes.

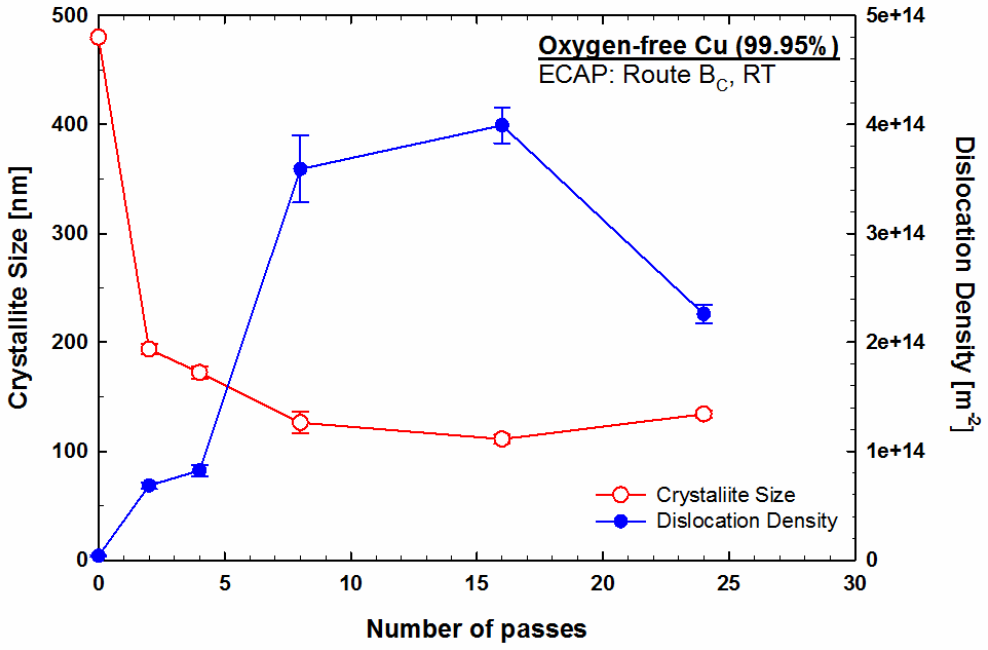

Figure 4.11 Crystallite size and dislocation density plotted as a function of number of ECAP passes.

4.2.4 Microhardness measurements after ECAP

The Vickers microhardness was measured across the diameter in the cross-sectional plane, and over the whole surface in the cross-sectional and longitudinal planes.

4.2.4.1 Hardness values across the diameters of the cross-sectional planes

Vickers microhardness measurements were taken across the diameters in the cross-sectional planes of billets processed by ECAP for 1, 2, 4, 6, 8, 16 and 24 passes. The cross-sectional plane lies perpendicular to the pressing direction (X-plane), as indicated in Figure 2.21. Figure 4.12 shows the values of microhardness with respect to their position on the disc after different number of ECAP passes and Table 4.1 summarizes the average microhardness values along the diameter of the cross-sectional planes.

The average microhardness value for the annealed sample prior to processing is ~41 Hv, represented by the lower dashed line in Figure 4.12. There was significant increase in hardness from the annealed condition after only one pass of ECAP. After the first pass, hardness increased significantly to an average value of ~90 Hv. The hardness measurements along the diameter showed relative homogeneity in the early stages of pressing. After the second pass, average microhardness values increased to ~105 Hv. After pressing the billet through 4–6 passes, average microhardness values were ~112 Hv. After 8 passes the hardness showed relative homogeneity, with an average value of ~115 Hv. With further straining and 16 passes the hardness increased to ~121 Hv. After an additional eight passes, 24 passes in total, the hardness decreased to an average value of ~112 Hv.

The results indicate that the average hardness rises with increasing the strain (ECAP passes) up to a certain level then decreases as displayed in Table 4.1 and Figure 4.12.

Table 4.1 Average microhardness values along the diameter of cross-sectional planes measured after processing oxygen-free copper by ECAP for annealed, 1, 2, 4, 6, 8, 16 and 24 passes.

No. of ECAP passes	Hv
Annealed (unprocessed)	41
1 P	90
2 P	105
4 P	110
6 P	112
8 P	115
16 P	121
24 P	112

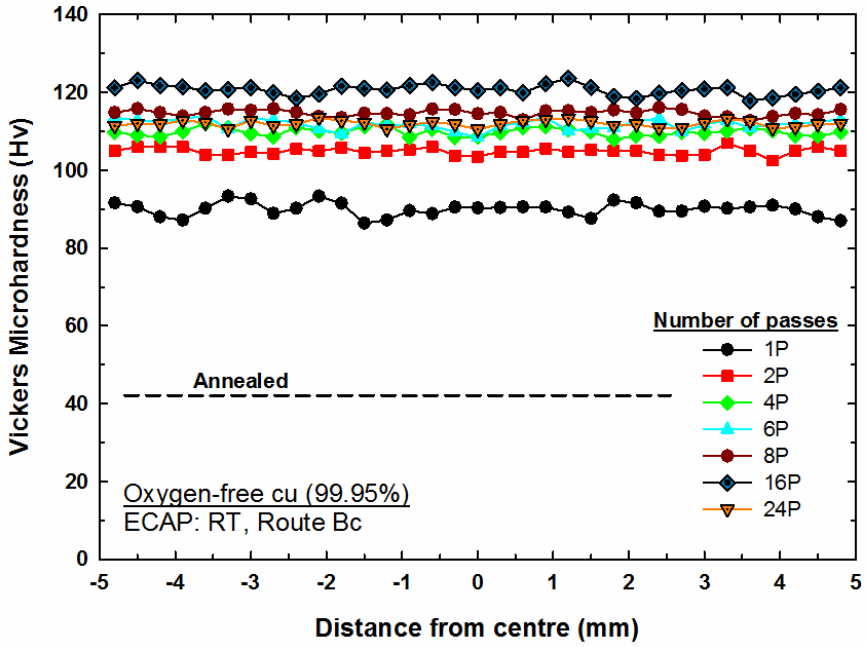

Figure 4.12 Vickers microhardness measurements across the diameter of the cross-sectional plane of oxygen-free copper processed by ECAP for 1, 2, 4, 6, 8, 16 and 24 passes.

4.2.4.2 Microhardness over the entire surface of the cross-sectional plane

After processing the copper billets by ECAP through 1, 2, 4, 6, 8, 16 and 24 passes, the microhardness values were recorded on the cross-sectional planes (X-planes) on a rectilinear grid pattern to produce colour-coded contour maps. Figure 4.13 shows the hardness distribution over the surface of the X-plane for oxygen-free copper processed by ECAP through: (a) 1 pass, (b) 2 passes, (c) 4 passes, (d) 8 passes, (e) 16 passes and (f) 24 passes. The colour key on the lower left shows the hardness values in the range of 40 to 180. Each sequential change in colour represents an incremental step of 20. The (Y, Z) = (0, 0) point shown in Figure 4.13 represents the centre of the X-plane of the ECAP billet. The Z axis corresponds to the direction perpendicular to the Z plane of the billet, and the Y axis corresponds to the direction perpendicular to the Y-plane, see Figure 2.21.

Figure 4.13(a) shows relative homogeneity in hardness distribution over the X-plane after one pass, with an average hardness value of ~100 Hv. After 2 passes, the average hardness increases to ~108 Hv. Increasing the passes to 4 raises the average microhardness value over the surface of the sample, as shown in Figure 4.13(c). After the eighth pass, hardness values increase over the surface of the X-plane and reach approximately ~115 Hv, as shown in Figure 4.13(d). With further straining up to 16 passes, as shown in Figure 4.13(e), the average hardness value over the surface of the specimen increased further to a value of ~135 Hv. However, this was followed by a decrease in the microhardness to ~120 Hv after 24 passes, as shown in Figure 4.13(f).

In short, microhardness values rose with increasing number of ECAP passes, but decreased after a certain limit. The average microhardness values recorded over the surfaces of the X-planes are in a good agreement with the values recorded across the diameter of the discs.

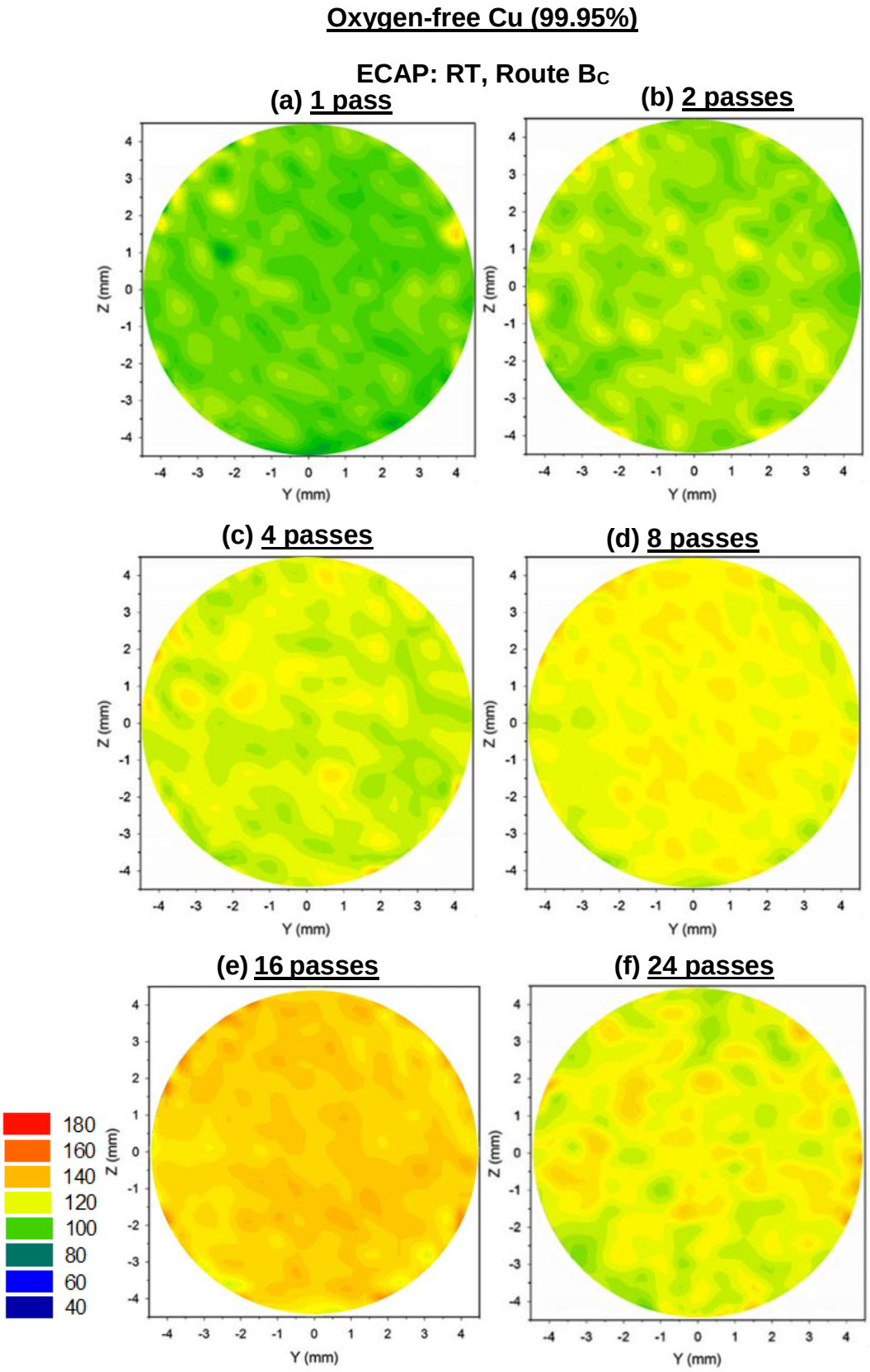

Figure 4.13 Colour-coded maps showing the distribution of microhardness over the cross-sectional planes of oxygen-free copper processed by ECAP for: (a) 1 pass, (b) 2 passes, (c) 4 passes, (d) 8 passes, (e) 16 passes and (f) 24 passes.

4.2.4.3 Microhardness measurements over the entire surface of longitudinal plane

Figure 4.14 displays the microhardness distribution over the longitudinal planes (Y-planes) of samples processed by ECAP through: (a) 1 pass, (b) 2 passes, (c) 4 passes, (d) 8 passes, (e) 16 passes and (f) 24 passes. The figure employs the same scale as Figure 4.13, showing the value of each colour from 40 Hv to 180 Hv in the same incremental steps of 20 Hv. The same colour-coded contour mapping was used for the Z and X directions. The Z direction denotes the vertical axis and the X direction represents the horizontal. Note that X = 40 mm represents the head of the billet and X = 0 represents the tail, while Z = 0 represents the centre line of each billet along the horizontal axis.

Inspection of Figure 4.14 shows a similar trend in results for the cross-sectional planes as shown in Figure 4.13, in that the average microhardness values increase with the number of ECAP passes then slightly decreased after a critical value, and that there is a degree of hardness homogeneity for each number (1 to 24) of passes.

The conclusions were obtained from the Vickers microhardness test. First, hardness increases significantly after the first pass, see Table 4.1. Second, there is a clear trend of increasing hardness with increasing numbers of ECAP passes, however the hardness decreased at a certain level of straining. Third, there is no significant difference in average Hv values between the X and Y planes. Fourth, there is a reasonable homogeneity in hardness observed for all passes of ECAP on both planes.

The microhardness measurements recorded on the longitudinal plane can be shown in the form of histograms presenting the number fraction of Vickers microhardness values of oxygen-free copper after ECAP through number of passes: (a) 1, (b) 2, (c) 4, (d) 8, (e) 16 and (f) 24, see Figure 4.15, where the red vertical lines represent the average microhardness values. It is apparent that the average microhardness value increases with increasing number of passes up to 16 then decreases after 24 passes. These histograms also show that the width of the distribution becomes smaller with number of passes increases indicating the increase in microhardness homogeneity at higher number of passes.

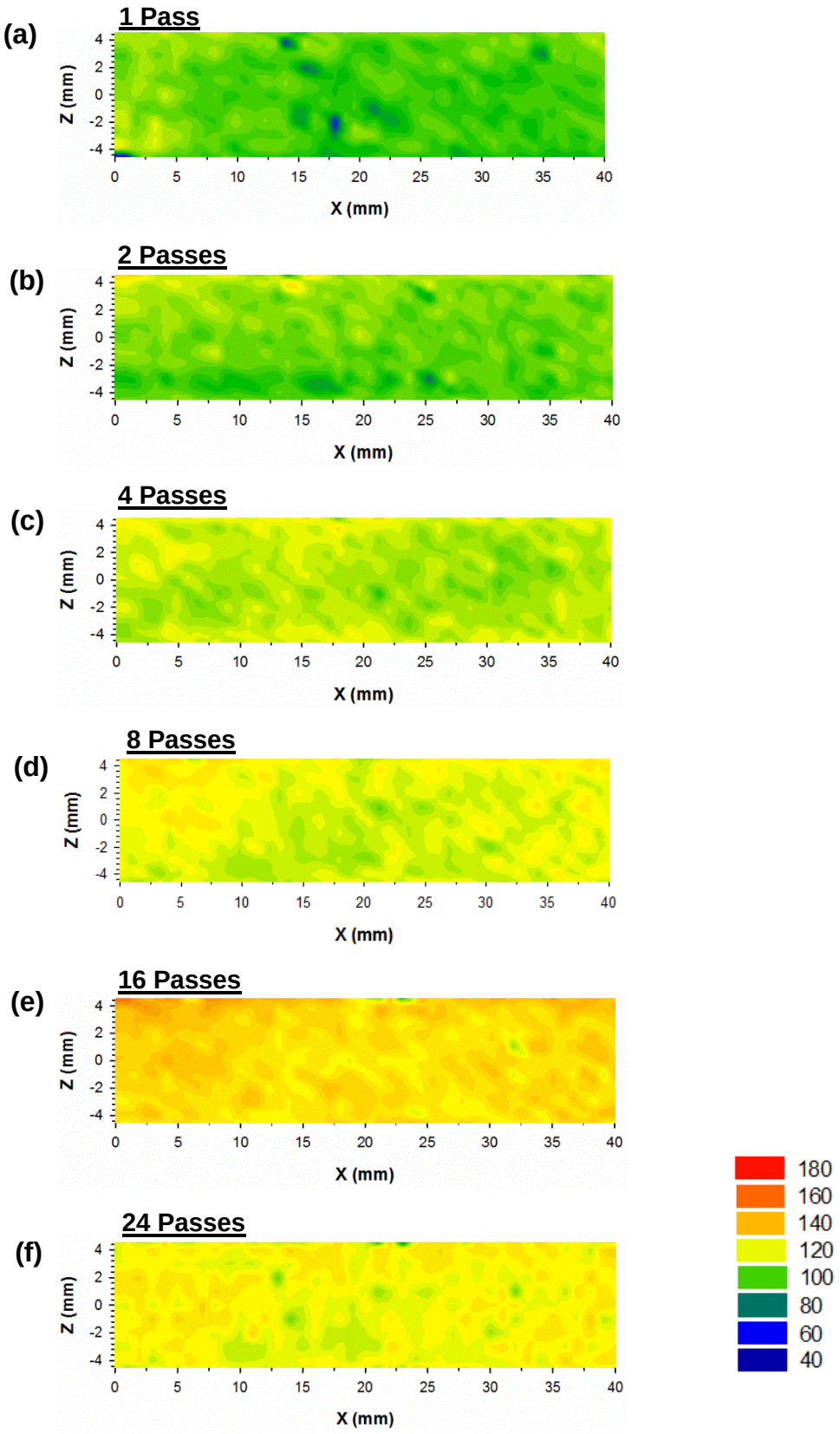

Figure 4.14 Colour-coded maps showing the distribution of microhardness on the longitudinal planes of oxygen-free copper discs processed by ECAP for: (a) 1 pass; (b) 2 passes; (c) 4 passes; (d) 8 passes; (e) 16 passes and (f) 24 passes.

(a)

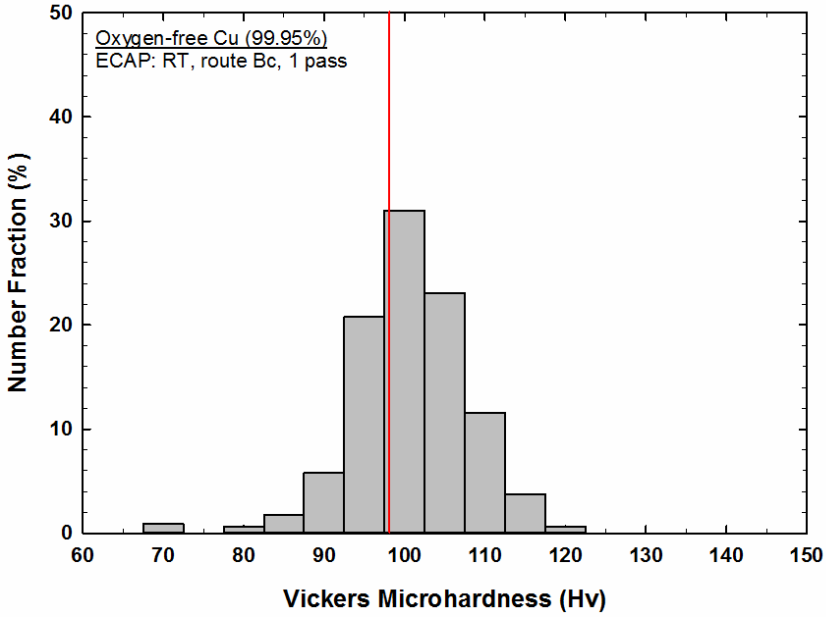
Oxygen-free Cu (99.95%)
ECAP: RT, route Bc, 1 pass
Number Fraction (%)
Vickers Microhardness (Hv)
0
10
20
30
40
50
60
70
80
90
100
110
120
130
140
150

(b)

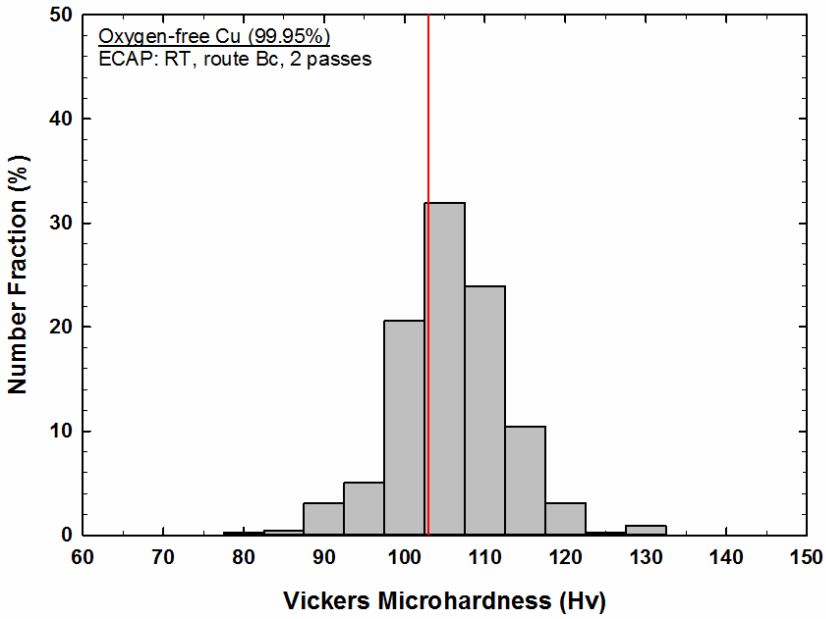
Oxygen-free Cu (99.95%)
ECAP: RT, route Bc, 2 passes
Number Fraction (%)
Vickers Microhardness (Hv)
0
10
20
30
40
50
60
70
80
90
100
110
120
130
140
150

(c)

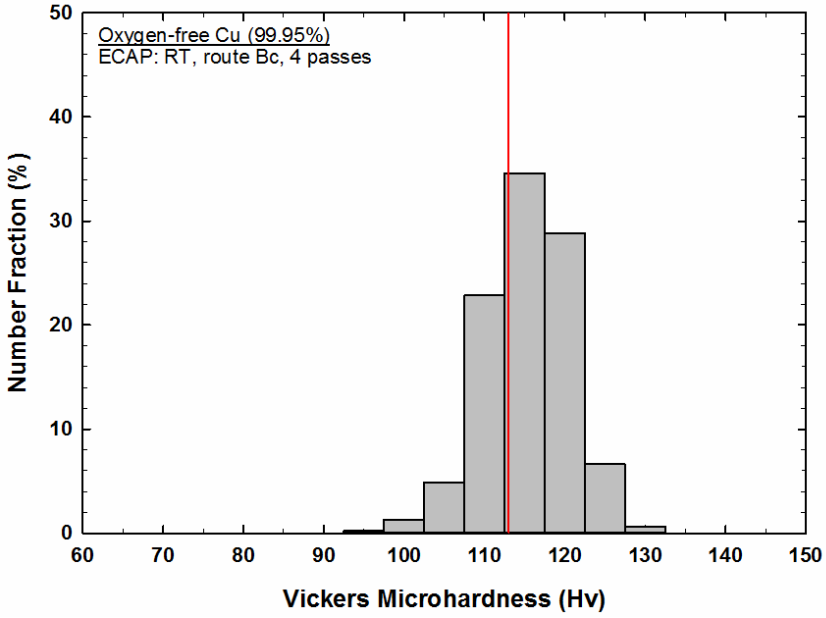
Oxygen-free Cu (99.95%)
ECAP: RT, route Bc, 4 passes
Number Fraction (%)
Vickers Microhardness (Hv)
0
10
20
30
40
50
60
70
80
90
100
110
120
130
140
150

(d)

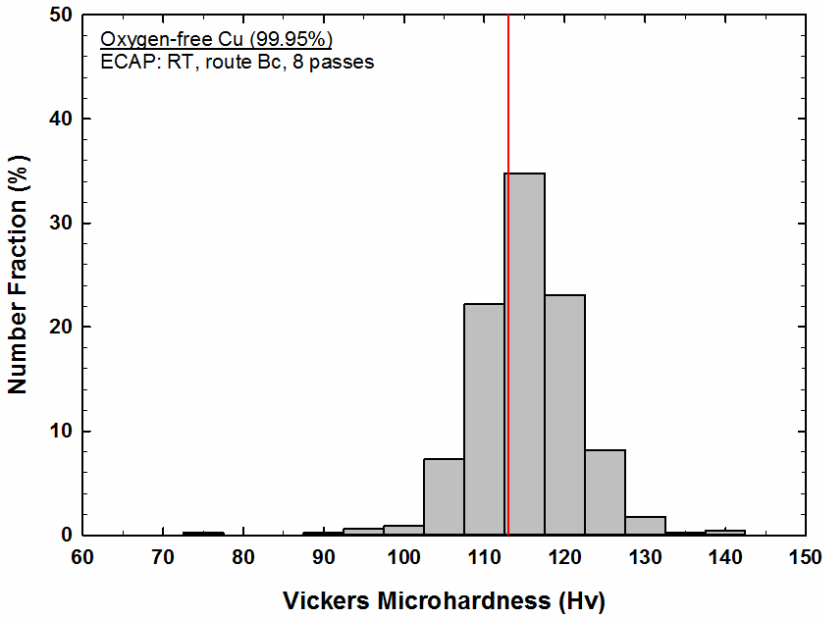
Oxygen-free Cu (99.95%)
ECAP: RT, route Bc, 8 passes
Number Fraction (%)
Vickers Microhardness (Hv)
0
10
20
30
40
50
60
70
80
90
100
110
120
130
140
150

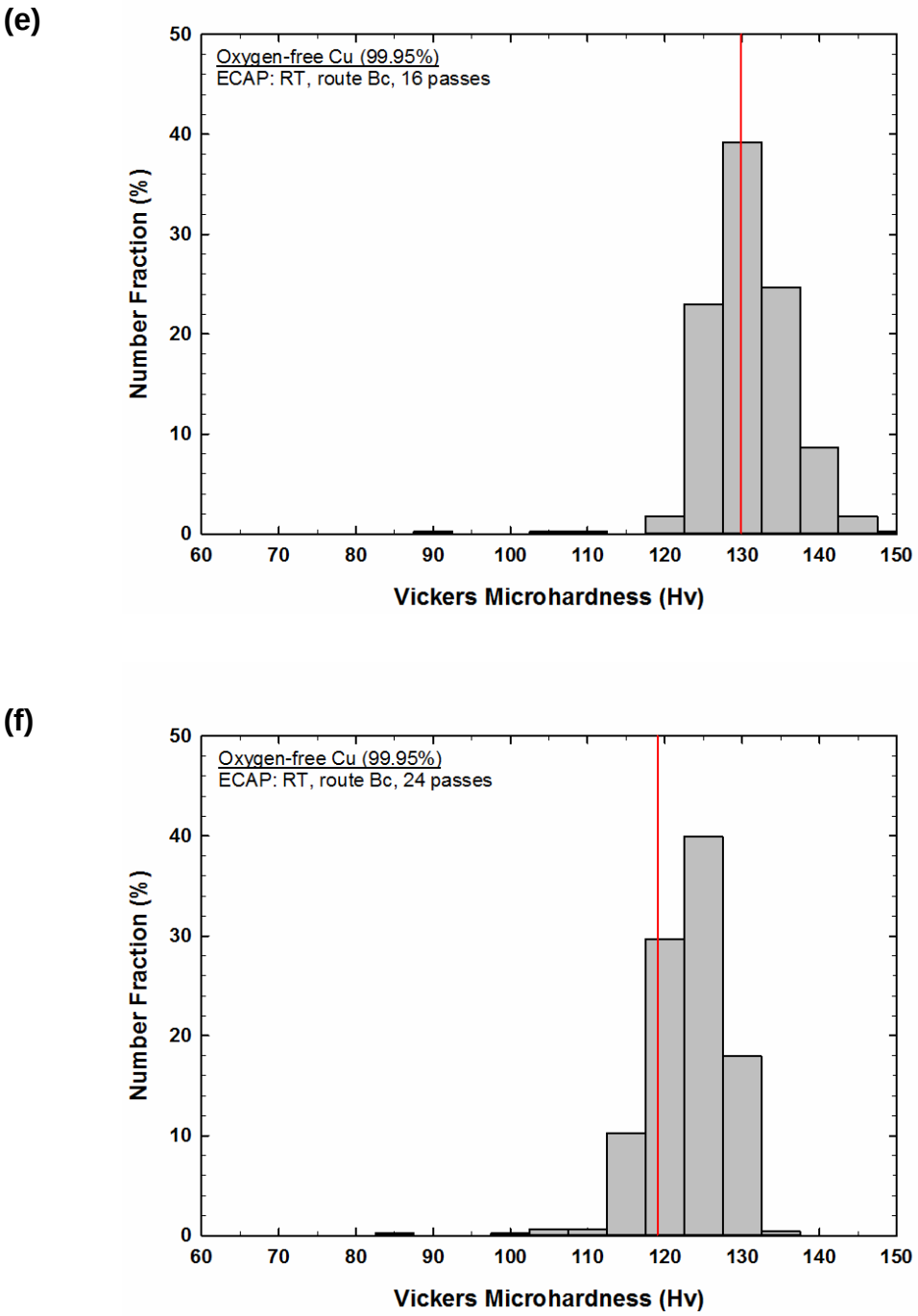

Figure 4.15 Histograms presenting the number fraction of Vickers microhardness values of oxygen-free copper after ECAP through number of passes: (a) 1, (b) 2, (c) 4, (d) 8, (e) 16 and (f) 24. (The red vertical lines represent the average microhardness values).

4.3 Discussion

4.3.1 Microstructural evolution during ECAP

The present study provides clear evidence that ECAP is an effective method of SPD for achieving an equiaxed small grain size with a high proportion of high-angle boundaries. Several reports have shown that the refinement of grain size is influenced by strain [157], pressing route [158] and temperature [82]. Also, prior studies have noted three types of refinement mechanisms: dislocation subdivision [159]; shear deformation [160]; and twin fragmentation [161]. A previous report describing the nature of grain refinement in FCC metals processed by ECAP [162] concludes that grain refinement in FCC metals takes place by the development of arrays of cells 'subgrains' separated by low angle boundaries in the initial passes through ECAP pressing. This subgrain structure evolves into an array of equiaxed grains separated by high-angle boundaries as the number of passes increases.

A second study developed a simple model for grain refinement in FCC metals processed by ECAP [163]. This provides important insights into the microstructure on the Y-plane for 1, 2 and 4 passes using Routes A, B_C and C, as shown in Figure 4.16. Since the present experiment was performed using Route B_C, only this route will be discussed.

According to the model presented by Langdon, an array of cells or subgrain boundaries is developed after the first pass with an average width of d and positioned at 45° to the X axis, see Figure 4.16 (1P). After two passes, another slip system with a set of subgrain boundaries is formed with a total angular range of $\eta = 18°$, as shown in Figure 4.16 (2P). It can be seen from Figure 4.16 (4P) that these subgrain boundaries are created at each pass, and after four passes the total angular range is $\eta = 63°$. These subgrain boundaries start to intersect, rearrange and annihilate each other in order to reach a lower energy state. Thus, equiaxed grains of average size d with a high fraction of HAGBs are formed, as depicted by Route B_C in Figure 4.17.

EBSD results demonstrate an achievement of exceptional grain refinement in oxygen-free copper of initial grain size of ~24 μm processed by ECAP at room temperature, using a die with an internal angle of 110°. The average grain size is reduced

to ~600 nm after 24 passes. This is larger than the average grain size of ~345 nm reported for pure copper processed by ECAP after 24 passes through a die with an internal angle of 90° at room temperature [164]. Another important finding is the increase in the fraction of high-angle boundaries to ~88% after 24 passes; this is higher than the proportion of ~60% reported for pure copper processed by ECAP for 24 passes through a die with an internal angle of 90° at room temperature [164]. This is consistent with earlier studies that ECAP processing increases the proportion of high-angle boundaries [74,159,164–168]. Ultrafine and equiaxed grains were achieved at high strain, unlike the elongated subgrains/grains with low-angle boundaries found when deforming metals by conventional techniques such as rolling [169]. The evolution of the grain size and HAGBs with respect to the numbers of ECAP passes is illustrated in Figure 4.18. It can be seen that the average grain size decreased whereas the fraction of HAGBs increased with increasing number of passes.

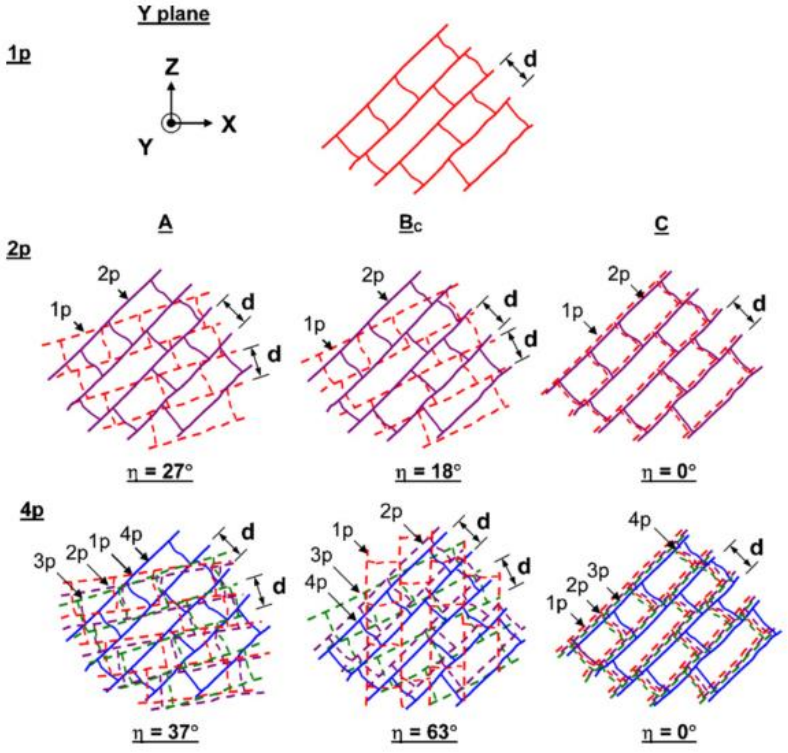

Figure 4.16 Grain refinement model in ECAP demonstrating the formation of subgrain bands on the Y-planes for 1, 2 and 4 passes using pressing Routes A, B_C and C [163].

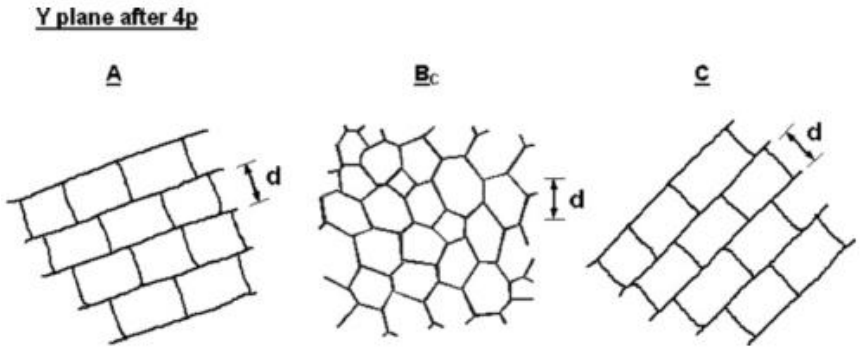

Figure 4.17 Schematic illustration of microstructure after pressing the Y-plane by ECAP for 4 passes using Routes A, B_C and C [163].

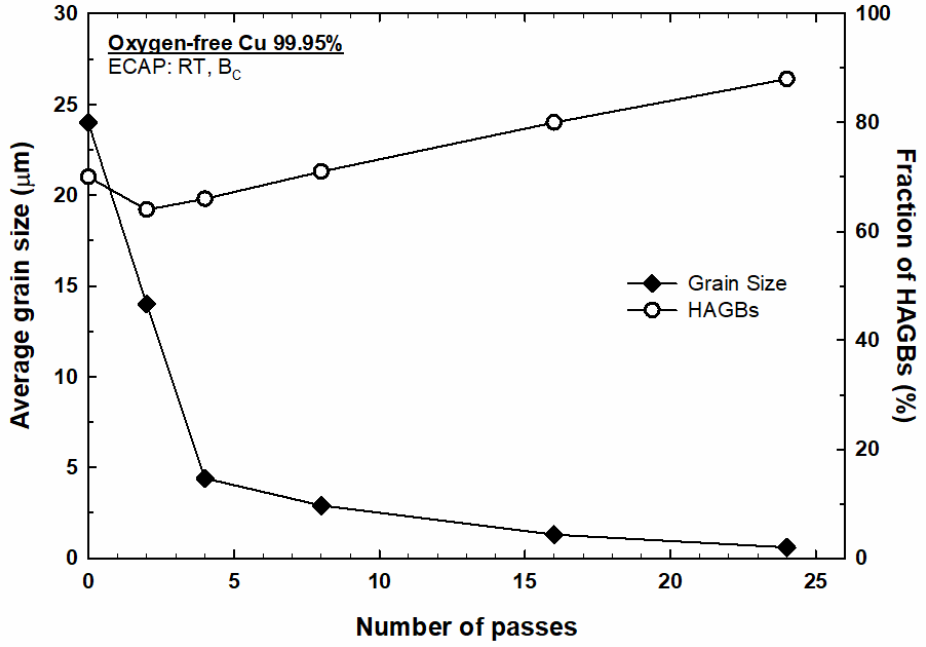

Figure 4.18 Average grain size and proportion of HAGBs as a function of number of ECAP passes.

4.3.2 Significance of ECAP processing route and channel angle

As mentioned in the literature review, there are four processing routes commonly used in ECAP. These are shown in Figure 2.23 [65] and termed: Route A, where these is no rotation of the sample between each separate pass; Route B_A, where the sample is rotated by 90º in alternate directions after each pass; Route B_C, where the sample is rotated by 90º in the same direction after each pass; and lastly Route C, where the sample is

rotated by 180º after each pass. Of these four processing routes, Route B_C has been demonstrated to be the most effective route in rapidly achieving an array of equiaxed UFGs [74] and it produces the largest angular ranges of slip on each orthogonal plan (X, Y and Z) [163].

The current study was conducted by pressing oxygen-free copper through a die with an internal angle of 110° for up to 24 passes at room temperature, using Route B_C. Figure 4.4 to Figure 4.8 show the evolution of the microstructure from large and elongated grains in the early stages of pressing to an array of equiaxed ultrafine grains after a high numbers of passes. These results are in agreement with the results obtained from an experiment performed on oxygen-free copper processed by ECAP for 25 passes using a die with a channel angle of $\Phi = 90°$ [74], where Route B_C was successful in obtaining the smallest size for the structural elements and producing an equiaxed grain structure. It is clear from Figure 4.8 that the microstructure in oxygen-free copper produced by ECAP using Route B_C is an equiaxed grain structure with a high proportion of HAGBs with a very small grain size.

Another factor that plays a significant role in the development of microstructure in metals is the channel angle. As presented in Equation 2.7, this is a critical parameter in determining the total imposed strain at each pass of ECAP. Previous experiments have studied the significance of the channel angle [77,78,170] and noted that channel angle $\Phi = 90°$ is the best choice to achieve an array of UFG most easily, with boundaries having high angles of misorientation.

Due to difficulties encountered during initial trials in pressing oxygen-free copper through a channel angle of $\Phi = 90°$, a larger channel angle of $\Phi = 110°$ was used in this study. These difficulties included deformation, and billets becoming stuck inside the die at higher numbers of passes. Several experiments have shown that using a channel angle of $\Phi = 110°$ leads to easier pressing of ECAP billets through the die than a channel angle of $\Phi = 90°$ [78]. Other experiments have reported an improvement in the deformability of billets and a decrease in ECAP temperature when a channel angle larger than $\Phi = 90°$ is used [79]. Decreasing the temperature in ECAP processing leads to better grain refinement. Furthermore, the total accumulative strain imposed by a channel angle of $\Phi = 90°$ is higher than the total accumulative strain imposed by a channel angle of $\Phi = 110°$, as illustrated in Table 4.2. Previous studies have reported that while the total accumulative

strain does not have a major influence in determining the microstructure, it is crucial in guaranteeing the imposition of very high strain on the billet on each separate pass during ECAP [77].

The present results are in a good agreement with these earlier reports. The channel angle of Φ = 110° led to an enhancement in the deformability of the oxygen-free copper billets during ECAP at room temperature through high numbers of passes. Thus, a more effective grain refinement was achieved after 24 passes, as shown in Figure 4.8.

Table 4.2 Total cumulative strain imposed on each separate pass for channel angles of Φ = 90° and Φ = 110°.

Number of passes	**Equivalent strain**	
	Φ = 90°	**Φ = 110°**
1	1	~0.8
2	2	~1.5
4	4	~3
8	8	~6
16	16	~12
20	20	~15
24	24	~18

Table 4.3 shows grain size measurements of pure copper processed by ECAP for various number of passes, die angles and processing routes. Generally, the difference in average grain size between these studies arises due to the difference in the processing parameters including die angles, number of passes and processing route. The average grain size recorded in this study was ~600 nm after 24 passes and it is larger than the average grain size of 345 nm produced after 24 passes using Φ = 90° [164]. It is readily apparent that processing copper using a die with an internal angle, Φ, of 90° leads to a smaller grain size than 110°. Another factors that can affect the grain size measurements are the initial heat treatment prior to ECAP, purity of copper and method of measurements. Apparently, the average grain sizes measured by TEM are relatively smaller than those measured by EBSD. This might be due to the scanning step distance used in EBSD.

Table 4.3 Average grain size (d) measurements of pure copper processed by ECAP for various number of passes, die angles and processing routes.

Φ	**Ψ**	**Passes**	**Route**	**Method**	**d (nm)**	**HAGB (%)**	**Ref.**
110°	20°	1-24	B_C	EBSD	600	88	Current study
110°	20°	12	B_C	EBSD	500	56	[171]
90°	0	$4 \geq P \leq 16$	B_C	EBSD	200	45	[172]
90°	–	4-24	B_C	EBSD	345	60	[164]
90°	–	12	B_C	EBSD	340	61	[173]
90°	–	12	B_C	TEM	210	–	[10]
90°	–	4	B_C	TEM	200-300	–	[174]
90°	–	14	C	TEM	200	70	[175]
90°	45°	8	B_C	TEM	200-2000	37	[176]
90°	0	8	B_C	TEM	200-2000	29	[176]
90°	–	1-12	B_C	TEM	250	–	[177]
90°	–	8	B_C	TEM	300-400	–	[178]
90°	–	8	B_C	TEM	300	–	[179]
90°	20°	8	B_C	TEM	500	30	[84]
90°	20°	8	C	TEM	950	20	[84]
90°	–	4	B_C	TEM	300	–	[180]
90°	20°	1-8	B_C	TEM	250	–	[181]
90°	20°	20	B_C	TEM	200-400	–	[182]
90°	–	12	B_C	TEM	240	–	[173]

4.3.3 Microhardness evolution during ECAP

Vickers microhardness measurements were made on the cross-sectional (X-planes) and longitudinal (Y-planes) of billets processed by ECAP. The results show a significant increase in microhardness values after the first pass. The average microhardness value was ~41 Hv before processing by ECAP and became ~90 Hv after one pass. Despite this substantial increase in microhardness values, the microstructure is not homogenous.

The microhardness values increase with increasing numbers of passes, however; this increase in microhardness is minor after 2 passes of ECAP, as illustrated in Table 4.1. On the other hand, the microhardness results and the microstructural analysis of this study confirm the gradual evolution towards relative microhardness homogeneity with increasing numbers of passes for oxygen-free copper, as shown in Figure 4.12. These results are consistent with previous reports for pure aluminium [100], aluminium alloys [98] and copper alloys [99] processed by ECAP. The results show that even though the hardness increment is small, the increase in homogeneity is significant with higher numbers of passes. In contrast to this results, an Al-7034 alloy processed by ECAP at 473 K for up to 6 passes demonstrated a significant decrease in hardness after the first pass and the loss of hardness became small in the following passes [183]. The weakening of the strength is due to the transformation of the metastable phase at the higher processing temperature of 473 K [184].

Oxygen-free copper reached a reasonable hardness homogeneity after 24 passes of ECAP as shown in Figure 4.13 and Figure 4.14. The results obtained from the cross-sectional planes presented in Figure 4.13 and the longitudinal planes presented in Figure 4.14 are compared in Figure 4.19. The data used to construct Figure 4.19 are the average values of microhardness recorded at all the measurements points on each sectional plane. A comparison of the two sets of results reveals almost the same microhardness values at each pass of ECAP. Also, it shows that the microhardness values increase rapidly after one pass of ECAP by a factor of approximately 2.5 for both planes, and thereafter continue to increase slowly with increasing numbers of passes up to 16 passes, after which there is a decrease with increasing strain after 24 passes. This result suggests that saturation occurs by means of recovery mechanism that takes place at a certain level of strain when deforming oxygen-free Cu at high strain.

In addition, both sectional planes reach good hardness homogeneity after processing by ECAP through 24 passes. These results are in line with a previous study which used Cu-0.1 wt.% Zr processed by ECAP for 8 passes at room temperature [99]. It was found that the microhardness values rose with increasing numbers of ECAP passes and the hardness values were similar on both X and Y-planes. Another study using Al-6061 processed by ECAP for up to 6 passes at room temperature shows consistent results of increasing hardness with increasing number of passes, and obtained microhardness homogeneity after pressing by ECAP, as well as showing the same hardness values for the X, Y and Z orthogonal planes [183].

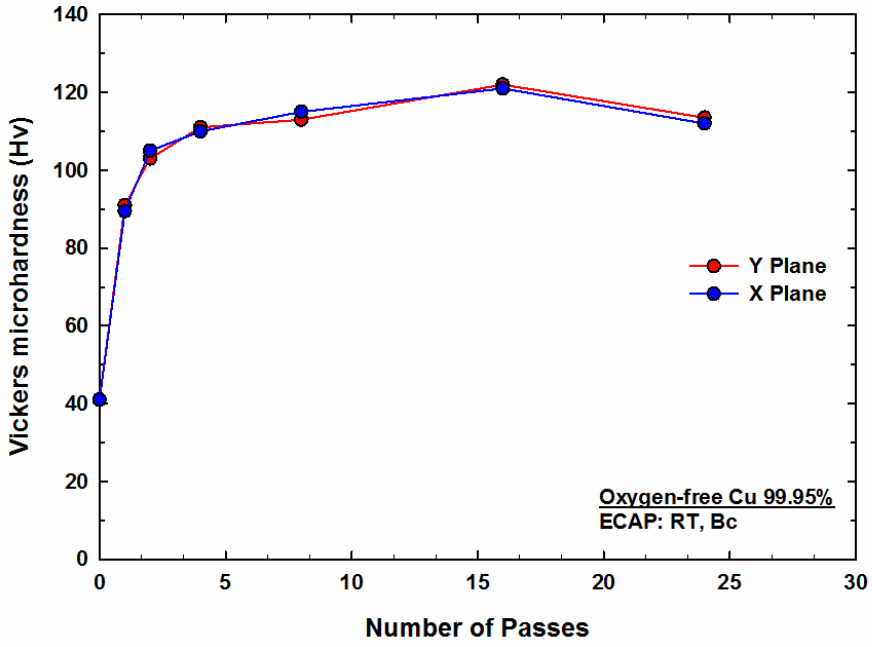

Figure 4.19 Average values of Vickers microhardness recorded on the cross-sectional and longitudinal planes of the ECAP billets as a function of the number of passes.

4.3.4 Hardness homogeneity after ECAP

Microstructural homogeneity of oxygen-free copper is achieved after processing a billet by ECAP through 24 consecutive passes. This is consistent with an earlier study on Cu-0.1%Zr alloy that reported full homogeneity of hardness after 8 passes [99]. The development of homogeneity is demonstrated by the differences in material properties, including the rates of strain hardening and recovery [100]. Materials with high SFEs have

fast recovery rate, thus materials with higher SFEs show a faster development of homogeneity than materials with low SFEs, because it is easier to accommodate a higher density of dislocations under a fixed applied strain. Another factor affecting the development of homogeneity is the purity of the material. Pure metals show faster development towards microstructural homogeneity, because they have only a dislocation hardening mechanism. By contrast, metal alloys demonstrate a slower development towards microhardness homogeneity as the alloying elements act as barriers and hinder the dislocation movement, which provides additional hardening of the metal [100].

The results obtained from this study are dissimilar to previous studies that have reported smaller hardness values in the lower region of the billet in the early stages of processing [93,96,99,185]. This is due to its lack of contact with the die walls at the outer corner of the channel, termed the 'corner gap' or the 'dead zone'. Here, the imposed strain is greatly reduced and creates a non-uniform microstructure. However, in this study the dead zone had only a minor effect on the billet and the hardness results show a reasonable uniformity in the early stages of ECAP. This is due to a difference in strain between outside and inside the billet which causes inhomogeneous strain distribution. The outside of the billet flows faster during the deformation process in which the strain decreases on the outer side and increases inside the billet, with the average strain decreased. This is confirmed by finite element simulation, showing that the region with smaller hardness values in the billet is related to the strain hardening rates of the material [185]. The current outcome is also contrary to that of Ebrahimi *et al*. [186] who found that the bottom region of the OFHC Cu billet exhibits lower hardness values than the top region after the first pass. It is suggested that both bending and shear mechanisms are imposed on the lower region of the billet simultaneously. These studies have commonly reported that the effect of the dead zone disappears with further processing of the material through increasing number of passes.

In addition, the grain size contributes to the measured microhardness, as expressed through the empirical Hall-Petch relationship [1,2]:

$$H_V = H_0 + Kd^{-1/2} \qquad (4.1)$$

where d is the grain diameter and H_0 and K are materials constants.

Equation 4.1 shows an inverse relationship between grain size and hardness. The hardness of the material increases with reducing the grain size. Figure 4.20 shows the variation in Vickers microhardness with the reciprocal square root of the average grain size. It is readily apparent that the sample processed by 24 passes deviates from the Hall-Petch relationship and softening has taken place with decreasing the grain size.

The hardness and grain size relationship during ECAP is shown in Figure 4.21. It can be seen that the decrease in average grain size leads to an increase in microhardness with increasing numbers of ECAP passes. These results are in accord with the recent studies indicating that ECAP was effective in reducing grain size and enhancing the hardness of pure copper [48,49,168,181,182,187–190]. It is readily apparent that processing oxygen-free Cu up to 16 passes follows the Hall-Petch relationship, however, it deviates from the Hall-Petch relationship when deformed beyond 16 passes.

The correlation between the measured microhardness and the equivalent strain is depicted in Figure 4.21 where the top horizontal axis represents the equivalent strain and the bottom horizontal axis is the number of passes. Equation 2.7 is used to calculate the equivalent strain. As can be seen from the figure, there is a rapid increase in hardness when the applied strain is small and then the rate of increase slows with increasing strain. At a certain point when the imposed strain is large, after a higher numbers of ECAP passes, the hardness decreases. Initially, the hardness increases continuously in relation to the equivalent strain and reaches maximum when the equivalent strain approaches ~12. Beyond this point, the hardness value decreases, indicating that the annihilation of dislocations becomes faster than the generation of dislocations. This trend suggests that another deformation mechanism might become dominant beyond a critical equivalent strain of ~12.

The decrease in microhardness observed in this study is in agreement with the XRD measurements shown in Figure 4.11 that show a decrease in dislocation density and increase in the crystallite size after 24 passes suggesting the occurrence of dynamic recovery during ECAP processing.

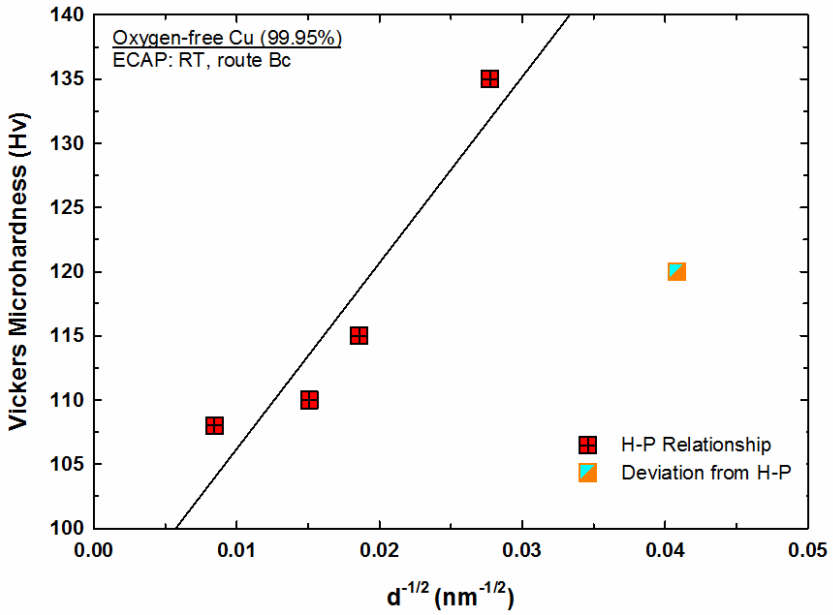

Figure 4.20 The variation in Vickers microhardness with the reciprocal square root of the average grain size of oxygen-free copper processed by ECAP at room temperature.

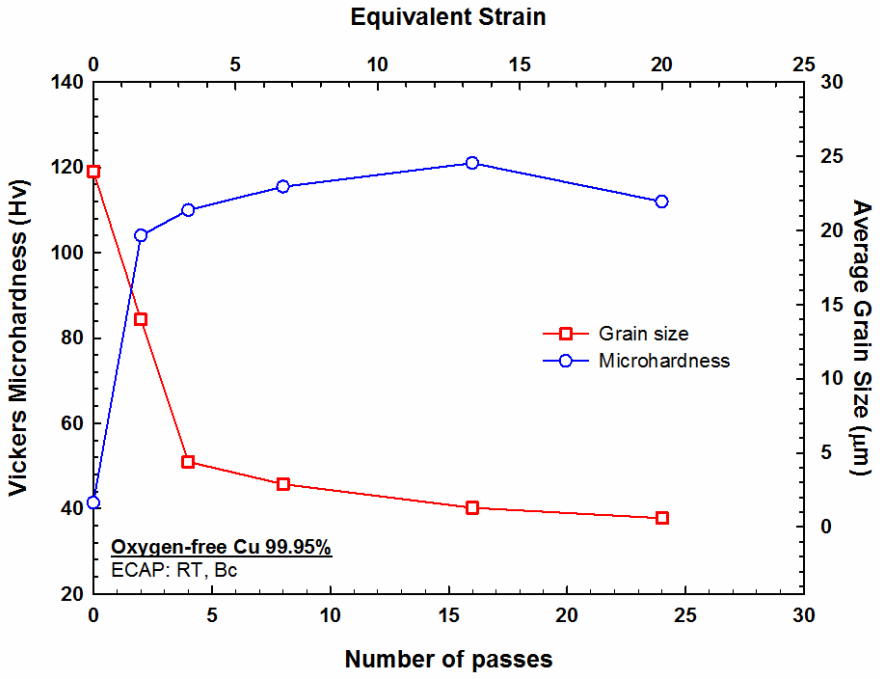

Figure 4.21 Average microhardness and grain size as a function of the number of ECAP passes and equivalent strain for oxygen-free copper processed by ECAP at room temperature.

4.3.5 Significance of processing method and SFE in determining minimum grain size

Recent studies have shown that each metal subjected to SPD there is a minimum grain size, the equilibrium grain size, when the material reaches saturation with progressive strain [3]. SFEs plays a major role in determining this grain size in metals and alloys. Table 4.4 shows the minimum grain sizes ($d_{\min}$), equivalent strain (ε_{sat}) and SFE (γ) for several metals processed by HPT and ECAP. It can be seen that materials with lower SFE values than the pure copper used in this study, such as Cu-10 wt% Zn and Cu-30 wt% Zn, have a smaller grain size, whereas material with higher SFE values, such as pure aluminium, have larger grain size. These results are in a good agreement with previous studies reporting that decreasing SFE produces smaller grain sizes [48,71,153,191,192]. Minimum grain size is attributed to the dynamic balance between the generation and recovery of dislocations [161,193]. The recombination of the dissociated dislocations and cross-slip become challenging in low SFE materials, which hinders recovery and produces a smaller grain.

In addition, minimum grain size depends on the processing technique where HPT, for example, has proven to produce smaller grain sizes than ECAP when the same metal is used [34]. As can be seen in Table 4.4 the average grain size measured by EBSD in this study is ~510 nm by HPT (Chapter 5) and is smaller than the average grain size of ~600 nm produced by ECAP. Also, by comparing the Al values obtained from previous studies, one can see that processing by HPT produced smaller grain sizes than by ECAP.

Table 4.4 Minimum grain size ($d_{\min}$), equivalent strain (ε_{sat}) and SFE (γ) for several metals processed by HPT and ECAP.

Material	**Processing method**	$d_{\min}$ **(nm)**	ε_{sat}	**SFE (mJ/m^2)**
Oxygen-free Cu (present study Ch.5)	HPT	~510	~50	78
Oxygen-free Cu (present study)	ECAP	~600	~18	78
Al [41]	HPT	~700	6	166
Al [71]	ECAP	~1300	4	166
Cu-10 wt% Zn [48]	HPT	~50	34	35
Cu-30 wt% Zn [48]	HPT	~10	14	14

4.4 Summary

1. Oxygen-free copper billets with a commercial purity of 99.95% were processed at room temperature by ECAP through a $\Phi = 110°$ channel angle using Route B_C for 1, 2, 4, 6, 8, 16, 20 and 24 passes.

2. EBSD measurements on the longitudinal planes of the ECAP-processed samples show significant grain refinement. The average grain size reduced from ~24 μm to ~600 nm after 24 passes. The grains were large and elongated in the early stages of deformation and became well-defined, equiaxed grains after 24 passes. The proportion of HAGBs rose with increasing number of passes to approximately 88%.

3. The XRD measurements obtained from ECAP samples revealed an increase in the dislocation density and a decrease in the crystallite size with increasing numbers of passes up to 16, followed by a decrease in the dislocation density and an increase in the crystallite size after 24 passes.

4. The evolution of microhardness of ECAP billets was measured by recording individual measurements along the diameter of cross-sectional planes and plotting colour-coded contour maps over the entire surface of the cross-sectional and longitudinal planes. The microhardness values increased with increasing numbers of passes and reached a maximum value after 16 passes and decreased after 24 passes.

5. A deviation from Hall-Petch relationship was observed after 24 passes of ECAP. The drop in dislocation density and microhardness together with the increase in the crystallite size suggests that recovery mechanism took place during the ECAP process after reaching a critical equivalent strain of ~12.

Chapter 5 Microstructural and Microhardness Evolutions in Oxygen-free Copper Processed by HPT at Room Temperature

5.1 Results

Microstructural evolution of oxygen-free copper discs processed by HPT at room temperature is investigated using optical microscopy, EBSD and X-ray diffraction while the hardness evolution is examined using Vickers microhardness test. This chapter deliberately follows the same structure as Chapter 4, *Microstructural and Microhardness Evolutions of Oxygen-free Copper Processed by ECAP at Room Temperature*, for ease of comparison of results.

5.1.1 Optical microscopy observations

The microstructure of unprocessed oxygen-free copper annealed at 600 ºC for 1 hour is shown in Figure 4.1(b). It consists of equiaxed grains with some annealing twinning. The optical microstructures at the centre, half-radius and near the edge of oxygen-free copper discs processed by HPT at room temperature through 1/2, 1, 3, 5 and 10 turns under an applied pressure of 6.0 GPa under quasi-constrained conditions are shown in Figure 5.1. Inspection showed a variation in the microstructures of the three regions in the early stages of deformation (lower numbers of turns), and this variation became less with increasing numbers of turns. There is a clear trend to grain size reduction from the edge towards the centre of the disc.

After only a 1/2 turn, at the edges grain refinement took place rapidly so the grain boundaries were not visible, while in the half-radius region only a trace of deformation was observed. Although grain refinement occurred also in the central region of the disc after 1/2 turn, the grains were larger than those in the half-radius and peripheral regions, retaining well-defined grain boundaries. Increasing the number of turns increased grain refinement in the central and half-radius regions, while there was no change detected by optical microscopy in the microstructure at the edges of the disc. After 10 turns, the

microstructure across the diameter of the disc reached approximately the same level of refinement, and the grain boundaries could no longer be detected by optical microscopy.

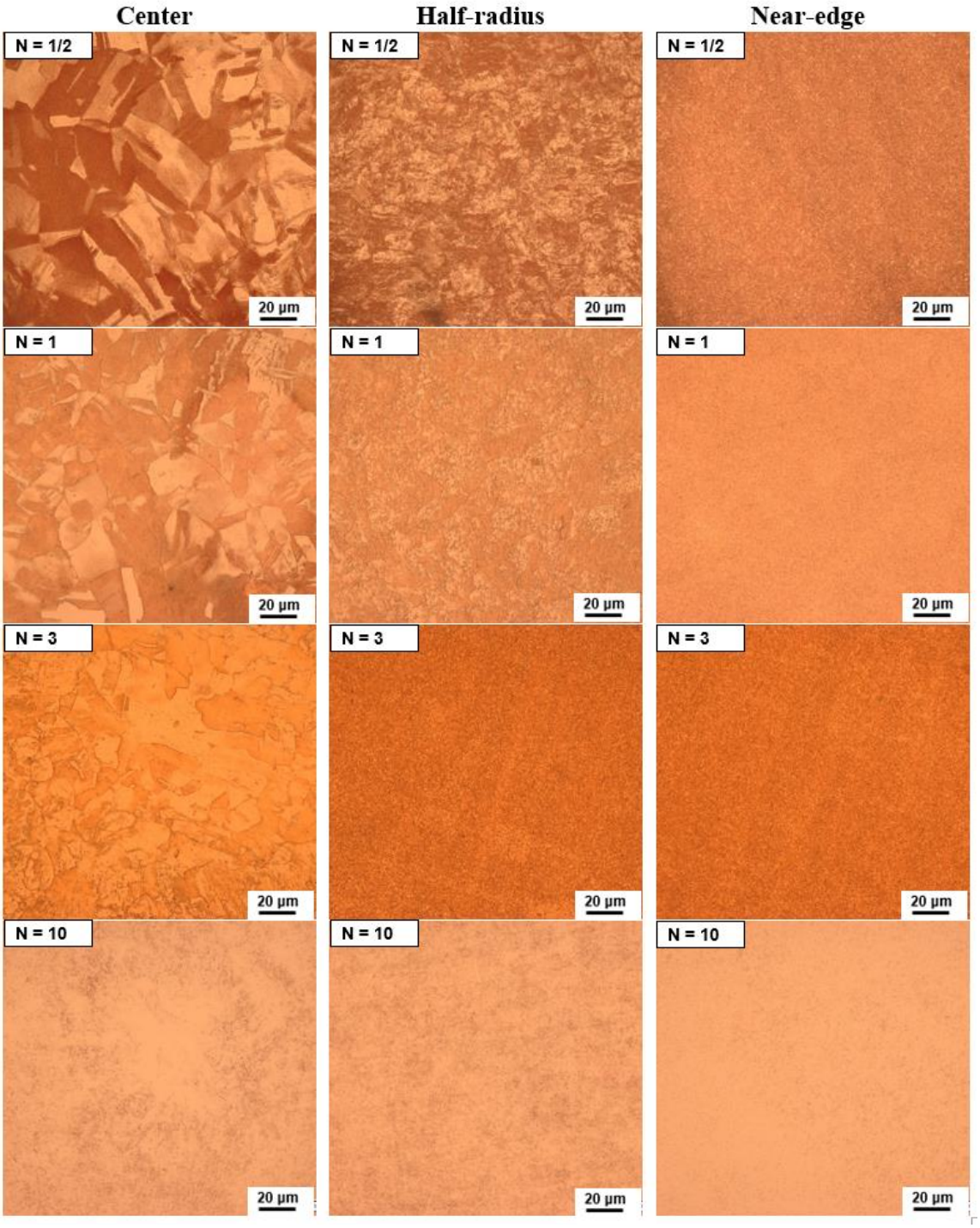

Figure 5.1 Optical microstructures at the centre, half-radius and near the edge of oxygen-free copper discs processed by HPT at room temperature through 1/2, 1, 3 and 10 turns under an applied pressure of 6.0 GPa.

The evolution of microstructures in the central region is presented at higher magnification in Figure 5.2. It is clear that few coarse grains with grain boundaries are still detectable after 1 turn and these diminish with increasing numbers of turns. Also, after 1turn a reduction in brightness can be seen around the central region with increasing distance from the disc centre, due to subdivision of the original grain structure [33,194].

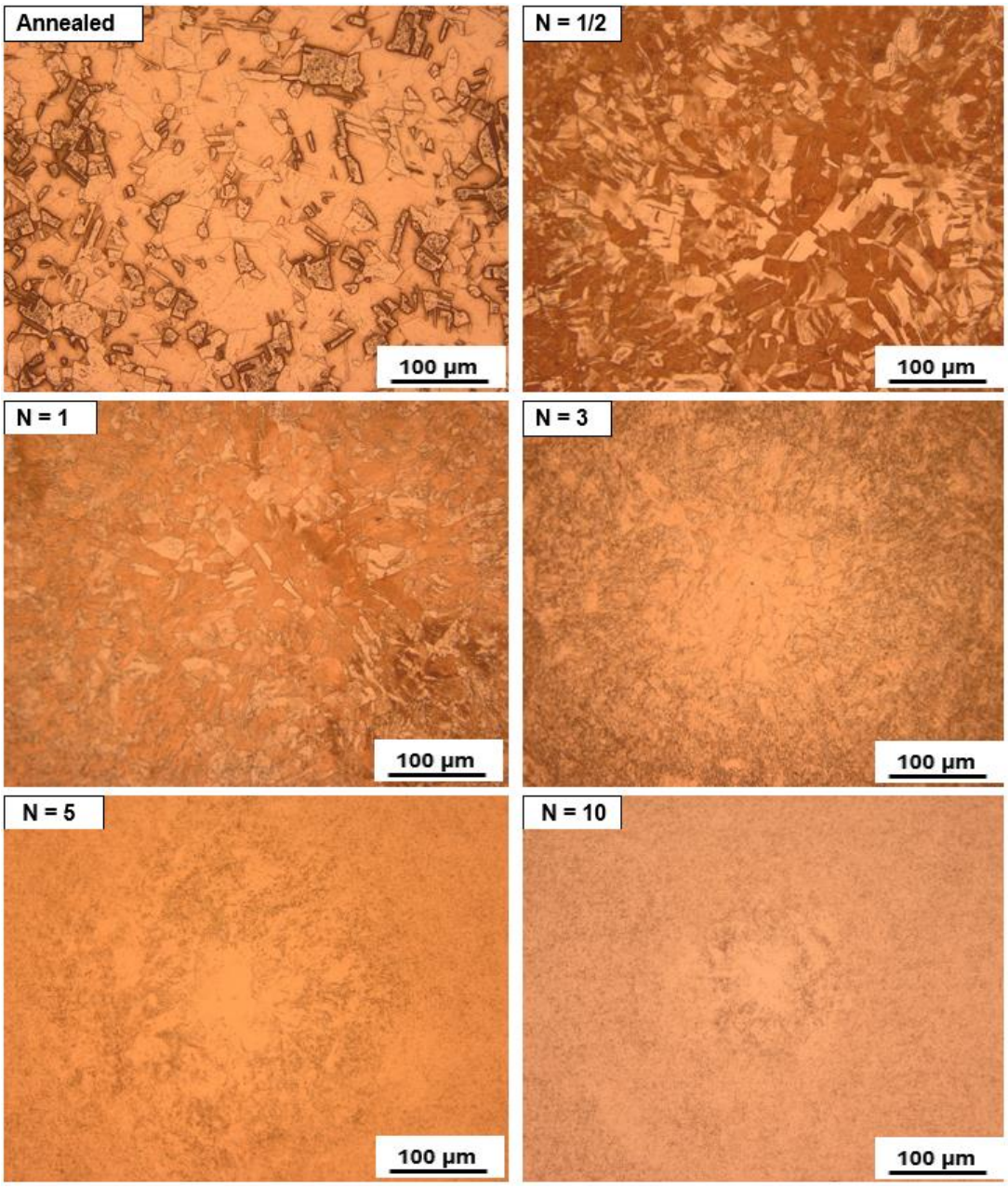

Figure 5.2 Optical micrographs showing microstructural evolution in central region of oxygen-free copper discs processed by HPT by up to 10 turns.

5.1.2 Electron Backscatter Diffraction measurements

The microstructures of samples processed by HPT were examined by EBSD. Figure 5.3 to Figure 5.6 shows the OIM images at the centre and periphery of each processed disc and the information regarding the grain size distribution is shown in Figure 5.7 to Figure 5.10 and the distribution of the misorientation angles are shown in Figure 5.11 to Figure 5.14. The microstructures evolved during HPT processing, and a close inspection of Figure 5.3(b) indicates that the edges had undergone significant grain refinement after 1/2 turn, while a bimodal grain structure of fine and coarse grains is apparent in the central region of the disc as shown in Figure 5.3(a). Thus, a variation in average grain size is observed between the centre and edge of the disc, as in Figure 5.7(a) and Figure 5.7(b). Average grain sizes of ~0.82 μm and ~0.69 μm were measured in the central and peripheral regions, respectively. At the centre of the disc the proportion of misorientation angles that are HAGBs is ~74% as shown in Figure 5.11(a), and at the periphery is ~86%, as shown in Figure 5.11(b). It should be noted that the distribution of misorientation angles is linked to the conventional pixel-to-pixel distributions recorded by OIM and thus may not be related to the grain-to-grain misorientation distribution. The annealing twins are significantly reduced to ~3% after processing the sample by HPT.

As processing increased to a full turn, there was a decrease in grain size at the centre and periphery, as shown in Figure 5.8(a) and Figure 5.8(b). An average grain size of ~0.7 μm was measured at the centre of the disc, and ~0.63 μm at the edge. At the centre the percentage of HAGBs was slightly reduced to ~71% and at the periphery the change was also minor, as illustrated in Figure 5.12(a) and Figure 5.12(b), respectively.

As shown in Figure 5.5(a) and Figure 5.5(b), after 3 turns the microstructure became more defined, with more equiaxed grains in the central and peripheral regions. Average grain size became more uniform and measurements showed ~0.60 μm at the centre, see Figure 5.9(a) and ~0.57 μm at the edge, see Figure 5.9(b). Also, the distribution of misorientation angles in the central region, as depicted in Figure 5.13(a), shows a significant increase in HAGBs to ~83%, but there is no noticeable change at the edge, see Figure 5.13(b).

After 10 turns, the microstructure become more defined, with more equiaxed grains, as shown in Figure 5.6(a) and Figure 5.6(b) of average size of ~0.51 μm in the

centre and periphery as shown in Figure 5.10(a) and Figure 5.10(b), respectively. Figure 5.14(a) and Figure 5.14(b) show that the proportion of HAGBs is almost identical at the centre and edges, with approximately 83% of HAGBs.

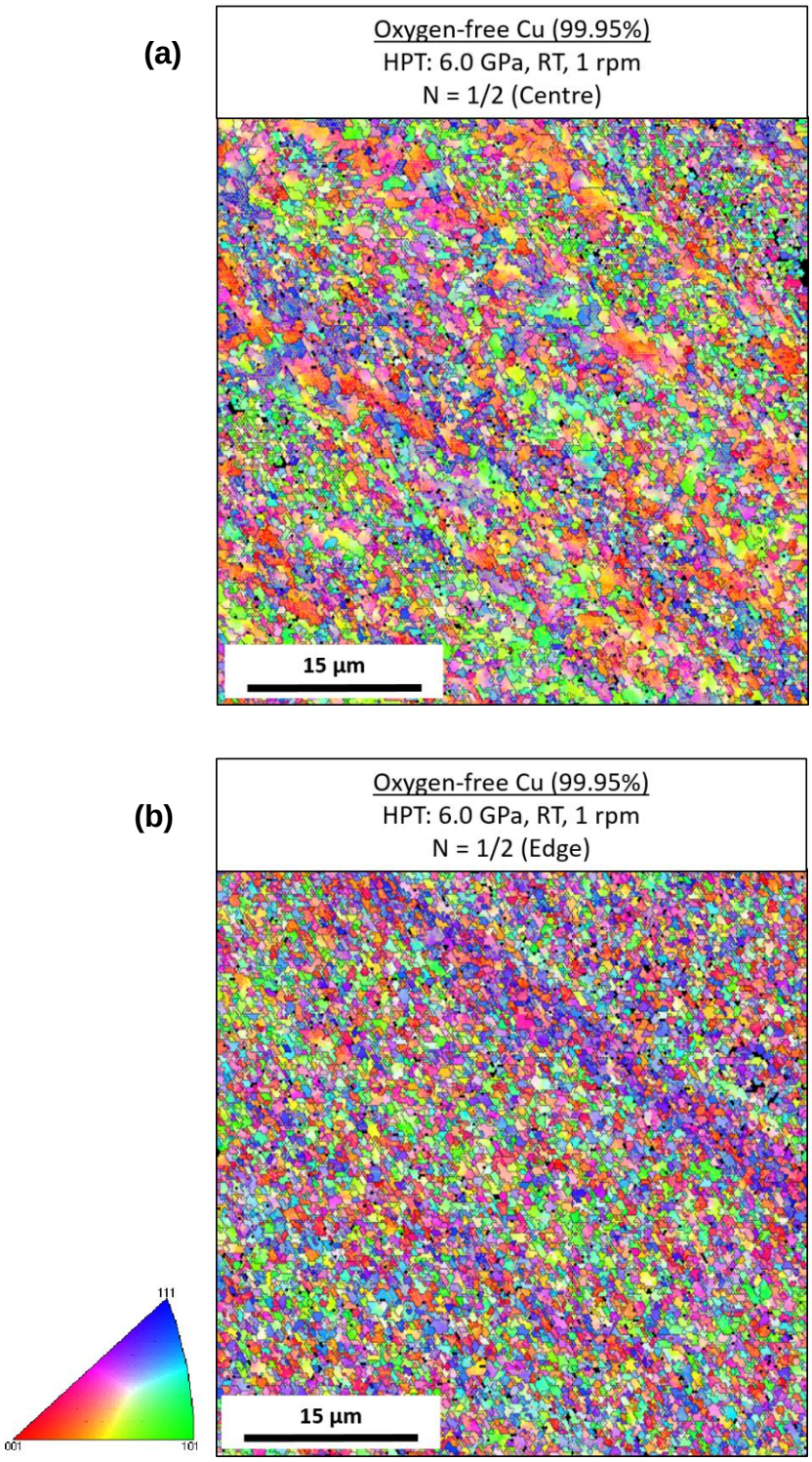

Figure 5.3 OIM Images of oxygen-free copper processed by HPT for 1/2 turn: (a) centre and (b) edge of the disc.

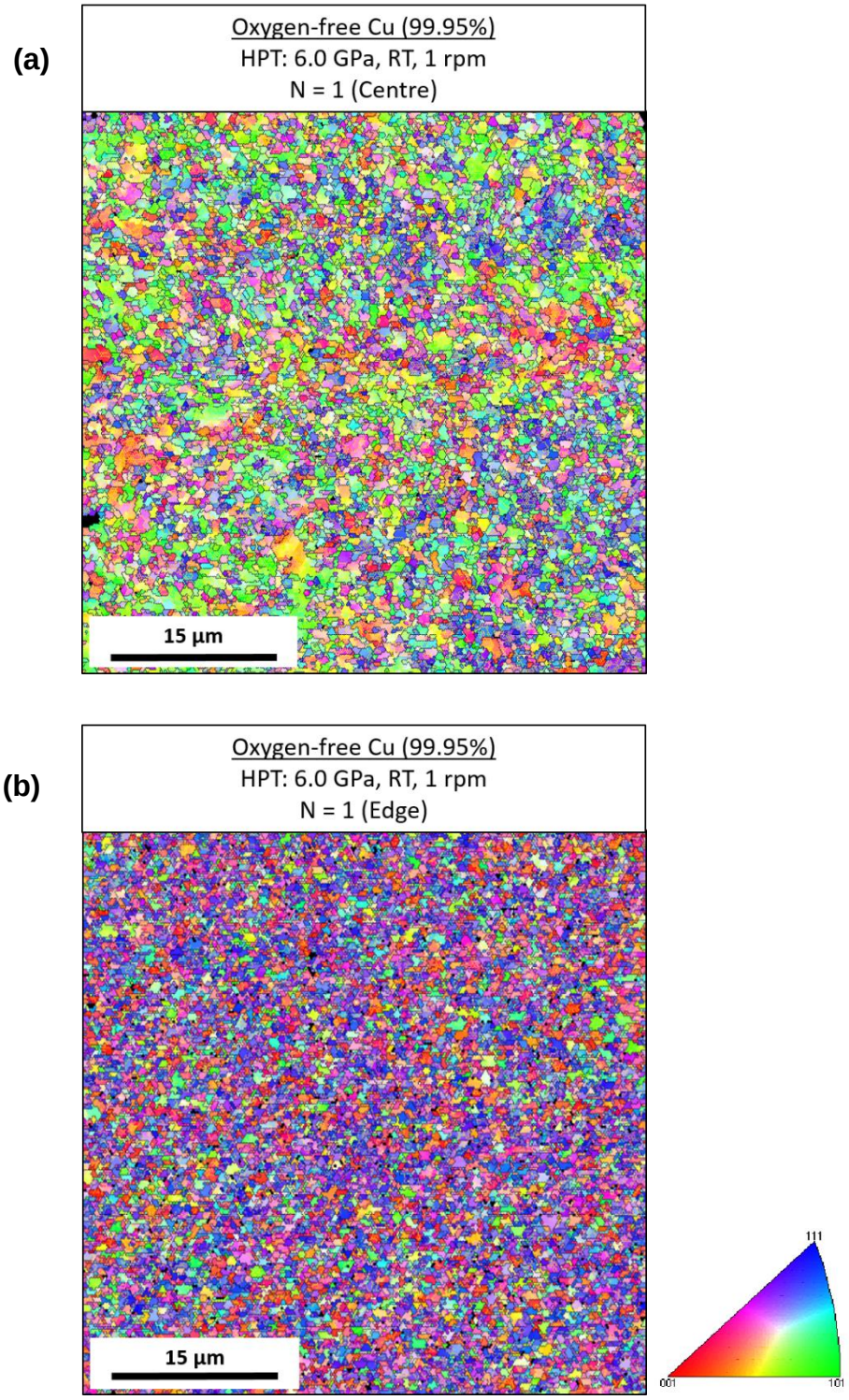

Figure 5.4 OIM Images of oxygen-free copper processed by HPT for 1 turn: (a) centre and (b) edge of the disc.

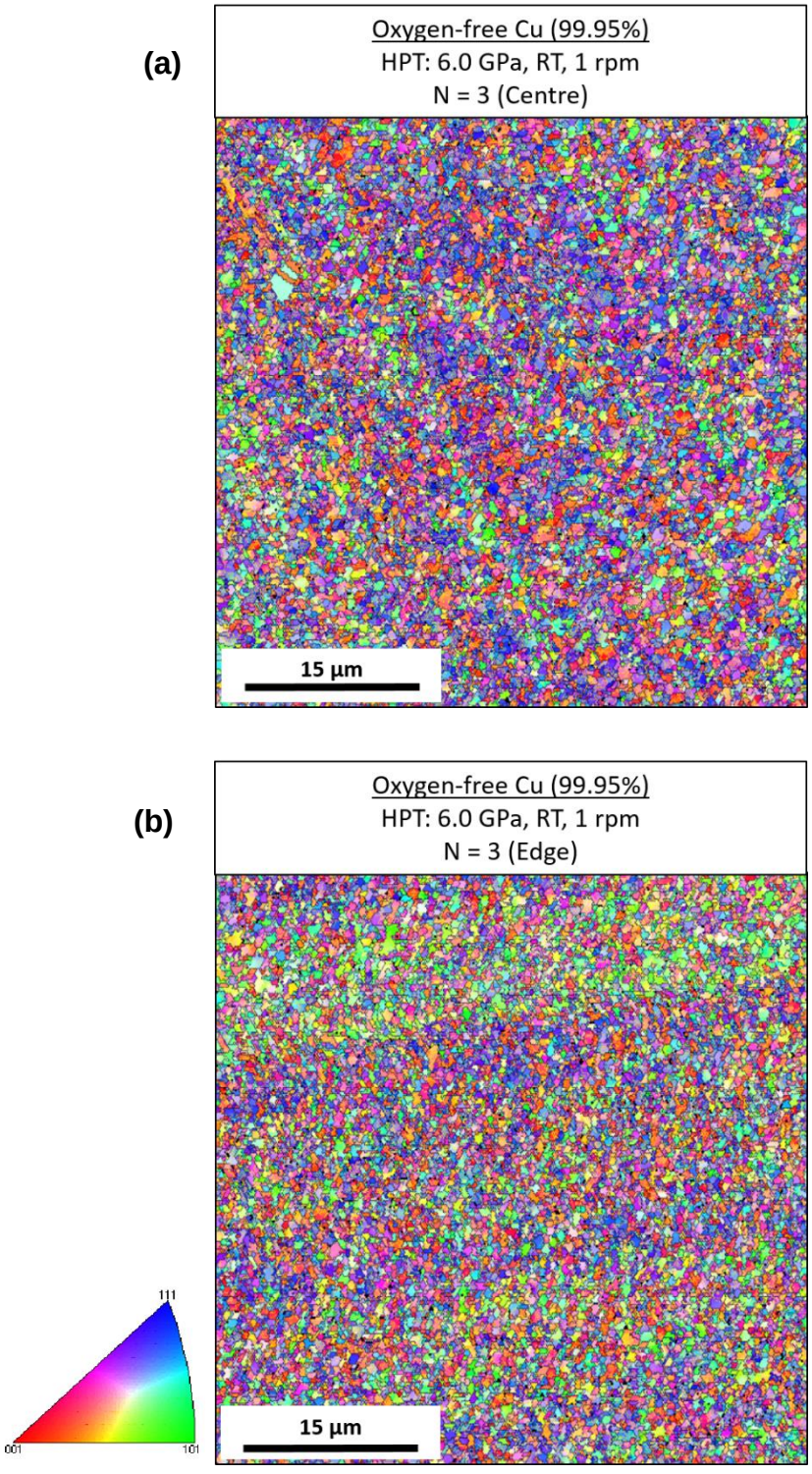

Figure 5.5 OIM Images of oxygen-free copper processed by HPT for 3 turns: (a) centre and (b) edge of the disc.

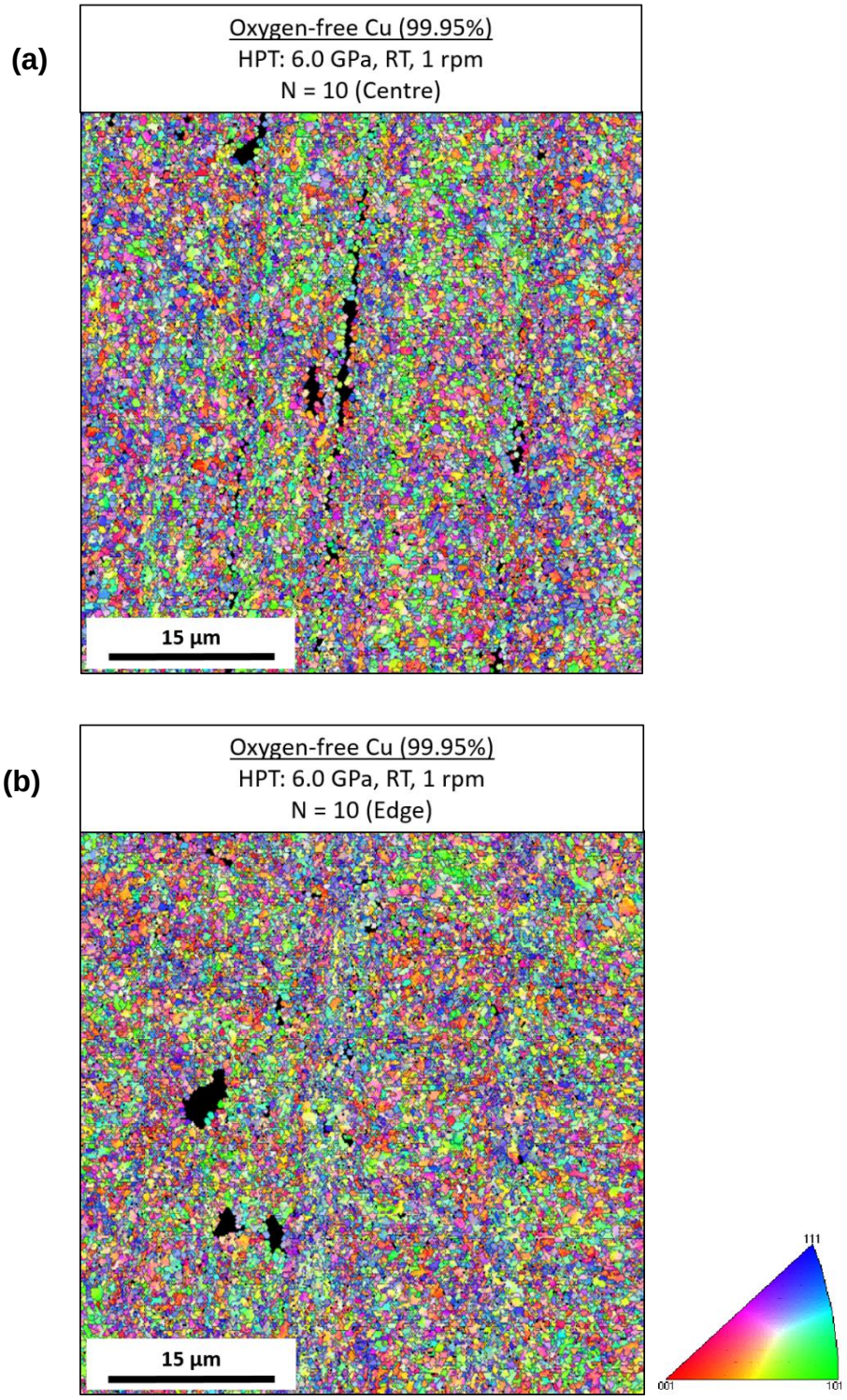

Figure 5.6 OIM Images of oxygen-free copper processed by HPT for 10 turns: (a) centre and (b) edge of the disc.

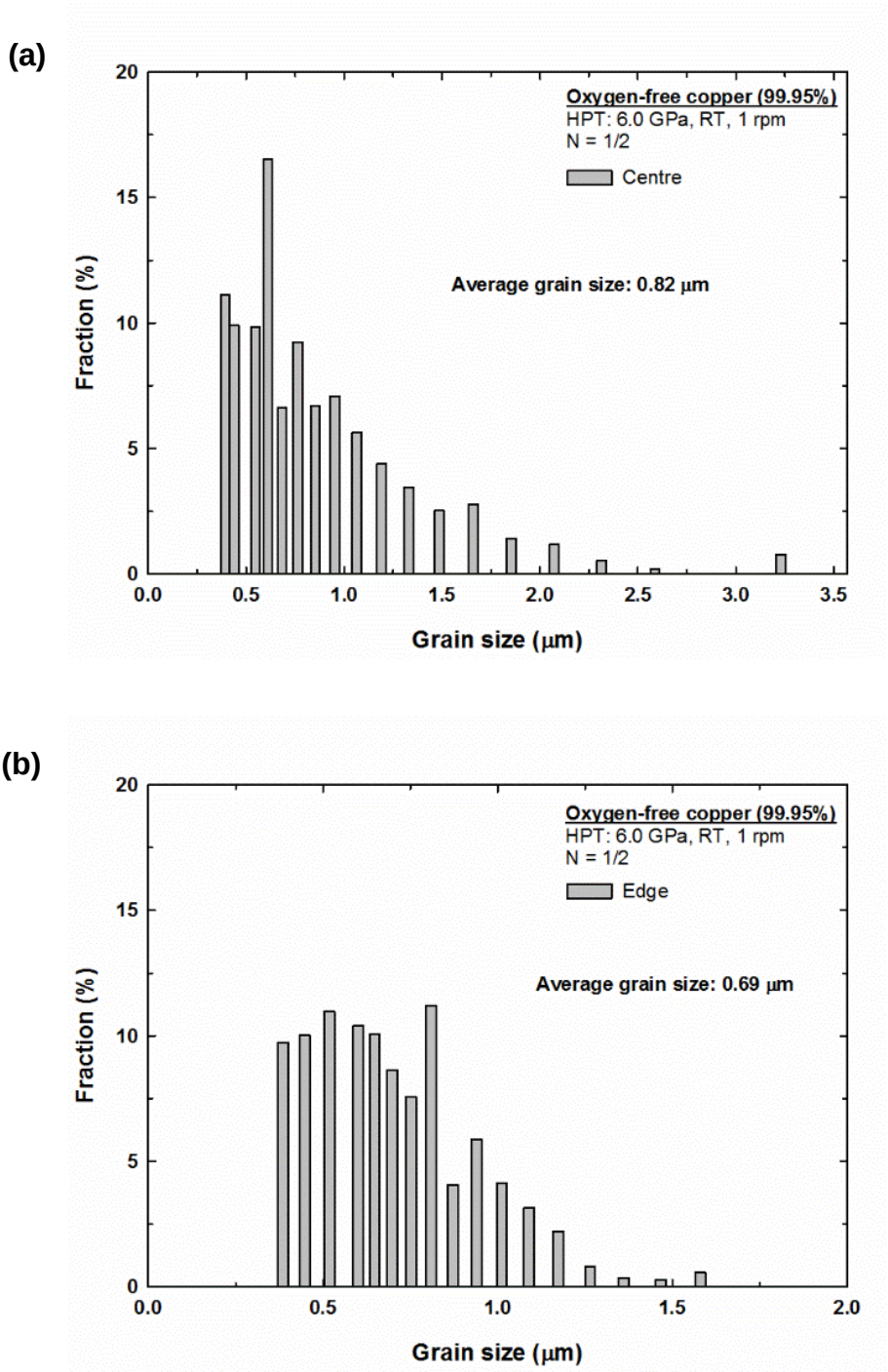

Figure 5.7 Grain size distribution of oxygen-free Cu processed by HPT for 1/2 turn: (a) centre and (b) edge of the disc.

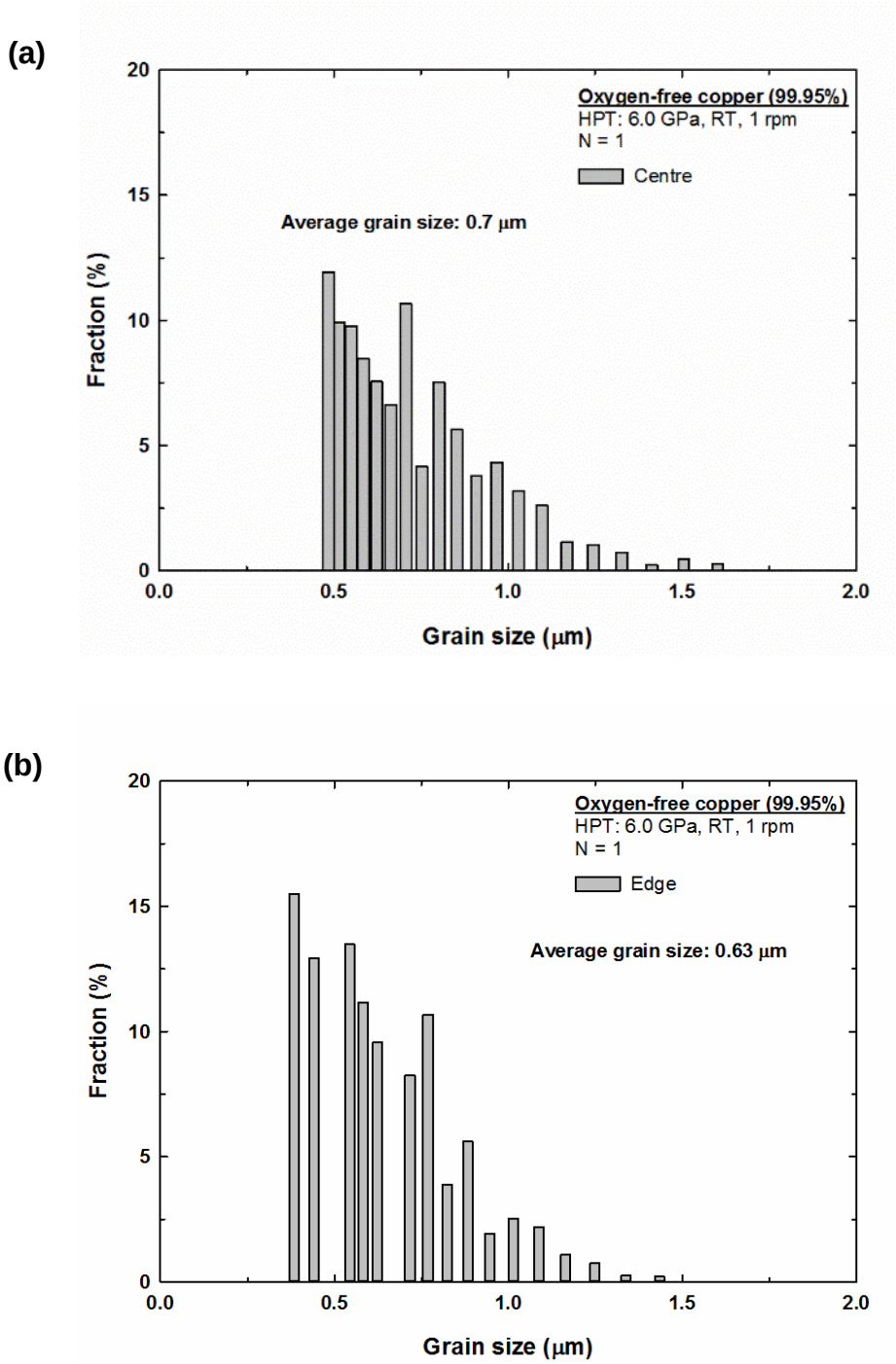

Figure 5.8 Grain size distribution of oxygen-free Cu processed by HPT for 1 turn: (a) centre and (b) edge of the disc.

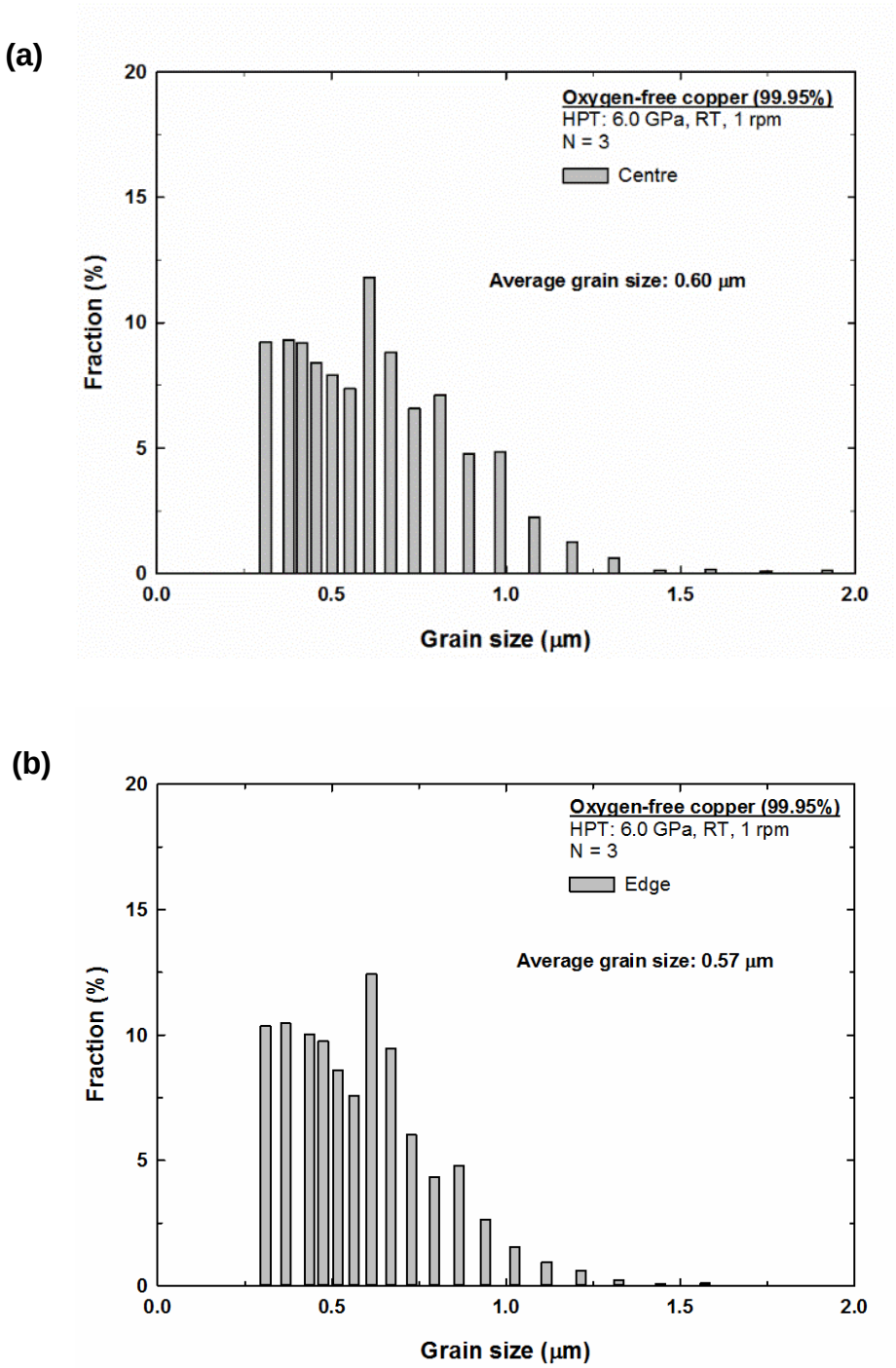

Figure 5.9 Grain size distribution of oxygen-free Cu processed by HPT for 3 turns: (a) centre and (b) edge of the disc.

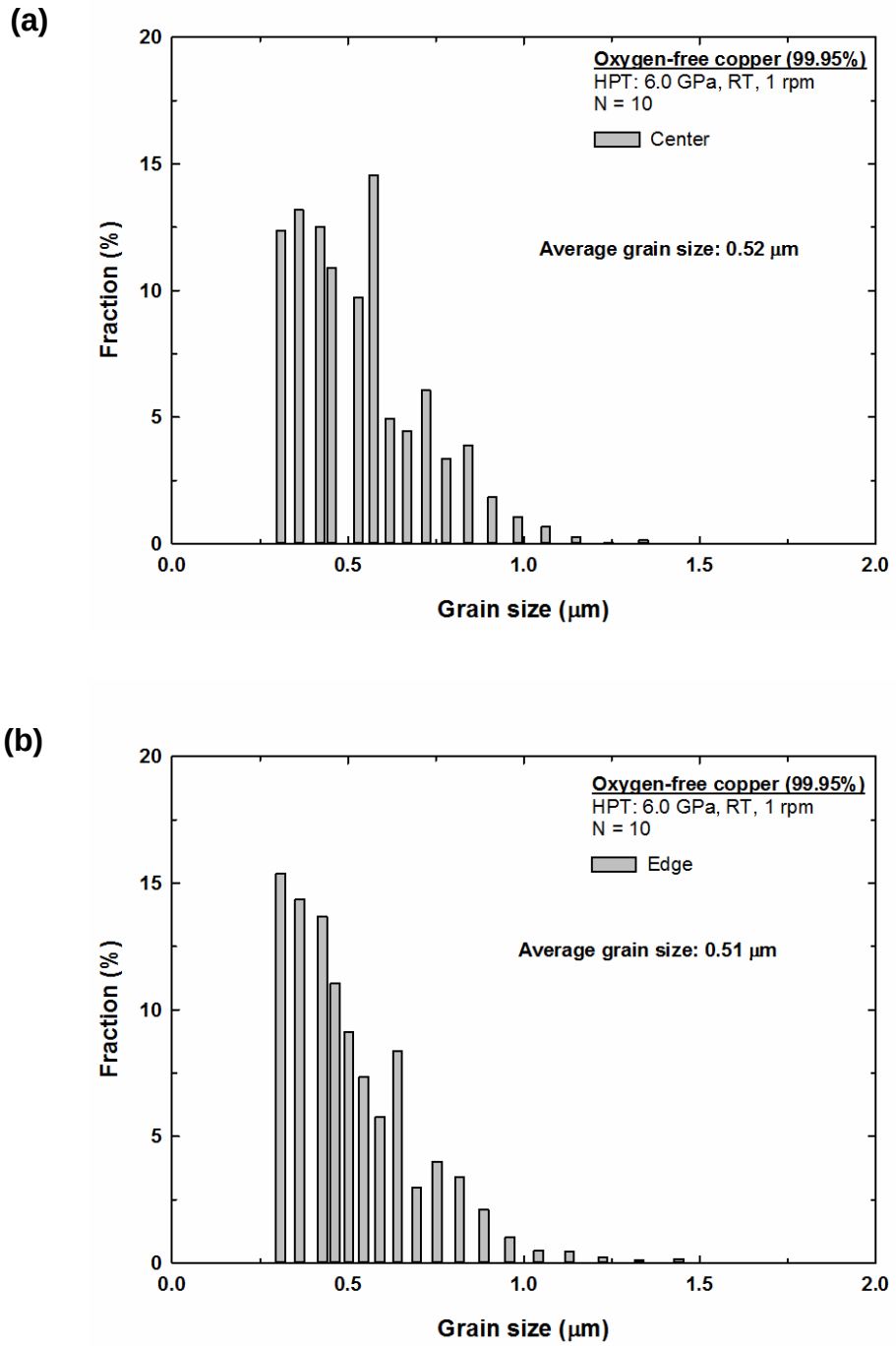

Figure 5.10 Grain size distribution of oxygen-free Cu processed by HPT for 10 turns: (a) centre and (b) edge of the disc.

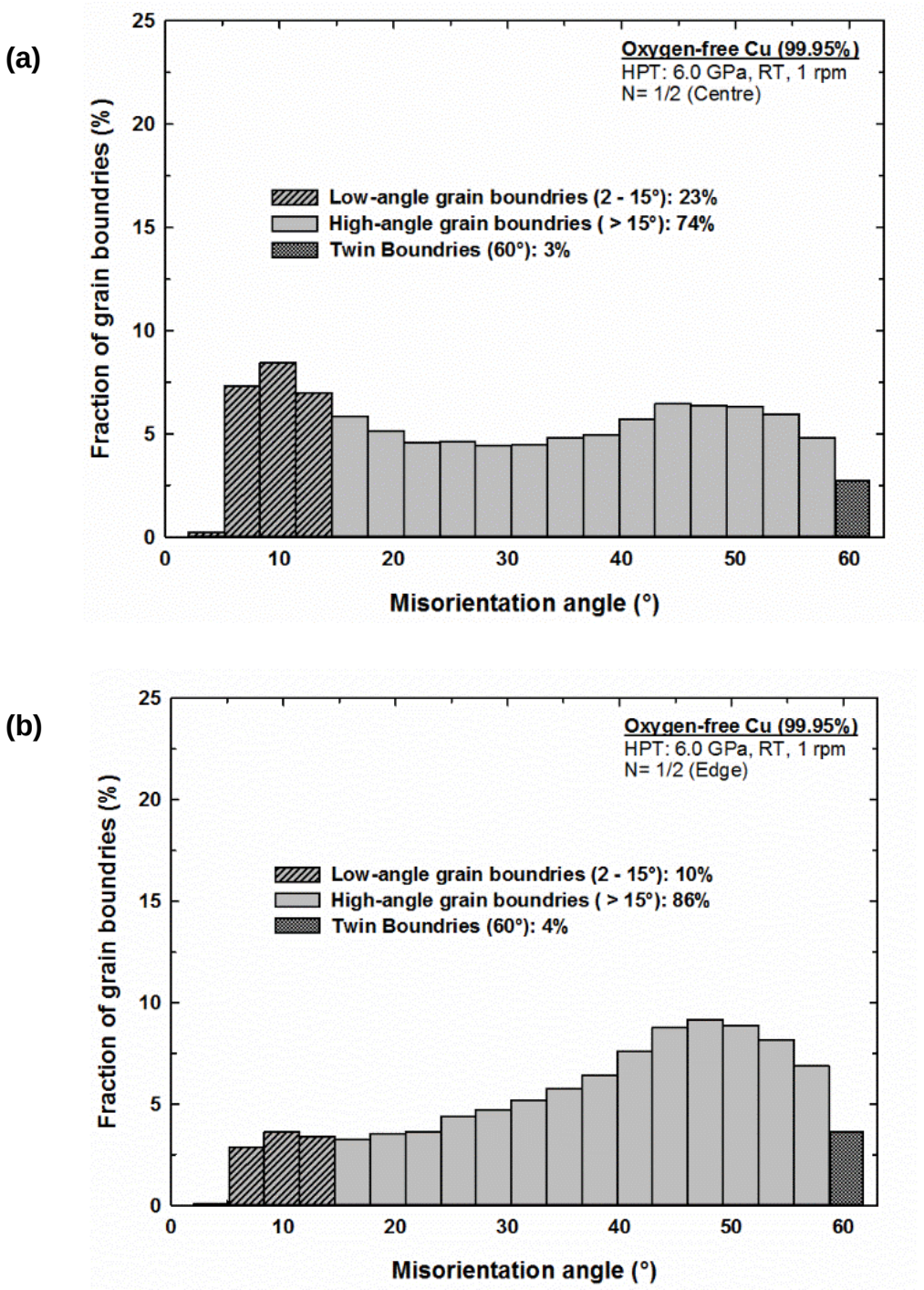

Figure 5.11 The distribution of proportion of misorientation angles of grain boundaries for oxygen-free Cu processed by HPT for 1/2 turn: (a) centre and (b) edge of the disc.

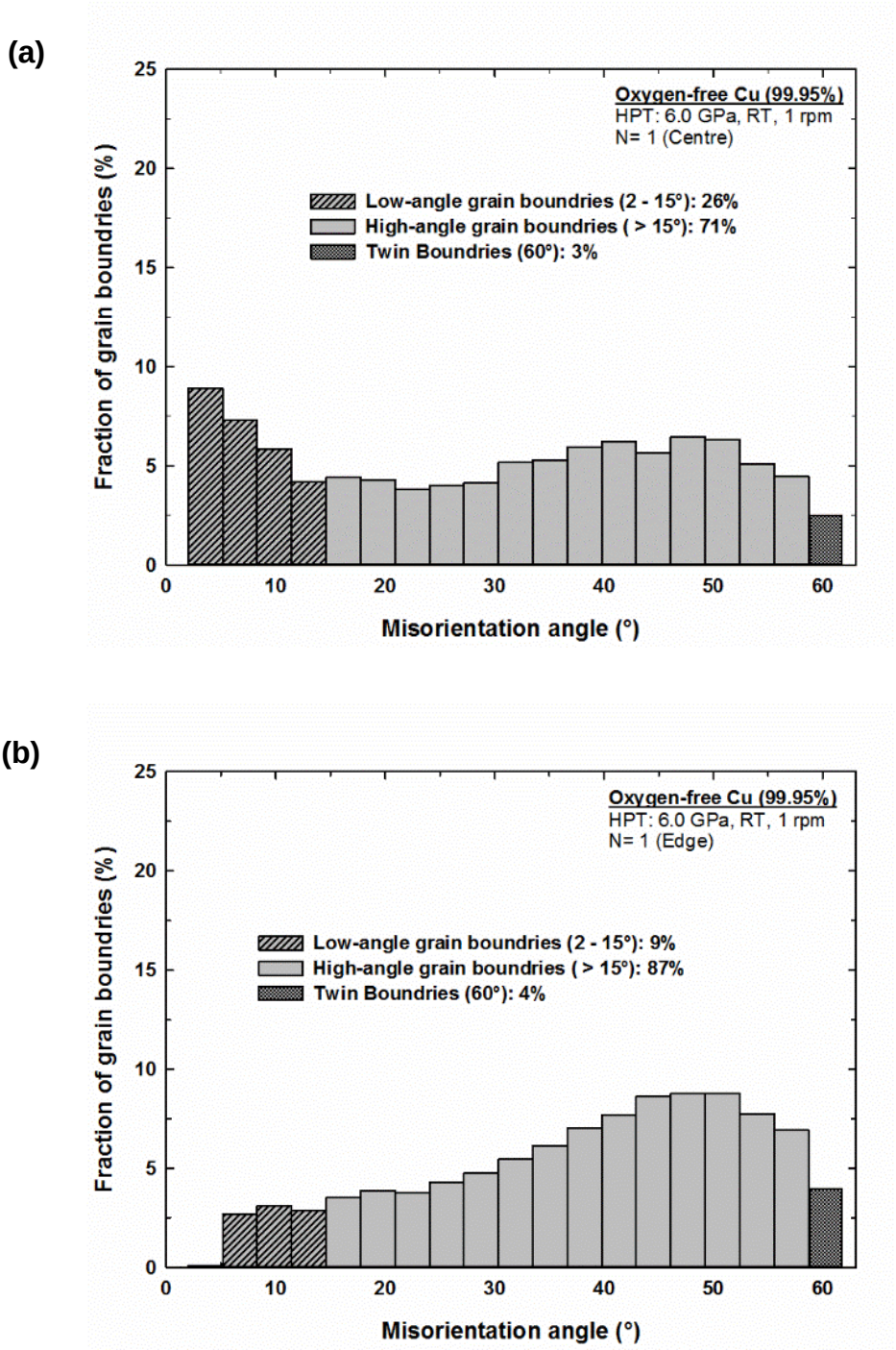

Figure 5.12 The distribution of proportions of misorientation angles of grain boundaries for oxygen-free Cu processed by HPT for 1 turn: (a) centre and (b) edge of the disc.

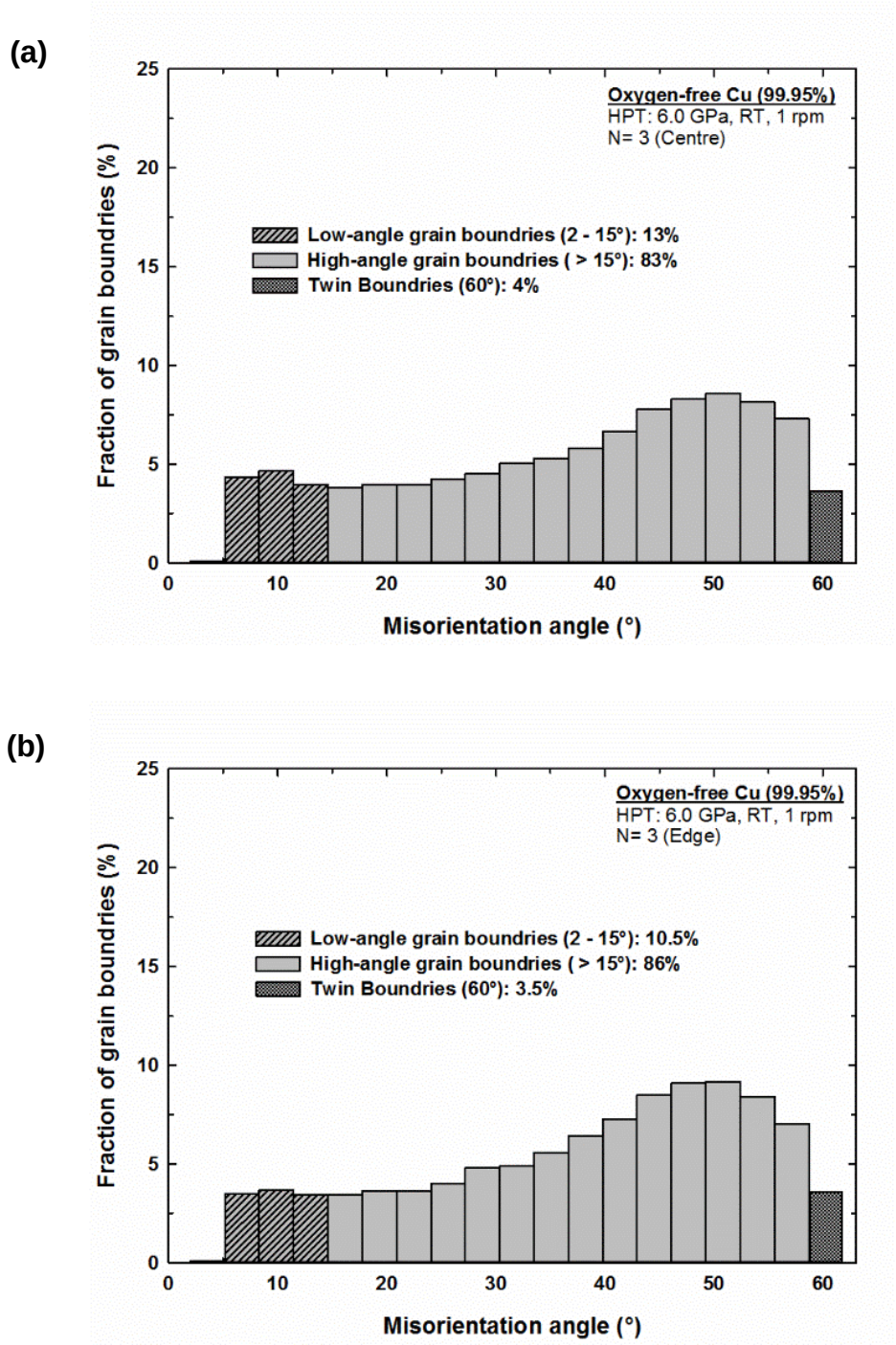

Figure 5.13 The distribution of proportion of misorientation angles of grain boundaries for oxygen-free Cu processed by HPT for 3 turns: (a) centre and (b) edge of the disc.

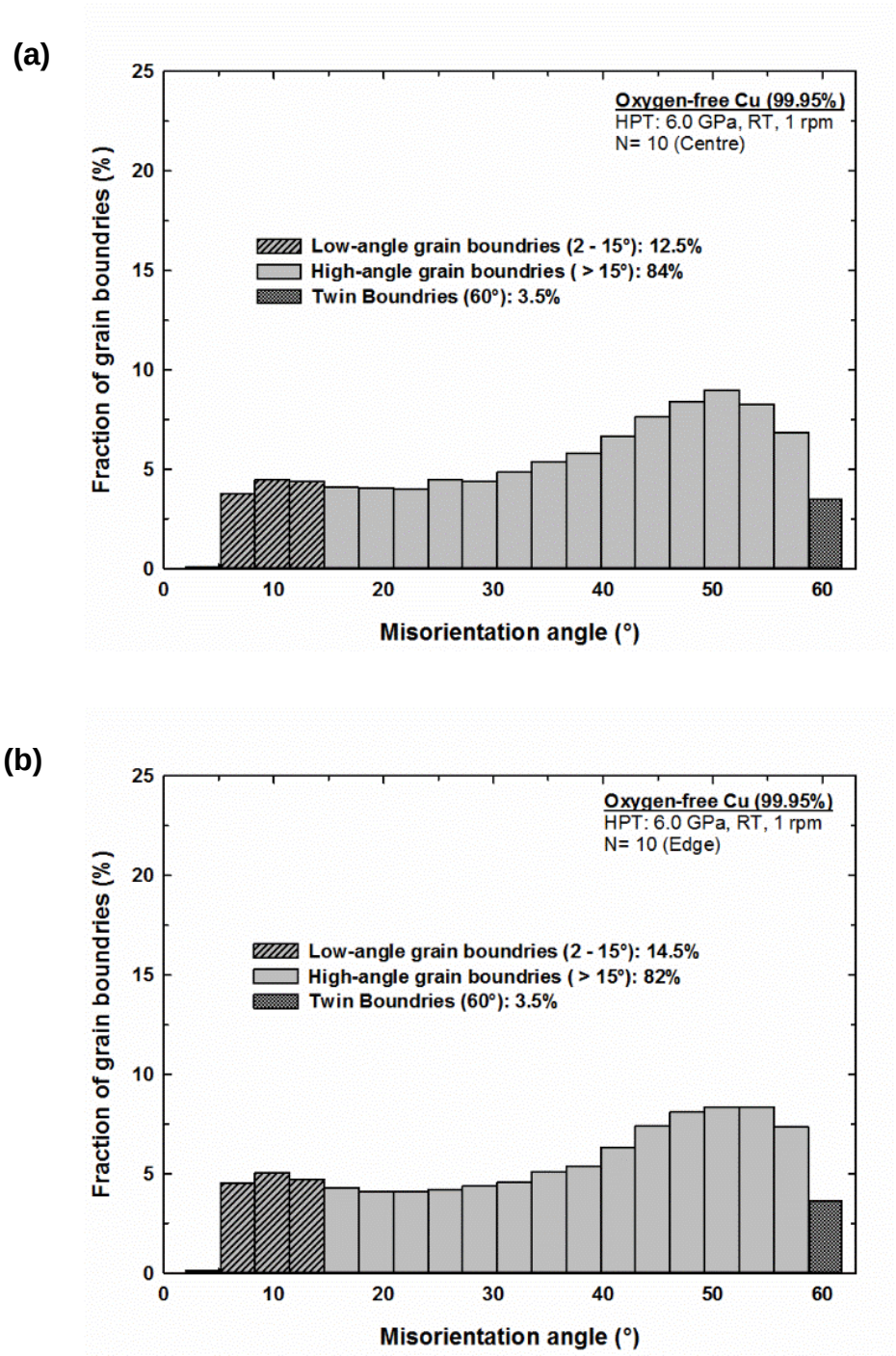

Figure 5.14 The distribution of proportion of misorientation angles of grain boundaries for oxygen-free Cu processed by HPT for 10 turns: (a) centre and (b) edge of the disc.

5.1.3 X-ray diffraction analysis

The XRD patterns of the annealed oxygen-free copper and the samples after processing by HPT through 1/2, 1, 3 and 10 turns are shown in Figure 5.15. Each diffraction peak is marked with its related reflection plane: (111), (002), (022), (113) and (222). Comparing the annealed and processed samples, the line-broadening grew after increasing the rotation to N = 1/2 and was followed by very minor changes with increased numbers of turns. It can be seen from Figure 5.15 that an increasing number turns increased the intensity of the (111) peak but reduced the intensity of the (002) peak.

XRD profile broadening is mainly affected by two parameters: the internal microstrain and the size of the small grains. Line-broadening is used to calculate the crystallite size for each condition [151,152]. The crystallite size and microstrain values obtained from the analysis of the XRD line-broadening are shown in Figure 5.16. The error bars were calculated using Maud software. A significant decrease in crystallite size was observed after 1/2 turn, followed by a minor recovery with further straining. The crystallite sizes of ~132 nm, ~154 nm, ~176 nm and ~179 nm are less than the near-edge grain sizes of ~690 nm, ~630 nm, ~570 nm and ~510 nm, measured after 1/2, 1, 3 and 10 turns respectively. It can be seen that the crystallite size values determined by XRD are smaller than the grain sizes measured by EBSD. This is due to the fact that EBSD measures the size of the grains with HAGBs, while XRD measures the mean size of the domains [153,154]. The concentration of crystallite defects in the oxygen-free copper samples is represented by the measured microstrain obtained from the XRD peak-broadening depicted in Figure 5.16. It is apparent from these results that microstrain increases after 1/2 turn followed by a decrease with further rotations up to 10 turns.

The dislocation density ρ was calculated from the X-ray data using Equation 3.1 [140,141]. Figure 5.17 shows the calculated values for the dislocation density and the crystallite size as a function of the number of turns. It is obvious from Figure 5.16 and Figure 5.17 that the dislocation density and microstrain demonstrate similar behaviour after deformation. The dislocation density initially increased from ~3.9×10^{12} m^{-2} to ~5.6×10^{13} m^{-2} after 1/2 a turn and then decreased to a values of ~3.2×10^{13} m^{-2}, ~2.8×10^{13} m^{-2} and ~1.4×10^{13} m^{-2} after 1, 3 and 10 turns, respectively. The decrease in the dislocation density between 1 and 10 turns is evidence that a rapid dynamic recovery took place during HPT processing.

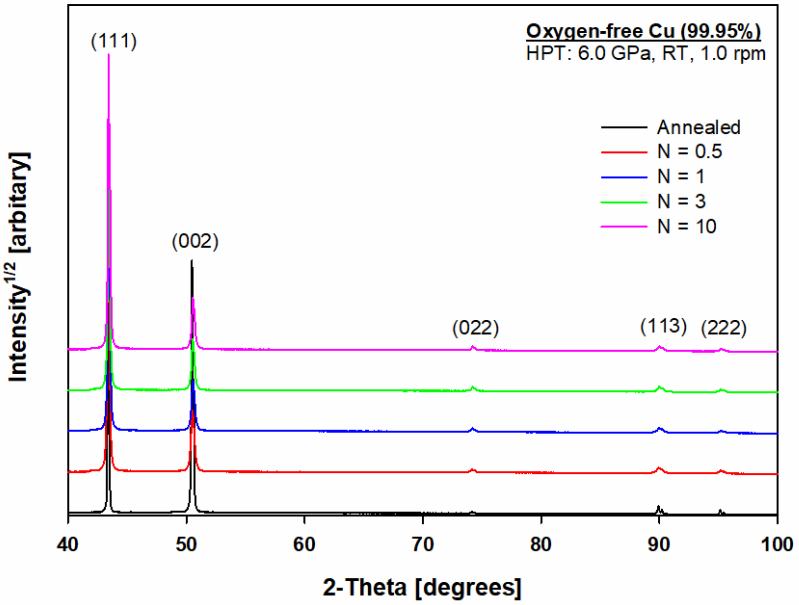

Figure 5.15 XRD patterns for oxygen-free copper, showing the annealed condition and after processing by HPT through 1/2, 1, 3 and 10 turns.

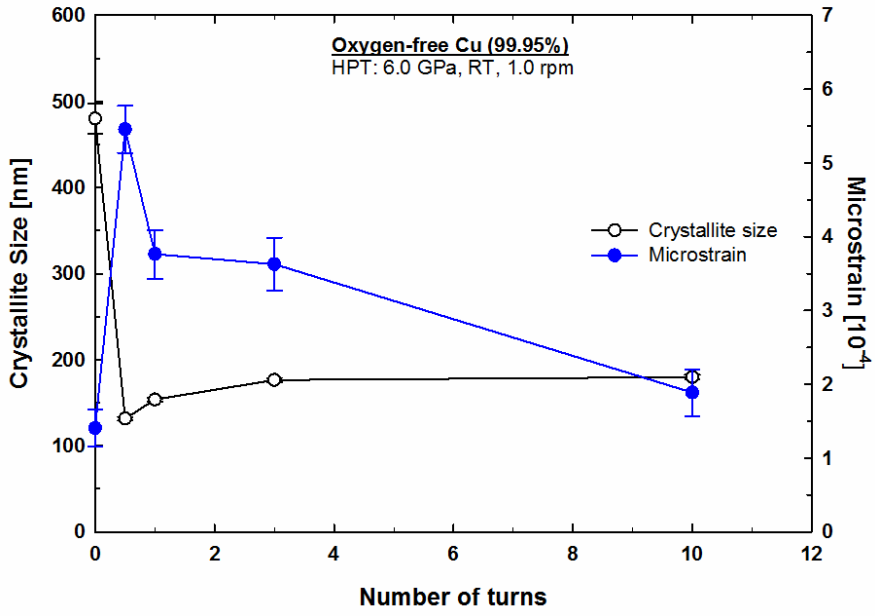

Figure 5.16 Crystallite size and microstrain plotted as a function of number of HPT turns.

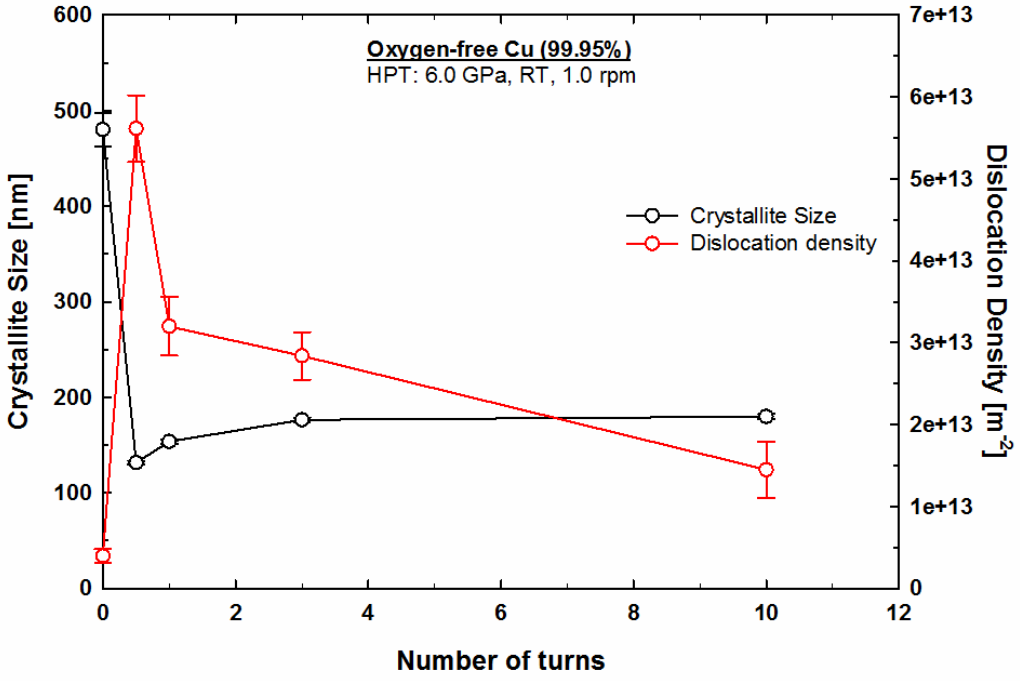

Figure 5.17 Crystallite size and dislocation density plotted as a function of number of HPT turns.

5.1.4 Microhardness measurements after HPT

The microhardness of UFG oxygen-free copper with a commercial purity of 99.95% is measured by the Vickers microhardness test. Two different methods are used to record the measurements: one takes the microhardness in a line across the diameter of each disc, see Figure 3.7, and the other the microhardness over the whole surface as shown in Figure 3.8 (X-plane).

Nanocrystalline materials consolidated from nanopowders are highly contaminated with porosity, a major problem that affects microhardness and makes it difficult to study [195]. In this research, the UFG oxygen-free copper processed by HPT has no porosity; as mentioned earlier, this is one of the advantages of UFG materials processed by SPD. The intrinsic microhardness behaviour relating to the structure of bulk UFG copper is investigated in this section.

5.1.4.1 Microhardness measurements measured across the diameter of HPT discs

Values of microhardness, in Hv, were plotted with respect to their position on the disc. Figure 5.18 shows the Vickers microhardness measurements across a diameter of each disc after HPT processing under a pressure of 6.0 GPa for 1/4, 1/2, 1, 3, 5 and 10 turns, respectively. The lower dashed line indicates the hardness value of ~41 Hv measured after annealed for 1 hour at 600 ºC before processing. An assessment of Figure 5.18 shows that the microhardness values increased significantly by a factor of two to three after a 1/4 turn, with higher values at the edges of the disc with an average of ~138 Hv, and lower at the centre of the disc with an average of ~96 Hv. The incremental increase in microhardness at the centre is approximately 135%, and near the edges approximately 235%.

Increasing the number of turns to N = 1/2 turn increased the hardness at the centre of the disc to ~101 Hv, but the hardness at the edge dropped slightly to ~135 Hv. With further increases in torsional straining (a higher number of turns), the hardness values continued to rise in the central region and the area of lower hardness was significantly reduced after 3 turns as shown in Figure 5.18. In contrast, the hardness values recorded at the edge of the disc remained almost constant, undergoing no major change with increasing number of turns. After 10 turns, the hardness value in the central region of the disc had increased to ~128 Hv, approximately ~210% higher than the value of the annealed condition. A reasonable homogeneity was achieved across the disc by increasing strain up to 10 turns.

The error bars in the central region of the discs were noticeably higher than at the periphery, as shown in Figure 5.19. These results illustrate the evolution of a reasonable homogeneity in hardness across the discs with increasing number of turns during HPT processing.

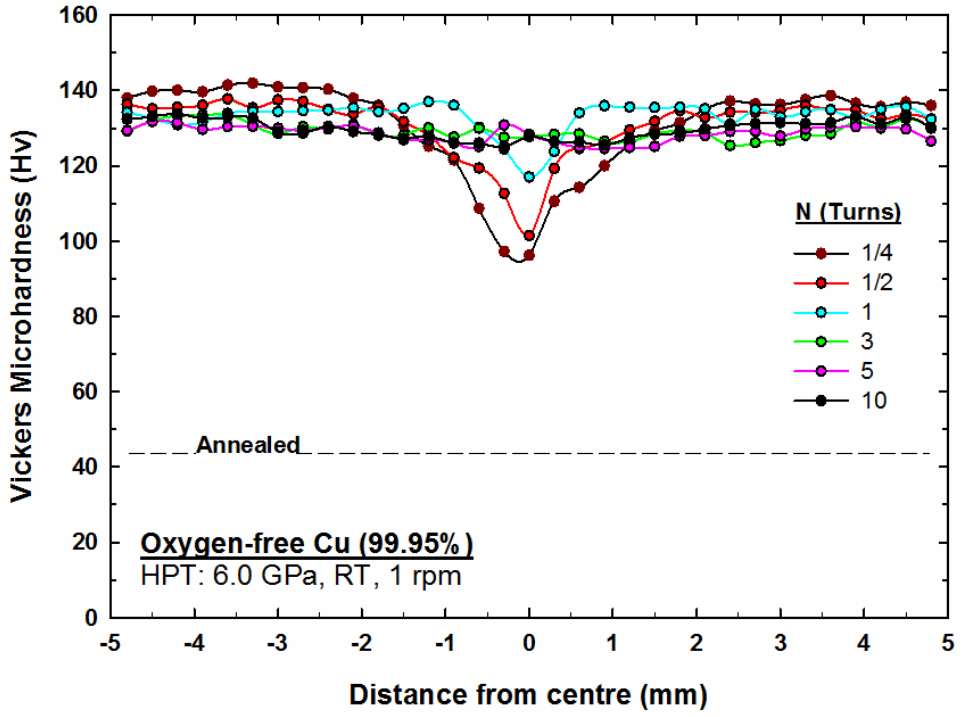

Figure 5.18 Vickers microhardness measurements along a diameter of oxygen-free copper discs processed by HPT for several numbers of turns.

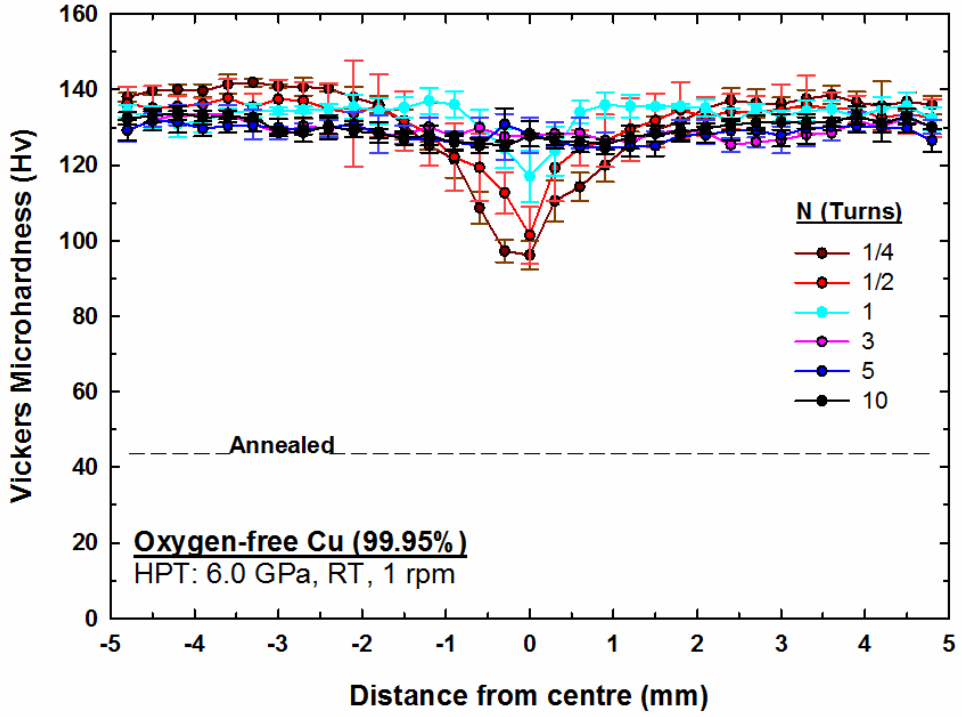

Figure 5.19 Individual error bars for the microhardness measurements along a diameter of oxygen-free copper discs processed by HPT for various numbers of turns.

Table 5.1 lists the hardness values with their error margins. Each value represents the average of two hardness measurements at the same distance along the diameter either side of the disc centre as follows: -4.8 mm to -0.3 mm, 0, 0.3 mm to 4.8 mm. It is clear that after processing the disc by N = 1/4, 1/2 and 1 turn, the central region shows lower hardness values than the periphery. However; after N = 3 turns the variation in hardness values decreases significantly and all values become closer. Likewise, the error bars are quite large at N = 1/4 and N = 1/2 along the diameters of the discs, but decrease with further turns N = 1, 3, 5 and 10 (greater strain). Thus, Table 5.1 shows increasing homogeneity in hardness across the diameter of the discs after processing by HPT.

Figure 5.20 shows the development of hardness in the central region and the edge of the discs after processing by HPT by up to 10 turns. It is clear that there is an increase in the hardness at both positions after a 1/4 turn, when compared with the values of the annealed (unprocessed) condition. Nevertheless, the hardness at the centre of the disc ~96 Hv is lower than at the edges ~138 Hv. The difference between hardness values at the centre and edge of the discs tends to decrease with further turns. A reasonable degree of homogeneity of hardness is attained after 3 turns.

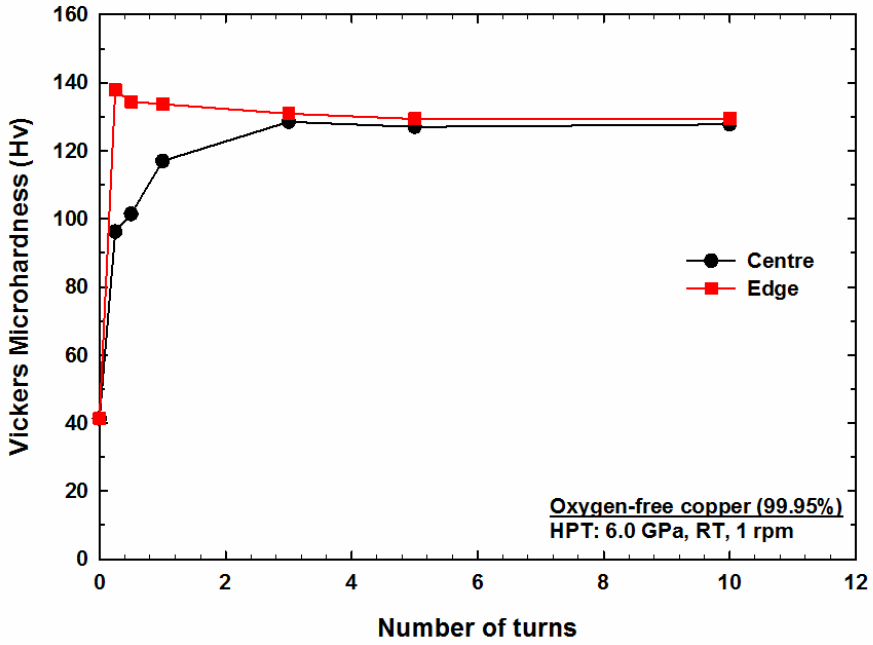

Figure 5.20 Hardness evolution at central region and edges of oxygen-free copper discs processed by HPT by up to 10 turns.

Table 5.1 Microhardness values along the radii of oxygen-free copper discs processed by HPT.

Distance from center (mm)	Vickers Microhardness (Hv)					
	0.25 turn	1/2 turn	1 turn	3 turns	5 turns	10 turns
0	96.2 ± 3.7	101.4 ± 6.5	117.0 ± 6.5	127.9 ± 4.0	128.3 ± 3.0	127.8 ± 1.6
0.3	103.9 ± 9.4	115.9 ± 4.7	124.1 ± 0.5	127.9 ± 0.5	128.6 ± 3.1	125.7 ± 0.4
0.6	111.5 ± 3.9	122.0 ± 3.6	132.1 ± 2.7	129.2 ± 1.1	124.9 ± 0.2	126.2 ± 0.2
0.9	120.8 ± 1.1	124.3 ± 3.0	136.0 ± 0.1	127.1 ± 0.8	125.3 ± 1.1	125.7 ± 0.3
1.2	125.4 ± 0.3	128.8 ± 0.9	136.3 ± 0.1	128.2 ± 2.6	125.9 ± 1.4	127.6 ± 0.3
1.5	130.0 ± 1.0	131.8 ± 0.0	135.4 ± 0.2	128.3 ± 0.2	126.1 ± 1.3	127.8 ± 0.8
1.8	133.7 ± 3.3	135.2 ± 0.7	135.0 ± 0.8	128.7 ± 0.8	128.3 ± 0.6	128.5 ± 0.2
2.1	136.5 ± 2.0	133.2 ± 0.6	135.3 ± 0.2	129.8 ± 1.5	129.3 ± 1.8	129.4 ± 0.5
2.4	138.7 ± 2.2	134.6 ± 0.5	132.9 ± 2.6	127.6 ± 3.1	129.7 ± 0.7	130.6 ± 0.2
2.7	138.5 ± 3.0	135.6 ± 2.1	134.8 ± 0.3	128.3 ± 3.0	129.2 ± 0.2	129.9 ± 1.8
3.0	138.6 ± 3.3	136.1 ± 1.9	133.7 ± 0.9	127.6 ± 1.4	129.0 ± 1.5	130.2 ± 1.7
3.3	139.7 ± 3.1	135.7 ± 0.4	134.4 ± 0.1	129.5 ± 2.0	130.1 ± 0.5	131.9 ± 1.1
3.6	140.0 ± 2.0	136.3 ± 2.0	134.4 ± 0.6	131.0 ± 3.6	130.3 ± 0.1	132.2 ± 1.0
3.9	138.1 ± 2.1	135.5 ± 0.9	132.3 ± 0.8	132.5 ± 1.4	130.0 ± 0.5	132.9 ± 0.3
4.2	137.8 ± 3.1	134.0 ± 2.2	132.9 ± 2.9	131.8 ± 2.1	130.7 ± 1.0	132.5 ± 1.9
4.5	138.3 ± 2.1	134.4 ± 1.1	134.1 ± 2.2	132.2 ± 0.3	130.8 ± 1.4	133.0 ± 0.1
4.8	137.4 ± 0.9	134.4 ± 2.7	133.3 ± 1.3	129.6 ± 0.6	127.9 ± 2.0	131.2 ± 1.7

5.1.4.2 Microhardness measurements over whole surface of HPT discs

Microhardness was measured on a rectilinear grid pattern to produce colour-coded contour maps, as in Figure 5.21, of the surface of discs processed by HPT for: (a) 1/4 turn; (b) 1 turn; (c) 5 turns; and (d) 10 turns. The significance of the hardness values are denoted by a set of colours corresponding to hardness values ranging from 40 Hv to 180 Hv in incremental steps of 20, as shown in the key to the right of Figure 5.21. The point (X, Y) corresponds to the centre of each disc, and the external X and Y orthogonal axes were randomly selected on discs.

A detailed inspection of Figure 5.21(a) shows an inhomogeneous microhardness distribution in 1/4 turn sample, with an area of lower hardness around the centre of the disc, with a diameter of approximately 3 mm. This region of lower hardness shrinks to about 1 mm in diameter when increasing the strain to 1 turn, as shown in Figure 5.21(b). At higher numbers of turns, it can be seen in Figure 5.21(c) and (d) that the area of lower hardness in the central region completely disappears and the whole surface of the disc shows a relatively similar level of microhardness.

The microhardness measurements recorded over the whole surfaces of HPT discs can be shown in the form of histograms presenting the number fraction of Vickers microhardness values of oxygen-free copper after HPT through number of turns: (a) 1/4, (b) 1, (c) 5 and (d) 10, see Figure 4.22, where the red vertical lines represent the average microhardness values. It is apparent that the average microhardness value increases with increasing number of turns then reaches saturation after 1 turn. These histograms also show that the width of the distribution becomes smaller after 1 turn and remains similar up to 10 turns indicating that microhardness homogeneity can be achieved at number of turns higher than 1.

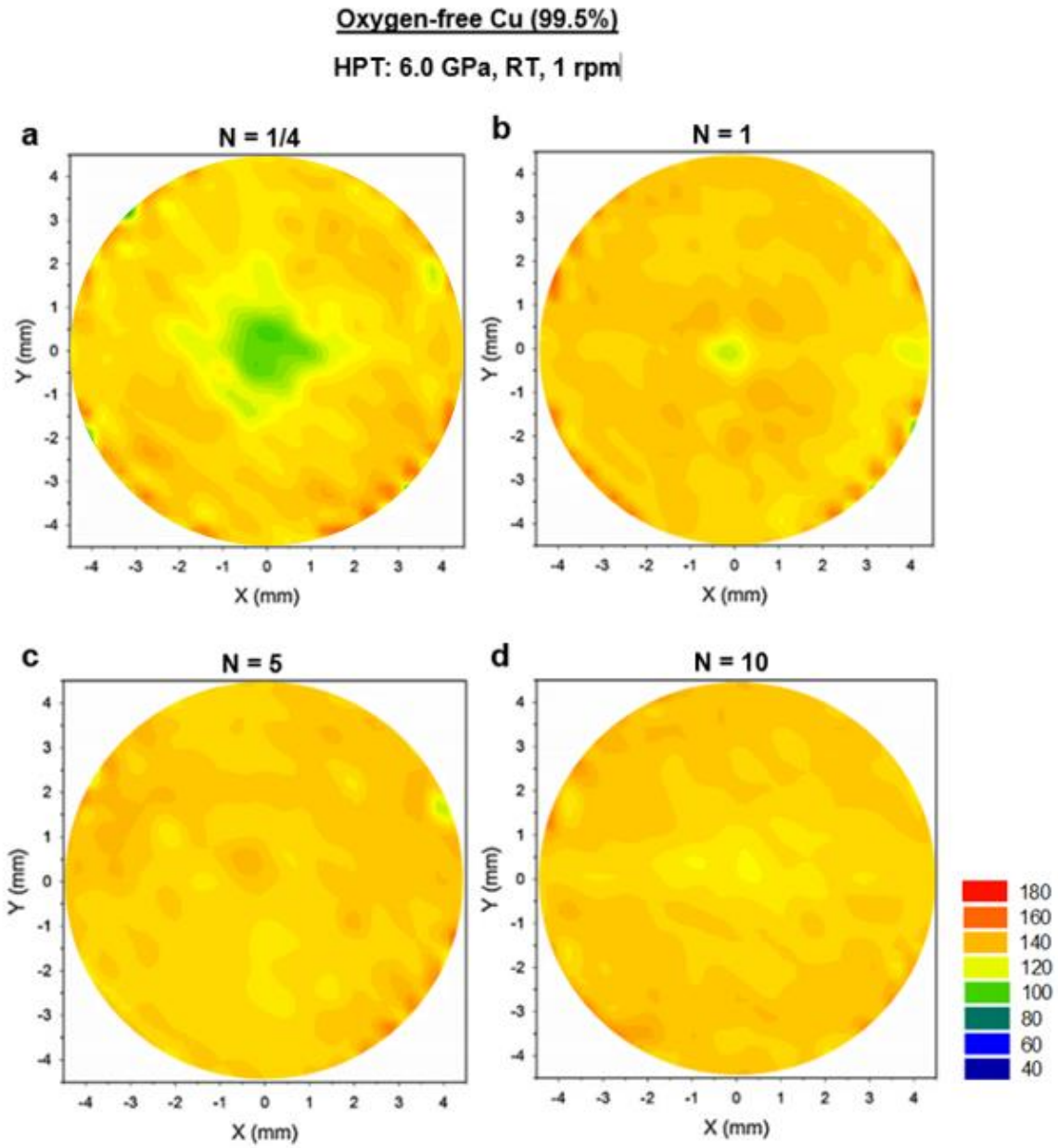

Figure 5.21 Colour-coded contour maps of the microhardness measurements over the surfaces of oxygen-free copper discs processed by HPT at a pressure of 6.0 GPa for: (a) 1/4 turn; (b) 1 turn; (c) 5 turns; and (d) 10 turns.

(a)

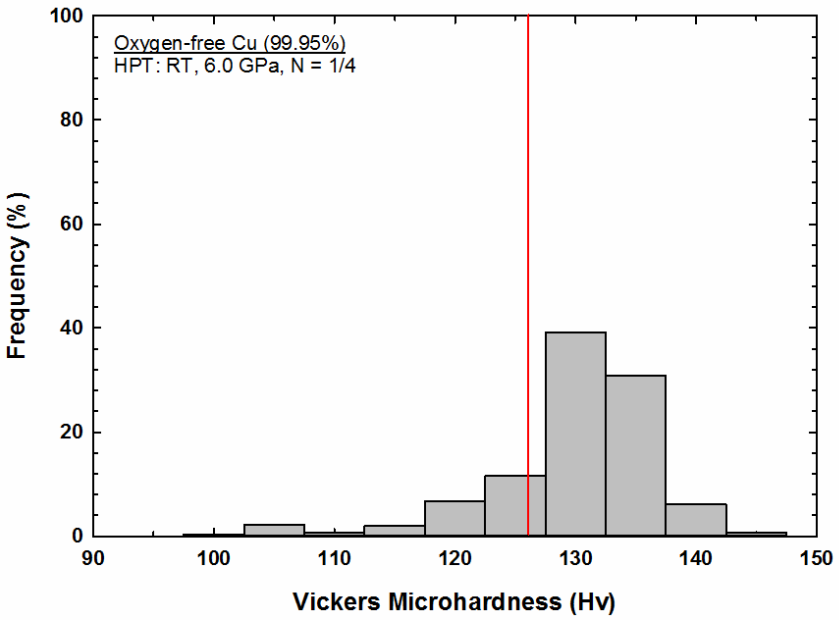
Oxygen-free Cu (99.95%)
HPT: RT, 6.0 GPa, N = 1/4
Frequency (%)
Vickers Microhardness (Hv)
0
20
40
60
80
100
90
100
110
120
130
140
150

(b)

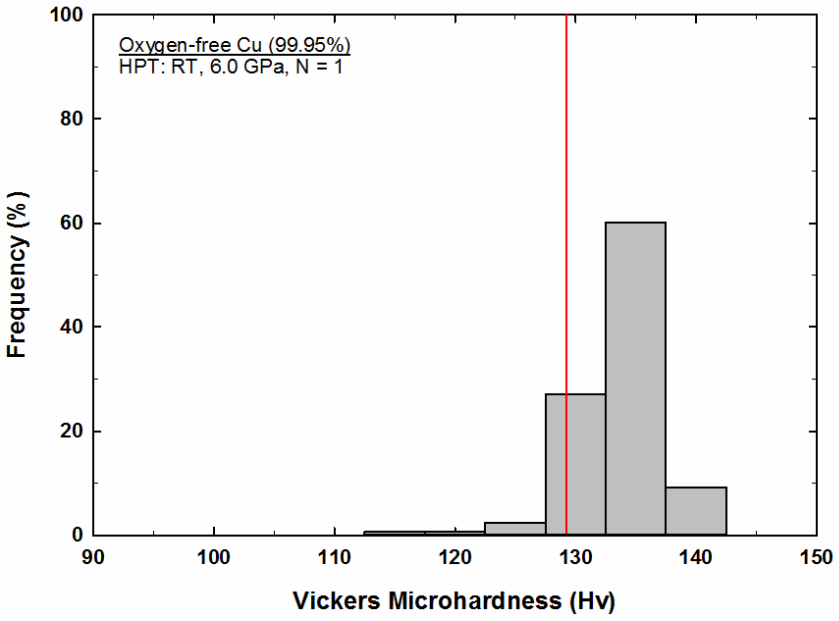
Oxygen-free Cu (99.95%)
HPT: RT, 6.0 GPa, N = 1
Frequency (%)
Vickers Microhardness (Hv)
0
20
40
60
80
100
90
100
110
120
130
140
150

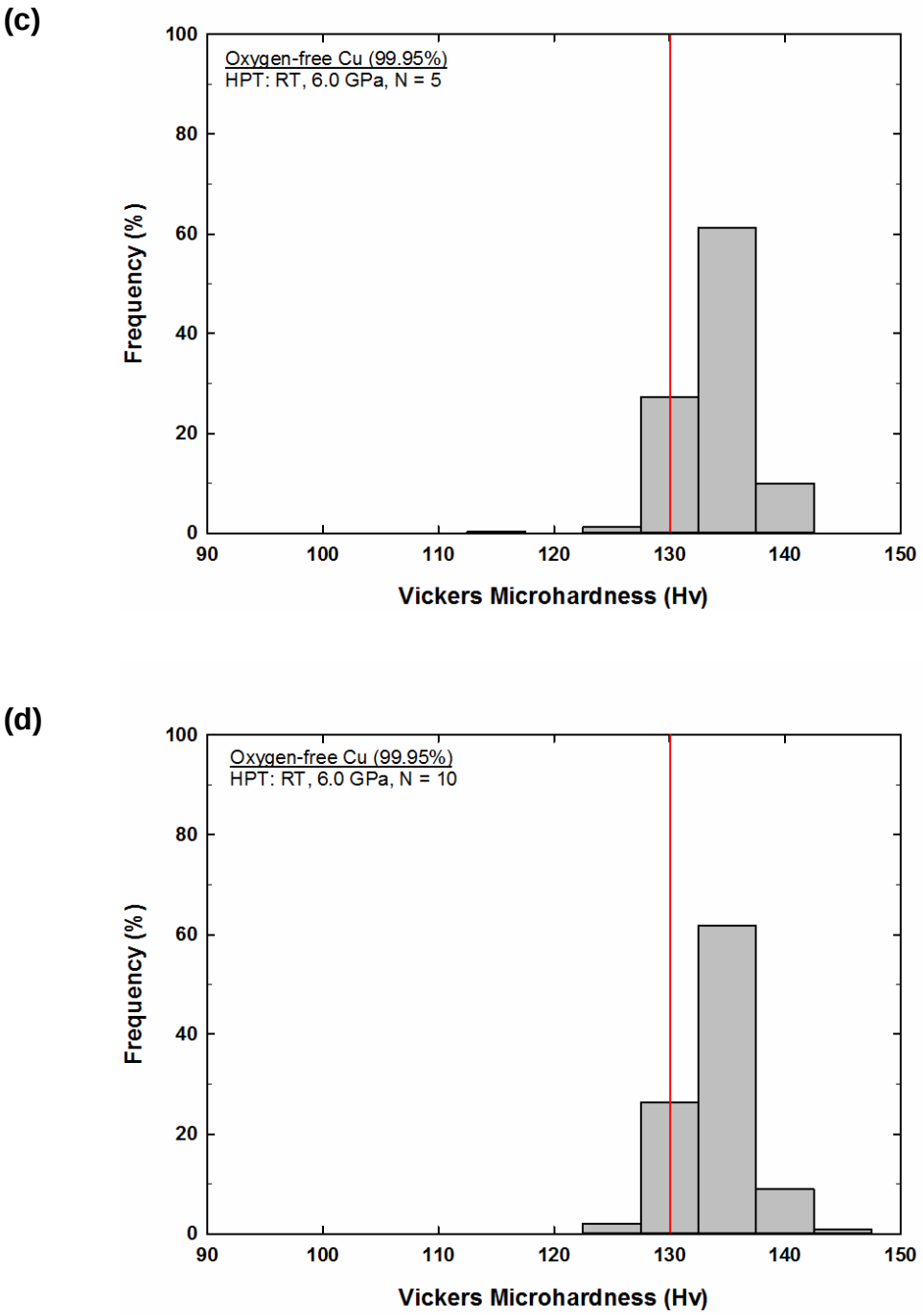

Figure 5.22 Histograms presenting the number fraction of Vickers microhardness values of oxygen-free copper after HPT through number of turns: (a) 1/4, (b) 1, (c) 5 and (d) 10. (The red vertical lines represent the average microhardness values).

5.2 Discussion

5.2.1 Microstructural evolution during HPT

Grain refinement is caused by dislocation gliding, accumulation, interaction, tangling and spatial rearrangement, and is influenced by the melting temperature, SFE and ordering degree, and solid-solution concentration [17]. Due to the higher melting point and the limited number of slip systems in body centred cubic structure (BCC) metals, their grain refinement and microhardness are higher than those of face centred cubic structure (FCC) metals. The schematic model of microstructural evolution is shown in Figure 5.23, as presented in a previous study [44]. It is suggested that microstructural evolution occurs in three stages. At the early stages of deformation (Region I), dislocations start to accumulate and subgrain boundaries form due to the agglomeration of dislocations. By further increasing the strain, Region II, the dislocation density and misorientation angle increase while the subgrain size decreases. The microstructure then reaches saturation due to a balance in generation and recovery of dislocations as shown in Figure 5.23, Region III.

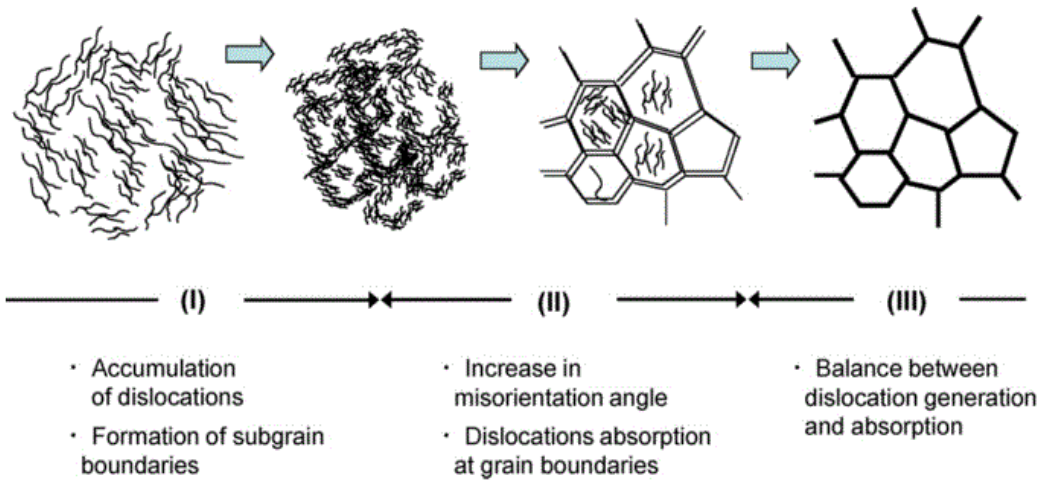

Figure 5.23 Stages of microstructural evolution with straining for grain refinement in pure Al [44].

Grain refinement observed in the present study starts initially at the edges of the disc with an equivalent strain of ~6.0 after 1/4 turn. The effect of torsional strain on the refinement is believed to be minor at the centre of the disc at this stage, when the equivalent strain is ~1, as shown in Table 5.2. The centre of the disc shows less grain refinement than the edge, and this inhomogeneity of the microstructure is confirmed by microhardness values, as shown in Figure 5.21(a). It is believed that dislocation accumulation occurs, and a subdivision starts to occur, within individual grains to form subgrain boundaries in the central region, accommodated by a large proportion of low-angle boundaries due to the applied compression force and torsional strain.

After increasing the number of turns to N = 1/2 (Figure 5.3), the average grain size fell from 24 μm (annealed condition) to 820 nm in the central region of the disc having high fraction of LABs, mostly associated with the subdivision process (formation of subgrain boundaries). Also, the twin boundaries are significantly reduced in both regions (centre and edge) after 1/2 turn. Figure 5.24, is an enlarged image of Figure 5.3(a), and shows that there are both fine and some elongated coarse grains in the centre of the disc. A close inspection on the equivalent strain in Table 5.2 shows values of ~1.3 at the centre of the disc and ~12.6 at the periphery, which is sufficient to initiate grain refinement but insufficient to reach full microhardness and microstructural homogeneity in pure copper.

Table 5.2 Equivalent strains at different distances from disc centre for oxygen-free copper processed by HPT.

No. of turns	Thickness (mm)	Distance from the centre of the disc (mm)						
		0.5	**1**	**1.5**	**2.5**	**3.5**	**4.5**	**5**
0.25	0.75	0.6	1.2	1.8	3.0	4.2	5.5	6.0
0.5	0.72	1.3	2.5	3.8	6.3	8.8	11.3	12.6
1	0.69	2.6	5.3	7.9	13.1	18.4	23.6	26.3
3	0.65	8.4	16.7	25.1	41.8	58.6	75.3	83.7
5	0.64	14.2	28.3	42.5	70.8	99.2	127.5	141.7
10	0.63	28.8	57.6	86.4	143.9	201.5	259.1	287.9

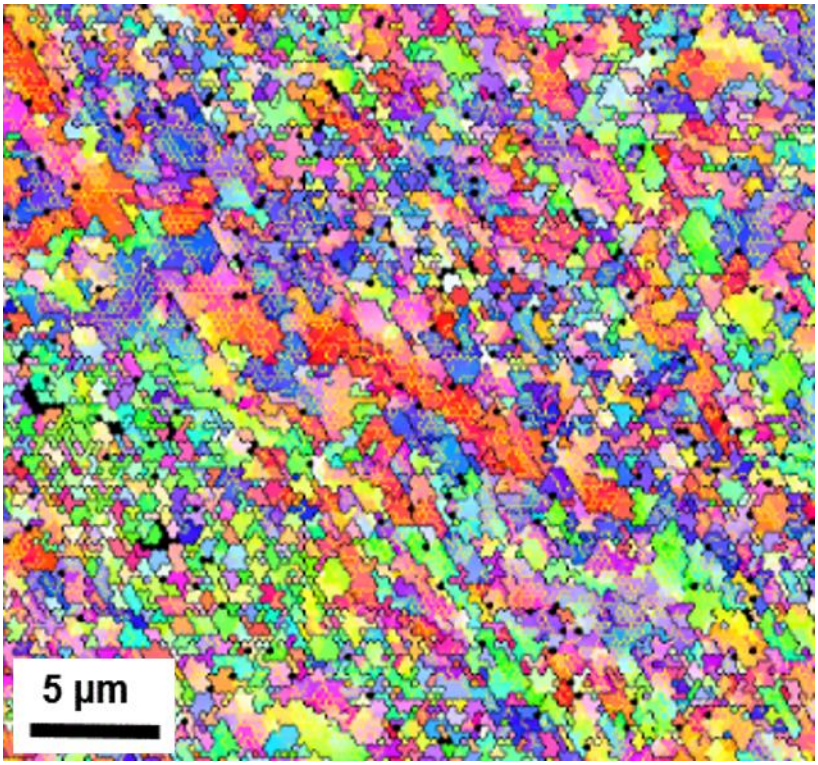

Figure 5.24 An enlarged image of Figure 5.3(a) showing fine and elongated coarse grains in the centre of oxygen-free copper disc processed by HPT for 1/2 turn.

The greater strain in the peripheral area contributes to producing UFGs with an average grain size of 690 nm containing a large proportion of HABs. The dislocation density increases with additional strain and reaches a maximum value of 5.6×10^{13} m^{-2} after 1/2 turn. A close inspection to Figure 5.17 shows a difference in the crystallite size between 1 and 10 turns. This difference is compensated by the change in the dislocation density, which indicates saturation of the dislocation storage after 1/2 turn of HPT.

After one turn, the recovery leads to a decrease in the dislocation density, while crystallite size increases. This was attributed to a softening mechanism occurred as a result of annihilation of dislocations [172,196,197]. This structural recovery at great strain increases the proportion of HAGBs. It is clear in Figure 5.4, Figure 5.5 and Figure 5.17 that there is a greater ratio of HAGBs, accompanied by a greater degree of relaxation in the microstructure after 1 and 3 turns. Also during this stage, as per other studies, thinning in the grain boundaries occurs due to evolution of the microstructure from non-equilibrium [198] to equilibrium grain boundaries at high values of the strain [199].

Non-equilibrium boundaries are defined as distorted grain boundaries with a high density of dislocations that are not needed to accommodate misorientation across the grain boundary [200]. The existence of non-equilibrium grain boundaries were observed in materials deformed by SPD techniques such as ECAP [201] and HPT [202]. Despite the decrease in the dislocation density, the average grain size was reduced with increasing number of turns up to 10. In addition, the reduction in microstrain at the same time as an increase in the crystallite size confirms the occurrence of a dynamic recovery process after 1 turn.

The microstructure is reasonably homogeneous after 10 turns, producing an average grain size of approximately 510 nm. This is larger than that for pure copper produced by HPT, where reported grain sizes have been ~150 nm after 5 turns at 5.0 GPa [34], ~140 nm after 5 turns at 2.0 GPa [37], ~140 nm after 5 turns at 6.0 GPa [46] and ~75 nm after 5 turns at 6.0 GPa [48]. This might be due to the occurrence of recovery mechanism during the HPT processing of oxygen-free copper in the current research.

Figure 5.25 shows the average grain size measured with respect to the number of turns and demonstrates a comparison between the values at the centre and edge of the disc. It can be seen that the plot of grain size against number of turns is not linear and it is assumed that the average grain size was larger after 1/4 turn than after 1/2 turn. The difference between consecutive measurements reduced with increasing number of turns. It should also be noted that the average grain size at both centre and edge reached the same value after 10 turns.

The evolution of microstructure in the central, mid-radius and near-edge regions of the disc with increasing numbers of turns is shown in Figure 5.1. It shows good agreement with microhardness measurements, depicted as colour-coded contour maps in Figure 5.21 where the central region shows limited grain refinement by shear strain in the early stages of deformation. This coarse area becomes more refined with increased number of turns (N = 5) and reaches almost the same average grain size as at the edges, indicating that the overall microstructure reaches nearly full refinement. This is consistent with earlier reports for high-purity copper of 99.99+ wt% [52].

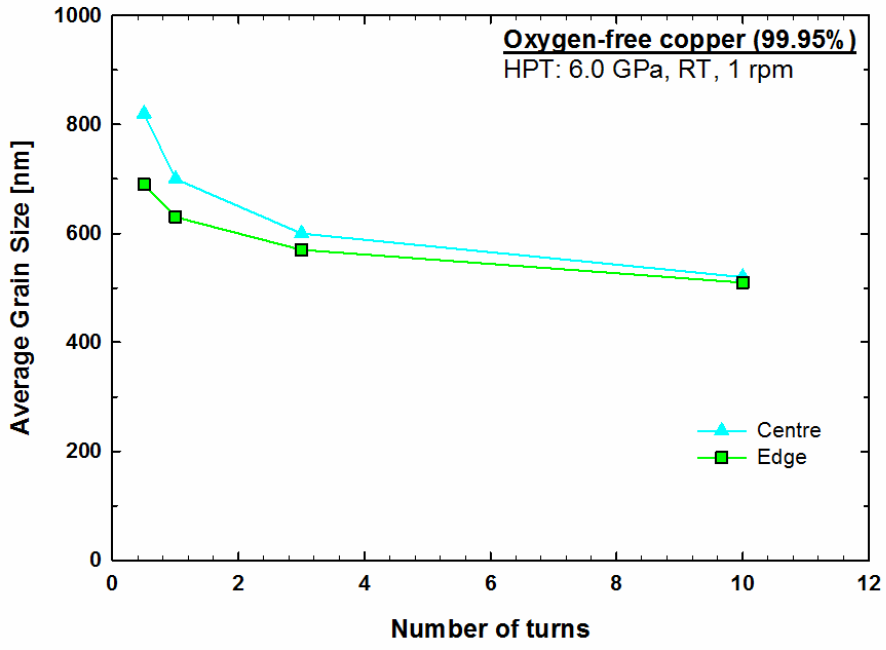

Figure 5.25 Average grain size at centre and edge as a function of number of HPT turns for oxygen-free copper.

The present study provides clear evidence that HPT is an effective SPD method of achieving an equiaxed UFG structure with a high proportion of high-angle boundaries. These results are consistent with previous studies of pure copper [37,46], Al–Mg–Sc alloy [37] and pure aluminium [203]. The evolution of grain size and HAGBs as a function of the number of turns for the centre and edge areas is shown in Figure 5.26 and Figure 5.27, respectively. It can be seen from Figure 5.26 that the decrease in the average grain size with number of turns is accompanied with an increase in HAGBs at the centre of the disc whereas the decrease in the average grain size at the edge of the disc is accompanied with very minor change in HAGBs with increasing number of turns as shown in Figure 5.27. Moreover, both figures shows a difference in the average grain size and HAGBs values between the centre and edge of the disc in the early stages of deformation and this difference is diminished after 10 turns.

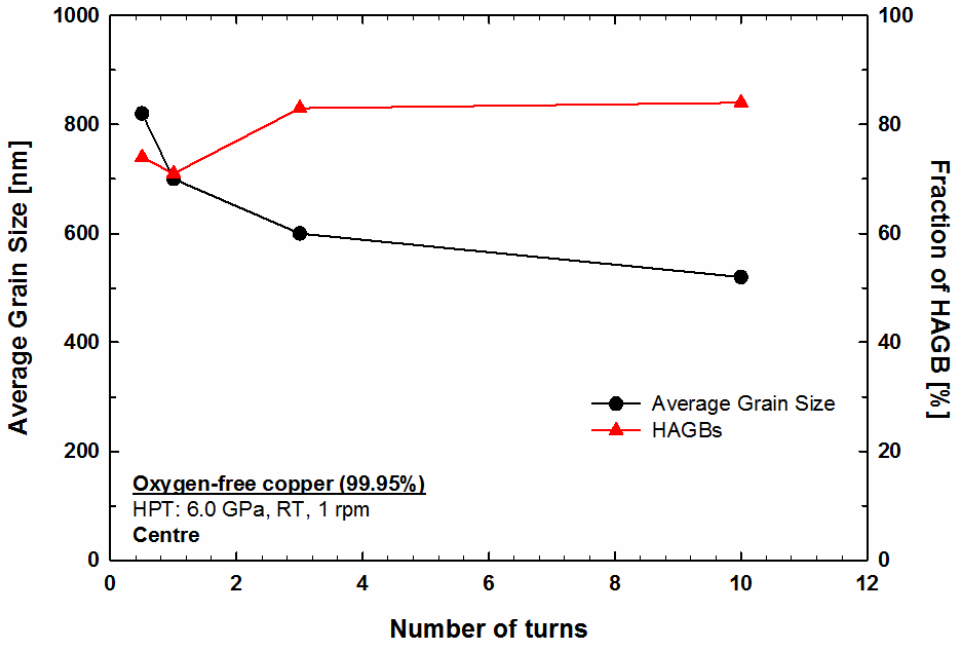

Figure 5.26 Average grain size and proportion of HAGBs at disc centre as a function of number of HPT turns for oxygen-free copper.

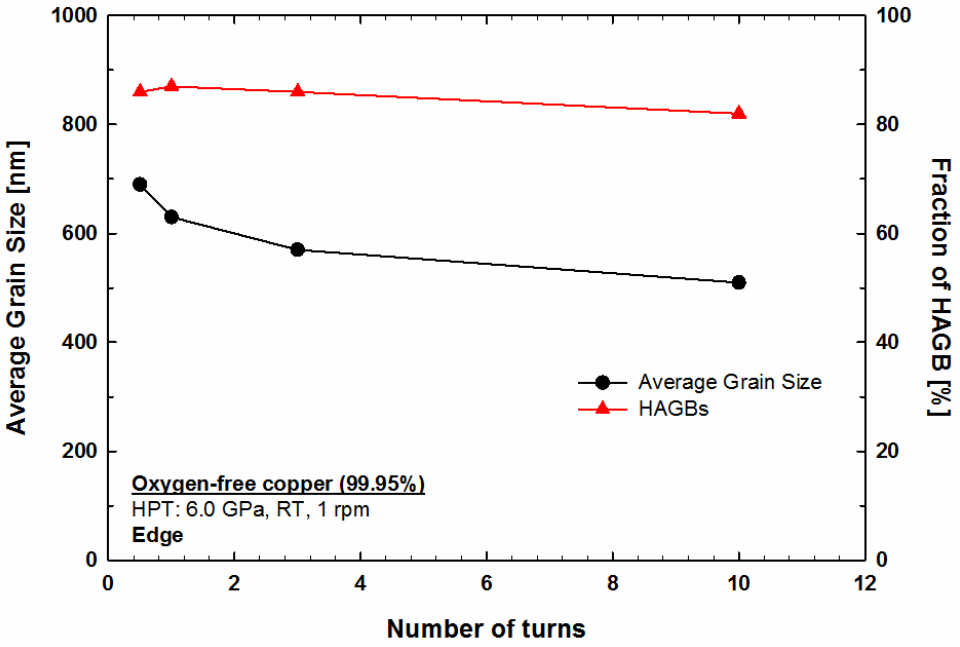

Figure 5.27 Average grain size and proportion of HAGBs at disc edges as a function of number of HPT turns for oxygen-free copper.

5.2.2 Microhardness homogeneity after HPT

The Vickers microhardness test was conducted across the diameter and over the whole surface of oxygen-free copper discs after processing by HPT for up to 10 turns. The microhardness investigation confirmed that the values are lower at the centre of the disc than at the outer regions in the early stages of HPT processing. Microhardness increases and a gradual evolution towards homogeneity is noticed with increasing number of revolutions and torsional strain, as shown in Figure 5.18. This result is consistent with previous reports for pure copper [37,48,49,52,204] and copper alloys [34,48,50,51,205] processed by HPT.

The variation of hardness between the central and peripheral regions of the disc corresponds to the local variation of the imposed strain across the disc given by the von Mises equivalent strain presented in Equation 2.6 where it gives a proportional relationship between the imposed strain and the distance from the disc centre. Thus, the imposed strain is equal to zero at the centre of the disc, where $r = 0$, which leads to lower microhardness in this region. The hardness increases in a linear fashion towards the maximum strain value near the edge according to Equation 2.6, where $r > 0$. The strain increases with increasing revolutions, which contribute to further increases in hardness. This shows a good agreement with the obtained results.

The hardness in the central region increases gradually with increased number of turns and the difference in hardness values between the centre and edges diminishes. Theoretically, no strengthening effect will take place in centre of the disc because the equivalent strain in this region is zero based on Equation 2.6. However, hardness measurements have shown that the hardness increases with increasing number of turns. This might be due to straining introduced to the centre of the disc by a small misalignment between the anvils and causes deformation to this area [206]. Also, the difficulty in precisely detecting the centre of the disc while taking hardness measurements [206].

This is similar to earlier reports for nickel processed by HPT that show a gradual evolution towards microstructural and microhardness homogeneity by increasing both applied pressure and the total number of revolutions [6,7]. After 10 turns, a reasonable hardness homogeneity is achieved by the increased torsional strain. Thus, in order to understand clearly the behavior of oxygen-free copper during HPT processing, it is crucial

to correlate the measured microhardness values (in Hv) and the equivalent strain, calculated using Equation 2.6. An average value of h = 0.80 mm is used to calculate equivalent strain and it is clear that there is local variation in the equivalent strain with microhardness values across the diameter of the disc as shown in Figure 5.28(a). These results are in agreement with previous studies on austenitic steel [33], pure copper [46,204], pure aluminium [44] and Cu-36Zn-2Pb alloy [207].

Figure 5.28(b) is a schematic drawing of the hardness variations with equivalent strain presented in Figure 5.28(a) divided into three regions [44]. The first region (I) in Figure 5.28(b) shows an initial increase in hardness with equivalent strain. With further increase of equivalent strain, the hardness reached an optimum value of ~12 due to a clustering of dislocations combined with the formation of subgrain boundaries. The hardness increases due to the increase in dislocation density during HPT deformation because there is greater probability of interaction between dislocations within grains, and the presence of subgrain boundaries obstructs the movement of the dislocations.

Region (II) shows hardness decreasing with increased strain due to decreasing dislocation density within grains, because the dislocations are extinguished at subgrain boundaries. Simultaneously, this annihilation increases the misorientation angles so that more grains are surrounded by higher angle boundaries and the likelihood is increased that dislocations will be absorbed at these boundaries.

Region (III), shows the hardness remaining constant, because the increase in production of dislocations is balanced by the absorption of dislocation at high angle boundaries. The material then enters into a steady state where it becomes saturated by additional strain at an equivalent strain of ~50. This is larger than the saturation value of ~15 reported in a previous study for pure copper [46], but the behaviour is similar to the hardness variation model of Kawasaki *et al*. [53], with equivalent strain showing hardening with recovery after HPT processing, as displayed in Figure 5.28(b). This is consistent with previous studies on pure Cu [150,208] and pure Al [38,41,44,146,209–213].

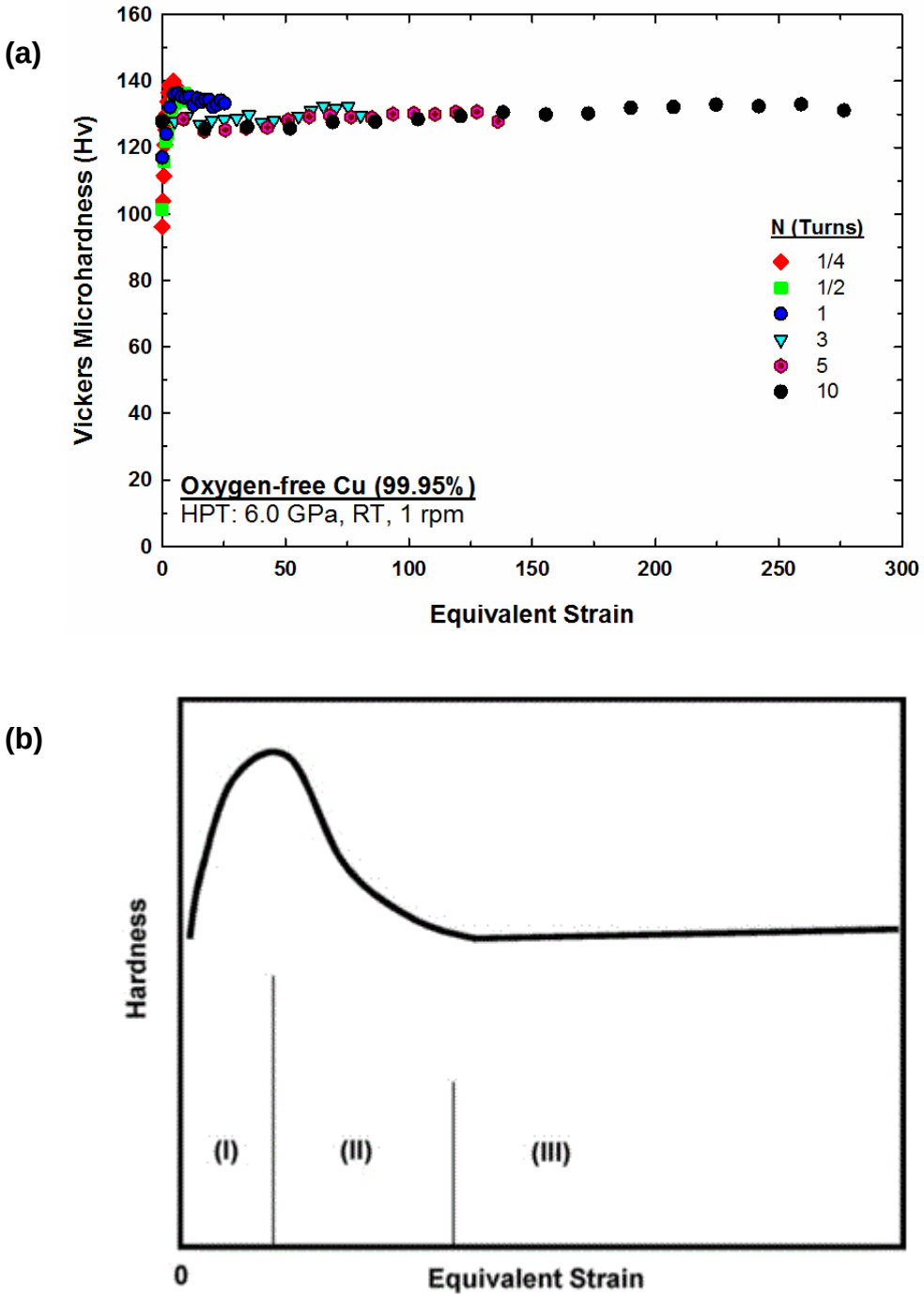

Figure 5.28 (a) Measured microhardness values against equivalent strain in oxygen-free copper processed by HPT at room temperature for up to 10 turns, (b) A schematic drawing of the hardness variations with equivalent strain presented in Figure 5.28(a) [44].

The non-homogeneity of the HPT process generates a strain gradient across the disc [147]. The edges of the disc reveal a minor strain gradient and a low density of geometrically necessary dislocations (GNDs), while the central region of the disc has bigger strain gradient and greater GNDs density. The delayed development of plastic strain (deformation) in the central region causes an increment in the strain gradient and improvement in the generation of GNDs near the centre of the disc, which leads to a delay in the onset of plastic deformation in that region. This leads to further enhancement of the strain gradient and further accumulation of GNDs. The centre of the disc shows high error bars for the microhardness measurements compared to low error bars at the periphery as shown in Figure 5.19. The high values for the error bars at the centre tend to fall off with increasing numbers of turns, pointing towards microstructural homogeneity, as shown in Table 5.1. Contrary to the present results, a study conducted on high-purity aluminium processed by HPT [41] found that hardness values at the centre of the disc are higher than at the edges in the early stages of processing and decrease with increasing numbers of turns. However, the hardness in the central and peripheral regions does reach the same level and displays hardness uniformity.

Furthermore, the microstructural homogeneity of oxygen-free copper attained after HPT can be evaluated by using the degree of homogeneity parameter (α), where a lower value of α indicates greater microstructural homogeneity [46].

$$\alpha = \frac{(HV_R - HV_C)}{HV_R}, \tag{5.1}$$

where HV_R and HV_C are hardness values in the peripheral and central regions, respectively.

Figure 5.29 shows the homogeneity parameter with respect to the number of turns, and it can be seen that the values of the homogeneity parameter, α, decrease with increasing number of HPT turns, indicating an increase in the microstructural homogeneity. This accords with results observed in earlier studies for copper [46,194] and Cu-Al alloys [194].

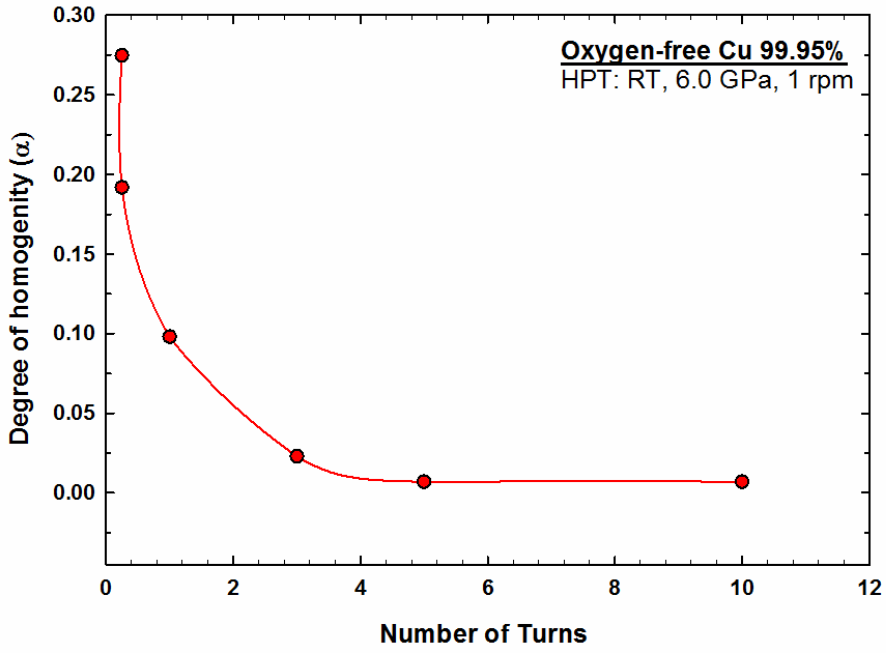

Figure 5.29 Evolution of homogenity parameter α in oxygen-free Cu with respect to the number of HPT turns.

Microhardness measurement can be affected by grain size, high dislocation density and high internal stresses. The relationship between the hardness and grain size is expressed in the empirical Hall-Petch relationship presented in Equation 4.1 [1,2]. Significant reduction in grain size results in increased hardness in the oxygen-free copper after HPT and follows the Hall-Petch relationship. However, reducing the grains to a size smaller than the critical size will trigger the inverse Hall-Petch relationship, where hardness decreases with decreasing the grain size. The average grain size after 10 turns is ~510 nm as shown in Figure 5.25, which is higher than ~7 nm, the critical size of copper [214]. This is consistent with earlier studies in pure copper [34,37,46,48].

Table 5.3 shows the average grain size and maximum Vickers microhardness value of pure copper processed by HPT at room temperature for various numbers of turns and different applied pressures. It is readily apparent that HPT is an effective method for reducing grain size and enhancing the hardness of the material. The differences in the average grain size reported in these studies is due the differences in the number of turns, applied pressure, purity of copper, initial grain size and method of measurement. In addition, it is suggested that recovery mechanism has taken a part in producing larger

average grain size for oxygen-free copper reported in the present study in comparison with other pure coppers reported in earlier studies as listed in Table 5.3.

Table 5.3 The average grain size and maximum Vickers microhardness value of pure copper processed by HPT at room temperature for various numbers of turns and different applied pressures.

Pure Copper	**Processing parameters**		**Grain size (μm)**		**Maximum Vickers Microhardness value (Hv)**	**Ref.**
	Pressure (GPa)	**No. of turns**	**Before HPT**	**After HPT**		
OF (99.95%)	6.0	10	~24	~0.51	~128	Present study
99.99%	2.0	12	–	~0.2	~130	[215]
99.99%	2.0	12	~150	~0.2-0.4	~132	[182]
99.90%	6.0	5	–	~0.075-0.345	~150	[48]
99.98%	6.0	5	~60	~0.1-0.3	~140	[49]
99.97%	6.0	5	~57	~0.12	~141	[194]
99.97%	6.0	5	~57	~0.14	~140	[46]
99.96%	6.0	5	~50	~0.14-0.3	~135	[37]
99.95%	4.0	25	–	~0.2-0.3	~150	[216]

5.2.3 Effect of SFE on microstructural homogeneity during HPT processing

This variation of hardness across the disc is directly related to the SFE of the materials that controls the nature of their recovery. Materials with low SFE tend to have slower recovery rates than materials with high SFE. Thus, the hardness values in the

central region of oxygen-free copper discs are less than at the periphery in the early stages of deformation, consistent with several studies on low SFE materials such as commercial-purity aluminium and aluminium alloys [29,31,39,45], and copper and copper alloys [37,46–52]. These studies show a gradual evolution towards hardness homogeneity with increasing torsional strain in the absence of recovery. On the other hand, materials with high SFE have a fast recovery rate due to their easy cross-slip. These materials show higher hardness values in the central region than the periphery at the early stages of deformation due to dynamic recovery at the edges. Also, there is a gradual evolution towards hardness homogeneity with increasing torsional strain through a greater numbers of turns. This is consistent with earlier reports on high-purity aluminium [38,41,44].

A schematic illustration showing the variation of Vickers microhardness values across the diameter of the disc in the early stages of deformation for materials with fast and slow recovery rates is depicted in Figure 2.19 [41]. Since the rate of dislocation recovery is controlled by the SFE, materials with low SFEs will achieve microstructural homogeneity more slowly than materials with high SFEs, due to the wide separation between the partial dislocations that make cross-slip more difficult, thus requiring higher strain to reach homogeneity [29,41,194]. SFE is also an important factor in the deformation mechanism in metals, which affects the evolution of microstructural homogeneity [46,161,194,217].

5.3 Summary

1. Oxygen-free copper discs with a commercial purity of 99.95% were processed at room temperature by HPT under an applied pressure of 6.0 GPa using quasi-constrained conditions by 1/4, 1/2, 1, 3, 5 and 10 turns.

2. EBSD measurements of the HPT-processed samples indicate a substantial grain refinement. The average grain size was reduced from ~24 μm to ~510 nm after 10 turns. A noticeable difference in the average grain size between the centre and edge of the disc was observed in the early stages of deformation, but diminished with increasing torsional strain and a higher number of turns. Coarse grains were observed in the centre of the disc while fine grains were produced at the edges at

a low number of turns, and the microstructure reached homogeneity with equiaxed grains of an average size of ~510 nm after 10 turns. Also, the proportion of HAGBs increased and the variation between the centre and edges of the disc diminished with increasing number of turns to reach ~84% across the diameter of the disc.

3. The evolution of microhardness homogeneity on HPT discs was measured by recording individual measurements along a diameter of each disc and plotting colour-coded contour maps over the entire surfaces. The microhardness values increased significantly in the central and peripheral regions with a modest torsional strain, however the microhardness distribution was inhomogeneous, and the peripheral region showed higher values than the central region. The variation in hardness corresponds to the local variation of imposed strain and the strain gradient across the disc, as well as the SFE. The difference in hardness values diminished and a homogenous hardness distribution was reached across the disc after 3 turns and became saturated at an equivalent strain of ~50. The average microhardness value of ~128 Hv was recorded after 10 turns.

4. The degree of homogeneity parameter was calculated and it decreased with increasing number of HPT turns from 1/4 to 10. This indicated that microhardness and microstructural homogeneity increased with increasing strain.

5. The analysis based on XRD measurements shows an increase in the dislocation density and a decrease in the crystallite size after HPT processing for up to 1/2 turn, followed by a decrease in dislocation density and an increase in the crystallite size associated with a higher number of turns. This indicates that dynamic recovery took place during the process of HPT after reaching a critical equivalent strain of ~12.

Chapter 6 Paradox of Strength and Ductility in UFG Oxygen-free Copper Processed by ECAP and HPT at Room Temperature

6.1 Background

Strength and ductility are the key mechanical properties of any material. It is widely known that bulk UFG materials produced by SPD usually exhibit high strength but relatively low ductility at room temperature. These properties can be enhanced, but usually the one at the expense of the other, and it is a challenge to enhance both at once [119,218]. Many studies have reported that materials processed by ECAP exhibit high strength, yet only limited elongation to failure [158,219,220]. Similar findings of high strength and low ductility are obtained when metals are deformed by conventional techniques such as extrusion, drawing or rolling.

Strain rate sensitivity and work hardening rate are major factors affecting the ductility of materials due to their contribution to the delay of the onset of localized deformation during tensile testing. Materials with high work hardening rate and high strain rate sensitivity tend to have higher tensile ductility than those with low values of the same parameters. High rate of work hardening is caused by the accumulation of dislocations within the grains; however, in UFG metals the grains are very small which makes the dislocation storage more difficult. Dislocations are emitted and absorbed at the grain boundaries instead of accumulating inside the grain interior. Thus, most UFG metals exhibit limited ductility at room temperature.

Several studies have reported the achievement of a significant grain refinement in pure Cu using ECAP [124,168,170,178,192,221–224] and HPT [34,37,46,47,49,52,149,204,215,225–227]. To date, most studies have suggested that pure Cu shows hardening behavior without recovery during both HPT [34,204,215] and ECAP [89,181] at room temperature. Nevertheless, two recent studies have reported a softening behavior of pure Cu with recovery during HPT processing [150,208]. This softening is a well-documented behavior of pure Al [38,41,44,146,209–213] and has been observed in other materials such as pure Zn [212] and pure Mg [228].

A third recent study also reported the occurrence of a recovery mechanism in pure Cu that contributed to the enhancement of ductility during 1-16 passes of ECAP at room temperature [124]. This latter report confirmed the results published in the classic study [89] that high ductility was achieved after 16 passes of ECAP as a result of grain boundary sliding. These findings were unexpected because it was previously claimed that the increase in strength in UFG materials is associated with a decrease in ductility at ambient temperature [219,229], and the poor ductility of UFG materials is due to their limited strain hardening ability [229–231].

Two different deformation mechanisms are proposed for the simultaneous gain in strength and ductility after processing pure Cu by ECAP for 16 passes at room temperature: one is grain boundary sliding [89] and the other is a recovery mechanism [124]. The present study is designed to clarify the mechanism leading to the enhancement in ductility by processing oxygen-free Cu for 24 passes at room temperature. Twenty-four passes was chosen instead of 16 to impose similar maximum strain on the specimen as in [89,124] because the die angle used in this study was 110° whereas 90° was used in the previous studies. In addition, the potential for achieving high strength and ductility by imposing very high strain on the specimens using HPT was investigated, as imposing a high strain using ECAP was limited because processing specimens beyond 24 passes led to the initiation of cracks.

This chapter investigates the direct influence of recovery behaviour on mechanical properties in oxygen-free copper processed using different SPD techniques (ECAP and HPT), and critically examines the relation between strength and ductility in UFG copper processed by ECAP for up to 24 passes and HPT for up to 10 turns, at room temperature. The aim of this section is to explore the relationship between the recovery mechanism of oxygen-free copper with respect to ductility, and to evaluate the mechanism contributing to the increase in strength and ductility.

6.2 Results

Strength and ductility of oxygen-free Cu processed by ECAP and HPT at room temperature are examined using a uniaxial tensile test. Specimens were pulled in tension at room temperature using initial strain rates of $1.0\times10^{-2}\ s^{-1}$, $1.0\times10^{-3}\ s^{-1}$ and $1.0\times10^{-4}\ s^{-1}$.

6.2.1 Strength and ductility behaviour after ECAP

The engineering stress–engineering strain curves of oxygen-free copper deformed by ECAP at room temperature are shown in Figure 6.1. The specimens were pulled in tension to failure using initial strain rates of: (a) 1.0×10^{-2} s^{-1}, (b) 1.0×10^{-3} s^{-1} and (c) 1.0×10^{-4} s^{-1}. In the present study, the value of the yield stress was measured using the 0.2% strain offset method [155]. The data relating to the yield strength and elongation to failure are summarized in Table 6.1. As can be seen from Figure 6.1(a) and the corresponding tensile data shown in Table 6.1, for the specimens tested at a strain rate of 1.0×10^{-2} s^{-1}, annealed copper exhibits a low yield stress of ~90 MPa with an elongation to failure of ~95%, which is typical of coarse-grained metals. The strength increased significantly after the first pass, accompanied by a dramatic decrease in ductility. Yield strength increased with the number of ECAP passes and reached a maximum value of ~430 MPa in the samples subjected to 16 passes, corresponding to a strain of ~12. Beyond 16 passes, the yield strength fell slightly to a value of ~410 MPa. Total elongation increased with further ECAP passes, and reached an elongation percentage of ~43% after 24 passes.

The same behaviour was observed when specimens were pulled in tension at a strain rate of 1.0×10^{-3} s^{-1}, as shown in Figure 6.1(b) and Table 6.2. Oxygen-free Cu specimens exhibit a yield stress of ~365 MPa and a total elongation of 43% after 2 passes, as shown in Table 6.2. Increasing number of passes increases the yield strength to ~422 MPa after 16 passes. The yield stress decreased to ~391 MPa while the elongation increased to ~52% after 24 passes.

Testing the specimens at a slower strain rate of 1.0×10^{-4} s^{-1} provide similar trend. As shown in Figure 6.1(c), the yield stress of ~349 MPa and a total elongation of 44% were measured after deforming the oxygen-free Cu by ECAP for 2 passes, as shown in Table 6.3. The yield stress increased to ~398 MPa, ~408 MPa and ~412 MPa with increasing number of passes to 4, 8 and 16, respectively. Increasing the number of passes to 24, decreases the yield stress to ~373 MPa and elongation to failure increased to ~55%.

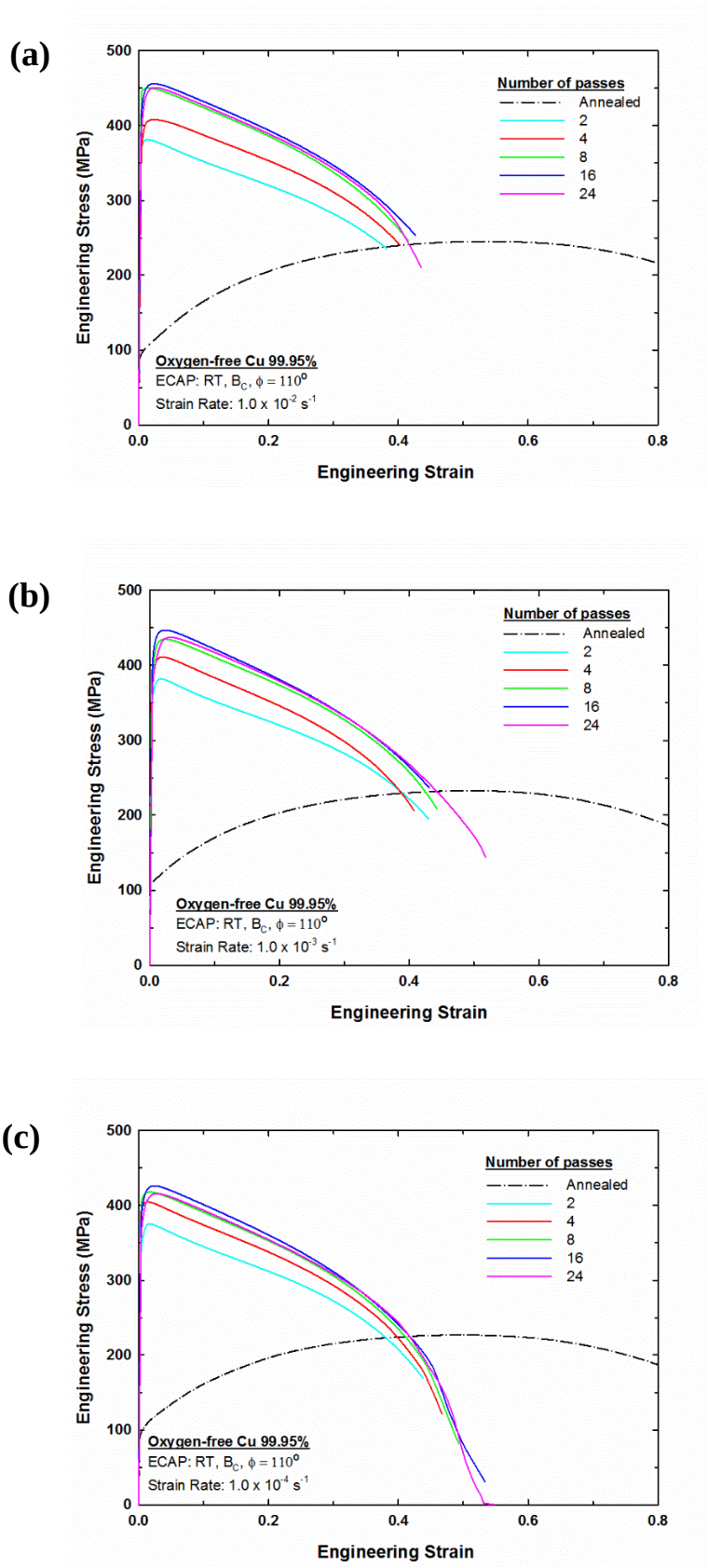

Figure 6.1 Engineering stress–engineering strain curves of oxygen-free copper deformed by ECAP at room temperature using strain rates of: (a) 1.0×10^{-2} s^{-1}, (b) 1.0×10^{-3} s^{-1} and (c) 1.0×10^{-4} s^{-1}.

Table 6.1 Values of yield strength and total elongation to failure of specimens subjected to various numbers of ECAP passes when pulled in tension using strain of 1.0×10^{-2} s^{-1}.

$\dot{\varepsilon}$ = 1.0×10^{-2} s^{-1}, T = 298 K

No. of passes	Yield strength (0.2%) (MPa)	Total elongation to failure (%)
0 (Annealed)	90 ± 5	95 ± 6
2	371 ± 4	38 ± 5
4	386 ± 2	40 ± 3
8	447 ± 3	41 ± 2
16	430 ± 1	42 ± 4
24	410 ± 5	43 ± 3

Table 6.2 Values of yield strength and total elongation to failure of specimens subjected to various numbers of ECAP passes when pulled in tension using strain of 1.0×10^{-3} s^{-1}.

$\dot{\varepsilon}$ = 1.0×10^{-3} s^{-1}, T = 298 K

No. of passes	Yield strength (0.2%) (MPa)	Total elongation to failure (%)
0 (Annealed)	110 ± 6	100 ± 4
2	365 ± 11	43 ± 6
4	386 ± 5	41 ± 3
8	405 ± 1	44 ± 2
16	422 ± 3	43 ± 5
24	391 ± 7	52 ± 4

Table 6.3 Values of yield strength and total elongation to failure of specimens subjected to various numbers of ECAP passes when pulled in tension using strain of 1.0×10^{-4} s^{-1}.

$\dot{\varepsilon}$ = 1.0×10^{-4} s^{-1}, T = 298 K

No. of passes	Yield strength (0.2%) (MPa)	Total elongation to failure (%)
0 (Annealed)	93 ± 3	104 ± 8
2	349 ± 6	44 ± 4
4	398 ± 5	47 ± 3
8	408 ± 4	49 ± 5
16	412 ± 5	53 ± 3
24	373 ± 3	55 ± 5

6.2.2 Uniform elongation after ECAP

Uniform elongation can be defined as the elongation that occurs at the maximum load, just before necking begins during tensile testing. Uniform elongation was investigated in this study, and the values of the ultimate tensile stress (UTS) and uniform elongation are summarized in Table 6.4, Table 6.5 and Table 6.6 for oxygen-free Cu specimens processed by ECAP for various number of passes using strain rates of 1.0×10^{-2} s^{-1}, 1.0×10^{-3} s^{-1} and 1.0×10^{-4} s^{-1}, respectively. The UTS increased gradually with increasing number of passes from ~381 MPa (2 passes) to ~456 MPa (16 passes) as shown in Table 6.4, then slightly decreased to ~450 MPa after 24 passes. The uniform elongation increased with increasing number of passes from ~1.4% to ~2.6% for the specimens pulled in tension at a strain rate of 1.0×10^{-2} s^{-1}.

Pulling oxygen-free Cu specimens at a strain rate of 1.0×10^{-3} s^{-1} shows that UTS increased and reached a maximum value of ~447 MPa in the sample subjected to 16 passes, followed by a minor decrease to ~437 MPa after 24 passes. Uniform elongation increased from ~1.7% to ~3.3% up to 24 passes as shown in Table 6.5.

Inspection of Table 6.6 reveals that specimens pulled in tension at a strain rate of 1.0×10^{-4} s^{-1} shows similar trend observed when using strain rates of 1.0×10^{-2} s^{-1} and 1.0×10^{-3} s^{-1}. Increasing number of passes increased the UTS from ~375 MPa to ~426 MPa, followed by a drop to 415 after 24 passes. Uniform elongation increased from ~1.7% to ~2.8% with increasing numbers of ECAP passes.

It can be seen from Table 6.4, Table 6.5 and Table 6.6 that the UTS shows a similar trend to the yield strength observed during tensile testing. The uniform elongation also shows similar behaviour to the elongation to failure. Both parameters were increased by further passes.

Table 6.4 Values of UTS and uniform elongation of specimens subjected to various numbers of ECAP passes when pulled in tension using a strain rate of 1.0×10^{-2} s^{-1}.

$\dot{\varepsilon} = 1.0\times10^{-2}$ s^{-1}, T = 298 K		
No. of passes	**UTS (MPa)**	**Uniform elongation (%)**
2	381 ± 5	1.4 ± 0.4
4	408 ± 5	2.3 ± 0.2
8	450 ± 2	1.5 ± 0.6
16	456 ± 4	2.4 ± 0.5
24	450 ± 5	2.6 ± 0.4

Table 6.5 Values of UTS and uniform elongation of specimens subjected to various numbers of ECAP passes when pulled in tension using a strain rate of 1.0×10^{-3} s^{-1}.

$\dot{\varepsilon} = 1.0\times10^{-3}$ s^{-1}, T = 298 K		
No. of passes	**UTS (MPa)**	**Uniform elongation (%)**
2	382 ± 7	1.7 ± 0.7
4	411 ± 5	1.9 ± 0.3
8	434 ± 2	2.2 ± 0.3
16	447 ± 5	2.4 ± 0.4
24	437 ± 3	3.3 ± 0.3

Table 6.6 Values of UTS and uniform elongation of specimens subjected to various numbers of ECAP passes when pulled in tension using a strain rate of 1.0×10^{-4} s^{-1}.

$\dot{\varepsilon} = 1.0\times10^{-4}$ s^{-1}, T = 298 K		
No. of passes	**UTS (MPa)**	**Uniform elongation (%)**
2	375 ± 5	1.7 ± 0.7
4	404 ± 2	1.4 ± 0.3
8	418 ± 3	1.7 ± 0.2
16	426 ± 1	2.4 ± 0.3
24	415 ± 6	2.8 ± 0.4

6.2.3 Strength and ductility behaviour after HPT

Figure 6.2 shows the resulting stress–strain curves for copper samples processed at different numbers of turns at initial strain rate of: (a) 1.0×10^{-2} s^{-1}, (b) 1.0×10^{-3} s^{-1} and (c) 1.0×10^{-4} s^{-1}. The values of the yield stresses measured were obtained using the 0.2% strain offset method [155], and the data relating to the yield strength and elongation to failure are summarized in Table 6.7, Table 6.8 and Table 6.9. The annealed samples show behaviour typical of coarse-grained metals, namely low stress and high ductility. A significant increase in the yield strength of the copper samples was observed after only 1/4 turn as shown Figure 6.2(a) and Table 6.7, however this was accompanied by a dramatic loss in ductility. The yield strength increased from ~104 MPa to ~475 MPa. Additional straining to 1/2 turn led to a further increment in the yield strength to ~530 MPa, yet there was a noticeable regain in elongation to failure from ~45% to ~50% at this stage. Beyond 1 turn, there was a drop in strength in the material to ~472 MPa, while the increase in ductility continued to ~55%. A regain in the yield strength was observed after 3 turns, followed by a very minor decrease, then saturation beyond 5 turns at a value of ~494 MPa. On the other hand, total elongation to failure increased to approximately ~70% after 10 turns of HPT.

Specimens exhibit high strength of ~510 MPa after only 1/4 turn, data for specimens pulled in tension at strain rate of 1.0×10^{-3} s^{-1} are shown in Figure 6.2(b) and Table 6.8. The yield stress reached maximum value of ~542 MPa after 1 turn then decreased with further straining to ~491 MPa after 10 turns. The elongation to failure increased with increasing number turns from ~45% to ~65%.

A similar trend was observed after pulling the specimens at slower strain rate of 1.0×10^{-4} s^{-1}, see Figure 6.2(c) and Table 6.9. After HPT processing to 1/4 turn, the yield stress increased to ~490 MPa in comparison to ~104 MPa for the annealed specimen and reached maximum value of ~500 MPa after 1 turn. The yield strength dropped with increasing number of turns to ~465 MPa after 10 turns. Meanwhile, increasing number of turns increased the total elongation to ~72%. It can be seen from the previous results that the ductility of oxygen-free copper increases with further HPT turns.

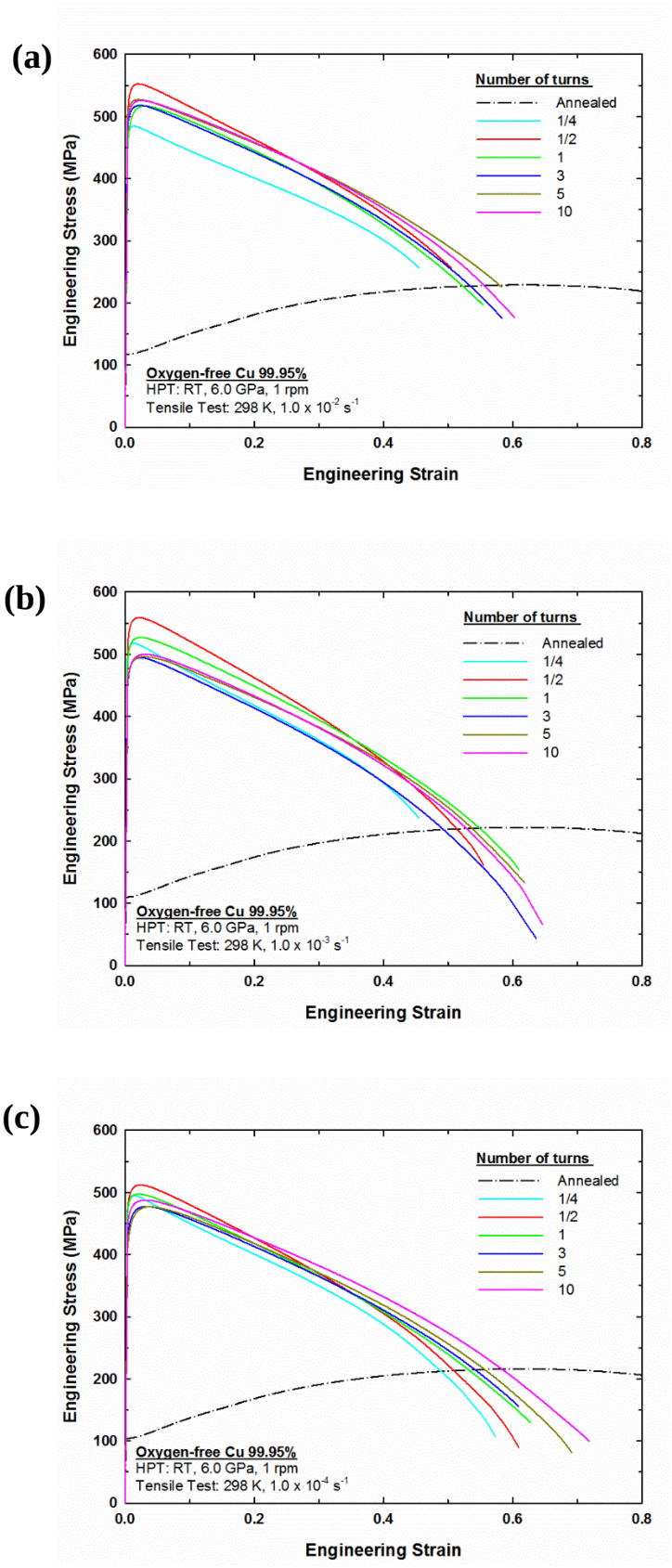

Figure 6.2 Plots of engineering stress-engineering strain for oxygen-free Cu after HPT processing up to 10 turns at room temperature at initial strain rate of: (a) 1.0×10^{-2} s^{-1}, (b) 1.0×10^{-3} s^{-1} and (c) 1.0×10^{-4} s^{-1}.

Table 6.7 Values of yield strength and total elongation to failure of specimens subjected to various numbers of HPT turns when pulled in tension using strain of 1.0×10^{-2} s^{-1}.

$\dot{\varepsilon} = 1.0\times10^{-2}$ s^{-1}, T = 298 K		
No. of turns	**Yield strength (0.2%) (MPa)**	**Total elongation to failure (%)**
0 (Annealed)	116 ± 5	114 ± 5
1/4	475 ± 6	45 ± 4
1/2	530 ± 6	50 ± 2
1	472 ± 1	55 ± 4
3	496 ± 8	58 ± 5
5	494 ± 5	58 ± 3
10	491 ± 4	60 ± 6

Table 6.8 Values of yield strength and total elongation to failure of specimens subjected to various numbers of HPT turns when pulled in tension using strain of 1.0×10^{-3} s^{-1}.

$\dot{\varepsilon} = 1.0\times10^{-3}$ s^{-1}, T = 298 K		
No. of turns	**Yield strength (0.2%) (MPa)**	**Total elongation to failure (%)**
0 (Annealed)	110 ± 4	121 ± 4
1/4	510 ± 7	45 ± 5
1/2	542 ± 2	55 ± 2
1	505 ± 4	61 ± 4
3	467 ± 5	64 ± 3
5	470 ± 3	62 ± 2
10	473 ± 5	65 ± 8

Table 6.9 Values of yield strength and total elongation to failure of specimens subjected to various numbers of HPT turns when pulled in tension using strain of 1.0×10^{-4} s^{-1}.

$\dot{\varepsilon} = 1.0\times10^{-4}$ s^{-1}, T = 298 K		
No. of turns	**Yield strength (0.2%) (MPa)**	**Total elongation to failure (%)**
0 (Annealed)	104 ± 6	130 ± 5
1/4	490 ± 3	57 ± 3
1/2	500 ± 5	61 ± 2
1	487 ± 2	63 ± 5
3	442 ± 3	61 ± 3
5	438 ± 4	69 ± 2
10	465 ± 4	72 ± 2

6.2.4 Uniform elongation after HPT

The measured values of the UTS and uniform elongation are summarized in Table 6.10, Table 6.11 and Table 6.12 for specimens pulled in tension at strain rates of 1.0×10^{-2} s^{-1}, (b) 1.0×10^{-3} s^{-1} and (c) 1.0×10^{-4} s^{-1}, respectively. It can be seen from Table 6.10 that the UTS increased from ~484 MPa to ~552 MPa with increasing deformation, from 1/4 to 1/2 turn. Beyond 1 turn, there was a decrease in the UTS to a measured value of ~516 MPa, and approximately the same value after 3 turns. A regain in the UTS was observed after 5 turns to a value of ~527 MPa and it was saturated by 10 turns. On the other hand, an increase in the uniform elongation from ~1.4% to approximately ~3% was observed after processing the samples from 1/4 turn to 10 turns, respectively.

Table 6.11 shows that the UTS increased from ~517 MPa to ~558 MPa when deformed from 1/4 to 1/2 turns, respectively. The UTS decreased after 1 passes with further straining and reached a value of ~499 MPa after 10 turns. On the other hand, the uniform elongation increased from ~1.3% to ~3.2% with increasing number of turns.

The UTS reached a maximum value of ~512 MPa after 1 turn at a strain rate of 1.0×10^{-4} s^{-1} as shown in 6.12 followed by a decrease to a value of ~487 MPa after 10 turns. An increase in the uniform elongation from ~1.3% to ~4% was observed with increasing number of turns.

This indicates the increase in the UTS and uniform elongation of oxygen-free copper upon increasing torsional strain at room temperature. In addition, UTS displays a similar trend to the yield strength shown in Table 6.7, Table 6.8 and Table 6.9.

Table 6.10 Values of UTS and uniform elongation of specimens subjected to various numbers of HPT turns when pulled in tension using strain of 1.0×10^{-2} s^{-1}.

$\dot{\varepsilon} = 1.0\times10^{-2}$ s^{-1}, T = 298 K		
No. of turns	**UTS (MPa)**	**Uniform elongation (%)**
1/4	484 ± 3	1.4 ± 0.4
1/2	552 ± 6	2.3 ± 0.3
1	516 ± 4	3.1 ± 0.6
3	517 ± 4	2.5 ± 0.1
5	527 ± 1	2.9 ± 0.6
10	525 ± 5	3.0 ± 0.7

Table 6.11 Values of UTS and uniform elongation of specimens subjected to various numbers of HPT turns when pulled in tension using strain of 1.0×10^{-3} s^{-1}.

$\dot{\varepsilon} = 1.0\times10^{-3}$ s^{-1}, T = 298 K		
No. of turns	**UTS (MPa)**	**Uniform elongation (%)**
1/4	517 ± 1	1.3 ± 0.2
1/2	558 ± 3	2.0 ± 0.4
1	526 ± 4	2.3 ± 0.6
3	494 ± 5	2.6 ± 0.2
5	496 ± 3	3.0 ± 0.3
10	499 ± 2	3.2 ± 0.1

Table 6.12 Values of UTS and uniform elongation of specimens subjected to various numbers of HPT turns when pulled in tension using strain of 1.0×10^{-4} s^{-1}.

$\dot{\varepsilon} = 1.0\times10^{-4}$ s^{-1}, T = 298 K		
No. of turns	**UTS (MPa)**	**Uniform elongation (%)**
1/4	495 ± 2	1.3 ± 0.3
1/2	512 ± 1	2.4 ± 0.3
1	497 ± 2	2.6 ± 0.1
3	477 ± 4	3.3 ± 0.5
5	477 ± 5	3.7 ± 0.2
10	487 ± 5	4.0 ± 0.1

6.2.5 Strain rate sensitivity

UFG copper tends to have higher strain rate sensitivities than its coarser counter parts [232]. The strain rate sensitivity for oxygen-free copper samples processed by ECAP and HPT at room temperature were calculated based on [233]:

$$m = \left(\frac{\partial ln\sigma}{\partial ln\dot{\varepsilon}}\right)_{\varepsilon} \tag{6.1}$$

where σ is the true stress and ε̇ the strain rate.

The strain rate sensitivity was calculated after testing the copper samples by the uniaxial tensile test at strain rates of 1.0×10^{-2} s^{-1}, 1.0×10^{-3} s^{-1} and 1.0×10^{-4} s^{-1}. Figure 6.3 shows flow stress-strain rate curves and the calculated values of the strain rate sensitivities for oxygen-free Cu processed by ECAP at room temperature. It is readily apparent that the strain rate sensitivity is higher when samples are pulled in tension at a slower strain rate. The annealed sample has a strain rate sensitivity value of ~0.004, increasing to ~0.011 after 2 passes. The strain rate sensitivity increased with increasing number of passes and reached values of ~0.021 and ~0.028 after 16 and 24 passes, respectively.

Figure 6.4 shows flow stress-strain rate curves showing the calculated values of the strain rate sensitivities for oxygen-free Cu processed by HPT at room temperature. The calculated strain rate sensitivity for the annealed samples is ~0.015. The results show a value of ~0.020 after a 1/4 turn, increasing to ~0.036 after 1/2 a turn, followed by a subsequent decrease from 1 to 10 turns to values of ~0.027 to ~0.014, respectively.

The calculated values of strain rate sensitivities for ECAP and HPT samples are higher than for the annealed samples, but is not sufficient to delay the onset of early necking [234].

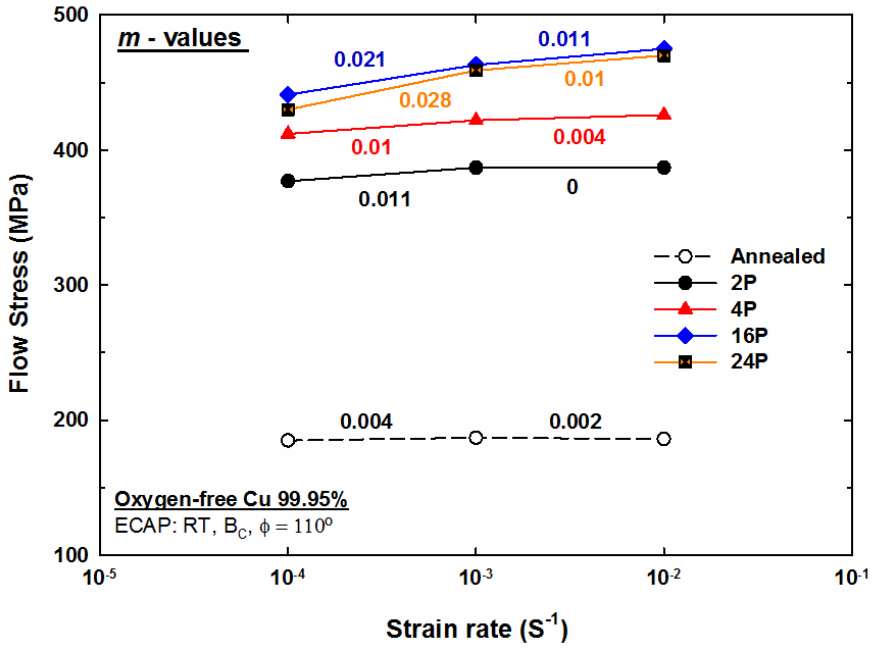

Figure 6.3 Flow stress-strain rate curves showing the calculated values of the strain rate sensitivities for oxygen-free Cu processed by ECAP at room temperature.

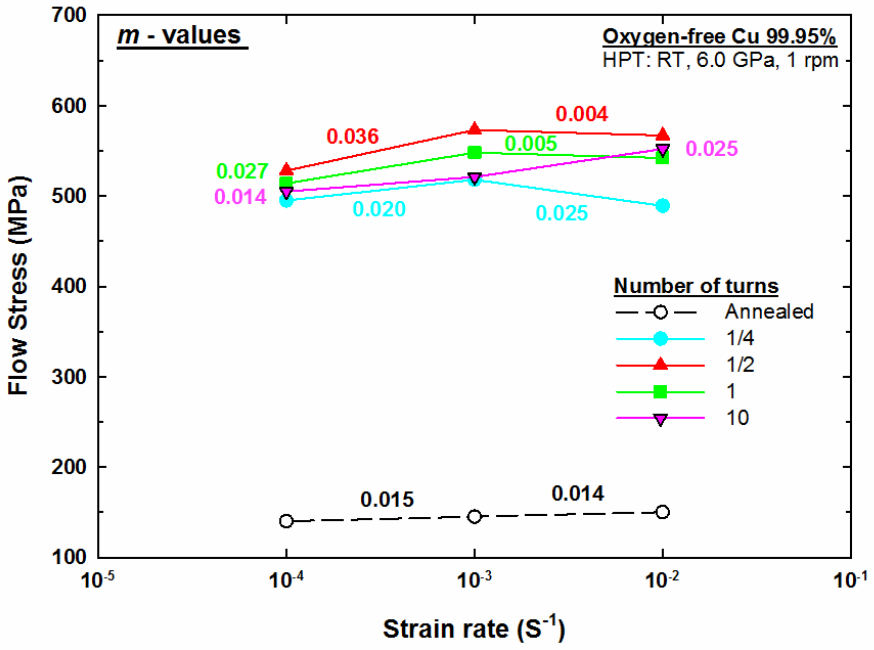

Figure 6.4 Flow stress-strain rate curves showing the calculated values of the strain rate sensitivities for oxygen-free Cu processed by HPT at room temperature.

6.2.6 Work hardening rate

In order to evaluate the onset of localized deformation during tensile testing, the work-hardening rate, Θ , was calculated using the following equation [43,235]:

$$\Theta = \left(\frac{\partial \sigma}{\partial \varepsilon} \right), \tag{6.2}$$

where σ and ε are the true stress and true strain, respectively.

Figure 6.5 shows the tensile true stress–true strain curves for the copper samples processed by ECAP for 2 to 24 passes. Figure 6.6 demonstrates that the sample processed by 24 passes had a higher work-hardening rate than samples processed by fewer passes, indicating a greater uniform elongation with increasing number of passes.

Figure 6.7 shows the tensile true stress–true strain curves for copper samples processed by HPT for 1/4 to 10 turns. The variation of the calculated work-hardening rate with true stress is shown in Figure 6.8. It is readily apparent that the work-hardening rate increased with increasing number of HPT turns. The sample processed by 10 turns provided a higher work-hardening rate than samples processed by lower number of turns. This supports the observation of increase in uniform elongation with increasing number of turns.

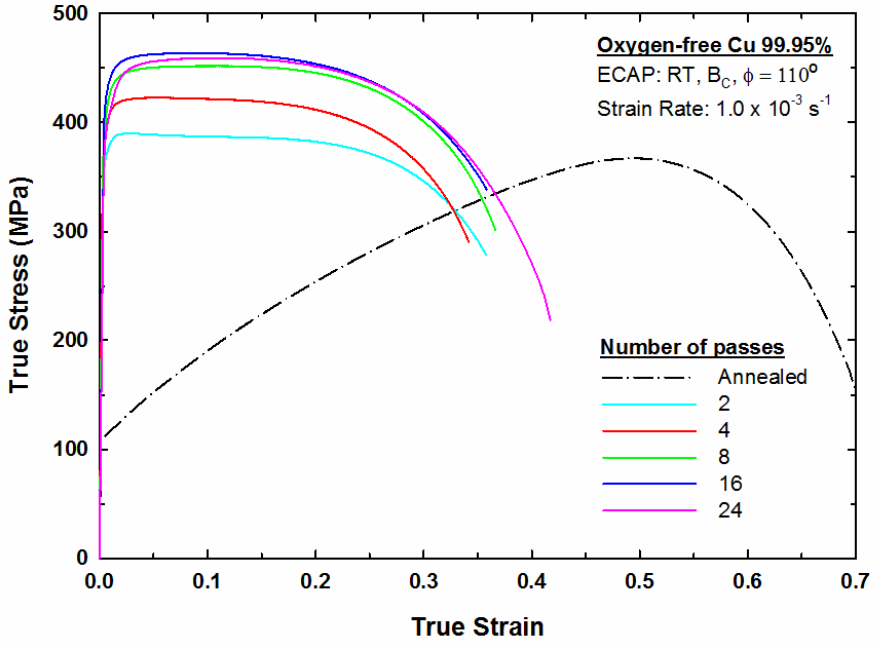

Figure 6.5 True stress against true strain curves for oxygen-free copper (99.95%) in an annealed specimen and after ECAP processing by up to 24 passes at room temperature at an initial strain rate of 1.0×10^{-3} s^{-1}.

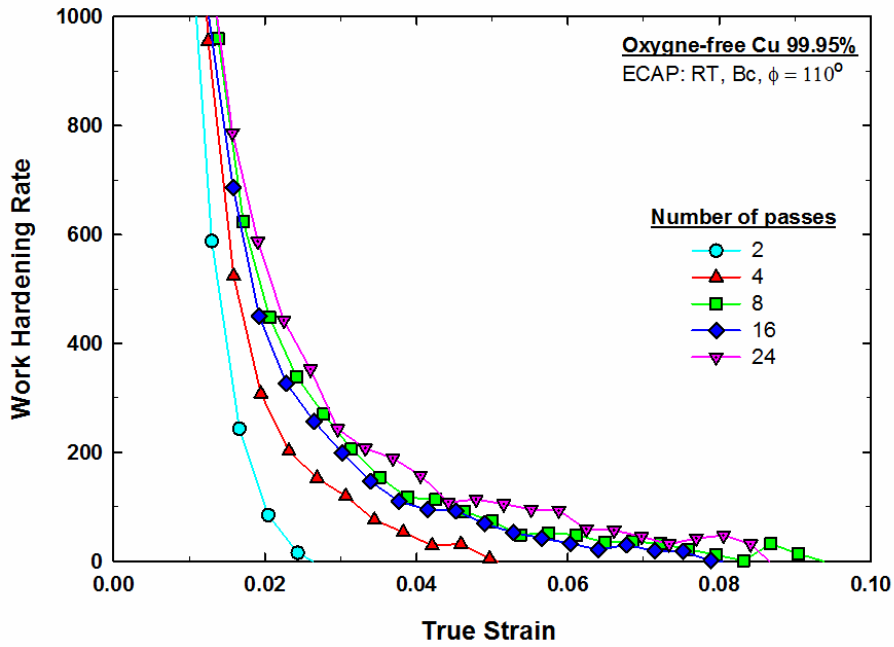

Figure 6.6 Work-hardening rate as a function of true strain for oxygen-free copper deformed by ECAP by up to 24 passes.

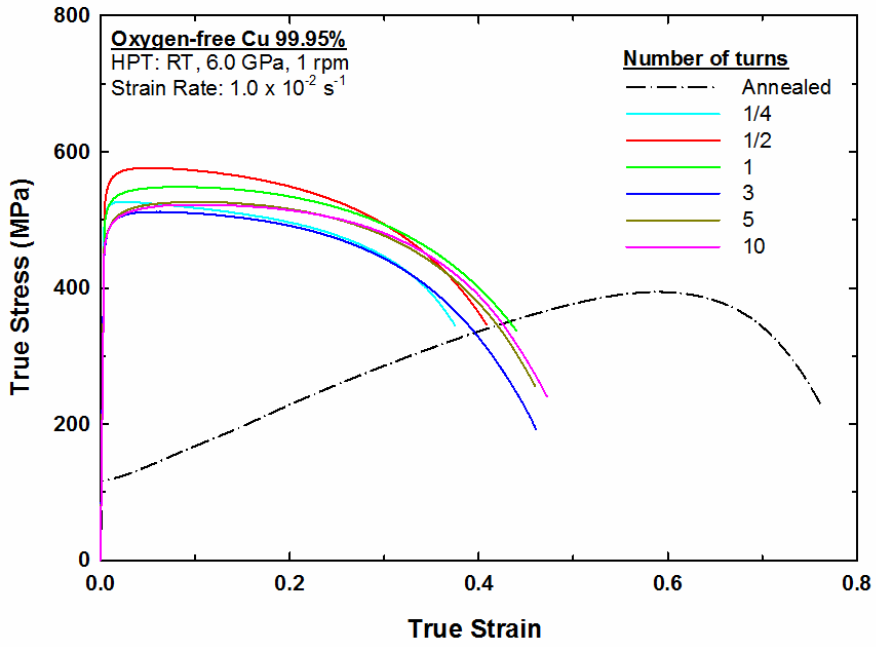

Figure 6.7 True stress against true strain curves for oxygen-free copper (99.95%) in an annealed specimen and after HPT processing by up to 10 turns at room temperature and at an initial strain rate of 1.0×10^{-2} s^{-1}.

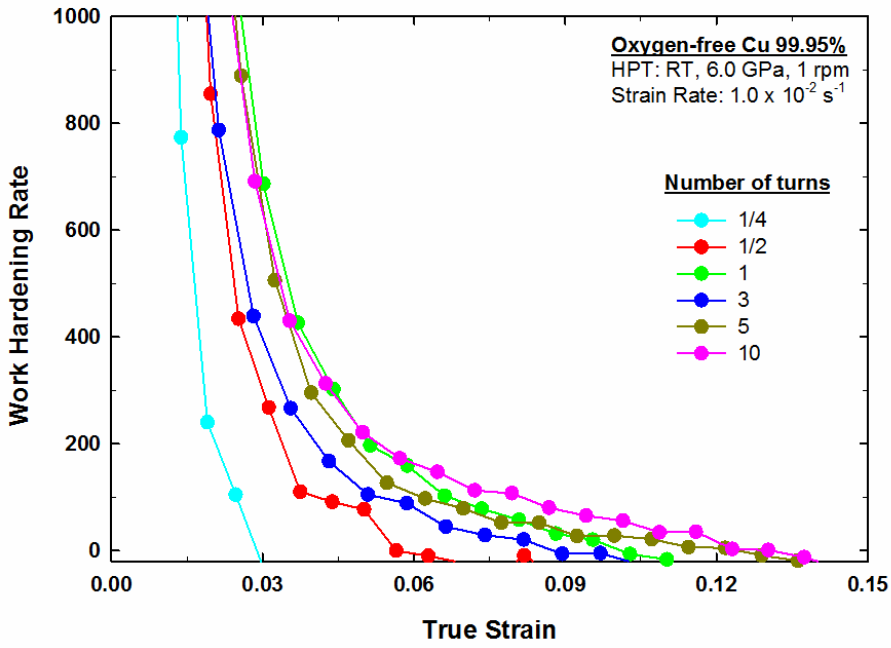

Figure 6.8 Work-hardening rate as a function of true stress for oxygen-free copper deformed by HPT by up to 10 turns.

6.3 Discussion

Several studies have proposed different approaches to simultaneously attain both high strength and ductility in UFG metals. The first is the formation of a bimodal structure, where nanocrystalline grains increase the strength, and larger grains provide enhanced ductility [123]. Another approach is the formation of second-phase particles in the nanostructured metallic matrix, where an increase in ductility is due to the shear band propagation created during straining [219]. The third approach is the formation of a UFG structure having high-angle boundaries, which have a grain boundary sliding (GBS) ability with increasing strain [3,89,119,236].

Earlier research demonstrated that grain boundary sliding is the reason for the enhancement ductility in UFG Cu and Ti due to the increase of strain rate sensitivity [89]. The paradox of strength and ductility was first observed by processing pure Cu by ECAP for up to 16 passes and pure Ti by HPT for 5 turns at room temperature [89]. However, the study was not focused on the intrinsic properties of the material. In the present study, oxygen-free Cu was processed by ECAP and HPT and then the crystallite size and dislocation density were examined and correlated with mechanical properties such as microhardness and tensile properties. It was found that the hardness and strength decreased slightly at a certain strain while ductility of the specimens was enhanced by processing using either ECAP or HPT.

6.3.1 Hall-Petch relationship

It has been well established that reducing the grain size increases the strength of polycrystalline materials, as described by the Hall-Petch relationship [1,2]. However, softening behaviour may occur when the grains are reduced below a certain critical size and the deformation mechanism can change from a dislocation activity to a grain boundary related process [237–240]. In order to have a better understanding of the Hall-Petch relationship for oxygen-free copper, the yield stress is plotted as a function of the average grain size for oxygen-free copper processed by ECAP and HPT as shown in Figure 6.9 and Figure 6.10, respectively. It is readily apparent from both figures that Hall-Petch plots are not linear.

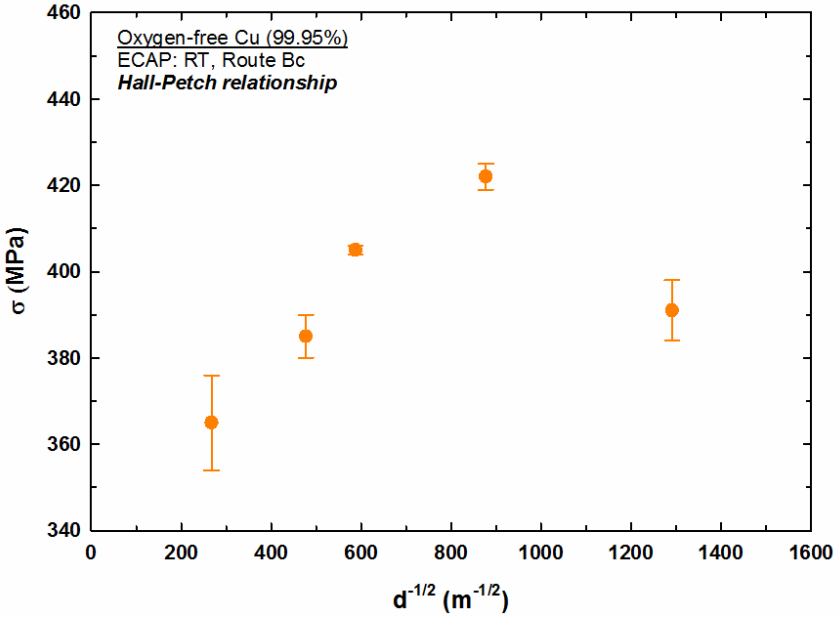

Figure 6.9 Evolution of yield stress as a function of the average grain size for oxygen free copper processed by ECAP at room temperature.

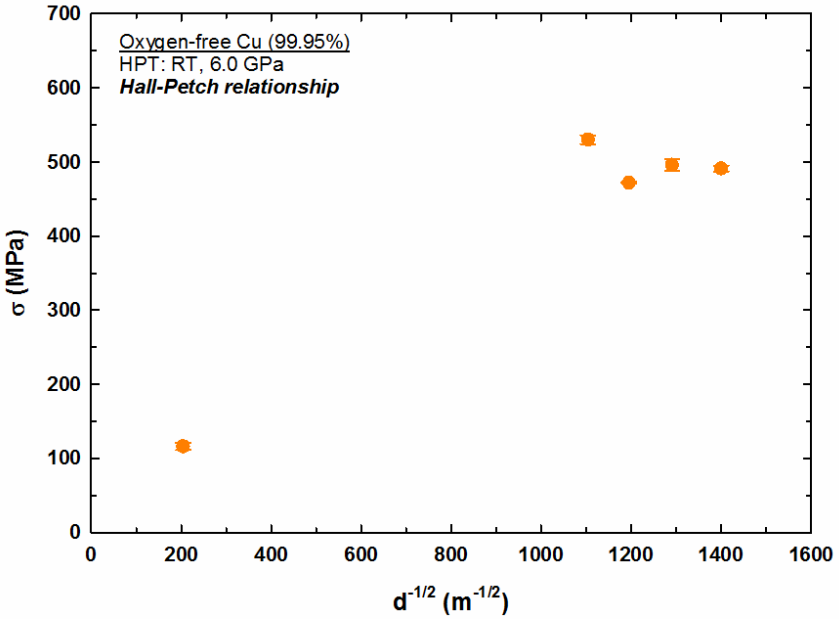

Figure 6.10 Evolution of yield stress as a function of the average grain size for oxygen-free copper processed by HPT at room temperature.

ECAP results, presented in Figure 6.9, show that the strength increases with the decrease of grain size in the range of $d^{-1/2}$ <880 $m^{-1/2}$, but it decreases with a continuous decrease of the grain size in the region of $d^{-1/2}$ >880 $m^{-1/2}$. A Similar trend is observed in the HPT results, see Figure 6.10. The strength increases with the decrease of grain size in the region of $d^{-1/2}$ <1100 $m^{-1/2}$, but it decreases with a continuous decrease of the grain size in the region of $d^{-1/2}$ >1100 $m^{-1/2}$. Both regions of $d^{-1/2}$ >880 $m^{-1/2}$ and $d^{-1/2}$ > 1100 $m^{-1/2}$ have a negative constant k.

The present study shows a transition from strengthening to softening (inverse Hall-Petch effect) at a larger grain size than the critical sizes of ~7 nm [214] and ~25 nm [239] that have been reported for copper and ~12 nm obtained from molecular dynamic (MD) simulations for copper and nickel [241–243]. Earlier studies have reported that annealing of nanocrystalline materials creates a range of grain sizes that leads to the inverse Hall-Petch relationship [214,244].

According to the data reported here and those observed in earlier studies [147,245,246], we can infer that grain boundary strengthening is not the dominant strengthening mechanism in nanocrystalline materials. Thus, the strengthening mechanism observed in Figures 6.9 and 6.10 is a combination of grain boundary strengthening and dislocation strengthening.

6.3.2 Strengthening mechanisms of ECAP and HPT processes

The present experiments provide clear evidence for a simultaneous increase in strength and ductility of oxygen-free copper after processing by ECAP for up to 24 passes (Figure 6.1) and by HPT for 10 turns (Figure 6.2) at room temperature. The increase in elongation was associated with a drop in the strength at a certain strain level observed in both ECAP and HPT experiments, which provide an evidence of softening. This finding is contrary to prior studies in copper which have shown that the strength increases with increasing strain and reaches a steady state at high strain without the occurrence of softening during the deformation process of ECAP [89,181,182,186,247] and HPT [34,182,194,204,212,215,248]. Reduction in the thickness of twins leads also to softening in the strength which contributes to ductility enhancement as observed in nano-twinned

copper [249]. The strain softening observed in this study is due to the reduction in dislocation density and increase in the crystallite size after critical strain during ECAP and HPT as shown in Figure 4.11 and Figure 5.17, respectively.

The microstructure of oxygen-free Cu after deformation by ECAP and HPT contains of both HAGBs and LAGBs which have a prominent role in the strength. Two strengthening mechanisms contribute to the strength of oxygen-free Cu: grain boundary strengthening (σ_{GB}) and dislocation strengthening (σ_{dis}). The total strength of oxygen-free copper is the combination of these strengthening mechanisms, with the assumption that each mechanism is independent of the other. This can be estimated as [26,156,186,250–253]

$$\sigma = \sigma_0 + \sigma_{GB} + \sigma_{dis} \tag{6.3}$$

where σ_0 is the lattice friction stress needed to move individual dislocations.

Grain boundary strengthening is basically the contribution of HAGBs to the strength of the material and it is related to the inverse average grain size, as presented by the Hall-Petch strengthening as follows [1,2]:

$$\sigma_{GB} = \sigma_{HAGBs} = Kd^{-1/2} \tag{6.4}$$

where K is a constant and d is the average grain size.

The reduction in grain size increases the overall strength of oxygen-free copper as shown in Figure 6.11(a) and Figure 6.11(b) for ECAP and HPT, respectively. Reducing grain sizes with increasing ECAP passes or HPT turns decreases the amount of dislocation pile-up at the grain boundary. Therefore, this increases the stress required to move dislocations across the grain boundary. The grain boundary acts as a barrier to dislocation motion because of the orientation mismatch of adjacent grains, which requires an increased amount of energy for the dislocation to change its direction. Also, the grain boundary region has more atomic disorder than the grain interior, which stops the dislocations from moving in continuous slip planes from one grain to another [155]. Hindering dislocation movement delays the onset of plasticity in oxygen-free copper and therefore increases its yield strength.

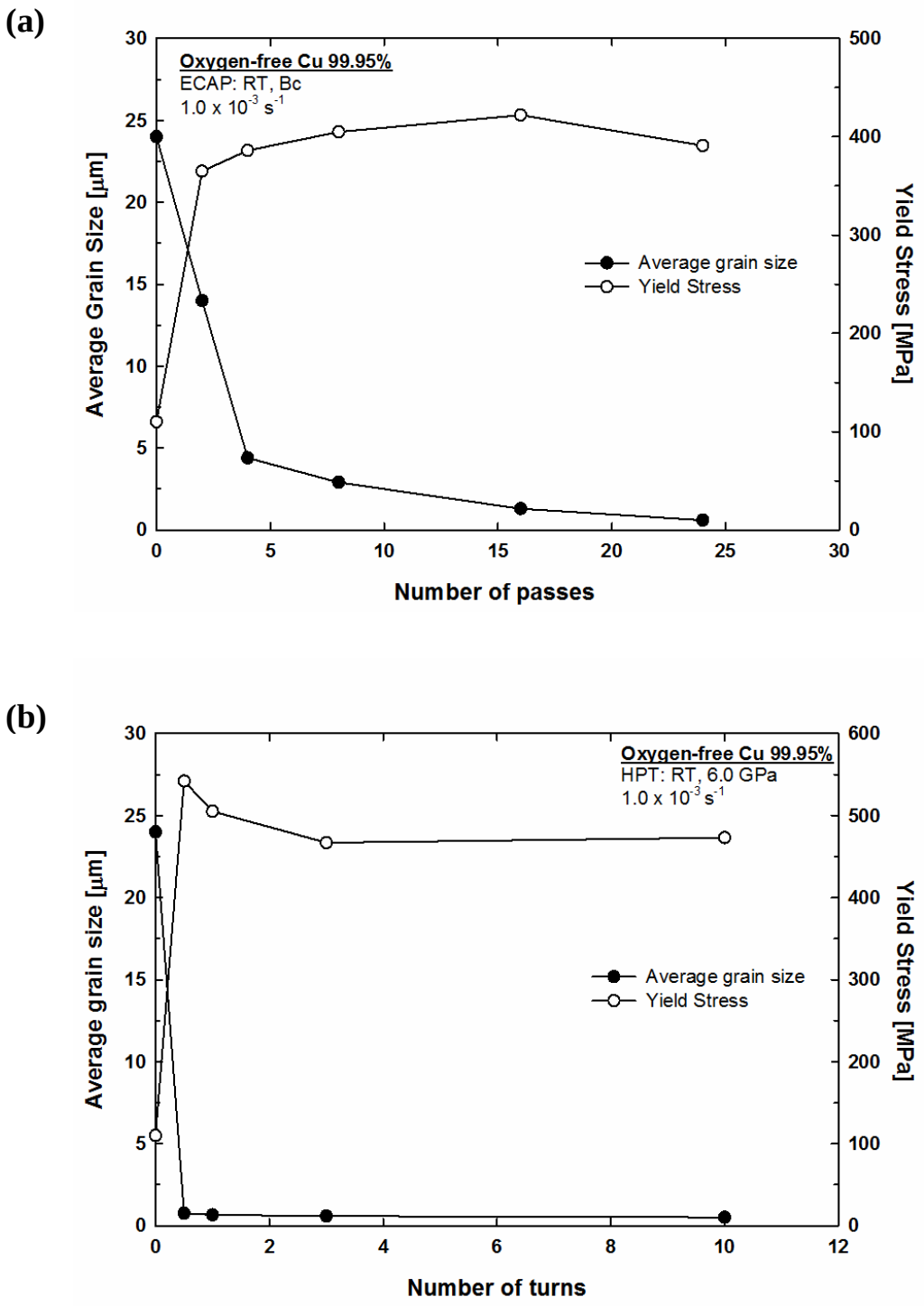

Figure 6.11 Average grain size and yield strength for oxygen-free copper as a function of number of: (a) ECAP passes and (b) HPT Turns.

LAGBs contributes to the strength of the material through dislocation strengthening mechanism and it is related to the dislocation density accumulated inside the boundaries [254]. Dislocation strengthening is described by Taylor equation:

$$\sigma_{dis} = \sigma_{LAGBs} = \alpha M G b \rho^{1/2} \tag{6.5}$$

where α is a numerical factor depending on the arrangement of dislocations, M is the Taylor factor, G is the shear modulus, b is the magnitude of the Burgers vector and ρ is the dislocation density.

Dislocation density shows a similar evolution to yield strength, as a function of strain for metals processed by ECAP, and both reach a steady state at the same strain [255]. The relationship between the saturation values of dislocation density and yield strength is characterized by the Taylor equation. Equation 6.5 indicates that the interactions between dislocations are what determines the saturation value of the yield strength in FCC metals. The close correlation between dislocation density and yield strength has been presented in a previous study for several metals [256].

Similarly, dislocation density inside the grain/subgrain contributes to the overall strength of oxygen-free copper. The dislocation density increases, whereas individual crystallite size decreases, with further strain during the deformation process [255,257]. Increasing the yield strength is normally associated with a refinement in grain size and an increased proportion of HAGBs, but the strength can be reduced by a lower dislocation density [258]. Hence, by inserting Equation 6.4 and Equation 6.5 into Equation 6.3, the yield stress can written as:

$$\sigma = \sigma_0 + \alpha M G b \rho^{1/2} + K d^{-1/2} \tag{6.6}$$

Using multi linear regression method, the values of σ_0, $\alpha M G b$ and K were obtained for each of ECAP and HPT experiments. The yield stress is calculated by Equation 6.6 by using the measured values from experiments in Table 6.2 for copper samples processed by ECAP and Table 6.7 for copper samples processed by HPT. The calculated and measured yield stresses are plotted with respect to the number of passes for ECAP samples and with respect to the number of turns for HPT samples as shown in Figure 6.12 and Figure 6.13, respectively. It is readily apparent from both figures that the calculated yield stress exhibit similar trend to the yield stress measured by tensile test

which indicates that both of grain boundary strengthening and dislocation strengthening contribute to the strengthening mechanism of oxygen-free copper during ECAP and HPT. Thus, the observed softening after 24 passes of ECAP shown in Figure 6.12, and after 1/2 turn of HPT shown in Figure 6.13, is related to the decrease in dislocation density and increase in the crystallite size, see Figure 4.11 and Figure 5.17.

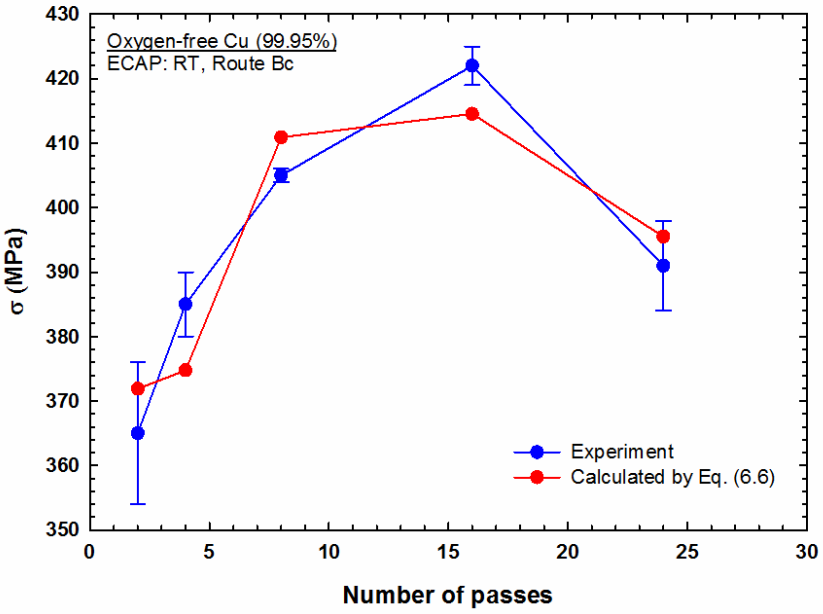

Figure 6.12 The value of yield stress measured by mechanical test and the value calculated using Eq. (6.6) after processing oxygen-free copper by ECAP at room temperature from 2 – 24 passes.

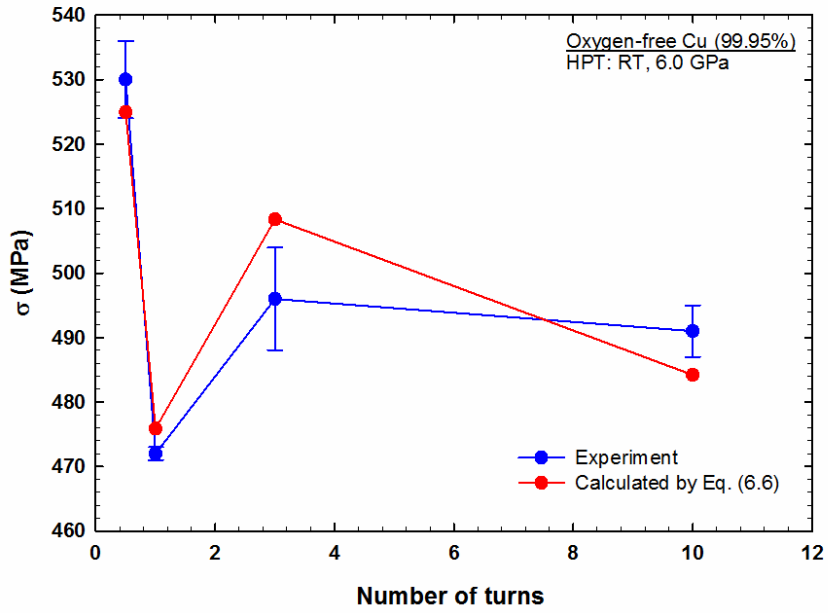

Figure 6.13 The value of yield stress measured by mechanical test and the value calculated using Eq. (6.6) after processing oxygen-free copper HPT at room temperature from 1/2 – 10 turns.

6.3.3 Gain in ductility with increasing numbers of passes or turns

As can be seen from the results, an increase in the uniform plastic elongation and the total elongation to failure can be achieved in oxygen-free copper by processing through a high number of passes by ECAP and high number of turns by HPT. ECAP results are consistent with earlier studies of Valiev *et al*. [89] and Torre *et al*. [124]. However, Valiev did not report any drop in strength with increasing numbers of passes. The outcome of this study is contrary to that observed on Cu-OFHC [186], Cu-0.1%Mg [186] and 2024 Al alloy [259] where the elongation to failure reduced with ECAP passes due to the existence of shear bands within the microstructure. The HPT results are inconsistent with previous studies reporting that the highest value of yield strength is recorded after 5 and 10 turns [51,260,261].

Uniform plastic deformation is usually characterized by the ultimate engineering stress before necking. UFG metals normally show an onset of early necking when pulled in tension, due to their low work hardening ability and low strain rate sensitivity after SPD processing, which leads to the fall in their uniform plastic deformation. The high

rate of work hardening is caused by the accumulation of dislocations within the grains; however in UFG metals the grains are small which makes dislocation storage more difficult [231]. Dislocations are emitted and absorbed at the grain boundaries instead of accumulating within the grain interior. Thus, most UFG metals exhibit limited ductility at room temperature [262]. The low hardening capacity in nanostructured metals produced by SPD has been discussed in an earlier study and three strategies were suggested to prolong the uniform tensile deformation [179]. These strategies included creating a microstructure with a bimodal grain size distribution, deforming the material at a low temperature and/or high strain rates and increasing the strain rate sensitivity [179].

The strain rate sensitivity is a crucial factor when evaluating the strain hardening of a material. According to Hart's criterion, increasing the strain rate sensitivity can delay the onset of localized deformation and prolong the ductility of the material [233]. UFG materials tend to exhibit higher strain rate sensitivity at low temperatures in comparison to their coarse-grained counterparts [263,264]. In practice, it is well documented that a large value of strain rate sensitivity in the presence of small grains and a large fraction of HAGBs can trigger grain boundary sliding [258]. It has been reported that grain boundary sliding has occurred in UFG Cu during the ECAP process at room temperature [10,89]. The occurrence of grain boundary sliding generally requires a high homologous temperature (~$0.5T_m$) [265,266], however, it has been reported that grain boundary sliding also occurs at lower temperatures during ECAP and HPT processing [10,267–269]. The grain boundaries are in a non-equilibrium state during processing by ECAP or HPT due to the surplus of extrinsic dislocations which are not geometrically necessary [60] and grain boundary sliding is therefore facilitated by their movement [119].

The increase in the proportion of HAGBs enhances the ductility of pure copper by facilitating grain boundary sliding, as reported in earlier studies [89]. The strain rate sensitivity was calculated for HPT and ECAP samples and the results show an increase in the strain rate sensitivity with increasing numbers of passes or turns; it is higher than the strain rate sensitivity in the annealed copper. An increase in the strain rate sensitivity from ~0.015 to ~0.027 is obtained by increasing the number of HPT turns, and to a value of ~0.028 after 24 passes of ECAP. This is in agreement with an earlier report showing an increase in the strain rate sensitivity from 0.007 to 0.023 after processing pure Cu (99.95%) by ECAP from 1 to 12 passes [234].

Despite the fact that strain rate sensitivity is increased after HPT and ECAP processing to a value significantly higher than the value of the annealed sample, it is still not high enough to delay the onset of early necking. However, there may be a small contribution towards the delay of the onset of early necking by increasing the strain rate sensitivity with ECAP passes and HPT turns, but the value is very small to facilitate grain boundary sliding. This trend of increasing strain rate sensitivity with increasing ECAP passes is in agreement with results obtained by Valiev *et al*. [89] and Torre *et al*. [124]. However, the value of the strain rate sensitivity obtained by Valiev after pressing copper for 16 passes was 0.14, indicating a mixture of deformation mechanisms including crystallographic slip and grain boundary sliding, which leads to an increase in ductility. On the other hand, the increase in the ductility observed in the present investigation is associated with a recovery mechanism similar to that observed by Torre *et al*. [124].

The work hardening rate of the material is another factor contributing to the onset of localized deformation during tensile testing. The microstructural evolution of copper from large grains into UFGs with low- and high- angle boundaries is reached through the accumulation and rearrangement of dislocations introduced during SPD. The dislocation density and strength increase significantly and often reach saturation level where the strain hardening rate becomes very low. This is due to the dynamic balance between the dislocations generated during SPD processing and the dislocations annihilated in the dynamic recovery process, and UFG metals often have higher dynamic recovery at room temperature than normal polycrystalline metals [179]. Non-uniform deformation in a nanostructured metal occurs when its strain hardening rate is lower than its strength, which in this case is the onset of early necking at modest strain during a tensile test. This condition is predicted by the Considére criterion [43]:

$$\left(\frac{\partial\sigma}{\partial\varepsilon}\right)_{\dot{\varepsilon}} \leq \sigma, \tag{6.7}$$

where σ is the true stress, ε is the true strain and $\dot{\varepsilon}$ is the strain rate.

In other words, plastic instability occurs when the work hardening rate $\left(\frac{\partial\sigma}{\partial\varepsilon}\right)$ becomes equal to or less than the flow stress during tension. Generally, the grains become smaller with increasing strain during SPD processing which decreases the dislocation storage capacity and limits the uniform deformation. Figure 6.6 and Figure 6.8

demonstrate the work hardening rate as a function of the true strain for oxygen-free Cu processed by ECAP and HPT, respectively. It is readily apparent that the specimens processed by the highest number of passes in ECAP and the highest number of turns in HPT have the highest strain hardening rate, and this is in a close agreement with the high uniform elongation obtained in the samples processed by 10 turns and 24 passes. This indicates that the work hardening rate increases with numbers of passes or turns. This finding is contrary to a previous study on pure Cu which has reported minimum uniform elongation after 8 passes of simple shear extrusion (SSE) [156].

The influence of the presence of HAGBs on the strain hardening is still not well understood. It is possible that HAGBs causes tangling and accumulation of dislocations near the boundaries by hindering the dislocations from slipping [258]. Thus, strain hardening is increased. Another possible mechanism by which HAGBs enhance the strain hardening is by grain boundary sliding [258]. Grain boundary sliding was reported in UFG materials processed by SPD such as aluminium [267], copper [89] and titanium [89] and it is well-known that random HAGBs slide more easily than LAGBs [270].

As shown in Figure 4.11 the crystallite size decreases with increasing numbers of passes and reaches a minimum value in the region of 16 passes but then increases at 24 passes. On the other hand, there is a maximum in the dislocation density for a specimen processed by 16 passes, after which the density decreases. Similar trends were observed in Figure 5.17 during the HPT process, where the crystallite size reached a minimum after 1/2 turn then increased with further straining, whereas the maximum value of the dislocation density occurred with the specimen subjected to 1/2 turn after which a rapid drop was observed at 1 turn followed by a continuous and gradual decrease in the dislocation density up to 10 turns. These trends of crystallite size and dislocation density displayed in Figure 4.11 for ECAP specimens and in Figure 5.17 for HPT specimens and match the drop in microhardness values shown in Figure 4.12 and Figure 5.18 and are also in a good agreement with the decrease in the strength shown in Figure 6.1 and Figure 6.2. As stated previously, these observations suggest the occurrence of a recovery mechanism during ECAP and HPT processing.

In the present study, the occurrence of the recovery mechanism highly influences the work hardening rate of oxygen-free Cu. The increase of the uniform plastic deformation presented in Tables 6.4 – 6.6 for ECAP, and Tables 6.10 – 6.12 for HPT, is

due to the decrease in both strength and dislocation densities observed during both processes, as shown in Figure 4.11 and Figure 5.17. This decrease in the dislocation density with presence of HAGBs enhances the dislocation storage and increases the ability to accommodate more dislocations and regain the capacity for work hardening.

The decrease in the total dislocation density with the increase in the crystallite size is due to the annihilation of dislocations which attributed to the recovery mechanism occurring during ECAP and HPT processing that increases the mean free path of dislocations, thus increasing the work hardening ability of oxygen-free copper and enhances plastic elongation with increasing numbers of passes or numbers of turns. Part of this recovery mechanism is the transformation from non-equilibrium boundaries with LAGBs to more equilibrium boundaries with HAGBs, leading to a decrease in the grain boundary thickness [199,256,271], and it produces a more equilibrated structure and leads to the restoration of strength despite the decrease in the dislocation density. This mechanism of the enhancement of ductility with recovery is consistent with a previous study on pure Cu processed by ECAP for 16 passes at room temperature [124]. Previous studies reported an enhancement in the strain hardening rate due to the ability of the pre-existing twins to hinder and store dislocations [165,272,273], but the effect of twins is minor in this study and, thus, is neglected.

A close inspection of Figure 4.11 and Figure 5.17 shows that the occurrence of the recovery mechanism during HPT is faster than for ECAP. The drop in dislocation density was observed after 1 turn of HPT but it was after 24 passes of ECAP. This may be due to the intensive strain imposed by HPT. The equivalent strains for ECAP specimens are calculated using Equation 2.7, and the equivalent strains for 2, 4, 8, 16 and 24 passes are ~1.5, ~3, ~6, ~12 and ~18, respectively. On the other hand, the equivalent strains for HPT specimens were calculated using Equation 2.6, but since the strain varies across the disc, an average strain is calculated for each condition. The equivalent strains for 1/2, 1 and 10 turns are ~7, ~16 and ~173, respectively. It is readily apparent that the recovery mechanism takes place at an equivalent strain exceeding ~12. Thus, it is concluded that uniform plastic deformation can be prolonged by deforming the oxygen-free Cu beyond a certain equivalent strain.

A direct comparison with the original results on the paradox of strength and ductility obtained for nano Cu processed by ECAP for 16 passes and nano Ti processed

by HPT for 5 turns is presented in Figure 6.14 [89]. The yield stress against elongation to failure is plotted for various materials. The conventional behaviour of high strength and low ductility is located in the shaded region of the curve, and the clear area is the high strength–high ductility region. The datum points for copper and aluminium represent the percentages of the applied strains during the rolling process. These points are located in the shaded area of the curve, since processing by conventional methods such as rolling and extrusion normally increase strength and decrease ductility. However, processing materials by SPD normally increases their strength and ductility and the points fall in the clear area of the curve.

Figure 6.14 shows that oxygen-free copper processed through 10 turns of HPT and 24 passes of ECAP at room temperature exhibits both high strength and high ductility. The points lie within the high strength–high ductility region, along with nano Cu and nano Ti as referred to earlier. It can also be seen from the present study, and from Valiev *et al*. [89] and Torre *et al*. [124], that pure copper has to be deformed by ECAP at an equivalent strain above ~16 at room temperature in order for its ductility to be enhanced; however, the ductility increased in the current study after deforming oxygen-free copper beyond an equivalent strain of ~12 by ECAP or HPT.

In conclusion, SPD methods have proven their capability to produce materials possessing both high strength and high ductility.

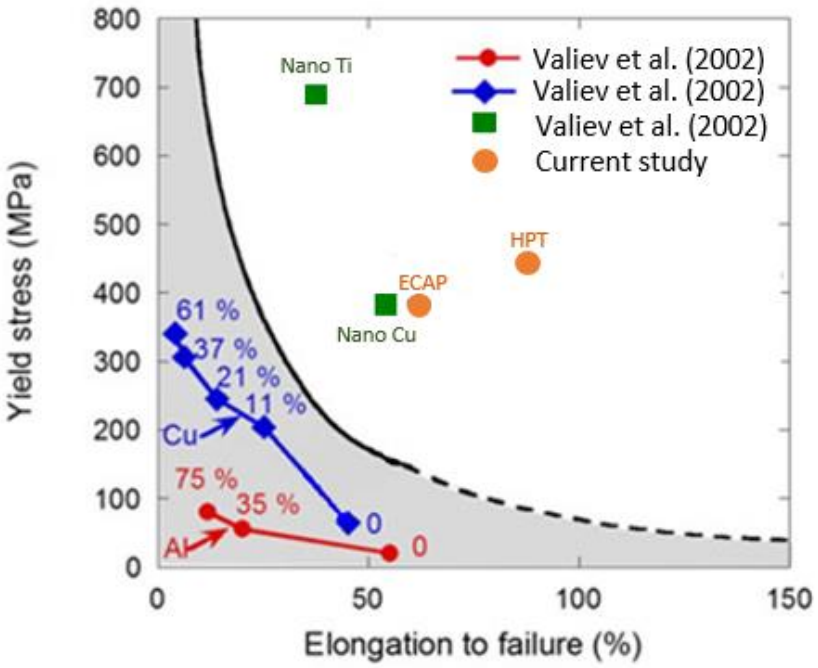

Figure 6.14 Strength and ductility paradox diagram for nanostructured metals, showing a direct comparison between oxygen-free copper processed by HPT for up 10 turns and ECAP for up to 24 passes, and earlier results obtained for copper and titanium processed by ECAP and HPT, respectively. Copper and aluminium show an increase in strength but a decrease in ductility when processed by several percentages of conventional cold rolling (red & blue datum points) [89].

6.3.4 Influence of strain rate on ductility

It has been shown from the tensile tests results conducted at room temperature that ductility is enhanced with increasing number of passes during ECAP and increasing number of turns during HPT. It is readily apparent also that decreasing the strain rate during tensile testing increases the ductility of oxygen-free copper. This is clearly demonstrated in Figure 6.15(a-f) for the specimens processed by ECAP and in Figure 6.16(a-f) for the specimens processed by HPT then pulled in tension to failure using strain rates of 1.0×10^{-2} s^{-1}, 1.0×10^{-3} s^{-1} and 1.0×10^{-4} s^{-1} at 298 K. It can be seen also that increasing the strain rate increases the values of the flow stress in the deformed specimens. This is due to the increase in the dislocation accumulation at the grain boundaries at high strain rate [274]. A minor drop in the flow stress is observed in the specimen processed by ECAP for 2 and 4 passes as shown in Figures 6.15(b) and 6.15(c) when decreasing the strain rate from 1.0×10^{-2} s^{-1} to 1.0×10^{-4} s^{-1}.

The influence of strain rate and number of ECAP passes in the tensile test is shown in Figure 6.17(a) and the influence of strain rate and number of HPT turns is shown in Figure 6.17(b). Both figures display the variation in the elongation to failure obtained during tensile testing at 298 K using three different strain rates for each specimen deformed by ECAP for a given number of passes, see Figure 6.17(a), and HPT for a given number of turns, see Figure 6.17(b). The ductility increases with increasing number of ECAP passes and it is in line with those of previous studies [89,124]. The ductility increases also with increasing number of HPT turns and it is consistent with the data obtained in Cu-0.1 %Zr [51]. The specimen deformed by low number of passes or turns exhibit low ductility because their microstructures are inhomogeneous as it was demonstrated in chapter 4 and chapter 5.

It is well documented that increasing the strain rate and decreasing the testing temperature increases the flow stress and promotes higher strain hardening behaviour [275]. These results confirm the association between the strain rate and elongation to failure. Curves in Figure 6.17(a) and Figure 6.17(b) demonstrate the effect of decreasing the strain rate on the final elongation of the specimens. Testing oxygen-free copper specimens at 298 K using lowest used strain rate of 1.0×10^{-4} s^{-1} promotes the optimum elongation at each given number of ECAP passes as shown in Figure 6.17(a) and at each given number of HPT turns as shown in Figure 6.17(b). This is attributed to the higher recovery achieved at the lowest strain rate during tensile test. Pulling the specimens at lower strain rates gives more time for dislocation annihilation to take place which leads to softening in the flow stress and thus increasing ductility. This behaviour was also observed in UFG Cu-5vol%Al_2O_3 nanocomposite that increasing the strain rate increases the flow stress and decreases the ductility due to the fast propagation of microcracks at and along the grain boundaries resulting in early fracture of the material [276].

(a)

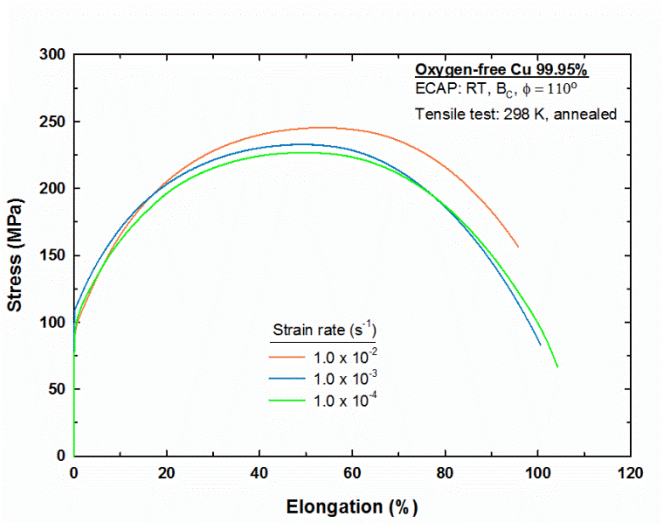
Oxygen-free Cu 99.95%
ECAP: RT, B_C, $\phi = 110^o$
Tensile test: 298 K, annealed
Strain rate (s^{-1})
1.0 x 10^{-2}
1.0 x 10^{-3}
1.0 x 10^{-4}
Stress (MPa)
Elongation (%)
0
50
100
150
200
250
300
0
20
40
60
80
100
120

(b)

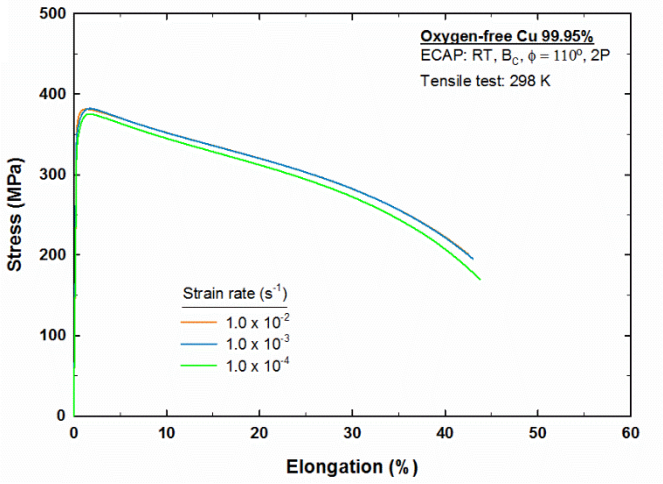
Oxygen-free Cu 99.95%
ECAP: RT, B_C, $\phi = 110^o$, 2P
Tensile test: 298 K
Strain rate (s^{-1})
1.0 x 10^{-2}
1.0 x 10^{-3}
1.0 x 10^{-4}
Stress (MPa)
Elongation (%)
0
100
200
300
400
500
0
10
20
30
40
50
60

(c)

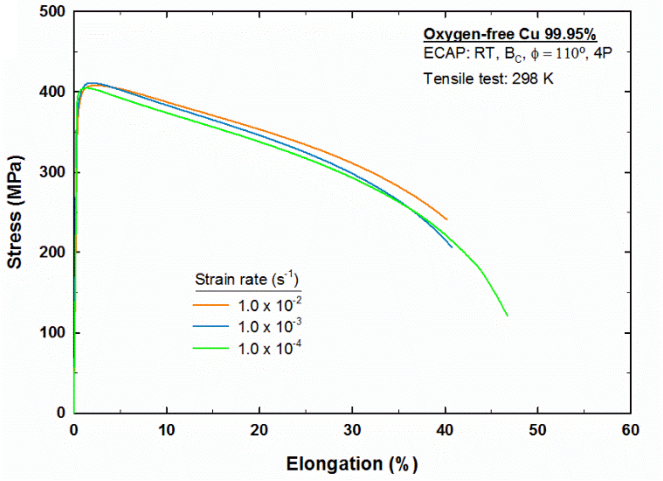
Oxygen-free Cu 99.95%
ECAP: RT, B_C, $\phi = 110^o$, 4P
Tensile test: 298 K
Strain rate (s^{-1})
1.0 x 10^{-2}
1.0 x 10^{-3}
1.0 x 10^{-4}
Stress (MPa)
Elongation (%)
0
100
200
300
400
500
0
10
20
30
40
50
60

(d)

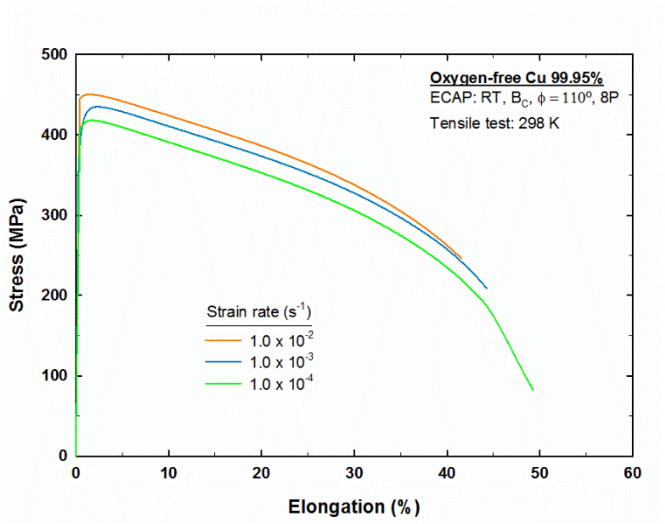

(e)

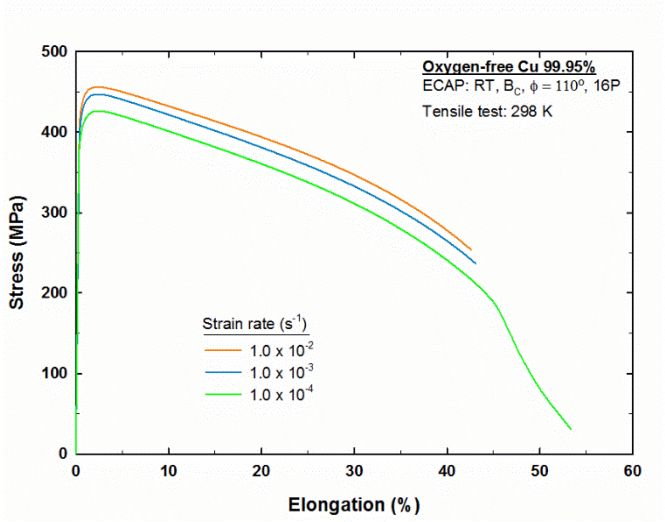

(f)

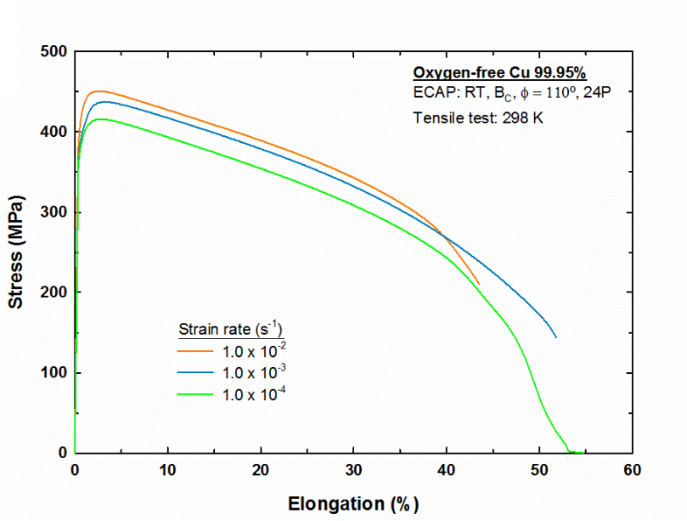

Figure 6.15 Stress-elongation % curves for oxygen-free copper processed by ECAP through different number of passes: (a) annealed, (b) 2, (c) 4, (d) 8, (e) 16 and (f) 24 and pulled in tension using different strain rates.

(a)

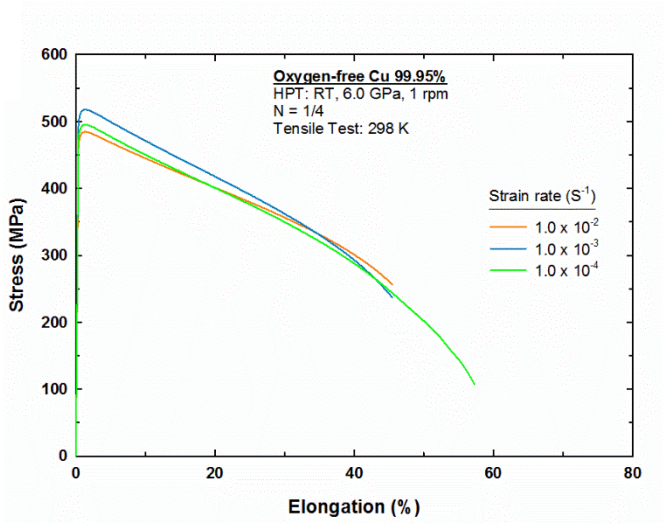
Oxygen-free Cu 99.95%
HPT: RT, 6.0 GPa, 1 rpm
N = 1/4
Tensile Test: 298 K
Strain rate (S-1)
1.0 x 10-2
1.0 x 10-3
1.0 x 10-4
Stress (MPa)
Elongation (%)
0
100
200
300
400
500
600
0
20
40
60
80

(b)

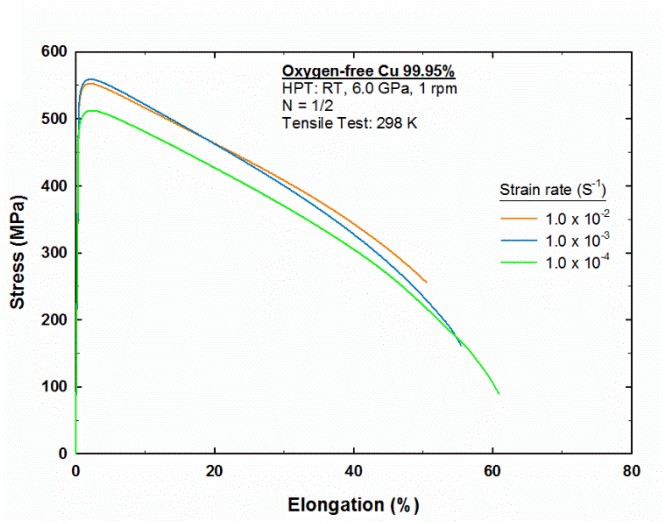
Oxygen-free Cu 99.95%
HPT: RT, 6.0 GPa, 1 rpm
N = 1/2
Tensile Test: 298 K
Strain rate (S-1)
1.0 x 10-2
1.0 x 10-3
1.0 x 10-4
Stress (MPa)
Elongation (%)
0
100
200
300
400
500
600
0
20
40
60
80

(c)

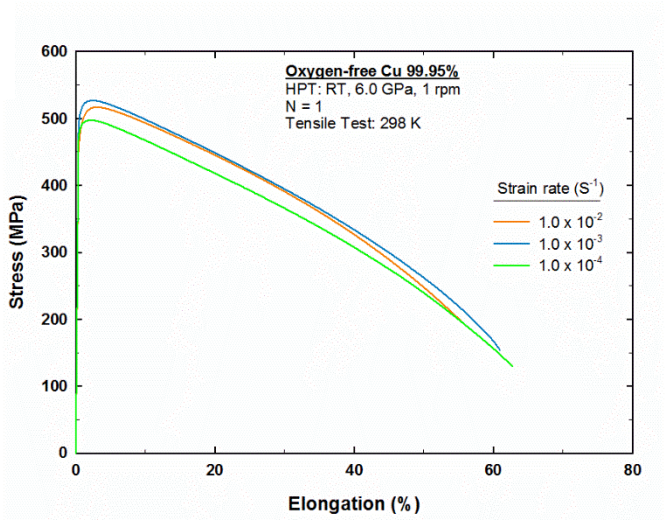
Oxygen-free Cu 99.95%
HPT: RT, 6.0 GPa, 1 rpm
N = 1
Tensile Test: 298 K
Strain rate (S-1)
1.0 x 10-2
1.0 x 10-3
1.0 x 10-4
Stress (MPa)
Elongation (%)
0
100
200
300
400
500
600
0
20
40
60
80

(d)

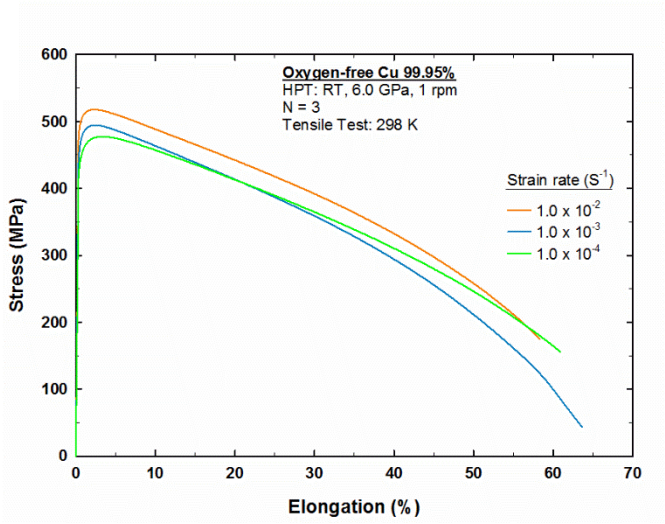

(e)

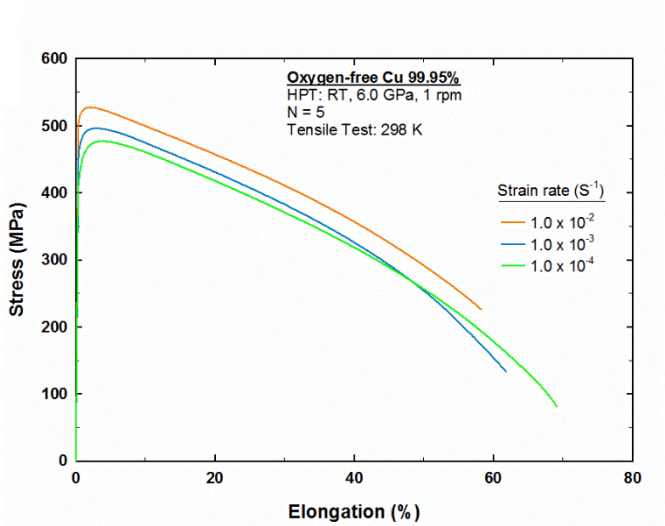

(f)

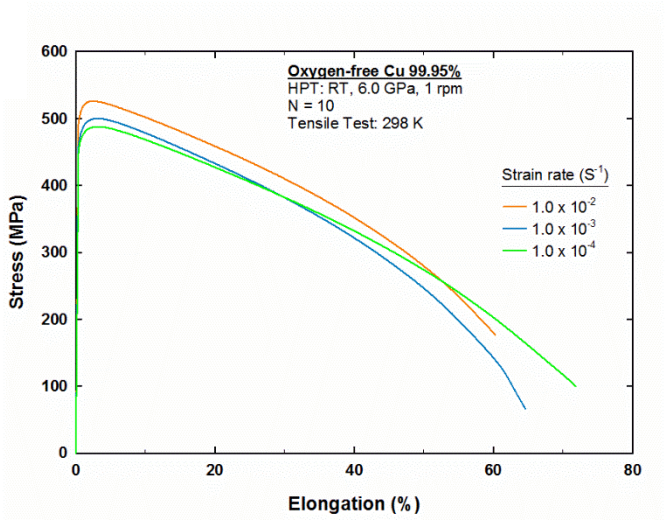

Figure 6.16 Stress-elongation % curves for oxygen-free copper processed by HPT through different number of turns: (a) 1/4, (b) 1/2, (c) 1, (d) 3, (e) 5 and (f) 10 and pulled in tension using different strain rates.

(a)

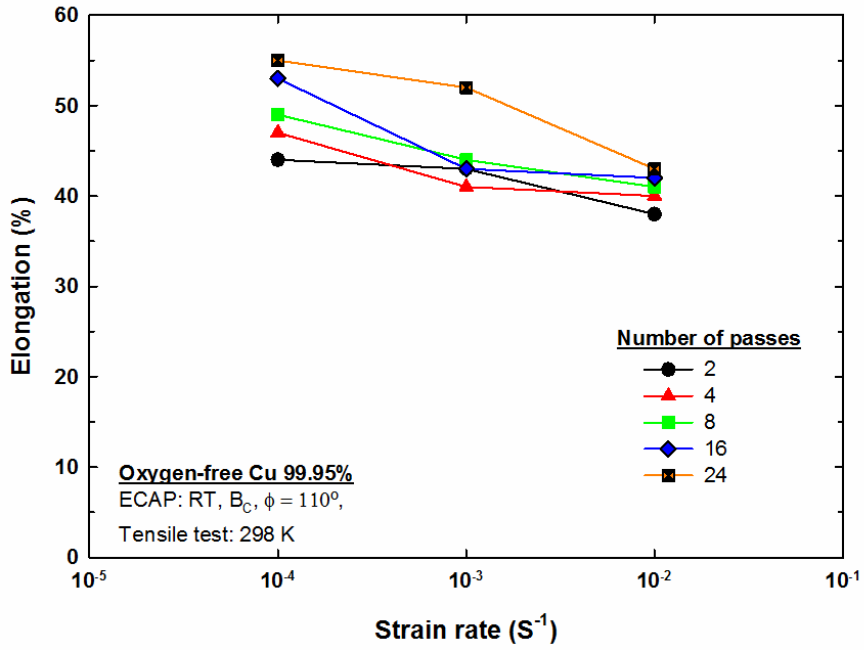

(b)

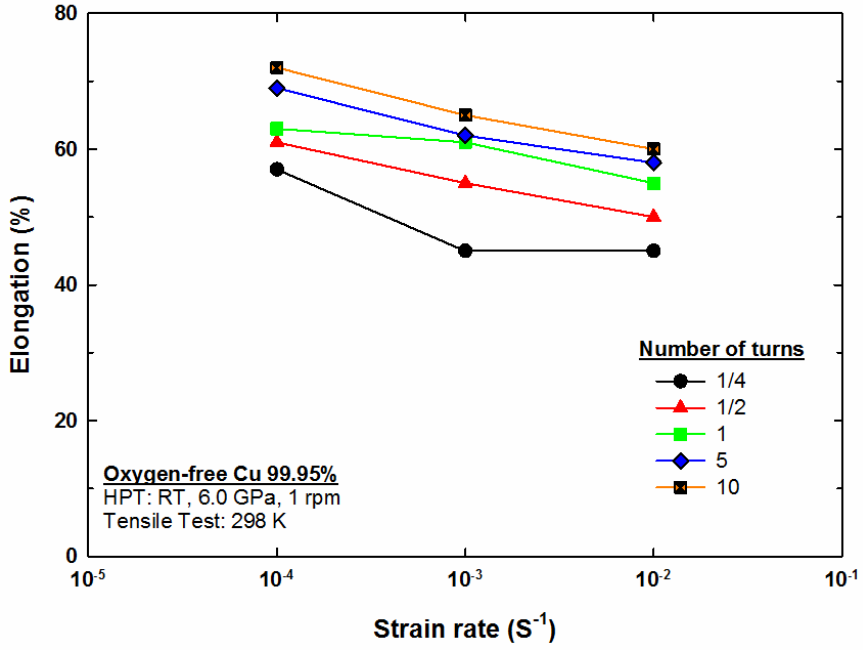

Figure 6.17 Elongation %-strain rate curves for oxygen-free copper processed at room temperature by: (a) ECAP and (b) HPT.

6.3.5 Formability index

In order to assess the performance of oxygen-free copper after ECAP and HPT processes, the formability index is calculated for each specific number of ECAP passes as shown in Figure 6.18(a) and number of HPT turns as shown in figure 6.18(b) at different strain rates. The formability index presenting strength and ductility is used in this study to provide more information regarding the mechanical performance of oxygen-free copper processed by ECAP and HPT. The formability index is calculated using the following equation [277]:

$$\text{Formability index (MPa\%)} = \text{UTS (MPa)} \times \text{El. (\%)} \quad (6.8)$$

where UTS is the ultimate tensile strength and El is the elongation to failure. As can be seen in Figure 6.18(a) that formability index increases with increasing number of passes and decreasing the strain rate. The highest formability index is observed in the specimen processed by 24 passes. Similar trend is noticed in Figure 6.18(b) for the specimens processed by HPT. It is readily apparent that the formability index is increasing with increasing number of turns as well as decreasing the strain rate and the highest formability index is observed in the specimen processed by 10 turns. Moreover, specimens processed by HPT exhibit higher formability index than specimens processed by ECAP.

It can be concluded from these results that deforming oxygen-free copper to higher strain levels by ECAP and HPT can provide better mechanical performance at room temperature. These results seem to be consistent with other research on Cu-OFHC and Cu-0.1%Mg processed by ECAP which found that the formability index increased with increasing number of passes from 1 to 4 [186]. However, this outcome is contrary to previous study on commercially pure Al that was processed by accumulative back extrusion (ABE) through 3 passes and the highest formability index was related to the specimen processed by 2 passes of ABE [253].

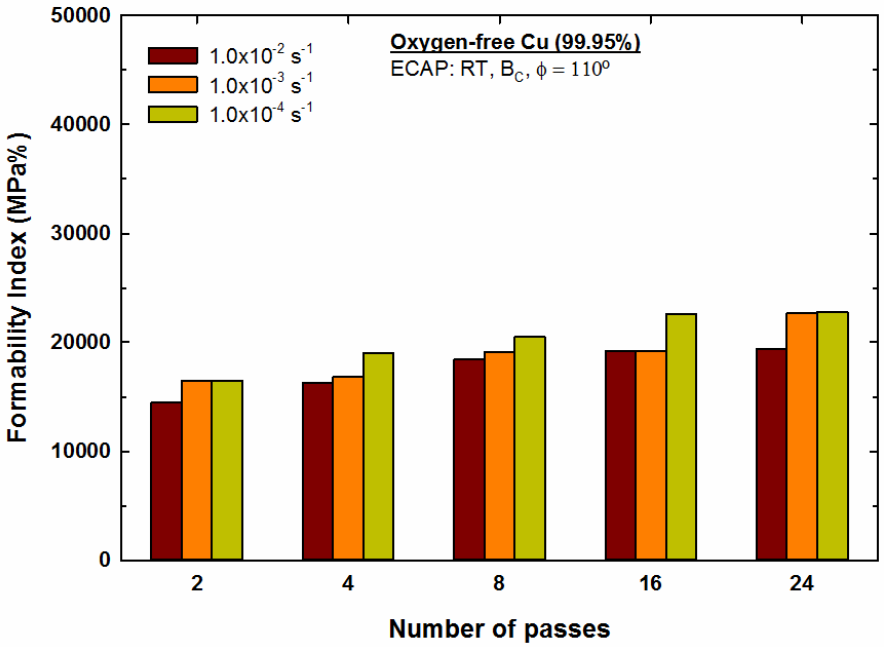

Figure 6.18 Formability index values of oxygen-free copper processed by ECAP for 2-24 passes at room temperature and pulled in tension using different strain rates.

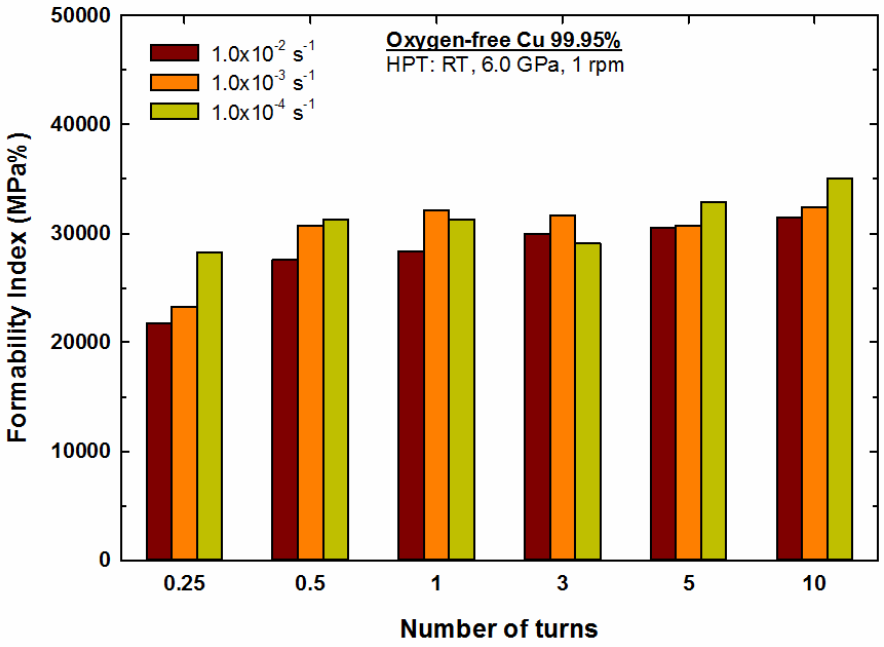

Figure 6.19 Formability index values of oxygen-free copper processed by HPT for 1/4-10 turns at room temperature and pulled in tension using different strain rates.

6.4 Summary

1. A simultaneous rise in strength and ductility was observed after pulling the oxygen-free copper samples processed by ECAP and HPT in tension with strain rates of 1.0×10^{-2} s^{-1}, 1.0×10^{-3} s^{-1} and 1.0×10^{-4} s^{-1}.

2. Dislocation density increased and crystallite size decreased after deformation by ECAP and HPT, however, at a certain strain the dislocation density decreased while the crystallite size increased indicating the occurrence of recovery mechanism. The occurrence of the recovery is much faster during HPT than ECAP. This is attributed to the intensive strain imposed by HPT. The occurrence of strength softening was observed after 24 passes in ECAP, while it was observed after 1/2 turn in HPT.

3. Yield stress, UTS, uniform elongation and elongation to failure increased with increasing strain during deformation. Grain size strengthening and dislocation strengthening are two mechanisms contributing to the enhanced strength of oxygen-free copper, while the increase in ductility is related to a recovery mechanism whereby the dislocation annihilation process reduces the dislocation density in the presence of HAGBs, and an increase in the crystallite size, which increases the mean free path of dislocations and restores the work-hardening ability of the material.

4. Although the strain rate sensitivity values are very small, it appears that it assists in the delay of early necking but not to the extent of facilitating a grain boundary sliding mechanism.

5. The ductility is improved in oxygen-free Cu by imposing equivalent strains higher than ~12.

6. Oxygen-free Cu samples exhibit higher elongation to failure at lower strain rates during tensile testing and the formability index increased with increasing the imposed strain and decreasing the strain rate.

Chapter 7 The Effect of Self-annealing Behaviour at Room Temperature on the Microstructure and Mechanical Properties of Oxygen-free Cu Processed by HPT

7.1 Background

Currently, there are few reports of the occurrence of self-annealing at room temperature in pure copper after HPT. One study has shown that self-annealing was not observed (no decrease in hardness) after 70 days storage at room temperature (RT) for pure Cu (99.99%) subjected to HPT for 5 turns at 6.0 GPa [278]. Another study on pure Cu processed by HPT for 1 turn and stored at RT for 96 hours revealed no significant change in hardness; however, there was a minor drop in microstrain as measured by XRD [279]. Long-term self-annealing after HPT was investigated using Cu (99.99%) that was processed through 10 turns at 6.0 GPa then stored at RT for 4.3 years [280]. The results showed that there was a minor drop in hardness value of ~22 Hv. A more recent study on Cu (99.99%) processed by HPT for 1/2, 1, 5 and 10 turns at 6.0 GPa showed a significant drop in hardness values at the edges of the disc processed by 1/2 turn after RT storage for 6 weeks. The self-annealing effect was not detected for 5 and 10 turns [150].

7.2 Aim

In this chapter, oxygen-free copper was processed by HPT at RT for various numbers of turns (N = 1/4, 1/2, 1, 3, 5 and 10). The microstructural stability was investigated by storing the samples at room temperature for 12 months. The microstructural development was investigated by EBSD and XRD techniques while mechanical properties were tested by Vickers microhardness and tensile tests. The aim of this chapter is to provide a systematic study of the influence of self-annealing in oxygen-free copper on the microstructural and mechanical properties.

7.3 Results

7.3.1 The evolution of microhardness after room temperature storage

The hardness measurements were recorded along a diameter of each disc. Figure 7.1 compares the hardness measurements recorded after 1 week and after 12 months from the HPT processing date for (a) 1/4, (b) 1/2, (c) 1, (d) 3, (e) 5 and (f) 10 turns. It can be seen from the microhardness results recorded 1 week after HPT that at the initial stages of deformation (N = 1/4 to 1) the microhardness values vary across the diameter of the disc. Low hardness values were recorded in the central region with higher values at the edges. At later stages of deformation (N = 3 to 10), the variations in the hardness values across the diameters of the discs are diminished and almost the same level of hardness is achieved. A steady-state condition was achieved after 10 turns with reasonable hardness homogeneity. In addition, the hardness values recorded at the peripheries after N = 1/4 are higher than the values recorded at the same positions after subsequent turns. These values slightly decreased with increasing number of turns till they became stabilized with the same average of hardness values across the diameter of the disc. The drop in hardness provided evidence of dynamic recovery taking place during the HPT process. This structural recovery had been observed previously in high purity OFHC copper of 99.99+wt% after processing by HPT at RT [150].

HPT specimens were stored at RT for a period of 12 months after processing then microhardness measurements were again recorded along diameters of each disc as shown in Figure 7.1. It is readily apparent in Figure 7.1(a) that there was a significant drop in hardness values around the periphery after 1/4 turn. The severity of hardness loss is reduced as the point of measurements moves towards the centre of the disc. The major drop was seen at a radial distance of ~4 mm up 4.8 mm, the measurement furthest from the centre, however it is reasonable to assume the drop in hardness extends to the edge of the disc. The average hardness value decreased from ~138 Hv to ~100 Hv within this region.

In Figure 7.1(b) the hardness values recorded after 12 months for the specimen processed by 1/2 turn revealed a substantial drop over a distance of ~2 to 4.8 mm from the centre of the disc. The average hardness value decreased from ~138 Hv to ~100 Hv within this region. The specimen processed by 1 turn shows that the hardness drop started

from a distance closer to the centre of the disc than specimens processed by lower numbers of turns as shown in Figure 7.1(c). The decrease in hardness began at ~0.5 mm from the centre of the disc and stabilised at an average value of ~118 Hv towards the periphery.

It can be seen that at higher numbers of turns (N = 3, 5 and 10), shown in Figure 7.1(d), (e), and (f), respectively, the drop in hardness was not localized and was almost constant across the diameters of the discs. These three conditions revealed a similar trend in which the drop in hardness values was relatively minor. The hardness reduced only ~8% after storage at RT for 12 months.

It is apparent from these results that the reduction in hardness was more pronounced in the specimens processed by low numbers of turns (N= 1/4 and 1/2) and had a major effect at the edges. After 1 turn, the area which hardness drop occurred, increased and was constant across the diameter of the disc after 3 turns.

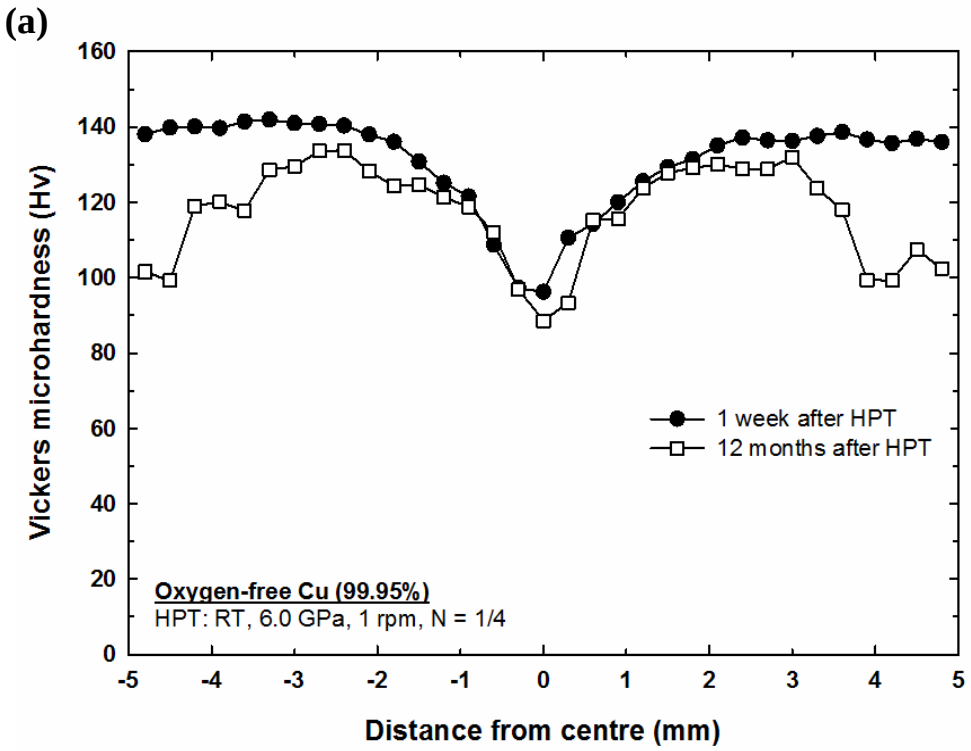

(b)

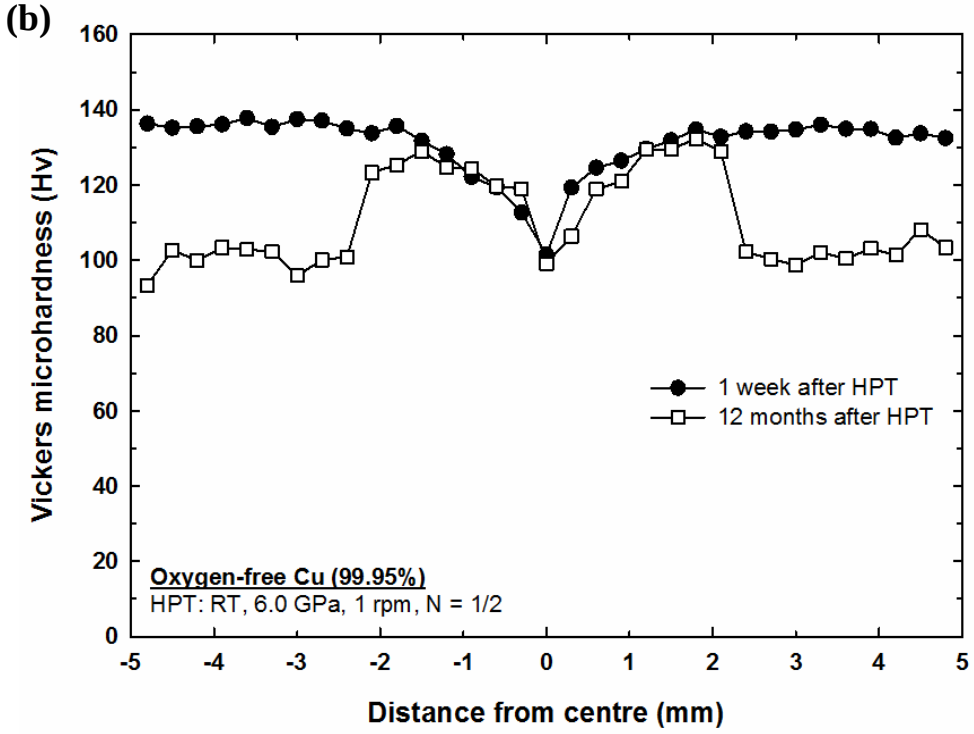
Vickers microhardness (Hv)
Distance from centre (mm)
1 week after HPT
12 months after HPT
Oxygen-free Cu (99.95%)
HPT: RT, 6.0 GPa, 1 rpm, N = 1/2

(c)

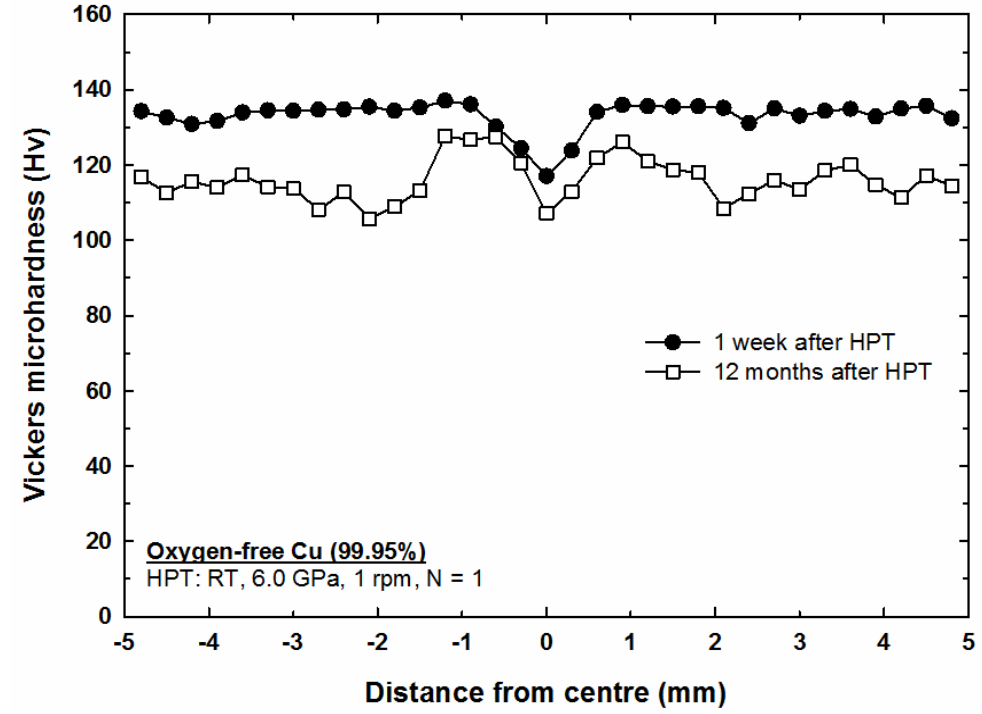
Vickers microhardness (Hv)
Distance from centre (mm)
1 week after HPT
12 months after HPT
Oxygen-free Cu (99.95%)
HPT: RT, 6.0 GPa, 1 rpm, N = 1

(d)

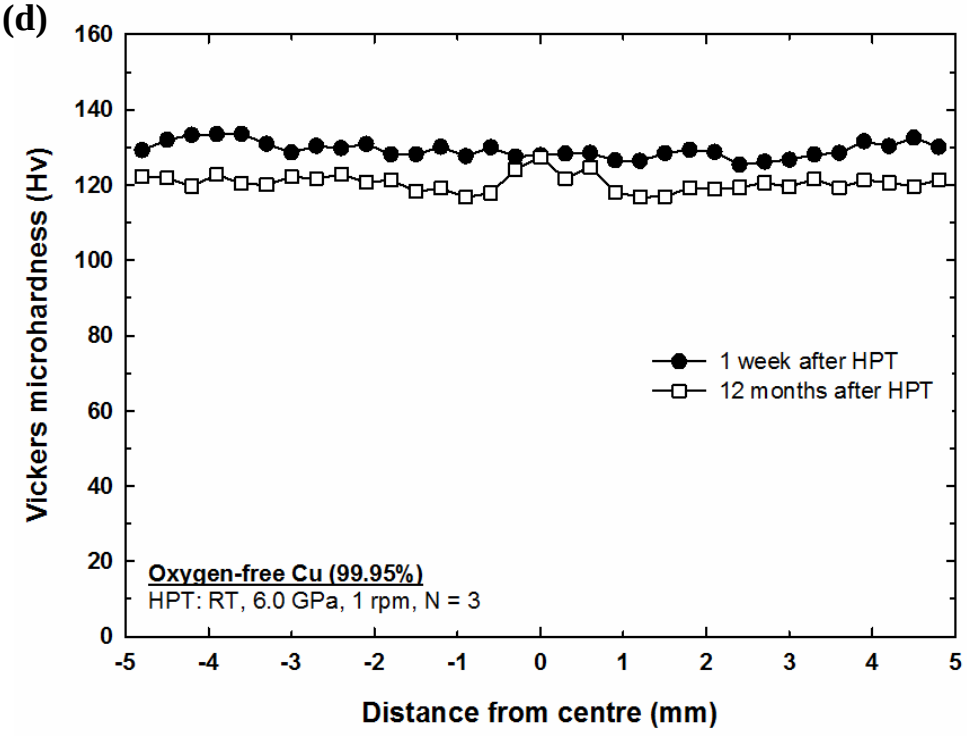
Vickers microhardness (Hv)
Distance from centre (mm)
1 week after HPT
12 months after HPT
Oxygen-free Cu (99.95%)
HPT: RT, 6.0 GPa, 1 rpm, N = 3

(e)

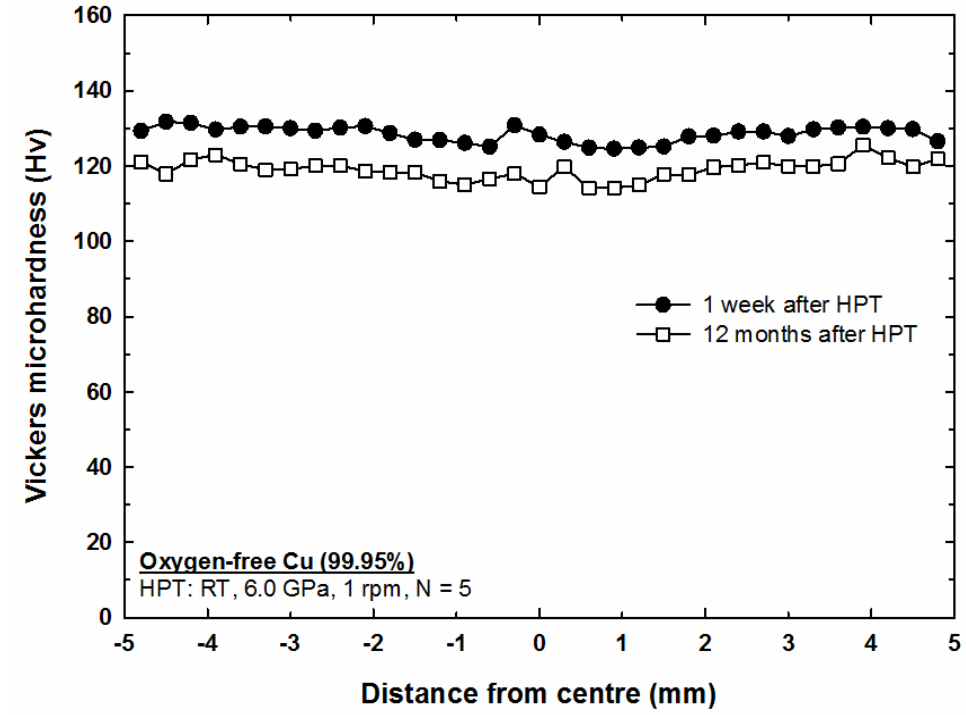
Vickers microhardness (Hv)
Distance from centre (mm)
1 week after HPT
12 months after HPT
Oxygen-free Cu (99.95%)
HPT: RT, 6.0 GPa, 1 rpm, N = 5

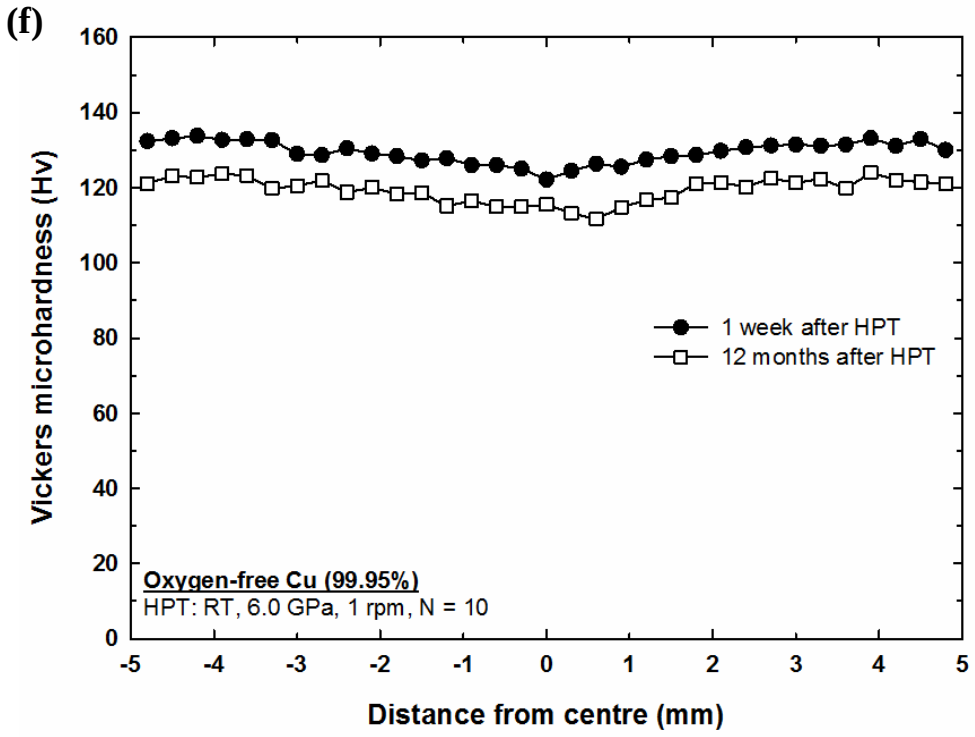

Figure 7.1 Vickers microhardness measurements recorded along diameters of oxygen-free Cu discs after 1 week and 1 year from date of the HPT processing for different numbers of turns (a) 1/4, (b) 1/2, (c) 1, (d) 3, (e) 5 and (f) 10 turns.

7.1.2 Microstructural evolution during post-HPT RT storage

The microstructural evolution at the centre and edge of oxygen-free Cu discs at 1 week after HPT processing was presented in Chapter 5 (Figures 5.3 – 5.14). It was documented that a significant reduction in the average grain size was observed after 1/2 turn. Before HPT processing, the annealed copper had an average grain size of ~24 μm and it this was reduced to ~820 nm and ~690 nm in the centre and at the periphery, respectively. The average grain size continued to decrease at both positions with increasing number of turns. After 10 turns, the variation in the average grain size between the centre and the periphery of the disc diminished and reached ~510 nm at both positions. This indicates that microstructural homogeneity was achieved at high torsional straining.

Figure 7.2 to Figure 7.9 illustrate the OIM images of the centre and edge of an oxygen-free copper disc 1 week and 12 months after HPT processing for 1/2, 1, 3 and 10 turns. Close inspection of these images shows that the grains at the periphery grew

significantly after 1/2 turn. It is also obvious that the peripheries of the discs processed by 1 and 3 turns then stored for 12 months have coarser grains than those present within 1 week after HPT processing.

Table 7.1 illustrates the average grain sizes of the centre and edge positions for oxygen-free Cu after HPT processing for various numbers of turns and subsequent storage at RT for 12 months. It can be seen that the average grain sizes at centre and edge after 12 months, for every number of turns, were larger than the average grain sizes measured after 1 week from HPT processing.

An abnormal grain growth was observed at the edge of the 1/2 turn specimen. The average grain size increased from ~0.69 μm to 3.1 μm. This shows a good correlation with the localized reduction in hardness observed in Figure 7.1(b). It was also noticed that the rate of grain growth was slower in the discs processed by a higher number of turns. In fact, the rate of grain growth decreased with increasing number of turns. For example, the average grain size at the edges after 1 turn increased from ~0.63 μm to ~1.96 μm after storage, while the average grain size after 10 turns increased from ~0.51 μm to ~0.71 μm. This can be clearly seen in Figure 7.5 and Figure 7.9.

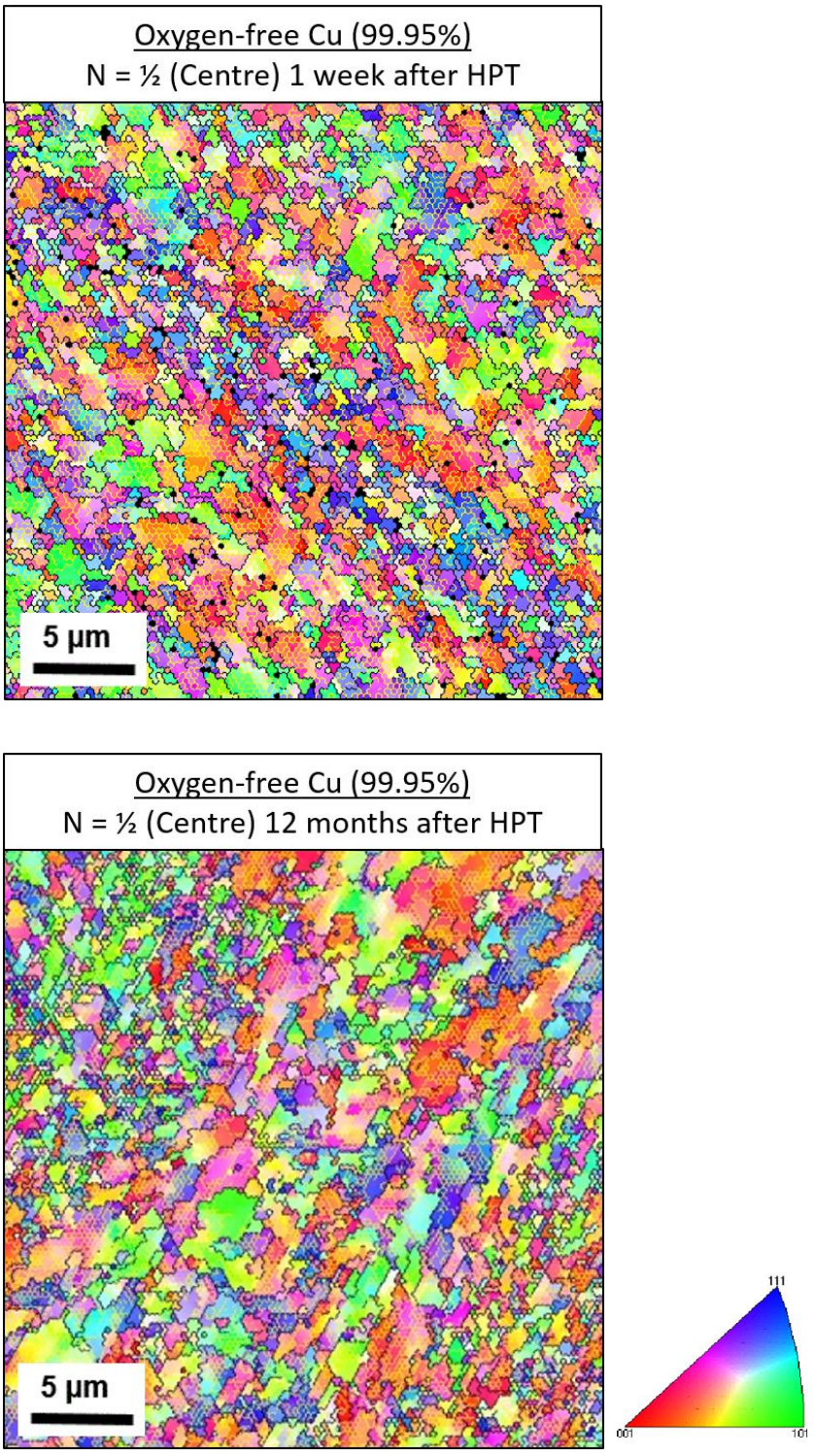

Figure 7.2 OIM images of the central region for oxygen-free copper disc; 1 week and 12 months after HPT processing for 1/2 turn.

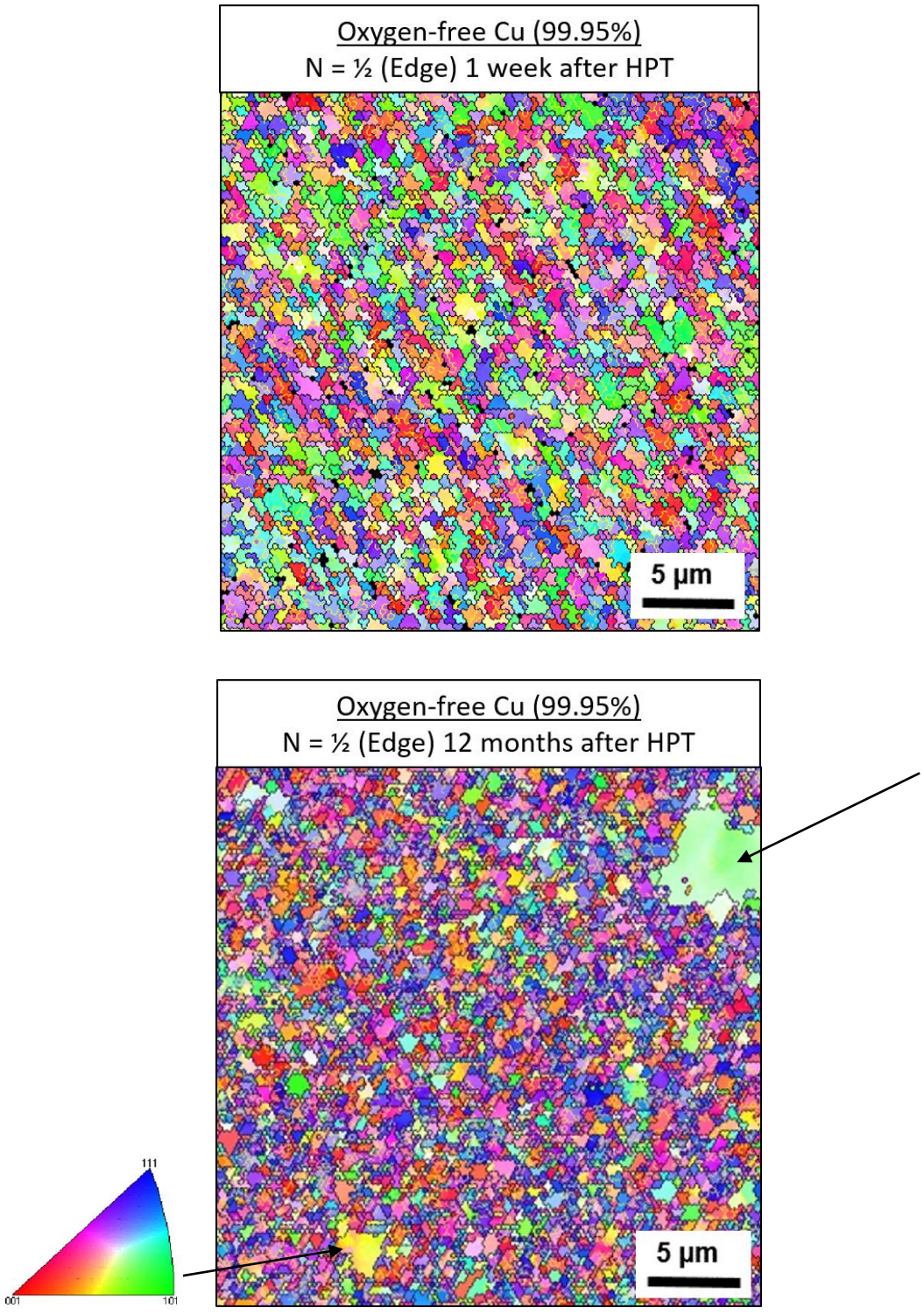

Figure 7.3 OIM images of the peripheral region for oxygen-free copper discs; 1 week and 12 months after HPT processing for 1/2 turn. (Abnormal grain growth are pointed by the arrows).

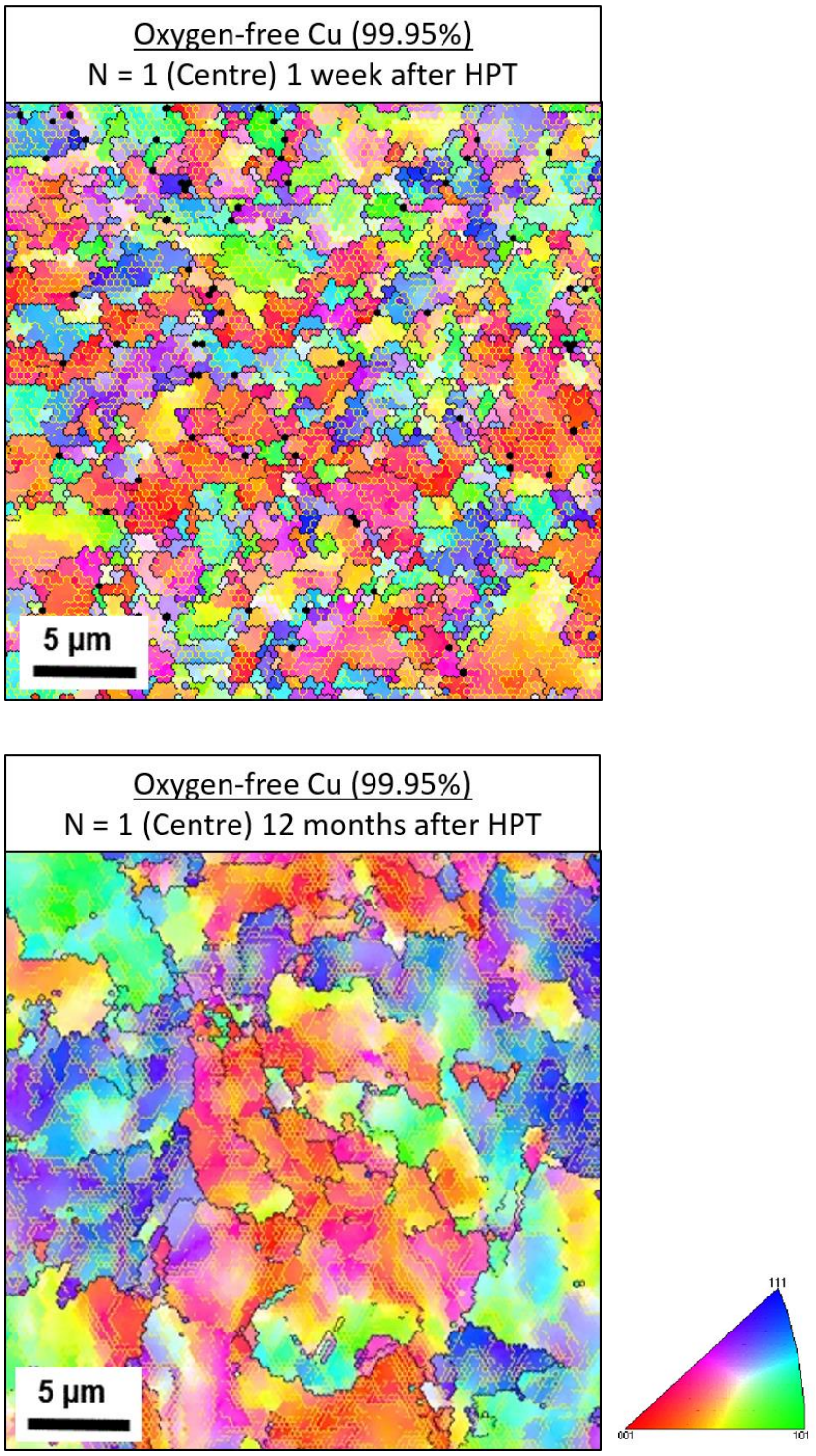

Figure 7.4 OIM images of the central region for oxygen-free copper disc; 1 week and 12 months after HPT processing for 1 turn.

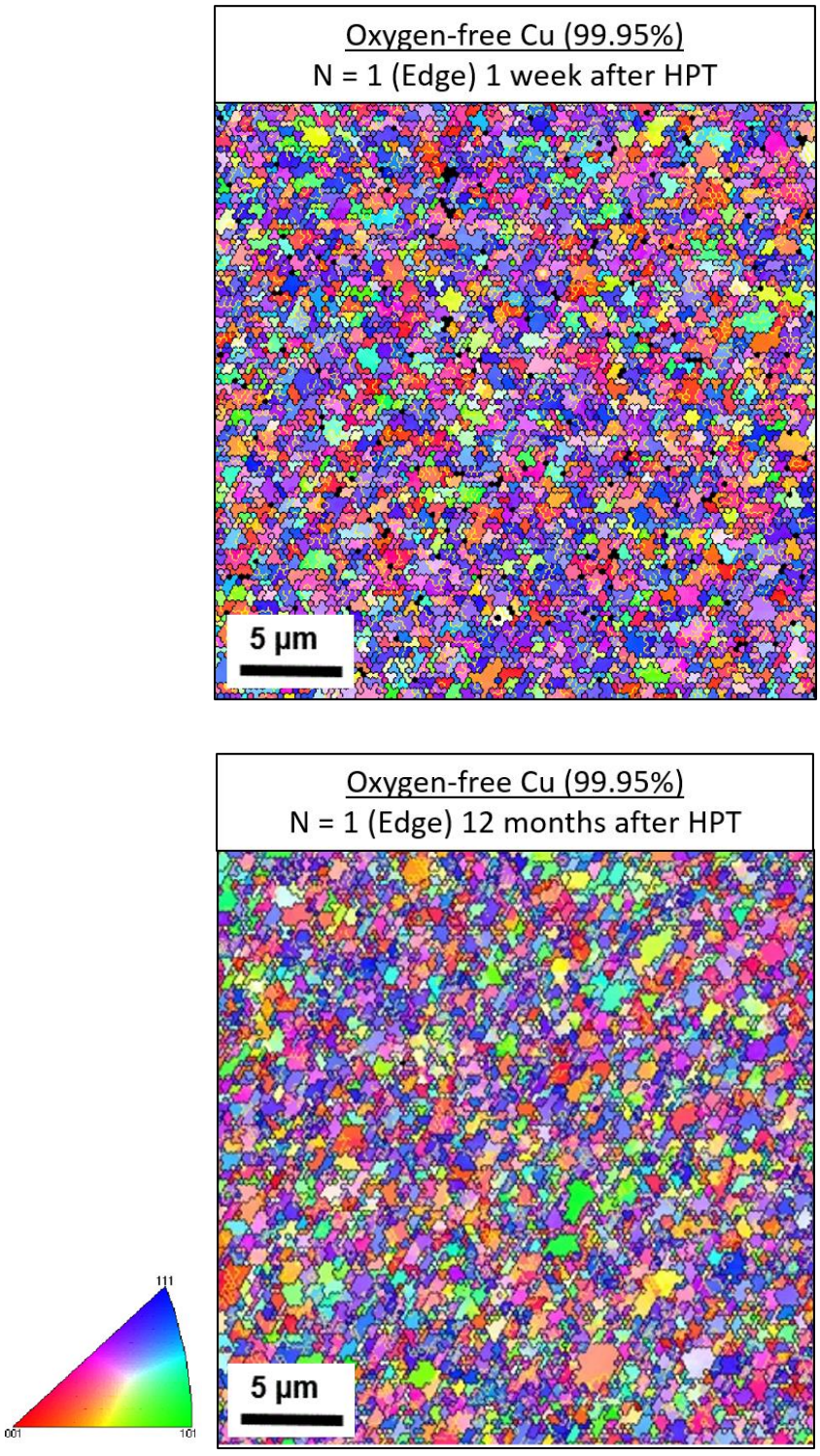

Figure 7.5 OIM images of the peripheral region for oxygen-free copper disc; 1 week and 12 months after HPT processing for 1 turn.

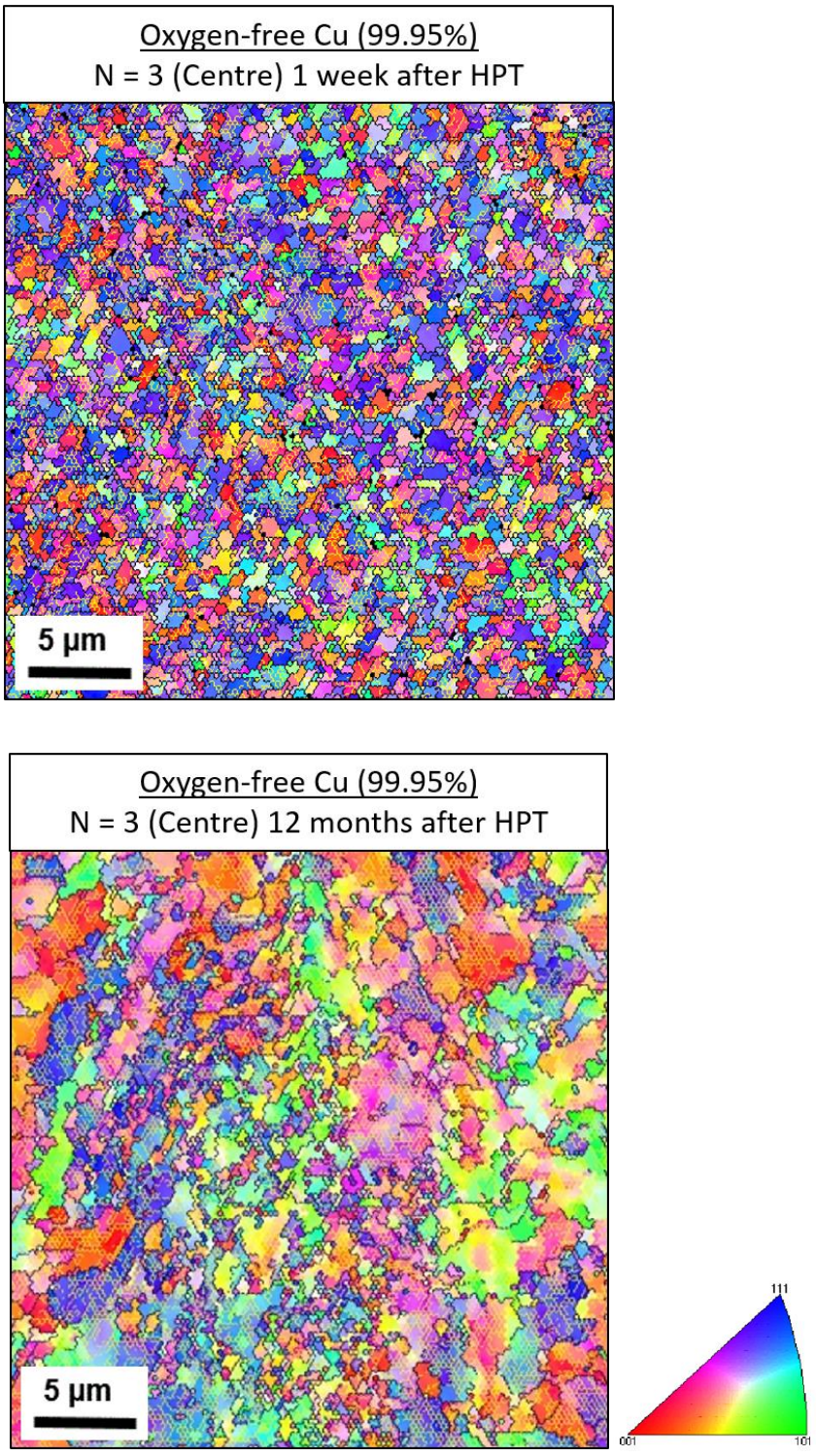

Figure 7.6 OIM images of the central region for oxygen-free copper disc; 1 week and 12 months after HPT processing for 3 turns.

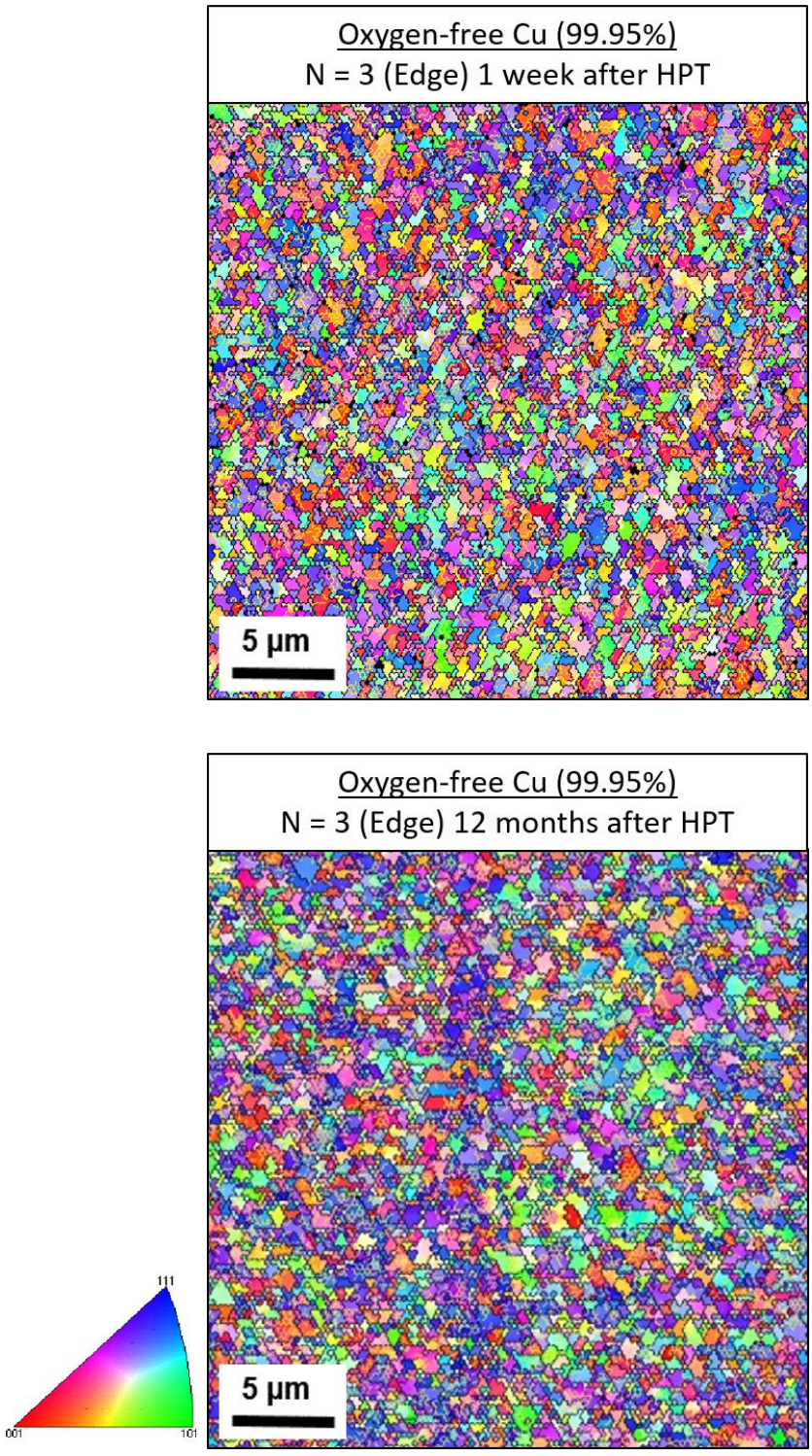

Figure 7.7 OIM images of the peripheral region for oxygen-free copper disc; 1 week and 12 months after HPT processing for 3 turns.

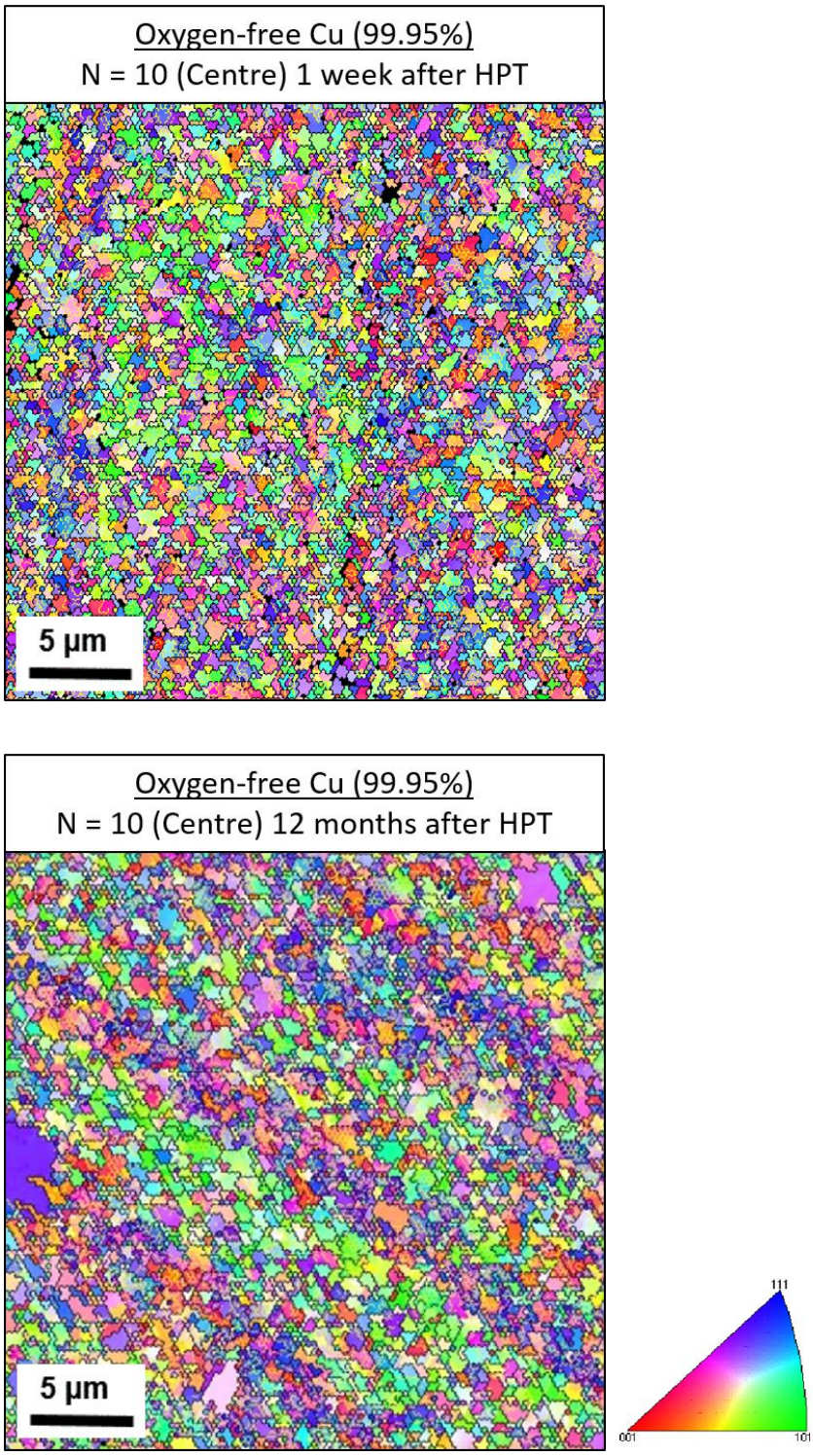

Figure 7.8 OIM images of the central region for oxygen-free copper disc; 1 week and 12 months after HPT processing for 10 turns.

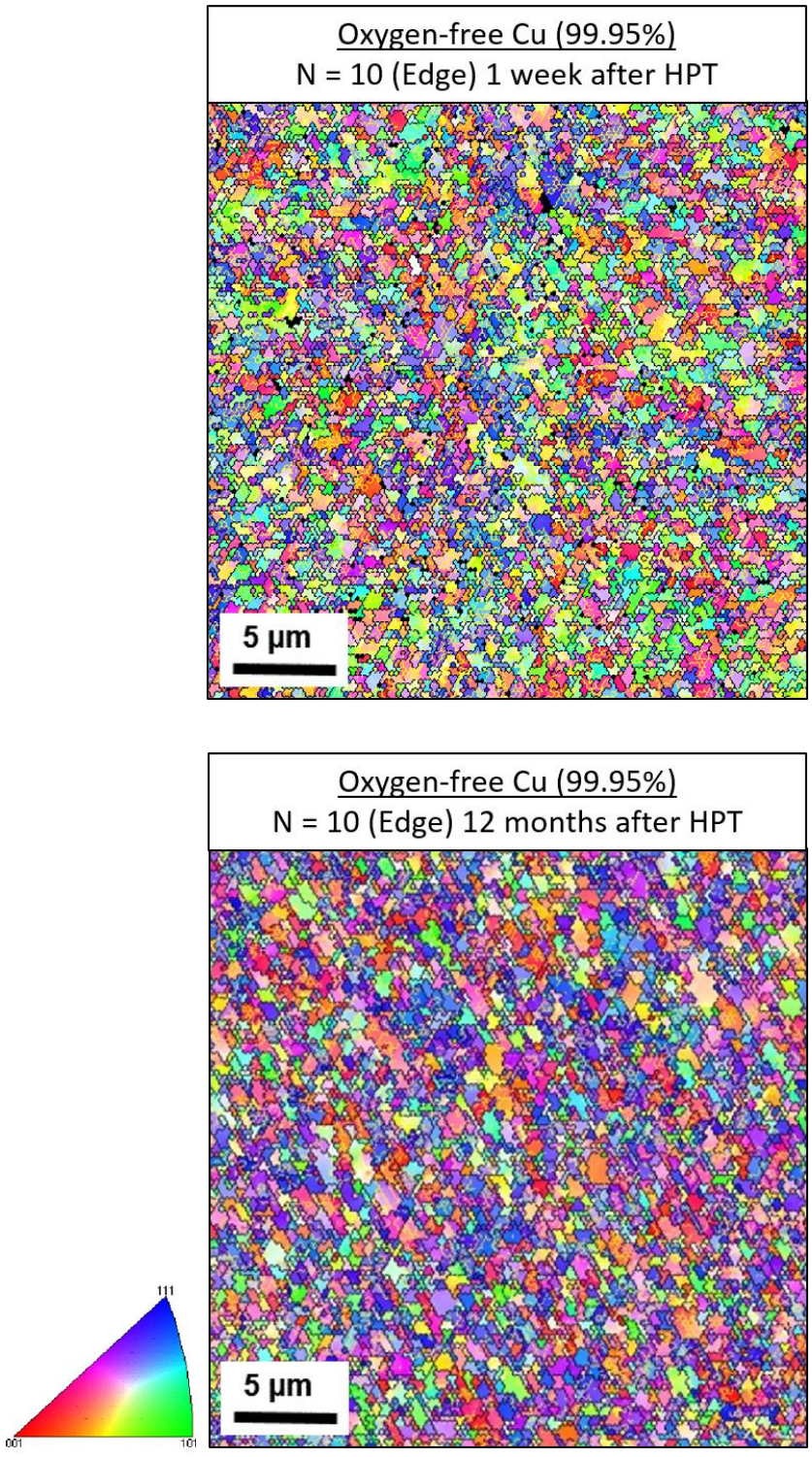

Figure 7.9 OIM images of the peripheral region for oxygen-free copper disc; 1 week and 12 months after HPT processing for 10 turns.

Table 7.1 The average grain sizes of the centres and edges of oxygen-free Cu discs after HPT processing for various number of turns and subsequent storage at RT for 12 months.

No. of turns	Position	Grain Size (μm)	
		1 week after HPT	**12 months after HPT**
1/2 turn	Centre	0.82	1.76
	Edge	0.69	3.1
1 turn	Centre	0.7	1.2
	Edge	0.63	1.96
3 Turns	Centre	0.60	0.70
	Edge	0.57	1.67
10 Turns	Centre	0.52	0.79
	Edge	0.51	0.71

The distributions of misorientation angles at the centre and edge positions for oxygen-free copper disc stored at RT for 12 months after HPT processing are shown in Figure 7.10 to Figure 7.13. It is apparent from these figures that the fractions of LAGBs are considerably higher at the centres of the discs processed by 1/2 and 1 turn, while there are high numbers of Σ3 twin boundaries at the edges. The Σ3 twin boundaries were not observed after 3 turns. Instead, the fraction of HAGBs at the centre of the disc was ~66% and at the edge was ~87%. This difference in the distributions of misorientation angles between the centre and edge is reduced at higher numbers of turns. For instance, the fractions of HAGBs for the speceimen processed by 10 turns at the centre and the edge were ~82% and ~89%, respectively.

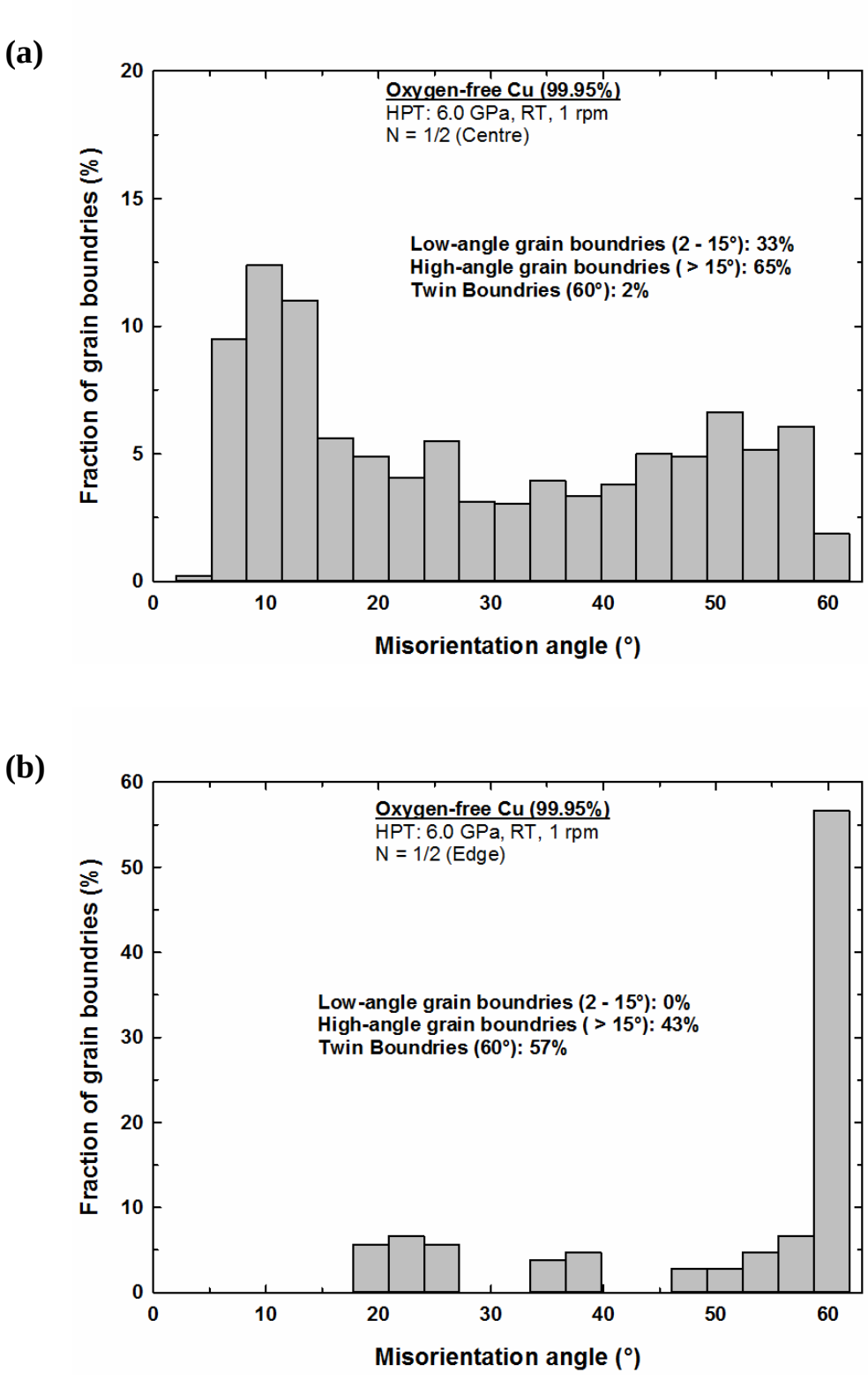

Figure 7.10 The distribution of misorientation angles for oxygen-free copper disc stored at RT for 12 months after HPT processing for 1/2 turn at a) centre and b) edge positions.

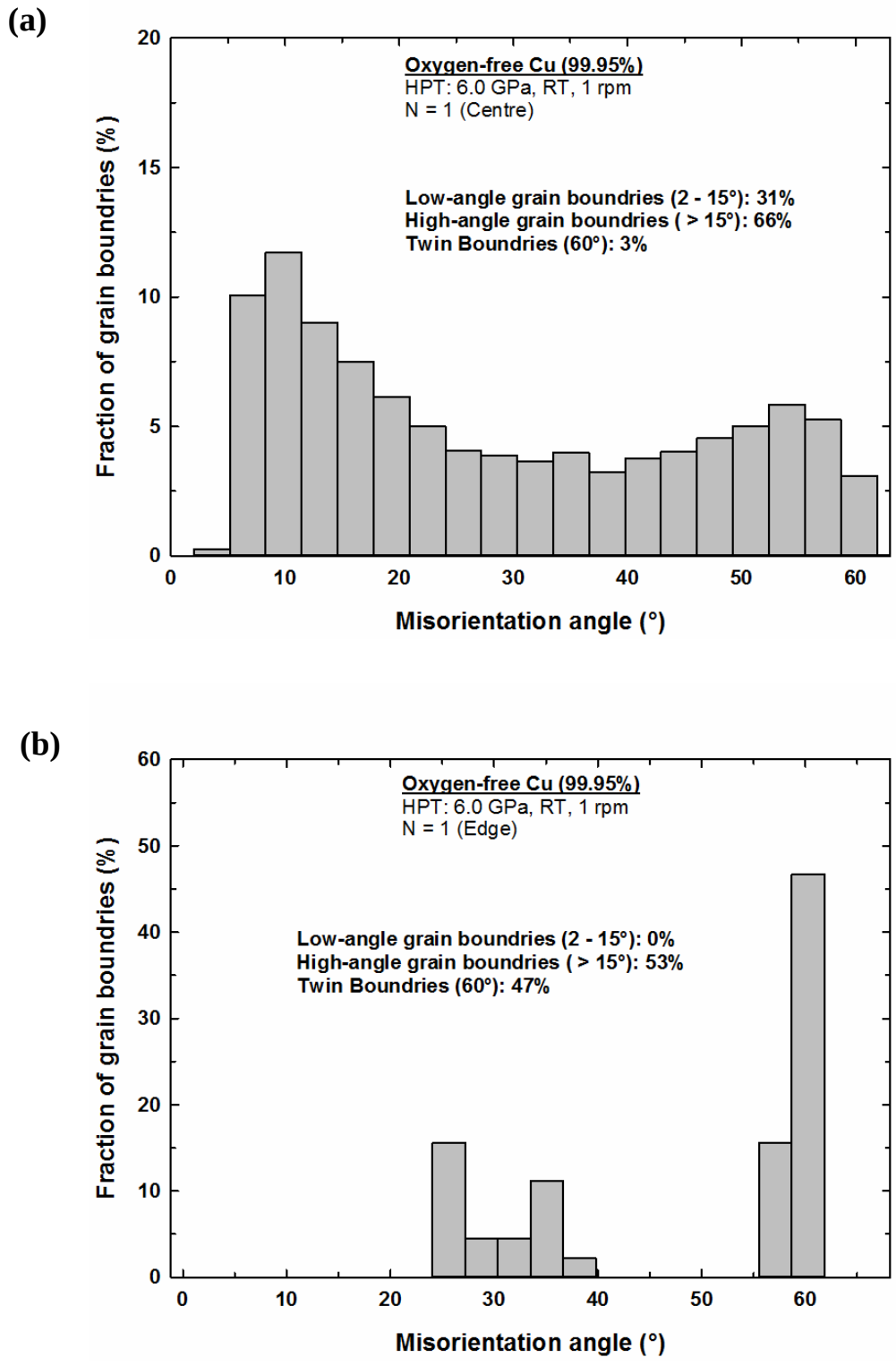

Figure 7.11 The distribution of misorientation angles for oxygen-free copper disc stored at RT for 12 months after HPT processing for 1 turn at a) centre and b) edge positions.

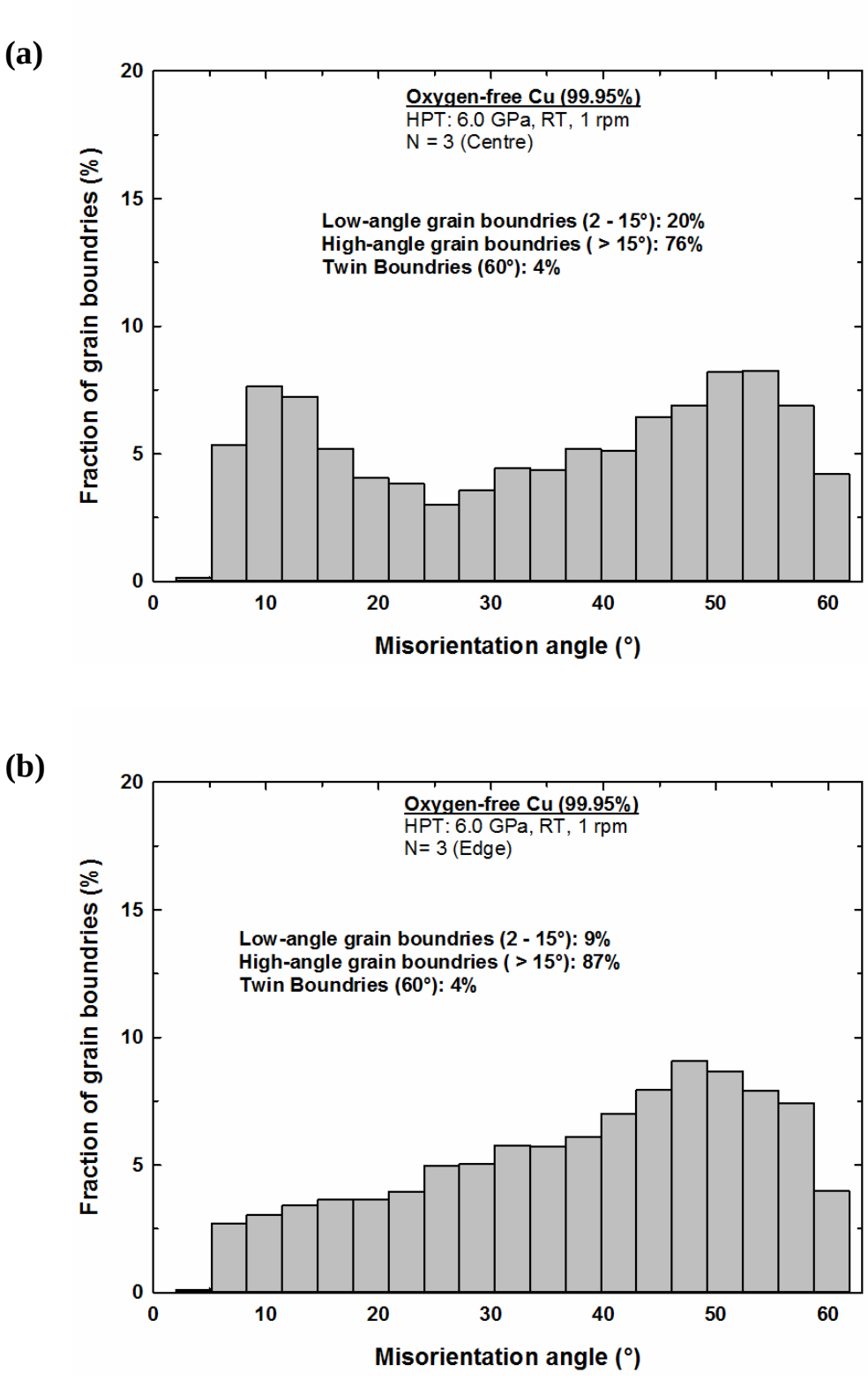

Figure 7.12 The distribution of misorientation angles for oxygen-free copper disc stored at RT for 12 months after HPT processing for 3 turns at a) centre and b) edge positions.

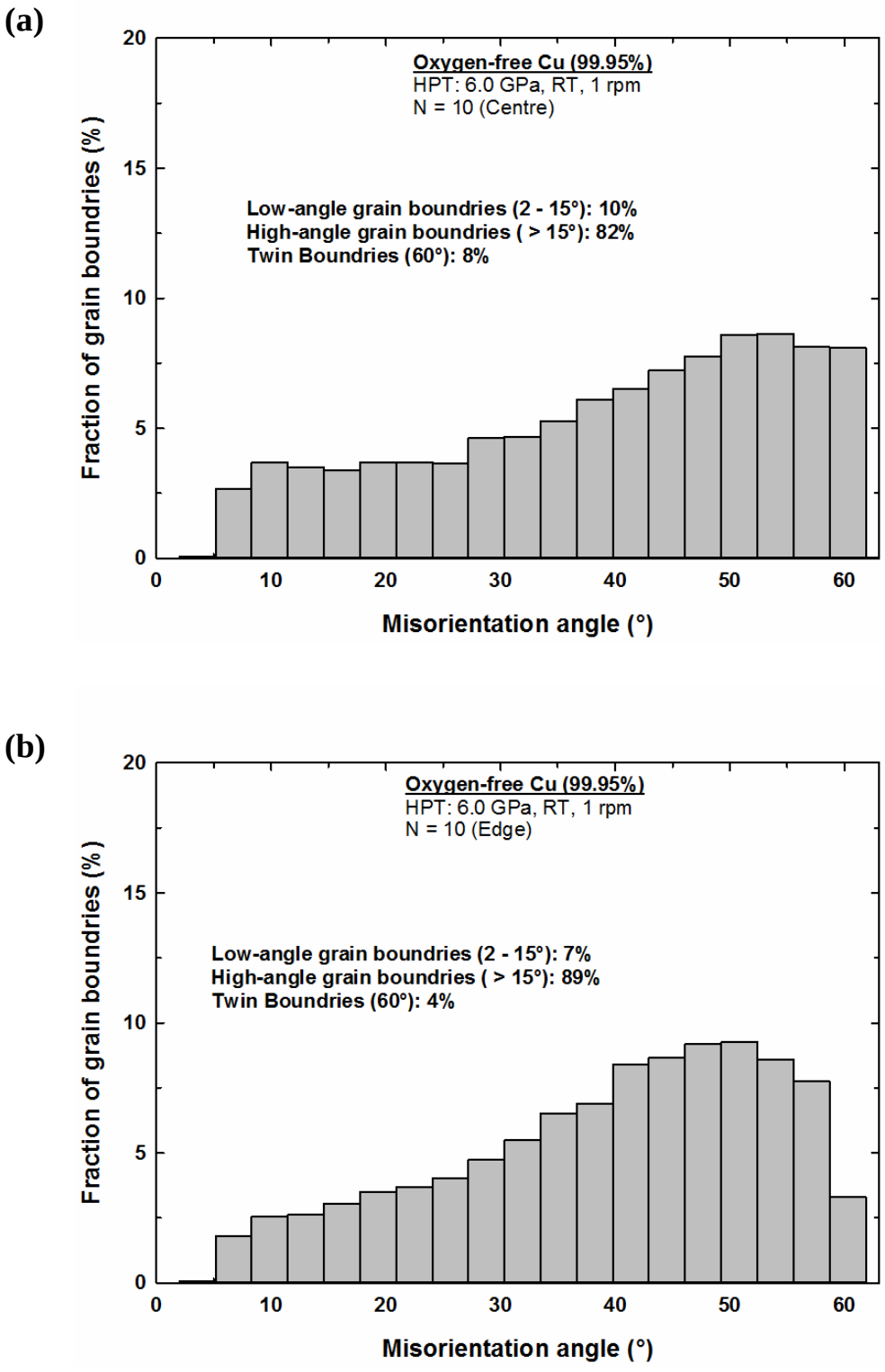

Figure 7.13 The distribution of misorientation angles for oxygen-free copper disc stored at RT for 12 months after HPT processing for 10 turns at a) centre and b) edge positions.

A direct comparison in the distributions of misorientation angles at the edges of the discs measured within 1 week after HPT processing and subsequently stored at RT for 12 months are shown in Figure 7.14. It is readily apparent that the fraction of Σ3 twin boundaries were significantly increased after 12 months storage in the specimens processed by 1/2 and 1 turns, as shown in Figure 7.14(a) and (b), and then almost disappears at higher numbers of turns (N = 3 and 10), see Figure 7.14(c) and (d). It was also noted that there was no major change in the fractional numbers of grain boundaries at different misorientation angles for specimens processed by 3 and 10 turns.

Figure 7.15(a-d) shows the fractional numbers of different grain boundary characters at the edges of oxygen-free Cu discs measured within 1 week after HPT processing and subsequent storage at RT for 12 months for a) 1/2 turn, b) 1 turn, c) 3 turns and d) 10 turns. These grain boundary characters are the LAGBs (2-15°), HAGBs (>15°) and Σ3 twin boundaries. It can be seen in Figure 7.15(a) and (b) that there was a drastic decrease in the fractional number of LAGBs after 12 months storage in those specimens processed by 1/2 and 1 turn, and the fractional number of HAGBs approximately halved. However, the fraction of Σ3 twin boundaries was significantly increased after storage at RT for 12 months. The grain boundary characters were relatively stable at higher number of turns (N = 3 and 10), and Figure 7.15(c-d) shows only minor changes in the fractional numbers.

On the other hand, Figure 7.15(e-h) presents the grain boundary character distributions at the centre of the Cu discs measured within 1 week after HPT processing and subsequent storage at RT for 12 months for e) 1/2 turn, f) 1 turn, g) 3 turns and h) 10 turns. It is readily apparent that there was a transformation from HAGBs to LAGBs in the specimens processed by 1/2, 1 and 3 turns whereas the specimen subject to 10 turns was relatively stable.

It can be concluded from the significant reduction in hardness at the peripheries of those specimens processed by 1/4, 1/2 and 1 turns, and the significant increase in the Σ3 twin boundaries, that recrystallization took place during storage for 12 months at RT. The recovery process that took place in the centres of the discs was based on the transformation of HAGBs to LAGBs during the storage time as shown in Figure 7.15(e) and Figure 7.15(f).

(a)

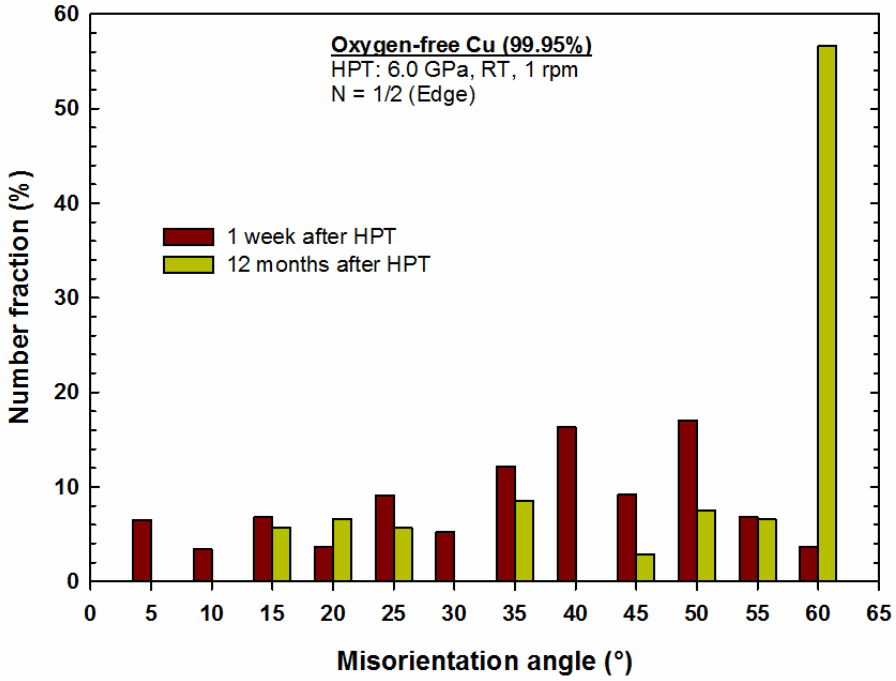
Oxygen-free Cu (99.95%)
HPT: 6.0 GPa, RT, 1 rpm
N = 1/2 (Edge)
1 week after HPT
12 months after HPT
Number fraction (%)
Misorientation angle (°)
0
10
20
30
40
50
60
0
5
10
15
20
25
30
35
40
45
50
55
60
65

(b)

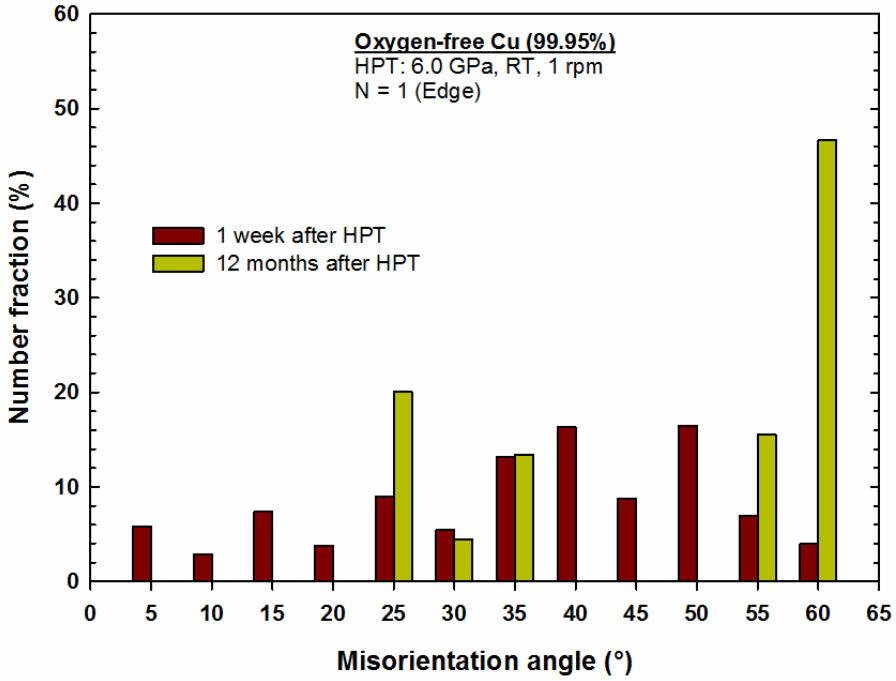
Oxygen-free Cu (99.95%)
HPT: 6.0 GPa, RT, 1 rpm
N = 1 (Edge)
1 week after HPT
12 months after HPT
Number fraction (%)
Misorientation angle (°)
0
10
20
30
40
50
60
0
5
10
15
20
25
30
35
40
45
50
55
60
65

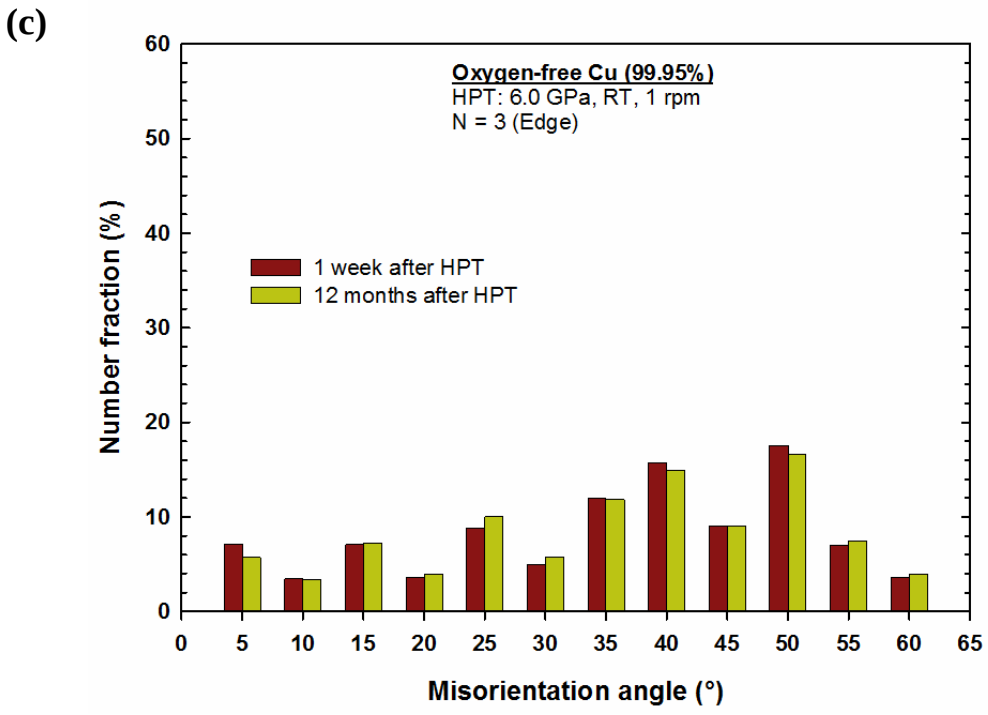

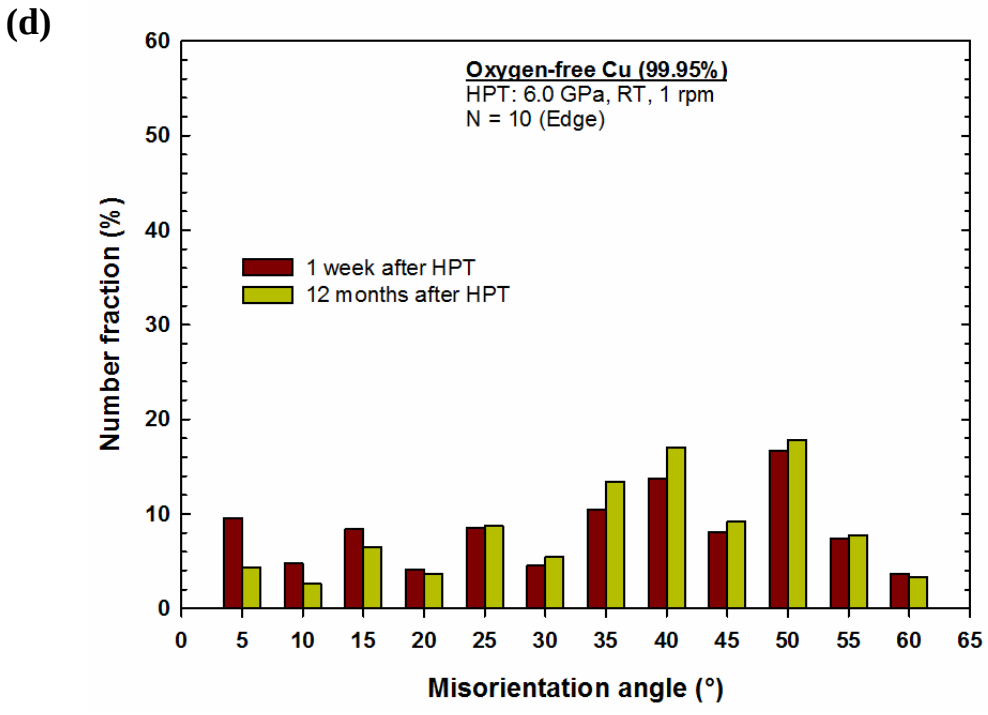

Figure 7.14 A direct comparison in the distributions of misorientation angles at the edges of the discs measured within 1 week after HPT processing and subsequent storage at RT for 12 months for a) 1/2 turn, b) 1 turn, c) 3 turns and d) 10 turns.

(a)

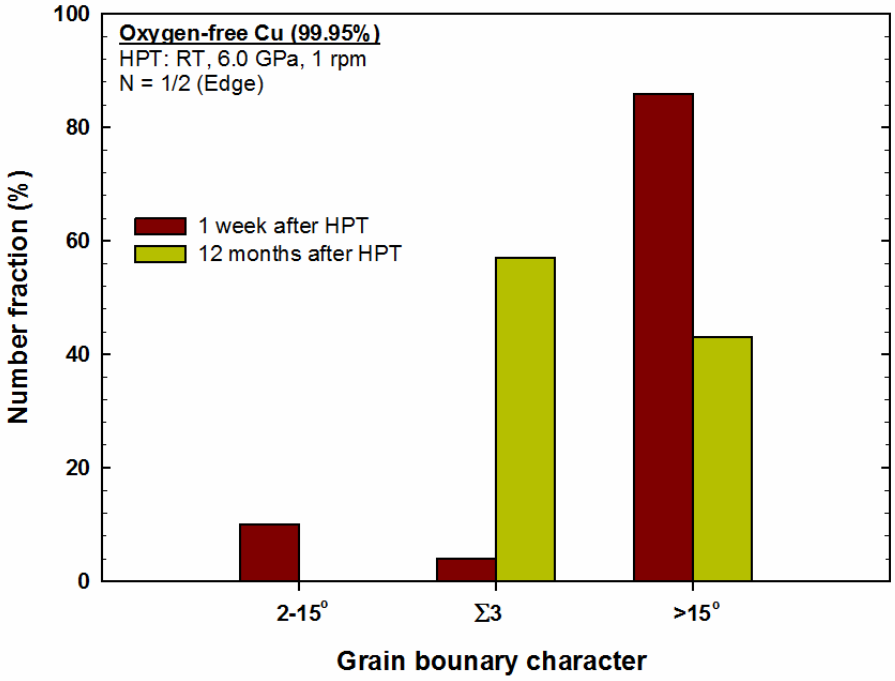
Oxygen-free Cu (99.95%)
HPT: RT, 6.0 GPa, 1 rpm
N = 1/2 (Edge)
1 week after HPT
12 months after HPT
Number fraction (%)
100
80
60
40
20
0
2-15°
Σ3
>15°
Grain bounary character

(b)

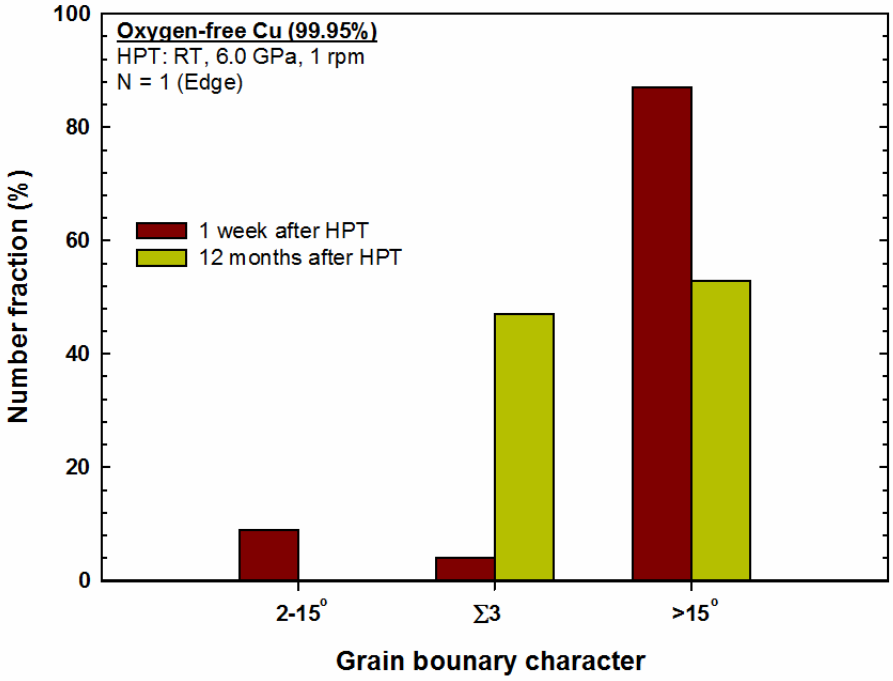
Oxygen-free Cu (99.95%)
HPT: RT, 6.0 GPa, 1 rpm
N = 1 (Edge)
1 week after HPT
12 months after HPT
Number fraction (%)
100
80
60
40
20
0
2-15°
Σ3
>15°
Grain bounary character

(c)

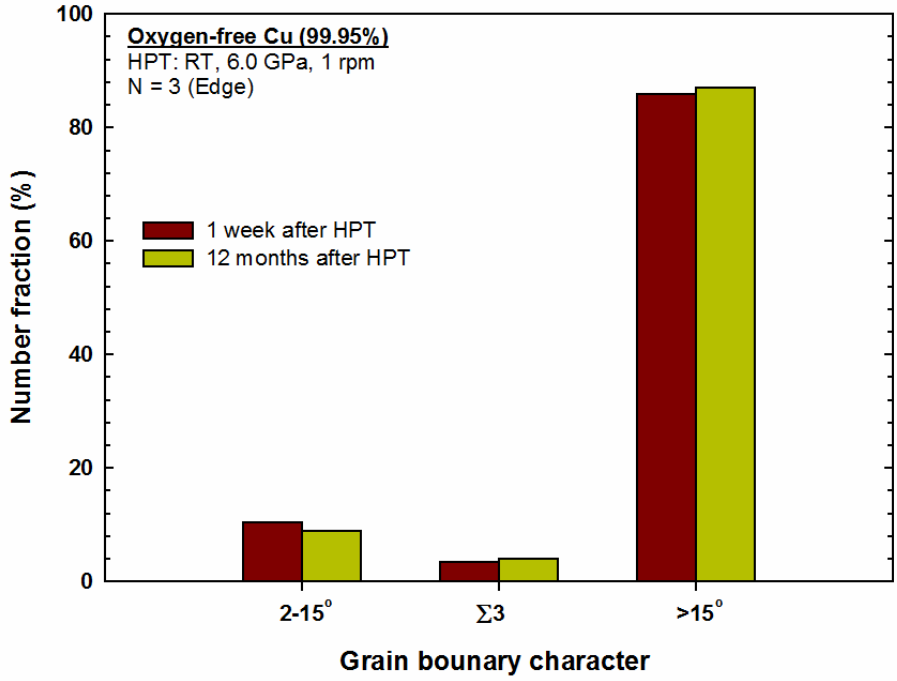
Oxygen-free Cu (99.95%)
HPT: RT, 6.0 GPa, 1 rpm
N = 3 (Edge)
1 week after HPT
12 months after HPT
Number fraction (%)
100
80
60
40
20
0
2-15°
Σ3
>15°
Grain bounary character

(d)

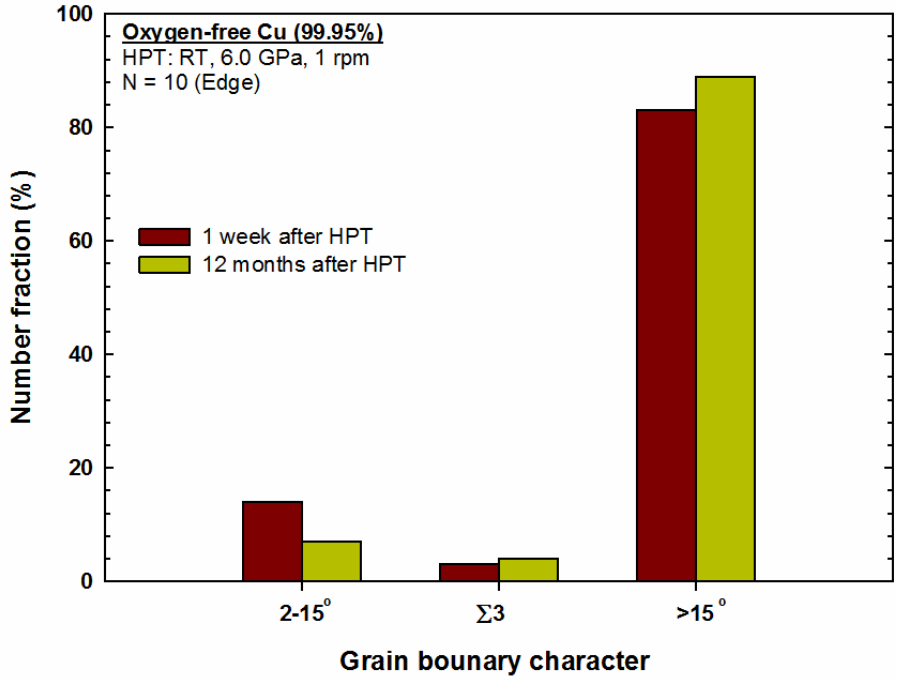
Oxygen-free Cu (99.95%)
HPT: RT, 6.0 GPa, 1 rpm
N = 10 (Edge)
1 week after HPT
12 months after HPT
Number fraction (%)
100
80
60
40
20
0
2-15°
Σ3
>15°
Grain bounary character

(e)

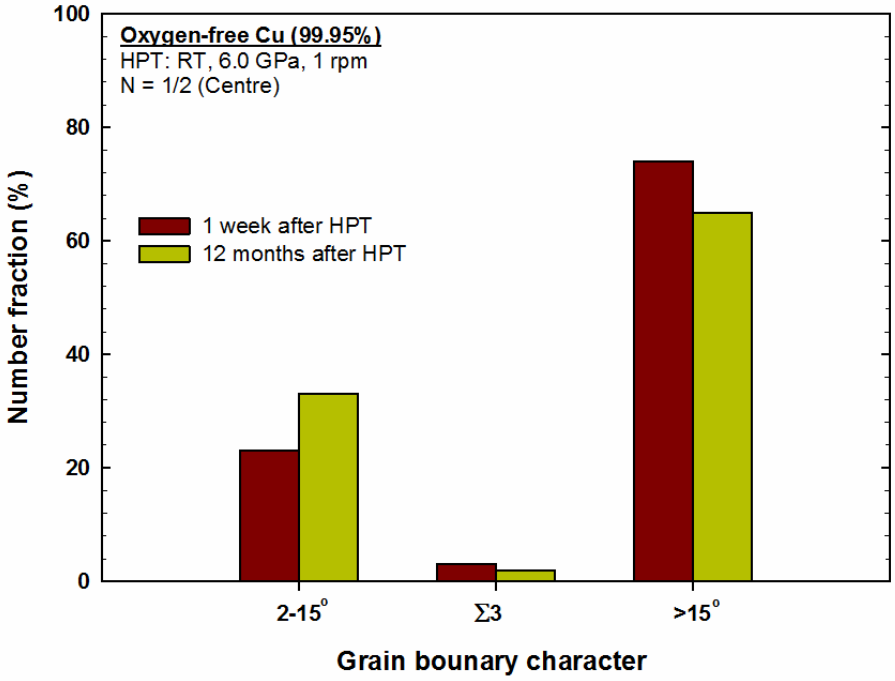
Oxygen-free Cu (99.95%)
HPT: RT, 6.0 GPa, 1 rpm
N = 1/2 (Centre)
1 week after HPT
12 months after HPT
Number fraction (%)
100
80
60
40
20
0
2-15°
Σ3
>15°
Grain bounary character

(f)

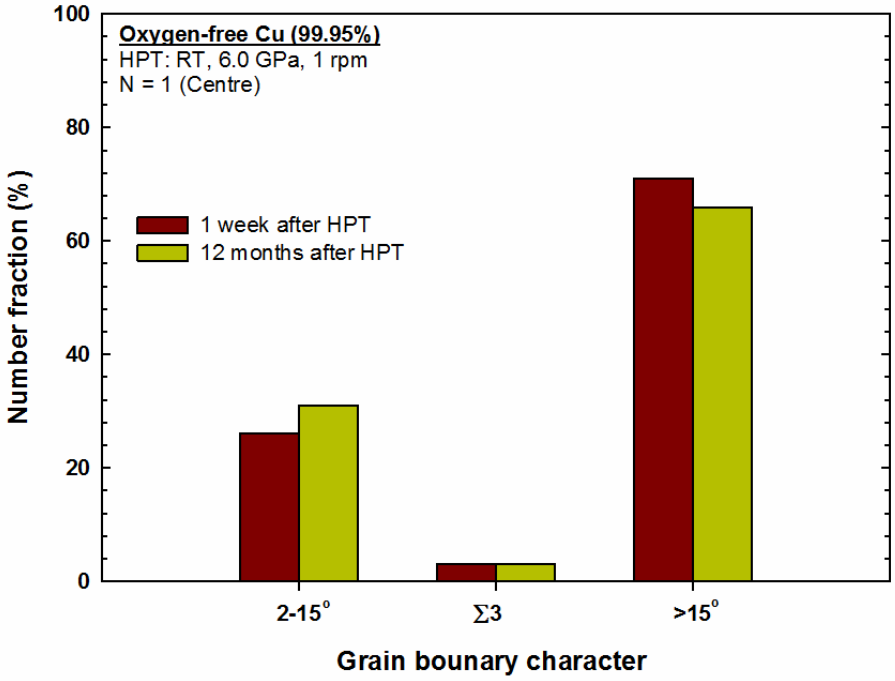
Oxygen-free Cu (99.95%)
HPT: RT, 6.0 GPa, 1 rpm
N = 1 (Centre)
1 week after HPT
12 months after HPT
Number fraction (%)
100
80
60
40
20
0
2-15°
Σ3
>15°
Grain bounary character

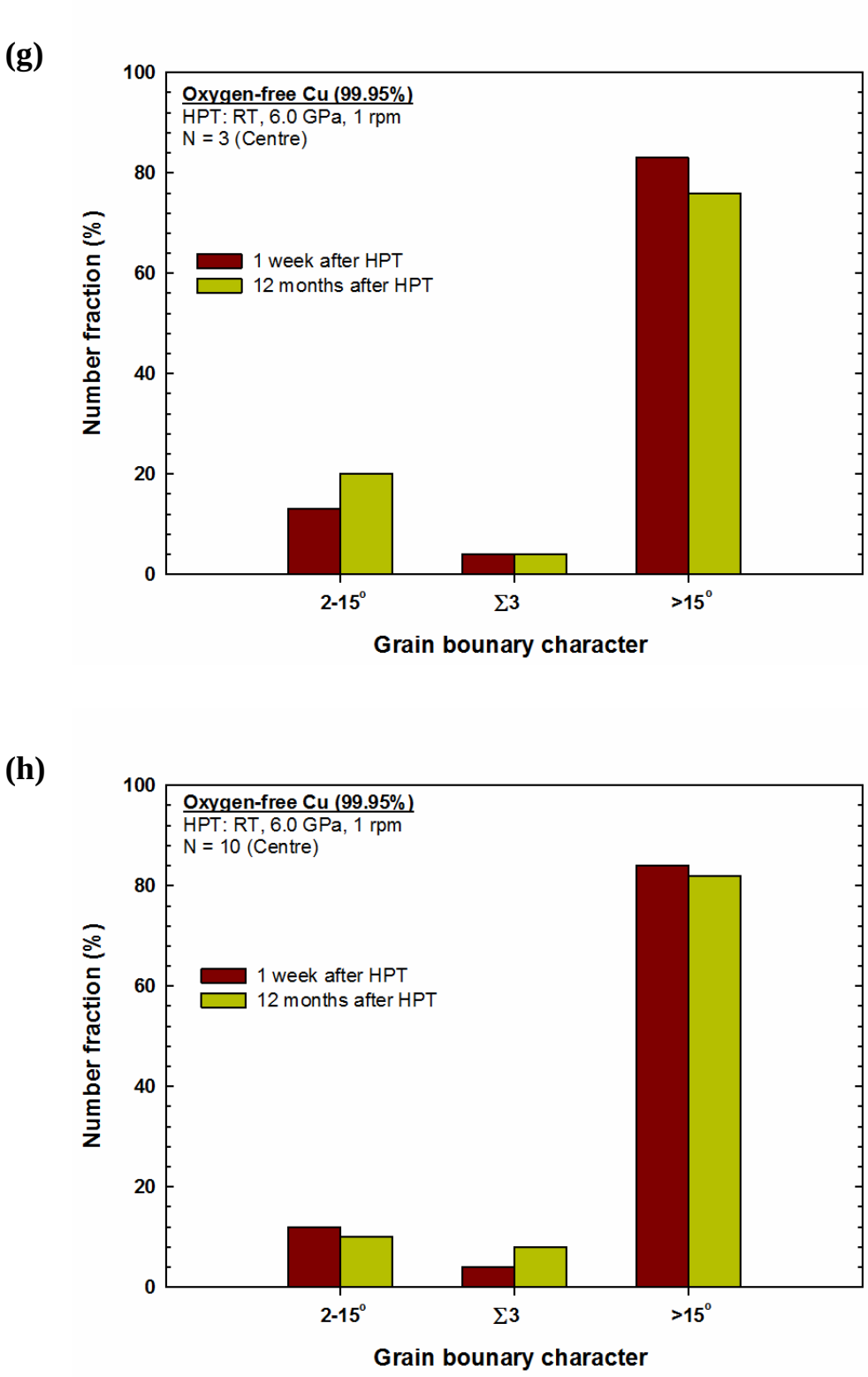

Figure 7.15 The fractional numbers of different grain boundary characters for oxygen-free Cu discs measured within 1 week after HPT processing and subsequent storage at RT for 12 months for a) N = 1/2 (Edge), b) N = 1 (Edge), c) N = 3 (Edge), d) N = 10 (Edge), e) N = 1/2 (Centre), f) N = 1 (Centre), g) N = 3 (Centre) and h) N = 10 (Centre).

7.1.3 X-ray diffraction analysis

XRD tests were conducted on the oxygen-free Cu discs, 1 week and 12 months after HPT processing. The results were analysed using Maud (XRD line profile analysis software). The microstrains for each condition are compared in Figure 7.16. It is readily apparent that the microstrains measured after 12 months follow the same trend as the microstrains measured after 1 week; however, lower values are observed after 12 months storage at RT. For both plots there is a clear increase in microstrain with increasing number of HPT turns from 0 to 1/2 turn. This is followed by a substantial decrease after 1 turn. The microstrain further decreased with the increase in HPT rotations by 3 and 10 turns.

The calculated dislocation density as a function of number of turns are shown in Figure 7.17. In the plot showing the dislocation density calculated after 1 week from HPT processing, there is a clear increase in the dislocation density with increasing number of HPT turns from 0 to 1/2 turn. This is followed by a significant decrease at 1 turn. The dislocation density further decreased with the increase in HPT turns, by 3 and 10. The drop in dislocation density that occurs from 1 to 10 turns suggests that dynamic recovery occurred during HPT processing.

The dislocation density results after 12 months storage at RT show the same trend as the results obtained 1 week after HPT processing. A comparison of the two plots shows that there was a drop in the dislocation density values for all samples, no matter how many HPT turns, after 12 months storage at RT. After 1/2 turn, there was a small drop in the dislocation density from ~5.6×10^{13} m^{-2} to ~5.3×10^{13} m^{-2} while a more significant drop occurred after 1 turn from ~2.6×10^{13} m^{-2} to ~1.3×10^{13} m^{-2}, for 3 turns, the dislocation density dropped from a value of ~9.7×10^{12} m^{-2} to ~2.5×10^{12} m^{-2} and for 10 turns the value after 1 week, ~5.3×10^{12} m^{-2} had decreased to ~1.2×10^{12} m^{-2} after 12 months storage.

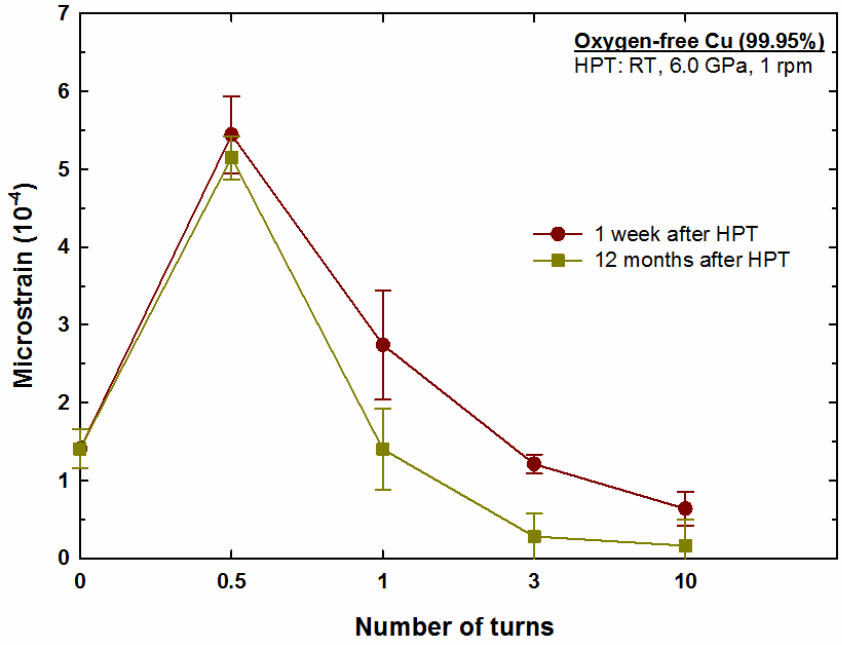

Figure 7.16 Microstrain as a function of number of turns for oxygen-free copper stored at room temperature for 1 week and 12 months after HPT processing.

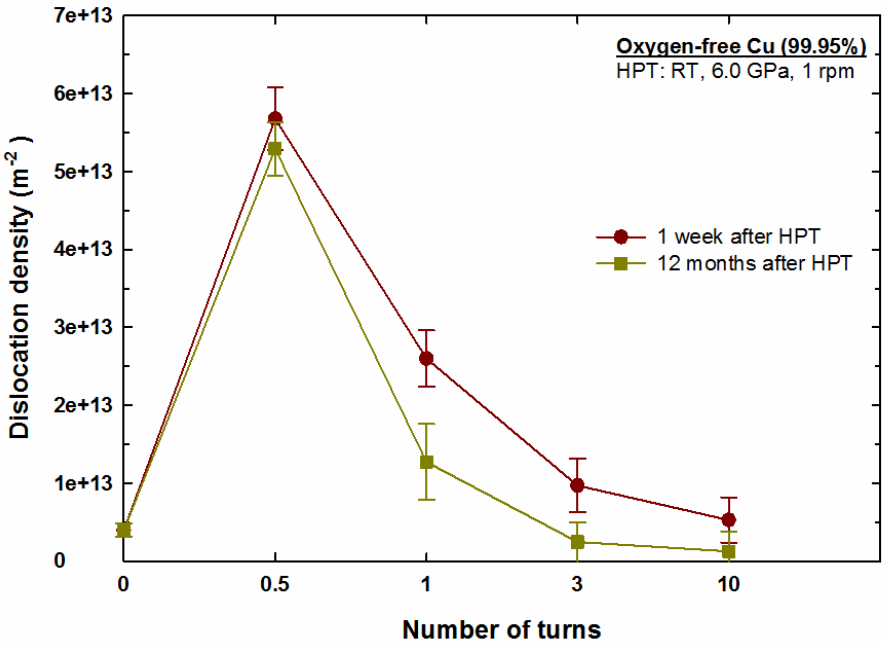

Figure 7.17 The calculated dislocation density as a function of number of turns for oxygen-free copper stored at room temperature for 1 week and 12 months after HPT processing.

7.3.4 Tensile Properties

Tensile tests were conducted on the oxygen-free copper samples, 1 week and 12 months after HPT processing. Figure 7.18 shows the engineering stress – elongation to failure curves for oxygen-free copper samples that were pulled in tension at a strain rate of 1.0×10^{-2} s^{-1} for different numbers of turns: (a) 1/2, (b) 1, (c) 3, (d) 10. Inspection of the curves presented in Figure 7.18(a-d) reveals that oxygen-free copper samples stored for 12 months exhibit lower mechanical strength but higher ductility in comparison with the samples stored for 1 week.

It is also evident that the strength observed during tensile testing is significantly reduced for the sample processed by 1/2 turn then stored for 12 months after HPT as shown in Figure 7.18(a). The yield stress was reduced from 530 MPa to 360 MPa as shown in Table 7.2. On the other hand, a minor decrease in the yield stress was observed after 12 months storage for the samples processed by 1, 3 and 10 turns, as shown in Figure 7.18(b-d). A similar trend was observed in the ultimate tensile stress as shown in Table 7.2. Comparing the values obtained 1 week and 12 months after HPT as shown in Table 7.2, it is apparent that the percentage increase in the uniform elongation and elongation to failure is the highest in the sample processed by 1/2 turn, and decreased with increasing numbers of turns.

From Figure 7.18(a), (b), (c) and (d), it is readily apparent that after storage of 12 months samples processed by a lower numbers of turns (N = 1/2 and 1) exhibit slightly a higher elongation to failure in comparison to the samples processed by 3 and 10 turns. Elongation to failure was 71% and 73 % for N = 1/2 and N = 1, respectively, where as 68% and 67% were recorded for N = 3 and N = 10, respectively as shown in Table 7.2. Additionally, the samples stored for 12 months show highest uniform elongation after 1/2 turn and reduced with further turns.

(a)

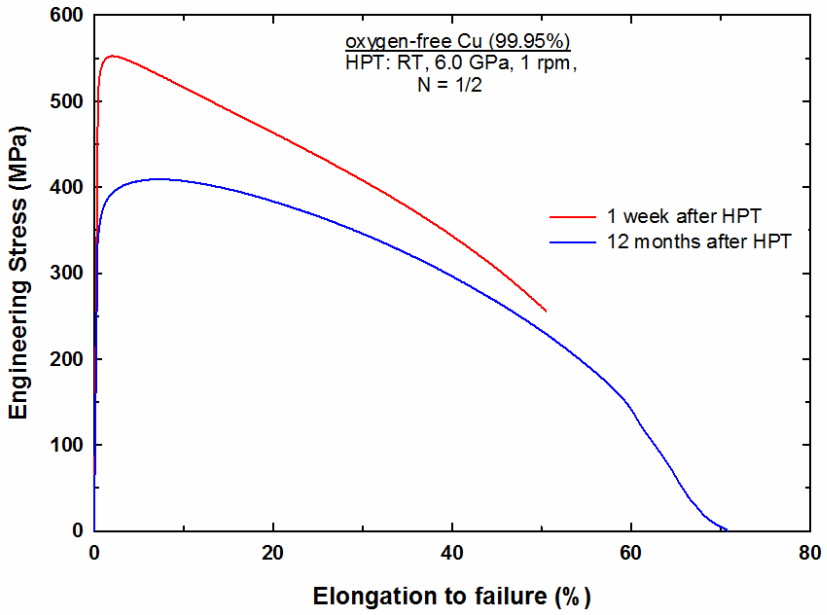
oxygen-free Cu (99.95%)
HPT: RT, 6.0 GPa, 1 rpm,
N = 1/2
1 week after HPT
12 months after HPT
Engineering Stress (MPa)
Elongation to failure (%)
0
100
200
300
400
500
600
0
20
40
60
80

(b)

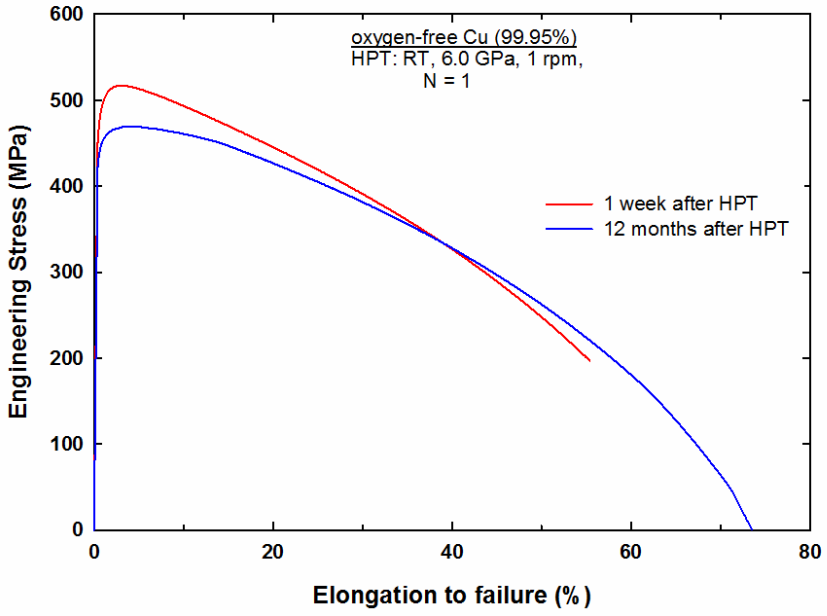
oxygen-free Cu (99.95%)
HPT: RT, 6.0 GPa, 1 rpm,
N = 1
1 week after HPT
12 months after HPT
Engineering Stress (MPa)
Elongation to failure (%)
0
100
200
300
400
500
600
0
20
40
60
80

(c)

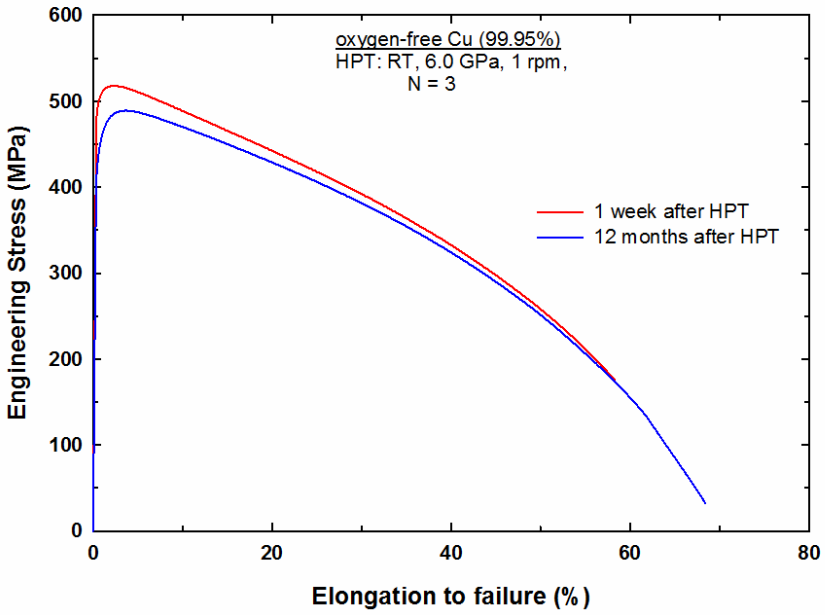

(d)

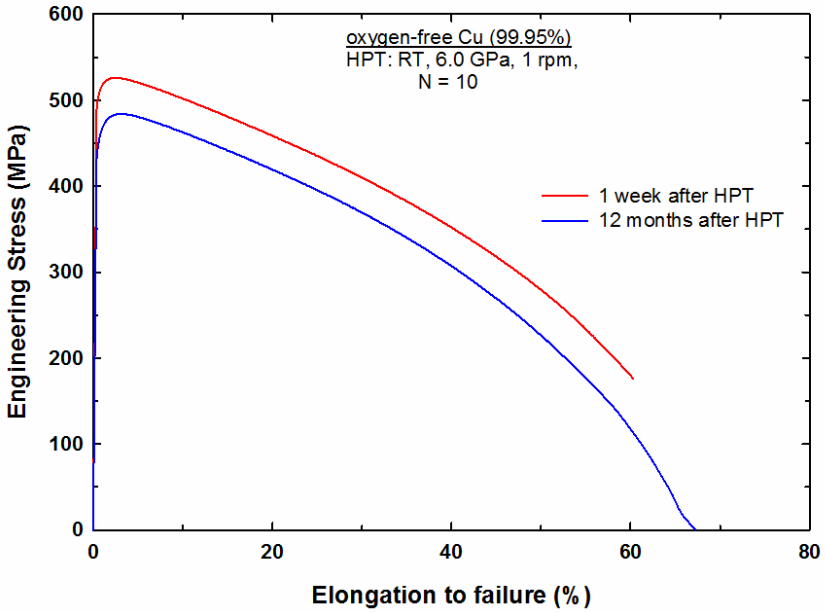

Figure 7.18 Engineering stress – elongation to failure curves for oxygen-free copper samples pulled in tension at a strain rate of 1.0×10^{-2} s^{-1} after 1 week and 12 months storage at RT after HPT processing for a) N = 1/2 , b) N = 1, c) N = 3, d) N = 10.

The data relating to the yield stress, ultimate tensile stress, uniform elongation and elongation to failure are summarized in Table 7.2.

Table 7.2 Values of yield stress (YS), ultimate tensile stress (UTS), uniform elongation (UEL) and elongation to failure (EL) of oxygen-free copper specimens subjected to various numbers of HPT turns when pulled in tension using strain of 1.0×10^{-2} s^{-1}, after 1 week and 12 months storage at RT after HPT.

No. of turns	Storage duration after HPT	YS (MPa)	UTS (MPa)	UEL (%)	EL (%)
1/2	1 week	530	552	2.3	50
	12 months	360	409	7.5	71
1	1 week	472	516	3.1	55
	12 months	443	469	4.5	73
3	1 week	496	517	2.5	58
	12 months	432	489	3.6	68
10	1 week	491	525	3.0	60
	12 months	450	484	3.3	67

7.4 Discussion

The first study that investigated the occurrence of self-annealing in pure copper (99.99%) subjected to HPT for 5 turns at 6.0 GPa, demonstrated there was no drop in hardness (self-annealing was not observed) after 70 days storage at RT [278]. Another study on pure Cu processed by HPT for 1 turn and stored at RT for 96 hours showed no major change in hardness; however, there was a minor drop in microstrain measured by XRD [279]. Edalati *et al*. investigated long-term self-annealing using Cu (99.99%) that was processed using HPT for 10 turns at 6.0 GPa, then stored at RT for 4 years and three months [280]. The results showed that there was a minor drop in hardness value of ~22 Hv.

These studies were generally limited to only high integer numbers of turns and the effect of self-annealing was usually by the microhardness test. They did not report any strong evidence of the occurrence of self-annealing during storage at RT after HPT processing. More recently, a study on high purity OFHC Cu (99.99+wt%) processed by HPT for 1/2, 1, 5 and 10 turns at 6.0 GPa showed a significant drop in hardness values at the edges of the disc processed by 1/2 turn after storage at RT for up to 6 weeks. The self-annealing effect was not detected after 5 and 10 turns [150]. It is concluded that these studies did not provide long-term self-annealing of pure copper (99.99%) subjected to HPT.

7.4.1 Instantaneous softening during HPT processing

It is observed from the microhardness measurements recorded across the diameters of the Cu discs, within 1 week after HPT processing, that the peripheral areas of the discs processed by 3, 5 and 10 turns exhibit lower hardness values than those processed by a lower number of turns. This indicates that dynamic recovery occurred during the HPT process. Several models have been developed to detect the nature of the recovery in the materials based on the variation of microhardness with the equivalent strain [42,53,148]. These models are illustrated in Figure 2.20. The variation of microhardness recorded in this study with respect to the equivalent strain is shown in Figure 5.28(a). Figure 7.19 is a schematic of Figure 5.28(a) that was drawn to highlight the transition from hardening to softening of oxygen-free copper during HPT. It is readily apparent that there is an abrupt increase in hardness in the initial stage of straining, followed by a drop in hardness at an equivalent strain of ~12 and then the hardness reaches a steady value of ~130 Hv at equivalent strain larger than ~50. These results exactly match those observed in an earlier study on OFHC Cu (99.99+ wt.%) [150]. Another study on high purity Cu (99.99 wt.%) shows that the hardness saturates at a value of ~130 Hv at an equivalent strain of ~15 [215] whereas another study on OFHC Cu (99.99+ wt.%) reveals a saturation hardness value of ~150 Hv at an equivalent strain of ~22 [149]. A later study of pure Cu (99.99 %) shows that hardness saturates at a ~142 Hv at an equivalent strain of ~80 [208].

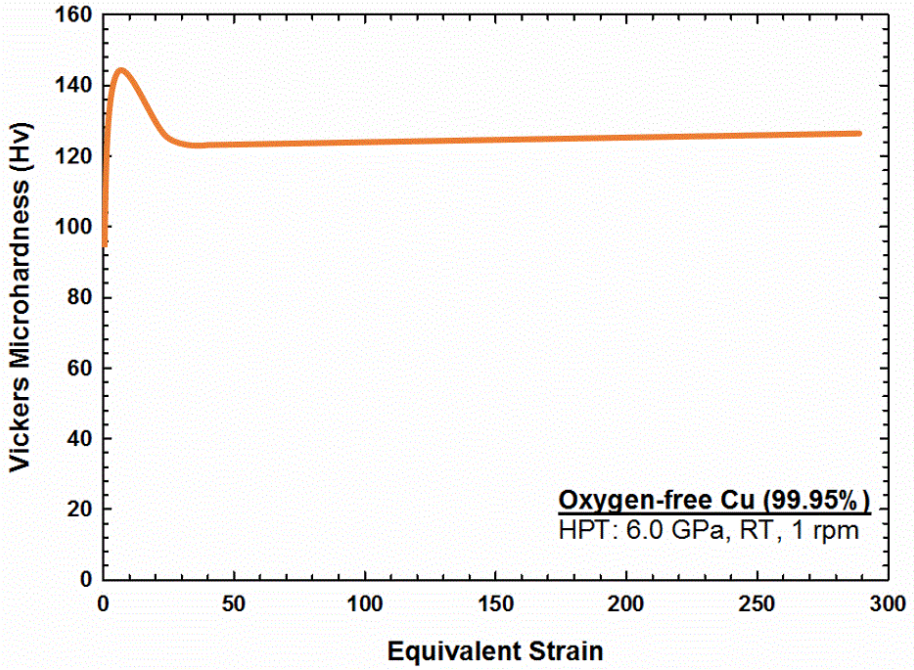

Figure 7.19 Vickers microhardness values with respect to equivalent strain for oxygen-free Cu processed by HPT at RT.

Softening with rapid recovery has been reported in high SFE materials such as high-purity Aluminum [38,44,146,209–213], and it has also been observed in pure Mg [228] and pure Zn [212]. However, it has been well documented that pure Cu saturates at large strains without recovery [34,37,46,182,204,213,215,216,225,281,282]. Recovery occurs easily in high-purity Al due to the narrow separation between the partial dislocations in high SFE materials which makes the cross-slip easier. On the other hand, pure copper is a low to medium SFE material that makes the cross-slip more difficult due to the wide separation between the partial dislocations. Thus, what is surprising in the present study is that softening with rapid recovery occurred in oxygen-free Cu (99.95 wt.%) during HPT processing. Similar findings were observed in earlier studies on OFHC Cu (99.99 +wt.%) processed by HPT at RT [149,150] and OFHC Cu processed by repetitive upsetting-extrusion (RUE) at RT [283]. These findings suggest that the nature of recovery in oxygen-free copper might be different from other pure copper materials regardless of their purity.

The direct correlation between the Vickers microhardness values and the equivalent strain shown in Figure 7.19 suggests hardness softening during the process which indicates the occurrence of recovery. Furthermore, the decrease in microstrain and

dislocation density values obtained by X-ray line profile analysis shown in Figure 7.16 and Figure 7.17 respectively, provide evidence that dynamic recovery occurred during HPT processing. In addition, Figure 5.17 illustrates that the crystallite size is ~176 nm after 10 turns which is larger than a crystallite size of ~132 nm after 1/2 turn. It is suggested from these figures that recovery has taken place after 1 turn and become more pronounced at higher numbers of turns. These results are in line with the previous study on OFHC Cu (99.99+ wt.%) [150].

One reason that can trigger the recovery is the temperature rise during the HPT process. This is well documented by finite element modelling [135]. The results from this modelling shows that the temperature rise is due to the heat generated during the plastic deforming of the sample, and due to the friction occurred when the material flows between the anvils during the rotation. Thus, it is important to investigate the influence of the temperature rise on the occurrence of recovery in the present study. The variation of temperature (ΔT) with time (t) is calculated by [284]:

$$\Delta T = 0.22\sigma\omega\left[1 + 1.28\left(1 - e^{-(t/482)}\right)\right] \quad (8.1)$$

where σ is the flow stress, ω is the rotation rate and t is the time.

The calculated temperature rise during each rotation is shown in Table 7.3. The results show that the temperature of oxygen-free Cu disc increased rapidly after 1/4 turn then the increase becomes slower with further turns. This is consistent with the earlier results obtained from finite element modelling that shows a rapid increase in the temperature at the initial stages of deformation followed by a slower rise [135]. The calculated temperature rise after 10 turns is ~ 57 C°. This value is different from a previous study on pure Cu that claimed a temperature rise of ~40 C° after 10 turns using the same experimental conditions [227].

A careful inspection of the microhardness results across the diameters of the HPT discs obtained in the present study and the results obtained in earlier studies in OFHC Cu shows two different trends in the initial stages of deformation (N = 1/4, 1/2 and 1). The first trend is low hardness value in the central region of the disc and high values at the edges [150]. This trend is also observed in the present study.

Table 7.3 The calculated temperature rise for different numbers of turns during HPT processing of Oxygen-free Cu.

NUMBER OF TURNS (N)	TEMP. RISE (K)
1/4	309
1/2	311
1	311
3	317
5	322
10	330

The second trend observed by Almazrouee *et al*. shows a low hardness value at the central region of the disc and a significant drop in hardness at the edges, with this drop in hardness moving towards the centre with increasing strain [149]. Reasonable hardness homogeneity is achieved after 10 turns in both cases. Studies, including the present study, have shown that both trends occur during HPT processing of oxygen-free Cu.

A close inspection of the study conducted on OFHC Cu (99.99+ wt%) shows the first trend was observed when the microhardness test was conducted 24 hours after HPT processing. The second trend appeared after 6 weeks of storage at RT and is due to the self-annealing effect [150]. This is consistent with the present study of oxygen-free Cu (99.95 wt.%); the first trend appeared during HPT processing and transformed into the second trend after 12 months storage at RT. Thus, it is believed that the second trend observed by Almazrouee *et al*. also conducted on OFHC Cu (99.99+ wt%) occurred several weeks after the HPT processing not during the process [149]. This conclusion is drawn because the study did not mention the storage time between the HPT processing and microhardness testing. However, the significance of self-annealing has been studied more recently on exactly the same material but with storage time systematically recorded [150].

It has been well established in the present study that dynamic recovery occurred at large strain during the HPT process. Also, it appears from the OIM image shown in Figure 7.9 that there are dislocation free grains which indicates that recrystallization might occur during or after the HPT process. An earlier report has confirmed that softening of pure Cu due to static recrystallization took place after the HPT process [215], whereas dynamic recrystallization has been reported in other studies [285,286]. In addition, several studies have reported the occurrence of dynamic recrystallization in pure Cu in the early stages of deformation [52,149,208]. To verify the validity of this phenomena, it is crucial to record the storage duration between the time of processing occurred and the time of mechanical testing and microstructure characterization.

7.4.2 The occurrence of self-annealing after 12 months storage at RT

Figure 7.1(a) to (f) show the microhardness values recorded across the diameters of the copper discs 1 week and 12 months after HPT processing. It is well documented in Figure 5.18 that specimens processed by a low number of turns (N = 1/4, 1/2 and 1) display a V-shaped plot due to the variations of the imposed strain across the disc, whereas the specimens processed by high number of turns (N = 3, 5 and 10) display relatively uniform hardness distributions across the diameters of the discs. The present results reveal that self-annealing took place in oxygen-free copper after 12 months storage at RT. The self-annealing effect is most significant in the specimens processed by a small number of turns (1/4, 1/2 and 1 turn) and was reduced at higher numbers of turns. Results, therefore, need to be interpreted with caution.

It is readily apparent from microhardness measurements across the diameters of the discs shown in Figure 7.1(a), (b) and (c) that the hardness values drop drastically at the periphery. Figure 7.3 provides evidence of abnormal grain growth after 12 months of storage at RT, in the specimen processed by 1/2 turn. It can be seen that there is a mixture of large and ultrafine grains. It is apparent that these large grains are free of dislocations as indicated by the arrows in Figure 7.3. This abnormal grain growth is associated with a significant increase in the fraction of Σ3 boundaries as shown in Figure 7.15(a), indicating the recrystallization during the time of storage. These results appear to be consistent with other research which found an abnormal grain growth containing large fraction of Σ3

boundaries mixed with ultrafine grains after 6 weeks of storage at RT of OFHC Cu that was processed by HPT for 1/2 turn [150]. Several studies have reported the occurrence of recrystallization and increase in the fraction of Σ3 boundaries in Cu due to adiabatic heating during the HPT process [52,149]. The fractions of LAGBs increased at the expense of HAGBs in the central region of the disc indicating the occurrence of recovery after 12 months storage at RT.

The difference in the softening mechanisms between the centre and the edge is due to the difference in the internal stored energy between the two positions as a result of the variation of the strain imposed during the initial stages of HPT processing. A higher energy is stored at the edges of the disc in the form of additional dislocations which provide a driving force for recrystallization. It is well documented that recrystallization can occur in metals having heterogeneous microstructures as a result of a high strain energy gradient [287,288]. Another contribution to the driving force for recrystallization is the grain boundary energy. The edges have smaller grain sizes, a higher fraction of HAGBs and a higher fraction of Σ3 twin boundaries compared to the centre of the disc. Thus, it is to be expected that recrystallization is more pronounced at the peripheries. This is supported by a report that shows for pure copper recrystallization starts at positions with HAGBs during annealing at 160 °C. Similar results are observed in the specimen processed by 1 turn, but to a smaller extent. Large dislocation free grains were also observed at the edge of the disc as shown in Figure 7.5 and the fraction of Σ3 twin boundaries is high for HPT 1 turn or less as seen in Figure 7.15(a & b).

It is apparent from inspection of Figure 7.1(d) to (f) that a small decrease in hardness occurs, right across the discs, after 12 months storage at RT for those discs processed by 3, 5 and 10 turns. The decrease in hardness is relatively uniform across the diameters of the discs. This finding is contrary to the previous study by Huang *et al*. which showed no drop in hardness for OFHC Cu discs processed by 5 and 10 turns then stored for up to 6 weeks at RT [150]. The change in the fractions of HAGBs and Σ3 twin boundaries is insignificant during the storage time as shown in Figure 7.15(c) and (d), whereas the microstrain and dislocation densities are reduced as seen in Figure 7.16 and Figure 7.17, respectively. These results suggest that recovery took place after 12 months of storage at RT in those specimens processed through a high number of turns.

The most interesting finding is that the occurrence of self-annealing is significant at the edges of the discs processed by a low number of turns but is minor for those discs processed by a large number of turns. This is due to the dynamic recovery which took place during the HPT process at the edges of the discs at large numbers of turns, which reduces the dislocation density and thus reduces the driving force for recrystallization. It is readily apparent that recrystallization occurs at positions which experience slow or no recovery.

Recovery reduces the internal stresses and dislocation density by the rearrangement of dislocations and as a result the driving force for recrystallization is diminished [289]. This conclusion is supported by the calculation of dislocation density from X-ray data using Equation (3.1). It is found that there is a high dislocation density after processing by 1/2 turn and a low dislocation density after 10 turns, see Figure 7.17.

Microhardness, EBSD and XRD tests provide clear evidence that the occurrence of self-annealing is due to recovery and recrystallization. Recovery is a process in which cross-slip eradicates screw dislocations and climb annihilates edge dislocations. It is well documented that recovery is associated with the SFE of the material which control the degree of the dislocation dissociation. Cross-slip occurs easily in high SFE materials due to the small splitting distance between the partial dislocations. The waiting time for cross-slip was calculated in an earlier study for FCC metals and the results show that recovery occurs easily in UFG Cu that has an intermediate SFE [290].

Both the SFE of Cu, and the nature of the HPT process affect the cross-slip and, consequently, the recovery process. During the HPT process, internal stresses are created by additional dislocations with differences in their magnitudes across the disc and, therefore, different activation energy for cross-slip. It is possible that the internal stresses in the centre of the disc pin the cross-slip and delay the recovery in which the dislocations are annihilated, after a long time of storage at RT. The waiting time for dislocation annihilation is different between the centres and edges of the discs as well as between low and high numbers of turns.

Climb is less affected by the increase of the degree of dislocation dissociation than cross-slip [291]. The velocity of cross-slip is higher than climb at room temperature in FCC metals such as pure copper [292]. Furthermore, it is well established that climb is a

diffusion-controlled mechanism is highly influenced by temperature. The climb process is more pronounced at high temperatures and climb velocity is determined by the absolute melting temperature, T_m, which is proportional to the diffusion-activation energy.

Nevertheless, recovery might occurs at room temperature by climb due to the high concentration of deformation-induced vacancies produced during the SPD process [293]. The concentration of these vacancies varies across the disc and increases with increasing distance (strain) from the centre. Thus, high dislocation density and larger vacancy clusters are produced at the periphery compared with the centre [216]. In addition, HPT produces a high dislocation density in oxygen-free Cu and reduces the grain size, which increases the volume of grain boundaries and thus enhances grain boundary diffusion. Thus, climb might have an influence on the recovery mechanism after HPT, and high dislocation density is the driving force for self-annealing during the 12 months storage at RT.

A close inspection of an earlier study on OFHC Cu (99.99+%) [150] reveals that the self-annealing effect was observed after 6 weeks of storage whereas it occurred after 12 months in the present study. A possible explanation for this might be the impurity content in the copper. The occurrence of self-annealing becomes slower with decreasing purity because impurities hinder dislocation movement and supress the self-annealing [280].

In order to make an assessment of the influence of self-annealing on the mechanical properties of oxygen-free copper, the average microhardness values were recorded in a distance between ~1.5 mm to ~2.5 mm from the centre of the disc and these values are presented in Table 7.4. This distance corresponds to the position of the gauge length of the tensile specimen on the disc. It can be seen that reduction in hardness in the gauge area is in agreement with the decrease in strength shown in Table 7.2. It is apparent that softening is higher in the samples with low numbers of turns due to the higher amount of stored energy in comparison to the samples with higher numbers of turns. The occurrence of recovery and/or recrystallization increases the ability of strain hardening by dislocation annihilation and production of dislocation-free grains which lead to the enhancement of ductility after 12 months storage at RT after HPT.

Table 7.4 The average microhardness values recorded ~1.5 mm to ~2.5 mm from the centre of disc. This distance corresponds to the position of gauge length of the tensile specimen on the disc.

	Microhardness (Hv)			
No. of turns	**1/2**	**1**	**3**	**10**
1 week after HPT	~134	~135	~128	~129
12 months after HPT	~117	~112	~120	~120

7.5 Summary

1. The microstructural stability of UFG oxygen-free copper processed by HPT was investigated after storing the samples for 1 week and 12 months at room temperature.

2. A significant decrease in microhardness values was observed near the edge of the disc for the samples processed by low number of turns (N = 1/4, 1/2 and 1) after 12 months of storage at room temperature. However, the drop in hardness was not localized and was almost constant across the diameters of the discs for the samples processed through 3, 5 and 10 turns.

3. Microstructural investigation shows that self-annealing is related to recrystallization and grain growth at low number of turns samples where as it was related to recovery mechanism at higher number of turns samples.

4. The occurrence of self-annealing in the samples processed by lower number of turns is related to the higher stored energy in comparison with the samples processed by higher number of turns where the stored energy is lower due to the occurrence of the dynamic recovery during HPT that diminished the driving force for recrystallization.

5. The difference in the softening mechanisms between the centre and the edge in the discs processed by 1/4 and 1/2 turn is due to the difference in the internal stored energy between the two positions as a result of the variation of the strain imposed during the initial stages of HPT processing. A higher energy is stored at the edges of the disc in the form of additional dislocations which provide a driving force for recrystallization.

6. The strength and ductility were studied by the means of tensile test. The occurrence of recovery and/or recrystallization increases the ability of strain hardening by dislocation annihilation and producing dislocation-free grains which leads to a decrease in the strength and enhancement in ductility.

Chapter 8 Microstructural Stability and Deformation Mechanisms of UFG Oxygen-free Copper Deformed by a High Strain Rate Dynamic Test

8.1 Background

The mechanical properties of UFG materials produced by ECAP have been widely examined using quasi-static strain rates such as tensile [120,159,165,294–297] and compression tests [294,298]. However, these tests operate only over limited ranges of strain rates. Thus, several experiments were necessary to investigate the deformation mechanisms and mechanical properties of pure copper at high strain rates using dynamic tests [106–108,112,299,300]. Grain size, strain rate, and test temperature are three major factors affecting the microstructure and mechanical properties of copper. Earlier studies demonstrated that the flow stress of pure copper increased with increasing the strain rate at 298 K [103,112,301], or decreasing the temperature [112,302]. Strain rate sensitivity is temperature dependent during dynamic testing and increases with increase in temperature [301,302]. Also, it has been shown that, at high strain rates, UFG copper has a greater strain rate sensitivity than coarse-grained copper [301].

These studies focused on the influence of temperature, strain rate and their coupling effect on the deformation mechanisms and mechanical properties of pure copper during dynamic testing. However, there are no reports discussing the influence of the initial microstructural condition on the mechanical properties, nor on grain refinement mechanisms after dynamic testing. Recent studies have shown a direct relationship between the initial unprocessed condition of the material and the minimum grain size obtained after processing by HPT [303] and ECAP [304]. In this investigation, we will focus on the initial microstructural condition of copper produced after processing by ECAP, rather than coarse-grained copper

Oxygen-free copper billets having a purity of 99.95 wt% were processed by ECAP at room temperature through 1, 4 and 8 passes using route B_C. Then these billets

were further tested at high strain rates of 10 s^{-1} using a Gleeble 3500 system and at 5.5×10^3 s^{-1} with a split Hopkinson pressure bar (SHPB). The dynamic compression tests were performed at 298 K and 473 K. Although several reports have discussed the influence of strain rate and temperature on UFG copper using dynamic tests [103,112,301,302,305], relatively few have discussed the influence of the initial microstructure of the ECAP processed material on the results of the dynamic testing.

The primary aim of this chapter is to investigate the effect of the preliminary microstructural state of the oxygen-free copper produced by ECAP at room temperature on the microstructure and the mechanical properties attained after dynamic testing at a high strain rate. A second aim is to examine the influence of strain rate and temperature on the microstructure and mechanical properties of oxygen-free copper deformed by ECAP and further dynamic testing.

8.2 Results

8.2.1 True stress-true strain curves

All true stress vs true strain curves in this section were obtained during dynamic tests. The true stress vs true strain curves for oxygen-free copper specimens tested at strain rates of 10 s^{-1} using the Gleeble 3500 at temperatures of 298 K and 473 K and at a strain rate of 5.5×10^3 s^{-1} using the SHPB at the same temperatures are shown in Figure 8.1 and Figure 8.2, respectively. The samples tested at 298 K using a strain rate of 10 s^{-1} show true stresses of ~390 MPa, ~470 MPa and ~500 MPa for the samples processed by ECAP for 1, 4 and 8 passes, respectively, as shown in Figure 8.1(a). The other samples tested at 298 K using a strain rate of 5.5×10^3 s^{-1} shown in Figure 8.2(a) show higher true stresses of ~440 MPa, ~560 MPa and ~590 MPa for the samples processed by ECAP for 1, 4 and 8 passes, respectively.

Figure 8.1(b) and Figure 8.2(b) show that lower stresses are required to deform oxygen-free copper specimens processed by ECAP + dynamic testing at 473 K compared to the same specimens tested at 298 K shown in Figure 8.1(a) and Figure 8.2(a). For the curves obtained at 10 s^{-1}, see Figure 8.1(b), the true stresses are ~310 MPa, ~340 MPa and ~325 MPa for the samples processed by ECAP for 1, 4 and 8 passes, respectively, whereas for the curves obtained at 5.5×10^3 s^{-1} shown in Figure

8.2(b), the true stresses are ~465 MPa, ~490 MPa and ~505 MPa for the samples processed by ECAP for 1, 4 and 8 passes, respectively.

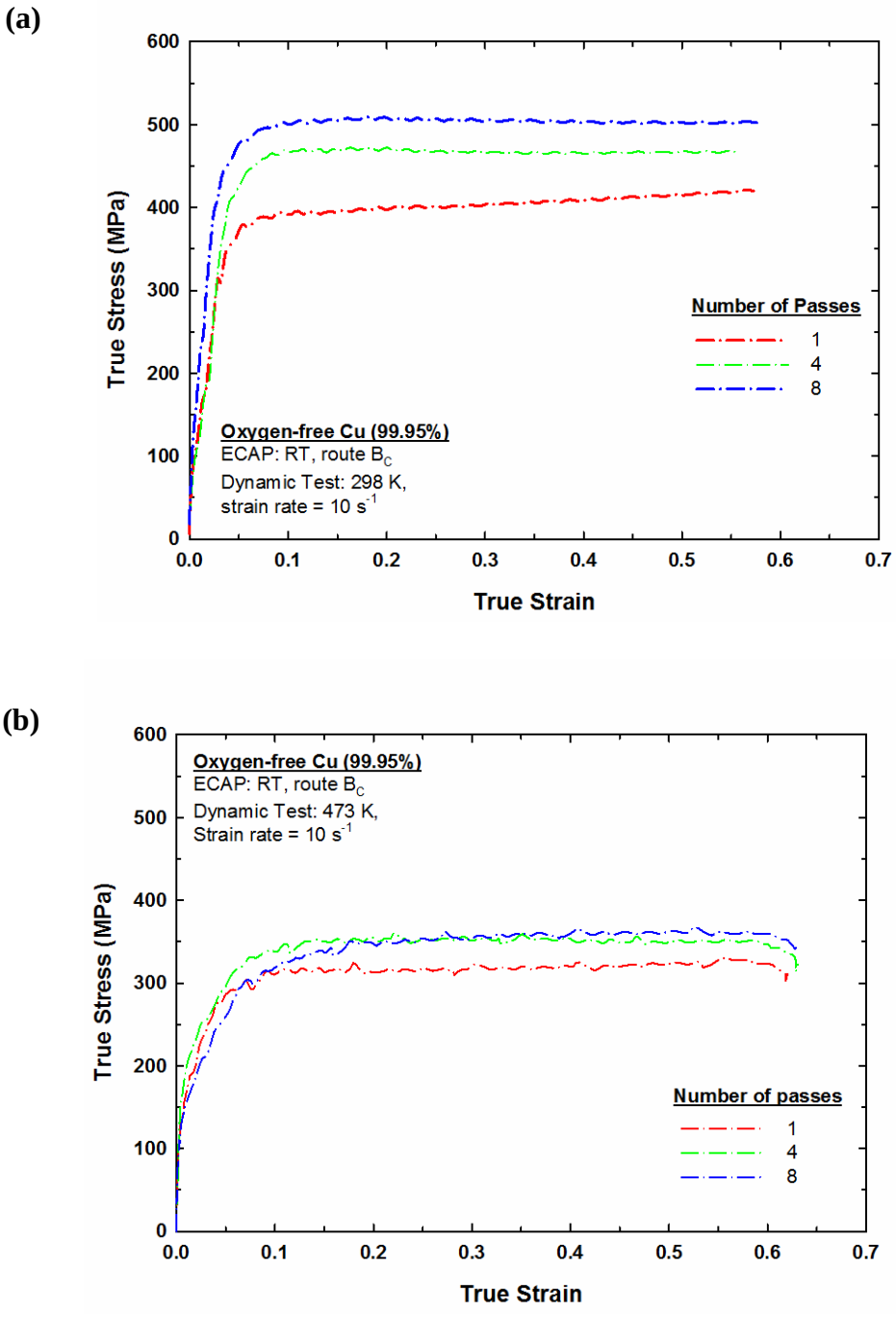

Figure 8.1 True stress vs true strain curves for oxygen-free copper specimens tested using SHPB at strain rate of 10 s^{-1} at (a) 298 K and (b) 473 K.

(a)

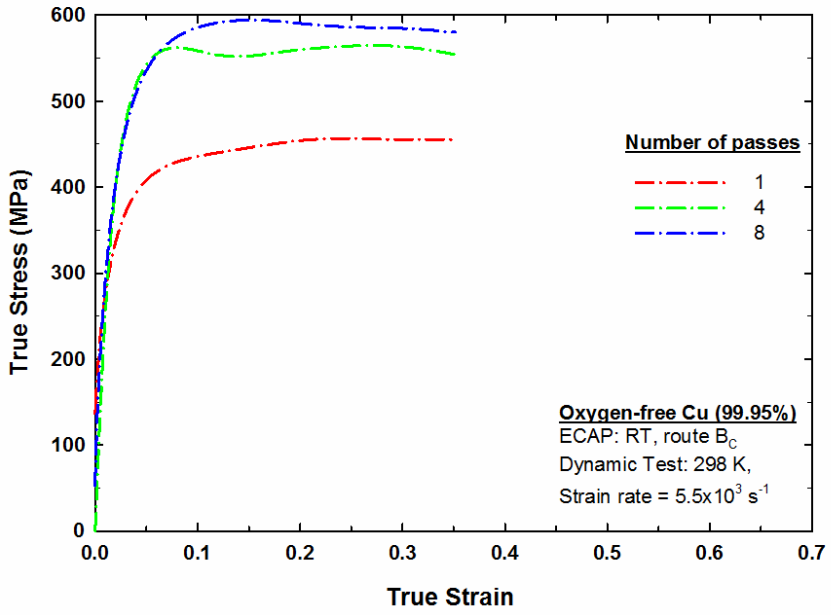

(b)

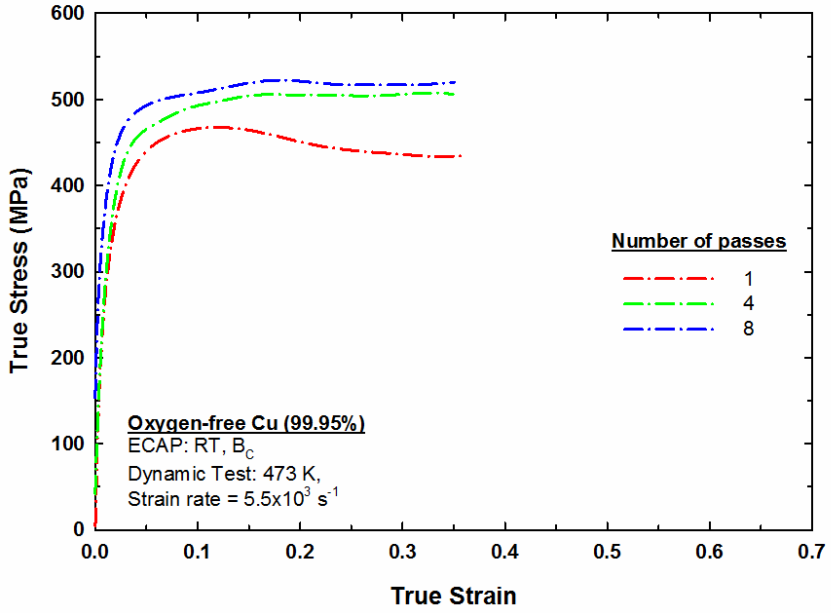

Figure 8.2 True stress vs true strain curves for oxygen-free copper specimens tested using SHPB at strain rate of 5.5×10^3 s^{-1} at (a) 298 K and (b) 473 K.

It is apparent from the dynamic compression test results that there was a general increase in the flow stress after initial yielding with increasing number of passes, regardless of the test temperature and strain rate. Also, the true stress decreased with increasing test temperature at a specific strain rate. It was also observed that the

true stresses increased with increasing the strain rate at a specific temperature. This is due to the increase in rate of dislocation multiplication and increase of dislocation density.

8.2.2 Microhardness measurements

Figure 8.3 displays Vickers microhardness values recorded after dynamic tests at strain rates of 10 s^{-1} and 5.5×10^3 s^{-1} for oxygen-free copper specimens processed by ECAP for 1, 4 and 8 passes. The figure shows that the hardness of the copper increased with increasing number of passes from 1 to 8 for specimens deformed at 298 K for both strain rates.

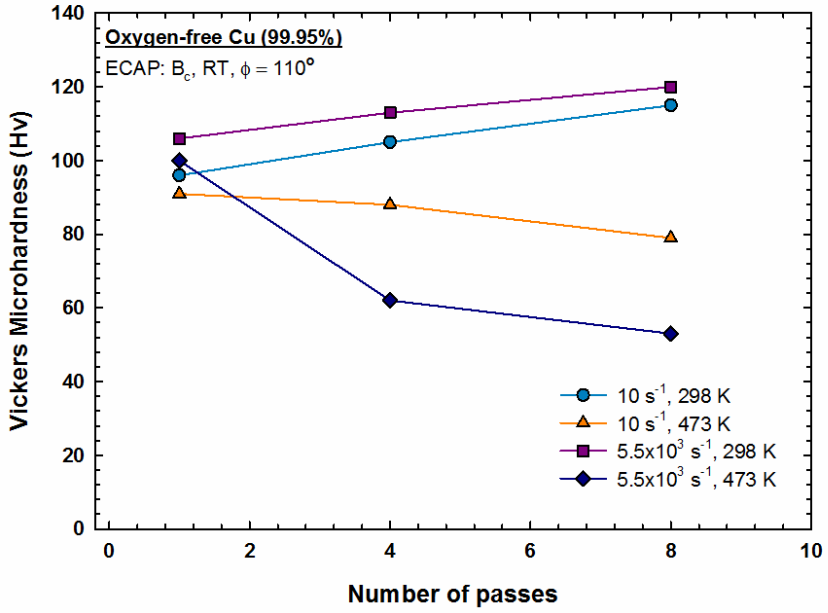

Figure 8.3 Vickers microhardness values recorded after dynamic tests at strain rates of 10 s^{-1} and 5.5×10^3 s^{-1} for oxygen-free copper specimens processed by ECAP for 1, 4 and 8 passes.

Contrary to expectations, Figure 8.3 shows the microhardness values decreased with increasing number of passes for specimens deformed at 473 K for both strain rates. This is inconsistent with the corresponding true stress-true strain curves obtained during the dynamic tests. Overall there was a very noticeable decrease in hardness from ~100 Hv to ~53 Hv in specimens deformed at a strain rate of 5.5×10^3

s^{-1} which is the opposite to the trend found during the dynamic tests and seen in the true stress-true strain curves shown in Figure 8.2(b). The microhardness results indicate that softening has taken place after dynamic testing, between the time of testing and the time of measuring the hardness for the samples tested at 473 K.

8.2.3 EBSD measurements

8.2.3.1 Microstructure after ECAP

The microstructural evolution of oxygen-free copper processed by ECAP for a) 1, b) 4 and c) 8 passes at 298 K is shown as OIM images in Figure 8.4. Inspection of Figure 8.4(a) shows that the microstructure after 1 pass of ECAP has large and elongated grains and the average size is significantly reduced from ~24 μm for the annealed condition to ~16 μm after 1 ECAP pass. The grains appear to be aligned in the same direction and have almost the same orientation, see the triangular legend located alongside the OIM images. As the imposed strain increased from 4 to 8 passes, the microstructure evolved into smaller grains resulting in an average grain size of ~4.4 μm and ~2.9 μm as shown in Figure 8.4(b) and Figure 8.4(c), respectively. The microstructure after 8 passes is composed of small and large grains that are randomly oriented, some of which are elongated. These results are consistent with previous results that 4 and 8 passes were not sufficient to create a homogeneous microstructure [164].

Figure 8.5 presents histograms of the distribution of misorientation angles for the specimens processed by ECAP. After just 1 pass, as shown in Figure 8.5(a), the fraction of low-angle grain boundaries which dictates the formation of dislocation cells is very high (75%). The percentage of high-angle grain boundaries increased to ~66% and ~71% after 4 and 8 passes respectively, as displayed in Figure 8.5(b) and Figure 8.5(c). This is higher than ~43% of high-angle grain boundaries achieved when pure copper was processed by ECAP for 8 passes through a die with an internal angle of 90° [164]. It is readily apparent that 8 passes are not sufficient to produce equiaxed ultrafine grains with a high proportion of high-angle grain boundaries. Therefore, the saturation state is not attained at this level of deformation and it requires an imposed strain higher than $\varepsilon_N = 6.1$ as calculated in Section 3.2.2.

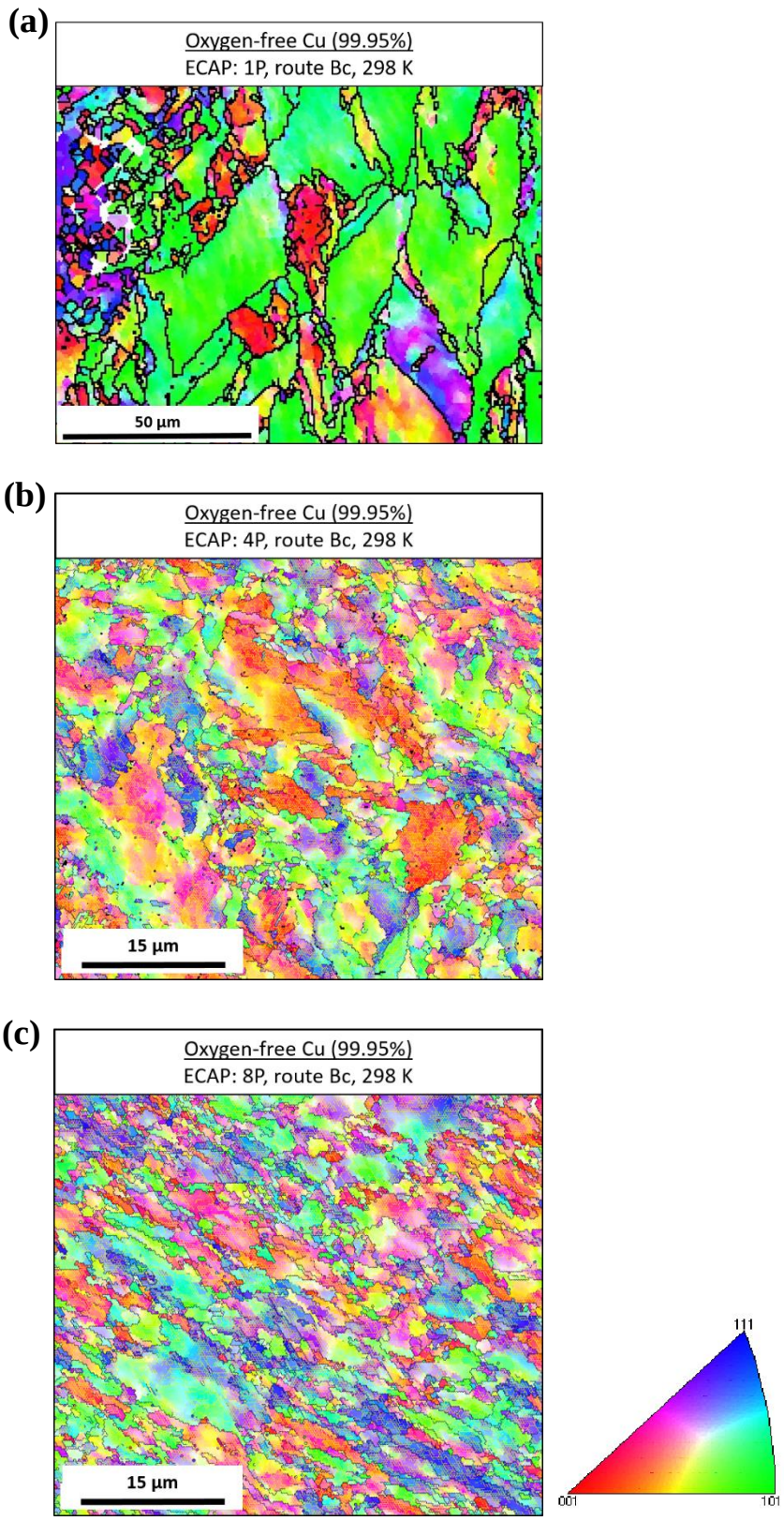

Figure 8.4 The OIM images for oxygen-free copper processed by ECAP for (a) 1, (b) 4 and (c) 8 passes at 298 K.

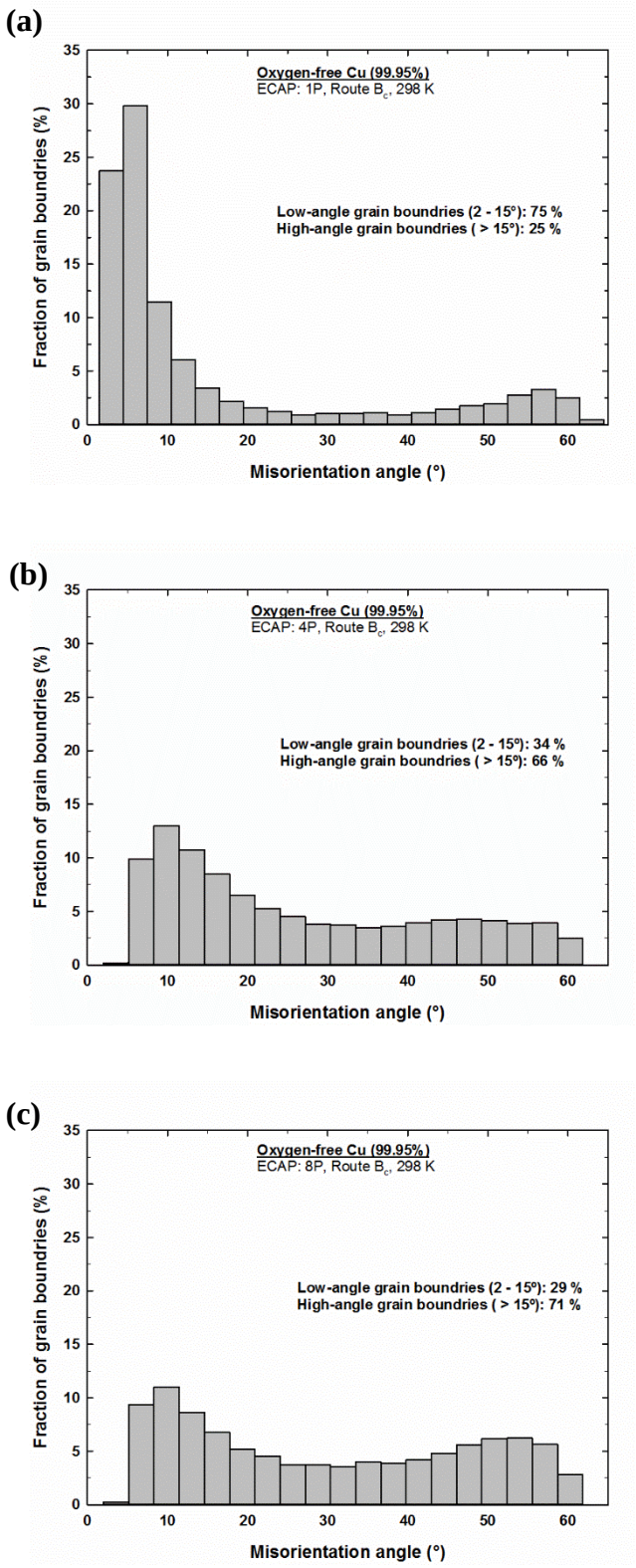

Figure 8.5 Histograms of the misorientation angles of grain boundaries for oxygen-free copper processed by ECAP for (a) 1 pass, (b) 4 passes and (c) 8 passes at 298 K.

8.2.3.2 Microstructure after further dynamic testing

Figure 8.6, Figure 8.7, Figure 8.8 and Figure 8.9, present the OIM images for oxygen-free copper processed by ECAP for 1, 4 and 8 passes and further deformed by dynamic testing at strain rate of 10 s^{-1} at 298 K, 10 s^{-1} at 473 K, 5.5×10^3 s^{-1} at 298 K and 5.5×10^3 s^{-1} at 473 K, respectively. These images were taken from the longitudinal sections of the specimens. The difference in colours represents different grain misorientation as shown in the unit triangles alongside each figure. Inspection of Figure 8.6 reveals that the microstructure after dynamic test for the specimen processed by 1 ECAP pass has an average grain size of ~0.4 µm. Measurements gave smaller grain sizes for the specimens produced at higher numbers of passes; ~0.33 µm for 4 passes and ~0.30 for 8 passes. The average grain size was estimated using the linear intercept method. It can be seen that the grains for the specimen processed by 1 pass appear to be elongated. These grains reduced in size and evolved into more equiaxed shapes after dynamic testing of the specimens processed by 4 and 8 passes. Increasing the testing temperature to 473 K for the same tests shown in Figure 8.7 reveals an increase in the average grain size for the 1 pass specimen to ~0.50 µm, and to ~0.62 µm and ~0.69 µm for the specimens processed by 4 and 8 passes, respectively. By examining Figure 8.7, it is readily observed that grain growth occurred during dynamic testing at 473 K in all specimens.

More information regarding the microstructural evolution of oxygen-free copper during dynamic testing at higher strain rates for the same test temperatures is provided by Figure 8.8 which shows the microstructure after dynamic testing at a strain rate of 5.5×10^3 s^{-1} and at temperature of 298 K. The average grain sizes measured after the dynamic test for the specimens processed by 1, 4 and 8 passes are ~0.40 µm, ~0.41 µm and ~0.42 µm, respectively. It follows from Figure 8.9 that average grain size is increased to ~0.36 µm, ~0.75 µm and ~0.79 µm for the specimens processed by 1, 4 and 8 passes respectively when tested at the higher temperature of 473 K.

It is apparent that specimens deformed at a higher number of passes by ECAP prior to dynamic testing produced smaller grain sizes when further deformed by a dynamic test at 298 K.

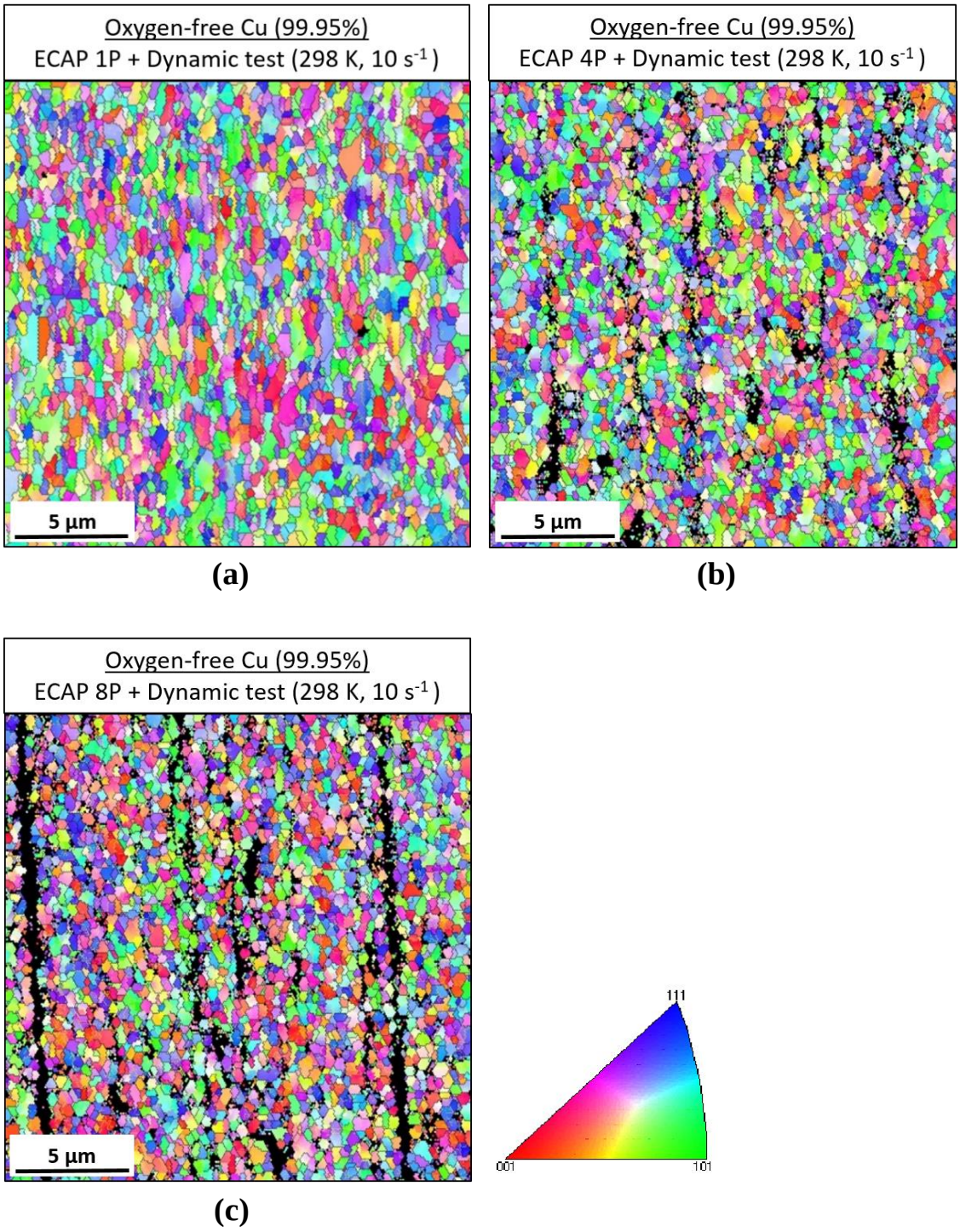

Figure 8.6 The OIM images for oxygen-free copper processed by ECAP for (a) 1 pass, (b) 4 passes and (c) 8 passes and further deformed by dynamic testing at strain rate of 10 s^{-1} at a temperature of 298 K.

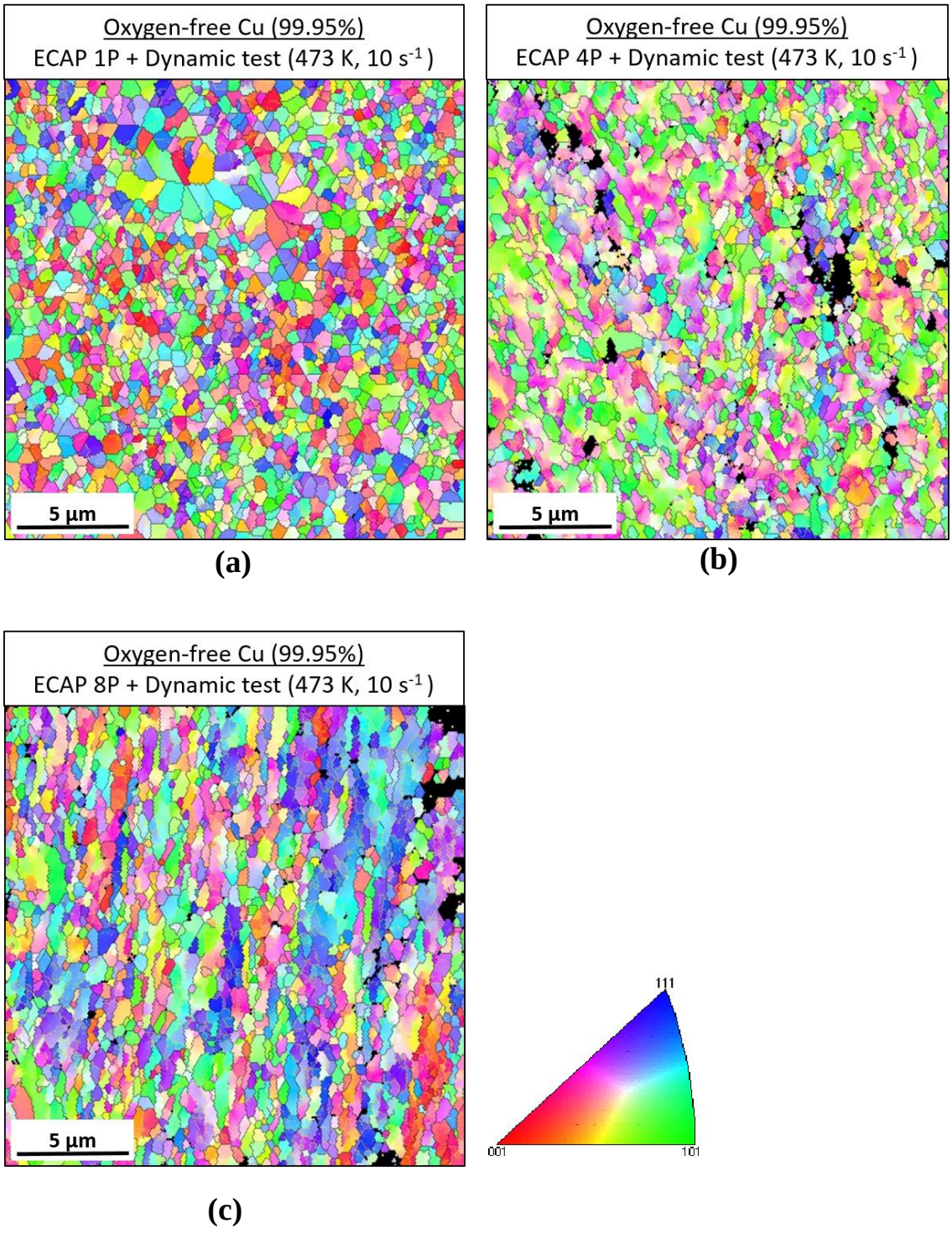

Figure 8.7 The OIM images for oxygen-free copper processed by ECAP for (a) 1 pass, (b) 4 passes and (c) 8 passes and further deformed by dynamic testing at strain rate of 10 s^{-1} at a temperature of 473 K.

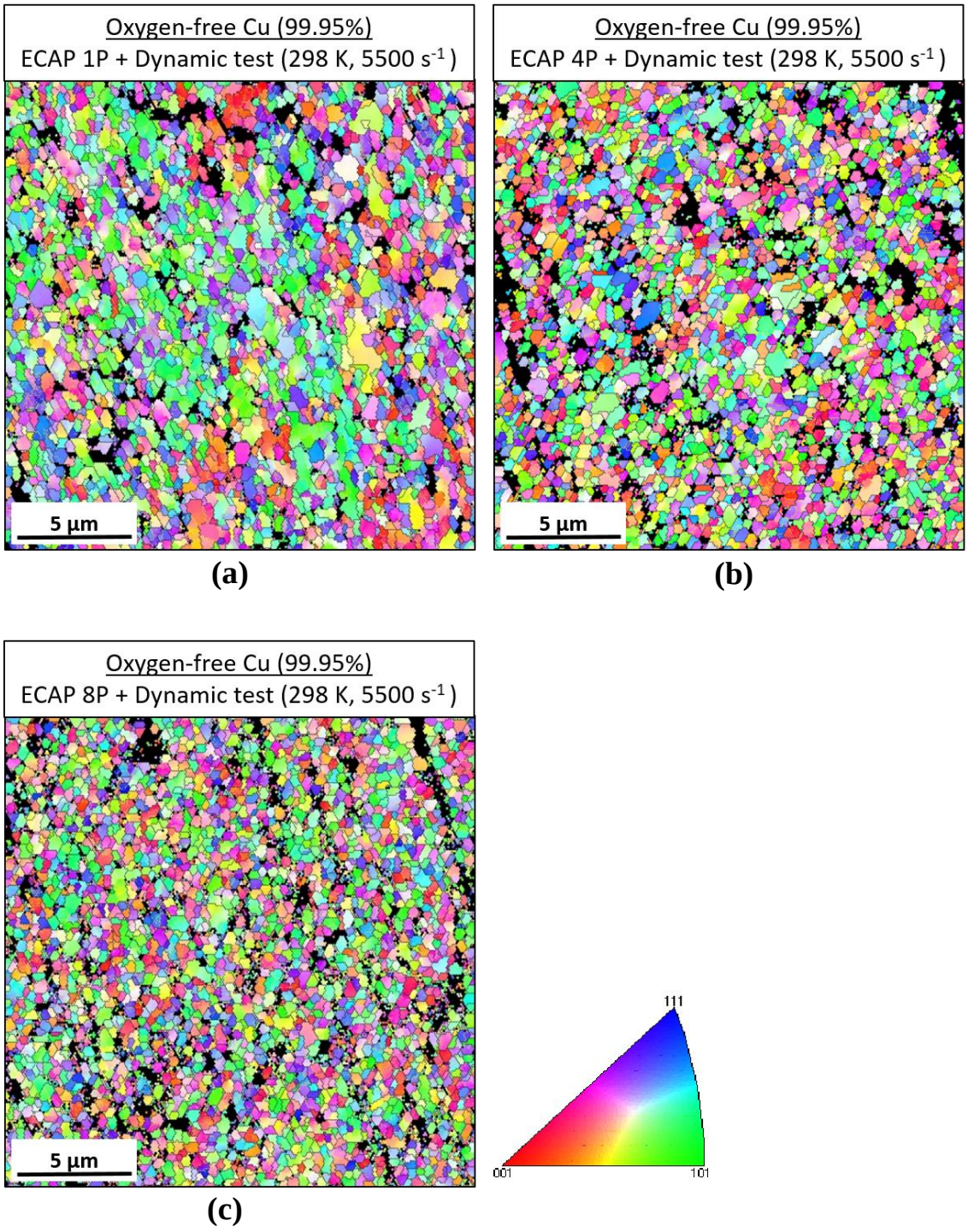

Figure 8.8 The OIM images for oxygen-free copper processed by ECAP for (a) 1 pass, (b) 4 passes and (c) 8 passes and further deformed by dynamic testing at strain rate of 5.5×10^3 s^{-1} at a temperature of 298 K.

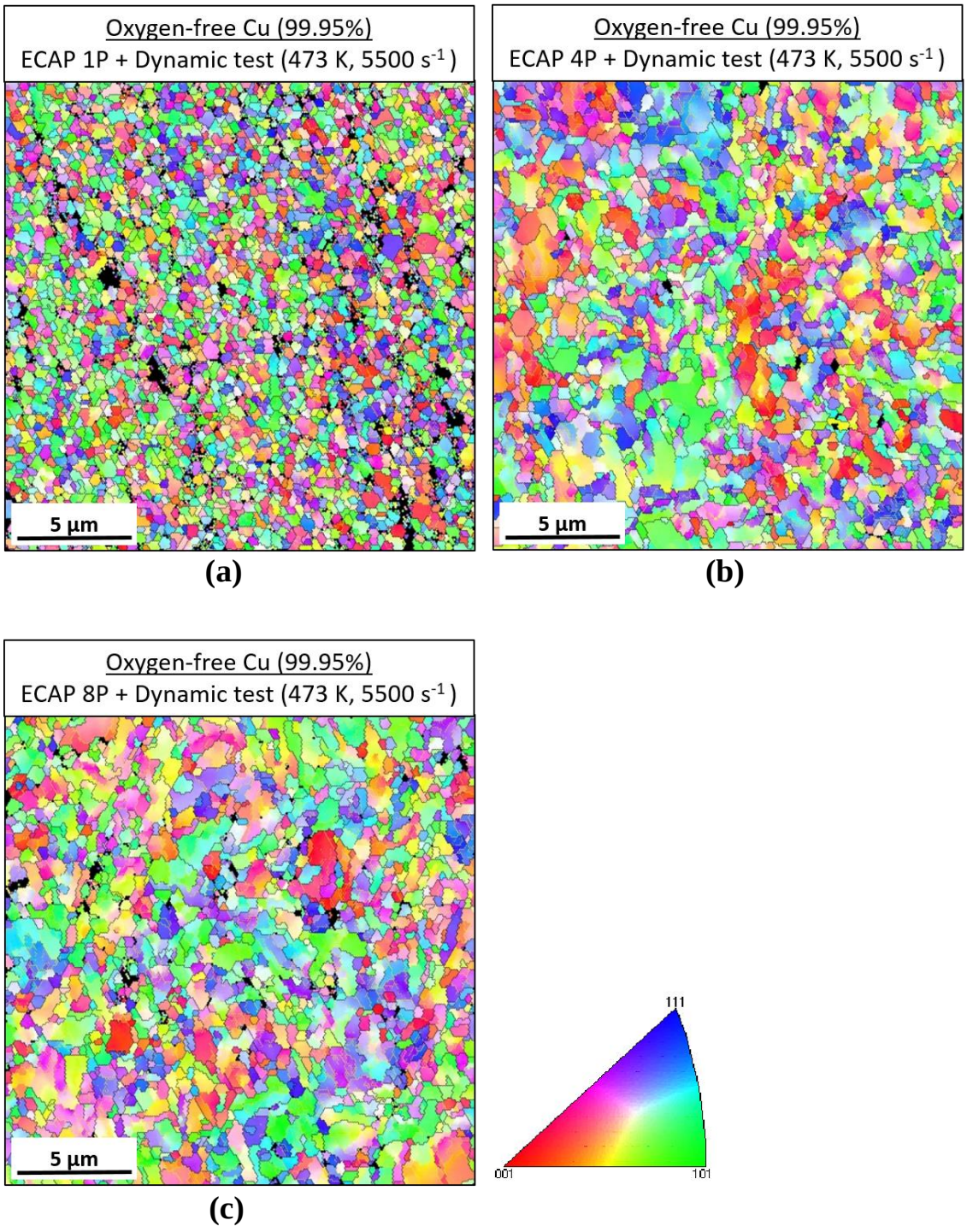

Figure 8.9 The OIM images for oxygen-free copper processed by ECAP for (a) 1 pass, (b) 4 passes and (c) 8 passes and further deformed by dynamic testing at strain rate of 5.5×10^3 s^{-1} at a temperature of 473 K.

For a better understanding of the microstructural evolution of UFG oxygen-free copper after dynamic testing, it is worth examining the nature of the grain boundaries. Histograms of the distributions of grain boundary misorientation angles for oxygen-free copper specimens processed by ECAP by 1, 4 and 8 passes, then further deformed by dynamic test at strain rates of 10 s^{-1} at 298 K, 10 s^{-1} at 473 K, 5.5×10^3 s^{-1} at 298 K and 5.5×10^3 s^{-1} at 473 K are given in Figures 8.10, 8.11, 8.12 and 8.13, respectively. Each figure records the percentages of low-angle grain boundaries where the misorientation is 2°-15° and high-angle grain boundaries where the misorientation is > 15°. In the present study, it should be noted that the distributions of grain boundary misorientation angles shown in the histograms are not an accurate grain-to-grain misorientation distribution, but rather a pixel-to-pixel misorientation distribution [306].

A detailed examination of the histogram in Figure 8.10 shows that oxygen-free copper continues to have almost the same fraction of high-angle grain boundaries (HAGBs ≈ 85 %) for 1, 4 and 8 ECAP pass specimens when subsequently deformed by a dynamic test at a strain rate of 10 s^{-1} at a temperature of 298 K. However, deforming the specimens at the higher strain rate of 5.5×10^3 s^{-1} at the same temperature, shown in Figure 8.12, clearly shows a higher percentage of high-angle grain boundaries in the specimen processed by 8 passes prior to dynamic testing. It is readily apparent that the percentage of high-angle boundaries increased from 80% to 89% for specimens deformed by 1 and 8 passes, respectively.

It is clearly noted from the histogram depicted in Figure 8.11 that the proportion of high-angle boundaries decreased significantly with increasing number of passes when subjected to a dynamic test at 473 K using a strain rate of 10 s^{-1}. The percentages of high-angle boundaries are 89%, 65% and 67% for specimens processed by 1, 4 and 8 passes, respectively. On the other hand, Figure 8.13 also reveals a dramatic and consistent decrease in the proportion of high-angle boundaries from 87% for 1 pass, to 71% for 4 passes to 69 % for 8 passes, when further deformed by dynamic testing using the higher strain rate of 5.5×10^3 s^{-1} at the higher testing temperature of 473 K.

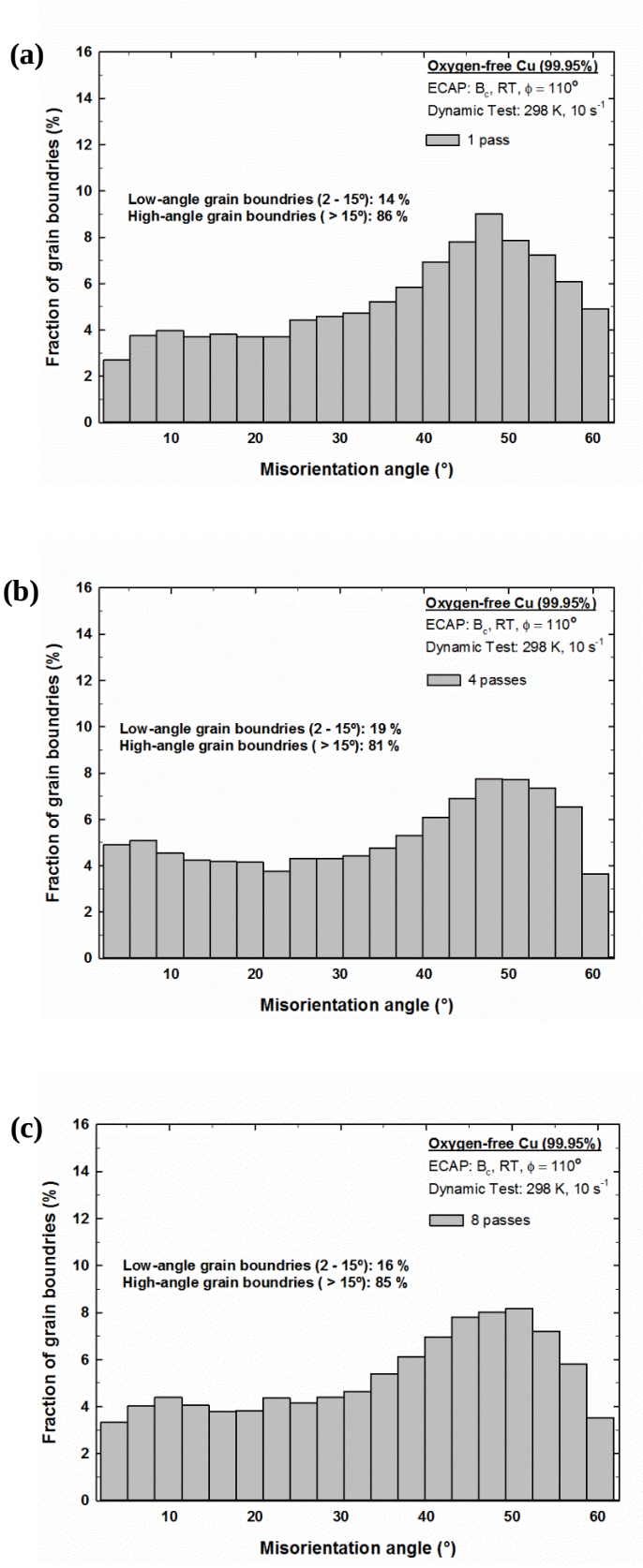

Figure 8.10 Histograms of the distribution of misorientation angles of grain boundaries for oxygen-free copper processed by ECAP for (a) 1 pass, (b) 4 passes and (c) 8 passes and further deformed by dynamic testing at 10 s^{-1} at 298 K.

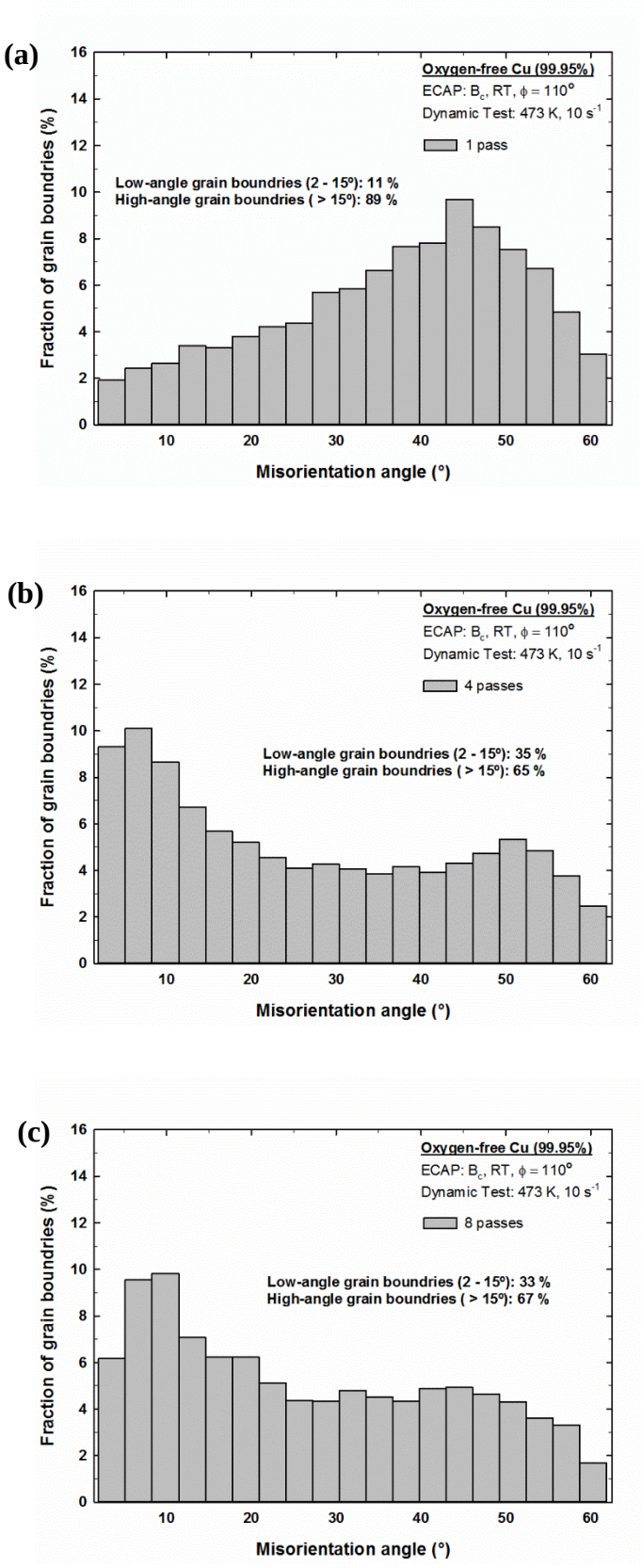

Figure 8.11 Histograms of the distribution of misorientation angles of grain boundaries for oxygen-free copper processed by ECAP for (a) 1 pass, (b) 4 passes and (c) 8 passes and further deformed by dynamic testing at 10 s^{-1} at 473 K.

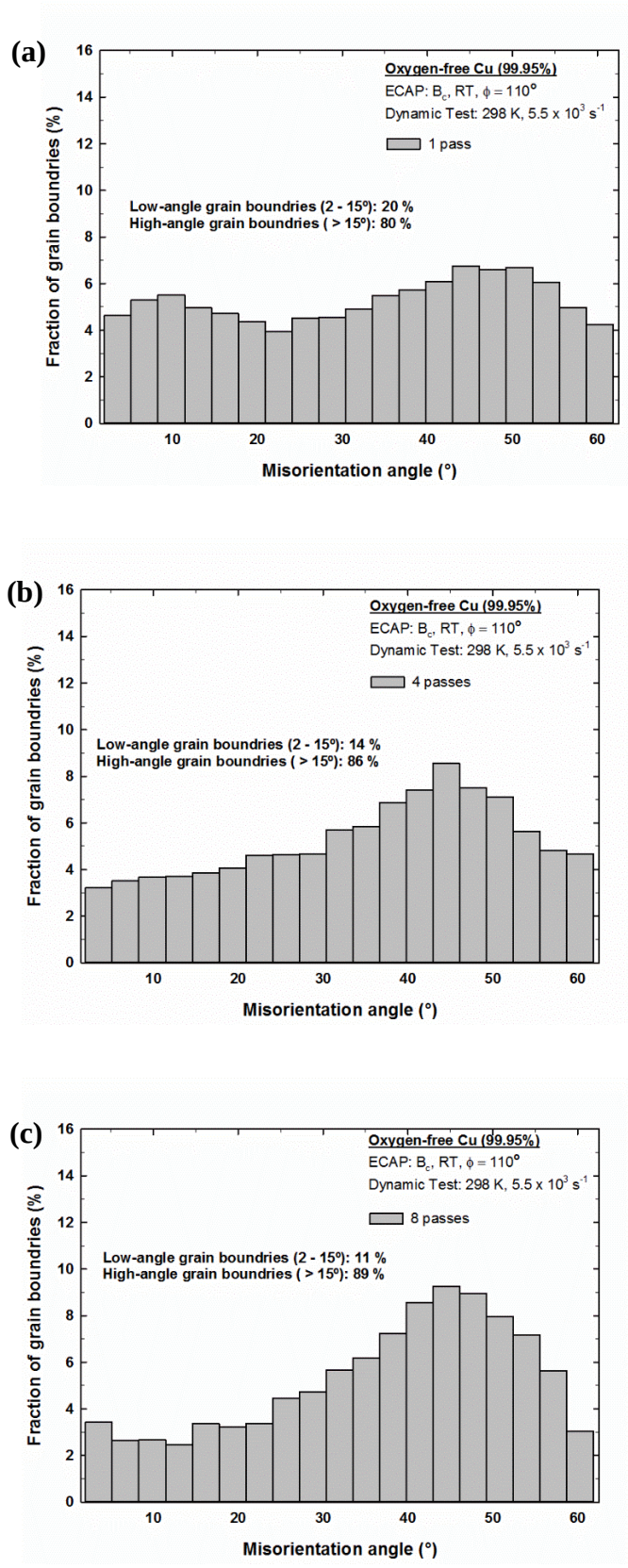

Figure 8.12 Histograms of the distribution of misorientation angles of grain boundaries for oxygen-free copper processed by ECAP for (a) 1 pass, (b) 4 passes and (c) 8 passes and further deformed by dynamic testing at 5.5×10^3 s^{-1} at 298 K.

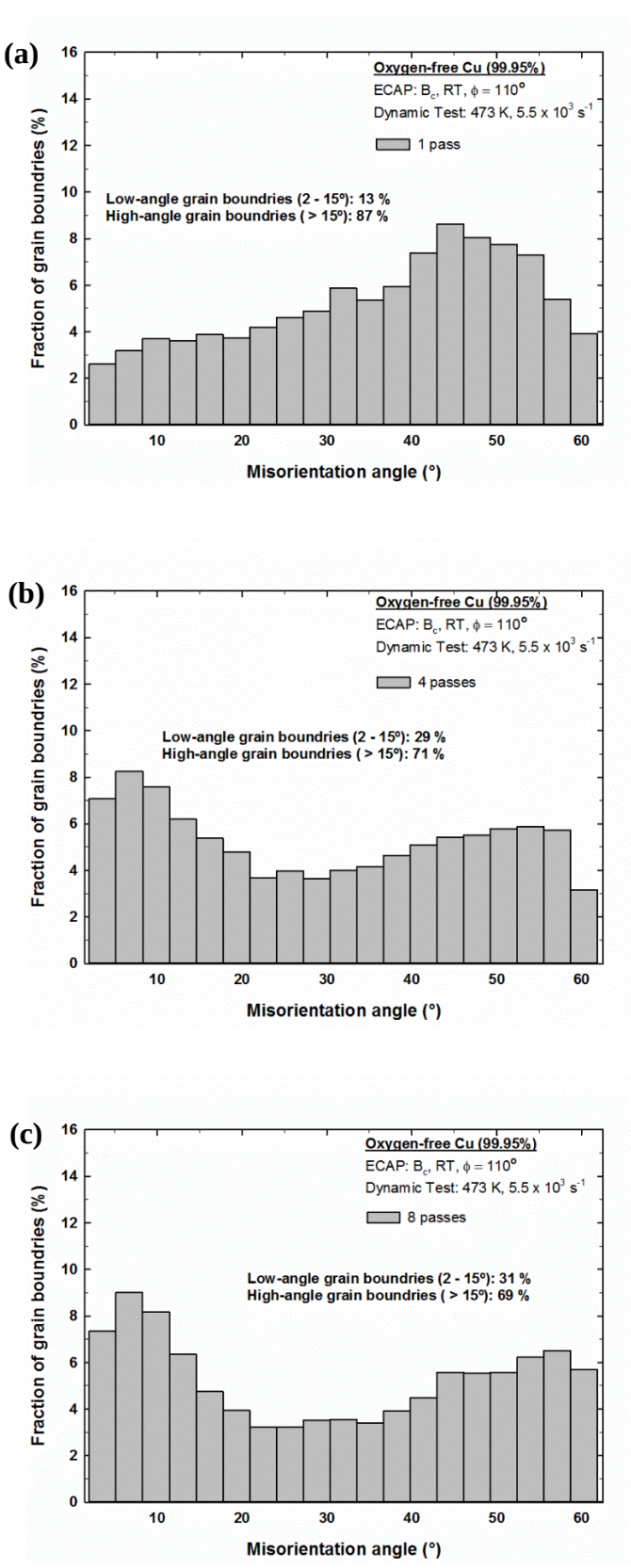

Figure 8.13 Histograms of the distribution of misorientation angles of grain boundaries for oxygen-free copper processed by ECAP for (a) 1 pass, (b) 4 passes and (c) 8 passes and further deformed by dynamic testing at 5.5×10^3 s^{-1} at 473 K.

8.2.4 X-ray diffraction analysis

X-ray diffraction test were performed to provide a clear insight into the deformation mechanisms and microstructural evolution of oxygen-free copper processed by ECAP and further deformed by dynamic testing at two different strain rates and temperatures. Inspection of the plots displayed in Figure 8.14 shows that dislocation density increased while crystallite size decreased with increasing number of ECAP passes of the copper specimens followed by dynamic testing with a strain rate of 10 s^{-1} at 298 K. The calculated dislocation density after testing the 1 pass specimen was ~6.11×10^{13} m^{-2} which increased to ~1.12×10^{14} m^{-2} and ~1.78×10^{14} m^{-2} for the 4 and 8 pass specimens, respectively.

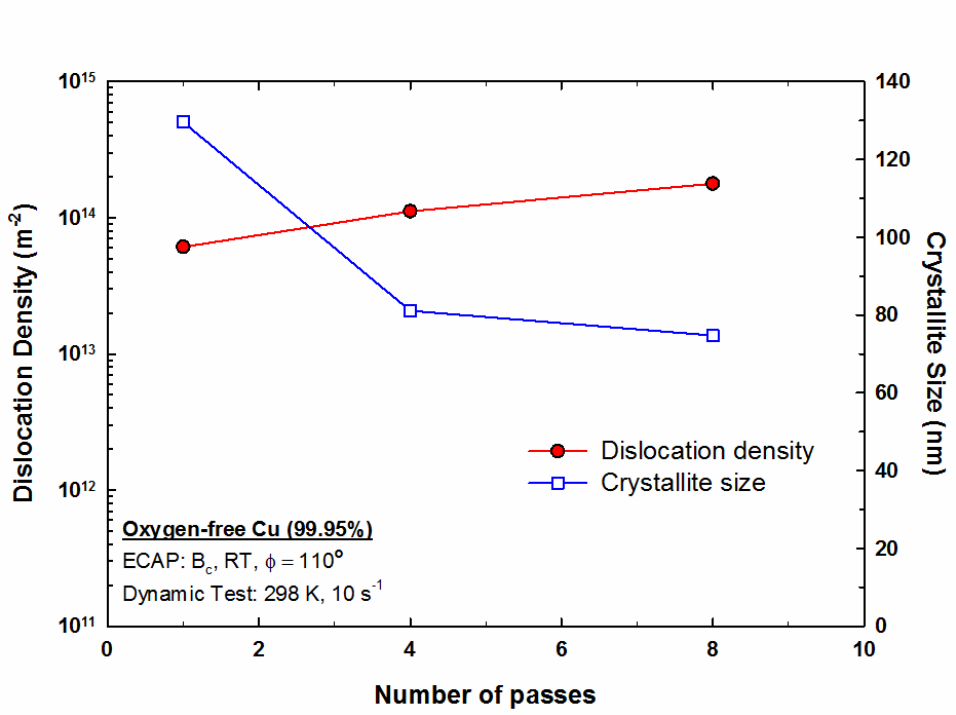

Figure 8.14 Dislocation density and crystallite size as a function of number of ECAP passes for oxygen-free copper further deformed by dynamic testing using strain rate of 10 s^{-1} at 298 K.

The results for the increased dynamic testing temperature, 473 K, at the same strain rate of 10 s^{-1} is shown in Figure 8.15 and it can be seen that there is a small decrease in the dislocation density and an increase in crystallite size of copper specimens with increase in the number of passes. Note there was a small increase in

initial deformation state prior to dynamic testing. The calculated dislocation density decreased from ~8.14×10^{13} m^{-2} to ~8.05×10^{13} m^{-2} and then to ~7.81×10^{13} m^{-2} for the specimens processed through 1, 4 and 8 passes of ECAP, respectively.

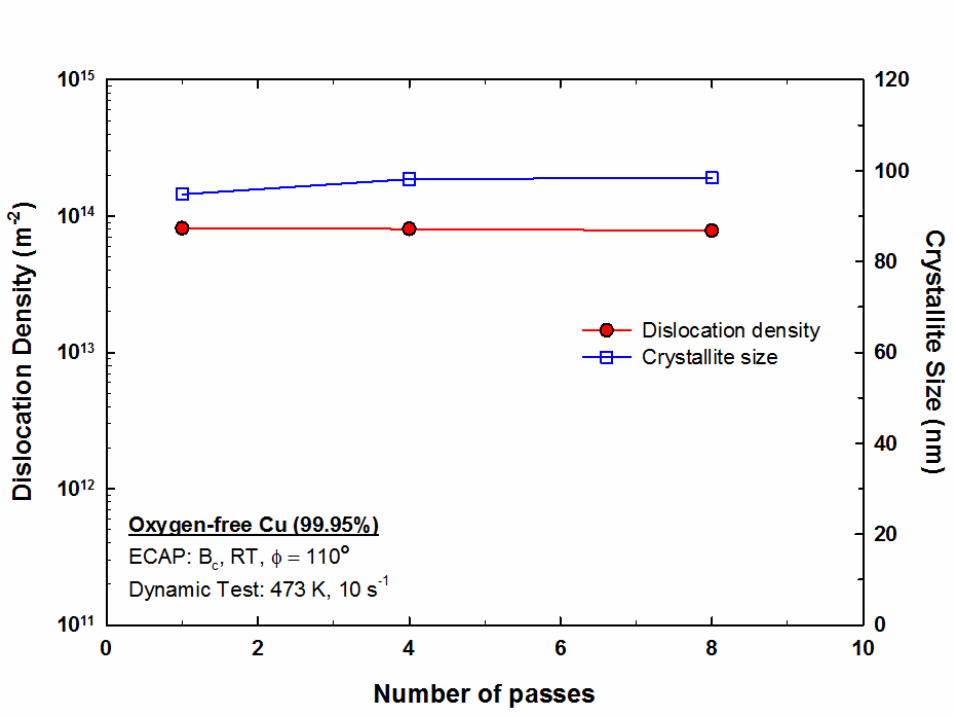

Figure 8.15 Dislocation density and crystallite size as a function of number of ECAP passes for oxygen-free copper further deformed by dynamic testing using strain rate of 10 s^{-1} at 473 K.

It is readily apparent also from Figure 8.16 that dislocation density increased with number of ECAP passes during dynamic testing at 298 K with strain rate of 5.5×10^{3} s^{-1}. The calculated dislocation density increased from ~7.6×10^{13} m^{-2} to ~1.0×10^{14} m^{-2} and then to ~1.25×10^{14} m^{-2} for specimens processed through 1, 4 and 8 passes of ECAP, respectively. Crystallite size decreased with prior number of ECAP passes from 1 to 8. The results displayed somewhat similar trends to those shown in Figure 8.14.

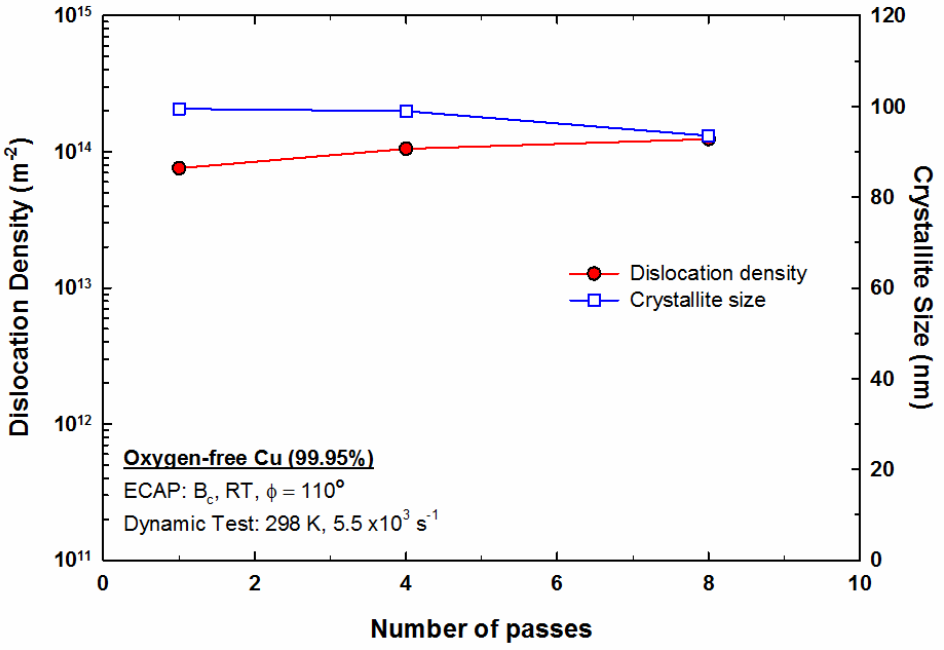

Figure 8.16 Dislocation density and crystallite size as a function of number of ECAP passes for oxygen-free copper further deformed by dynamic testing using strain rate of 5.5×10^3 s^{-1} at 298 K.

In Figure 8.17 there is a clear decrease in dislocation density and a trend for increasing crystallite size for the dynamic test performed at the higher temperature of 473 K with strain rate of 5.5×10^3 s^{-1}. These plots are unique because only under these conditions there is a trend for decrease in calculated dislocation density and increase in crystallite size with increase in number of ECAP passes. The calculated dislocation densities are ~7.15×10^{13} m^{-2}, ~2.1×10^{11} m^{-2} and ~3.40×10^{11} m^{-2} for the specimens processed through 1, 4 and 8 passes of ECAP, respectively.

The results obtained by the samples tested at 298 K shown in Figures 8.14 and 8.16 are in good agreement with the earlier results obtained by true stress-true strain curves and Vickers microhardness test. The results observed by XRD for the samples tested at 473 K shown in Figure 8.15 and 8.17 are in agreement with microhardness results that show softening with increasing number of passes. A possible explanation for this might be that softening occurred after the dynamic test.

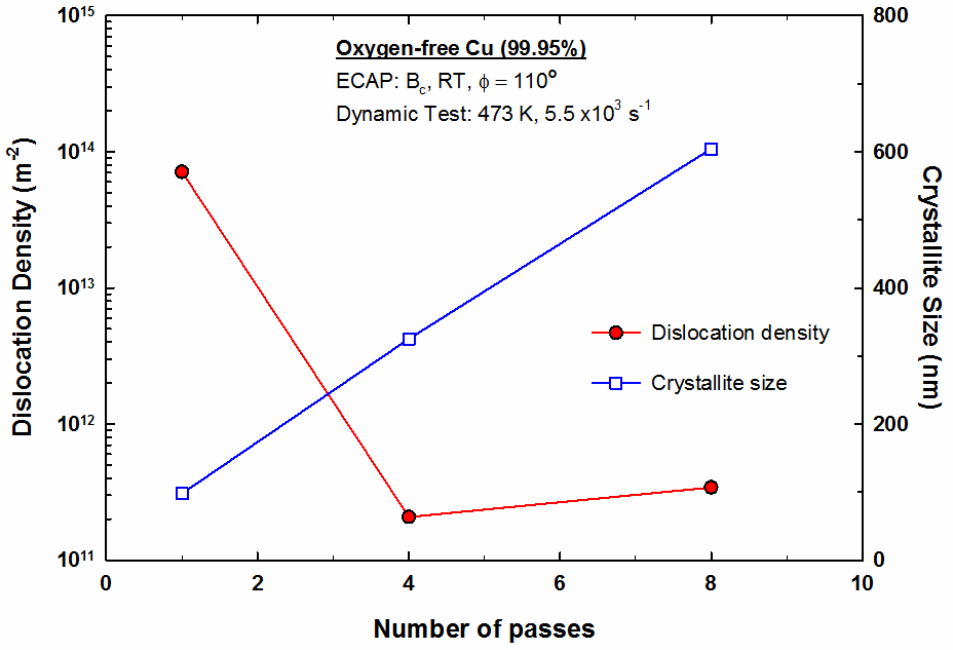

Figure 8.17 Dislocation density and crystallite size as a function of number of ECAP passes for oxygen-free copper further deformed by dynamic testing using strain rate of 5.5×10^3 s^{-1} at 473 K.

8.2.5 A direct comparison between the initial conditions and dynamic test results

In order to fully analyse the results of the dynamic tests, it is necessary to consider the initial microstructural condition prior to the dynamic test. In this case the number of ECAP passes; 1, 4 or 8. Thus, the properties produced by ECAP will be compared to the same properties after dynamic testing for each condition.

Figure 8.18 shows a direct comparison of dislocation density and grain size with respect to the annealed condition, after ECAP and after the dynamic test for: a) 1 pass, b) 4 passes and c) 8 passes. Dynamic tests were conducted at 298 K using a strain rate of 10 s^{-1}. For all three ECAP conditions, grain size reduced after dynamic testing. The dislocation density increased for both 1 pass and 4 passes with dynamic testing. However, the dislocation density appeared to decrease after dynamic testing for 8 passes. In addition, it is apparent from Figure 8.18(a-c) that consistently higher values of dislocation densities are produced after processing copper by ECAP, and ECAP

followed by dynamic testing, in comparison to the annealed condition. The calculated dislocation density for the annealed specimen is ~3.9×10^{12} m^{-2}. Despite the fact that dynamic testing was successful in reducing the grain sizes for the specimens processed by ECAP, it should be noted that the dislocation density of ~6.11×10^{13} m^{-2} for 1 pass ECAP + dynamic testing, is higher than the ~3.98×10^{13} m^{-2} for 1 pass ECAP as shown in Figure 8.18(a). Dislocation density increases from ~8.20×10^{13} m^{-2} to ~1.12×10^{14} m^{-2} for 4 pass ECAP + dynamic testing, in comparison to 4 pass ECAP as depicted in Figure 8.18(b). The dislocation density of ~1.78×10^{14} m^{-2} calculated after 8 pass ECAP + dynamic testing is lower than the ~3.60×10^{14} m^{-2} calculated after 8 pass ECAP as shown in Figure 8.18(c).

Figure 8.19 shows the dislocation density and grain size with respect to the annealed condition, after ECAP and after dynamic testing conditions for: a) 1 pass, b) 4 passes and c) 8 passes. Dynamic tests were conducted at 298 K using a strain rate of 5.5×10^{3} s^{-1}. Similar trends as shown in Figure 8.18, were observed for dislocation density and grain size for each condition when testing oxygen-free copper samples at 298 K using the higher strain rate of 5.5×10^{3} s^{-1}. Under all three conditions, grain size reduced after dynamic testing, but the dislocation density increased for 1 pass and 4 pass specimens while decreased for the 8 pass specimen after the subsequent dynamic testing.

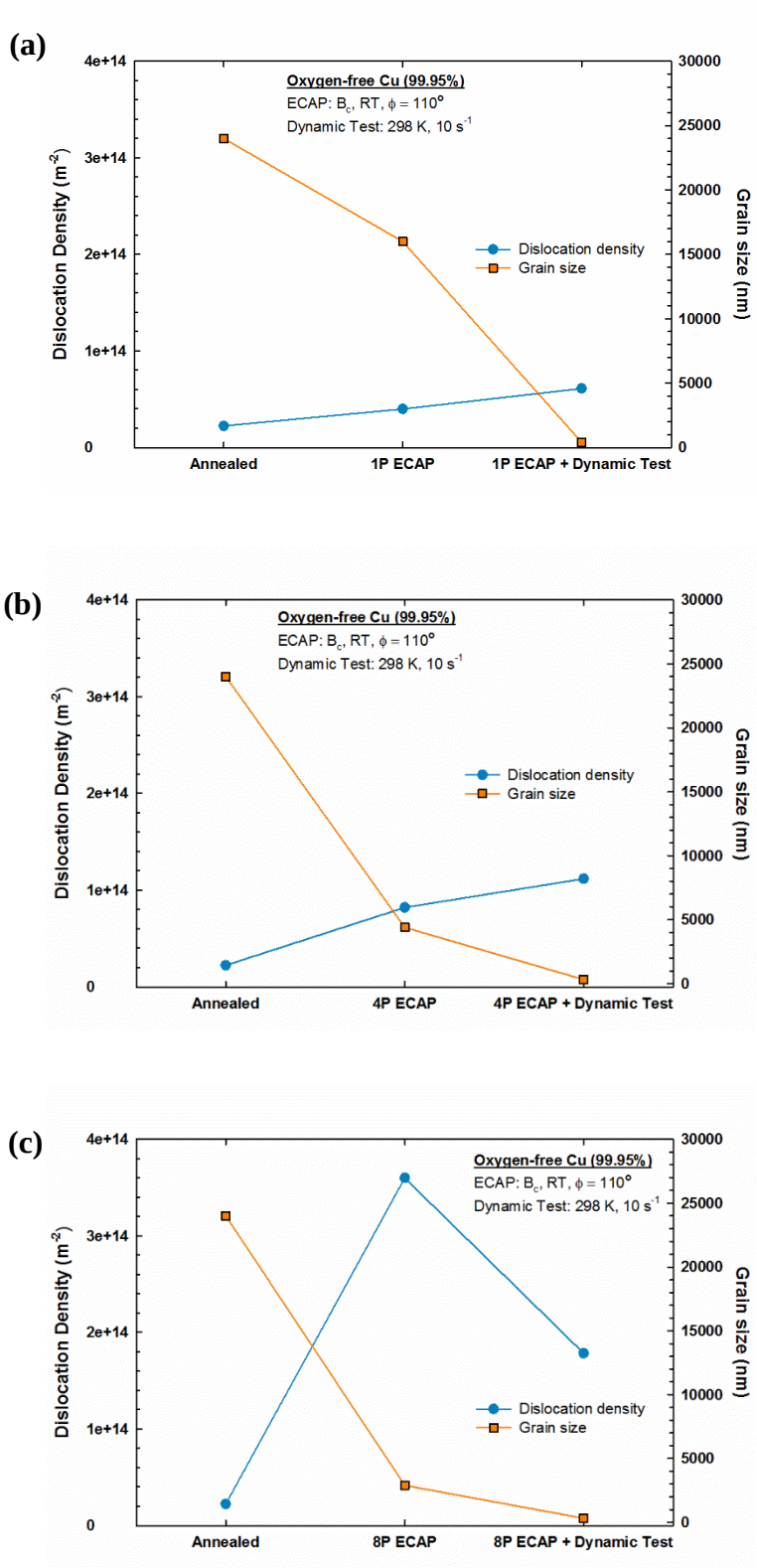

Figure 8.18 Dislocation density and grain size with respect to the annealed specimen, after ECAP and after dynamic testing for: (a) 1 pass, (b) 4 passes and (c) 8 passes. Dynamic tests were conducted at 298 K using a strain rate of 10 s^{-1}.

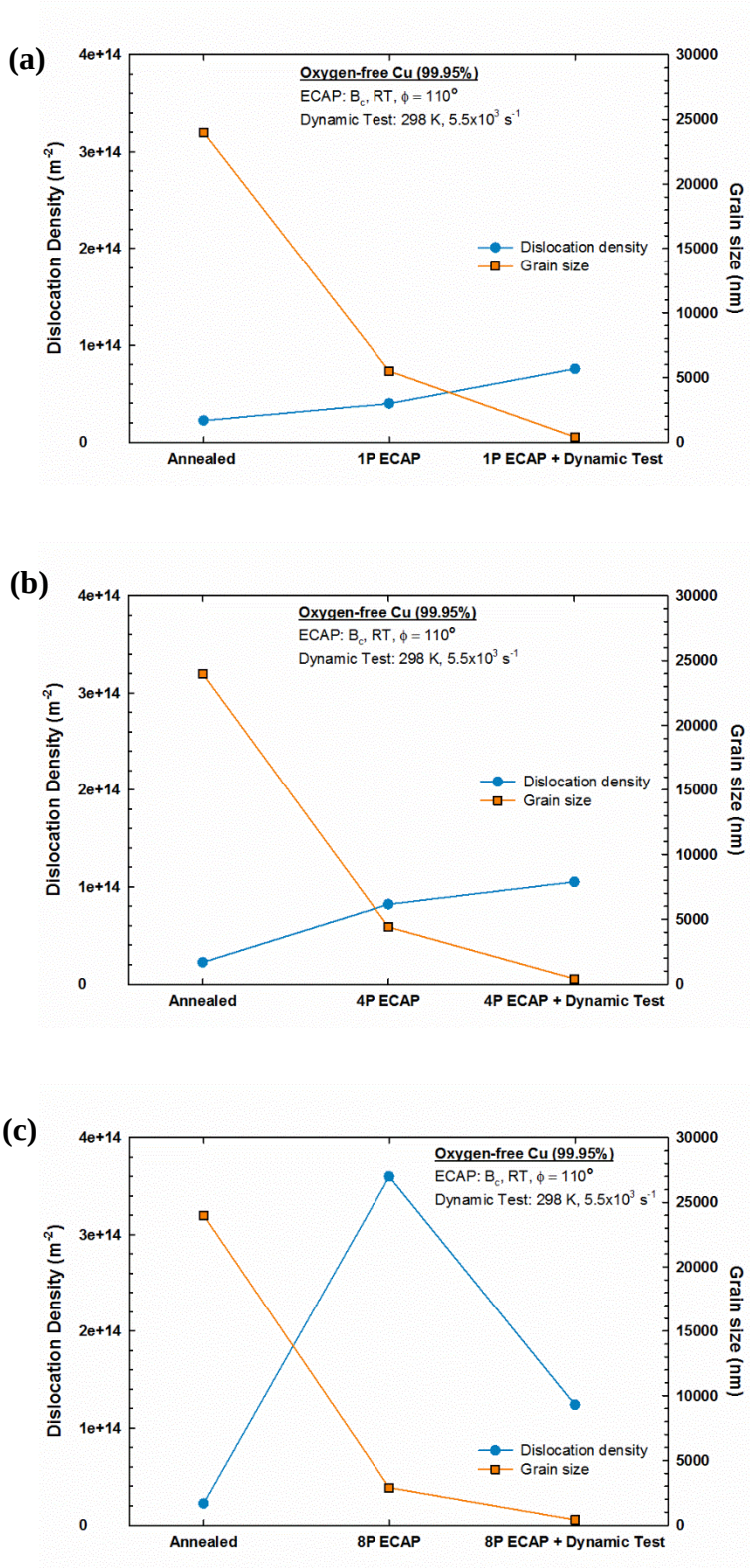

Figure 8.19 Dislocation density and grain size with respect to the annealed specimen, after ECAP and after dynamic testing conditions for: (a) 1 pass, (b) 4 passes and (c) 8 passes. Dynamic tests were conducted at 298 K using a strain rate of 5.5×10^3 s^{-1}.

The influence of temperature on the mechanical strength of oxygen-free copper is demonstrated in Figure 8.20, which shows plots of true stress vs true strain for specimens tested using the SHPB system with strain rates of 5.5×10^{3} s^{-1} at temperatures of 298 K and 473 K for a) 1 pass, b) 4 passes and c) 8 passes. It follows from Figure 8.20(a) that the flow stress of ~470 MPa at $\varepsilon = 0.1$ for tests carried out at a temperature of 473 K is higher than the flow stress of ~440 MPa obtained at 298 K. It is also apparent that the curve at 298 K shows an increase in work-hardening behaviour and reached a true stress of ~455 MPa at $\varepsilon = 3.5$, while the curve at 473 K exhibited flow softening and reached a true stress of ~435 MPa at $\varepsilon = 3.5$. In contrast, it is apparent from the curves for 4 passes shown in Figure 8.20(b) and 8 passes shown in Figure 8.20(c) that superior mechanical strength is obtained during dynamic testing at 298 K rather than 473 K. After increasing the testing temperature from 298 K to 473 K, the flow stress dropped from ~555 MPa to ~490 MPa for the specimen processed by 4 ECAP passes, as shown in Figure 8.20(b), and dropped from ~585 MPa to ~505 MPa for the 8 pass specimen as shown in Figure 8.20(c).

Figure 8.21 shows the dislocation density and crystallite size as a function of processing conditions for oxygen-free copper processed by ECAP through a) 1 pass, b) 4 passes and c) 8 passes and further deformed by dynamic testing using a strain rate of 5.5×10^{3} s^{-1}, at two temperatures, 298 K and 473 K. These measurements are taken using Maud software based on analysis of XRD line broadening. Figure 8.21(a) presents the dislocation density of the 1 pass specimen after ECAP as ~3.98×10^{13} m^{-2}, this increased after deformation by dynamic test at 298 K to ~7.57×10^{13} m^{-2}. However, at 473 K the dislocation density was ~7.13×10^{13} m^{-2}. Figure 8.21(a) also presents the crystallite sizes for the 1 pass specimen after deforming by ECAP, and by ECAP + dynamic testing at 298 K and 473 K; these were measured as ~205, ~99 and ~98 nm, respectively. It is apparent from Figure 8.21(b) and Figure 8.21(c) that for both the 4 pass and the 8 pass specimens, the dislocation density decreased when raising the temperature of the dynamic test from 298 K to 473 K. For the 4 pass specimen the dislocation density was reduced from ~1.05×10^{14} m^{-2} to ~2.08×10^{11} m^{-2}. For the 8 pass specimen the dislocation density was reduced from ~1.24×10^{14} m^{-2} to ~3.42×10^{11} m^{-2}. The specimen subjected to 4 ECAP passes at 298 K had a crystallite size of ~172 nm. After dynamic testing at 298 K and 5.5×10^{3} s^{-1}, this was reduced to

~99 nm. However, after dynamic testing at 473 K and 5.5×10^3 s^{-1}, a larger crystallite size of ~325 nm was measured.

Microhardness measurements show a minor drop in hardness value with increase in testing temperature from 298 K to 473 K for the 1 pass specimen as shown in Figure 8.22(a) and no noticeable change in the average grain size. A significant drop in the hardness values and increase in the average grain size were observed for 4 pass and 8 pass specimens with increased testing temperature as shown in Figure 8.22(b) and Figure 8.22(c), respectively. For the 4 pass specimen shown in Figure 8.22(b), the hardness decreased from ~115 Hv to ~60 Hv while the average grain size increased from ~410 nm to ~750 nm. Figure 8.22(c) shows that the hardness decreased from ~120 Hv to ~50 Hv with increased testing temperature of 473 K for the 8 pass specimen, whereas the average grain size increased from ~420 nm to ~790 nm.

The influence of strain rate on the dislocation density and crystallite size of oxygen-free copper is presented in Figure 8.23 and Figure 8.24, respectively. Both figures show specimens processed by only ECAP at room temperature then followed by dynamic testing using strain rates of 10 s^{-1} and 5.5×10^3 s^{-1} at 298 K and 473 K for: a) 1 pass, b) 4 passes and c) 8 passes.

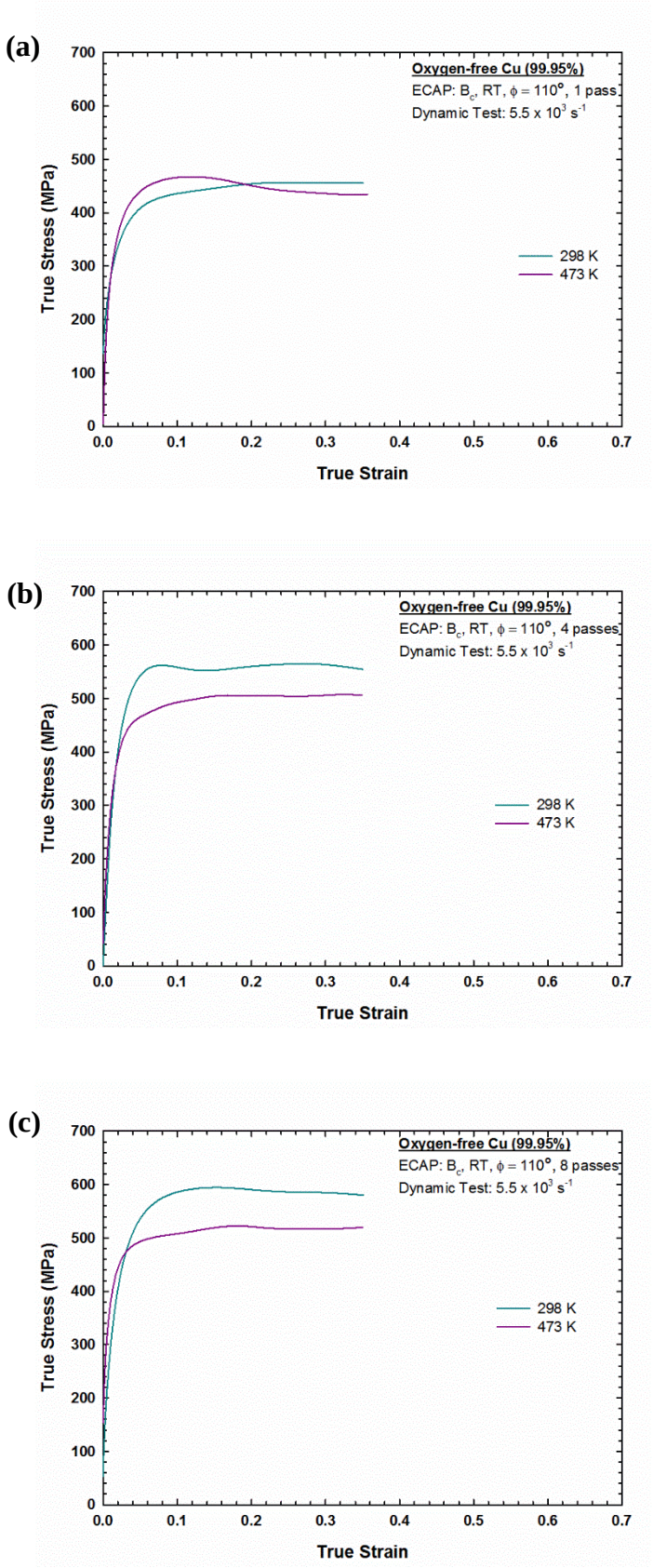

Figure 8.20 True stress vs true strain curves for oxygen-free copper specimens tested using SHPB at strain rates of 5.5×10^3 s^{-1} and at temperatures of 298 K and 473 K for (a) 1 pass, (b) 4 passes and (c) 8 passes.

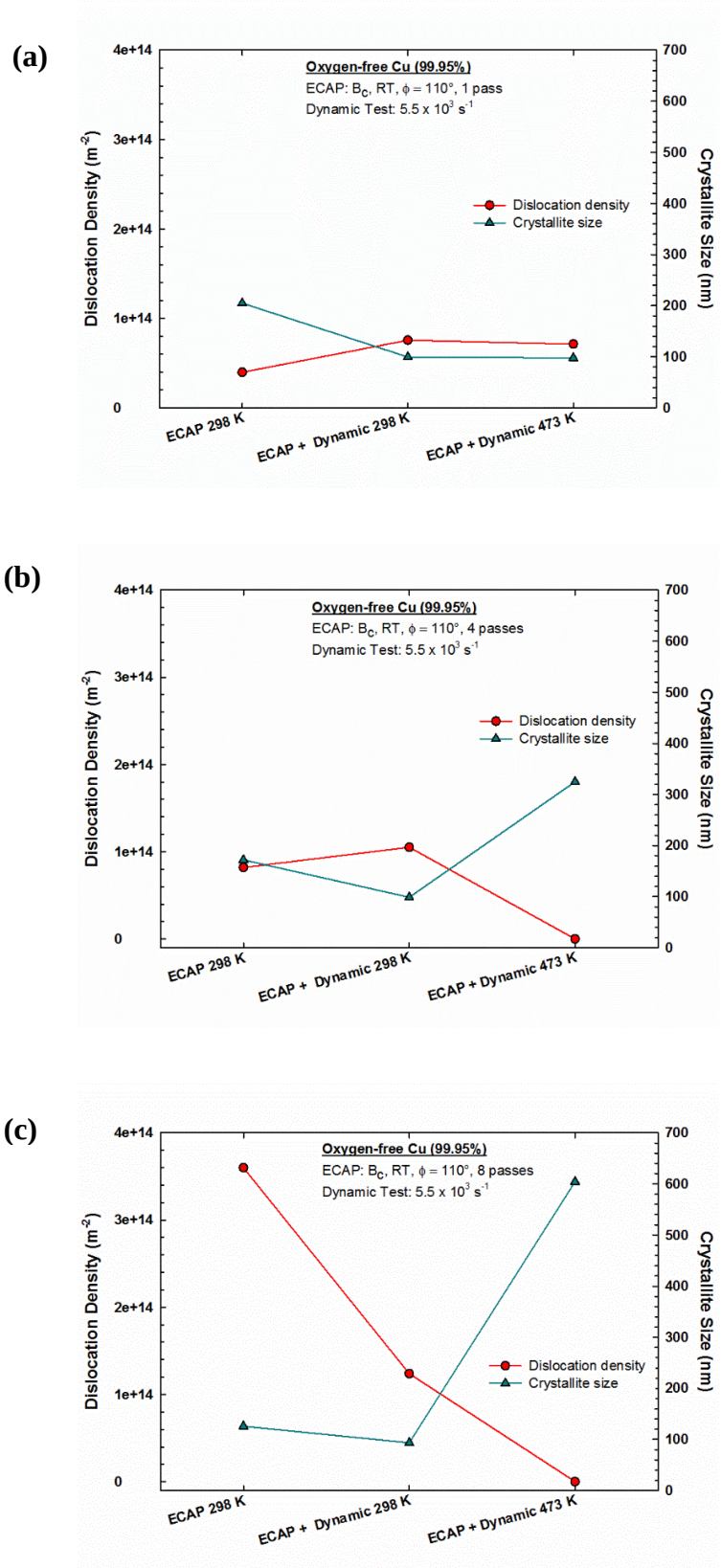

Figure 8.21 Dislocation density and crystallite size for oxygen-free copper processed by ECAP through (a) 1 pass, (b) 4 passes and (c) 8 passes and further deformed by dynamic testing using strain rate of 5.5×10^3 s^{-1} at the two temperatures 298 K and 473 K.

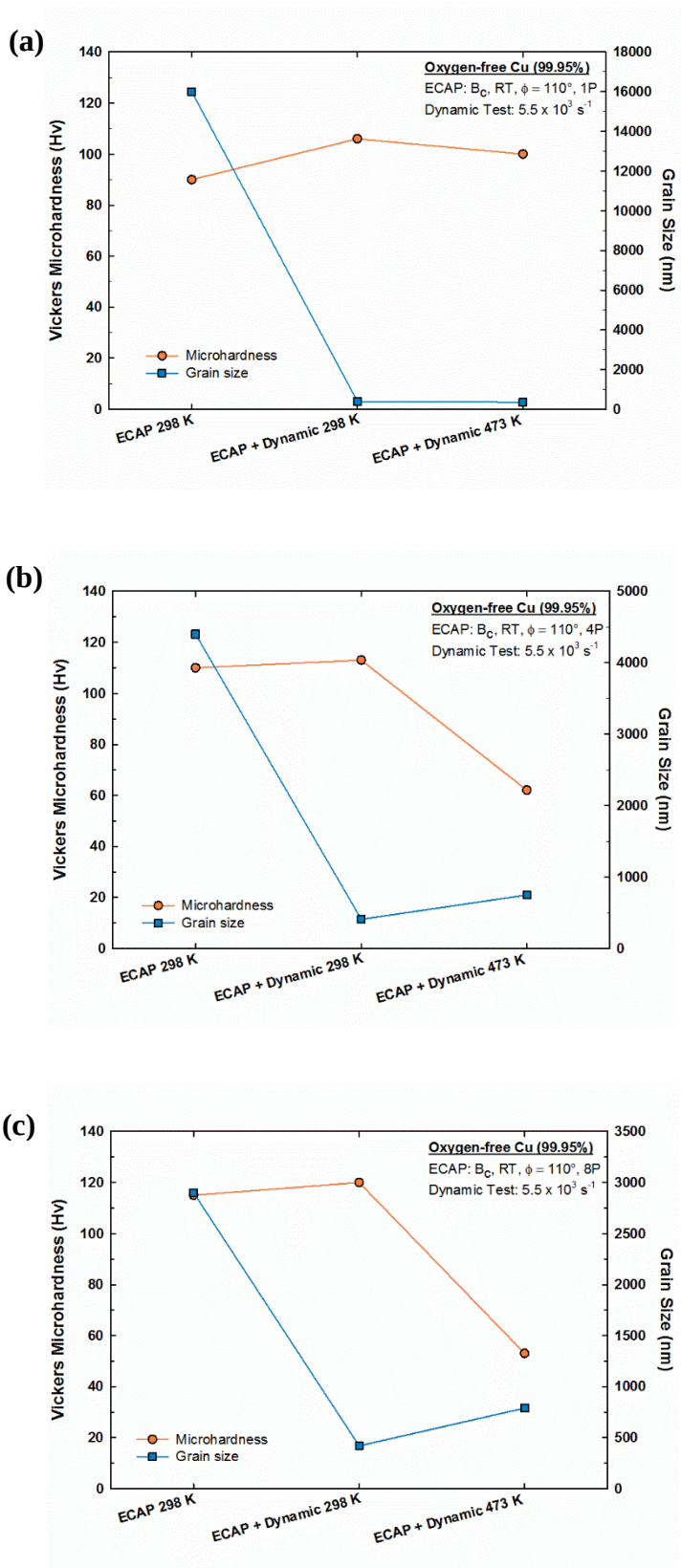

Figure 8.22 Microhardness and grain size as a function of processing condition for oxygen-free copper processed by ECAP through (a) 1 pass, (b) 4 passes and (c) 8 passes and further deformed by dynamic testing using strain rate of 5.5×10^3 s^{-1} at 298 K and 473 K.

For the 1 pass specimen, it is readily apparent in Figure 8.23(a) that the dislocation density increases after dynamic testing at both 298 K and 473 K, but that the crystallite size decreases as shown in Figure 8.24(a). The strain rate at 10 s^{-1} produced a higher dislocation density at 473 K than at 298 K. However, a strain rate of 5.5×10^3 s^{-1} produced much the same dislocation density at both temperatures. At 298 K the higher strain rate produced the greater dislocation density. On the other hand, the crystallite size was reduced after dynamic testing. The value of the crystallite size was slightly smaller at 473 K than 298 K, for the strain rate 10 s^{-1} but at the strain rate of 5.5×10^3 s^{-1} the crystallite size was the same at both temperatures, as shown in Figure 8.24(a).

For the 4 pass specimen, Figure 8.23(b) shows that the dislocation density increases slightly after dynamic testing at 298 K for both strain rates. It is also apparent that dislocation density produced by the strain rate of 5.5×10^3 s^{-1} is slightly lower than the value produced by the strain rate of 10 s^{-1} at 298 K. At 473 K the dislocation density for the strain rate of 5.5×10^3 s^{-1} is much lower than the one produced using the strain rate of 10 s^{-1}. The crystallite size decreases for both temperatures at the strain rate of 10 s^{-1}, as shown in Figure 8.24(b). The crystallite size slightly increases when deformed using a strain rate of 5.5×10^3 s^{-1} at a temperature of 298 K, in comparison to the value obtained for 10 s^{-1}. However, there is a substantial increase in crystallite size when using a strain rate of 5.5×10^3 s^{-1} at 473 K, in comparison to the value obtained for 10 s^{-1} as shown in Figure 8.24(b).

For the 8 pass specimen the dislocation density decreases after dynamic testing for both strain rates and both temperatures, see Figure 8.23(c). Comparatively, the dislocation density is lower at 473 K than at 298 K for both strain rates. It can be seen that the 8 pass specimen is more sensitive to strain rate than the 1 pass and 4 pass specimens. Dynamic testing at a strain rate of 10 s^{-1} reduced the crystallite size for both temperatures, as shown in Figure 8.24(c). The crystallite size increased very slightly in comparison to the value obtained for 10 s^{-1} at 298 K, when deformed using a strain rate of 5.5×10^3 s^{-1} at a temperature of 298 K. However, there was a very substantial increase in crystallite size when using a strain rate of 5.5×10^3 s^{-1} at 473 K, as shown in Figure 8.24(c).

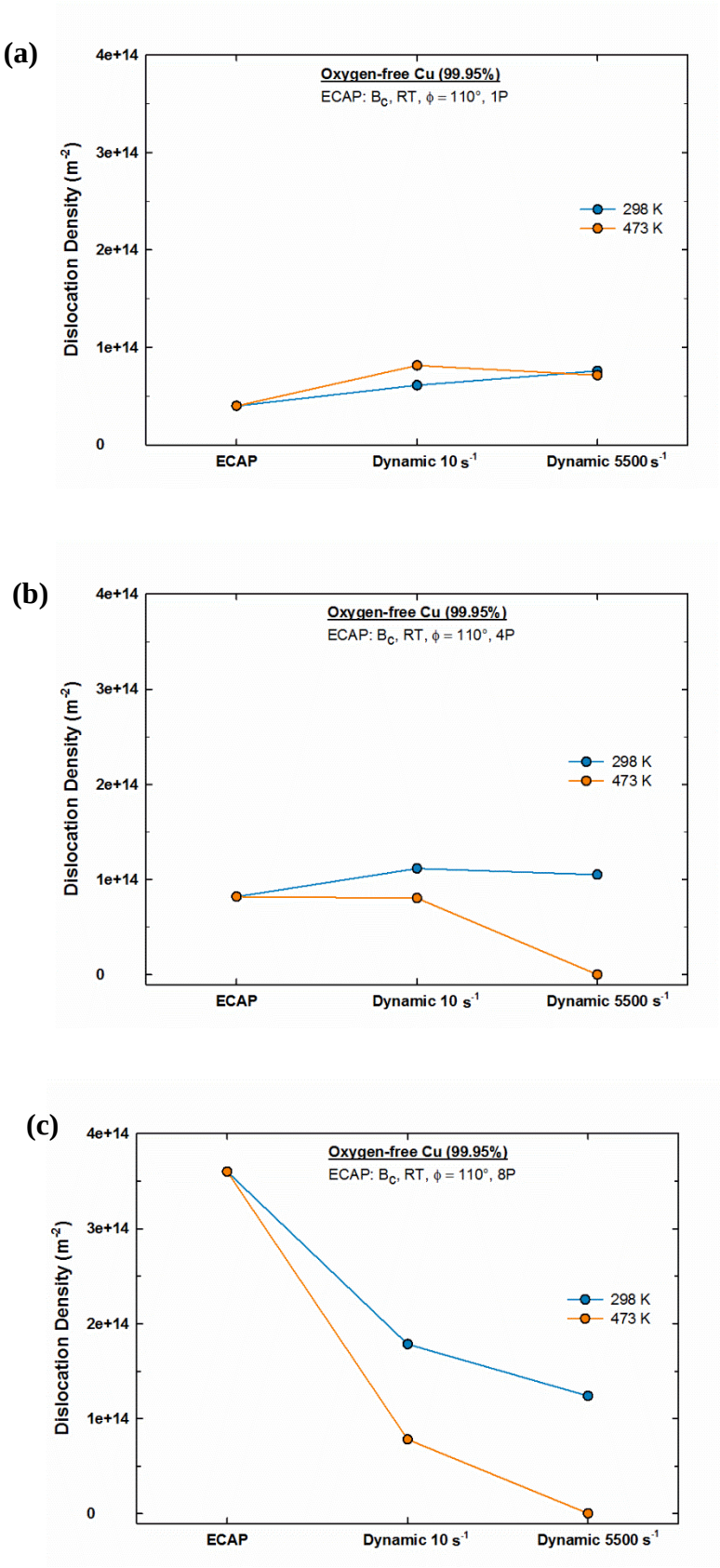

Figure 8.23 Dislocation density for oxygen-free copper specimens processed by only ECAP at room temperature followed by dynamic tests using strain rates of 10 s^{-1} and 5.5×10^{3} s^{-1} at 298 K and 473 K.

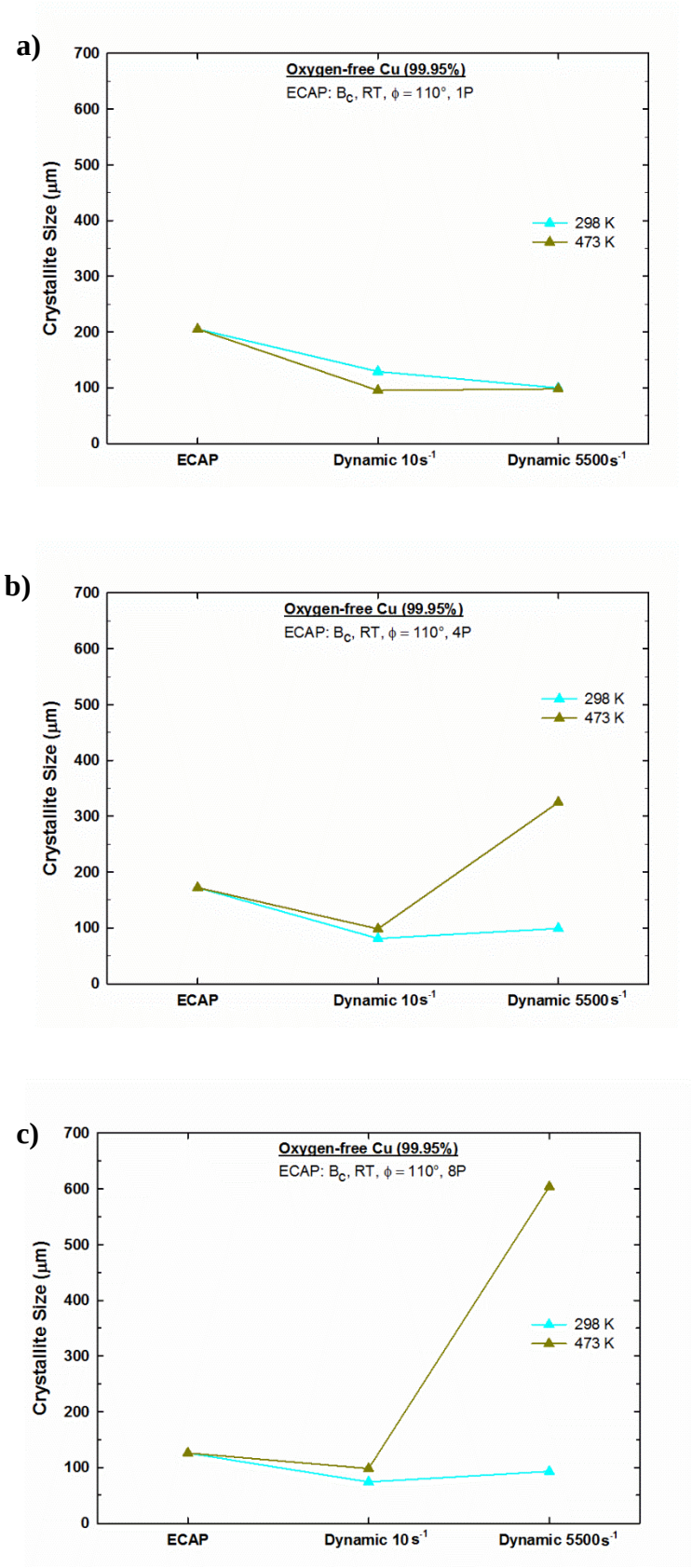

Figure 8.24 Crystallite size for oxygen-free copper specimens processed by only ECAP at room temperature followed by dynamic tests using strain rates of 10 s^{-1} and 5.5×10^{3} s^{-1} at 298 K and 473 K.

8.3 Discussion

8.3.1 Influence of the initial microstructure on the strength of oxygen-free copper

Since there was uncertainty regarding the influence of the initial microstructural condition produced by ECAP on the microstructure and mechanical properties attained after the high strain rate dynamic test, the results of the present study need to be interpreted with caution and systematically examined. The copper samples underwent a significant plastic deformation due to the ECAP process and the strain accumulated after each pass generates more dislocations and further grain refinement.

The 8 pass sample has the highest level of internal stresses and dislocation density (as compared to the 1 and 4 pass specimens), thus it is in a state of relatively high-stress. A possible consequence of this might be strain hardening induced by ECAP prior to the dynamic test. The dislocation densities of oxygen-free copper samples processed by ECAP were given in Section 4.2.3. As seen in Figure 8.5 the 8 pass specimen has a higher percentage of HAGBs than specimens with lower numbers of passes (1 and 4). The prominent work-hardening noticed in ECAP processed copper after 8 passes at 298 K at a strain rate of 10 s^{-1} shown in Figure 8.1(a) and at a strain rate of 5.5×10^{3} s^{-1} shown in Figure 8.2(a) is due to grain boundary and dislocation strengthening mechanisms as discussed in Chapter 6. Also, the 8 pass specimens exhibit higher hardness values than specimens with lower numbers of passes at 298 K as shown in Figure 8.3. The higher strain imposed during processing to a higher number of passes generates more dislocations and forms smaller grains having high-angle grain boundaries that hinder dislocation motion.

It is readily apparent from Figure 8.6 and Figure 8.8 that dynamic testing generates further grain refinement in the microstructure at 298 K using each strain rate of 10 s^{-1} and 5.5×10^{3} s^{-1} and therefore, greater strain hardening as shown in Figure 8.1(a) and Figure 8.2(a). So, the variation of strength observed after the dynamic test and shown in Figure 8.1(a) and Figure 8.2(a) is related to the difference in the initial microstructural conditions produced by ECAP. During deformation by ECAP, the level of the internal stresses and dislocation density in copper specimens increases and

creates non-equilibrium boundaries [199]. Different numbers of passes generate different amounts of geometrically necessary dislocations. This is clearly reflected in the strength of oxygen-free copper specimens after the dynamic test at the higher strain rate as shown in Figure 8.1(a), Figure 8.2(a) and Figure 8.3. It is seen in Figure 8.14 ($\dot{\varepsilon}$ = 10 s^{-1}) and Figure 8.16 ($\dot{\varepsilon}$ = 5.5×10^3 s^{-1}) that copper specimens processed through ECAP by 8 passes exhibit higher dislocation density and smaller crystallite size after dynamic testing as compared to the specimens processed by a lower number of passes.

Inspection of Figure 8.1(a) shows that, initially, the strength increases with increase in the preliminary imposed strain. However, the gain in strength slows as the strain increases above about 0.05. Once the curves have levelled off, there is a bigger gap in stress between 1 pass and 4 passes than between 4 passes and 8 passes. Similarly, there is a larger decrease in crystallite size due to increasing the ECAP passes from 1 to 4, than increasing the number of ECAP passes from 4 to 8 as shown in Figure 8.14. This is related to the increase of the geometrically necessary dislocations. The accumulation of these dislocations increases their density with increasing strain, and as their density increases it becomes more difficult to accommodate additional dislocations. Consequently, microstructural saturation is reached when strain exceeds a critical value. This saturation state occurs when the process of generation and annihilation of dislocations is balanced. Thus, strain hardening decreases as the microstructure becomes close to saturation.

It can be seen in Figure 8.4 that 1, 4 and 8 ECAP passes were only initial stages in the process of fragmentation, and not sufficient to form a homogeneous microstructure with equiaxed grains. Thus, the imposed strain is much lower than the critical strain required to achieve a steady-state condition. In short, the initial microstructural condition of oxygen-free copper produced by ECAP and deformed at a strain which is much lower than saturation strain prior to dynamic testing, can still influence the mechanical properties produced by dynamic testing.

Different low strain conditions produced by ECAP create different microstructures since dynamic testing under a specific strain rate adds the same level of strain hardening to each condition. The condition with the highest level of internal stresses and dislocation density prior to dynamic testing has higher mechanical strength, this can be seen by comparing Figure 8.1(a) and Figure 8.2(a) to Figure 8.4.

These results are in agreement with a study that has shown that the initial microstructural condition produced by ECAP prior to further processing by HPT can highly affect the grain size [307]. A second study has shown that the maximum shear stress increases with increasing number of passes prior to a dynamic torsional test [305]. However, a previous investigation has stated that the initial state of the copper sample has only a minor influence on the mechanical properties measured with a compression test performed at a strain rate of 0.1 s^{-1} [190].

Higher number of ECAP passes will not have a major influence on the mechanical properties after dynamic testing. This is because the intensive hardening produced by ECAP is close to the saturation state. Thus, further strain hardening induced by dynamic testing will be very slow and will not be as effective as it would have been when the initial strain was low (lower number of passes). Also, the variation in strength between different conditions will be minor or may even diminish. Similar phenomena were reported in an earlier study on commercial purity Niobium that was processed by ECAP for 16 passes then further deformed by HPT for 5 turns [308]. The results showed that there was no noticeable change in microstructure after HPT and saturation was rapidly reached. Another study has shown that the initial microstructural condition of single-phase materials could be neglected once processed at high strain using only HPT [309].

8.3.2 Grain refinement after dynamic testing at 298 K

After ECAP processing, dynamic testing at a temperature of 298 K was conducted using strain rates of 10 s^{-1} and 5.5×10^{3} s^{-1}. It is readily apparent that a significant grain refinement occurred after dynamic testing at strain rate of 10 s^{-1}, as shown in Figure 8.6, and a strain rate of 5.5×10^{3} s^{-1}, as shown in Figure 8.8. The grain structure formed by ECAP contained large and elongated grains as shown in Figure 8.4 which evolved into a microstructure composed of fine grains with nearly equiaxed shapes as displayed in Figure 8.6 and Figure 8.8. Materials with small grain sizes tend to move faster (faster kinetics) towards grain refinement when deformed by large strain [310]. It can also be seen that the microstructure evolved towards greater homogeneity and the grains became more equiaxed with increasing the number of ECAP passes from 1 to 8, prior to dynamic testing. This grain refinement is associated with an increase in the percentage of HAGBs as shown in Figure 8.10 and 8.12.

The most interesting finding is that dynamic testing is effective in producing an UFG structure within the specimens that underwent preliminary processing by ECAP. Table 8.1 shows a comparison between the average grain sizes produced by ECAP + dynamic test with the average grain sizes produced by various SPD techniques. It follows from Table 8.1 that deforming copper by dynamic testing is effective in producing exceptionally small grain sizes, in the nanometer range, similar to those obtained after processing by a single or combination of SPD methods at room temperature such as HPT [37,49,52,311,312], ECAP [49,74,181,192,311], ECAP + HPT [49,311,313] and surface mechanical attrition treatment (SMAT) [314].

By Comparing the OIM images after ECAP displayed in Figure 8.4 with the images after dynamic testing displayed in Figure 8.6 and Figure 8.8, it can be seen that the microstructure of oxygen-free copper is exceptionally refined after the dynamic test for each condition: a) 1 pass, b) 4 passes and c) 8 passes. The deformation mechanism at high strain rates is discussed in several studies, which show that during dynamic testing at high strain rates, regions of highly localized deformation called adiabatic shear bands are likely to be formed in polycrystalline metals [101,103,107,110,315–323].

Adiabatic shear bands are formed due to the very short duration of plastic deformation at high strain rate which significantly reduces the heat dissipated and causes a localized temperature rise in the deformed region [324]. It is believed that shear bands play a major role in the grain refinement process [106,107]. Grain refinement models for the adiabatic shear bands were developed in earlier studies [315,317]. These models illustrate that during high strain rate deformation, dislocations are distributed homogeneously, then these dislocations are rearranged and form elongated dislocation cells. These cells evolve into elongated subgrains as the misorientation increases. With increasing deformation, these elongated subgrains start to break up and the subgrain boundaries are reoriented and form equiaxed ultrafine grains.

During dynamic testing, high strain rate deformation is induced in the specimen by the high-velocity impact. Dislocation activities (gliding, accumulation, interaction, tangling and spatial rearrangement) take place to accommodate the high strain. This will result in an increase of dislocation density. The pile-up of dislocation

lines forms dislocation tangles and dislocations walls which transform into subgrain boundaries inside the grains and cause a break in the boundaries of the original grains and produces ultrafine grains. This is similar to the grain refinement mechanism observed in SPD for various metals such as copper [34,325]. It is also similar to the mechanism that has been reported in 7075 aluminum alloy processed by laser shock processing (LSP) impacts [326] and Mg/Ti joints by high energy shot peening (HESP) [327].

It follows from Figure 8.18(a & b) and Figure 8.19(a & b) that grain refinement after dynamic testing is associated with a substantial increase in the dislocation density and this is consistent with earlier studies that show higher dislocation density is produced by multiple SPD processing than a single process [285,311,328]. However, dynamic testing is not considered as an SPD method since the shape and size of the specimen are not retained after the test.

On the other hand, the microstructures for the 8 pass specimen developed after dynamic testing at 298 K consists of ultrafine grains that are free of dislocations as shown in Figure 8.6(c) and Figure 8.8(c). It is suggested from the drop of dislocation density of the 8 pass specimen shown in Figure 8.18(c) and Figure 8.19(c), that the microstructure might be changed by dynamic recrystallization (DRX) during the dynamic testing. The possibility of the occurrence of DRX in pure copper during high strain rate was introduced by Chokshi and Meyers through a preliminary study [329]. Earlier studies have reported that DRX may take place in the subgrain boundaries and produce ultrafine grains having HAGBs [330]. This is in agreement with earlier studies reporting the evolution of small grains with HAGBs through DRX at high strain rates [106,107,110,329].

An earlier report has suggested that the thermal effects by the adiabatic temperature rise can greatly enhance the DRX during high strain rate deformation [106,108]. The high speed compression generates adiabatic heating and stores considerable energy within the material which might provide a driving force for dynamic recrystallization as microstructural reorganisation, with the material undergoing migration of HAGBs during the process of deformation [107,331,332]. The adiabatic temperature rise in oxygen-free copper during high strain deformation can be calculated using [333]:

$$\Delta T = \frac{0.9}{\rho C_V} \int_0^{\varepsilon} \sigma d\varepsilon \quad (8.1)$$

Where σ and ε are the true stress and true strain, respectively, ρ is the density of the material (8.96 g/cm^3) and C_V is the specific heat capacity of copper (383 J/kg K). The calculated temperature rise for the 8 pass specimen deformed at strain rates of 10 s^{-1} and 5.5×10^3 s^{-1} are ~375 K and ~450 K, respectively. This is lower than the adiabatic temperature rise in the range of 500 - 800 K that were calculated by Andrade *et al.* [106] for copper during dynamic deformation at a high strain rate of 10^4 s^{-1}, whereas it is higher than the adiabatic temperature rise of 300 K reported by Meyers *et al.* [108] for copper during shock-loading impacts. Both of these studies proposed that the adiabatic temperature rise can cause a microstructure to be developed by DRX. A later study by Hines and Vecchio [107] reported an adiabatic temperature rise of 500 K under compression for shock-hardened copper at high strain rates, however the total time for cooling the specimen to RT was calculated to be less than 1600 μs, thus temperature has a minor influence on DRX. It can be also noted that the homologous temperatures calculated for this study is 0.28 and 0.33 which are less than 0.4 T_m for copper.

It is readily noted from the results observed in this study that grain refinement in oxygen-free copper can be produced by DRX depending on the initial microstructure prior to the dynamic test. The 1 pass specimen has large grain size and a high proportion of low-angle boundaries and so can accommodate more dislocations during dynamic testing. Thus the grain refinement mechanism is mainly due to dislocation activities. Conversely, the 8 pass specimen has smaller grain size, a higher fraction of HAGBs and a higher dislocation density which provide more potential for DRX. Since the adiabatic temperature rise during high strain dynamic tests has a minor influence on the microstructure, it is proposed that the microstructure was evolved through mechanically induced DRX [107,111]. The mechanism for grain refinement witnessed with the 8 pass specimen was similar to previous studies [334] on aluminium alloy, and ANSI type 304 stainless steel when processed by LSP [335].

Table 8.1 Comparison between the average grain sizes produced by ECAP followed by dynamic testing with the average grain sizes produced by various SPD techniques in pure copper at room temperature.

Material	**Reference**	**Grain size (nm)**	**Technique**
Oxygen-free Cu (99.95)	Present study	400	1P ECAP + dynamic test
Oxygen-free Cu (99.95)	Present study	330	4P ECAP + dynamic test
Oxygen-free Cu (99.95)	Present study	300	8P ECAP + dynamic test
Pure Cu (99.96%) [37]	Horita *et al*. (2005)	140	HPT
Pure Cu (99.98%) [181]	Lugo *et al*. (2010)	500	ECAP
Pure Cu (99.995%) [314]	Wang *et al*. (2006)	100	SMAT
Pure Cu (99.9%) [311]	Zhilyaev *et al*. (2008)	320	HPT
Pure Cu (99.9%) [311]	Zhilyaev *et al*. (2008)	500	ECAP
Pure Cu (99.9%) [311]	Zhilyaev *et al*. (2008)	310	ECAP + HPT
Oxygen-free Cu (99.98%) [74]	Dobatkin *et al*. (2007)	230	ECAP
OFHC Cu (99.99+%) [52]	Al-Fadhalah *et al*. (2013)	450	HPT
Pure Cu [312]	Zhilyaev *et al*. (2014)	370	HPT
Pure Cu (99.96%) [192]	Komura *et al*. (1999)	270	ECAP
Pure Cu (99.98%) [49]	Lugo *et al*. (2008)	150 - 300	ECAP
Pure Cu (99.98%) [49]	Lugo *et al*. (2008)	100 - 300	HPT
Pure Cu (99.98%) [49]	Lugo *et al*. (2008)	400 - 700	ECAP + HPT
Pure Cu (99.99%) [313]	Zhilyaev *et al*. (2013)	210	ECAP + HPT

8.3.3 Influence of temperature on grain refinement at a strain rate of 5500 s^{-1}

A detailed inspection of Figure 8.20 shows that the flow stress of oxygen-free copper is dependent on temperature during dynamic testing for the specimens processed by 4 and 8 ECAP passes. It is obvious from Figure 8.20(b and c) that the strength decreases when the temperature is increased to 473 K. This is consistent with previous studies on UFG-copper [301,302], pure titanium [101], 7075 aluminum alloy [113] and AZ31 magnesium alloy [336]. Surprisingly, the temperature has only a minor effect on the 1 pass specimen, see Figure 8.20(a). No loss in strength was observed in the 1 pass specimen when dynamic testing was carried out at 473 K. Obviously, both the 4 pass and 8 pass specimens lost strength with increase in temperature, with the loss appearing to be greater for the 8 pass specimen, see Figure 8.20(b) and Figure 8.20(c). Figure 8.20(c) shows bigger strength gap between 298 K and 473 K in 8 pass and smaller gap in 4 pass as shown in Figure 8.20(b).

It is well established that high strain rate deformation due to dynamic testing enhances the strength of materials [106,108,112], however this factor decreases with increase in test temperature [101,113,301,302,336]. These studies are in a good agreement with the present study of oxygen-free copper. Nonetheless, the 1 pass specimen is thermally stable and no change in the true stress is observed due to deformation at a higher temperature, 473 K compared to 298 K, whereas the strength of both 4 pass and 8 pass specimens decreased with increase in temperature as shown in Figure 8.20.

The loss in strength is larger in the 8 pass than the 4 pass specimen. This could be attributed to the difference in the initial microstructure in the two specimens prior to the dynamic testing. In this case the initial microstructure was produced by ECAP at 298 K and each specimen was subjected to a different level of deformation by ECAP, the different grain sizes and dislocation densities meant different amounts of stored energy. A close inspection to Figure 8.21(a) shows that the dislocation density of the 1 pass specimen was increased to the same level after dynamic testing at either 298 K or 473 K. The increase of dislocation density is due to the addition of the new dislocations generated during deformation to the existing dislocations.

On the other hand, the 4 pass specimen shown in Figure 8.21(b) shows a similar trend to that of the 1 pass specimen when dynamic testing was carried out at 298 K (the dislocation density increased), however, when the dynamic testing was carried out at 473 K the dislocation density decreased. Examining the OIM image shown in Figure 8.9(b), the microstructure of the 4 pass specimen consisted of an array of dislocation-free grains with UFGs mixed with large grains, indicating the occurrence of recrystallization and grain growth.

The behavior of the 8 pass specimen is different from either the 1 pass or 4 pass specimens after dynamic testing at 298 K. The dislocation density decreased as shown in Figure 8.21(c) and dislocation-free grains shown in Figure 8.9(c) produced after testing, indicate the occurrence of DRX. This was discussed earlier in Section 8.3.2. Inspection of the OIM image of the 8 pass specimen shows a mixture of small and large grains after deformation at 473 K. Also, the significant drop in dislocation density shown in Figure 8.21(c) along with the substantial decrease of the fraction of HAGBs shown in Figure 8.13(c) after testing at 473 K, provide evidence of the occurrence of recrystallization and grain growth.

These results agree with the microhardness measurements shown in Figure 8.22. A significant drop in microhardness values is observed with increasing the testing temperature from 298 K to 473 K for both the 4 pass and 8 pass specimens as shown in Figure 8.22(b) and Figure 8.22(c), respectively. Only a minor drop is observed for the 1 pass specimen, see Figure 8.22(a). For all three ECAP conditions (1, 4, 8 passes) there was a sharp drop in grain size after dynamic testing at room temperature. For the 1 pass specimen there is no noticeable change in the grain size when testing temperature was raised from 298 K to 473 K, see Figure 8.22(a), and both microstructures show reasonable homogeneity with ultrafine and equiaxed grains as shown in Figures 8.8(a) and 8.9(a) as well as high fraction of HAGBs as shown in Figures 8.12(a) and 8.12(b). However, grain coarsening was observed for both 4 pass and 8 pass specimens, as shown in Figure 8.22(b) and Figure 8.22(c), respectively.

It can be seen from these results that there was no major effect due to temperature on the 1 pass specimen, but for the 4 and 8 pass specimens there was a significant temperature effect and the hardness value is similar to the annealed condition indicating that the microstructure evolved by recrystallization.

To visualize the temperature effect on the flow stress, the change of flow stress with increase in temperature from 298 K to 473 K is shown in Figure 8.25 for 1 pass, 4 passes and 8 passes then further deformed by a SHPB dynamic test at a strain rate of 5.5×10^{3} s^{-1}. For the case of 1 pass, as can be seen from Figure 8.25(a), the flow stress increased with increase in temperature for true strain values 0.05 to 0.15; for values of 0.20 and 0.25 it decreased. However, Figure 8.25(b - c) shows that the flow stress decreased with increasing temperature for all five true strain values for both the 4 pass and 8 pass specimens.

The temperature effect on the work hardening rate is shown in Figure 8.26. Similar work hardening rates are observed in the 1 pass specimen after dynamic testing at both 298 K and 473 K, as shown in Figure 8.26(a). However, with the 4 and 8 pass specimens, the work hardening rate decreases more rapidly when dynamic testing at 473 K compared to 298 K, as shown in Figure 8.26(b) and Figure 8.26(c), respectively. It is readily apparent that the decrease in the work hardening rate due to change in temperature is faster for the 8 pass specimen than the 4 pass.

It is well established that the amount of stored energy during deformation is a critical factor driving the onset of recrystallization [337]. As the strain increases during the ECAP process with increasing number of passes (from 1 to 8), the amount of the stored energy increases: the 1 pass specimen has the lowest, and the 8 pass specimen has the highest stored energy. Recrystallization is initiated when sufficient deformation is reached, this occurs faster (or at a lower temperature) in the more highly deformed specimen.

Initial grain size is another factor influencing recrystallization [337]. Specimens with larger initial grain size (the 1 pass specimen) tend to have less nucleation sites in the grain boundaries and therefore slower recrystallization than specimens with smaller initial grain size (8 pass specimen). In addition, increasing the testing temperature increases the nucleation rate and leads to faster recrystallization [337]. Thus, we can say the 1 pass specimen was least deformed and the stored energy was not sufficient to initiate recrystallization during SHPB testing at either 298 K or 473 K. On the other hand, the 4 pass specimen was deformed by ECAP to higher strain so the stored energy was higher, however, it did not have sufficient stored energy to

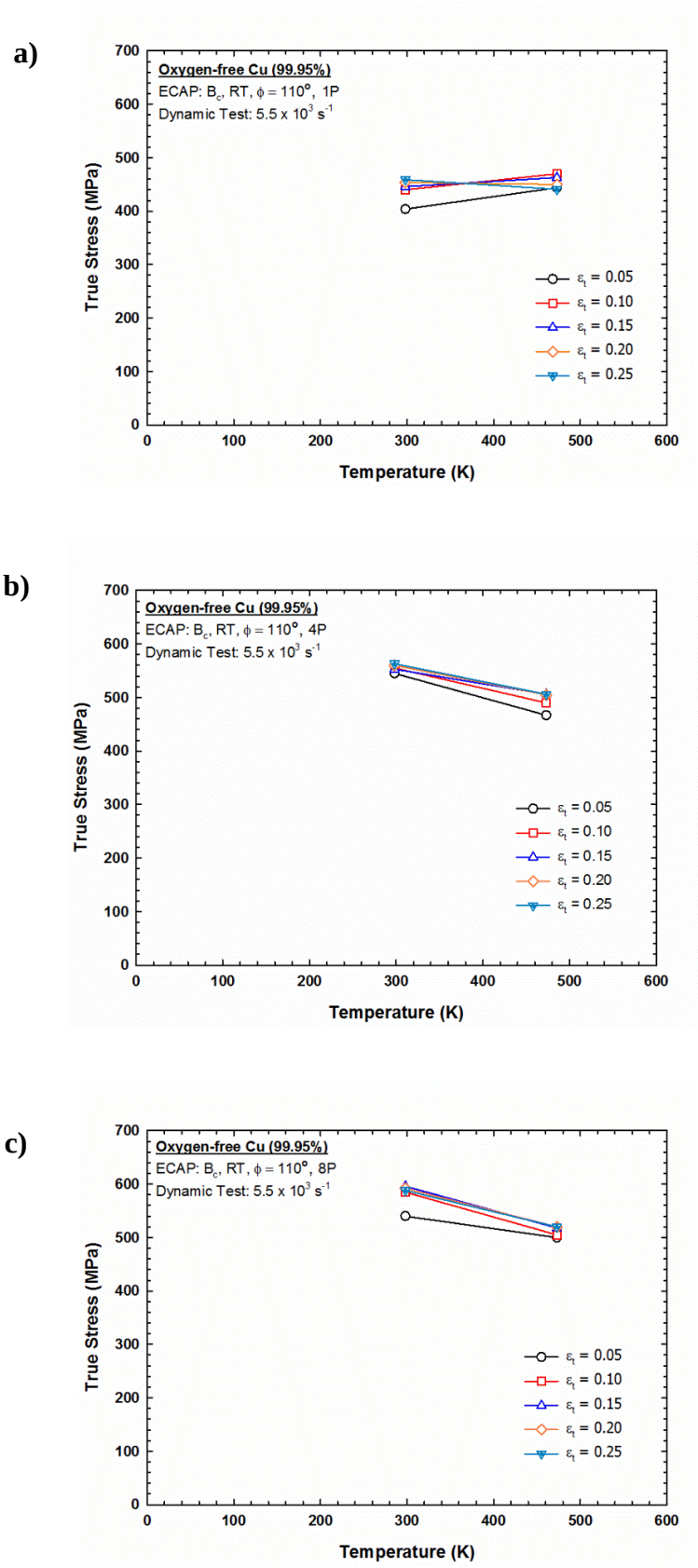

Figure 8.25 The variation of flow stress with respect to temperature for various true strains in oxygen-free copper processed by ECAP for a) 1 pass, b) 4 passes and c) 8 passes, then further deformed by SHPB dynamic test at a strain rate of 5.5×10^3 s^{-1}.

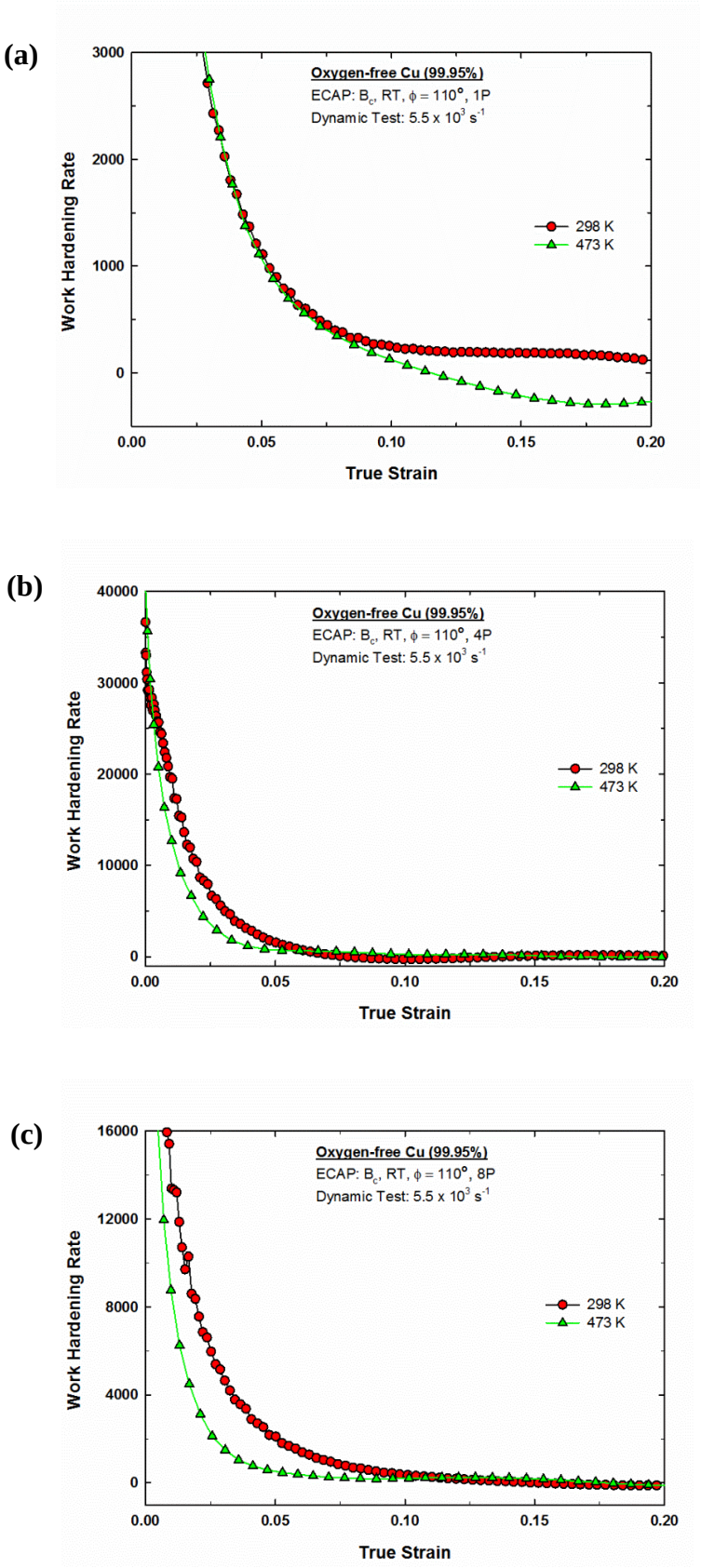

Figure 8.26 Work hardening rate with respect to the true strain for oxygen-free copper processed by ECAP for (a) 1 pass, (b) 4 passes and (c) 8 passes, then further deformed by SHPB dynamic test at a strain rate of 5.5×10^3 s^{-1} at 298 K and 473 K.

start recrystallization when deformed by SHPB at 298 K. Increasing the test temperature to 473 K led to recrystallization and grain growth as shown in Figure 8.6.

There was more stored energy in the 8 pass specimen than for the 4 pass specimen and it was enough for recrystallization to take place during SHPB testing at 298 K. The stored energy was high enough to cause the onset of recrystallization at a lower temperature. However, grain growth was observed in the 8 pass specimen deformed at 473 K because the stored energy produced by ECAP and the higher testing temperature was sufficient to start recrystallization and grain growth.

The discrepancy observed between the dynamic curves obtained during the test at 473 K as shown in Figure 8.2(b) and the microhardness and XRD results, see Figure 8.3 and Figure 8.17, obtained after the dynamic test could be attributed to the occurrence of softening after the test. A possible explanation for this might be that recrystallization occurred when the sample was in the heating device before or after the test, between the time of impact and the time of removing the sample from the device.

8.3.4 Influence of strain rate

The dislocation density and crystallite size after dynamic testing are shown in Figures 8.23 and 8.24, respectively, for each processing condition. These results demonstrate that the 1 pass specimen has low sensitivity to strain rate and temperature as shown in Figures 8.23(a) and 8.24(a), whereas the 4 pass specimen is less sensitive to strain rate at 298 K than at 473 K, as shown in Figures 8.23(b) and 8.24(b). On the other hand, the 8 pass specimen is sensitive to strain rate at both temperatures, and a drop in the dislocation density was observed as shown in Figure 8.23(c), however it was more pronounced at 473 K.

These results provide further support for the hypothesis that the mechanical properties of oxygen-free copper are highly affected by the initial microstructure produced by ECAP prior to dynamic testing. The initial microstructure can highly influence the strain rate and temperature sensitivities.

Figure 8.27 shows the variation of true stress with respect to strain rate for ECAP processed copper tested at 298 K within the strain rate range of 1.0×10^{-3} s^{-1} to 10 s^{-1}. Table 8.2 presents the strain rate sensitivity, m, calculated using Equation 6.1, $m = \left[\frac{\partial log\sigma}{\partial \log \dot{\varepsilon}}\right]$, where σ is the true stress and $\dot{\varepsilon}$ is the strain rate.

It can be seen from Figure 8.27 that the true stress of oxygen-free copper at 298 K increases with increasing strain rate and the strain rate sensitivity increases monotonically with increasing number of passes. Strain rate sensitivities for 1, 4 and 8 passes are 0.007, 0.009 and 0.014, respectively, were recorded when going from quasi-static to a dynamic strain rate of 10 s^{-1}. Similar results of strain rate sensitivity enhancement after dynamic testing have been reported in earlier studies [103,112,301,338].

The variation of true stress with respect to strain rate for oxygen-free copper processed by ECAP for (a) 1 pass, (b) 4 passes and (c) 8 passes then tested by dynamic test at 298 K and 473 K for strain rate range of 10 s^{-1} to 5.5×10^{3} s^{-1} is shown in Figure 8.28. It is readily apparent that the true stress increases with increasing strain rate for 1, 4 and 8 passes, for both 298 K and 473 K. It is also apparent the samples exhibit higher strain rate sensitivities at 473 K than 298 K.

Thus, based on the strain rate sensitivities in Table 8.2 it is anticipated that the 1 pass specimen will exhibit greater strength after dynamic testing and the 8 pass specimen will exhibit higher ductility after dynamic testing, in comparison to the specimens processed by ECAP only. This might also be due to the increase of HAGBs and the decrease in the dislocation density that is observed after dynamic testing the 8 pass sample as shown in Figure 8.18(c), which improves the dislocation storage and increases the capacity for work-hardening. Therefore, it is concluded that the initial microstructure of oxygen-free copper processed by ECAP can highly influence the grain refinement mechanism and mechanical properties during subsequent deformation by dynamic testing at high strain rate.

Table 8.2 Strain rate sensitivities values (m) for oxygen-free copper testing by dynamic tests at different ranges of strain rates and temperatures.

No. of ECAP passes	Dynamic Test Temperature (K)	Strain rate sensitivity (m)	
		$\dot{\varepsilon} = 10^{-3}$ s^{-1} – 10 s^{-1}	$\dot{\varepsilon} = 10$ s^{-1} – 5500 s^{-1}
1	298	0.007	0.019
	473	–	0.064
4	298	0.009	0.026
	473	–	0.058
8	298	0.014	0.025
	473	–	0.072

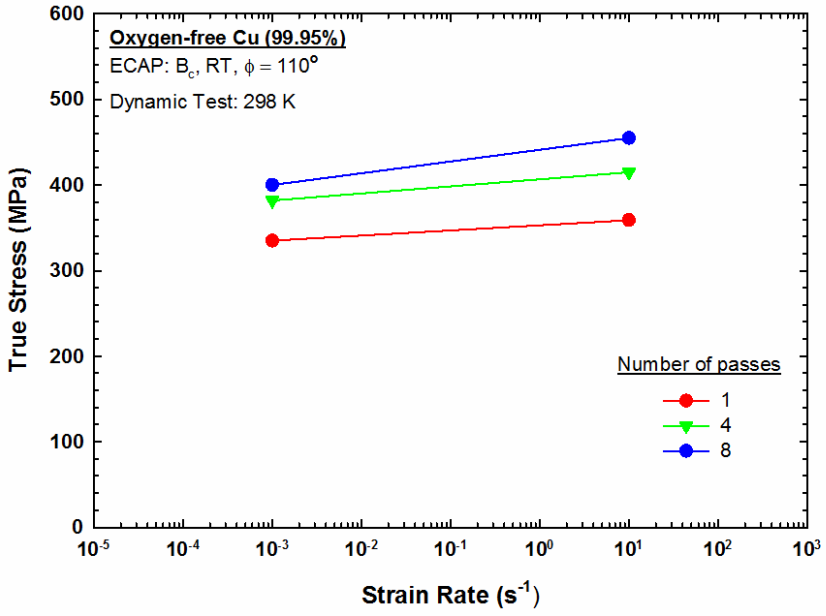

Figure 8.27 The variation of true stress with respect to strain rate for ECAP processed copper tested at 298 K for strain rates of 1.0×10^{-3} s^{-1} and 10 s^{-1}.

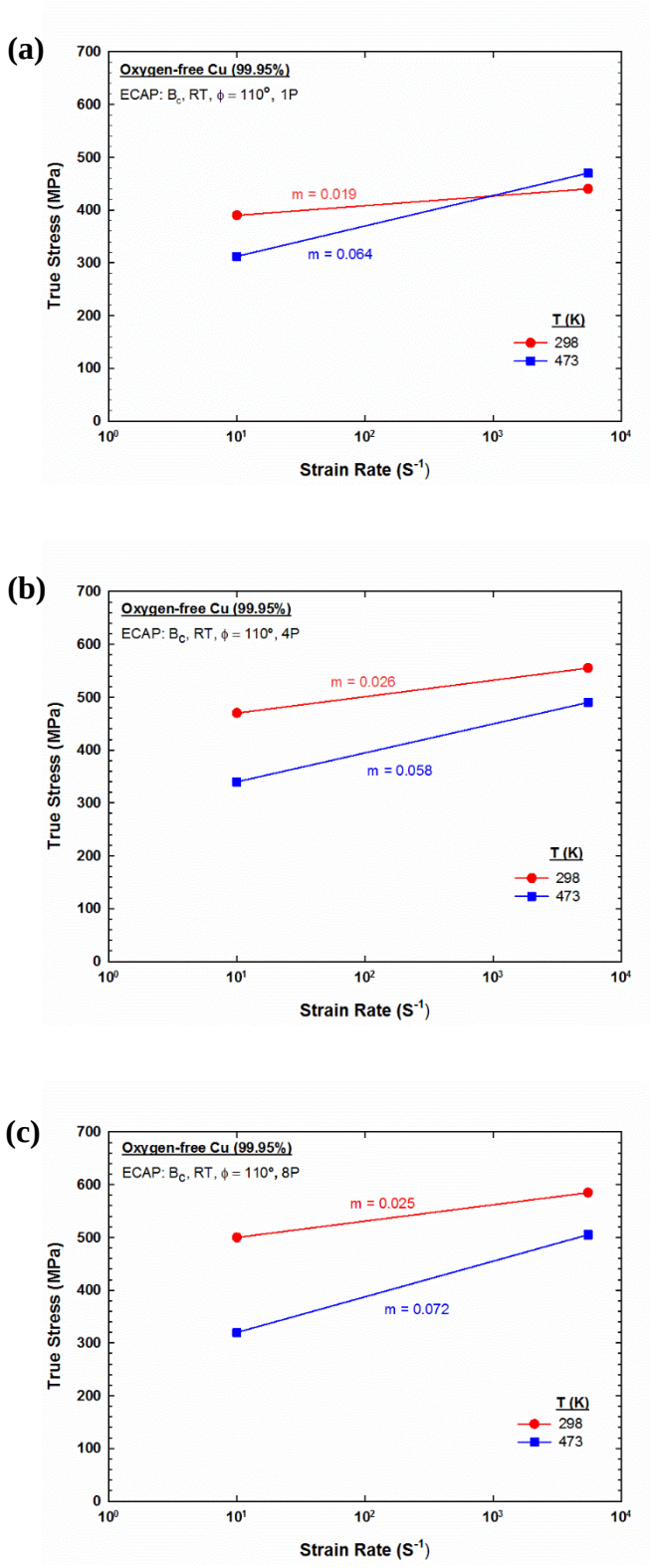

Figure 8.28 The variation of true stress with respect to strain rate for oxygen-free copper processed by ECAP for (a) 1 pass, (b) 4 passes and (c) 8 passes then tested by dynamic test at 298 K and 473 K for strain rate range of 10 s^{-1} to 5.5×10^{3} s^{-1}. (The number next to the line is the strain sensitivity value).

The influence of strain rate and deformation temperature on the microstructure and deformation mechanism of oxygen-free copper processed by dynamic testing can be expressed by the Zener-Hollomon parameter, Z [190], as follows:

$$Z = \dot{\varepsilon} \exp\left(\frac{Q}{RT}\right), \quad (9.3)$$

Where $\dot{\varepsilon}$ is the strain rate, Q is the activation energy for diffusion which is 203600 J m^{-2} [114], R is the universal gas constant and T is the absolute temperature. Table 8.3 shows the calculated values of Z for different strain rates and temperatures used during dynamic testing, and it can be seen that the value of Z increases with increasing the strain rate and/or decreasing temperature.

Table 8.3 Zener-Hollomon parameter (Z) values calculated at different strain rates and temperatures for oxygen-free copper processed by dynamic testing.

Temperature (K)	**Strain rate (s^{-1})**	**Z**
298	10	4.88×10^{36}
298	5.5×10^{3}	2.68×10^{39}
473	10	3.05×10^{23}
473	5.5×10^{3}	1.68×10^{26}

8.4 Summary

1. Oxygen-free copper was processed by ECAP for 1, 4 and 8 passes at room temperature then further deformed by dynamic tests at 298 K and 473 K using strain rates of 10 s^{-1} and 5.5×10^{-3} $s^{-1.}$

2. The results show that, after dynamic testing, each condition had different strengths, dislocation densities, average grain sizes and crystallite sizes. The yield strength and dislocation density increased while grain and crystallite sizes decreased with increasing the number of ECAP passes prior to dynamic testing.

3. The mechanical properties obtained after dynamic testing can be influenced by the initial microstructural conditions produced by ECAP, once these conditions are in the initial fragmentation stage. The closer these conditions are towards saturation prior to dynamic testing, the lower is the effect of dynamic testing on the mechanical properties and microstructure.

4. The pre-existing stresses and dislocation density produced in the specimen by ECAP will influence the grain refinement mechanism during dynamic testing. The highly stressed specimen (8 passes) provide a high driving force for DRX during dynamic testing while 1 pass specimen can accommodate more dislocations and the grain refinement mechanism mainly occurs due to by dislocation activities.

5. It is believed that the microstructure of the 8 pass specimen was evolved through mechanically induced DRX since the cooling time for the adiabatic heating was fast which did not provide a sufficient time for the kinetics of recrystallization to take place.

6. The initial microstructure produced by ECAP prior to dynamic testing will influence strain rates and temperature sensitivities. The highly pre-deformed specimen is more susceptible to temperature and strain rate whereas the lightly pre-deformed specimen is more stable.

7. Dynamic testing can be as effective as many SPD techniques in producing ultrafine and equiaxed grains with a high proportion of high-angle boundaries.

Chapter 9 General Discussion on the Different Softening Mechanisms Produced by SPD at Room Temperature

This study has shown that oxygen-free copper is an active material at room temperature and exhibits softening at large strains. Different softening mechanisms were observed during and after the SPD processing due to the intensive strain induced by various SPD techniques as listed in Table 9.1. It is was shown from ECAP (Chapter 4) and HPT (Chapter 5) experiments that dynamic recovery occurs at equivalent strain larger than 12 and it is associated with increasing the crystallite size and misorientation angles while decreasing the dislocation density. It can also be seen from Table 9.1 that there is a transition from hardening to softening at higher strains in each SPD experiment and this is described by the storage and annihilation of dislocations according to [339]:

$$\sigma \propto \rho_{total} = \rho_{storage} - \rho_{annihilation} \tag{9.1}$$

The total dislocation density is highest at 16 passes of ECAP and 1/2 turn of HPT indicating that dislocation storage reaches saturation at these conditions as shown in Table 9.1. Apparently, the annihilation of dislocations becomes more active at larger strains ($\varepsilon_{eq} \geq 12$) beyond 16 passes of ECAP, and 1/2 turn of HPT which leads to a decrease in the strength of oxygen-free copper as a consequence of the decrease in the total dislocation density.

Dislocation annihilation occurs by cross slip of screw dislocations and climb of edge dislocations. It is known that the extent of dislocation dissociation is dependent on the likelihood of cross-slip and, because copper's stacking fault energy is intermediate, dissociation is at a moderate level. In reality, thermal fluctuations in the crystalline lattice generate cross-slip and, on the assumption that constriction and cross-slip energies are equal, earlier calculation have shown that the expected cross-slip waiting time for UFG copper is such that easy recovery can occur [290].

When the density of deformation-induced vacancies and/or internal stresses attain a critical value, as might occur at high strain SPD processing, recovery can also take place due to climb. It has been stated that HPT-deformed copper contains miniature vacancy clusters which occur due to the accumulation of vacancies generated by deformations,

and an elevated dislocation density [216]. Such observations correspond to the existence of non-equilibrium grain boundaries in materials processed by SPD with surplus grain boundary energies [340].

Table 9.1 Softening mechanisms occurring in oxygen-free copper processed by different SPD techniques.

SPD Process	Temperature	Hardening	Softening	Mechanism
ECAP	298 K	1 – 16 passes	> 16 passes	Dynamic recovery
ECAP + Dynamic test	298 K	1 – 4 passes	8 passes	Dynamic recrystallization
ECAP + Dynamic test	473 K	1 pass	4 – 8 passes	Dynamic /Static recrystallization
HPT	298 K	1/4 – 1/2 turns	1–10 turns	Dynamic recovery
Post-HPT storage	298 K	−	1/4 – 1/2 turn	Static recrystallization
			1, 3 and 10 turns	Recovery

The present study also showed that self-annealing has taken place after storing the HPT samples of oxygen-free copper for 12 months at RT. Self-annealing occurred due to recovery and recrystallization. One interesting finding is that discs processed through lower numbers of turns (N = 1/4 and 1/2) exhibit different softening mechanisms than discs processed by higher numbers of turns (N = 3, 5 and 10) as shown in Table 9.1. Localized recrystallization was observed at the edges of discs processed by fractional numbers of turns whereas recovery occurred across the diameters of the discs processed by higher numbers of turns. This is attributed to the higher dislocation density generated

by HPT after 1/2 turn in comparison to the lower dislocation density in the subsequent turns as shown in Figure 7.17. The discs with higher numbers of turns have lower dislocation density because they exhibit strain softening by dynamic recovery during the HPT process which diminishes the driving force for recrystallization. If the high dislocation density produced by HPT is not recovered by cross-slip and/or climb, it will provide a driving force for recrystallization as shown in N = 1/4 and 1/2.

Recovery and recrystallization are related to the degree of dislocation dissociation. Materials with low SFE have a high degree of dislocation dissociation which hinders the annihilation of dislocations by cross-slip. In contrast, dynamic softening is faster in high SFE materials, where the degree of dislocation dissociation is low, due to the higher mobility of dislocations [215]. With an intermediate SFE, copper is a transitional material between low and high SFE. The internal stresses generated by HPT can highly influence the activation energy for the cross-slip and can assist or impedes its motion [290]. These internal stresses can increase the waiting time for the dislocation annihilation by cross-slip and delay the recovery process (which is 12 months in this study).

The localized softening occurring at the edges of the discs deformed by low numbers of turns is due to the higher dislocation densities in comparison to the central region. This is due to the variation of the imposed strain produced by HPT. Less time is needed to attain a steady dislocation density while stored at RT due to faster recovery rates which is directly related to the higher concentrations of dislocation that produced after HPT. The higher the dislocation density, the less the average spacing between dislocations, the higher the assisting stresses, and the faster annihilation by cross-slip [290]. A possible explanation of the stability in the central regions within the storage time of 12 months is the higher mean spacing between dislocations and lower assisting stresses.

Climb is a mechanism controlled by diffusion, and is significant only at higher temperatures. However, earlier studies reported that diffusion can be more rapid in materials subjected to severe plastic deformation than in their coarse-grained counterparts by as much as several magnitudes due to their high concentration of dislocations and their greater density of grain boundaries [341]. Thus, it is possible that climb can assist in dislocation annihilation, even at RT.

Processing oxygen-free copper by ECAP followed by the dynamic test at 298 K showed hardening in the samples deformed by 1 and 4 passes while recrystallization was observed in the samples deformed by 8 passes, as shown in Table 9.1. The grain refinement mechanism was mainly by dislocation activities in the specimen processed by 1 pass whereas it was through dynamic recrystallization for the specimen processed by 8 passes. This is due to the higher dislocation density and stored energy produced by 8 passes of ECAP that provide a higher driving force for recrystallization, as discussed earlier in this section. Increasing the strain reduces the temperature for the onset of recrystallization [337].

After increasing the temperature to 473 K, the sample processed by 4 passes became thermally unstable. Increasing the testing temperature increases the nucleation rate and leads to faster recrystallization [337]. Nucleation and growth become faster in the sample processed by 4 passes at 473 K, and larger grains were observed as shown in Figure 8.8. Figure 8.27 shows that the influence of strain rate became more significant with increasing number of passes. Softening was observed when increasing the strain rate in the highly deformed samples by ECAP (8 passes) at 298 K. This might be due to the high speed compression at a higher strain rate that stores considerable energy within the material which provides a driving force for recrystallization.

The amount of the annealing twins observed in the microstructure after deformation is an indicative of the type of the recrystallization. An earlier study on pure copper tested by hot torsion at high strain rates have shown that high numbers of annealing twins provide an evidence of static recrystallization whereas low numbers indicates the occurrence of dynamic recrystallization [342]. Also, smaller grains were observed in the microstructure evolved by dynamic recrystallization than the gains observed in the microstructure evolved by static recrystallization [342]. This is consistent with the present study where high fraction of annealing twins was observed after storing oxygen-free copper for 12 months after HPT whereas low fraction was observed after dynamic testing.

Dislocation behaviour can be influenced by purity, crystal structure, stacking-fault energy and homologous temperature (T_H), and it has been reported that the contributions of recrystallization and recovery (dynamic softening) to the decrease in hardness grow increasingly important as the stacking-fault energy and T_H increase [212]. Thus, the

dynamic softening would be assumed to be the prevailing mechanism for decrease in hardness in very low-melting point metals [212].

When processing by HPT, T_H is the controlling parameter in defining the steady-state grain size in high-purity metals. As the T_H rises there will be a corresponding increase in the impact of dynamic mechanical softening on reduction of hardness in the steady-state [212].

A T_H value of 0.35 is not sufficient for recrystallization to occur within metals subject to deformation by such established processing mechanisms as forging and rolling. There would be expected to be a substantial force pushing towards recrystallization in materials processed by SPD, because of the occurrence of extended areas of non-equilibrium grain boundaries and an elevated dislocation density [34,343].

Kilmametov *et al.* [226] have assessed vacancy concentrations in copper by means of X-ray diffraction, for HPT operated at RT. They found the excess vacancy distribution was as high as was normally found at thermal equilibrium near the metal's melting point. A vacancy concentration as high as this increases diffusivity by decreasing the activation energy necessary for atomic diffusion.

Previous experiments on copper had suggested that to explain the development of dislocation-free grains, the activation energy required for diffusion, should be between half and two-thirds of the activation energy for lattice diffusion [204]. These authors proposed that the HPT process generated an adequate number of lattice defects for the evolution of microstructure despite the T_H value being only 0.32.

For this research it is essential to consider that the decreased stability of UFG Cu could affect its feasibility as a structural material. However, from the results obtained in this research, difficulties related to softening can be forestalled by using a relatively low strain when processing using SPD, and so prevent substantial degradation of strength during the component's working life. Additionally, alloying can be used to delay softening of UFG copper and extend the stability of the microstructure for long periods of time; however, ductility could be affected. Thus, an additional heat-treatment method can be used such as short-term annealing after SPD processing to alter the microstructure and provide the best combination of strength and ductility.

Chapter 10 Conclusions and Future Work

10.1 Conclusions

Oxygen-free copper with a commercial purity of 99.95% was processed at room temperature by two SPD techniques: HPT and ECAP. Copper discs were processed by HPT under an applied pressure of 6.0 GPa using quasi-constrained conditions by 1/4, 1/2, 1, 3, 5 and 10 turns, and billets were processed by ECAP through $\Phi = 110°$ channel angle using Route B_C for 1, 2, 4, 6, 8, 16, 20 and 24 passes. The microstructural evolution was investigated using optical microscopy, EBSD and XRD, and the mechanical properties were investigated using Vickers microhardness and tensile tests. The conclusions of this study are summarized as follows:

Microstructural examination showed a significant grain refinement after ECAP. The average grain size reduced with increasing number of passes. The grains were large and elongated in the early stages of deformation with an average grain size of ~24 μm and became well-defined equiaxed grains with an average size of ~600 nm after 24 passes. The proportion of HAGBs increased with increasing numbers of passes to approximately 88%.

The evolution of microhardness on ECAP billets was measured by recording individual measurements along the diameter of each disc (cross-sectional plane) and plotting colour-coded contour maps over the entire surface of the cross-sectional and longitudinal planes. A significant increase in the microhardness value was observed after 1 pass (~90 Hv) in comparison to the hardness value of ~ 41 Hv for the annealed sample. The microhardness values increased with increasing numbers of passes up to 16 (at equivalent strain ~12) then decreased after 24 passes. Reasonable homogeneity in hardness distribution was achieved over the cross-sectional and longitudinal planes after 24 passes with an average hardness value of ~120 Hv.

The XRD measurements obtained from ECAP samples revealed an increase in the dislocation density and a decrease in the crystallite size with increasing numbers of passes up to 16, followed by a decrease in the dislocation density and an increase in the crystallite size after 24 passes. The drop in dislocation density and microhardness together with the

increase in the crystallite size suggests that recovery behaviour took place during the ECAP process after reaching a critical equivalent strain of ~12.

A substantial grain refinement was achieved after HPT. The average grain size was reduced from ~24 μm to ~510 nm after 10 turns. Due to the variation of the equivalent strain across the diameter of the disc, a noticeable difference in the average grain size between the centre and edge of the disc was observed in the early stages of deformation, but diminished with increasing torsional strain with higher numbers of turns. Coarse grains were observed in the centre of the disc while fine grains were produced at the edges at lower numbers of turns, and the microstructure reached reasonable homogeneity with equiaxed grain. Also, the proportion of HAGBs increased and the variance between the centre and edges of the disc diminished with increasing number of turns to reach ~84% across the diameter of the disc.

The evolution of microhardness homogeneity on HPT discs was measured by recording individual measurements along the diameter of each disc and plotting colour-coded contour maps for the entire surfaces. The microhardness values increased significantly in the central and peripheral regions with a modest torsional strain, however the microhardness distribution was inhomogeneous, and the peripheral region showed higher values than the central region. The variation in hardness corresponds to the local variation of imposed strain and the strain gradient across the disc, as well as the SFE. The difference in hardness values diminished and a homogenous hardness distribution was reached across the disc after 3 turns. The average microhardness value of ~128 Hv was recorded after 10 turns.

Oxygen-free copper showed hardening behaviour with recovery when the average microhardness values were plotted with respect to the equivalent strain. This behaviour is similar to the behaviour reported for Aluminium but, based on earlier studies, copper usually shows hardening without recovery. The hardness increased at low equivalent strain, then softening occurred when the equivalent strain reached ~12 then saturated at an equivalent strain of ~50.

The analysis based on XRD measurements was in agreement with the hardening behaviour with recovery observed in hardness measurements. The XRD results show an increase in the dislocation density and a decrease in the crystallite size after HPT

processing for up to 1/2 turn, followed by a decrease in dislocation density and an increase in the crystallite size associated with a higher number of turns. The softening is attributed to a recovery mechanism similar to the one observed during the ECAP process.

The direct influence of recovery behaviour on the tensile properties were investigated by pulling the samples processed by ECAP and HPT to failure with a strain rate of 1.0×10^{-2} $s^{-1,}$ 1.0×10^{-3} s^{-1} and 1.0×10^{-4} s^{-1}. A simultaneous rise in strength and ductility was observed. Yield stress, UTS, uniform elongation and elongation to failure increased with increasing strain during deformation. Grain size strengthening and dislocation strengthening are two mechanism contributing to the enhanced strength of oxygen-free copper, while the increase in ductility is related to a dynamic recovery mechanism whereby the dislocation annihilation process reduces the dislocation density in the presence of HAGBs, which increases the mean free path of dislocations and restores the work-hardening ability. Higher ductility but lower strength was attained with decreasing strain rate

The microstructural stability and self-annealing effect was investigated by storing HPT discs for 12 months at room temperature. The results show that softening has taken place during the storage period in all HPT discs but different softening mechanisms were observed. Hardness measurements show a significant decrease in the samples processed by a low number of turns, N = 1/4 and 1/2. The decrease in hardness was localized to an area near to the edge of the disc and the average hardness value decreased from ~138 Hv to ~100 Hv within this region. The microstructure consisted of a mixture of ultrafine and large grains which are free of dislocations. This grain growth was associated with a significant increase in the fraction of Σ3 boundaries indicating the occurrence of recrystallization during the time of storage. This is due to the higher dislocation density and stored energy at the edges of the disc produced by the variation of the imposed strain during HPT processing which provides a driving force for recrystallization.

Better microstructural stability was observed in the samples processed by a higher number of turns, N = 3, 5 and 10 and stored at room temperature for 12 months. The decrease in hardness was minor (~10 Hv) and it was relatively uniform across the diameters of the discs. The fractions of LAGBs increased at the expense of HAGBs indicating the occurrence of recovery after 12 months storage at RT. These discs did not experience a significant softening even though they were processed by very large strains

because the dynamic recovery which took place during the HPT process and reduced the dislocation density and thus diminished the driving force for recrystallization.

Tensile tests were repeated at strain rate of 1.0×10^{-2} s^{-1} after storage for 12 months and the results showed that the ductility was enhanced in compensation of strength. A minor decrease in the yield stress was attained in the samples processed by 1, 3 and 10 turns, but it was significantly reduced for lower numbers of turns. The samples processed by a lower number of turns (N = 1/2 and 1) exhibit a slightly higher elongation to failure in comparison to the samples processed by 3 and 10 turns. Additionally, the samples stored for 12 months show highest uniform elongation after 1/2 turn and reduced with further turns. The occurrence of recovery and/or recrystallization increases the ability of strain hardening by dislocation annihilation and produces dislocation-free grains which lead to the enhancement of ductility.

The thermal stability and deformation mechanism of UFG copper subjected to 1, 4 and 8 passes of ECAP under a high strain rate were investigated using dynamic testing at temperatures of 298 K and 473 K and at strain rates of 10 s^{-1} and 5.5×10^{3} s^{-1}. The average grain sizes of ~300 nm and ~400 nm produced by dynamic testing at 298 K and strain rates of 10 s^{-1} and 5.5×10^{3} s^{-1}, respectively, are smaller than the average grain size of ~600 nm produced by 24 passes of ECAP and ~510 nm produced by 10 turns of HPT. An ultrafine grained and relatively homogenous microstructure with equiaxed grains was observed, similar to those produced by SPD methods.

The grain refinement mechanism was mainly by dislocation slip in the specimen processed by 1 pass whereas it was through dynamic recrystallization for the specimen processed by 8 passes. This is due to the difference in the dislocation densities and stored energy between ECAP specimens. High speed compression stores considerable energy within the material which provides a driving force for recrystallization.

Increasing the testing temperature to 473 K and/or the strain rate to 5.5×10^{3} s^{-1} strongly influenced the deformation mechanism. It was observed that the 1 pass specimen had better stability than the 4 and 8 pass specimens during dynamic testing at high temperature. This was due to the amount of stored energy and dislocation density produced by ECAP prior to dynamic testing. The 1 pass specimen was least deformed by ECAP and the stored energy was not sufficient to initiate recrystallization by dynamic

testing at either 298 K or 473 K. Also, the 1 pass specimen had larger initial grain size before testing, and so had fewer nucleation sites in the grain boundaries for recrystallization. The dislocation densities, microhardness and work hardening rates decreased in the 4 pass specimen at 473 K even though it was stable at 298 K. This is due to the increase in the nucleation rate with increasing test temperature that leads to faster recrystallization. Recrystallization and grain growth were seen in the microstructure of both 4 pass and 8 pass specimens.

It was concluded that the initial microstructure condition (grain size, dislocation density, internal stresses and stored energy) produced by ECAP can highly influence the deformation mechanism and the mechanical properties of oxygen-free copper when deformed at high strain rates.

This study has shown that oxygen-free copper is an active material at room temperature. The behaviour of oxygen-free copper can change depending on the severity of the processing conditions. Imposing high strain stores energy within the sample but, apparently, oxygen-free copper has the tendency to release this energy during and after the processing which leads to a softening mechanism.

10.2 Recommendations for future work

Microstructural characterization using a transmission electron microscopy will provide a better understanding of the microstructural evolution and deformation mechanisms during ECAP and HPT. DSC analysis will provide information about the stored energy in the material after processing and regarding recrystallization, especially during high strain rate deformation by dynamic testing.

The study of the self-annealing effect could be extended examining the thermal stability of oxygen-free copper after long-term storage at cryogenic temperatures. This procedure tends to decrease the softening mechanisms by preventing or delaying recovery and recrystallization. The change in texture should be examined.

Using a special set up for each of the ECAP and HPT facilities, liquid nitrogen could be used during the processing to prevent the occurrence of dynamic recovery. This would assist in increasing the accumulation of dislocations and lead to enhancement in both strength and ductility. The microstructural evolution and mechanical properties would be examined.

Oxygen-free copper could be processed by HPT at room temperature through a high number of turns, say N = 20 and 30, in order to assess the softening mechanism at higher strain and examine the steady state microstructure with equilibrium grain size. Tensile testing could be conducted at room temperature at different strain rates in order to examine the influence of softening mechanisms on the strength and ductility.

Combining ECAP and HPT is considered to be an alternative procedure for reducing grain size. This procedure displays a high potential for achieving significant grain refinement in metals and decreases the fraction of LABs. Earlier studies have shown that an ECAP + HPT procedure increased the strength of the material, however, based on the outcomes of this study it would be expected that oxygen-free copper will soften at large strains. The microstructural stability during this procedure could be investigated and the microstructural features compared with those that have already been obtained in this study by ECAP and HPT. Also, tensile testing at room temperature could be conducted to study the mechanical properties.

Short-term annealing could be used after processing by ECAP and HPT and the thermal stability investigated. Different temperatures and times would be used to produce a microstructure with the best stability. EBSD and XRD would be performed on selected samples to analyze the microstructure. Short-term annealing after SPD processing has proven to be an effective method for achieving high strength and ductility. The aim of this work would be to find the optimum annealing condition for enhancing strength and ductility and developing a better understanding of the effects of this procedure on oxygen-free copper.

References

[1] E.O. Hall, Proc. Phys. Soc. Sect. B 64 (1951) 747–753.

[2] N.J. Petch, J. Iron Steel Inst. 174 (1953) 25–28.

[3] R.Z. Valiev, R.K. Islamgaliev, I. V Alexandrov, Prog. Mater. Sci. 45 (2000) 103–189.

[4] T.G. Langdon, Acta Mater. 61 (2013) 7035–7059.

[5] R.Z. Valiev, Y. Estrin, Z. Horita, T.G. Langdon, M.J. Zehetbauer, Y.T. Zhu, Jom 58 (4) (2006) 33–39.

[6] A.P. Zhilyaev, G. V. Nurislamova, B.-K. Kim, M.D. Baró, J.A. Szpunar, T.G. Langdon, Acta Mater. 51 (2003) 753–765.

[7] A.P. Zhilyaev, S. Lee, G. V. Nurislamova, R.Z. Valiev, T.G. Langdon, Scr. Mater. 44 (2001) 2753–2758.

[8] R.Z. Valiev, N. Krasilnikov, N.K. Tsenev, Mater. Sci. Eng. A. 137 (1991) 35–40.

[9] J. Wang, M. Furukawa, Z. Horita, M. Nemoto, R.Z. Valiev, T.G. Langdon, Mater. Sci. Eng. A 216 (1996) 41–46.

[10] R.Z. Valiev, E. V. Kozlov, Y.F. Ivanov, J. Lian, A.A. Nazarov, B. Baudelet, Acta Metall. Mater. 42 (1994) 2467–2475.

[11] ASM, ASM Specialty Handbook: Copper and Copper Alloys, ASM International, Materials Park, OH, 2001.

[12] Y. Liu, J. Zhao, Comput. Mater. Sci. 50 (2011) 1418–1424.

[13] U. Engel, R. Eckstein, J. Mater. Process. Technol. 125–126 (2002) 35–44.

[14] R.Z. Valiev, O.A. Kaibyshev, R.I. Kuznetsov, R.S. Musalimov, N.K. Tsenev, Dokl Akad Nauk SSSR (1988) 301–864.

[15] A.P. Zhilyaev, T.G. Langdon, Prog. Mater. Sci. 53 (2008) 893–979.

[16] T.C. Lowe, R.Z. Valiev, Jom 56 (10) (2004) 64–68.

[17] R.Z. Valiev, A.P. Zhilyaev, T.G. Langdon, Bulk Nanostructured Materials: Fundamentals and Applications, Wiley, Hoboken, NJ, USA, 2014.

[18] Y.T. Zhu, T.C. Lowe, T.G. Langdon, Scr. Mater. 51 (2004) 825–830.

[19] X. Zhao, W. Fu, X. Yang, T.G. Langdon, Scr. Mater. 59 (2008) 542–545.

[20] Z. Horita, T. Fujinami, T.G. Langdon, Mater. Sci. Eng. A 318 (2001) 34–41.

[21] V. Latysh, G. Krallics, I. Alexandrov, A. Fodor, Curr. Appl. Phys. 6 (2006) 262–266.

[22] W. Oelerich, T. Klassen, R. Bormann, J. Alloys Compd. 315 (2001) 237–242.

[23] G. Barkhordarian, T. Klassen, R. Bormann, J. Alloys Compd. 364 (2004) 242–246.

[24] R.Z. Valiev, M.J. Zehetbauer, Y. Estrin, H.W. Höppel, Y. Ivanisenko, H. Hahn, G. Wilde, H.J. Roven, X. Sauvage, T.G. Langdon, Adv. Eng. Mater. 9 (2007) 527–533.

[25] Y. Estrin, M. Janecek, G.I. Raab, R.Z. Valiev, A. Zi, Metall. Mater. Trans. A 38 (2007) 1906–1909.

[26] I. Sabirov, M.Y. Murashkin, R.Z. Valiev, Mater. Sci. Eng. A 560 (2013) 1–24.

[27] P.W. Bridgman, Studies in Large Scale Plastic Flow and Fracture, McGraw Hill, New York, 1952.

[28] N. Smirnova, V. Levit, V. Pilyugin, R. Kuznetsov, L. Davydova, V. Sazonova, Fiz Met. Met. 61 (1986) 1170.

[29] C. Xu, Z. Horita, T.G. Langdon, Acta Mater. 56 (2008) 5168–5176.

[30] R.Z. Valiev, Y. V. Ivanisenko, E.F. Rauch, B. Baudelet, Acta Mater. 44 (1996) 4705–4712.

[31] A.P. Zhilyaev, T.R. McNelley, T.G. Langdon, J. Mater. Sci. 42 (2007) 1517–1528.

[32] A. Hohenwarter, A. Bachmaier, B. Gludovatz, S. Scheriau, R. Pippan, Int. J. Mater. Res. 100 (2009) 1653–1661.

[33] A. Vorhauer, R. Pippan, Scr. Mater. 51 (2004) 921–925.

[34] H. Jiang, Y.T. Zhu, D.P. Butt, I. V. Alexandrov, T.C. Lowe, Mater. Sci. Eng. A 290 (2000) 128–138.

[35] Z. Yang, U. Welzel, Mater. Lett. 59 (2005) 3406.

[36] G. Sakai, Z. Horita, T.G. Langdon, Mater. Sci. Eng. A 393 (2005) 344–351.

[37] Z. Horita, T.G. Langdon, Mater. Sci. Eng. A 410–411 (2005) 422–425.

[38] M. Kawasaki, R.B. Figueiredo, T.G. Langdon, Acta Mater. 59 (2011) 308–316.

[39] C. Xu, T.G. Langdon, Mater. Sci. Eng. A 503 (2009) 71–74.

[40] M. Kawasaki, S.N. Alhajeri, C. Xu, T.G. Langdon, Mater. Sci. Eng. A 529 (2011) 345–351.

[41] C. Xu, Z. Horita, T.G. Langdon, Acta Mater. 55 (2007) 203–212.

[42] M. Kawasaki, B. Ahn, T.G. Langdon, Acta Mater. 58 (2010) 919–930.

[43] G.E. Dieter, Mechanical Metallurgy, McGraw-Hill, Singapore, 1988.

[44] Y. Ito, Z. Horita, Mater. Sci. Eng. A 503 (2009) 32–36.

[45] A. Loucif, R.B. Figueiredo, T. Baudin, F. Brisset, T.G. Langdon, Mater. Sci. Eng. A 527 (2010) 4864–4869.

[46] X.H. An, S.D. Wu, Z.F. Zhang, R.B. Figueiredo, N. Gao, T.G. Langdon, Scr. Mater. 63

(2010) 560–563.

[47] T. Ungár, L. Balogh, Y.T. Zhu, Z. Horita, C. Xu, T.G. Langdon, Mater. Sci. Eng. A 444 (2007) 153–156.

[48] L. Balogh, T. Ungár, Y. Zhao, Y.T. Zhu, Z. Horita, C. Xu, T.G. Langdon, Acta Mater. 56 (2008) 809–820.

[49] N. Lugo, N. Llorca, J.M. Cabrera, Z. Horita, Mater. Sci. Eng. A 477 (2008) 366–371.

[50] J. Wongsa-Ngam, M. Kawasaki, Y. Zhao, T.G. Langdon, Mater. Sci. Eng. A 528 (2011) 7715–7722.

[51] J. Wongsa-Ngam, M. Kawasaki, T.G. Langdon, J. Mater. Sci. 47 (2012) 7782–7788.

[52] K.J. Al-Fadhalah, S.N. Alhajeri, A.I. Almazrouee, T.G. Langdon, J. Mater. Sci. 48 (2013) 4563–4572.

[53] M. Kawasaki, B. Ahn, T.G. Langdon, Mater. Sci. Eng. A 527 (2010) 7008–7016.

[54] A.P. Zhilyaev, B.-K. Kim, J.A. Szpunar, M.D. Baró, T.G. Langdon, Mater. Sci. Eng. A 391 (2005) 377–389.

[55] F. Wetscher, A. Vorhauer, R. Stock, R. Pippan, Mater. Sci. Eng. A 387–389 (2004) 809–816.

[56] A.P. Zhilyaev, B.-K. Kim, G.V. Nurislamova, M.D. Baró, J.A. Szpunar, T.G. Langdon, Scr. Mater. 46 (2002) 575–580.

[57] G. Sakai, K. Nakamura, Z. Horita, T.G. Langdon, Mater. Sci. Eng. A 406 (2005) 268–273.

[58] V.M. Segal, I.J. Beyerlein, C.N. Tome, V.N. Chuvil'deev, V.I. Kopylov, Fundametals and Engineering of Severe Plastic Deformation, Nova Science, New York, USA, 2010.

[59] V.M. Segal, V.I. Reznikov, A.E. Drobyshevskiy, V.I. Kopylov, Russ. Met. 1 (1981) 99–105.

[60] R.Z. Valiev, A. V. Korznikov, R.R. Mulyukov, Mater. Sci. Eng. A 168 (1993) 141–148.

[61] R.Z. Valiev, T.G. Langdon, Prog. Mater. Sci. 51 (2006) 881–981.

[62] P.B. Berbon, M. Furukawa, Z. Horita, M. Nemoto, T.G. Langdon, Metall. Mater. Trans. A 30A (1999) 1989–1997.

[63] Y. Huang, T.G. Langdon, Mater. Today 16 (2013) 85–93.

[64] Y. Iwahashi, J. Wang, Z. Horita, M. Nemoto, T.G. Langdon, Scr. Mater. 35 (1996) 143–146.

[65] K. Nakashima, Z. Horita, M. Nemoto, T.G. Langdon, Mater. Sci. Eng. A 281 (2000) 82.

[66] M. Nemoto, Z. Horita, M. Furukawa, T.G. Langdon, Met. Mater. 4 (1998) 1181–1190.

[67] M. Furukawa, Z. Horita, T.G. Langdon, Met. Mater. Int. 9 (2003) 141–149.

[68] Z. Horita, M. Furukawa, M. Nemoto, T.G. Langdon, Mater. Sci. Technol. 16 (2000) 1239–

1245.

[69] K. Oh-ishi, Z. Horita, M. Furukawa, M. Nemoto, T.G. Langdon, Metall. Mater. Trans. A 29A (1998) 2011–2013.

[70] Y. Iwahashi, M. Furukawa, Z. Horita, M. Nemoto, T.G. Langdon, Metall. Mater. Trans. A 29A (1998) 2245–2252.

[71] Y. Iwahashi, Z. Horita, M. Nemoto, T.G. Langdon, Acta Mater. 46 (1998) 3317–3331.

[72] A. Gholinia, P.B. Prangnell, M.V. Markushev, Acta Mater. 48 (2000) 1115–1130.

[73] M. Furukawa, Z. Horita, T.G. Langdon, Mater. Sci. Eng. A 332 (2002) 97–109.

[74] S.V. Dobatkin, J.A. Szpunar, A.P. Zhilyaev, J.-Y. Cho, A.A. Kuznetsov, Mater. Sci. Eng. A 462 (2007) 132–138.

[75] S. Komura, M. Furukawa, Z. Horita, M. Nemoto, T.G. Langdon, Mater. Sci. Eng. A 297 (2001) 111–118.

[76] M. Furukawa, Y. Iwahashi, Z. Horita, M. Nemoto, T.G. Langdon, Mater. Sci. Eng. A 257 (1998) 328–332.

[77] K. Nakashima, Z. Horita, M. Nemoto, T.G. Langdon, Acta Mater. 46 (1998) 1589–1599.

[78] I. V. Alexandrov, G.I. Raab, L.O. Shestakova, R.Z. Valiev, R.J. Dowding, in:, M. Greenfield, J. Oaks (Eds.), Tungsten, Hard Met. Refract. Alloy., Princeton (NJ), 2000, p. 27.

[79] X. Zhao, X. Yang, X. Liu, X. Wang, T.G. Langdon, Mater. Sci. Eng. A 527 (2010) 6335–6339.

[80] K. Furuno, H. Akamatsu, K. Oh-ishi, M. Furukawa, Z. Horita, T.G. Langdon, Acta Mater. 52 (2004) 2497–2507.

[81] D. Yamaguchi, Z. Horita, M. Nemoto, T.G. Langdon, Scr. Mater. 41 (1999) 791–796.

[82] A. Yamashita, D. Yamaguchi, Z. Horita, T.G. Langdon, Mater. Sci. Eng. A 287 (2000) 100–106.

[83] Y.C. Chen, Y.Y. Huang, C.P. Chang, P.W. Kao, Acta Mater. 51 (2003) 2005–2015.

[84] W.H. Huang, C.Y. Yu, P.W. Kao, C.P. Chang, Mater. Sci. Eng. A 366 (2004) 221–228.

[85] A. Goloborodko, O. Sitdikov, R. Kaibyshev, H. Miura, T. Sakai, Mater. Sci. Eng. A 381 (2004) 121–128.

[86] P. Málek, M. Cieslar, R.K. Islamgaliev, J. Alloys Compd. 378 (2004) 237–241.

[87] Y. Nishida, T. Ando, M. Nagase, S. Lim, I. Shigematsu, A. Watazu, Scr. Mater. 46 (2002) 211–216.

[88] G.I. Raab, N.A. Krasilnikov, R.Z. Valiev, in:, Y. Zhu, T.G. Langdon, R.Z. Valiev, L.S. Semiatin, H. Dong, T.C. Lowe (Eds.), Ultrafine Grained Mater. III, TMS, Warrendale, PA, USA, 2004, p. 137.

[89] R.Z. Valiev, I. V Alexandrov, Y.T. Zhu, T.C. Lowe, J. Mater. Res. 17 (2002) 5–8.

[90] N. Krasilnikov, Russ. Met. 3 (2005) 35.

[91] Ry. Lapovok, Russ. Met. 1 (2004) 44.

[92] V.M. Segal, Mater. Sci. Eng. A 197 (1995) 157–164.

[93] Y. Wu, I. Baker, Scr. Mater. 37 (1997) 437–442.

[94] P.B. Prangnell, C. Harris, S.M. Roberts, Scr. Mater. 37 (1997) 983–989.

[95] S.L. Semiatin, D.P. Delo, E.B. Shell, Acta Mater. 48 (2000) 1841–1851.

[96] A. Shan, I. Moon, H. Ko, J. Park, Scr. Mater. 41 (1999) 353–357.

[97] H.S. Kim, Mater. Sci. Eng. A 315 (2001) 122–128.

[98] S.N. Alhajeri, N. Gao, T.G. Langdon, Mater. Sci. Eng. A 528 (2011) 3833–3840.

[99] J. Wongsa-Ngam, M. Kawasaki, T.G. Langdon, Mater. Sci. Eng. A 556 (2012) 526–532.

[100] C. Xu, T.G. Langdon, J. Mater. Sci. 42 (2007) 1542–1550.

[101] L. Wang, Y. Wang, A.P. Zhilyaev, A. V. Korznikov, S. Li, E. Korznikova, T.G. Langdon, J. Mater. Sci. 49 (2014) 6640–6647.

[102] J.E. Field, S.M. Walley, W.G. Proud, H.T. Goldrein, C.R. Siviour, Int. J. Impact Eng. 30 (2004) 725–775.

[103] A. Mishra, M. Martin, N.N. Thadhani, B.K. Kad, E.A. Kenik, M.A. Meyers, Acta Mater. 56 (2008) 2770–2783.

[104] G.T. Gray III, in:, ASM Met. Handb. Mech. Test. Eval., Vol. 8, ASM International, Metals Park, Ohio, 2000, p. 462.

[105] R.W. Armstrong, S.M. Walley, Int. Mater. Rev. 53 (2008) 105–128.

[106] U. Andrade, M.A. Meyers, K.S. Vecchio, A.H. Chokshi, Acta Metall. Mater. 42 (1994) 3183–3195.

[107] J.A. Hines, K.S. Vecchio, Acta Mater. 45 (1997) 635–649.

[108] M.A. Meyers, U.R. Andrade, A.H. Chokshi, Metall. Mater. Trans. A 26A (1995) 2881–2893.

[109] R. Kapoor, S. Nemat-Nasser, Mech. Mater. 27 (1998) 1–12.

[110] L.E. Murr, E. V. Esquivel, J. Mater. Sci. 39 (2004) 1153–1168.

[111] P.H.R. Pereira, Y.C. Wang, Y. Huang, T.G. Langdon, Mater. Sci. Eng. A 685 (2017) 367–376.

[112] G.T. Gray III, T.C. Lowe, C.M. Cady, R.Z. Valiev, I. V. Aleksandrov, Nanostructured Mater. 9 (1997) 477–480.

[113] W. Lee, W. Sue, C. Lin, C. Wu, J. Mater. Process. Technol. 100 (2000) 116–122.

[114] R. Nunes, J.H. Adams, M. Ammons, H.S. Avery, E. Al., Metals Handbook VOL 2, Properties and Selection: Nonferrous Alloys and Special-Purpose Materials, 10th ed., ASM International, Metals Park, Ohio, USA, 1990.

[115] J. Wongsa-Ngam, H. Wen, T.G. Langdon, Mater. Sci. Eng. A 579 (2013) 126–135.

[116] D. Setman, E. Schafler, E. Korznikova, M.J. Zehetbauer, Mater. Sci. Eng. A 493 (2008) 116–122.

[117] P. Müllner, C. Solenthaler, Mater. Sci. Eng. A 230 (1997) 107–115.

[118] J.T. Wang, C. Xu, Z.Z. Du, G.Z. Qu, T.G. Langdon, Mater. Sci. Eng. A 410–411 (2005) 312–315.

[119] R. Valiev, Nat. Mater. 3 (2004) 511–516.

[120] Z. Horita, T. Fujinami, M. Nemoto, T.G. Langdon, Metall. Mater. Trans. A 31A (2000) 691–701.

[121] Z. Horita, T. Fujinami, M. Nemoto, T.G. Langdon, J. Mater. Process. Technol. 117 (2001) 288–292.

[122] S.R. Agnew, B.R. Elliott, C.J. Youngdahl, K.J. Hemker, J.R. Weertman, Mater. Sci. Eng. A 285 (2000) 391–396.

[123] Y. Wang, M. Chen, F. Zhou, E. Ma, Nature 419 (2002) 912–915.

[124] F. Dalla Torre, R. Lapovok, J. Sandlin, P.F. Thomson, C.H.J. Davies, E.V. Pereloma, Acta Mater. 52 (2004) 4819–4832.

[125] Z. Horita, K. Ohashi, T. Fujita, K. Kaneko, T.G. Langdon, Adv. Mater. 17 (2005) 1599–1602.

[126] J. An, Y.F. Wang, Q.Y. Wang, W.Q. Cao, C.X. Huang, Mater. Sci. Eng. A 651 (2016) 1–7.

[127] R.Z. Valiev, A. V Sergueeva, A.K. Mukherjee, Scr. Mater. 49 (2003) 669–674.

[128] Y. Li, Y. Zhang, N. Tao, K. Lu, Scr. Mater. 59 (2008) 475–478.

[129] T.R. Lee, C.P. Chang, P.W. Kao, Mater. Sci. Eng. A 408 (2005) 131–135.

[130] M. Geiger, M. Kleiner, R. Eckstein, N. Tiesler, U. Engel, CIRP Ann. - Manuf. Technol. 50 (2001) 445–462.

[131] Y. Qin, J. Mater. Process. Technol. 177 (2006) 8–18.

[132] N.K. Tran, Y.C. Lam, C.Y. Yue, M.J. Tan, Int. J. Mech. Aerospace, Ind. Mechatron. Manuf. Eng. 6 (2012) 983–986.

[133] Y. Saotome, A. Inoue, IEEE (1994) 343–348.

[134] J. Xu, X. Zhu, D. Shan, B. Guo, T.G. Langdon, Mater. Sci. Eng. A 646 (2015) 207–217.

[135] R.B. Figueiredo, P.H.R. Pereira, M.T.P. Aguilar, P.R. Cetlin, T.G. Langdon, Acta Mater. 60 (2012) 3190–3198.

[136] L. Lutterotti, P. Scardi, J. Appl. Crystallogr. 23 (1990) 246–252.

[137] R.A. Young, The Rietveld Method, Oxford University Press, Oxford, England, 1993.

[138] L. Lutterotti, S. Gialanella, Acta Mater. 46 (1998) 101–110.

[139] P. Sahu, M. De, Mater. Sci. Eng. A 333 (2002) 10–23.

[140] G. Williamson, R. Smallman, Philos. Mag. 1 (1956) 34–46.

[141] R. Smallman, K. Westmacott, Philos. Mag. 2 (1957) 669–683.

[142] N. Maury, N.X. Zhang, Y. Huang, A.P. Zhilyaev, T.G. Langdon, Mater. Sci. Eng. A 638 (2015) 174–182.

[143] C. Xu, M. Furukawa, Z. Horita, T.G. Langdon, Mater. Sci. Eng. A 398 (2005) 66–76.

[144] M. Prell, C. Xu, T.G. Langdon, Mater. Sci. Eng. A 480 (2008) 449–455.

[145] R.B. Figueiredo, M.T.P. Aguilar, P.R. Cetlin, T.G. Langdon, Metall. Mater. Trans. A 42 (2011) 3013–3021.

[146] C. Xu, Z. Horita, T.G. Langdon, Mater. Trans. 51 (2010) 2–7.

[147] Y. Estrin, A. Molotnikov, C.H.J. Davies, R. Lapovok, J. Mech. Phys. Solids 56 (2008) 1186–1202.

[148] M. Kawasaki, J. Mater. Sci. 49 (2014) 18–34.

[149] A.I. Almazrouee, K.J. Al-Fadhalah, S.N. Alhajeri, T.G. Langdon, Mater. Sci. Eng. A 641 (2015) 21–28.

[150] Y. Huang, S. Sabbaghianrad, A.I. Almazrouee, K.J. Al-Fadhalah, S.N. Alhajeri, T.G. Langdon, Mater. Sci. Eng. A 656 (2016) 55–66.

[151] Y. Zhao, K. Zhang, K. Lu, Phys. Rev. B 56 (1997) 14322–14329.

[152] Y.H. Zhao, H.W. Sheng, K. Lu, Acta Mater. 49 (2001) 365–375.

[153] Y.H. Zhao, Y.T. Zhu, X.Z. Liao, Z. Horita, T.G. Langdon, Mater. Sci. Eng. A 463 (2007) 22–26.

[154] K. Máthis, J. Gubicza, N.H. Nam, J. Alloys Compd. 394 (2005) 194–199.

[155] W.D. Callister, D.G. Rethwisch, Materials Science and Engineering: An Introduction, 8th ed., Wiley, USA, 2010.

[156] E. Bagherpour, F. Qods, R. Ebrahimi, H. Miyamoto, Mater. Sci. Eng. A 679 (2017) 465–475.

[157] E. Hosseini, M. Kazeminezhad, Comput. Mater. Sci. 44 (2009) 962–967.

[158] V. V. Stolyarov, Y.T. Zhu, I. V Alexandrov, T.C. Lowe, R.Z. Valiev, Mater. Sci. Eng. A

299 (2001) 59–67.

[159] Z.J. Zhang, Q.Q. Duan, X.H. An, S.D. Wu, G. Yang, Z.F. Zhang, Mater. Sci. Eng. A 528 (2011) 4259–4267.

[160] V.M. Segal, Mater. Sci. Eng. A 338 (2002) 331–344.

[161] S. Qu, X.H. An, H.J. Yang, C.X. Huang, G. Yang, Q.S. Zang, Z.G. Wang, S.D. Wu, Z.F. Zhang, Acta Mater. 57 (2009) 1586–1601.

[162] R.B. Figueiredo, T.G. Langdon, Int. J. Mater. Res. 100 (2009) 1638–1646.

[163] T.G. Langdon, Mater. Sci. Eng. A 462 (2007) 3–11.

[164] C.X. Huang, H.J. Yang, S.D. Wu, Z.F. Zhang, Mater. Sci. Forum 584–586 (2008) 333–337.

[165] Y.H. Zhao, J.F. Bingert, X.Z. Liao, B.Z. Cui, K. Han, A. V. Sergueeva, A.K. Mukherjee, R.Z. Valiev, T.G. Langdon, Y.T. Zhu, Adv. Mater. 18 (2006) 2949–2953.

[166] M. Kawasaki, Z. Horita, T.G. Langdon, Mater. Sci. Eng. A 524 (2009) 143–150.

[167] O.F. Higuera-Cobos, J.M. Cabrera, Mater. Sci. Eng. A 571 (2013) 103–114.

[168] A.P. Zhilyaev, T.G. Langdon, Mater. Res. 16 (2013) 586–591.

[169] N. Hansen, D.J. Jensen, Phil. Trans. R. Soc. Lond. A 357 (1999) 1447–1469.

[170] W.H. Huang, L. Chang, P.W. Kao, C.P. Chang, Mater. Sci. Eng. A 307 (2001) 113–118.

[171] J. Xu, J. Li, D. Shan, B. Guo, Mater. Sci. Eng. A 664 (2016) 114–125.

[172] F.H. Dalla Torre, A.A. Gazder, E. V. Pereloma, C.H.J. Davies, J. Mater. Sci. 42 (2007) 9097–9111.

[173] Y.L. Wang, R. Lapovok, J.T. Wang, Y.S. Qi, Y. Estrin, Mater. Sci. Eng. A 628 (2015) 21–29.

[174] S. Ferrasse, V.M. Segal, K.T. Hartwig, R.E. Goforth, Metall. Mater. Trans. A 28 (1997) 1047–1057.

[175] O.V. Mishin, G. Gottstein, Philos. Mag. A 78 (1998) 373–388.

[176] O. V. Mishin, D. Juul Jensen, N. Hansen, Mater. Sci. Eng. A 342 (2003) 320–328.

[177] B. Mingler, H.P. Karnthaler, M. Zehetbauer, R.Z. Valiev, Mater. Sci. Eng. A 319–321 (2001) 242–245.

[178] H.W. Hoppel, Z.M. Zhou, H. Mughrabi, R.Z. Valiev, Philos. Mag. A 82 (2002) 1781–1794.

[179] Y.M. Wang, E. Ma, Acta Mater. 52 (2004) 1699–1709.

[180] S. Han, C. Lim, C. Kim, S. Kim, Metall. Mater. Trans. A 36 (2005) 467–470.

[181] N. Lugo, N. Llorca, J.J. Suñol, J.M. Cabrera, J. Mater. Sci. 45 (2010) 2264–2273.

[182] K. Edalati, K. Imamura, T. Kiss, Z. Horita, Mater. Trans. 53 (2012) 123–127.

[183] C. Xu, Z. Száraz, Z. Trojanová, P. Lukáč, T.G. Langdon, Mater. Sci. Eng. A 497 (2008) 206–211.

[184] C. Xu, M. Furukawa, Z. Horita, T.G. Langdon, Acta Mater. 53 (2005) 749–758.

[185] H.S. Kim, M.H. Seo, S.I. Hong, Mater. Sci. Eng. A 291 (2000) 86–90.

[186] M. Ebrahimi, C. Gode, Prog. Nat. Sci. Mater. Int. 27 (2017) 244–250.

[187] F. Salimyanfard, M.R. Toroghinejad, F. Ashrafizadeh, M. Hoseini, J.A. Szpunar, Mater. Des. 44 (2013) 374–381.

[188] C.F. Zhu, F.P. Du, Q.Y. Jiao, X.M. Wang, A.Y. Chen, F. Liu, D. Pan, Mater. Des. 52 (2013) 23–29.

[189] L. Kommel, A. Rõzkina, I. Vlasieva, Mater. Sci. 14 (2008) 206–209.

[190] A. Mishra, B.K. Kad, F. Gregori, M.A. Meyers, Acta Mater. 55 (2007) 13–28.

[191] Y. Iwahashi, Z. Horita, M. Nemoto, T.G. Langdon, Acta Mater. 45 (1997) 4733–4741.

[192] S. Komura, Z. Horita, M. Nemoto, T.G. Langdon, J. Mater. Res. 14 (1999) 4044–4050.

[193] F.A. Mohamed, Acta Mater. 51 (2003) 4107–4119.

[194] X.H. An, Q.Y. Lin, S.D. Wu, Z.F. Zhang, R.B. Figueiredo, N. Gao, T.G. Langdon, Philos. Mag. 91 (2011) 3307–3326.

[195] P.G. Sanders, C.J. Youngdahl, J.R. Weertman, Mater. Sci. Eng. A 234–236 (1997) 77–82.

[196] M. Goerdeler, G. Gottstein, Mater. Sci. Eng. A 309–310 (2001) 377–381.

[197] F. Roters, D. Raabe, G. Gottstein, Acta Mater. 48 (2000) 4181–4189.

[198] A.A. Nazarov, A.E. Romanov, R.Z. Valiev, Acta Metall. Mater. 41 (1993) 1033–1040.

[199] J. Wang, Y. Iwahashi, Z. Horita, M. Furukawa, M. Nemoto, R.Z. Valiev, T.G. Langdon, Acta Mater. 44 (1996) 2973–2982.

[200] R. Valiev, Vy. Gertsmann, O. Kaibyshev, Phys. Stat. Sol . A 97 (1986) 11.

[201] K. Oh-ishi, Z. Horita, D.J. Smith, T.G. Langdon, J. Mater. Res. 16 (2001) 583–589.

[202] Z. Horita, D.J. Smith, M. Furukawa, M. Nemoto, J. Mater. Res. 11 (1996) 1880–1890.

[203] A.P. Zhilyaev, K. Oh-ishi, T.G. Langdon, T.R. McNelley, Mater. Sci. Eng. A. 410–411 (2005) 277–280.

[204] K. Edalati, T. Fujioka, Z. Horita, Mater. Sci. Eng. A 497 (2008) 168–173.

[205] Y.Z. Tian, S.D. Wu, Z.F. Zhang, R.B. Figueiredo, N. Gao, T.G. Langdon, Acta Mater. 59 (2011) 2783–2796.

[206] K. Edalati, T. Fujioka, Z. Horita, Mater. Trans. 50 (2009) 44–50.

[207] H.Y. Zhang, C.T. Wang, Y.C. Wang, S.K. Li, H. Zou, T.G. Langdon, J. Mater. Sci. 50 (2015) 1535–1543.

[208] J. Xu, J. Li, C.T. Wang, D. Shan, B. Guo, T.G. Langdon, J. Mater. Sci. 51 (2016) 1923–1930.

[209] Y. Harai, Y. Ito, Z. Horita, Scr. Mater. 58 (2008) 469–472.

[210] K. Edalati, Z. Horita, Mater. Trans. 50 (2009) 92–95.

[211] M. Kawasaki, B. Ahn, T.G. Langdon, J. Mater. Sci. 45 (2010) 4583–4593.

[212] K. Edalati, Z. Horita, Mater. Sci. Eng. A 528 (2011) 7514–7523.

[213] K. Edalati, Z. Horita, T. Furuta, S. Kuramoto, Mater. Sci. Eng. A 559 (2013) 506–509.

[214] E.A. Brandes, G.B. Brook, in:, 7th ed., Butterworth-Heinemann, Oxford, 1992, p. 241.

[215] K. Edalati, Y. Ito, K. Suehiro, Z. Horita, Int. J. Mater. Res. 100 (2009) 1668–1673.

[216] J. Čížek, M. Janeček, O. Srba, R. Kužel, Z. Barnovská, I. Procházka, S. Dobatkin, Acta Mater. 59 (2011) 2322–2329.

[217] X.H. An, Q.Y. Lin, S.D. Wu, Z.F. Zhang, Mater. Sci. Eng. A 527 (2010) 4510–4514.

[218] R.Z. Valiev, Nature 419 (2002) 887–889.

[219] C. Koch, Scr. Mater. 49 (2003) 657–662.

[220] E. Ma, Scr. Mater. 49 (2003) 663–668.

[221] S.D. Wu, Z.G. Wang, C.B. Jiang, G.Y. Li, I.V. Alexandrov, R.Z. Valiev, Scr. Mater. 48 (2003) 1605–1609.

[222] Q.W. Jiang, X.W. Li, Mater. Sci. Eng. A 546 (2012) 59–67.

[223] N.D. Stepanov, A. V. Kuznetsov, G.A. Salishchev, G.I. Raab, R.Z. Valiev, Mater. Sci. Eng. A 554 (2012) 105–115.

[224] C.X. Huang, W. Hu, G. Yang, Z.F. Zhang, S.D. Wu, Q.Y. Wang, G. Gottstein, Mater. Sci. Eng. A 556 (2012) 638–647.

[225] T. Hebesberger, H.P. Stüwe, A. Vorhauer, F. Wetscher, R. Pippan, Acta Mater. 53 (2005) 393–402.

[226] A.R. Kilmametov, G. Vaughan, A.R. Yavari, A. LeMoulec, W.J. Botta, R.Z. Valiev, Mater. Sci. Eng. A 503 (2009) 10–13.

[227] K. Edalati, R. Miresmaeili, Z. Horita, H. Kanayama, R. Pippan, Mater. Sci. Eng. A 528 (2011) 7301–7305.

[228] K. Edalati, A. Yamamoto, Z. Horita, T. Ishihara, Scr. Mater. 64 (2011) 880–883.

[229] Y.T. Zhu, X. Liao, Nat. Mater. 3 (2004) 351–352.

[230] H. Van Swygenhoven, J.R. Weertman, Scr. Mater. 49 (2003) 625–627.

[231] Z. Budrovic, H. Van Swygenhoven, P.M. Derlet, S. Van Petegem, B. Schmitt, Science 304 (2004) 273–277.

[232] F.H. Dalla Torre, E. V. Pereloma, C.H.J. Davies, Acta Mater. 54 (2006) 1135–1146.

[233] M.A. Meyers, K.K. Chawla, in:, Prentice-Hall, Englewood Cliffs (NJ), 1984, pp. 570–585.

[234] F.H. Dalla Torre, E. V. Pereloma, C.H.J. Davies, Scr. Mater. 51 (2004) 367–371.

[235] E.W. Hart, Acta Metall. 15 (1967) 351–355.

[236] T. Mungole, P. Kumar, M. Kawasaki, T.G. Langdon, J. Mater. Res. 29 (2014) 2534–2546.

[237] S. Yip, Nature 391 (1998) 532–533.

[238] J. Schiøtz, K.W. Jacobsen, Science 301 (2003) 1357–1359.

[239] M.A. Meyers, A. Mishra, D.J. Benson, Prog. Mater. Sci. 51 (2006) 427–556.

[240] A. Loucif, R.B. Figueiredo, T. Baudin, F. Brisset, R. Chemam, T.G. Langdon, Mater. Sci. Eng. A 532 (2012) 139–145.

[241] J. Schiøtz, F.D. Di Tolla, K.W. Jacobsen, Nature 391 (1998) 561–563.

[242] J. Schiøtz, T. Vegge, F.D. Di Tolla, K.W. Jacobsen, Phys. Rev. B 60 (1999) 11971–11983.

[243] H. Van Swygenhoven, Science 296 (2002) 66–67.

[244] A.H. Chokshi, A. Rosen, J. Karch, H. Gleiter, Scr. Metall. 23 (1989) 1679–1684.

[245] M.J. Starink, X.G. Qiao, J. Zhang, N. Gao, Acta Mater. 57 (2009) 5796–5811.

[246] M.J. Starink, X. Cheng, S. Yang, Acta Mater. 61 (2013) 183–192.

[247] N.Q. Chinh, G. Horváth, Z. Horita, T.G. Langdon, Acta Mater. 52 (2004) 3555–3563.

[248] K. Edalati, Z. Horita, Mater. Trans. 51 (2010) 1051–1054.

[249] L. Lu, X. Chen, X. Huang, K. Lu, Science 323 (2009) 607–610.

[250] N. Hansen, Scr. Mater. 51 (2004) 801–806.

[251] M.M. Abramova, N.A. Enikeev, R.Z. Valiev, A. Etienne, B. Radiguet, Y. Ivanisenko, X. Sauvage, Mater. Lett. 136 (2014) 349–352.

[252] M. Reihanian, R. Ebrahimi, N. Tsuji, M.M. Moshksar, Mater. Sci. Eng. A 473 (2008) 189–194.

[253] N. Haghdadi, A. Zarei-Hanzaki, D. Abou-Ras, Mater. Sci. Eng. A 584 (2013) 73–81.

[254] N. Kamikawa, X. Huang, N. Tsuji, N. Hansen, Acta Mater. 57 (2009) 4198–4208.

[255] J. Gubicza, N.Q. Chinh, Z. Horita, T.G. Langdon, Mater. Sci. Eng. A 387–389 (2004) 55–59.

[256] J. Gubicza, N.Q. Chinh, J.L. Lábár, S. Dobatkin, Z. Hegedűs, T.G. Langdon, J. Alloys Compd. 483 (2009) 271–274.

[257] E. Schafler, G. Steiner, E. Korznikova, M. Kerber, M.J. Zehetbauer, Mater. Sci. Eng. A 410–411 (2005) 169–173.

[258] Y.H. Zhao, J.F. Bingert, Y.T. Zhu, X.Z. Liao, R.Z. Valiev, Z. Horita, T.G. Langdon, Y.Z. Zhou, E.J. Lavernia, Appl. Phys. Lett. 92 (2008) 10–13.

[259] M.H. Goodarzy, H. Arabi, M.A. Boutorabi, S.H. Seyedein, S.H. Hasani Najafabadi, J. Alloys Compd. 585 (2014) 753–759.

[260] F. Wetscher, A. Vorhauer, R. Pippan, Mater. Sci. Eng. A 410–411 (2005) 213–216.

[261] C. Xu, S. V. Dobatkin, Z. Horita, T.G. Langdon, Mater. Sci. Eng. A 500 (2009) 170–175.

[262] D. Jia, Y.M. Wang, K.T. Ramesh, E. Ma, Y.T. Zhu, R.Z. Valiev, Appl. Phys. Lett. 79 (2001) 611–613.

[263] Y. Zhao, Y.T. Zhu, E.J. Lavernia, Adv. Eng. Mater. 12 (2010) 769–778.

[264] E. Ma, JOM 58(4) (2006) 49–53.

[265] R.C. Gifkins, T.G. Langdon, J. Inst. Met. 93 (1965) 347.

[266] T.G. Langdon, J. Mater. Sci. 41 (2006) 597–609.

[267] N.Q. Chinh, P. Szommer, Z. Horita, T.G. Langdon, Adv. Mater. 18 (2006) 34–39.

[268] R.Z. Valiev, M. Yu, A. Kilmametov, B. Straumal, N.Q. Chinh, T.G. Langdon, J. Mater. Sci. 45 (2010) 4718–4724.

[269] A. V. Polyakov, I.P. Semenova, R.Z. Valiev, Y. Huang, T.G. Langdon, MRS Commun. 3 (2013) 249–253.

[270] M.Y. Gutkin, I.A. Ovid'ko, N. V. Skiba, J. Phys. D. Appl. Phys. 38 (2005) 3921–3925.

[271] J. Wang, Z. Horita, M. Furukawa, M. Nemoto, N.K. Tsenev, R.Z. Valiev, Y. Ma, T.G. Langdon, J. Mater. Res. 8 (1993) 2810–2818.

[272] E. Ma, Y.M. Wang, Q.H. Lu, M.L. Sui, L. Lu, K. Lu, Appl. Phys. Lett. 85 (2004) 4932–4934.

[273] B.Q. Han, Z. Lee, D. Witkin, S. Nutt, E.J. Lavernia, Metall. Mater. Trans. A 36 (2005) 957–965.

[274] Q. Guo, H.G. Yan, H. Zhang, Z.H. Chen, Z.F. Wang, Mater. Sci. Technol. 21 (2005) 1349–1354.

[275] L. Wen-quan, Q. Guo-zheng, Y. Chun-tang, Z. Lei, Z. Jie, Trans. Nonferrous Met. Soc. China 22 (2012) s650–s655.

[276] D. Zhou, H. Geng, D. Zhang, W. Zeng, C. Kong, P. Munroe, Mater. Sci. Eng. A 688 (2017) 164–168.

[277] A.Z. Hanzaki, P. Hodgson, S. Yue, ISIJ Int. 35 (1995) 79–85.

[278] H. Matsunaga, Z. Horita, Mater. Trans. 50 (2009) 1633–1637.

[279] A.P. Zhilyaev, T.G. Langdon, J. Mater. Sci. 49 (2014) 6529–6535.

[280] K. Edalati, J.M. Cubero-Sesin, A. Alhamidi, I.F. Mohamed, Z. Horita, Mater. Sci. Eng. A 613 (2014) 103–110.

[281] A. Dubravina, M.J. Zehetbauer, E. Schafler, I. V. Alexandrov, Mater. Sci. Eng. A 387–389 (2004) 817–821.

[282] A.P. Zhilyaev, A.A. Gimazov, T.G. Langdon, J. Mater. Sci. 48 (2013) 4461–4466.

[283] I. Balasundar, K.R. Ravi, T. Raghu, Mater. Sci. Eng. A 583 (2013) 114–122.

[284] P.H.R. Pereira, R.B. Figueiredo, Y. Huang, P.R. Cetlin, T.G. Langdon, Mater. Sci. Eng. A 593 (2014) 185–188.

[285] A.P. Zhilyaev, S. Swaminathan, A.A. Gimazov, T.R. McNelley, T.G. Langdon, J. Mater. Sci. 43 (2008) 7451–7456.

[286] M.V. Degtyarev, T.I. Chashchukhina, L.M. Voronova, A.M. Patselov, V.P. Pilyugin, Acta Mater. 55 (2007) 6039–6050.

[287] G. Wang, S.D. Wu, L. Zuo, C. Esling, Z.G. Wang, G.Y. Li, Mater. Sci. Eng. A 346 (2003) 83–90.

[288] M. Kumar, A.J. Schwartz, W.E. King, Acta Mater. 50 (2002) 2599–2612.

[289] H.P. Stüwe, A.F. Padilha, F. Siciliano Jr, Mater. Sci. Eng. A 333 (2002) 361–367.

[290] J. Gubicza, N.Q. Chinh, J.L. Lábár, Z. Hegedűs, T.G. Langdon, Mater. Sci. Eng. A 527 (2010) 752–760.

[291] A.S. Argon, W.C. Moffatt, Acta Metall. 29 (1981) 293–299.

[292] I. Kovács, L. Zsoldos, Dislocations and Plastic Deformation, Pergman Press, London, 1973.

[293] D. Setman, M. Kerber, H. Bahmanpour, J. Horky, R.O. Scattergood, C.C. Koch, M.J. Zehetbauer, Mech. Mater. 67 (2013) 59–64.

[294] S. Qu, C.X. Huang, Y.L. Gao, G. Yang, S.D. Wu, Q.S. Zang, Z.F. Zhang, Mater. Sci. Eng. A 475 (2008) 207–216.

[295] A. Ma, J. Jiang, N. Saito, I. Shigematsu, Y. Yuan, D. Yang, Y. Nishida, Mater. Sci. Eng. A 513–514 (2009) 122–127.

[296] M. Zha, Y. Li, R.H. Mathiesen, R. Bjørge, H.J. Roven, Scr. Mater. 105 (2015) 22–25.

[297] R.B. Figueiredo, T.G. Langdon, Adv. Eng. Mater. 10 (2008) 37–40.

[298] W. Blum, J. Dvořák, P. Král, P. Eisenlohr, V. Skleničkа, Mater. Sci. Eng. A 590 (2014) 423–432.

[299] W.S. Zhao, N.R. Tao, J.Y. Guo, Q.H. Lu, K. Lu, Scr. Mater. 53 (2005) 745–749.

[300] Y.S. Li, N.R. Tao, K. Lu, Acta Mater. 56 (2008) 230–241.

[301] S. Tao, L. Yu-long, X. Kui, Z. Feng, Z. Ke-Shi, D. Qiong, Mech. Mater. 43 (2011) 111–118.

[302] T. Suo, Y. Li, F. Zhao, X. Fan, W. Guo, Mech. Mater. 61 (2013) 1–10.

[303] F.A. Mohamed, S.S. Dheda, Mater. Sci. Eng. A 558 (2012) 59–63.

[304] F.A. Mohamed, S.S. Dheda, Mater. Sci. Eng. A 580 (2013) 227–230.

[305] Y.G. Kim, B. Hwang, S. Lee, C.W. Lee, D.H. Shin, Mater. Sci. Eng. A 504 (2009) 163–168.

[306] L.S. Tóth, B. Beausir, C.F. Gu, Y. Estrin, N. Scheerbaum, C.H.J. Davies, Acta Mater. 58 (2010) 6706–6716.

[307] S. Sabbaghianrad, T.G. Langdon, Mater. Sci. Eng. A 596 (2014) 52–58.

[308] V. V. Popov, E.N. Popova, A. V. Stolbovskiy, Mater. Sci. Eng. A 539 (2012) 22–29.

[309] R. Pippan, S. Scheriau, A. Taylor, M. Hafok, A. Hohenwarter, A. Bachmaier, Annu. Rev. Mater. Res. 40 (2010) 319–343.

[310] A. Belyakov, K. Tsuzaki, H. Miura, T. Sakai, Acta Mater. 51 (2003) 847–861.

[311] A.P. Zhilyaev, A.A. Gimazov, G.I. Raab, T.G. Langdon, Mater. Sci. Eng. A 486 (2008) 123–126.

[312] A.P. Zhilyaev, I. Shakhova, A. Belyakov, R. Kaibyshev, T.G. Langdon, J. Mater. Sci. 49 (2014) 2270–2278.

[313] A.P. Zhilyaev, I. Shakhova, A. Belyakov, R. Kaibyshev, T.G. Langdon, Wear 305 (2013) 89–99.

[314] K. Wang, N.R. Tao, G. Liu, J. Lu, K. Lu, Acta Mater. 54 (2006) 5281–5291.

[315] M.A. Meyers, G. Subhash, B.K. Kad, L. Prasad, Mech. Mater. 17 (1994) 175–193.

[316] S. Nemat-Nasser, J.B. Isaacs, M. Liu, Acta Mater. 46 (1998) 1307–1325.

[317] M.A. Meyers, V.F. Nesterenko, J.C. LaSalvia, Q. Xue, Mater. Sci. Eng. A 317 (2001) 204–225.

[318] Y.B. Xu, W.L. Zhong, Y.J. Chen, L.T. Shen, Q. Liu, Y.L. Bai, M.A. Meyers, Mater. Sci. Eng. A 299 (2001) 287–295.

[319] B.K. Kad, J.-M. Gebert, M.T. Perez-Prado, M.E. Kassner, M.A. Meyers, Acta Mater. 54 (2006) 4111–4127.

[320] M. Ping-li, Y. Jin-cheng, L. Zheng, D. Yang, J. Magnes. Alloy. 1 (2013) 64–75.

[321] B.F. Wang, Z.L. Liu, X.Y. Wang, Z.Z. Li, Mater. Sci. Eng. A 610 (2014) 301–308.

[322] C. Zheng, F. Wang, X. Cheng, J. Liu, T. Liu, Z. Zhu, K. Yang, M. Peng, D. Jin, Mater. Sci. Eng. A 658 (2016) 60–67.

[323] J. Yu, Z. Liu, Y. Dong, Z. Wang, J. Magnes. Alloy. 3 (2015) 134–141.

[324] C. Zener, J.H. Hollomon, J. Appl. Phys. 15 (1944) 22–32.

[325] X.Z. Liao, Y.H. Zhao, Y.T. Zhu, R.Z. Valiev, D. V. Gunderov, J. Appl. Phys. 96 (2004) 636–640.

[326] J.T. Wang, Y.K. Zhang, J.F. Chen, J.Y. Zhou, M.Z. Ge, Y.L. Lu, X.L. Li, Mater. Sci. Eng. A 647 (2015) 7–14.

[327] C. Xu, G. Sheng, H. Wang, Y. Jiao, X. Yuan, J. Alloys Compd. 695 (2017) 1383–1391.

[328] A.P. Zhilyaev, A.A. Gimazov, E.P. Soshnikova, Á. Révész, T.G. Langdon, Mater. Sci. Eng. A 489 (2008) 207–212.

[329] A.H. Chokshi, M.A. Meyers, Scr. Metall. Mater. 24 (1990) 605–610.

[330] M. Wen, G. Liu, J. Gu, W. Guan, J. Lu, Appl. Surf. Sci. 255 (2009) 6097–6102.

[331] R.D. Doherty, D.A. Hughes, F.J. Humphreys, J.J. Jonas, D.J. Jensen, M.E. Kassner, W.E. King, T.R. McNelley, H.J. McQueen, A.D. Rollett, Mater. Today 1 (1998) 14–15.

[332] R.D. Doherty, D.A. Hughes, F.J. Humphreys, J.J. Jonas, D.J. Jensen, M.E. Kassner, W.E. King, T.R. McNelley, H.J. McQueen, A.D. Rollett, Mater. Sci. Eng. A 238 (1997) 219–274.

[333] W.F. Hosford, R.M. Caddell, Metal Forming: Mechanics and Metallurgy, 3rd ed., Cambridge University Press, New York, 2007.

[334] J.Z. Lu, K.Y. Luo, Y.K. Zhang, C.Y. Cui, G.F. Sun, J.Z. Zhou, L. Zhang, J. You, K.M. Chen, J.W. Zhong, Acta Mater. 58 (2010) 3984–3994.

[335] J.Z. Lu, K.Y. Luo, Y.K. Zhang, G.F. Sun, Y.Y. Gu, J.Z. Zhou, X.D. Ren, X.C. Zhang, L.F. Zhang, K.M. Chen, C.Y. Cui, Y.F. Jiang, A.X. Feng, L. Zhang, Acta Mater. 58 (2010) 5354–5362.

[336] C.Y. Gao, L.C. Zhang, W.G. Guo, Y.L. Li, W.R. Lu, Y.L. Ke, Mater. Sci. Eng. A 613 (2014) 379–389.

[337] F.J. Humphreys, M. Hatherly, Recrystallization and Related Annealing Phenomena, 2nd ed., Elsevier, Oxford, 2004.

[338] H. Ma, L. Huang, Y. Tian, J. Li, Mater. Sci. Eng. A 606 (2014) 233–239.

[339] U.F. Kocks, J. Eng. Mater. Technol. 98 (1976) 76–85.

[340] X. Sauvage, G. Wilde, S. V. Divinski, Z. Horita, R.Z. Valiev, Mater. Sci. Eng. A 540 (2012) 1–12.

[341] S. Schumacher, R. Birringer, R. Strauβ, H. Gleiter, Acta Metall. 37 (1989) 2485–2488.

[342] H.J. McQueen, S. Bergerson, Met. Sci. J. 6 (1972) 25–29.

[343] E. Schafler, M.B. Kerber, Mater. Sci. Eng. A 462 (2007) 139–143.